DEVELOPMENT AND APPLICATION OF LASER DOPPLER ANEMOMETER INSTRUMENTATION FOR THE STUDY OF GAS-SOLID SUSPENSION FLOWS

by

Yiannis Demetrios Tridimas, M.A., B.Sc.

A thesis submitted as part of the
requirements for the degree of
Doctor of Philosophy of the
Council for National Academic Awards

Department of Mechanical, Marine
and Production Engineering,
Liverpool Polytechnic.

ICI Corporate Laboratory,
Runcorn, Cheshire.

June 1981

TEXT BOUND INTO

THE SPINE

To Kath

ACKNOWLEDGEMENTS

The author wishes to thank:

Dr. N.H. Woolley and Dr. M.J. Lalor, who supervised this research, for the support and encouragement they afforded him, during this difficult period.

Dr. C.A. Hobson, without whose digital electronic designs, this investigation would not have been possible.

Mr. K.W. Dean and Mr. L. Hale, for their technical support and advice.

Mr. D. Burton, for his help with the final stages of the experimental work.

Mr. Kasim Elhuni, for his help with electronic filter design.

All the technical staff of the Department of Mechanical, Marine and Production Engineering, for their help on many occasions.

The Science Research Council for providing funds for some of the equipment used in this work.

DEVELOPMENT AND APPLICATION OF LASER DOPPLER ANEMOMETER INSTRUMENTATION FOR THE STUDY OF GAS-SOLID SUSPENSION FLOWS

Ph.D. Thesis, Y.D. Tridimas, 1981

ABSTRACT

The work reported in this thesis can be broadly divided into three parts, i.e. optimization of the laser Doppler anemometer, development of "discrimination" techniques and velocity measurements in flowing gas-solid suspensions.

A study of the imaging characteristics of the beam waist and the beam intersection in a dual beam LDA, and the development of a beam diameter measuring technique led to the optimization of the laser anemometer.

Digital logic circuits were developed which made possible separation of signals from the two phases of a flowing gas-solid suspension, thus enabling a study of the interactions between the two phases to be carried out.

One component velocity measurements were carried out in upward flowing gas-solid suspensions in vertical pipes. Solids of mainly spherical shape and diameters between 40 and 1000 μm were conveyed with air. Glass pipes of 22, 25.8 and 31.4 mm diameters were used and the pipe Reynold's number varied between 5000 and 31 000. The results indicated that:

(i) A slip existed between the solids and the air, which was proportional to the particle size. The air and solids velocity profiles crossed near the wall.

(ii) The air turbulence was in some cases reduced by the addition of solids and in other cases increased.

(iii) The turbulence level of the solids was on average higher than that of the air except in the near wall region.

In conclusion, the use of LDA in the study of two phase flows seems promising. Further investigation is needed in order to fully understand the interactions between the two phases of a suspension.

..... current ignorance casts a longer and darker shadow.... the ways in which a dispersed second phase influences the turbulent properties of a supporting first phase are almost entirely unexplored. Influences there must be; but no-one is able to quantify them on the basis of knowledge.

D.B. Spalding

Recent Advances in Numerical Methods in Fluids, 1980, Vol. 1, Pineridge Press, Swansea.

LIST OF CONTENTS

		Page
NOMENCLATURE		
CHAPTER 1		
INTRODUCTION		1
1.1	GAS-SOLID SUSPENSIONS - THE PROBLEM	2
1.2	VELOCITY MEASUREMENTS IN GAS-SOLID SUSPENSIONS - ADVANTAGES OF LDA	5
1.3	SUMMARY OF THE WORK	6
REFERENCES FOR CHAPTER 1		12
CHAPTER 2		
OPTIMIZATION OF THE LASER DOPPLER ANEMOMETER		16
2.1	INTRODUCTION	17
2.2	THE DOPPLER SHIFT	
2.2.1	Single beam	18
2.2.2	Dual beam system	21
2.2.3	The fringe model	23
2.3	PROPAGATION OF GAUSSIAN LASER BEAMS	25
2.3.1	Laser cavity configuration	25
2.3.2	Beam geometry	28
2.3.3	Transformation of a beam by a lens	31
2.4	BRIEF REVIEW OF LASER DOPPLER ANEMOMETERS	34
2.4.1	General	34
2.4.2	Optical arrangements	34
2.4.3	Multichannel laser Doppler anemometer	38

		Page
2.5	THE DUAL BEAM LASER DOPPLER ANEMOMETER	39
2.5.1	Introduction	39
2.5.2	Basic parameters of a dual beam laser Doppler anemometer	40
2.5.3	Intensity distribution in the beam intersection region	46
2.6	DUAL BEAM LDA - ONE LENS SYSTEM	48
2.6.1	Imaging of beam waist and beam intersection	48
2.6.2	Conditions for coincidence of output waist and intersection	51
2.7	DUAL BEAM LDA - TWO LENS SYSTEM	57
2.7.1	Introduction	57
2.7.2	Imaging of beam waist	58
2.7.3	Conditions for coincidence of output waist and intersection	59
2.7.4	Practical considerations	61
2.8	BEAM DIAMETER MEASUREMENT	62
2.8.1	Introduction	62
2.8.2	Measurement of beam diameter - power ratio method	63
2.8.3	Experimental determination of unfocused beam dimensions	67
	(a) Pinhole method	67
	(b) Using the power ratio technique	69
2.8.4	Beam waist location	72
2.8.5	Experimental determination of beam waist dimensions	76
	(a) Using the power ratio technique	76
	(b) Using frequency shifting	77
	(c) Comparison of results	78
2.8.6	Concluding remarks	81
REFERENCES FOR CHAPTER 2		84

Page

CHAPTER 3

PRACTICAL ASPECTS OF VELOCITY MEASUREMENTS USING LDA 89

3.1 VELOCITY MEASUREMENTS IN FLUIDS - EFFECTS OF REFFRACTIVE INDEX 90
3.1.1 Probe traverse 90
3.1.2 Fringe spacing (fringe mode anemometer) 92

3.2 FREQUENCY SHIFTING 93
3.2.1 Introduction 93
3.2.2 Effect of frequency shifting on counter processed signals 95
3.2.3 Removal of directional ambiguity 97
3.2.4 Effects of frequency shift on signal filtering 98
3.2.5 The radial diffraction grating 100

3.3 LIMITATIONS IN THE ACCURACY OF FREQUENCY MEASUREMENTS 103
3.3.1 Introduction 103
3.3.2 Velocity biasing, sources and corrections 103
3.3.3 (a) General considerations 104
(b) Sources of biasing errors 105
(c) Biasing error corrections 108
(d) Velocity gradient bias corrections 111
(e) Corrections used 116
Effects of noise 118

3.4 COLLECTING OPTICS GEOMETRY 122

REFERENCES FOR CHAPTER 3 124

CHAPTER 4

EXPERIMENTAL EQUIPMENT 128

4.1 INTRODUCTION 129

		Page
4.2	LDA COMPONENTS	131
4.2.1	The laser	131
4.2.2	Photomultiplier and collecting optics	132
4.2.3	The radial diffraction grating	135
4.2.4	Other components	135
4.3	TRAVERSING MECHANISM	136
4.4	TWO-LENS DUAL-BEAM SYSTEM	138
4.5	FLOW RIGS	143
4.5.1	Water flow rig	143
4.5.2	Recirculating powder rig	145
4.5.3	Open type flow rig	147
4.6	SOLIDS USED	149
4.7	THE FREQUENCY METER	151
4.7.1	Principles of operation	151
4.7.2	Accuracy	152
4.7.3	Instrument capabilities	154
4.8	DATA RECORDING AND PROCESSING SYSTEM	156
4.9	LIST OF OTHER INSTRUMENTS	158
REFERENCES FOR CHAPTER 4		160
CHAPTER 5		
DEVELOPMENT OF DISCRIMINATION TECHNIQUES		161
5.1	INTRODUCTION	162
5.2	LDA SIGNAL CHARACTERISTICS	163
5.2.1	Signal visibility	163
5.2.2	Experimental investigation of LDA signal characteristics	168
	(a) Using an oscilloscope	168
	(b) Using velocity histograms	170
5.2.3	Concluding remarks	177

		Page
5.3	THE DISCRIMINATOR	186
5.3.1	Principles of operation	186
5.3.2	Testing of circuit operation	188
	(a) Using simulated signals	188
	(b) Using signals from a gas-solid suspension flow	191
5.3.3	Assessment of discriminator performance	192
5.4	CONCLUSIONS	195
REFERENCES FOR CHAPTER 5		210

CHAPTER 6

VELOCITY MEASUREMENTS IN GAS-SOLID SUSPENSION FLOWS		212
6.1	INTRODUCTION	213
6.2	EXPERIMENTAL PROCEDURE	216
6.3	RESULTS AND COMMENTS	221
6.4	ANALYSIS OF RESULTS	266
6.4.1	Particle slip velocity and drag coefficient	266
6.4.2	Particle velocity profiles	278
REFERENCES FOR CHAPTER 6		283

CHAPTER 7

CONCLUSIONS AND RECOMMENDATIONS		286
7.1	CONCLUSIONS	287
7.2	RECOMMENDATIONS FOR FUTURE WORK	290
7.2.1	Experimental techniques	290
7.2.2	Organisation of future experimental work	293
REFERENCES FOR CHAPTER 7		295

APPENDICES

NOMENCLATURE

a	pipe radius
a	wire radius in beam diameter measurements (chapter 2)
a	major semiaxis of probe volume (chapter 3)
b	minor semiacis of probe volume (chapter 3)
b_o	beam radius at crossover point
c	speed of light in vacuo
C	capacitance
C_D	drag coefficient
d	laser cavity length
d	distance between the lenses in a two lens dual beam system
d_p	pinhole diameter
d_r	line pair width in a diffraction grating
D	diameter of scattering particle
f	measured LDA signal frequency
f	lens focal length
f_d	Doppler difference (beat) frequency
f_D	Doppler shift frequency
f_F	beam propagation parameter ($f_F = \pi w_1^2/\lambda$)
f_1	frequency of incident light
f_o	filter cut off frequency
f_r	frequency of rotation of radial diffraction grating
f_s	frequency shift
f_{sc}	frequency of scattered light
F_D	drag force
h	differential manometer reading

I	light intensity
k	constant
L	radius of lens aperture
L	inductance (Appendix A4)
m	L-C filter constant
$\dot{m}$	mass flowrate
n	refractive index of a medium
n_a	refractive index of air
n_f	refractive index of fluid (chapter 3)
n_f	number of fringes
n_g	refractive index of glass
n_i	sample number
$\hat{n}_i$	unit vector in direction of incident radiation
$\hat{n}_{sc}$	unit vector in direction of scattered radiation
$\hat{n}_{sc1}, \hat{n}_{sc2}$	directions of scattered light collection
N	number of measurement cycles
N_d	number of line pairs of a diffraction grating
p	pressure
p	order of diffracted beams (chapter 3)
p_{at}	atmospheric pressure
P_m	minimum beam power
P_o	total beam power
q_1	complex beam parameter at beam waist
q_2	complex beam parameter
r	radial distance
R	nondimensionalised radius ($R = \frac{r}{a}$)
R	specific gas constant
R	radius of curvature of spherical resonator mirror (chapter 3)

R	pipe radius (chapter 3)
Re_f	pipe Reynold's number
Re_p	particle Reynold's number
R_o	electronic filter impedance
R_z	radius of curvature of beam phase front
s	distance between lens and beam waist
t	time
T	temperature
u	object distance from lens
u	velocity
$\bar{u}$	measured local mean velocity
$\bar{u}_c$	corrected local mean velocity
$\bar{u}_r$	actual flow velocity at the geometric centre of the probe volume
$\sqrt{u'^2}$	r.m.s. velocity
U	nondimensionalised velocity ($U = \frac{\bar{u}}{U_m}$)
U_m	pipe centreline velocity
U_p	particle velocity
U_{p_o}	particle velocity at pipe centreline
U_{p_w}	particle velocity at pipe wall
U_σ	particle slip velocity
v	image distance from lens
$\dot{V}$	volume flowrate
$\vec{V}$	particle velocity vector
V_p	nondimensionalised particle velocity ($V_p = \frac{U_p}{U_m}$)
V_{sca}	signal visibility
V_{Tl}	threshold voltage of frequency meter

V_{T2}	threshold voltage of discriminator
$\bar{V}_1$	component of vector $\vec{V}$ normal to optical axis
$\bar{V}_2$	component of vector $\vec{V}$ parallel to optical axis
w	beam waist radius (subscripts used 0, 1 and 2)
w_z	laser beam radius
x	coordinate normal to y and z directions
y	coordinate normal to fringes
y	distance from pipe wall
z	coordinate along optical axis
z_1	distance between input waist and lens
z_2	distance between lens and output waist
δ	fringd spacing
$\Delta\tau_i$	residence time of particle in probe volume
$\Delta\tau m_i$	measurement time
$\Delta x, \Delta y, \Delta z$	dimensions of probe volume in the x, y and z directions
θ	half-angle between beams in a dual beam system
θ_p	diffraction angle of beams emerging from diffraction grating
λ	wavelength of light
λ_i	wavelength of incident light
λ_o	wavelength of light in vacuo
μ_f	viscosity of air
ρ	mass density
ρ_f	mass density of air
ρ_p	mass density of particle material
ϕ	beam divergence angle

CHAPTER 1

INTRODUCTION

1.1 GAS-SOLID SUSPENSIONS - THE PROBLEM

A gas-solid suspension flow is a two-phase flow consisting of the conveying gas and the conveyed solids. Such types of flow exist in nature (dust, sand and snow carried by the wind) and have found many industrial applications - pneumatic conveying of particulate matter, such as grain, flour, plastic granules and even coal conveyed many hundreds of metres from mine shafts to the surface. Space and nuclear technologists have also an interest in this type of flow. Such methods of transport of solids have been very cost effective and very advantageous in cases where space limitations did not allow other conventional methods of transport, although one of the main problems in pneumatic transport of solids remains erosion of pipe bends.

In fully developed flow of a particulate suspension, effects accounted for include the Magnus effect due to fluid shear, electrostatic forces due to electric charges on the particles and Brownian or turbulent diffusion [1].

Experimental investigation of gas-solid suspension flows has made very slow progress over the years, due mainly to the difficulties in developing accurate methods of measurement and reliable instruments [2,3,4]. The lack of knowledge of the ways in which the two phases interact has been pointed out by Spalding [5].

It is now established that in gas solid suspension flows the local mean velocity of the solids can be very different

from that of the conveying gas due to the inertia of the solids [6]. This depends on particle size and also on the degree of turbulence [7]. In such flows velocity distributions are not easy to describe theoretically and experimental determination of flow parameters becomes of great importance. In vertical pipe flows the slip velocity which exists between solids and fluid due to gravity is very different for upward and downward flow [1].

With regard to the various properties of the conveying fluid, a range of results have been reported. The following is an outline of observations contained in the literature.

Velocity profile. For the velocity profiles of fluids conveying solids, a variety of results have been presented [4], ranging from no change, to significant flattening [8] and also to increased velocity at the centre-line [4].

Turbulence intensity. The presence of solids results in damping [9] or an increase of turbulence intensity, depending on solids concentration and wall distance [10]. Results indicating no significant change of turbulence intensity in the pipe centreline have also been reported [11].

Pressure drop. An increase of pressure drop was observed for low particle concentrations [10]. In an analytical study, Koronakis [12] states that turbulence friction is

significantly reduced by the injection of solid particulates or polymers. The fluid with the particulates requires a lower pressure gradient to move at a specified average velocity than the same fluid without the particulates.

Heat transfer. An increase in heat transfer with increase in turbulence at low particle concentrations was observed, as a possible result of fluid-particle interactions in the viscous sublayer [10] . Solids loading has been thought of as the most influential factor, which affects the heat transfer rate to a flowing gas-solid suspension.

Eddy diffusivity. The presence of solids with considerable inertia results in a reduction of eddy diffusivity [3,11,13] although an increase has also been realised [3,11] .

The slip velocity at the centre of the flow pipe has been found to be a function of loading ratio and particle terminal velocity [4] , and also of particle Reynold's number [8] . Solid density may be affected by electrostatic forces in which case the flow may become annular in nature [3,9] . Some investigators found a uniform particle distribution over the pipe cross-section [4,8] .

It is obvious that more experimental results are needed, so that the interactions between the two phases of a flowing gas-solid suspension may be fully understood.

1.2 VELOCITY MEASUREMENTS IN GAS-SOLID SUSPENSIONS - ADVANTAGES OF LDA

One of the main problems in the study of two phase flows has been a lack of suitable instrumentation, capable of coping with the often adverse conditions encountered in those situations [3,4,8] . Although theoretical treatment of such flows is abundant in the literature, experimental back-up is disproportionately small. This void is now being filled by the advances made in laser Doppler anemometry.

The laser Doppler anemometer has in recent years developed rapidly into a useful research tool with wide capabilities, varying from particle sizing to the measurement of velocity and length of moving solids [14]. Its advantage over other types of instrumentation lies in the fact that it is non intrusive and can perform in the most hostile of environments, such as corrosive fluids and high temperature gas streams, where other devices would be damaged and would cause flow disturbances. In addition the laser anemometer possesses the simplicity of a constant relationship between observed signal frequency and velocity. This removes the need for calibration prior to use, as other devices, such as hot wire anemometers require [15,16,17,18] . The measuring volume can be made very small and the frequency response is very high.

In this work the LDA was used in gas-solid suspension flows, an environment not suited to conventional instrumentation,

as it can affect the calibration [24] , or can result in blockage [2,20,21] . When the conveyed material is abrasive, rapid erosion of probes inserted into the flow will take place.

1.3 SUMMARY OF THE WORK

The object of this investigation was to carry out a study of fully developed gas-solid suspension flows, in the upward direction in vertical pipes, using laser Doppler anemometer (LDA) techniques. Such a study would then lead to a better understanding of the influence which the solids exert on the conveying air.

Two phase flows are very complex and the velocity spectrum depends not only on the degree of turbulence but also on the size distribution of the conveyed solids. Studying the effects of the presence of the solids on the air flow necessitates obtaining signals from each phase separately, a task which has defeated many efforts of workers in this field, as signals emitted from solid scatterers of any shape and size have the same basic characteristics. Thus measuring the velocity of the fluid has been an almost impossible task, since the solids often produced the majority of the signals [2] . In order to take measurements from the carrying fluid only, while solids were present, Zisselmar and Mollerus [10] developed a complex set up, in which matching of the refractive indices of the two phases,

optically eliminated the solids. Such applications, obviously, can only have a limited scope.

It was thus realised from the outset that in order to attempt an investigation into gas-solid suspensions, a basic technique needed to be developed, which would make such measurements possible. Associated with this, was the need to carry out an optimization of the optical set up, so that the beam parameters at the crossover region - the measuring volume - in a dual beam LDA, were accurately measured and set according to requirements. This led to the development of a method for measuring the beam size and, in particular, measuring the diameter of the beam waist [22]. Once developed, this method made possible measurements of the beam diameter in situ and by doing so, location of the beam waist was achieved, speedily and without disturbing the optics.

As a consequence of the above development, it was realised that the waist of the focused beams and the beam crossover point did not normally coincide. A number of optical arrangements were examined and it was found that such coincidence could only be achieved by proper design of the optical anemometer, based on the different imaging characteristics of the beam waist and the beam intersection point. As a result, an optical arrangement was developed, which consisted of ordinary optical components and made possible coincidence of beam waist and intersection [23].

The need to make the focused beam waists coincident with the crossover poiht, arose mainly from the realisation that a small probe volume would be thus obtained, which would allow measurements close to the wall in a relatively small bore pipe and would minimise errors arising from velocity gradients along the measuring volume.

Work carried out by Farmer [24], Robinson and Chu [25], Chu and Robinson [26] and other workers, has indicated a strong dependence of LDA signal characteristics on particle size/fringe spacing under certain light collecting conditions. An experimental study of this was undertaken as a first step to developing a method for distinguishing between signals obtained from the two phases in a gas-solid suspension.

Following the successful conclusion of this study, a digital logic circuit, a 'discriminator' was designed, which by exploiting the difference in amplitude of the two basic Doppler signal components, a.c. and d.c., effectively discriminated between signals resulting from 'small', micron size scatterers and larger solid particles.

All fluids contain very small particles such as dust, algae or air bubbles in the case of liquids. The laser anemometer makes use of these contaminants, whose size is of the order of 1 μm or less and which are, therefore, small enough to follow the flow [15]. Thus by assuming that the very small scatterers, normally fine dust particles

and often injected smoke, followed the air velocities everywhere, it was possible to measure the velocity of the air, while large solid particles were being transported by it. The major difficulty arose from the fact that to preserve the difference between the visibility of the small and large particle signals, a wide, on axis light collecting aperture was necessary, a requirement often conflicting with the need for low noise levels, in particular when measurements close to the pipe wall were carried out; large quantities of scattered light resulted in deterioration of signal to noise ratio and prohibited taking measurements very close to the boundary.

A series of tests to ascertain the effectiveness of the discriminator was undertaken and it was found that in the range of solids used (40 μm to 1 mm approximately) it was possible to record information separately from the two phases of the suspension. The discriminator could be set manually to any one of three options, i.e. 'all' - no discrimination, 'small' where only small particle signals were accepted and 'large' - only large particle signals accepted.

The optical anemometer used was designed and constructed from optical and electronic components most of which were not specifically designed for this purpose. It was part of this work to employ an optimised system, easy to assemble, inexpensive and, most important of all, adaptable to changing needs. The Doppler frequency meter, which

formed the basis of the velocity measuring system, was one of a number of prototypes designed by C.A. Hobson [14] . A more advanced type of this meter, with wide ranging capabilities, is currently under development.

A series of velocity measurements in gas-solid suspensions followed the development of the instrumentation, using an open type flow rig , in which the solids were reused.

The air flowrate was determined by means of a calibrated orifice plate. Glass tubes of bore between 22 and 31.4 mm. were used as working pipes and all pipe bends were made of soft rubber hose.

The main type of solids used was spherical glass beads - glass ballotini; other materials were also used to a lesser extent. No breaking up of the solids was observed, even after long usage, since direct impact of the solids with hard surfaces was completely avoided.

Seeding of the air was carried out by using either silicon carbide powder or smoke.

The measurements consisted of velocity profiles across the pipe and also of a number of centreline velocity measurements. Results from the two phases separately as well as from the suspension as a whole were recorded.

The results showed a varying slip between the solids and the air, depending on the size of the particles.

Dependence of slip on other flow parameters was also observed.

The presence of solids in the flow exerted an influence on the turbulence of the air; this influence varied in a complex manner. Particle size, particle concentration, loading ratio, and flow velocity were among the factors, which were thought to be of importance in the modification of air turbulence.

A number of suggestions for improvement of the experimental apparatus as well as an outline of a possible reorganisation of the testing procedures has been included at the end of this work.

REFERENCES

[1] Soo S L 1969 Pipe flow of suspensions. Appl. Sci. Res. 21 60-84

[2] Moller R E K and Norman B 1978 Simultaneous measurement of velocity and concentration in fibre suspension flow. Proc. Dyn. Flow Conference, Marseille & Baltimore, 745-754.

[3] Boothroyd R G 1971 Flowing gas-solid suspensions, Chapman and Hall

[4] Reddy K V S and Pei D C 1969 Particle dynamics in solid-gas flow in a vertical pipe. I and CE Fundamentals 8 3 490-497

[5] Spalding D B 1980 Recent advances in numerical methods in fluids. Vol. 1, Pineridge Press, Swansea

[6] Baw P S and Peskin R L 1967 Density profiles in gas-solid suspension flow, AIAA Journal, 5 4 815-817

[7] Stümke A and Umhauer H 1978 Local particle velocity distributions in two phase flows measured by laser-Doppler velocimetry. Proc. of the Dyn. Conference, Marseille & Baltimore, 417-423.

[8] Chandok A A and Pei D C T 1971 Particle dynamics in solids-gas flow in a vertical pipe, Pneumo-transport 1, Conf., Cambridge B5-53-67

[9] Muskett W J 1977 A study of rates of heat transfer to flowing gas-solid suspensions. MPhil Thesis Dept. of Mech. Mar. and Prod. Eng. Liverpool Polytechnic

[10] Zisselmar R and Molerus O 1978 Investigation of solid-liquid pipe flow with regard to turbulence modification. Intl. seminar on Momentum, Heat and Mass Transfer, Dubrovnik

[11] Boothroyd R G 1967 Turbulence characteristics of the gaseous phase in duct flow of a suspension of fine particles. Trans. Instn. Chem. Engrs. 45 T297-310

[12] Koronakis P S 1973 Reduction of turbulent energy and shear by particulates in a homologous turbulent shear flow field of low Reynolds number. PhD Thesis University of Illinois, USA

[13] Peskin R L and Rin C H 1967 The effect of suspended solids in turbulent dispersion. Fluids Eng. Conf., Chicago

[14] Hobson C A 1978 Digital analysis of opto-electronic data. PhD Thesis, Dept. of Electrical and Control Engineering, Liverpool Polytechnic

[15] Blake K A and Jespersen K I The NEL laser velocimeter. Dept. of Trade and Industry, National Eng. Laboratory, Report No. 510, May 1972

[16] Brayton D B Kalb H.T and Crosswy F L 1973 Two-component dual-scatter laser Doppler velocimeter with frequency burst signal readout. Appl. Opt. 12 6 1145-1155

[17] Spectra Physics Laser Review 1977 4 2

[18] Welch N E and Tomme W J 1967 The analysis of turbulence from data obtained with a laser velocimeter. AIAA paper No. 67-179

[19] Goldstein R J 1974 Measurement of fluid velocity with laser-Doppler techniques. Appl. Mech. Reviews 753-760

[20] Birchenough A and Mason J S 1976 Laser anemometry measurements in a gas-solid suspension flow. Opt. and Laser Technology 253-258

[21] Mobbs F R et al 1969 Influence of particle size distribution on the high-speed flow of gas-solid suspensions in a pipe. Proc. Inst. Mech. Eng. 1969-70. 184 3C 67-76

[22] Tridimas Y D Lalor M J and Woolley N H 1979 Beam waist location and measurement in a dual-beam laser Doppler anemometer. J. Phys. E: Sci. Instrum. 11 203-206

[23] Tridimas Y D Lalor M J and Woolley N H 1979 Criteria for achieving coincidence of beam waist and crossover region in a dual-beam laser Doppler anemometer. J. Phys. E: Sci. Instrum. 12 1176-1178.

[24] Farmer W M 1972 Measurement of particle size, number density and velocity using a laser interferometer Appl. Opt. 11 11 2603-2612

[25] Robinson D M and Chu W P 1975 Diffraction analysis of Doppler signal characteristics for a cross-beam laser Doppler velocimeter. Appl. Opt. 14 9 2177-2185

[26] Chu W P and Robinson D M 1977 Scattering from a moving spherical particle by two cross coherent plane waves Appl. Opt. 16 3 619-626.

CHAPTER 2

OPTIMIZATION OF THE

LASER DOPPLER ANEMOMETER

2.1 INTRODUCTION

Although laser Doppler anemometers have been extensively researched and used for a number of years, it was felt in the initial stages of this work that for reasons such as those given below, further investigation was necessary of beam geometry and in particular of waist position, in a focused laser beam.

In a dual beam LDA, control over the geometry of the cross-over region is of great importance, and the accuracy of measurements carried out with this instrument depends, to a large extent, on the precision with which the dimensions of the various parameters of the crossover region have been set, which in turn, depends on proper choice and alignment of the optical components. Due to the often very small dimensions of the beam intersection region, measurement of its geometric properties is rather difficult and reliance on calculated values has, in many instances, been the only solution possible.

The work presented in this chapter consists in the main of an extensive investigation of the properties of focused laser beams and the development of methods for the determination of optimum settings for a laser Doppler anemometer and the measurement of the beam size. A brief review of the basic principles and types of laser Doppler anemometers is also presented here.

2.2 THE DOPPLER SHIFT

In this analysis the laser light source is assumed to be fixed and only the scatterer is moving.

2.2.1 Single beam

Consider a monochromatic radiation of wavelength λ_1 and speed c, propagating in the direction of the unit vector $\hat{n}_1$ and illuminating a particle, which moves with velocity $\vec{V}$, where $\vec{V} \ll c$, as shown in figure 2.1. It can be shown [1,2,3] that the radiation scattered by the particle in

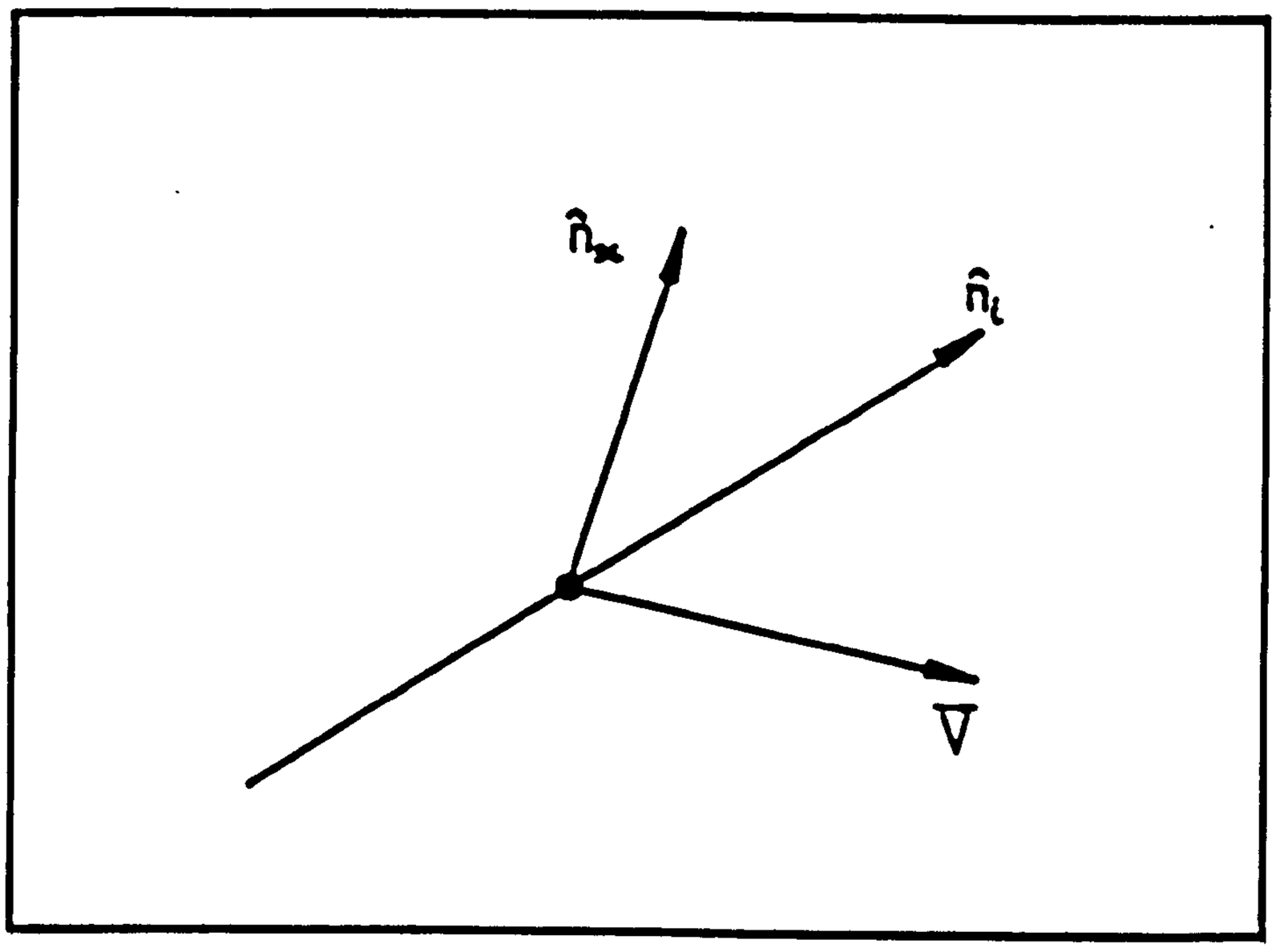

Figure 2.1 Scattering geometry

the direction of the unit vector $\hat{n}_{sc}$, has a frequency given by

$$f_{sc} = f_i \left(\frac{1 - \vec{v}.\frac{\hat{n}_i}{c}}{1 - \vec{v}.\frac{\hat{n}_{sc}}{c}} \right)$$

The apparent change in frequency, the Doppler shift, f_D, is then given by

$$f_D = f_{sc} - f_i = \frac{f_i}{c} \frac{\vec{v}.(\hat{n}_{sc} - \hat{n}_i)}{\left(1 - \frac{\vec{v}\,\hat{n}_{sc}}{c}\right)}$$

and since $|\vec{v}| < c$,

$$f_D = \frac{n\,\vec{v}}{\lambda_o} . (\hat{n}_{sc} - \hat{n}_i) \qquad (2.1)$$

where n is the index of refraction of the surrounding medium and λ_o is the wavelength of the incident radiation in vacuo (i.e. $\lambda_i = \frac{\lambda_o}{n}$).

It is seen from equation (2.1) that the observed Doppler shift depends on the position of the observer.

If scattered light is collected in two different directions, $\hat{n}_{sc1}$ and $\hat{n}_{sc2}$, the two detected frequencies are:

$$f_{sc1} = f_i \left(\frac{1 - \vec{v}.\frac{\hat{n}_i}{c}}{1 - \vec{v}.\frac{\hat{n}_{sc1}}{c}} \right)$$

and

$$f_{sc2} = f_i \left(\frac{1 - \vec{v}.\frac{\hat{n}_i}{c}}{1 - \vec{v}.\frac{\hat{n}_{sc2}}{c}} \right)$$

The Doppler difference frequency f_d is then:

$$f_d = f_{sc1} - f_{sc2} = f_i \frac{\left(1 - \vec{v}.\frac{\hat{n}_i}{c}\right)}{\left(1 - \vec{v}.\frac{\hat{n}_{sc1}}{c}\right)\left(1 - \vec{v}.\frac{\hat{n}_{sc2}}{c}\right)} \frac{\vec{v}}{c} .$$

$$(\hat{n}_{sc1} - \hat{n}_{sc2})$$

and as $|\vec{v}| < c$ then

$$f_d = \frac{n}{\lambda_o} \vec{v}.(\hat{n}_{sc1} - \hat{n}_{sc2}) \qquad (2.2)$$

In practice, the two waves are superimposed on the surface of a photodetector to yield the desired signal.

Equation (2.1) forms the theoretical basis for the "reference beam" laser Doppler anemometer or local oscillator heterodyne, whereas the "dual scatter" or symmetric heterodyne system is based on equation (2.2), see section 2.4.2.

2.2.2 Dual beam system.

In this arrangement a particle scatters light at the intersection of two beams as shown in figure 2.2.

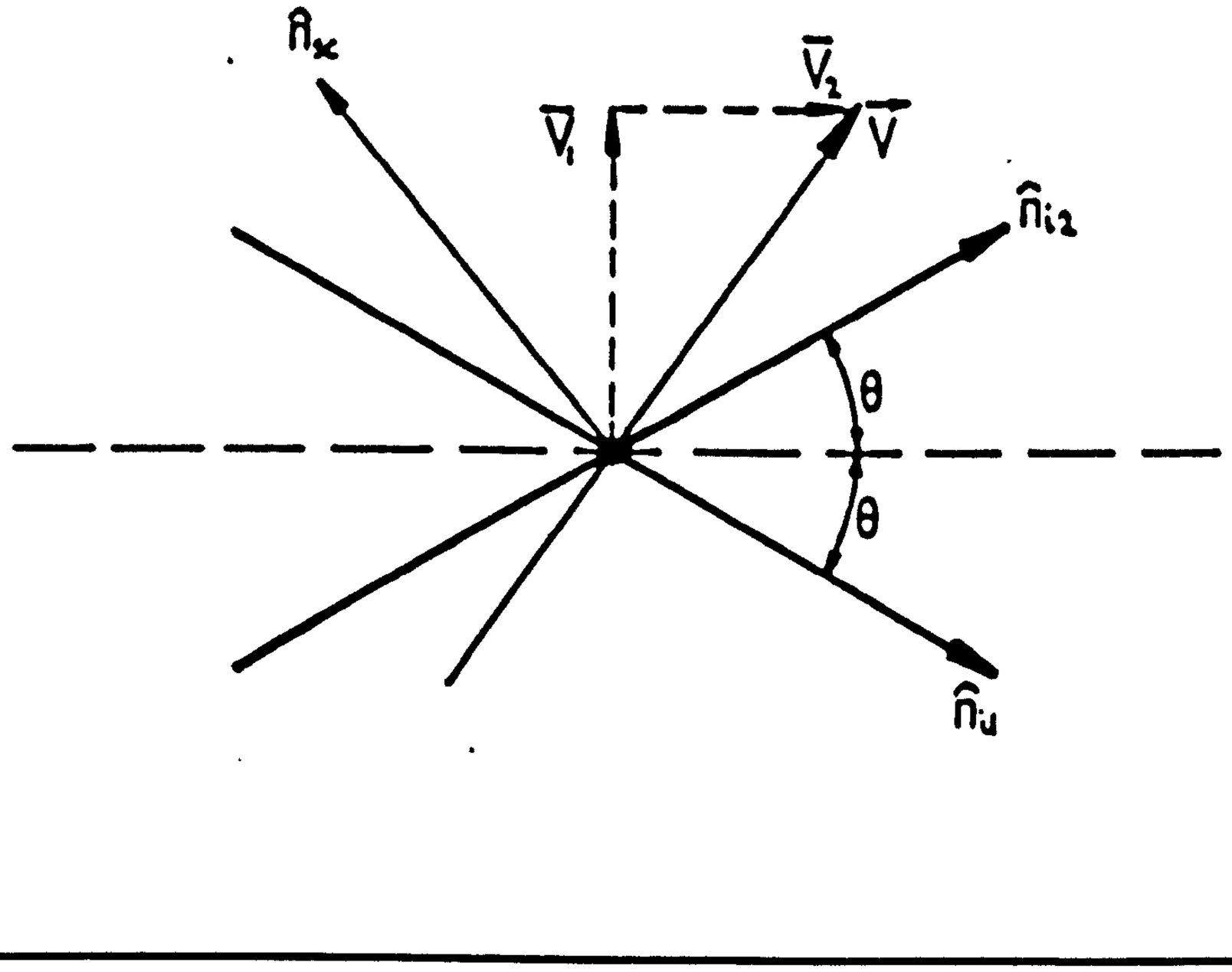

Figure 2.2 Dual beam scattering geometry

An observer viewing in the direction $\hat{n}_{sc}$ will detect a difference frequency $f_d = f_{D2} - f_{D1}$, where subscripts 1 and 2 refer to beams 1 and 2 and the quantities f_{D1} and f_{D2} are analogous to f_D in equation (2.1).

The two frequencies are usually mixed on the surface of a square law detector to give a Doppler difference,

$$f_d = \frac{n \vec{V}}{\lambda_o} \cdot (\hat{n}_{i1} - \hat{n}_{i2}) \qquad (2.3)$$

The following are observed:

(i) for fixed $\hat{n}_{i1}$ and $\hat{n}_{i2}$, f_d is independent of the direction of observation.

(ii) f_d depends on the angle between the two beams.

(iii) If $\bar{V}$ is normal to both $\hat{n}_{i1}$ and $\hat{n}_{i2}$, then $f_d = 0$.

If the angle between the two incident beams is equal to 2θ then equation (2.3) gives

$$f_d = \frac{n}{\lambda_o} (\bar{V}_1 + \bar{V}_2).(\hat{n}_{i1} - \hat{n}_{i2})$$

where $\bar{V}_2$ and $\bar{V}_1$ are the components of $\bar{V}$ in the direction of the bisector of the angle 2θ and at right angles to it respectively. Here $\bar{V}_2.(\hat{n}_{i1} - \hat{n}_{i2}) = 0$ and $\bar{V}_1(n_{i1} - n_{i2}) = V_1 [\cos(\frac{\pi}{2} - \theta) - \cos(\frac{\pi}{2} + \theta)]$. Hence

$$f_d = \frac{2n}{\lambda_o} \bar{V}_1 \sin\theta . \qquad (2.4)$$

It is thus seen that the Doppler shift is produced by that component of the particle velocity vector, which is normal to the axis of symmetry of the incident beams.

Equation (2.4) gives the Doppler shift for the "dual beam" or differential heterodyne laser Doppler anemometer (see section 2.4.2).

2.2.3 The fringe model

Equation (2.4) can be derived by a different approach [2]. Consider the intersection region of two beams and the three coordinate system, as shown in figure 2.3. At any point P(y,z) in the intersection region, interference of the two waves takes place, due to different path lengths. Thus bright fringes are formed if the path difference is equal to $m\lambda_i$ $(m = 1,2,...)$ and dark fringes when the path difference equals $(m \pm \frac{1}{2})\lambda_i$.

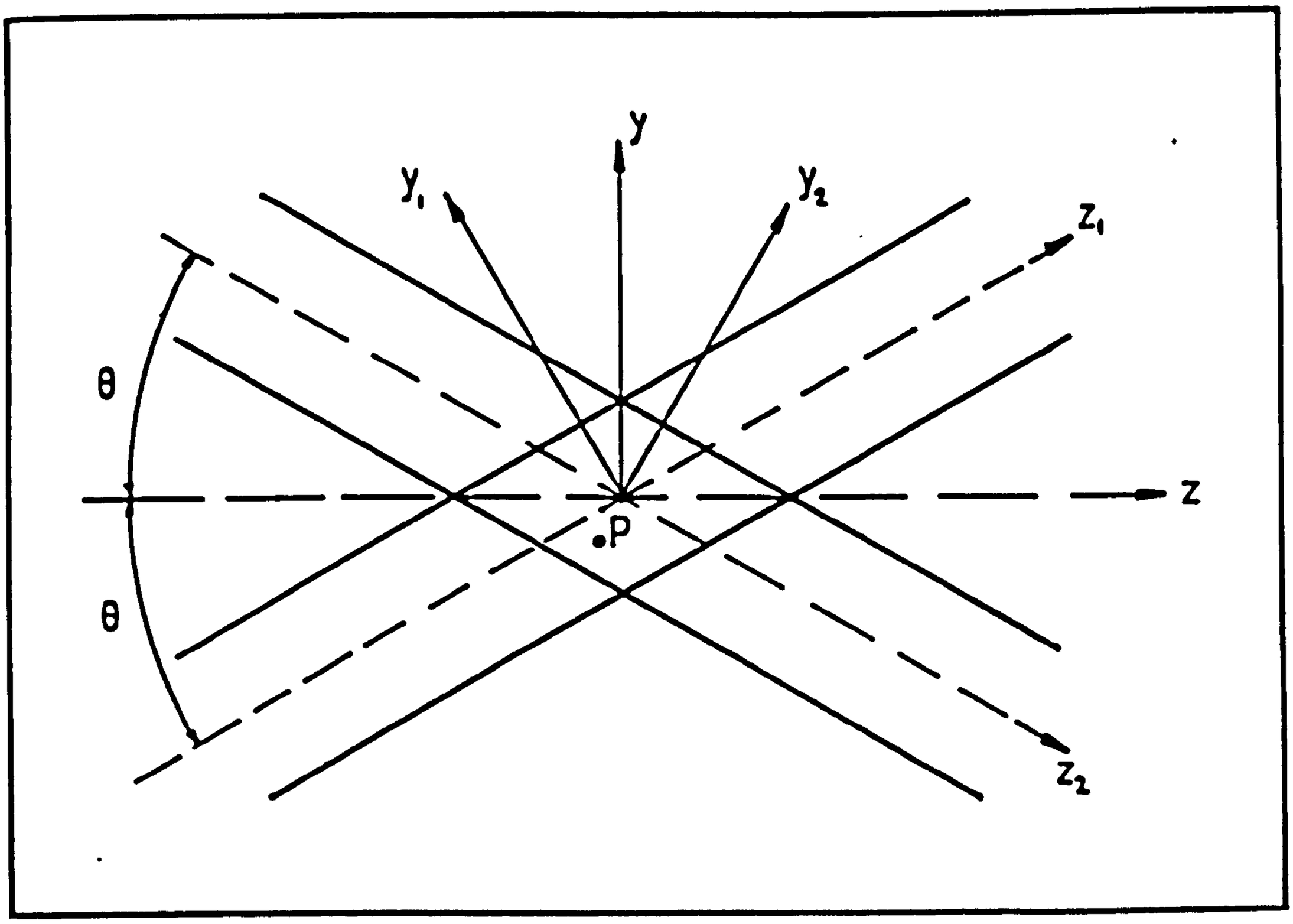

Figure 2.3 Fringe model scattering geometry

The path difference at P(y,z) is $z_1 - z_2$. Transforming (y_1,z_1) and $y_2,z_2)$ into the (y,z) coordinate system we obtain:

$$z_1 = z\cos\theta + y\sin\theta$$

$$z_2 = z\cos\theta - y\sin\theta \ .$$

This gives

$$z_1 - z_2 = 2y\sin\theta \ .$$

Thus bright fringes occur when $2y\sin\theta = m\lambda_1$, from which the distance δ between two consecutive fringes is given by

$$\delta = \frac{\lambda_1}{2\sin\theta}$$

or

$$\delta = \frac{\lambda_o}{2n\sin\theta} \qquad (2.5)$$

In a three-dimensional system (x,y,z), the fringes are parallel to x-z planes.

A particle moving inside the crossover region with velocity $\vec{V}$ will cross the fringes at a rate equal to

$$\frac{\bar{V}_1}{\delta} = \frac{2n\,\bar{V}_1\sin\theta}{\lambda_o}$$

where $\bar{V}_1$ is the component of $\vec{V}$ in the y-direction. This frequency is identical to the Doppler shift, as expressed by equation (2.4), i.e.

$$f_d = \frac{2n}{\lambda_o}\,\bar{V}_1\sin\theta$$

Equations (2.1), (2.2) and (2.3) yield only the magnitude

of the velocity component measured and not its direction, which must be determined by other means (see section 3.2).

2.3 PROPAGATION OF GAUSSIAN LASER BEAMS

2.3.1 Laser cavity configuration

It has been tacitly assumed in the preceeding theory that the laser beam is a collimated plane wave. This is often not the case because of the design of the laser cavity. The gas in a He-Ne laser acts solely as an amplifying medium. It will not oscillate until positive feedback is obtained by placing the gas between two reflectors which return the light back and forth between them [4]. The usual system is a Fabry-Perot cavity, which has two highly reflecting mirrors at the ends. One mirror is made slightly transparent so that about 2% of the light is emitted from the cavity.

A number of mirror configurations are possible. The simplest is the two plane mirror configuration, see figure 2.4(a). There is only one repeatable path between the two mirrors, so this system will produce a single spot output with little or no divergence. The only variable is the cavity length, d, which must be an integral number of half wavelengths i.e. $d = n(\lambda/2)$, where n is a positive integer. This is a necessary condition for the electric field of the standing wave to be zero on the two mirrors. It then follows that the resonant frequencies, ν (longitudinal modes), are given by $\nu = n\frac{c}{2d}$, where c is the velocity of

light.

This system is however very difficult to align since the mirrors must be perfectly parallel and not the least bit convex. Thus a combination of two concave mirrors or a plane and a concave mirror is generally employed. Figure 2.4(b) shows a concentric or spherical resonator in which two spherical mirrors of radius of curvature R, are separated by a disrance d, such that d = 2R.

Figure 2.4(c) shows a confocal configuration which consists of two spherical mirrors of the same radius of curvature, R, and separated by a distance d, such that the mirror foci are coincident.

Figure 2.4(d) shows a cavity with one plane and one concave mirror.

The use of these types of cavity has two important practical effects:

1. It introduces the possibility of off axis modes. If the number of radial phase changes across the wave front (mode order) is m, and the number of azimuthal phase changes is p, then a mode is described as TEM mpn where TEM stands for Transverse Electro-Magnetic. The 'n', which is a large number is often dropped and the mode referred to as TEM_{mp}. Typical values of m, p and the associated patterns are shown in figure 2.4(e). If many transverse modes are present there will be many different frequencies in the output of the laser,

(a) Plane mirrors

(b) concentric mirrors

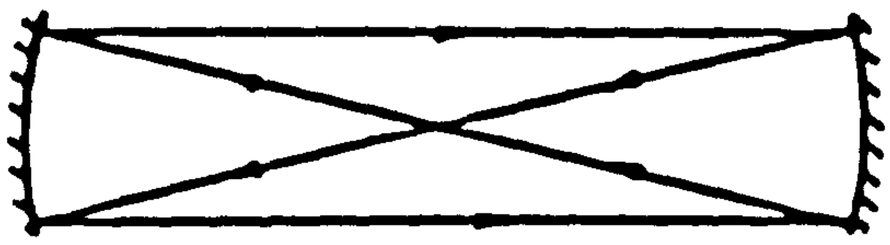

(c) confocal configuration

(d)

hemiconfocal

hemispherical

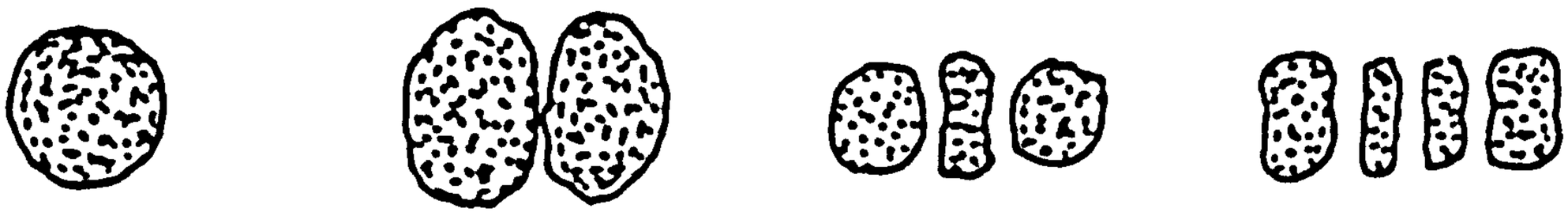

$T_{EM_{00}}$ $T_{EM_{01}}$ $T_{EM_{02}}$ $T_{EM_{02}}$

(e) Mode patterns

Figure 2.4 Resonator configurations and mode patterns.

which will be to the detriment of frequency measurements with a laser anemometer. Therefore the laser should only be operated in the uniphase or TEM_{oo} mode.

2. With concave mirrors used in the laser cavity the beam will be focused to a 'waist', either inside or just outside the cavity. Thus the laser beam will be diverging and not naturally collimated, see figure 2.5.

2.3.2 Beam Geometry

Two important beam parameters of the 'fundamental mode' are the radius of curvature of the phasefront R_z and the beam radius w_z. These parameters are related [5,6] by:

$$\frac{1}{q_z} = \frac{1}{R_z} - j\,\frac{\lambda}{\pi\, w_z^2} \qquad (2.6)$$

where q_z is a complex beam parameter, which describes the Gaussian intensity variation in the radial direction. The phasefront is spherical near the beam axis [6]; z denotes the direction of propagation. The intensity distribution in the radial direction is Gaussian and the beam radius or 'spot size', w, is measured from the beam axis up to the point where the intensity is $\frac{1}{e^2}$ of that on the axis. The beam radius has a minimum, or 'waist', w_1, usually in the laser resonator and thereafter the beam expands. At the waist the phasefront is plane and the complex beam parameter is

$$q_1 = j \frac{\pi w_1^2}{\lambda} \tag{2.7}$$

At a distance z from the waist we have

$$q_z = q_1 - z \tag{2.8}$$

The above beam parameters are shown in figure 2.5.

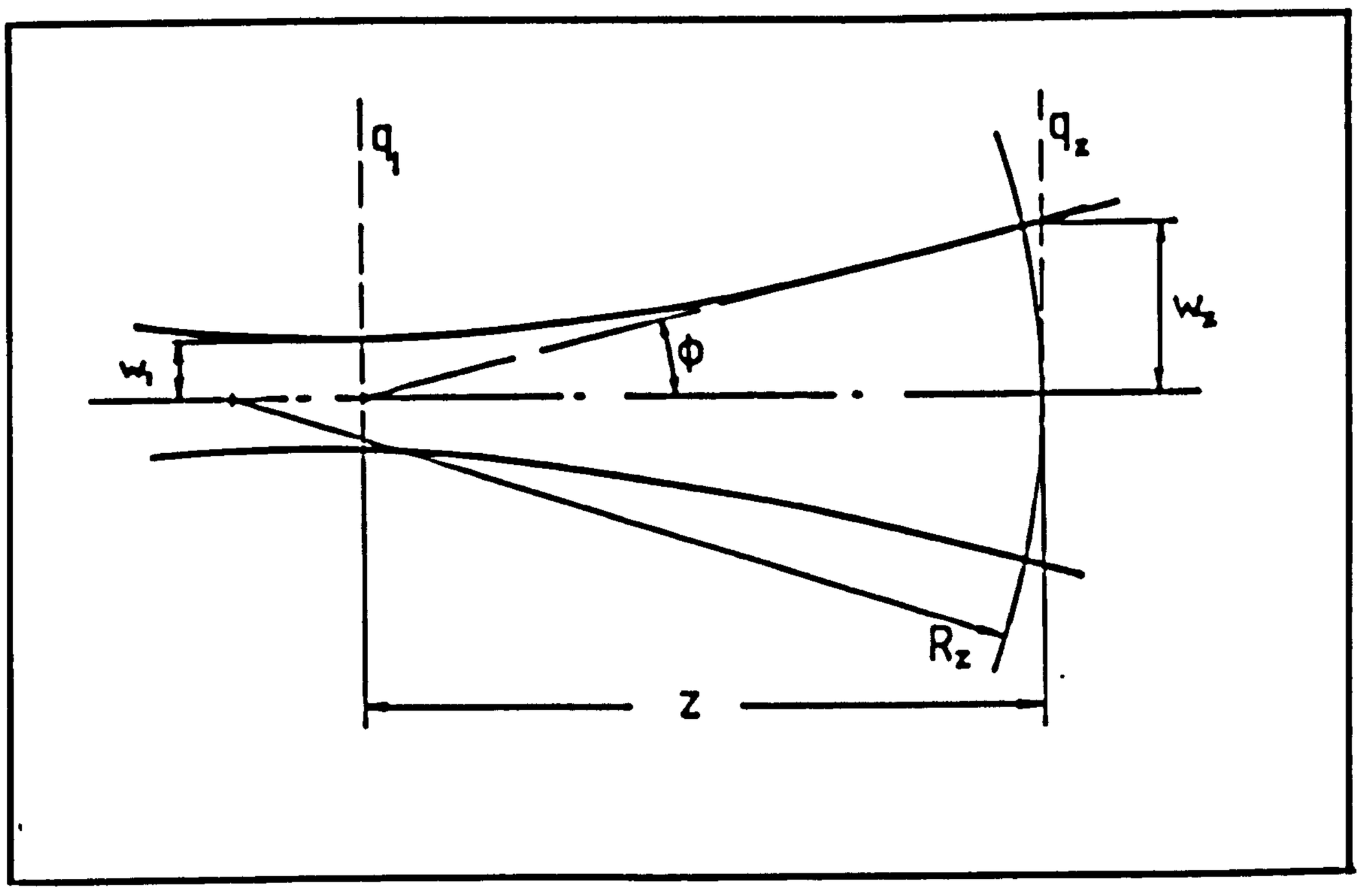

Figure 2.5 Beam parameters

From equations (2.6), (2.7) and (2.8) one obtains

$$w_z^2 = w_1^2 \left[1 + \left\{ \frac{z}{\frac{\pi w_1^2}{\lambda}} \right\}^2 \right] \tag{2.9}$$

and $$R_z = z\left[1 + \left\{\frac{\pi \frac{w_1^2}{\lambda}}{z}\right\}^2\right] \qquad (2.10)$$

where λ denotes the wavelength.

As $z \to \infty$,

$$w_z \to \frac{z}{\pi \frac{w_1}{\lambda}} ,$$

which is an asymptote inclined at an angle $\phi = \tan^{-1} \frac{w_z}{z}$ or

$$\phi = \frac{\lambda}{\pi w_1} \qquad (2.11)$$

Hence ϕ defines the beam divergence. The variation of the beam radius, w_z, with distance from the waist, z, is shown in figure 2.6.

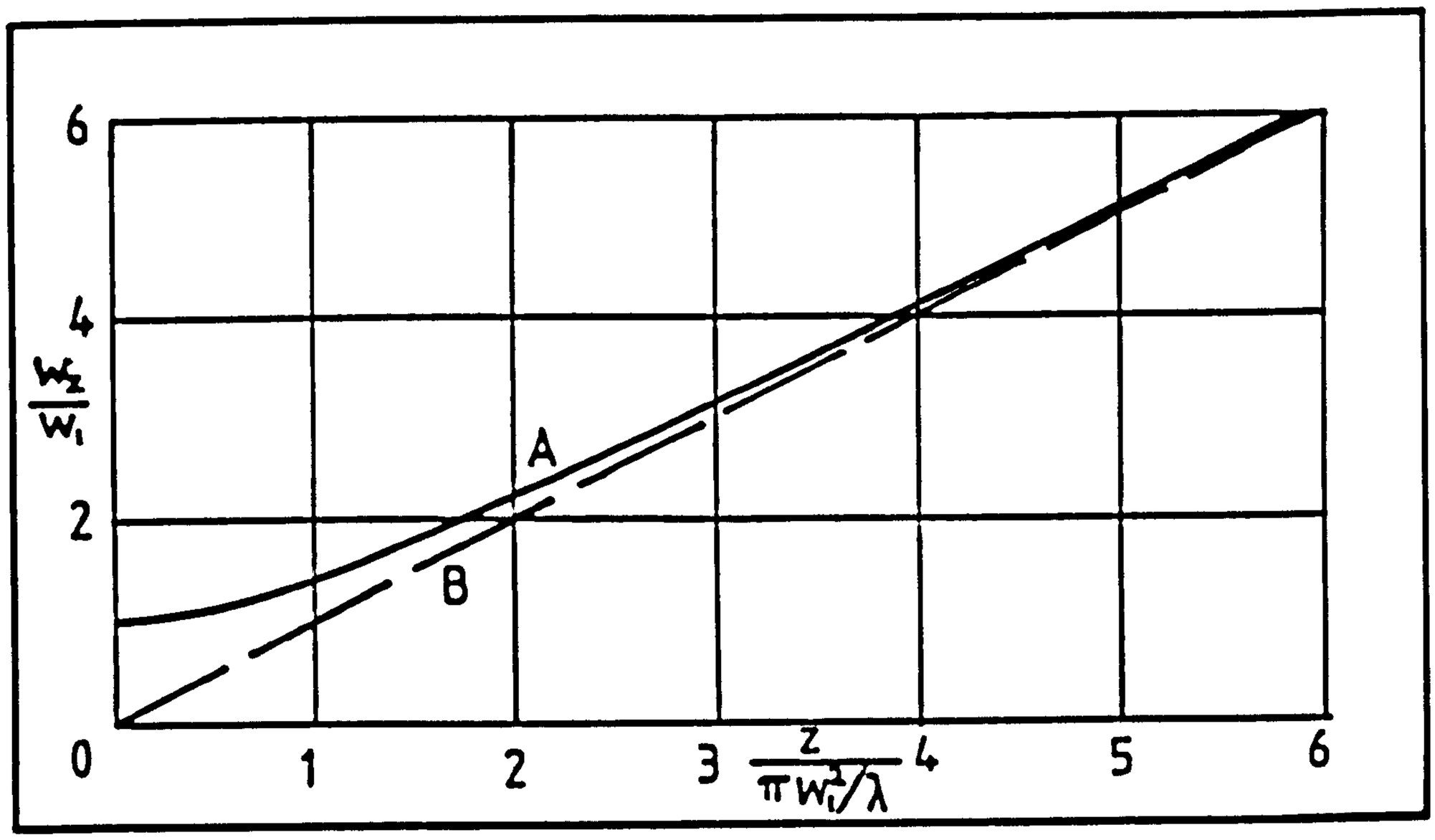

Figure 2.6 Beam propagation. A: equation (2.9), B: $\frac{w_z}{w_1} = \frac{z}{\pi \frac{w_1^2}{\lambda}}$.

2.3.3 Transformation of a beam by a lens

When a Gaussian beam passes through a lens the parameters R_z and w_z are changed and a new beam waist is formed. In the following, all beam parameters in front of the lens will be called input parameters and those behind the lens will be called output parameters. The radius of the new beam waist, w_2 and the distance of the waist from the lens, z_2, are given [7] by:

$$\frac{w_2}{w_1} = \frac{f}{\left[(z_1 - f)^2 + \left\{\frac{\pi w_1^2}{\lambda}\right\}^2\right]^{\frac{1}{2}}} \qquad (2.12)$$

$$\frac{z_2}{f} = \frac{(z_1 - f).f}{(z_1 - f)^2 + \left\{\frac{\pi w_1^2}{\lambda}\right\}^2} \qquad (2.13)$$

where f denotes the focal length of the lens and z_1 denotes the distance between the input waist and the lens, as shown in figure 2.7.

Equations (2.13) and (2.12) can be rewritten as [8]:

$$\left(\frac{z_2}{f} - 1\right) \Big/ \left(\frac{f}{f_F}\right) = \frac{\left(\frac{z_1}{f} - 1\right)\frac{f}{f_F}}{1 + \left(\frac{z_1}{f} - 1\right)^2 \left(\frac{f}{f_F}\right)^2} \qquad (2.14)$$

$$\left(\frac{w_2}{w_1}\right) \Big/ \left(\frac{f}{f_F}\right) = \left[1 + \left(\frac{z_1}{f} - 1\right)^2 \left(\frac{f}{f_F}\right)^2\right]^{\frac{1}{2}} \qquad (2.15)$$

where $f_p = \frac{\pi w_1^2}{\lambda}$. Graphs of the above expressions are shown in figure 2.8 and a summary of the relationships between input and output parameters is presented in table 2.1.

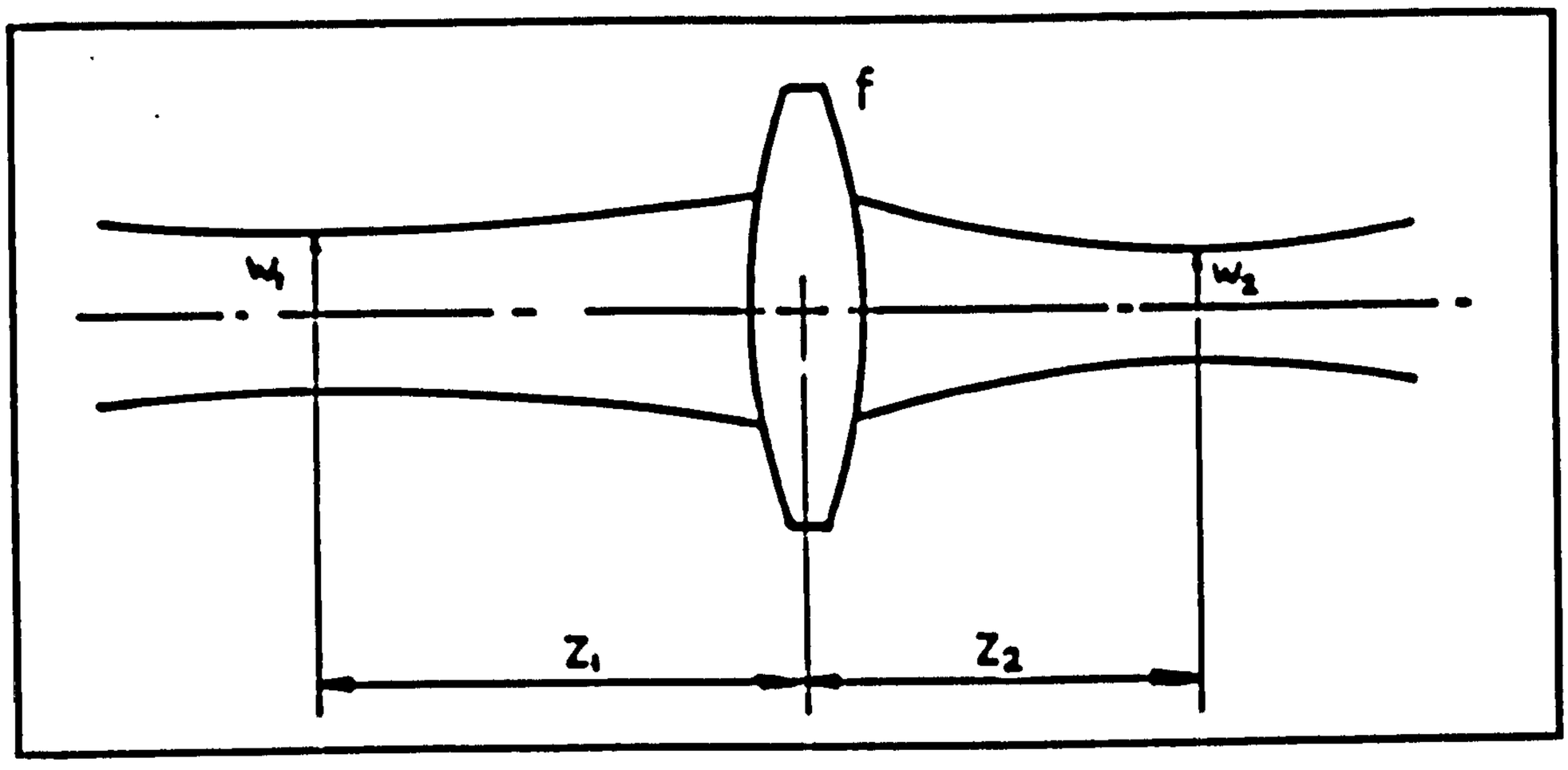

Figure 2.7 Focused beam parameters

z_1/f	z_2/f	w_2/w_0
$-\infty$	1	0
$1-\frac{1}{(f/f_F)}$	$1-\frac{1}{2}\frac{f}{f_F}$ (min)	$\frac{f/f_F}{\sqrt{2}}$
1	1	f/f_F (max)
$1+\frac{1}{(f/f_F)}$	$1+\frac{1}{2}\frac{f}{f_F}$ (max)	$\frac{f/f_F}{\sqrt{2}}$
∞	-1	0

Table 2.1 Relationships between input and output parameters of focused laser beams

It is observed that the distance of the output beam waist from the lens takes values from f, to a minimum (< f), to a maximum (> f) and finally back to f, as the input waist to the lens distance changes from $-\infty$ to $+\infty$. The output waist radius has a maximum when the input waist is at f.

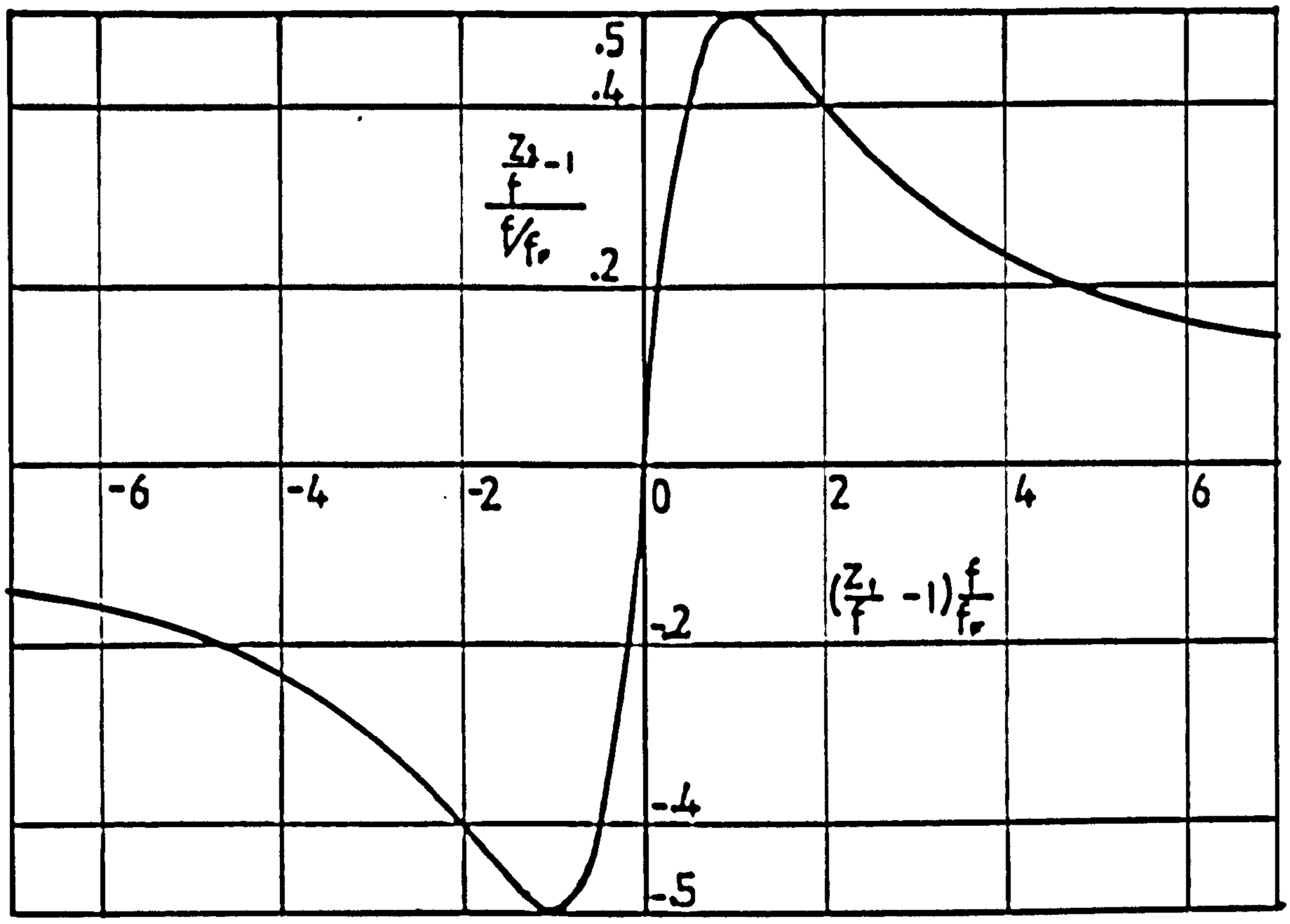

(a)

(b)

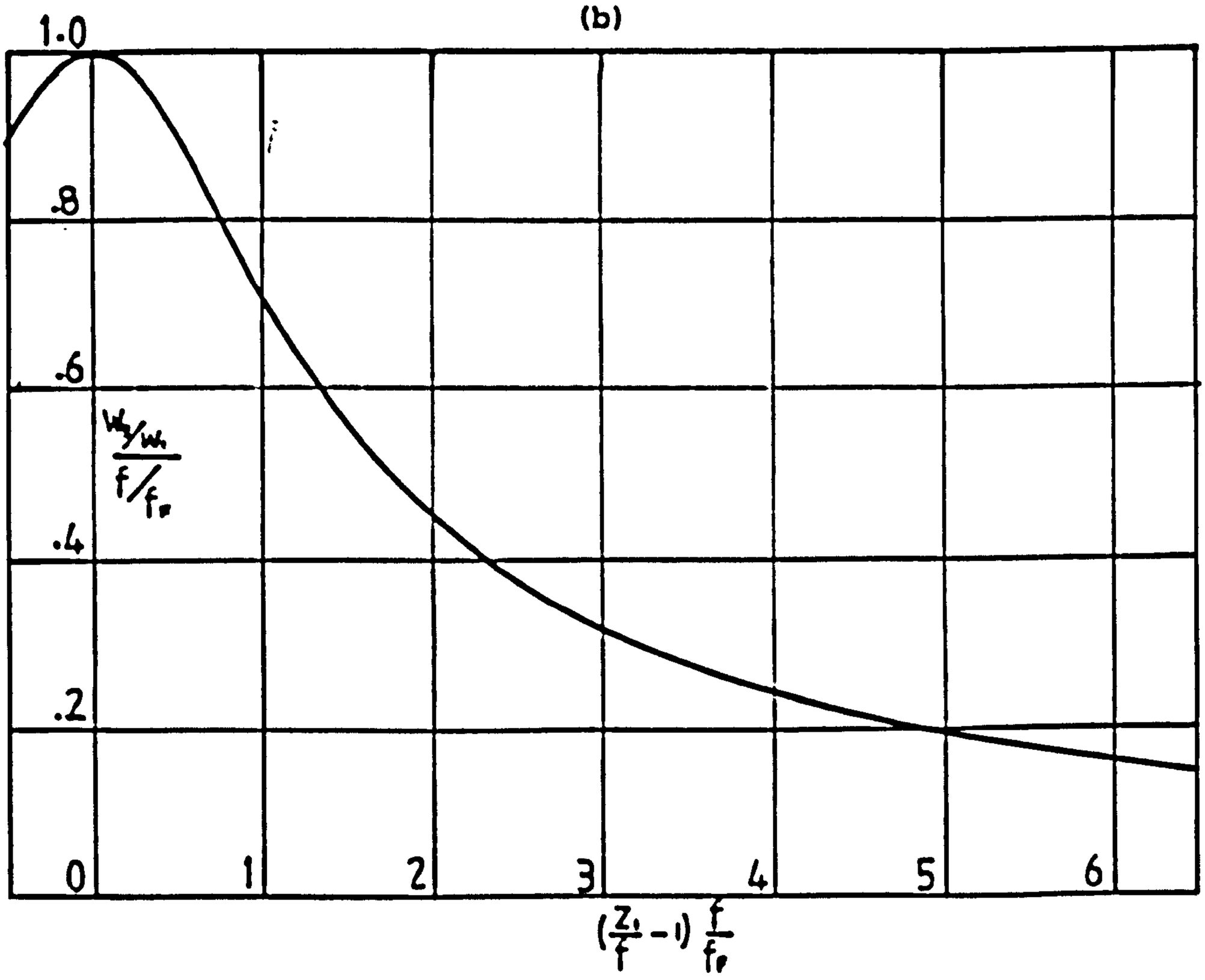

Figure 2.8 (a): Graph of equation (2.14); (b): equation (2.15)

2.4 BRIEF REVIEW OF LASER DOPPLER ANEMOMETERS

2.4.1 General

Since first introduced [9] the laser Doppler anemometer has developed fast as a tool for measuring velocities of flowing fluids and moving solids. It has found a wide scope as a research instrument and many variations from the basic instrument design can be found in the literature associated with it. The main reason for the development of various types of laser anemometer is basically the need to satisfy the requirements of particular applications, e.g. velocity measurements in pipe flows, investigation of gas velocities inside internal combustion engine cylinders, velocities of moving solids, dense or sparsely seeded two phase flows etc. In order to obtain the best results from each particular situation various workers in the field have developed and applied many variations of dual and reference beam anemometers, with forward and/or backscatter light collection either paraxially, or at various angles. Several types of LDA now exist which can measure one, two or three components of velocity simultaneously.

2.4.2 Optical arrangements

The laser Doppler anemometers used today can be classified into three main categories i.e. the 'reference beam' type, the 'dual scatter' and the 'dual beam' systems. A detailed study of these types has been presented by Wang

and Snyder [10], Durst and Whitelaw [1] and Durst, Melling and Whitelaw [11].

Figure 2.9(a) shows a reference beam configuration; in this system the scatterer is illuminated by a laser beam. The scattered light is collected by the collecting optics and heterodyned with a beam of lower intensity, directly from the laser. This gives rise to a beat frequency which is proportional to the velocity of the scatterer [12].

Figure 2.9(b) shows a dual scatter arrangement. The scatterer is illuminated by a single beam; scattered light is collected from two different angles and mixed at the photodetector surface to produce the shift frequency, which is related to the velocity of the scatterer. This is the simplest and easiest system to set up [10].

The third type, the 'dual beam' or 'fringe anemometer', is the most commonly used optical arrangement [13]. As shown in figure 2.9(c), the single beam from the laser is split into two equal intensity beams which are then made to intersect - usually after being focused by a lens. The intersection region, the 'probe volume', is a region of alternate planes of high and low light intensity - the interference fringes. When a particle crosses these fringes it scatters light of varying intensity. Some of that light is collected and directed on to a photodetector surface. The resulting a.c. signal has a frequency which is proportional to the velocity of the scattering object.

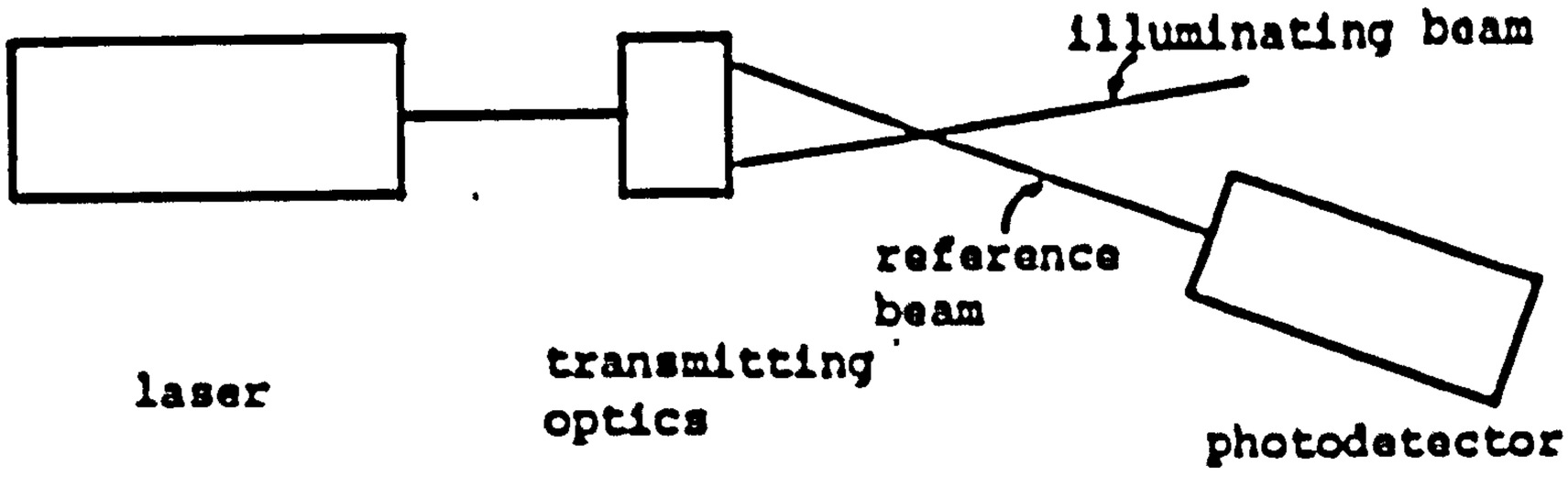

(a) Reference beam, L.D.A.

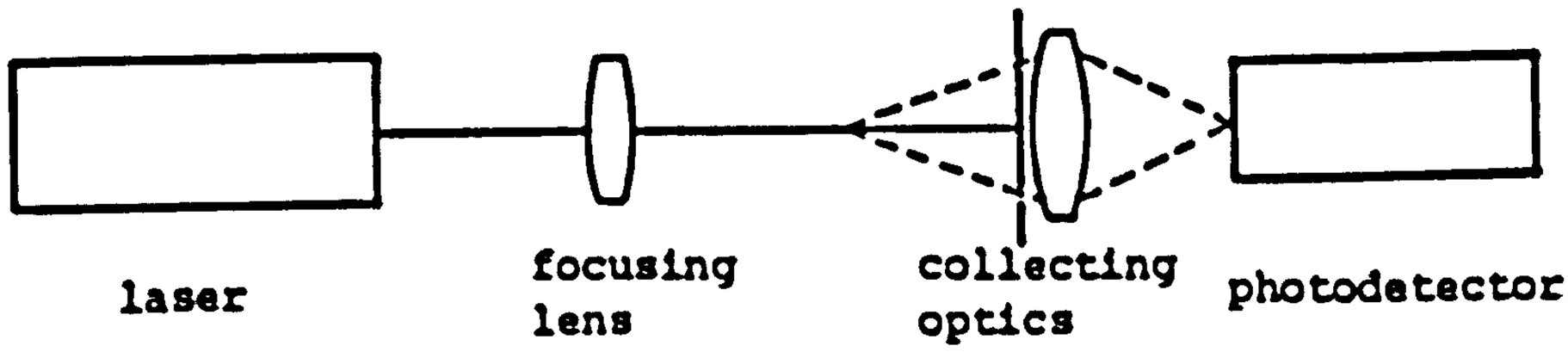

(b) Dual-scatter L.D.A.

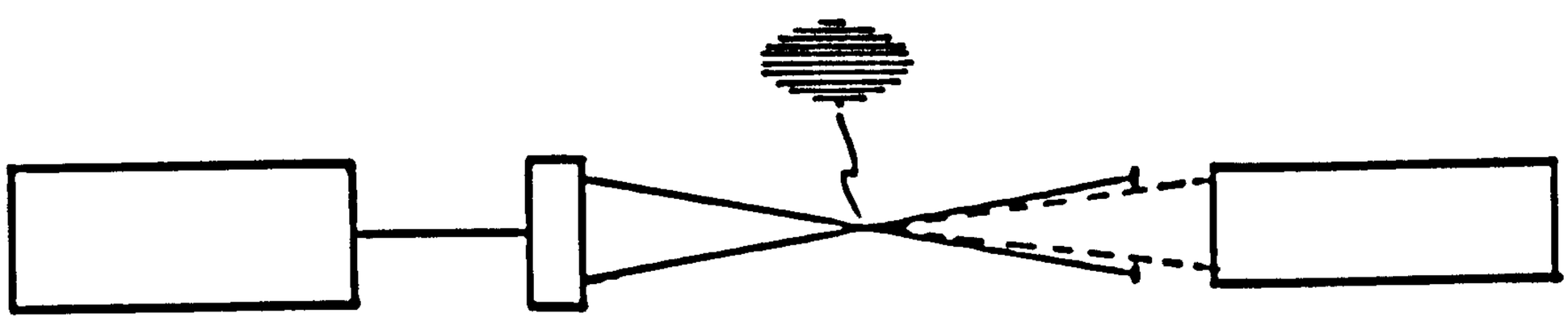

(c) Dual beam L.D.A.

Figure 2.9 Basic L.D.A. arrangements

Both the reference beam and the dual scatter systems suffer from the disadvantage of poor signal strength. This tends to limit their applications to situations where particle density is high and forward scatter can be utilised [13]. There are several advantages in the dual beam optical system, which make it the most widely used technique [10, 14]. The signal frequency is independent of detector orientation relative to the scattered light. This provides better signal to noise ratio and allows for less precise component alignment [15]. In addition, with signal frequency being independent of detector position, it becomes possible to utilise backscatter light collection. This has allowed the use of laser anemometers in situations where forward scatter was not possible. An example of such a situation is an internal combustion engine, where access into the combustion chamber is achieved through a small window. Figure 2.10 shows a dual beam anemometer used in the backscatter mode. Another advantage of the backscatter arrangement is its increased compactness [12,16] over its forward scatter counterpart.

Variations of the basic LDA configurations can be found in the literature [14,17,18,19].

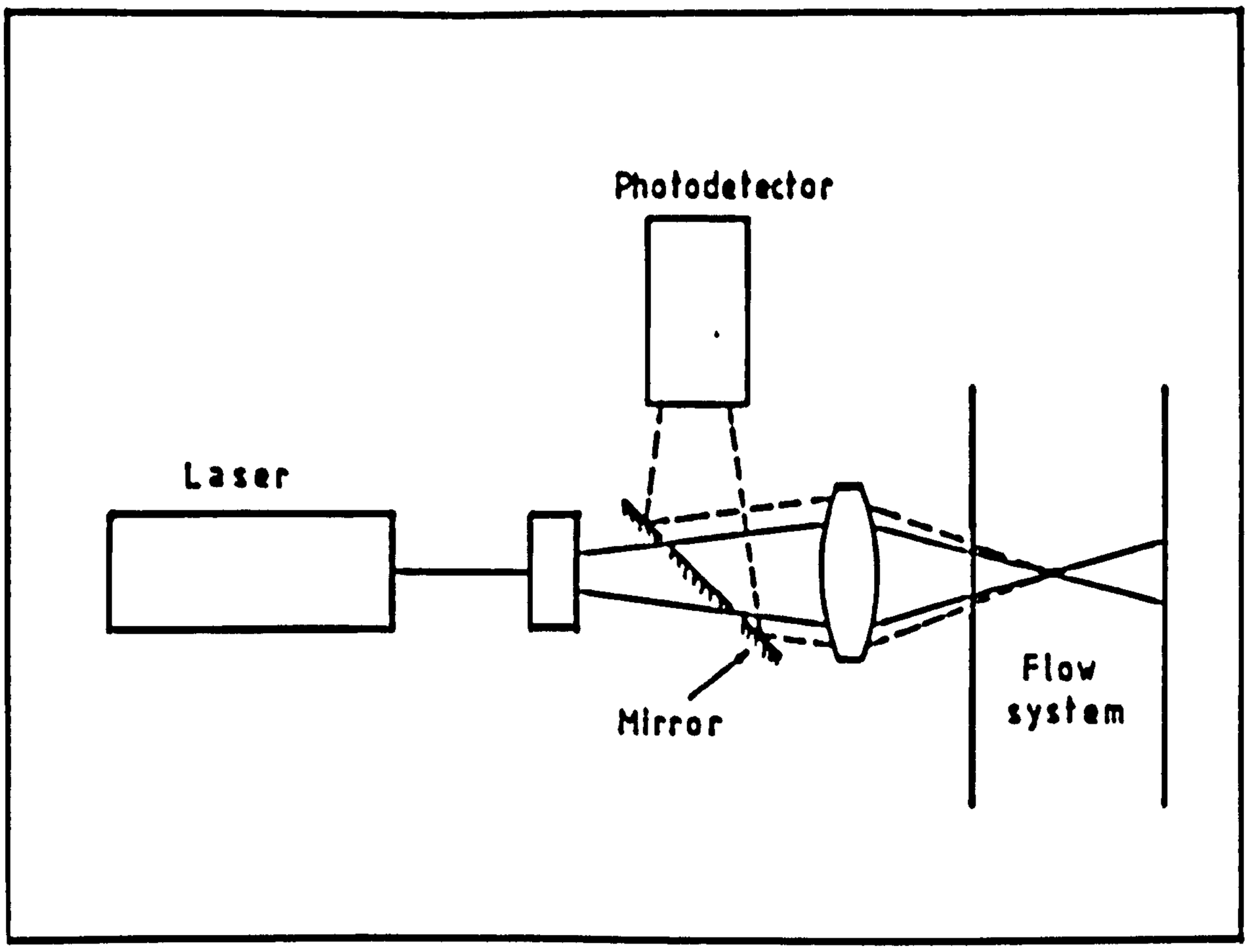

Figure 2.10 Dual beam anemometer in backscatter mode

2.4.3 Multichannel laser Doppler anemometer

Simultaneous measurements of two and three components of velocity are posisble, utilising either the reference [1,20], or the dual beam model [1,13,16,20,21]. Most of the multichannel laser Doppler anemometers, which have been used to date, operate in the dual beam mode [20].

In a multicomponent LDA more than one pair of beams are focused at the same point, producing an equal number of sets of fringes (if in the fringe mode), hence giving velocity components related to the angular disposition of those beams. Another method of obtaining simultaneous measurement of more than one velocity components, utilises

the multiwavelength capability of argon-ion lasers. Thus multicolour beam systems are possible [13]. A detailed account of such systems can be found in references [13] and [20].

2.5 THE DUAL BEAM LASER DOPPLER ANEMOMETER

2.5.1 Introduction

A simple dual beam laser anemometer or 'Doppler difference' anemometer consists of a laser source, a beam splitter and a converging lens. The single beam which has a waist in the laser resonator, is divided into two beams by the beam splitter. The directions of the two beams may be parallel, converging or diverging, depending on the type of beam splitter used. Finally those two beams are passed through the lens and made to cross at a point. The crossover region, usually called the 'probe volume' is the image of the input intersection point (real or virtual); beam waists are also formed on the two beams as images of the input waist. Equal path lengths are assumed throughout this work. In a different arrangement the single beam is focused first and then split into two converging beams [22].

The imaging laws for the beam waist and the beam intersection are different and as a result the output waist will not normally coincide with the intersection region unless the overall optical system is arranged to achieve this. In

an improved laser Doppler anemometer it is a basic requirement that the beam waists should coincide with the crossover region for reasons such as

(a) To eliminate interference plane gradients which cause signal broadening [22,23,24].

(b) To achieve a small crossover region and thus:

(i) Minimise signal broadening due to velocity gradients [25,26,27].

(ii) Improve measurements in some flow situations e.g. film flows [28]. Adjustment of the receiving optics to 'see' only the central portion of the probe volume can only be considered as second best, since it results in loss of a large part of the available laser power.

(c) The Mie theory of light scattering by particles on which, for example, particle sizing is based, requires plane wavefronts at the scattering region [29], a condition best achieved if the beams intersect at their waists.

2.5.2 Basic parameters of a dual beam laser Doppler anemometer

The most important feature of a dual beam laser Doppler anemometer is the crossover region, where interference between the two beams gives rise to bright and dark fringes. The distance between the fringes is given by

equation (2.5) as

$$\delta = \frac{\lambda}{2 \sin \theta} \quad .$$

The basic parameters of the beam intersection region are shown in figure 2.11. Figure 2.12 shows a photograph of the fringes projected on to a screen, using a microscope objective.

When a particle passes through the intersection region it will intercept the fringes with a frequency, given by equation (2.4) as

$$f_d = \frac{\bar{V}_1}{\delta} = \frac{2 \bar{V}_1 \sin \theta}{\lambda}$$

where V_1 is the velocity component normal to the fringes. The scattered light intensity varies with the position of the particle within the fringe system, between a low value and a maximum value as shown in figure 2.13. The maximum and minimum values of the signal depend, among other factors, on the size of the scatterer relative to the fringe spacing. The two components of the signal are a low frequency pulse, the d.c. component, also called the pedestal, which corresponds to the light intensity scattered from the crossover region in the absence of heterodyne mixing, and a sinusoidal Doppler component, the a.c. component, which oscillates at the Doppler frequency [30]. These two signal components can be separated by electronic filtering. The pedestal component is obtained after low pass filtering whereas the a.c. component is obtained by

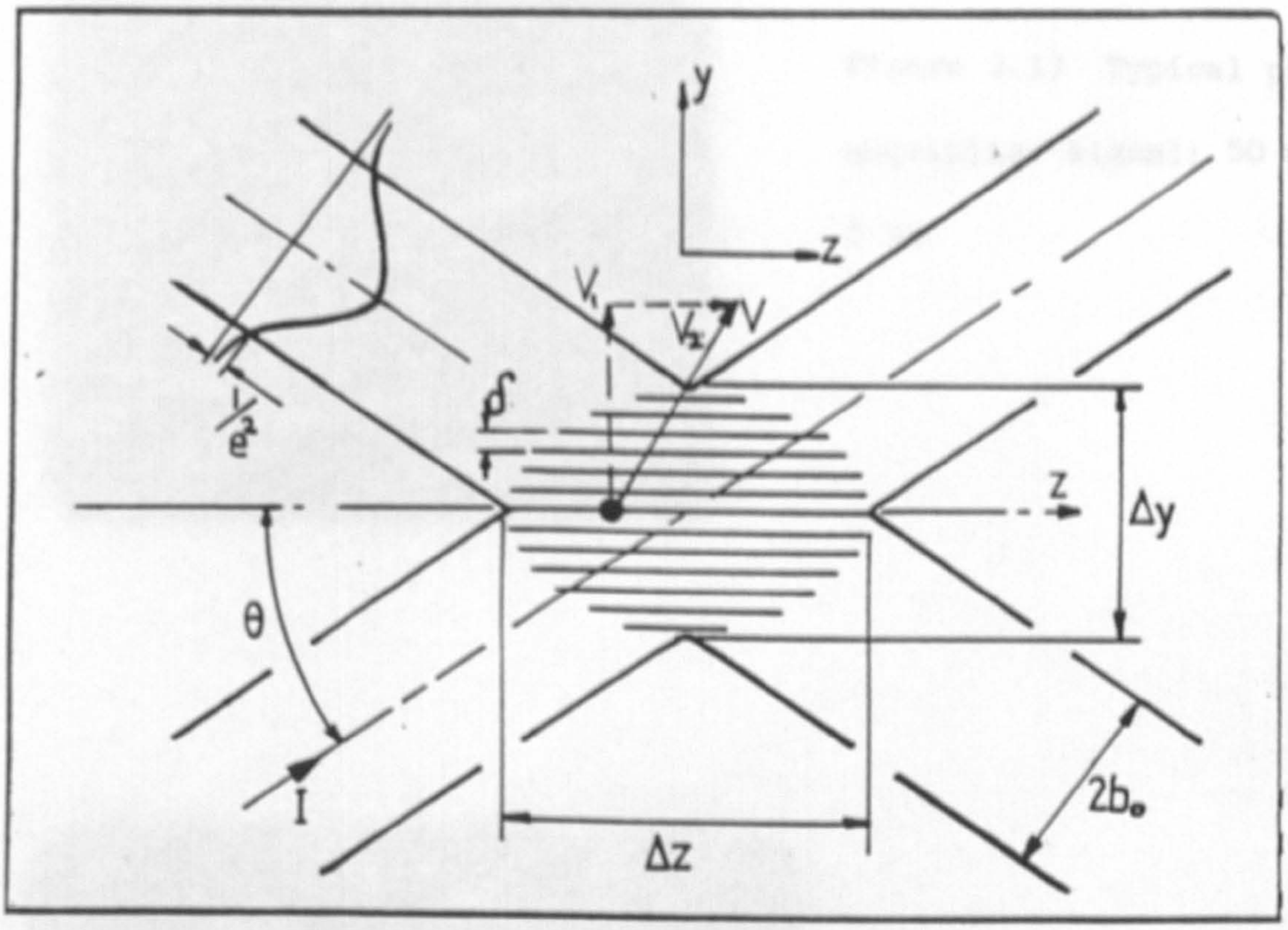

Figure 2.11 Beam intersection region

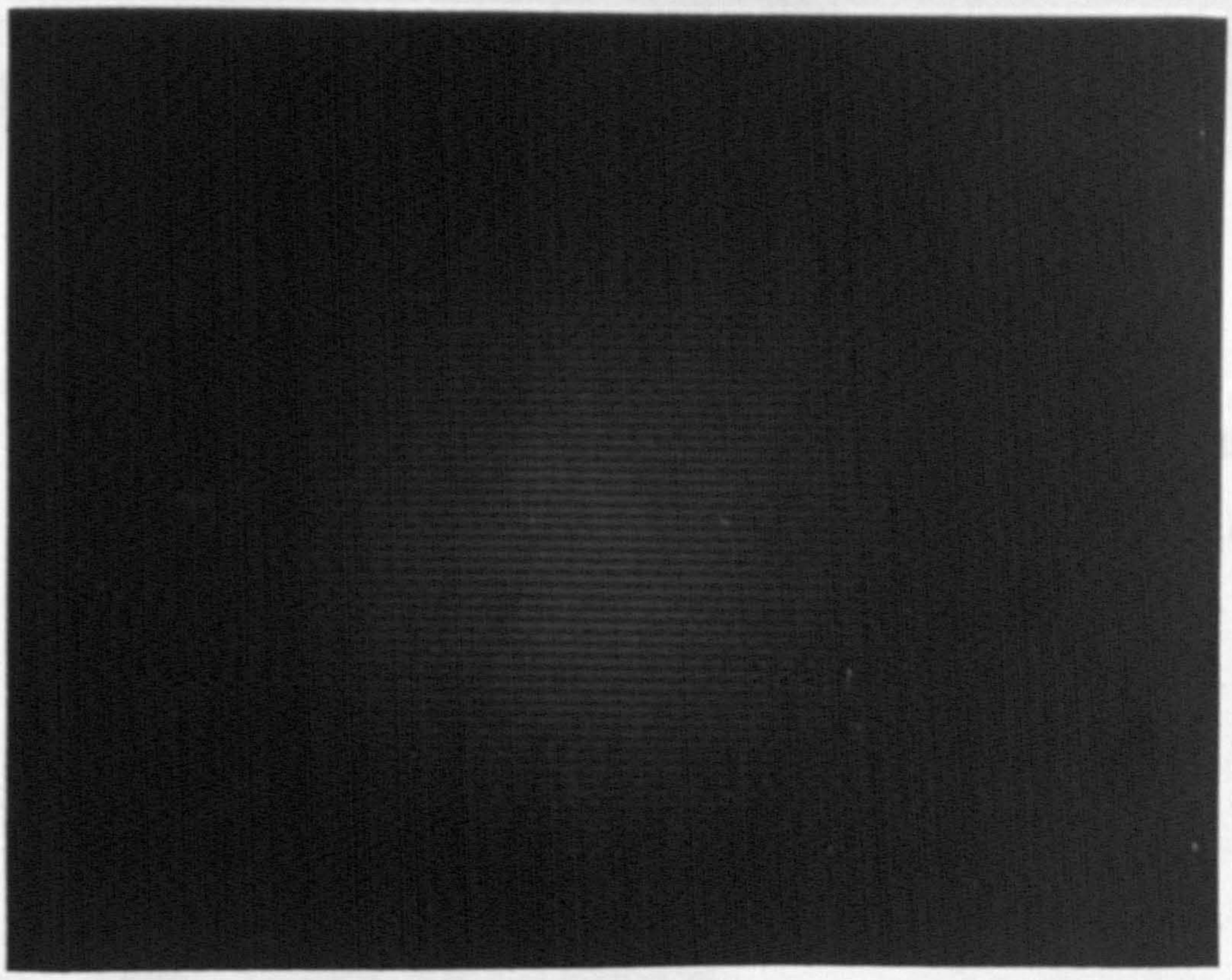

Figure 2.12 Photograph of fringes.

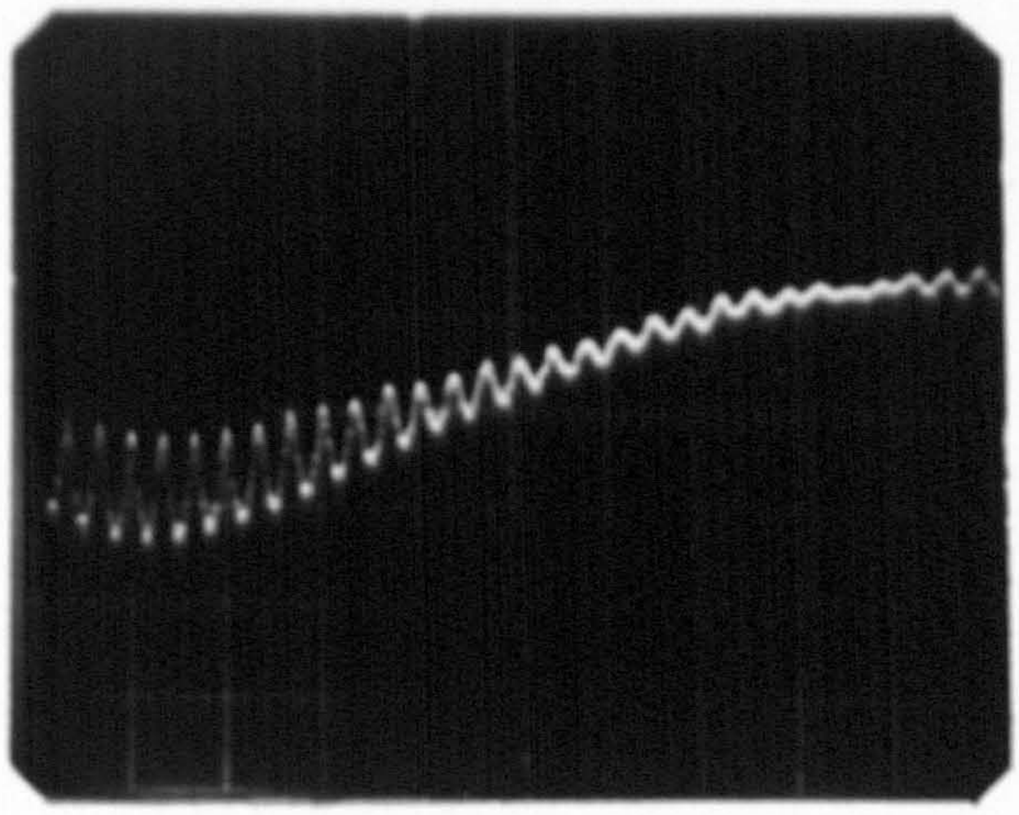

Figure 2.13 Typical photo-multiplier signal; 50 mV, 5 μs

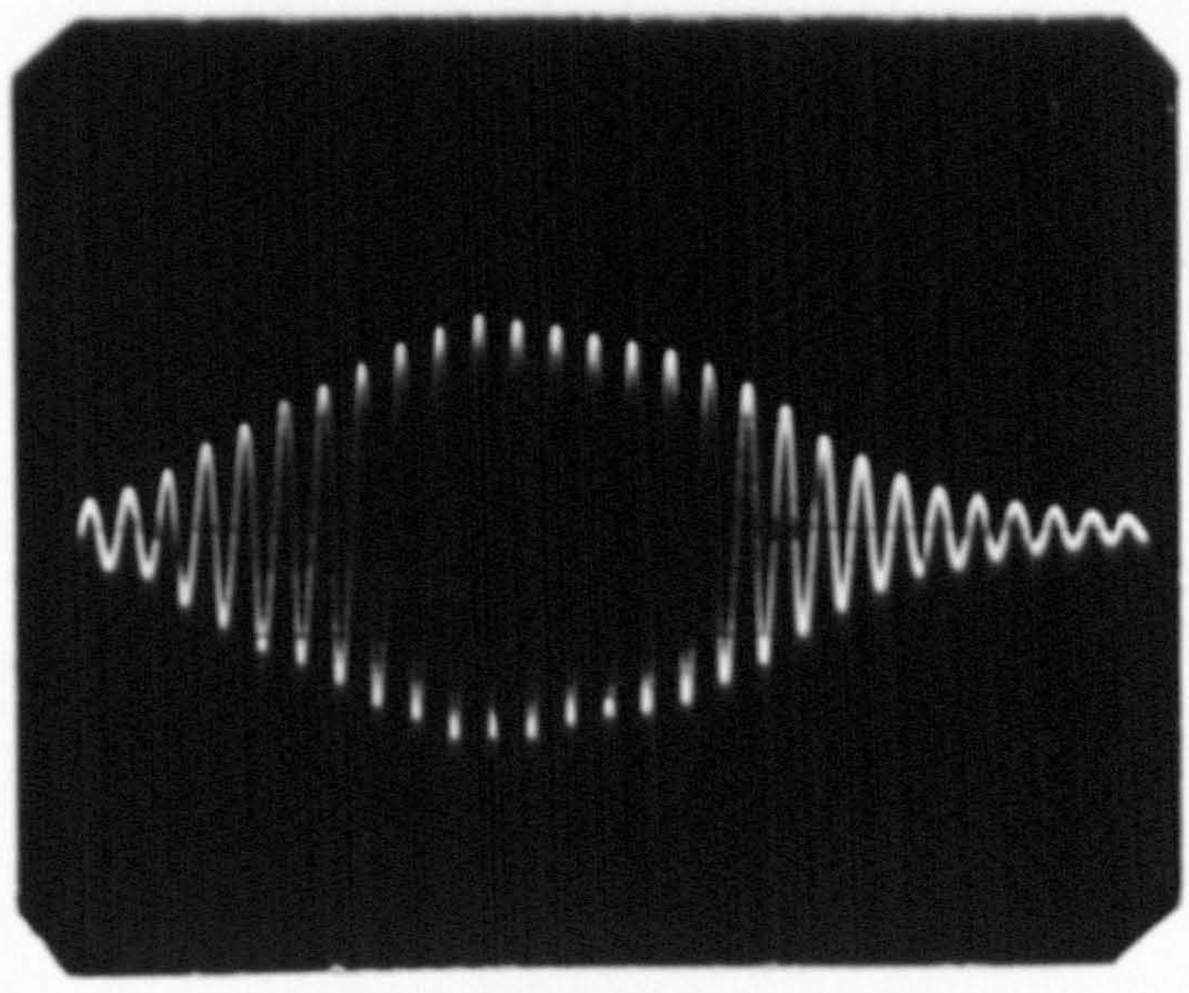

(a) (0.5 V, 0.2 μs)

Figure 2.14 High-pass filtered Doppler signals

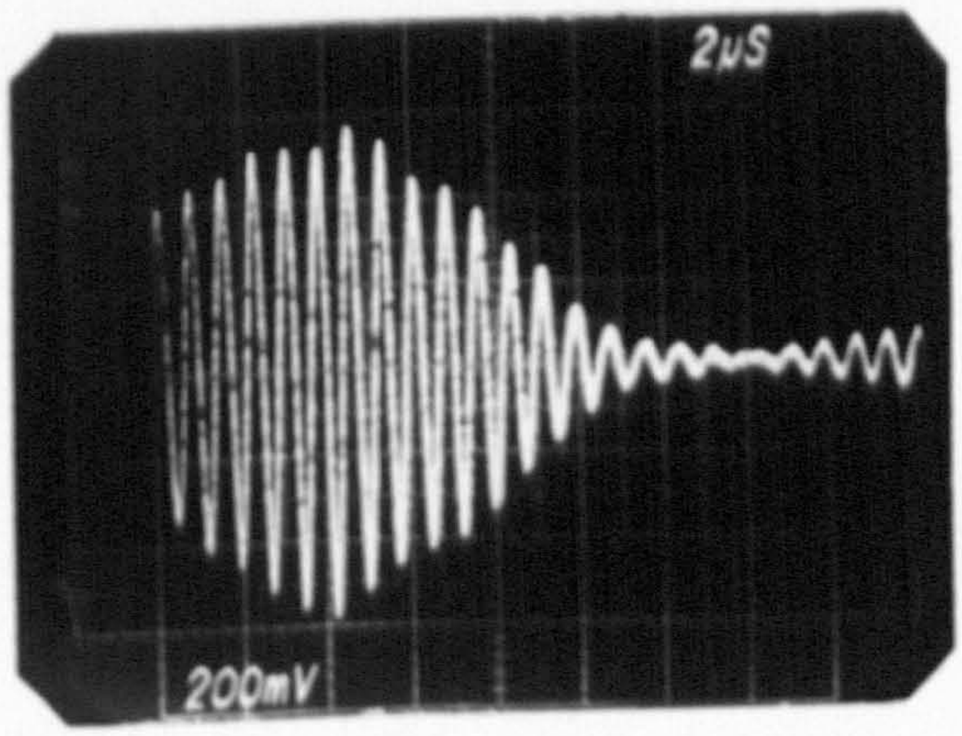

(b)

high pass filtering of the signal. High pass filtered signals are shown in figures 2.14(a) and (b).

The probe volume is an ellipsoid and its dimensions are usually defined as the region within which the combined intensity of the two beams is greater than $\frac{1}{e^2}$ or 0.135 of the peak intensity at the geometric centre of the crossover region. The $\frac{1}{e^2}$ probe volume is described [16,31] by the expression:

$$x^2 + y^2 \cos^2\theta + z^2 \sin^2\theta = b_o^2$$

where θ is the half-angle between the beams and b_o is the beam radius at the crossover. The x, y and z dimensions of the probe volume at the $\frac{1}{e^2}$ intensity limits are

$$\begin{aligned} \Delta x &= 2b_o \\ \Delta y &= \frac{2b_o}{\cos\theta} \\ \Delta z &= \frac{2b_o}{\sin\theta} \end{aligned} \qquad (2.16)$$

The number of fringes n_f in the probe volume is then

$$n_f = \frac{\Delta y}{\delta}$$

When the beams cross at the waists, as shown in figure 2.15, where the wavefronts are plane, the probe volume will be symmetrical and the interference fringes will be

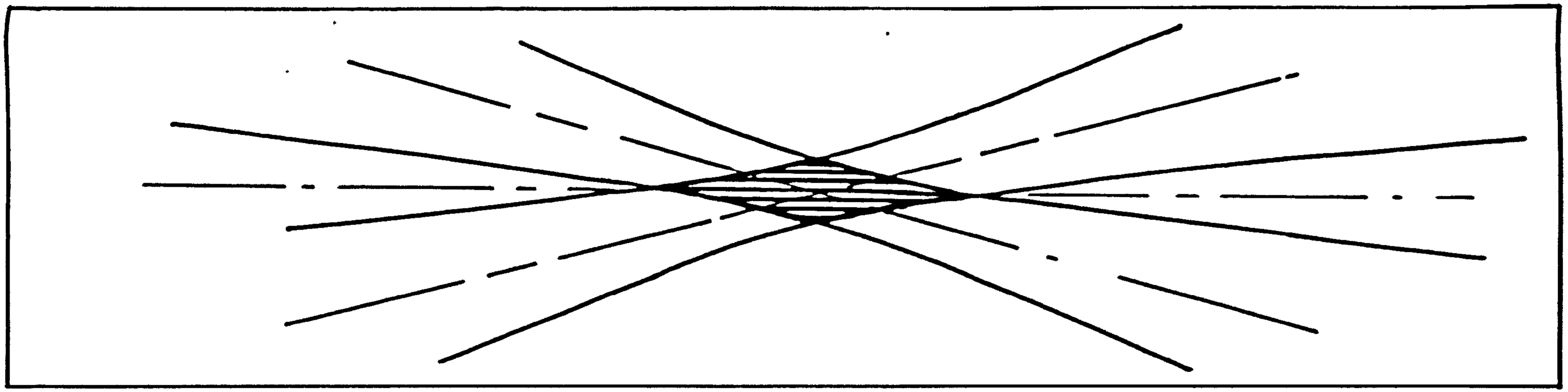

Figure 2.15 Beams crossing at the waist

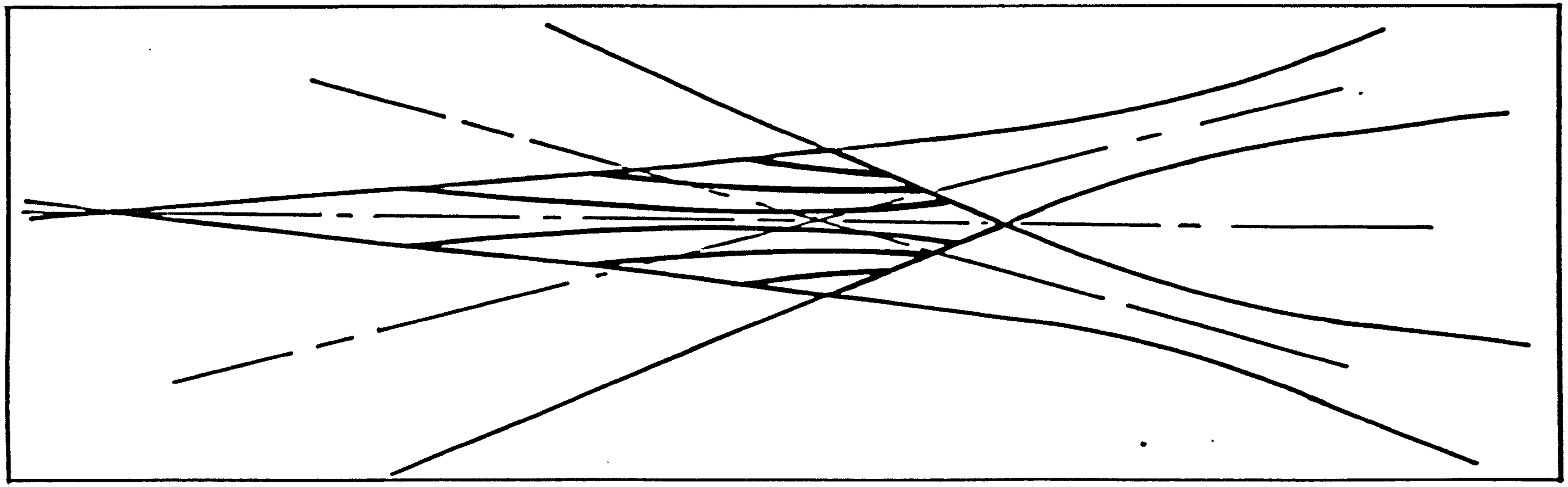

Figure 2.16 Crossover not coincident with beam waist

parallel. If the waists do not coincide with the cross-over region, as shown in figure 2.16, the result is an elongated probe volume and the fringes are no longer parallel [23].

2.5.3 Intensity distribution in the beam intersection region

Referring to figure 2.17, the intensity distribution I(x',y') in the Gaussian laser beam is given [32] by:

$$I(x',y') = \frac{2P_o}{\pi b_o^2} \exp\left(-2\,\frac{x'^2 + y'^2}{b_o^2}\right)$$

where P_o denotes total beam power

and b_o is the $\frac{1}{e^2}$ intensity radius.

For the intensity distribution along the z and y diagonals of the intersection region, the above expression can be transformed to

$$I'(z) = \frac{4P_o}{\pi b_o^2} \exp\left(-2\,\frac{z^2 \sin^2\theta}{b_o^2}\right) \qquad (2.17)$$

$$I'(y) = \frac{4P_o}{\pi b_o^2} \exp\left(-2\,\frac{y^2 \cos^2\theta}{b_o^2}\right) \qquad (2.18)$$

(note that the contribution from each beam is one half of this).

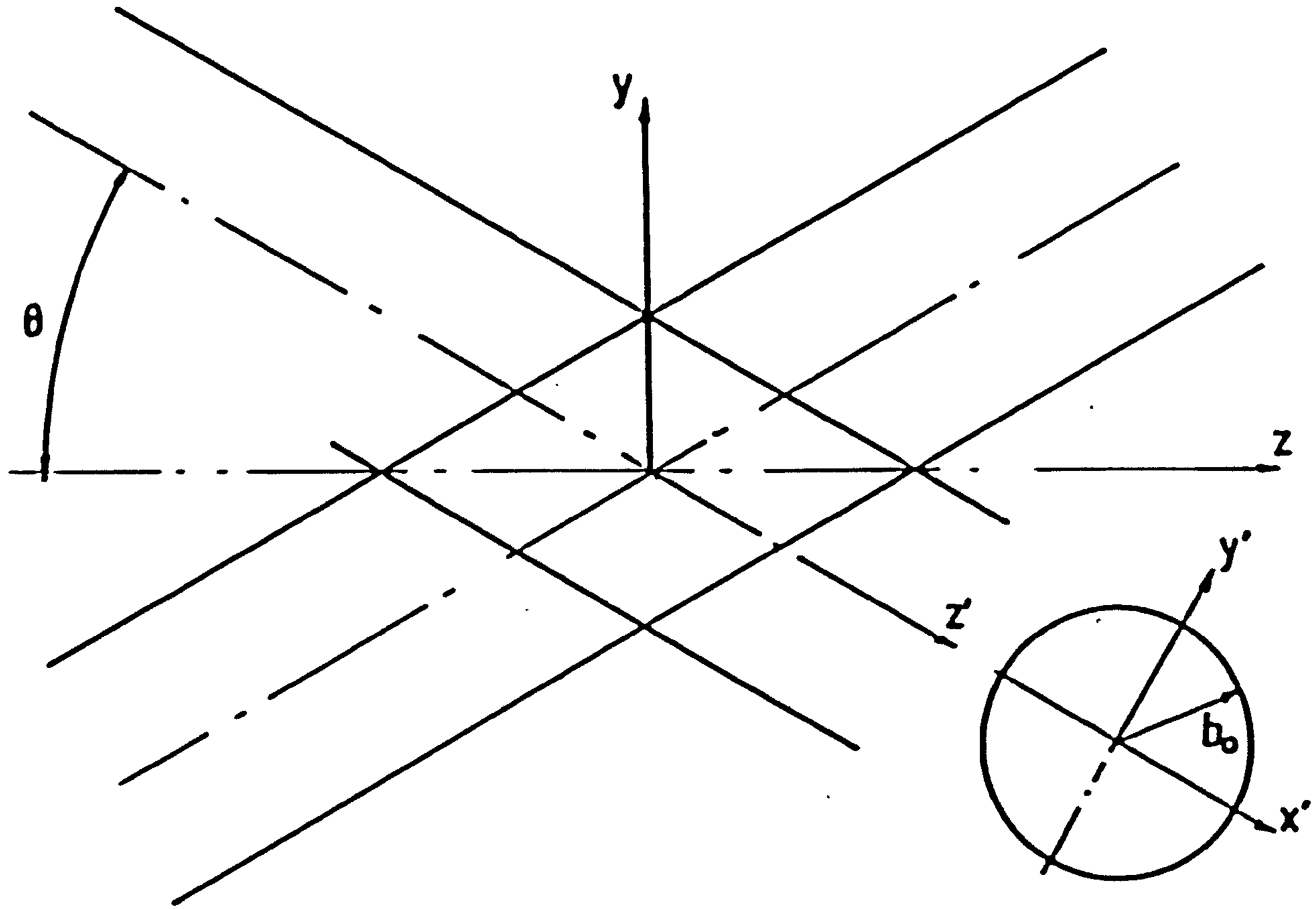

Figure 2.17 Coordinate system for intensity distribution in crossover region

Dividing equations (2.17) and (2.18) by I'(o), i.e. $\frac{4P_o}{\pi b_o^2}$, the nondimensionalised intensity distribution becomes

$$\frac{I'(z)}{I'(o)} = \left[\exp(-\ 2\ \sin^2\theta)\right]^{\frac{z^2}{b_o^2}} \qquad (2.19)$$

$$\frac{I'(y)}{I'(o)} = \left[\exp(-\ 2\ \cos^2\theta)\right]^{\frac{y^2}{b_o^2}} \qquad (2.20)$$

If the beams intersect at or near the waist, b_o is approximately constant along the diagonals. However if this is not the case account must be taken of the radius variation in equations (2.19) and (2.20).

2.6 DUAL BEAM LDA - ONE LENS SYSTEM

2.6.1 Imaging of beam waist and beam intersection

The position and size of the image of a Gaussian beam waist produced by a lens, are given by equations (2.14) and (2.15). When two coplanar beams pass through a converying lens, their point of intersection may be considered as a point source and its distance from the lens, real or virtual, is given by the geometric optics relationship

$$\frac{1}{u} + \frac{1}{v} = \frac{1}{f} \qquad (2.21)$$

where u and v are the object and image distances from the lens and are taken positive as shown in figure 2.18.

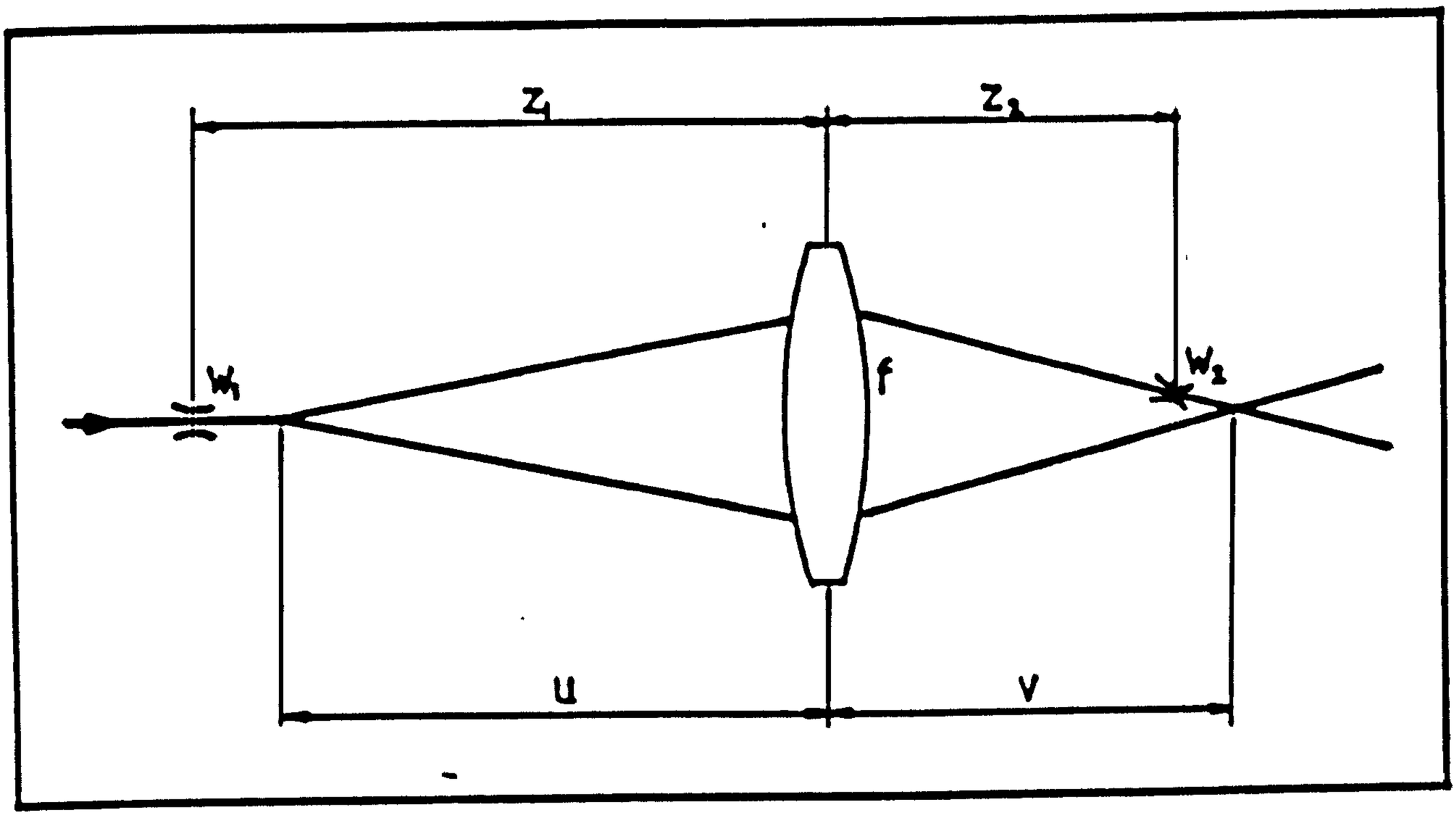

Figure 2.18 One lens system

It is noted that: as $u \to \infty$ the input beams are parallel, $u > 0$ gives converging beam directions. Furthermore we note that:

$$0 < \frac{u}{f} < 1; \quad \frac{v}{f} < 0, \qquad \text{virtual image}$$

$$1 < \frac{u}{f} < \infty; \quad \infty > v > 1, \quad \text{real image}$$

$$-\infty < \frac{u}{f} < 0; \quad 1 > \frac{v}{f} > 0, \quad \text{real image}$$

The above relationships between object and image are shown in figure 2.19.

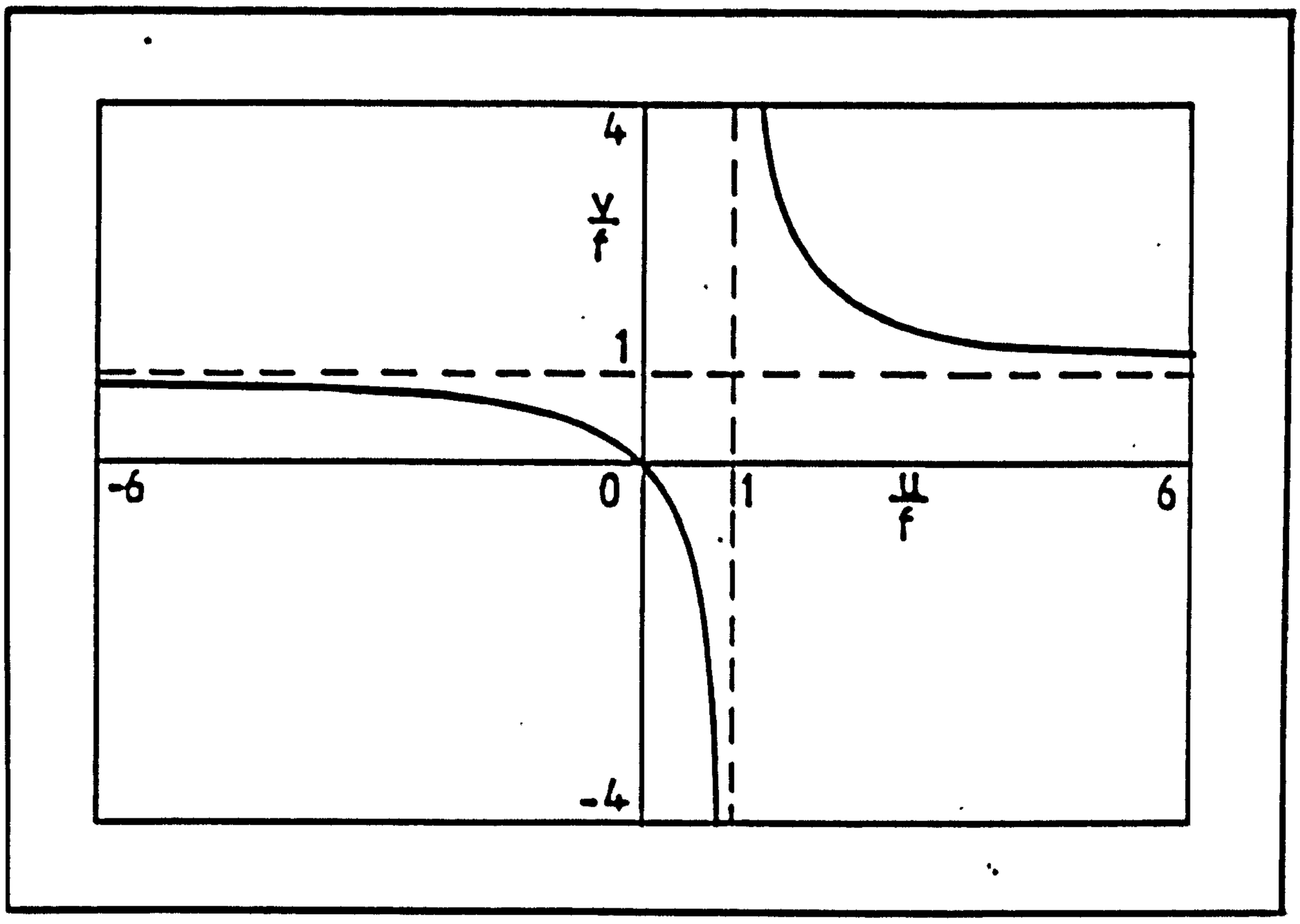

Figure 2.19 Image-object relationships

If a prism type beamsplitter is used, one can, with suitable adjustments obtain parallel, converging or diverging beams, whose intersection lies some distance away from the beam splitter, depending on the angle between the two beams. With a diffraction grating, used throughout this work as a beam splitter, only diverging beams are obtained and their intersection is real and lies on the grating. Other devices such as mirrors can be used to alter the directions of the beams according to requirements.

2.6.2 Conditions for coincidence of output waist and intersection

Coincidence of output beam waist and intersection is achieved if $\frac{v}{f} = \frac{z_2}{f}$. Hence after combining equations (2.13) and (2.20), one obtains

$$\left(\frac{u}{f} - 1\right)\frac{f}{f_F} = 1 + \frac{\left(\frac{z_1}{f} - 1\right)^2\left(\frac{f}{f_F}\right)^2}{\left(\frac{z}{f} - 1\right)\frac{f}{f_F}} \qquad (2.22)$$

Equation (2.22) relates the input variables f, z, w_1 and u for the case when the output variables v and z_2 are equal. Thus z_2 and u are related according to the geometric optics law

$$\left(\frac{z_2}{f} - 1\right) = \frac{1}{\left(\frac{u}{f} - 1\right)} \qquad (2.23)$$

Figure 2.20 shows graphs relating the various beam parameters. A summary of the main points regarding the relationships between the output variables z_2 and w_2 and the input variables z_1, w_1 and u is given in table 2.2. The following are noted:

(i) When $\frac{z_1}{f} = 1$, then $\frac{u}{f} \to \infty$. The input beam directions are parallel and $\frac{z_2}{f} = 1$.

(ii) When $1 < \frac{z_1}{f} < \infty$, $\frac{u}{f}$ takes values greater than 1, as shown in table 2.2. The input beam directions are diverging and since, as it can be seen from equation

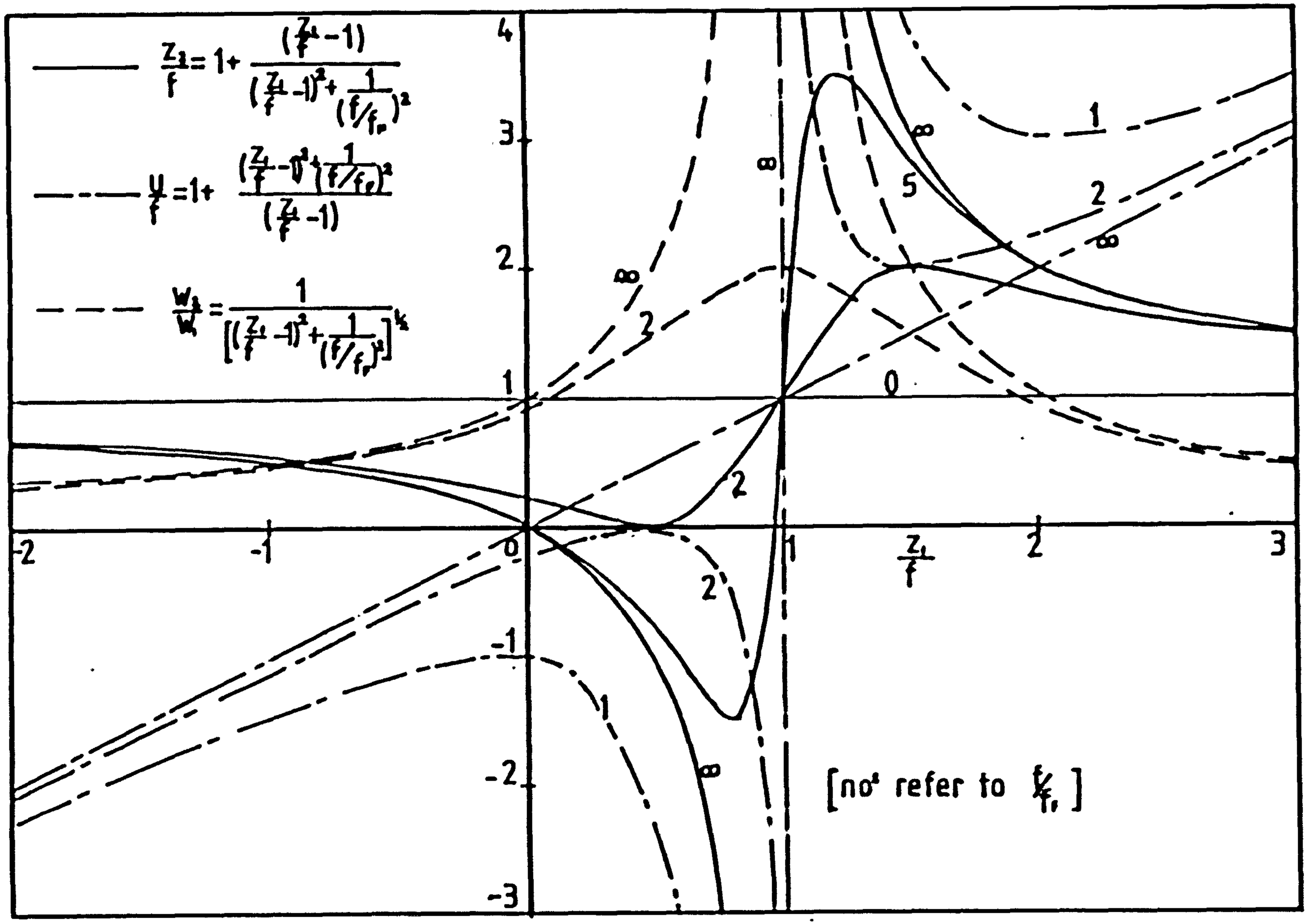

Figure 2.20 Graphs of $\frac{Z_2}{f}$, $\frac{u}{f}$ and $\frac{w_2}{w_1}$ against $\frac{Z_1}{f}$, for different $\frac{f}{f_p}$.

$\frac{z_1}{f}$	$\frac{z_2}{f}$	$\frac{u}{f}$	$\frac{w_2}{w_1}$
$-\infty$	1	$-\infty$	0
$1 - \frac{1}{\frac{f}{f_P}}$	$1 - \frac{1}{2}\frac{f}{f_P}$ (MIN)	$1 - \frac{2}{\frac{f}{f_P}}$ (MAX)	$\frac{\frac{f}{f_P}}{\sqrt{2}}$
1	1	∞	$\frac{f}{f_P}$ (MAX)
$1 + \frac{1}{\frac{f}{f_P}}$	$1 + \frac{1}{2}\frac{f}{f_P}$ (MAX)	$1 + \frac{2}{\frac{f}{f_P}}$ (MIN)	$\frac{\frac{f}{f_P}}{\sqrt{2}}$
∞	1	∞	0

Table 2.2 Relationships between input and output variables

(2.22), $\left|\frac{u}{f}\right| > \left|\frac{z_1}{f}\right|$, this arrangement requires that the input beam intersection be located before the input waist. This condition cannot be met by beam splitters producing real intersection, such as diffraction gratings.

(iii) When $0 < \frac{z_1}{f} < 1$, then $\frac{u}{f}$ takes values less than 1. The range $0 < \frac{u}{f} < 1$ gives virtual image. In the range $\frac{u}{f} < 0$ the input beams are converging and $\frac{v}{f} < 1$.

(iv) The case when $\frac{z_1}{f} < 0$ is of no practical use

In practice, case (i) is not suited to small focal length lenses ($f_1 = z_1$), the limit being the physical dimensions of the optical components between the lens and the input waist in the laser resonator. Case (ii) offers the widest choice of focal lengths. Case (iii) is also limited to large focal length lenses. The optical arrangements corresponding to cases (i) to (iii) above are shown in figure 2.21. The main difference between the three arrangements lies in the distance of the intersection image from the lens. In the parallel beam configuration, $\frac{v}{f} = 1$, in the diverging and converging beam arrangements $\frac{v}{f} > 1$ and $\frac{v}{f} < 1$ respectively.

With reference to figure 2.20 the following observations are made:

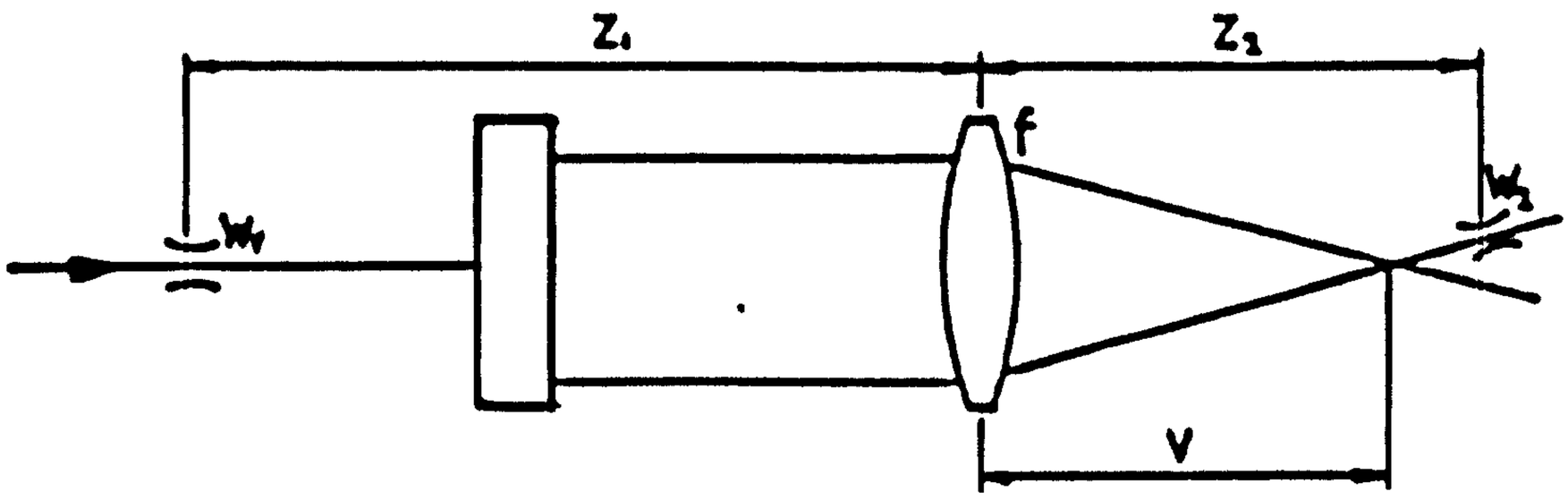

(a) parallel input beams

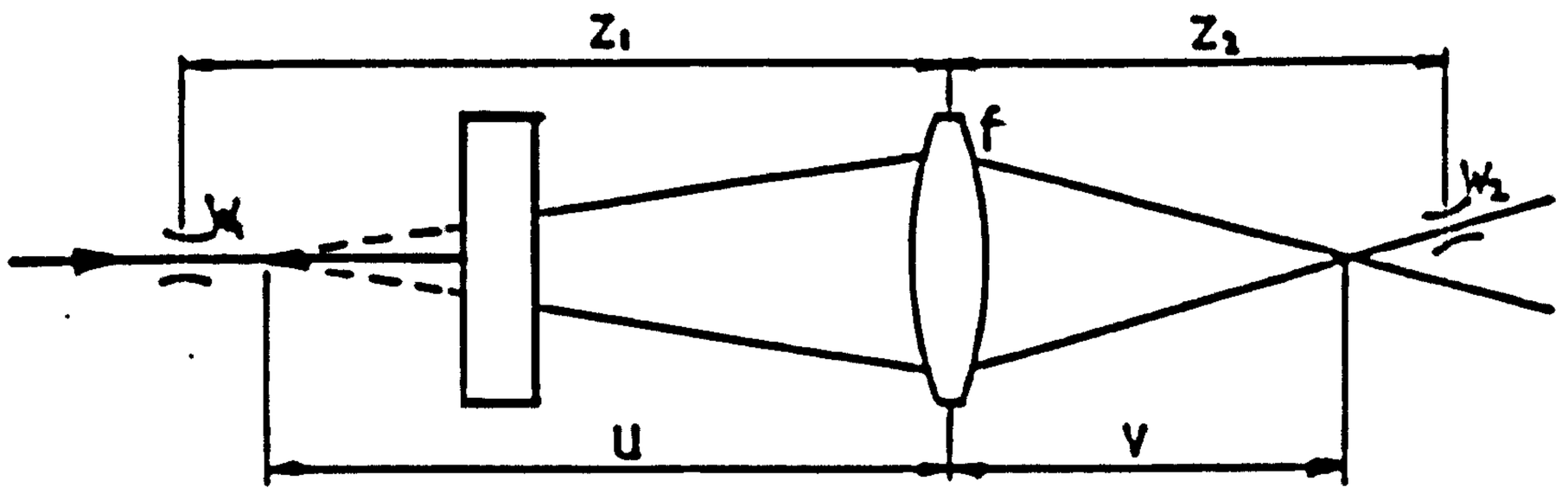

(b) diverging input beams

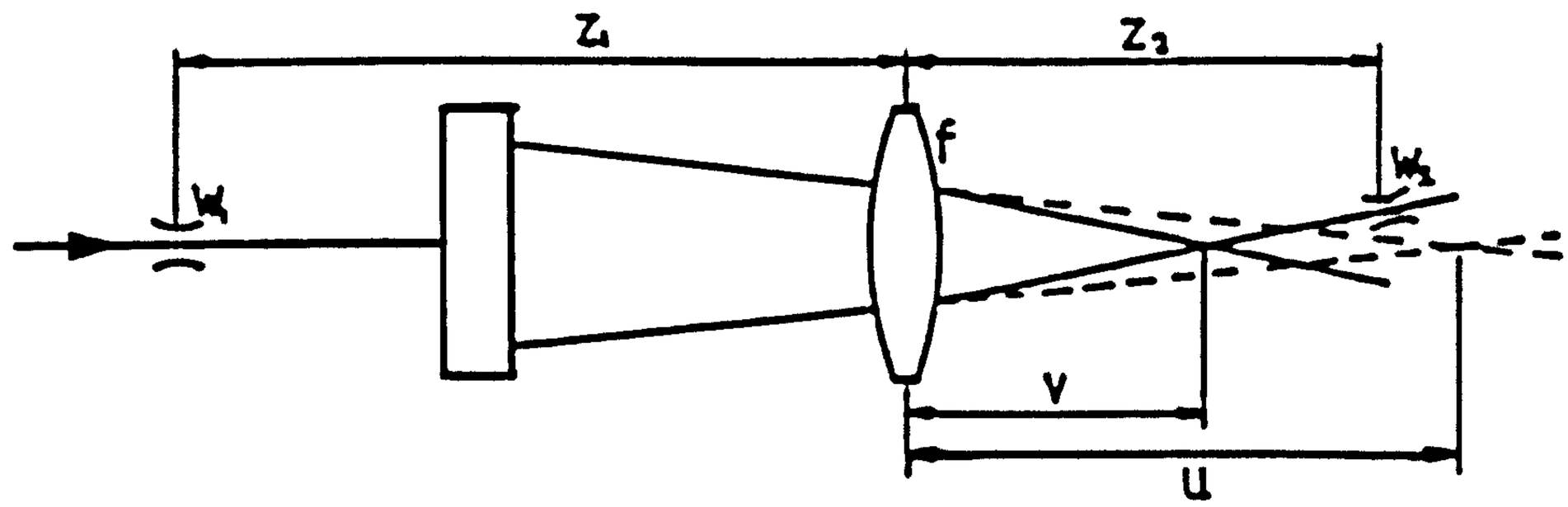

(c) converging input beams

Figure 2.21 One lens system arrangements

1. For every value of $\frac{z_2}{f} > 1$ there are two values of $\frac{z_1}{f}$, between 1 and ∞ and one (double root) when $\frac{z_2}{f}$ is a maximum.
2. For every value of $\frac{z_2}{f} < 1$ there are two values of $\frac{z_1}{f}$ between 1 and -∞ and a double value when $\frac{z_2}{f}$ is a minimum.
3. For every value of $\frac{w_2}{w_1}$ there are two values of $\frac{z_1}{f}$ displaced symmetrically about $\frac{z_1}{f} = 1$, where $\frac{w_2}{w_1}$ is a maximum. It is also noted that for any particular value of $\frac{z_2}{f}$ there is only one value for $\frac{w_2}{w_1}$.

Radial diffraction gratings have been used as beam splitters throughout this work and thus we are mainly concerned with case (ii), i.e. diverging input beams. As already mentioned it is not possible to make $\frac{u}{f} > \frac{z_1}{f}$, in order to achieve coincidence when using a diffraction grating as beam splitter, in a single lens system. As an example of the difficulties encountered in the setting up of the optics, let z_1 = 60 cm and f = 15 cm; then $\frac{z_2}{f}$ = 1.106 and for coincidence $\frac{u}{f}$ must be 10.55. If the lens focuses the two beams this implies that the input intersection must lie about 1.6 m in front of the lens which is not possible with a diffraction grating. If now one sets u = 25 cm, then $\frac{v}{f}$ = 2.5 and this gives a distance between output waist and intersection of 21 cm.

It was due to this difficulty in achieving coincidence that the effect of adding a second lens to the optical system

was investigated.

2.7 DUAL BEAM LDA - TWO LENS SYSTEM

2.7.1 Introduction

It was shown in paragraph 2.7 that in a one lens system, when the input beams are parallel, small focal length lenses cannot be used since $\frac{z_1}{f}$ must be equal to 1. In the case of converging beams $\frac{z_1}{f}$ must be less than unity, which also prohibits the use of small focal length lenses. It was also pointed out that in the case of diverging beams, coincidence could not be achieved when using a diffraction grating as beam splitter. In order to overcome these limitations a two lens arrangement was proposed. In this arrangement an additional lens is placed before the beam splitter. Such a system is shown in figure 2.22 where w_o denotes the input waist radius to the first lens. The first lens produces a new beam waist, whose position and size can be adjusted by suitable choice of focal length so that the requirement for coincidence, $\left|\frac{u}{f}\right| > \left|\frac{z_1}{f}\right|$, may be met. The effect of this lens is to reduce the value of w_1 and hence increase the value of $\frac{f}{f_F}$ in equation (2.14). It is seen from figure 2.20 that as $\frac{f}{f_F}$ increases, $\frac{u}{f}$ tends towards $\frac{z_1}{f}$ asymptotically and this allows the input waist to the second lens to be located near the input intersection. In the case when a radial diffraction grating is being used, this gives the added benefit that the incident

beam on it has a reduced spot size and consequently the ellipticity of the output beam cross section is reduced [33,34]

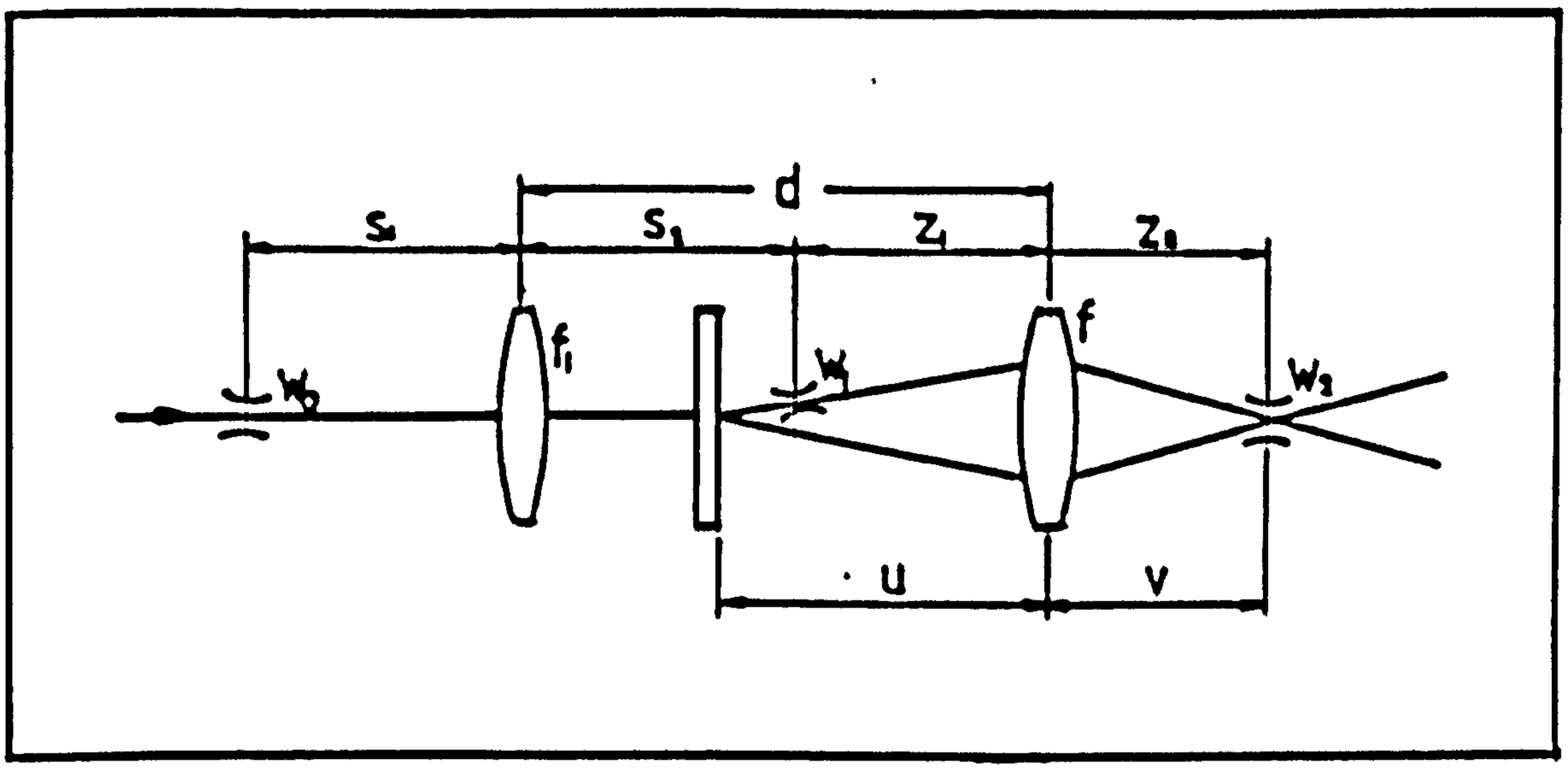

Figure 2.22 Two lens system geometry

2.7.2 Imaging of beam waist

In the two lens system shown in figure 2.22 equations (2.12 and (2.13) apply to the second lens. For the first lens two similar expressions apply:

$$\frac{w_1}{w_0} = \frac{f_1}{\left[(s_1 - f_1)^2 + \left(\frac{\pi w_0^2}{\lambda}\right)^2\right]^{\frac{1}{2}}} \qquad (2.24)$$

$$\frac{s_2}{f_1} = 1 + \frac{(s_1 - f_1)f_1}{(s_1 - f_1)^2 + \left(\frac{\pi w_0^2}{\lambda}\right)^2} \qquad (2.25)$$

By eliminating the intermediate parameters s_2, z_1 and w_1 the output variables z_2 and w_2 can be expressed in terms of the input variables s_1, w_o, f_1 f and d, where d = $s_2 + z_1$, as follows:

$$\frac{w_2}{w_o} = \frac{w_o}{\left[\left\{\left(\frac{d}{f} - 1\right) - \frac{s_2}{f}\right\}^2 + \left(\frac{f_F}{f}\right)^2\left(\frac{w_1}{w_o}\right)^4\right]^{\frac{1}{2}}} \qquad (2.26)$$

$$\frac{z_2}{f} = 1 + \frac{\left(\frac{d}{f} - 1\right) - \frac{s_2}{f}}{\left\{\left(\frac{d}{f} - 1\right) - \frac{s_2}{f}\right\}^2 + \left(\frac{f_F}{f}\right)^2\left(\frac{w_1}{w_o}\right)^4} \qquad (2.27)$$

where s_2 and w_1 are given by equations (2.25) and (2.24).

2.7.3 Conditions for coincidence of output waist and intersection

As in the case of the single lens system if we set $\frac{v}{f} = \frac{z_2}{f}$ in equations (2.21) and (2.27) we obtain

$$\left(\frac{u}{f} - 1\right) = \frac{\left\{\left(\frac{d}{f} - 1\right) - \frac{s_2}{f}\right\}^2 + \left(\frac{f_F}{f}\right)^2\left(\frac{w_1}{w_o}\right)^4}{\left(\frac{d}{f} - 1\right) - \frac{s_2}{f}} \qquad (2.28)$$

By suitable rearrangements, equations (2.28) as well as equations (2.26) and (2.27) can be reduced to forms which

can be represented by the graphs in figure 2.20, although due to their complexity direct interpretation of these three expressions is not possible as in the case of their single lens counterparts. For practical purposes, numerical solutions were obtained in the following manner: choosing suitable ranges of values for f_1, s_1, f and d, equations (2.26), (2.27) and (2.28) were solved by computer for w_2, z_2 and u. The choice of the input parameters depended on available optical components and practical considerations, such as overall dimensions of the set up. Since a diffraction grating was used as beam splitter, only the case of diverging input beams to the second lens and $u < d$ was examined. Several solutions were tested and in all cases it was found that the output beam waists were displaced slightly from the output beam intersection. This was attributed to low accuracy of measurement of the distances between the optical components using a ruler graduated in mm, possible difference between the actual and nominal focal lengths of the lenses, non-paraxial focusing of the beams by the second lens and probable error in estimating the location of the beam waist in the laser resonator. This problem was remedied by a small readjustment of the position of the diffraction grating. The size of the output waists as well as their location relative to the beam intersection were determined using the 'power ratio' technique [32], see section 2.8.

2.7.4 Practical considerations

In a practical laser Doppler anemometer some of the variables are limited to a particular range of values, dictated by the following requirements:

(i) Positive input waist to lens distance, i.e. $\frac{z_2}{f} > 0$.

It can be shown from equation (2.13) that when $\frac{z_2}{f} = 0$, then

$$\frac{z_1}{f} = \frac{1 \pm \sqrt{1 - \left(\frac{2}{\frac{f}{f_F}}\right)^2}}{2} .$$

Thus $\frac{z_2}{f} < 0$ if $\frac{f}{f_F} > 2$ in the range of values of $\frac{z_1}{f}$ given by the above expression. This condition also satisfies the requirement for a real beam intersection image ($v > 0$).

(ii) It is usually required that $\frac{w_2}{w_1} < 1$. It is noted that $\frac{w_2}{w_1} < 1$ if $\frac{f}{f_F} < 1$ (all $\frac{z_1}{f}$) and also if $\frac{f}{f_F} > 1$ and $\frac{z_1}{f}$ lies outside the range of values given by

$$1 \pm \sqrt{1 - \frac{1}{\left(\frac{f}{f_F}\right)^2}}$$

(iii) The minimum value of z_1 in a single lens system, or s_1 in the case of a two lens system, is determined by the actual physical size of the laser.

(iv) The lens aperture, 2L, the value of u, the angle between the input beams, the value of z_2 and the angle between the output beams must all be taken

into account when designing a laser anemometer. Referring to figure 2.23, ϕ and θ are the half-angles between the input and output beams, where $\tan \phi = \frac{L}{u}$ and $\tan \theta = \frac{L}{v}$. Angles θ and ϕ must be such that L is as small as possible if undesirable aberrations are to be avoided.

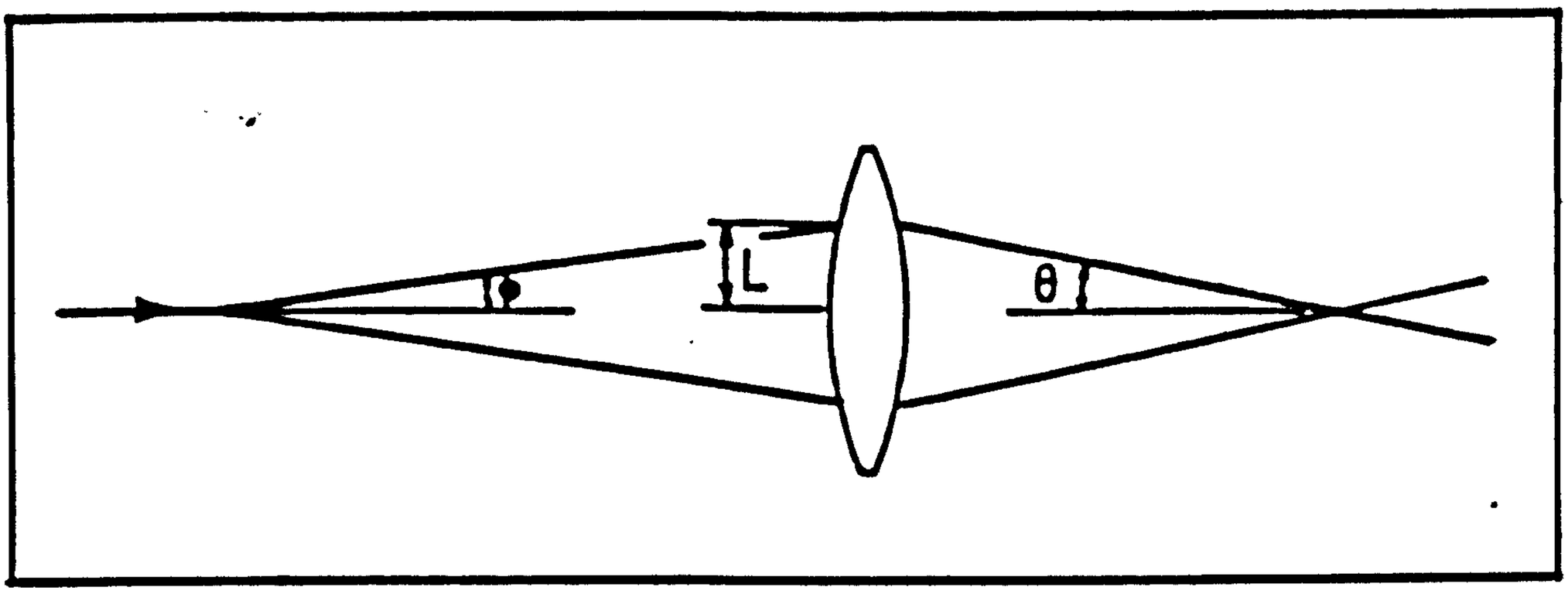

Figure 2.23 Focusing lens parameters

2.8 BEAM DIAMETER MEASUREMENT

2.8.1 Introduction

As it was pointed out in section 2.5.1 it is important to make the waists of the focused beams coincident with the beam intersection. A related problem is to know the physical dimensions of the beam crossover region, which is important when making biasing corrections in flows with velocity gradients [35]. To achieve this, a method was developed for measuring laser beam diameters and also determining the exact position of the beam waist.

As seen from equation (2.8) the divergence of a laser beam increases in proportion to the inverse of the beam waist radius. In the vicinity of the waist the beam radius can be considered constant; when two beams cross at the waists the probe volume is symmetric. At that point also the beams are plane waves and the resulting interference planes are parallel. If two beams intersect some distance away from the waist, the intersection region is no longer symmetric, due to a change in beam radius; the waves are no longer plane and the result is interference plane gradients [36]. This has been demonstrated in figures 2.15 and 2.16; the difference between the shapes and sizes of the probe volumes is marked.

2.8.2 Measurement of beam diameter, power ratio method

A technique for measuring the spotsize of Gaussian beams [37] was adapted and applied to the location and measurement of the beam waist. The theoretical basis of the method is as follows:

The intensity I(x,y) of a Gaussian beam is given [38,39] by:

$$I(x,y) = \frac{2p_o}{\pi b_o^2} \exp\left(-2\,\frac{x^2+y^2}{b_o^2}\right) \qquad (2.29)$$

where p_o denotes the total beam power and b_o the beam radius at the $\frac{1}{e^2}$ intensity points; x and y are normal to the beam axis.

The beam power is $\iint I(x,y)\, dx\, dy$.

If, as shown in figure 2.24 a thin wire of radius a is placed symmetrically about a diameter of the beam cross section, the detected beam power becomes a minimum, P_m and is given by

$$P_m = 2\,\frac{2P_o}{\pi r^2}\int_{x=a}^{x=\infty}\int_{y=-\infty}^{y=\infty} \exp\left(-2\,\frac{x^2+y^2}{b_o^2}\right) dy\, dx \qquad (2.30)$$

Letting $t^2 = \frac{2y^2}{b_o^2}$ and noting that $\int_0^\infty e^{-t^2}\, dt = \frac{\sqrt{\pi}}{2}$, equation (2.30) can be reduced to

$$\frac{P_m}{P_o} = \frac{4}{b_o\sqrt{2\pi}}\int_a^\infty \exp\left(-\frac{2x^2}{b_o^2}\right) dx$$

or
$$\frac{P_m}{P_o} = \frac{2}{\sqrt{\pi}}\int_{\frac{a}{b_o}\sqrt{2}}^\infty e^{-z^2}\, dz \qquad (2.31)$$

where $z^2 = \frac{2x^2}{b_o^2}$

Also $\frac{P_m}{P_o} = 1 - \frac{2}{\sqrt{\pi}}\int_0^{\frac{a}{b_o}\sqrt{2}} e^{-z^2}\, dz = 1 - \mathrm{erf}(\frac{a}{b_o}\sqrt{2})$

$$\frac{P_m}{P_o} = \mathrm{erfc}\,(\tfrac{a}{b_o}\sqrt{2}) \qquad (2.32)$$

Using tabulated values for the error function the graph in figure 2.25 was constructed. With P_m and P_o measured, b_o can be calculated for a given value of a.

Alternatively one can use tabulated values for percentage points of the normal distribution. In this case letting $\frac{x^2}{2} = z^2$ in equation (2.31) one obtains

$$\frac{1}{2}\frac{P_m}{P_o} = \frac{1}{\sqrt{2\pi}} \int_{\frac{2a}{b_o}}^{\infty} \exp\left(-\frac{x^2}{2}\right) dx$$

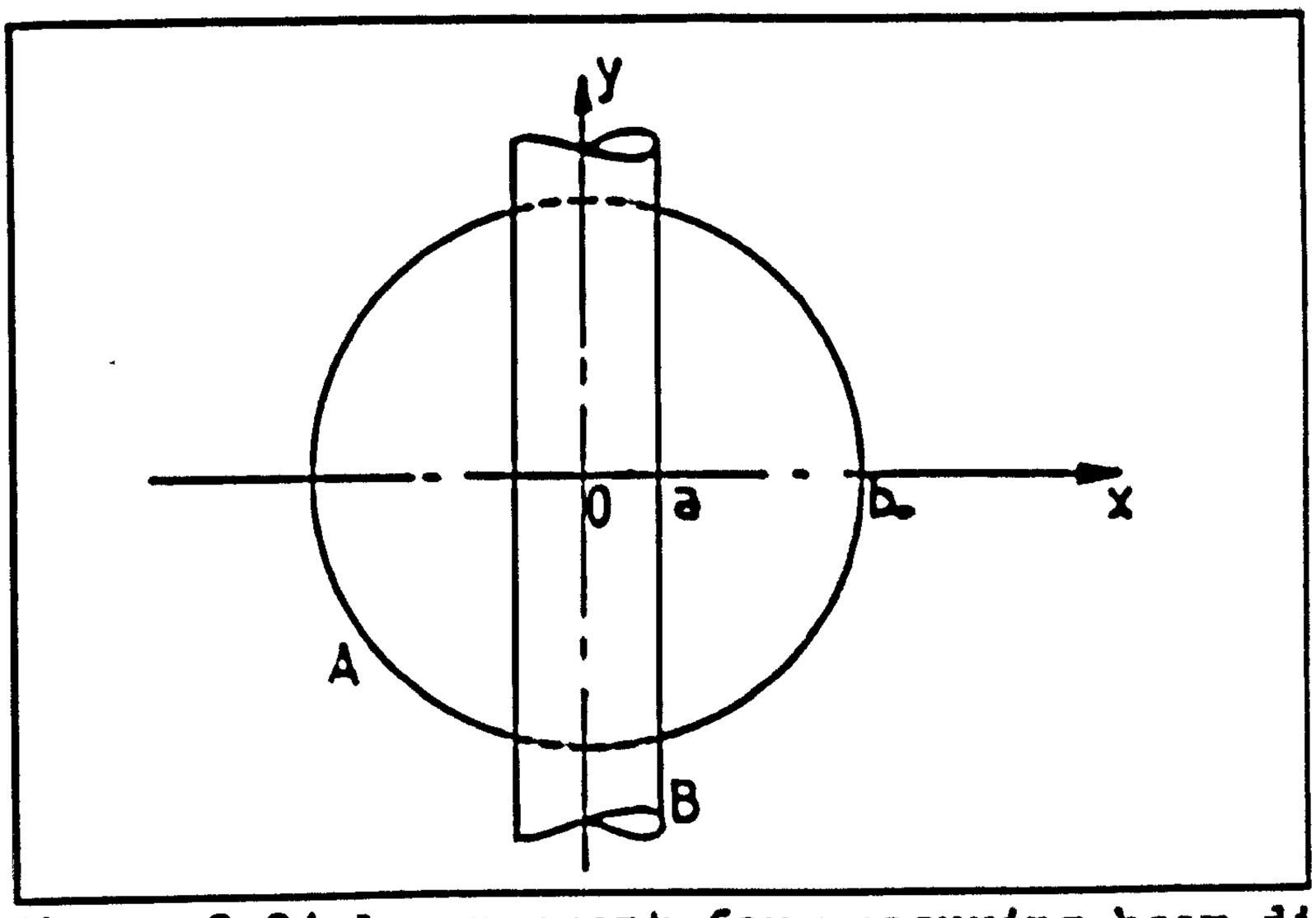

Figure 2.24 Arrangement for measuring beam diameter:

A: beam cross section, B: wire.

Statistical tables contain tabulated values for α and u_α, where $\alpha = \frac{1}{\sqrt{2\pi}} \int_{u_\alpha}^{\infty} \exp\left(-\frac{x^2}{2}\right) dx$.

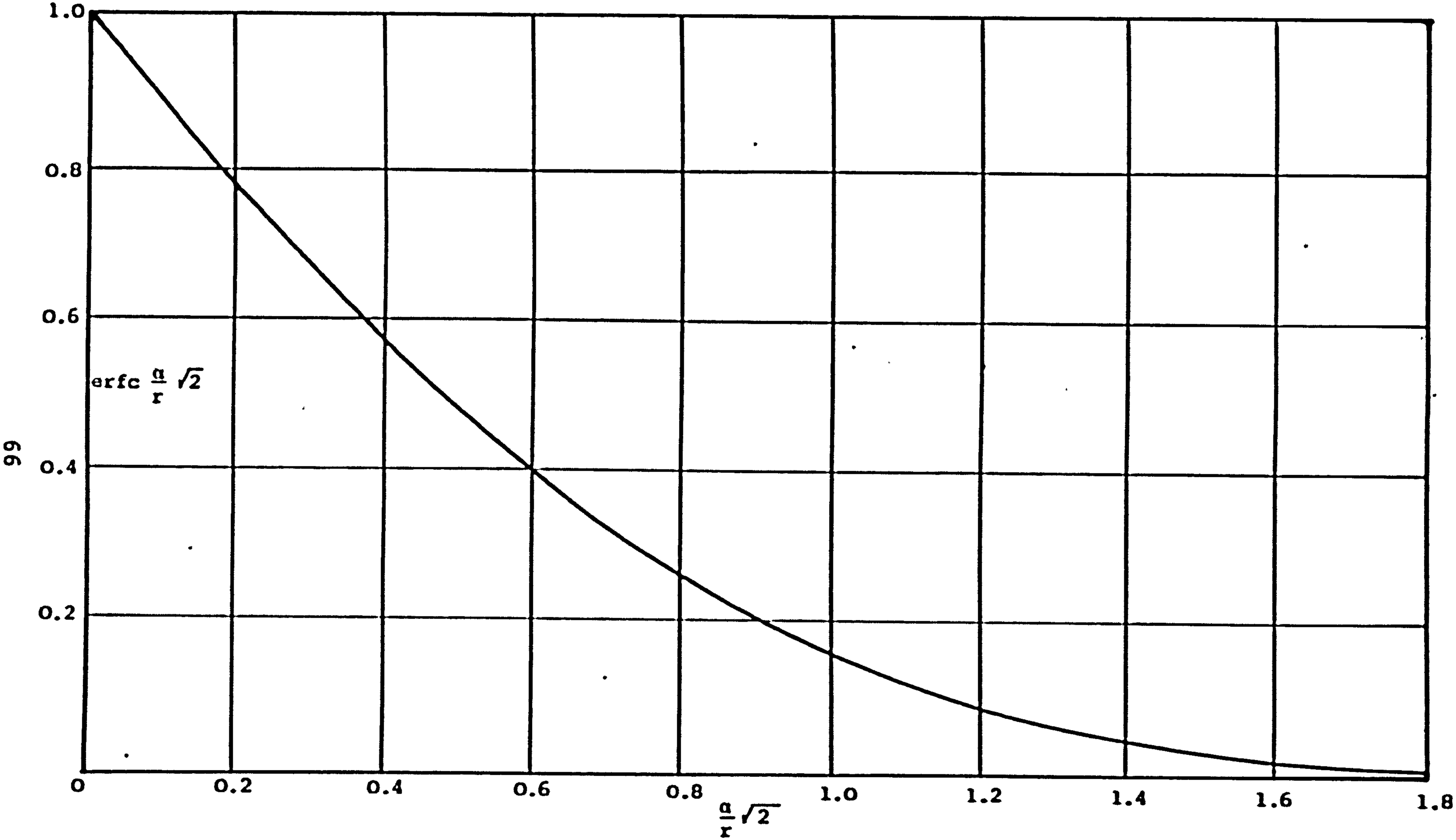

Figure 2.25 The complementary error function, equation (2.32)

2.8.3 Experimental determination of unfocused beam dimensions

(a) Pinhole method

The object of this investigation was to check whether the intensity distribution of the laser beam was Gaussian and to measure the beam diameter for later comparison.

The traditional method of scanning the beam with a pinhole was used. The distance between the laser exit and the pinhole was 7.1 m; the beam cross section appeared as a large and clearly defined disc, with very little background light from the laser plasma tube. The pinhole, of 0.69 mm diameter, was drilled in a thin steel disc on which concentric circles and two diameters at right angles to each other were scribed, to assist in traversing the pinhole along a diameter of the beam cross section. The steel disc was mounted on a large area photodiode so that the pinhole was positioned centrally to it and the whole arrangement was fixed on a translation stage with micrometric movement. With this set up measurements of laser power were made along a diameter of the beam cross section using a laser power monitor (Scientifica and Cook Electronics Ltd.), with an analogue display. The readings were divided by the pinhole area and non-dimensionalised with the estimated peak value.

The results are shown in figure 2.26 with a theoretical Gaussian profile superimposed on them. The non-dimensionalised expression for the theoretical curve is derived from

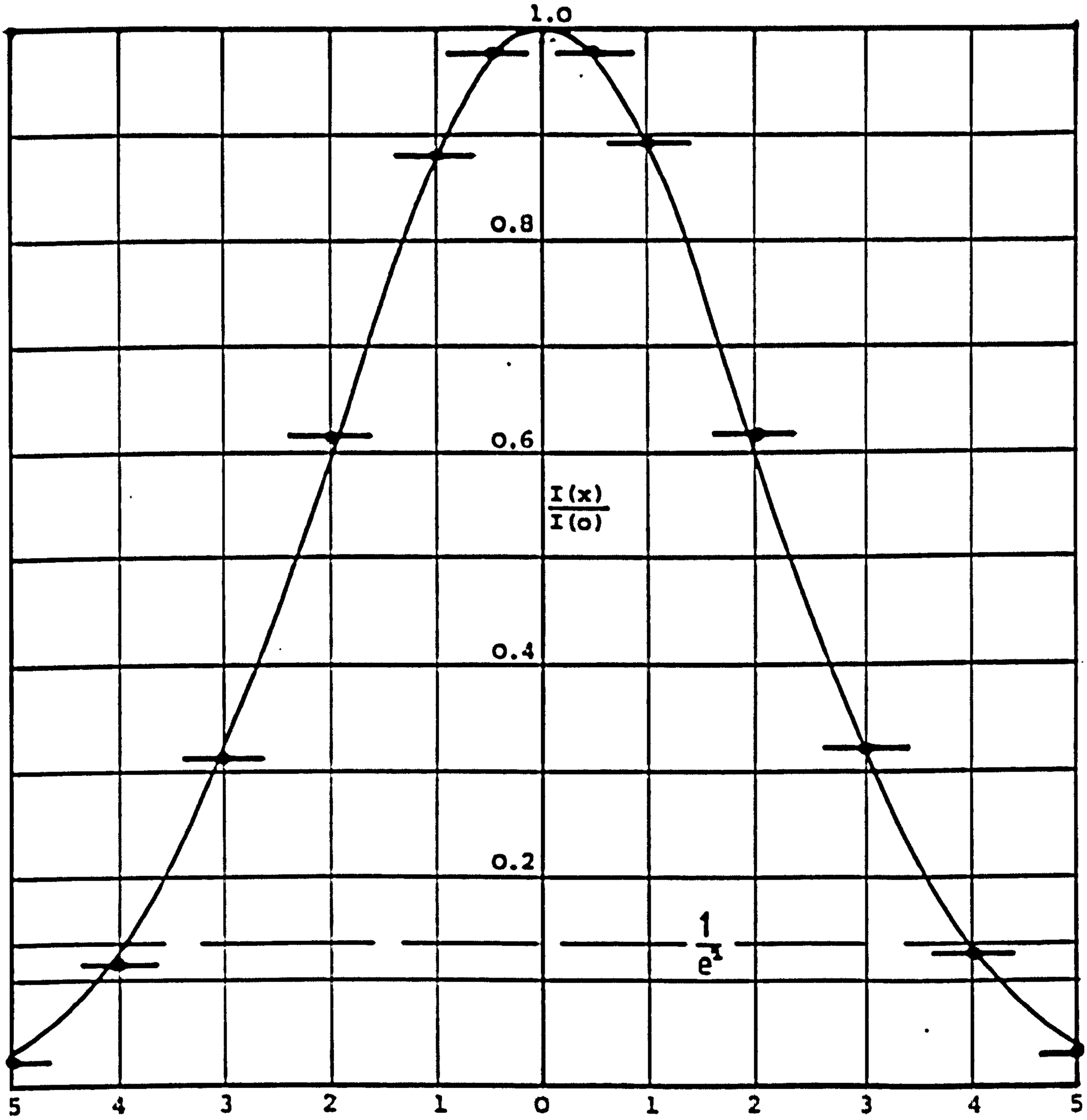

Figure 2.26 Intensity distribution along a diameter of the beam cross section. Solid line: equation (2.33); —•— : experiment

equation (2.29) by letting y = 0 and noting that $I(o) = \frac{2P_o}{b_o^2}$, i.e.

$$\frac{I(x)}{I(o)} = \exp\left(-\frac{2x^2}{b_o^2}\right) \qquad (2.33)$$

where b_o the $\frac{1}{e^2}$ intensity radius of the beam cross section was taken as 3.9 mm from the experimental results.

The results showed that the intensity distribution of the laser light was Gaussian.

(b) Using the power ratio technique

The measurements were carried out at the same point as with the previous method. Three different diameter wires were used to measure the beam size. The experimental set up for these measurements is shown in figure 2.27. Three steel strips of widths corresponding to the wire diameters were also used in order to investigate any possible differences in the measurements between using wires and flat strips. The various wire and strip sizes together with the results are shown in table 2.3. It is seen from the results that:

(i) There is no difference between readings obtained with flat strips and wires of similar dimensions.

(ii) The three different sized wires and strips gave results which are in close agreement.

(iii) The beam diameter was about 7.8 mm.

Similar measurements using this method were carried out on

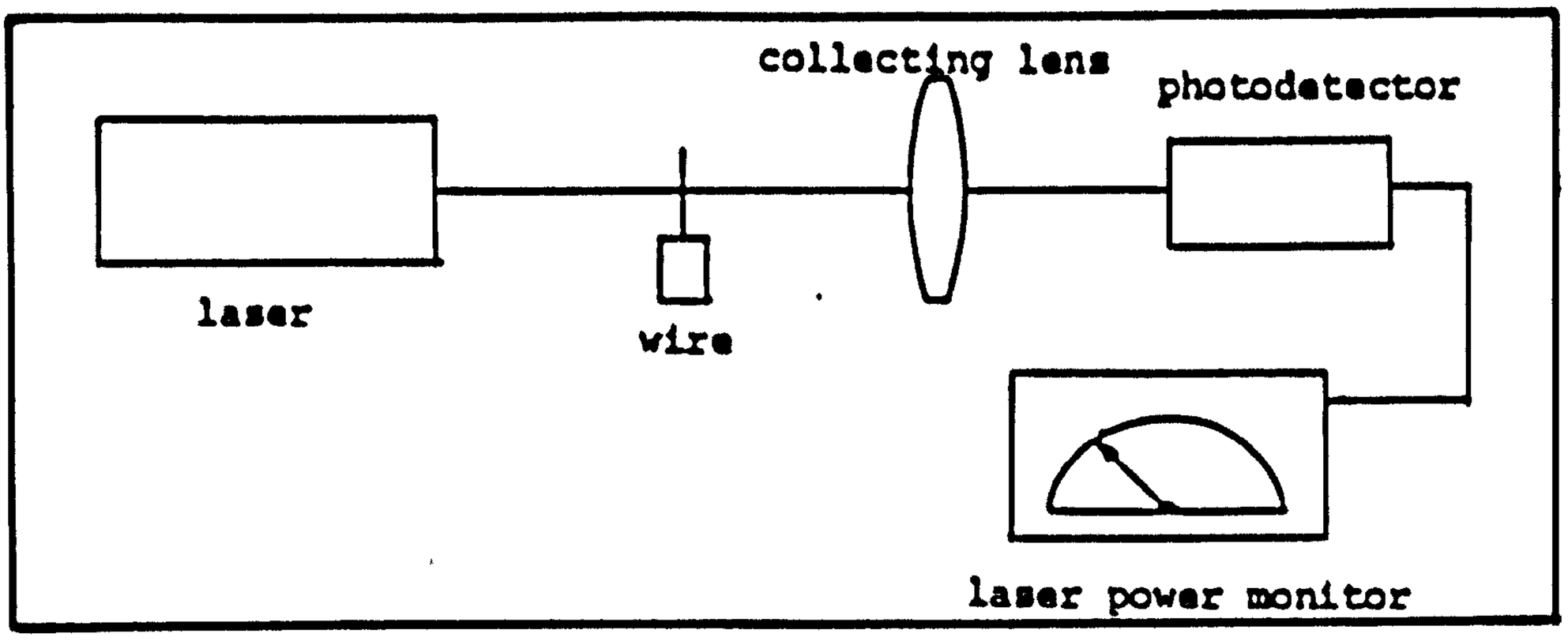

Figure 2.27 Experimental set up for power ratio method

	WIRES			FLAT STRIPS		
2a (mm)	P_m (mW)	P_o (mW)	$2b_o$ (mm)	P_m (mW)	P_o (mW)	$2b_o$ (mm)
4.83	1.69	8.50	7.51	1.65	8.50	7.48
2.57	4.40	8.53	7.99	4.40	8.53	7.99
1.10	6.72	8.60	7.86	6.73	8.60	7.89

Table 2.3 Results from beam diameter measurements. 2a = wire diameter or strip width; b_o = beam radius.

the unfocused beam near the laser, where the background light from the laser tube appeared to be more intense. There it was found necessary to place an iris diaphragm between the laser and the wire, with an aperture of about 2-3 times the theoretical beam diameter at that point, to avoid truncating the beam [8]. If no iris diaphragm was used, the measured beam diameters increased slightly with wire diameter. This may be explained as follows: An almost constant amount of background radiation is being added to the parameters P_m and P_o regardless of the wire size. As a percentage, this radiation is higher when those parameters have small values. Since P_o remains approximately constant and P_m becomes smaller as the wire diameter increases, the error in $\frac{P_m}{P_o}$ becomes correspondingly larger, thus resulting in an increase in the measured beam diameter with increasing wire diameter. It was observed that this problem became more severe if a collecting lens was used, as shown in figure 2.27 and no iris diaphragm to cut out the background illumination.

For measurements near the laser, where the beam diameter is small, or in the case of focused beams, it was found necessary to solder the fine wires on a steel plate, on which a hole of a few mm diameter was drilled. The wire was aligned along a diameter of the hole. With this arrangement no other means of cutting out the background radiation was needed and tests carried out under a variety of conditions gave consistent results.

2.8.4 Beam waist location

Having established the validity of the method for measuring beam diameters, attention was turned to the location of the waist of the focused beams relative to the point of intersection between the two beams in a dual beam LDA.

A very popular arrangement for a dual beam anemometer at the time of this investigation consisted of two beams made parallel by using either a prism type beam splitter [2,16] or a radial diffraction grating and a lens [20,28, 40], and a focusing lens. This type of optical system was based on the assumption that the parallel beams were collimated and when focused by a lens, coincidence of waist and crossover was guaranteed. This claim was investigated using the optical system shown in figure 2.28.

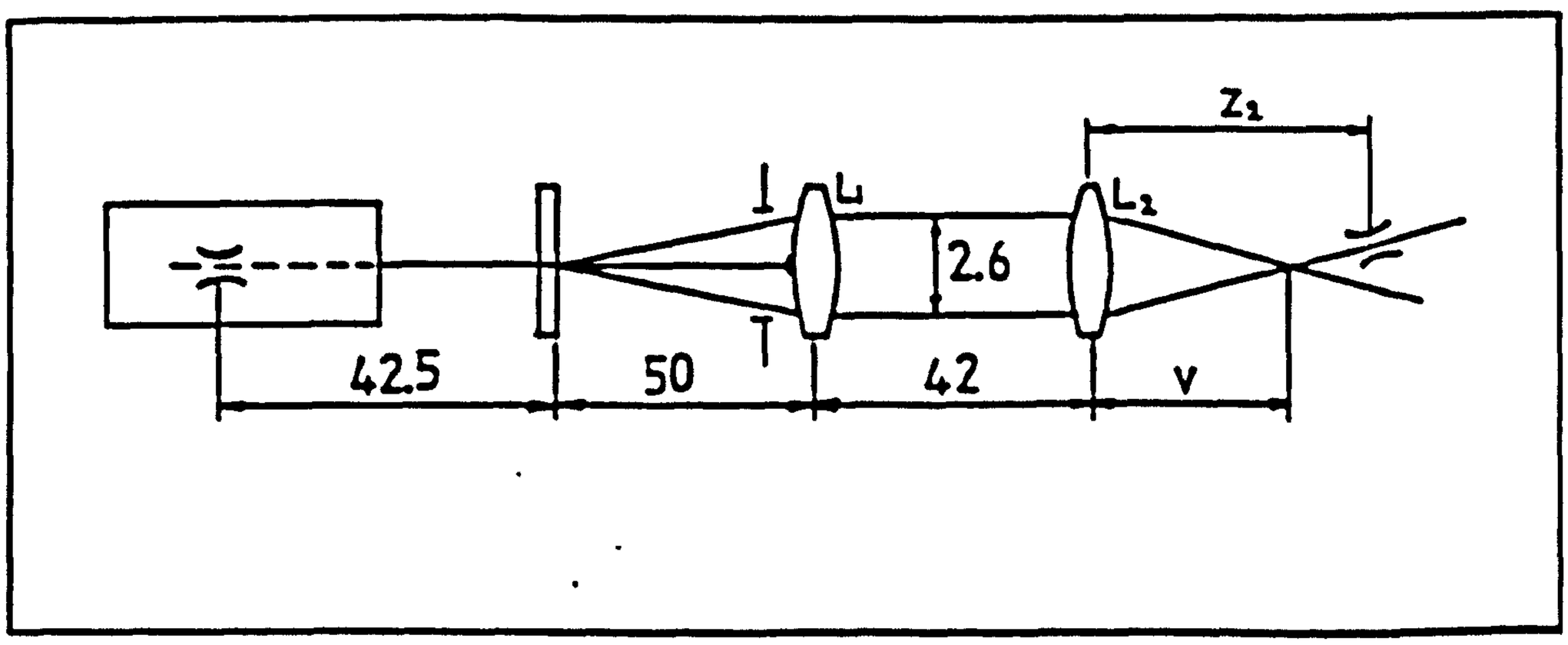

Figure 2.28 Dual beam arrangement for investigation of beam waist location. Dimensions in cm; f_1 = 50 cm; f_2 = 5 cm; v = 5.08 mm.

A wire of diameter 100 μm was used, mounted on a translation stage with micrometric movement in two directions. Measurements were taken after L_2 in steps of 1 mm on both beams. The initial distance of the wire from the lens was measured using a ruler and a small error is expected. The results of the measurements are shown in figure 2.29.

It is noted that:

(i) the waists of the two focused beams occurred at slightly different distances from the focusing lens and

(ii) neither of the waists coincided with the beam intersection.

Following this, measurements of the beam diameters between lenses L_1 and L_2 were carried out and the results are shown in figure 2.30. It is seen that the beams converge to a waist, at a distance of approximately 59 cm after L_1. The above findings invalidated the suggestion of collimated beams between lenses L_1 and L_2 and guaranteed coincidence of waist and intersection after L_2. Subsequent attempts to achieve coincidence by varying the distance between the lenses within practical limits, proved fruitless, although it was possible, if different focal length lenses were used. Figure 2.31 shows the effect of varying the distance between the lenses on the position of the focused waist.

As a result of the above no further use was made of this

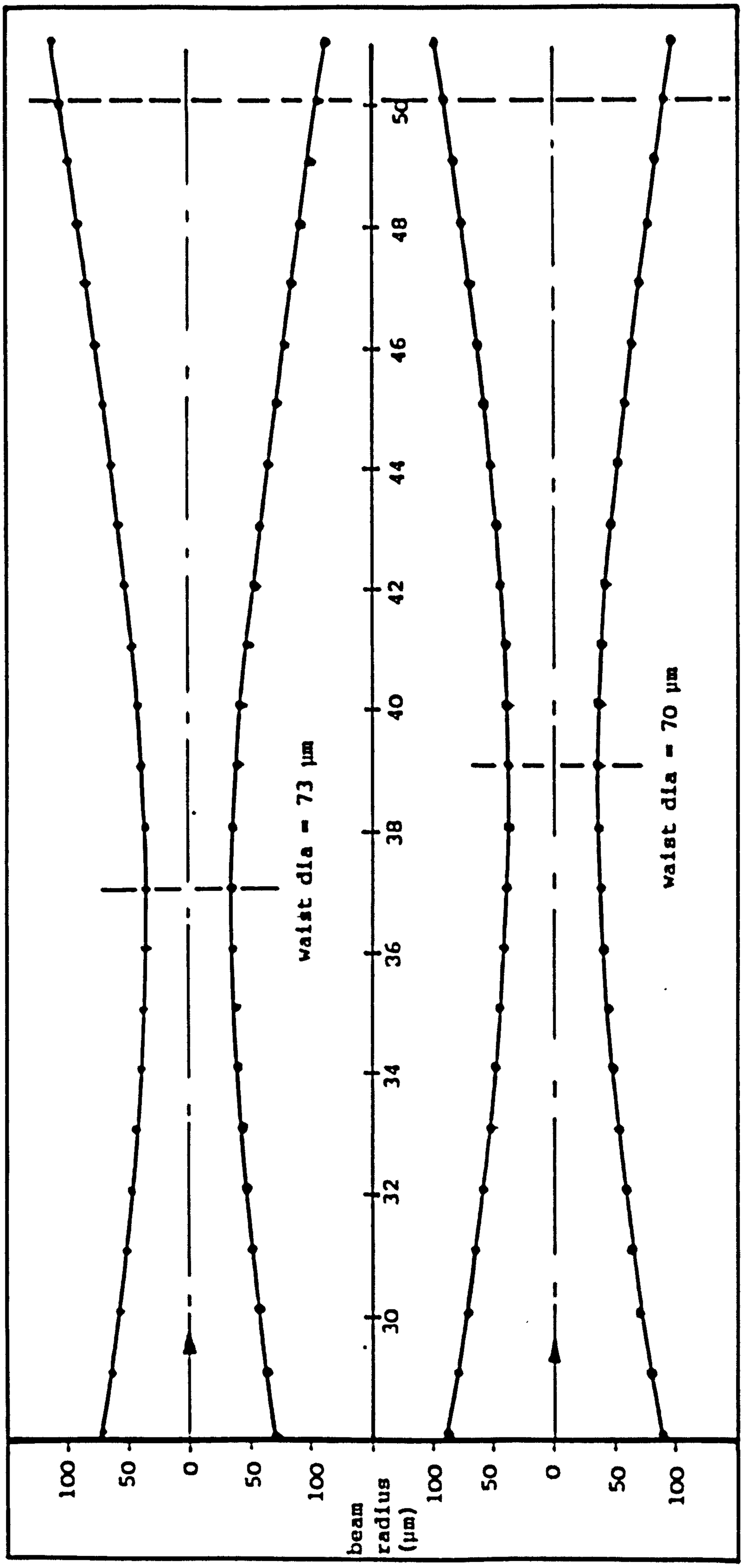

Figure 2.29 Distance of beam waist from lens

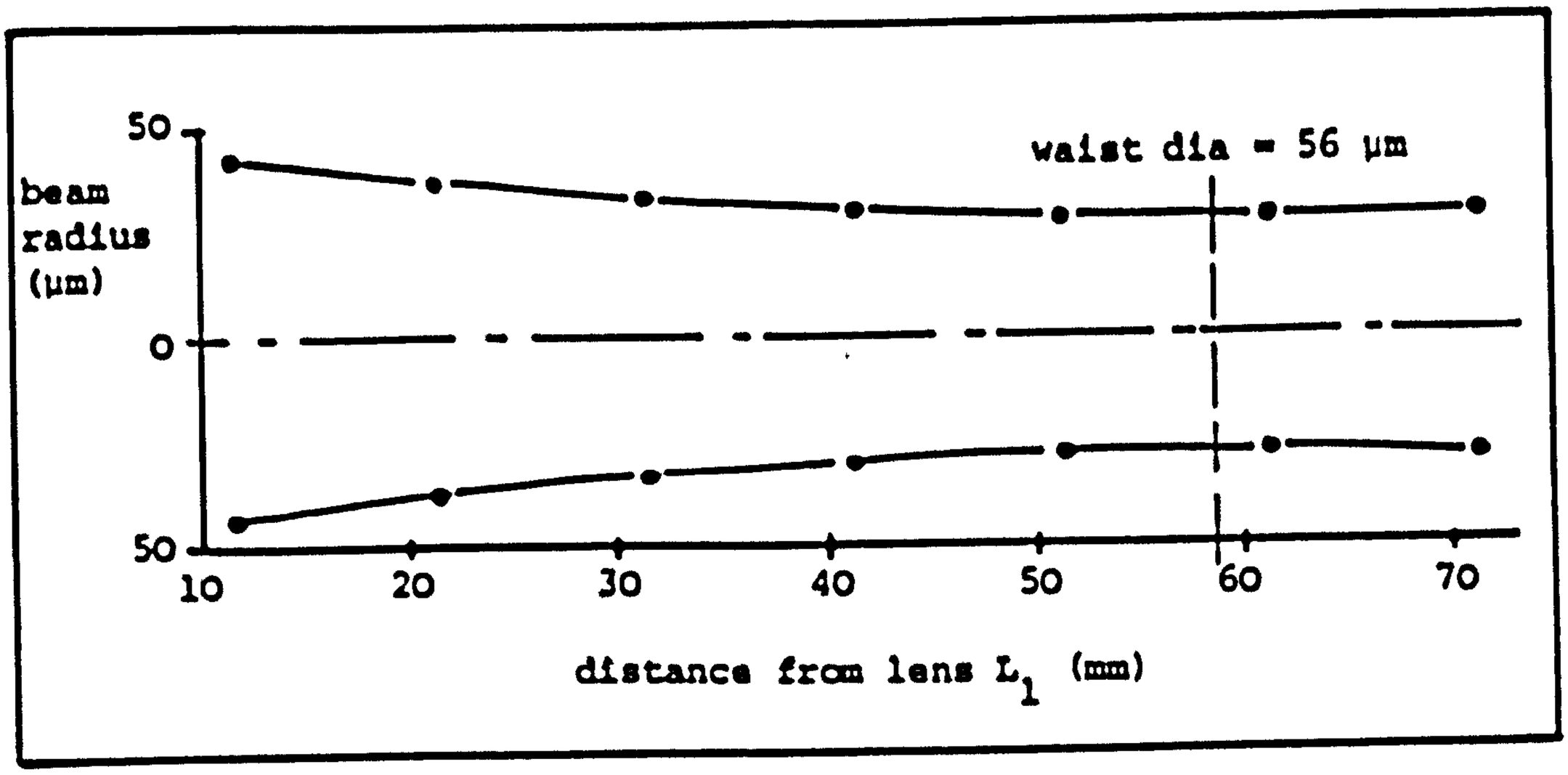

Figure 2.30 Beam propagation between L_1 and L_2 (average values for two beams)

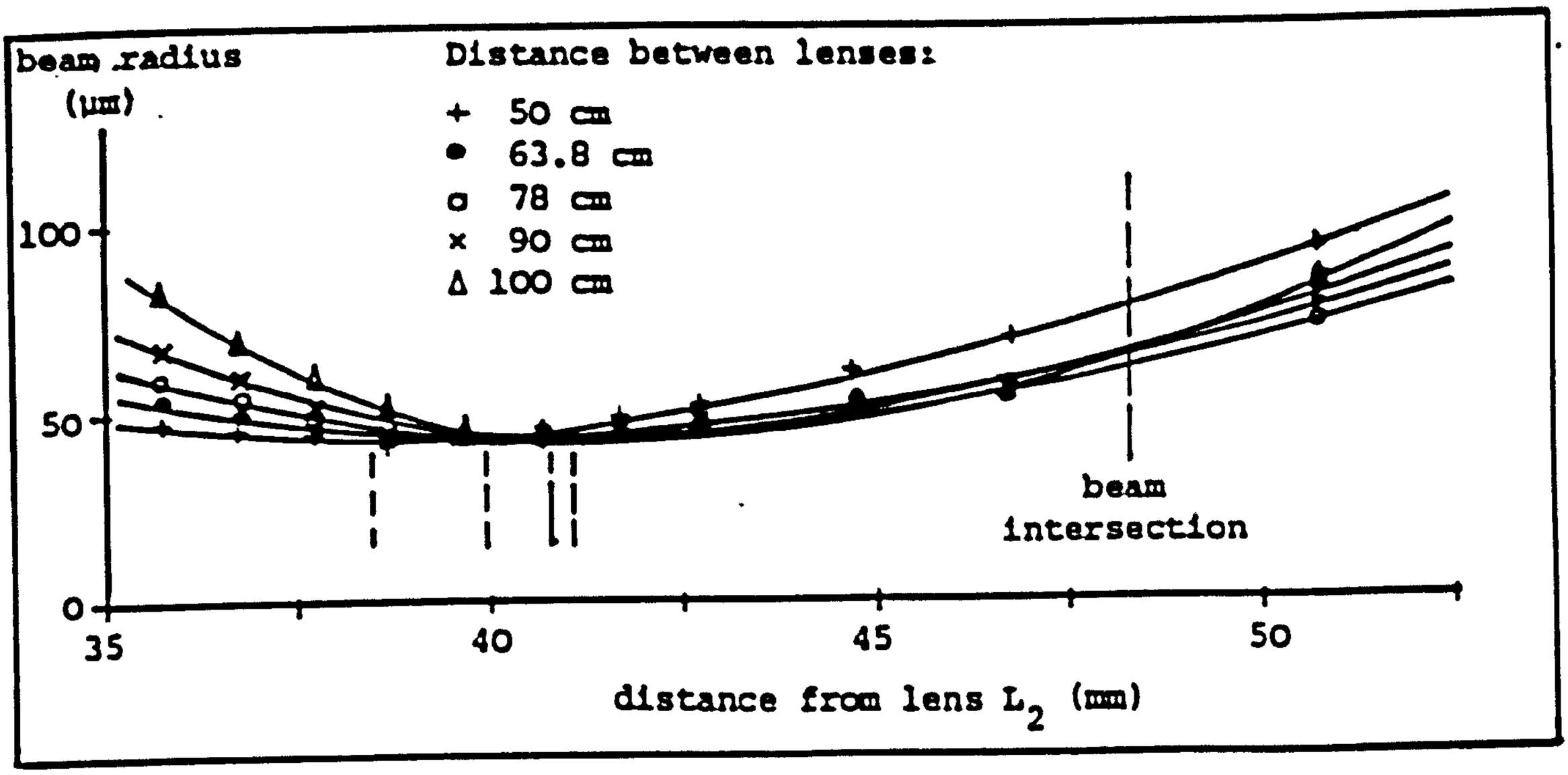

Figure 2.31 Focused beam waist position for various L_1 - L_2 distances

type of optical arrangement for a dual beam laser Doppler anemometer.

2.8.5 Experimental determination of beam waist dimensions

(a) Using the power ratio technique

The optical arrangement used was an optimised two lens system, giving coincidence of beam waist and intersection and it is shown in figure 2.32.

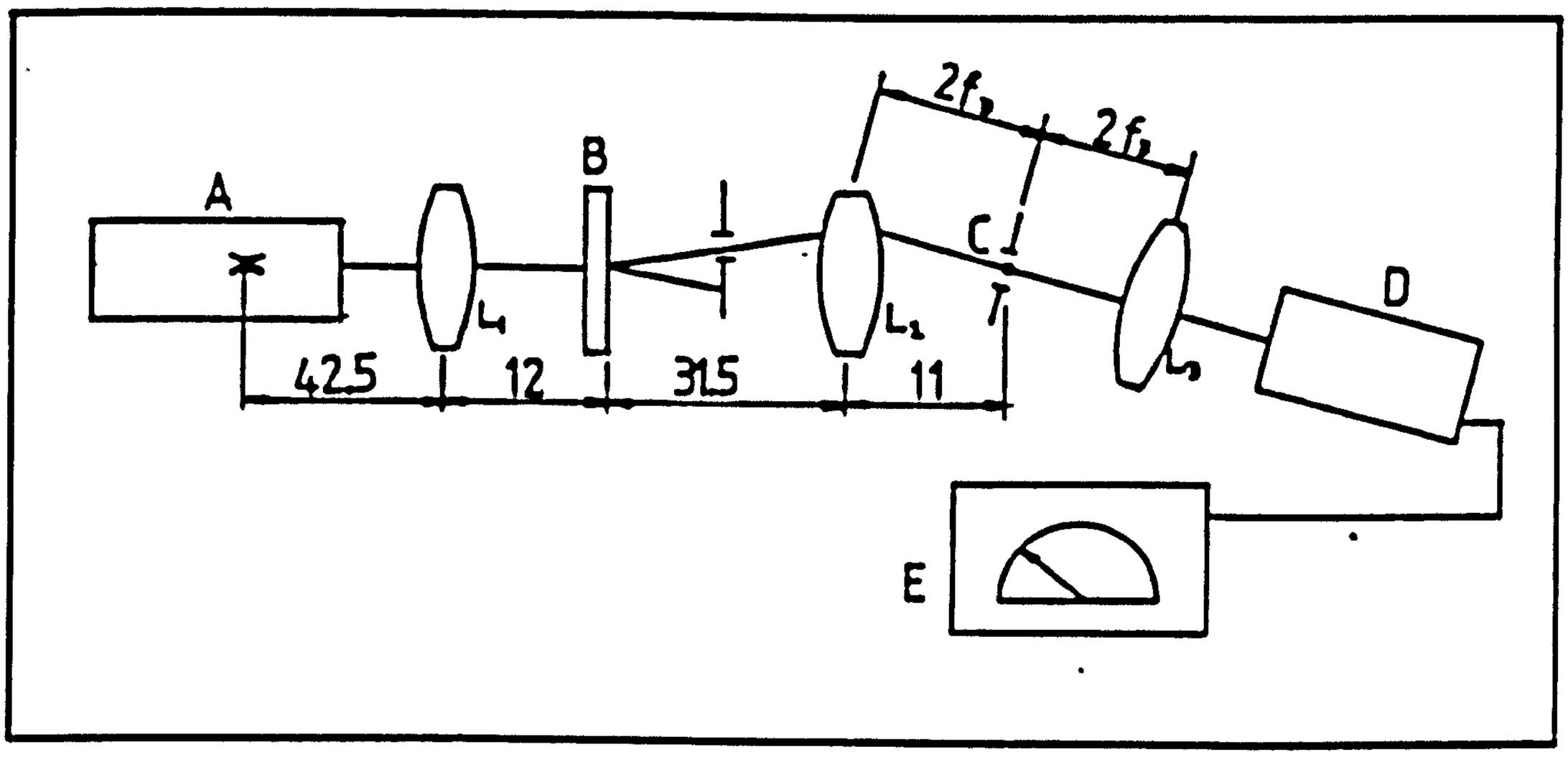

Figure 2.32 Set up for measuring beam waist diameter. Dimensions in cm.

A: laser, B: grating, C: wire, D: photodiode, E: laser power meter. f_1 = 15 cm, f_2 = 8 cm, f_3 = 5 cm.

The diffraction grating which had 18600 lines was rotated at approximately 350 rpm to average out any variations in its transmissivity.

Three different size wires were used and their dimensions and the results obtained are shown in table 2.4.

$2a$ (μm)	P_m (mW)	P_o (mW)	$2b_o$ (μm)
20	0.945	1.835	62
30	0.580	1.815	60
40	0.350	1.800	62

Table 2.4 Results from beam waist measurements. a = wire radius, b_o = beam radius.

From the results it is seen that the beam waist diameter was about 61.5 μm. The half angle, θ, between the beams was calculated by measuring the beam separation at two different distances from the intersection of the beams and taking the average. Thus for this arrangement, θ was found to be 4.92°. Using expressions (2.16) the dimensions of the measuring volume were found to be Δz = 717 μm and Δy = 62 μm.

(b) Using frequency shifting

The two lens dual beam LDA used was that shown in figure 2.32. A photomultiplier collected light scattered from the intersection region in the forward paraxial direction.

Frequency shifting was provided by the rotating radial diffraction grating. A fine wire of 20 μm diameter was placed in the intersection point at right angles to the y-z plane defined in figure 2.11. Translation of the wire was possible along the z and y directions. A telescope was attached to the photomultiplier to focus the scattered light on a pinhole in front of the photomultiplier. Readings of the photomultiplier a.c. voltage output were taken, using a digital voltmeter, at a number of positions of the wire along z and y. Values of the photomultiplier output, which is proportional to the light intensity, divided by the estimated peak value are shown in figure 2.33, from which the z and y dimensions of the measuring volume were estimated as 943 and 82 μm respectively.

(c) Comparison of results

The theoretical dimensions of the probe volume given by equations (2.25) and (2.15) are Δz = 730 μm and y = 62.8 μm. The results obtained using the power ratio method are in good agreement with the theoretical ones but those in (b) above differ considerably. This difference can be explained as follows:

Figure 2.34 shows two intersecting beams. If paraxial forward light detection is employed, a wire of radius a traversing the intersection region in the z direction, will first produce signal of intensity ratio equal to $\frac{1}{e^2}$ at

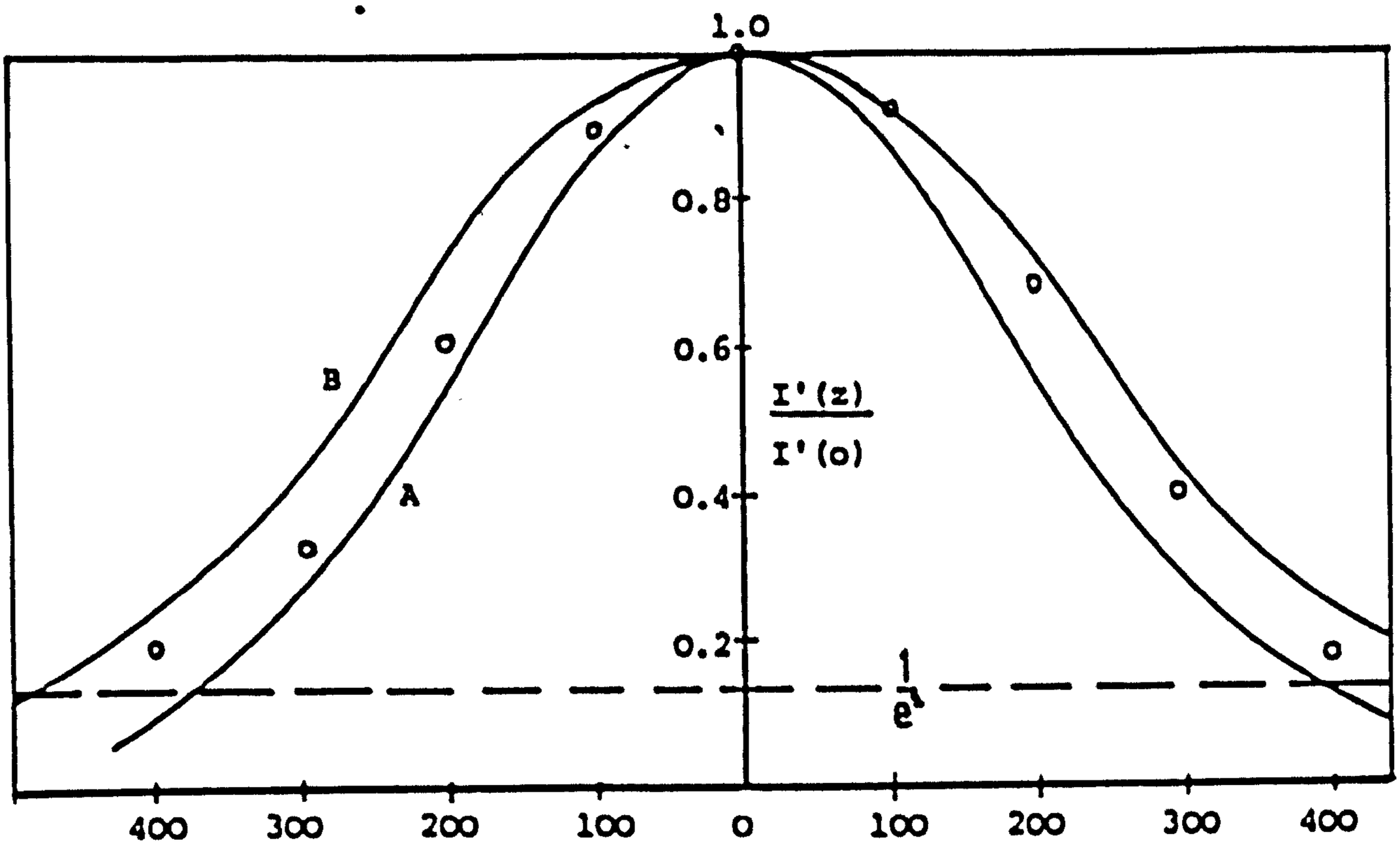

(a)

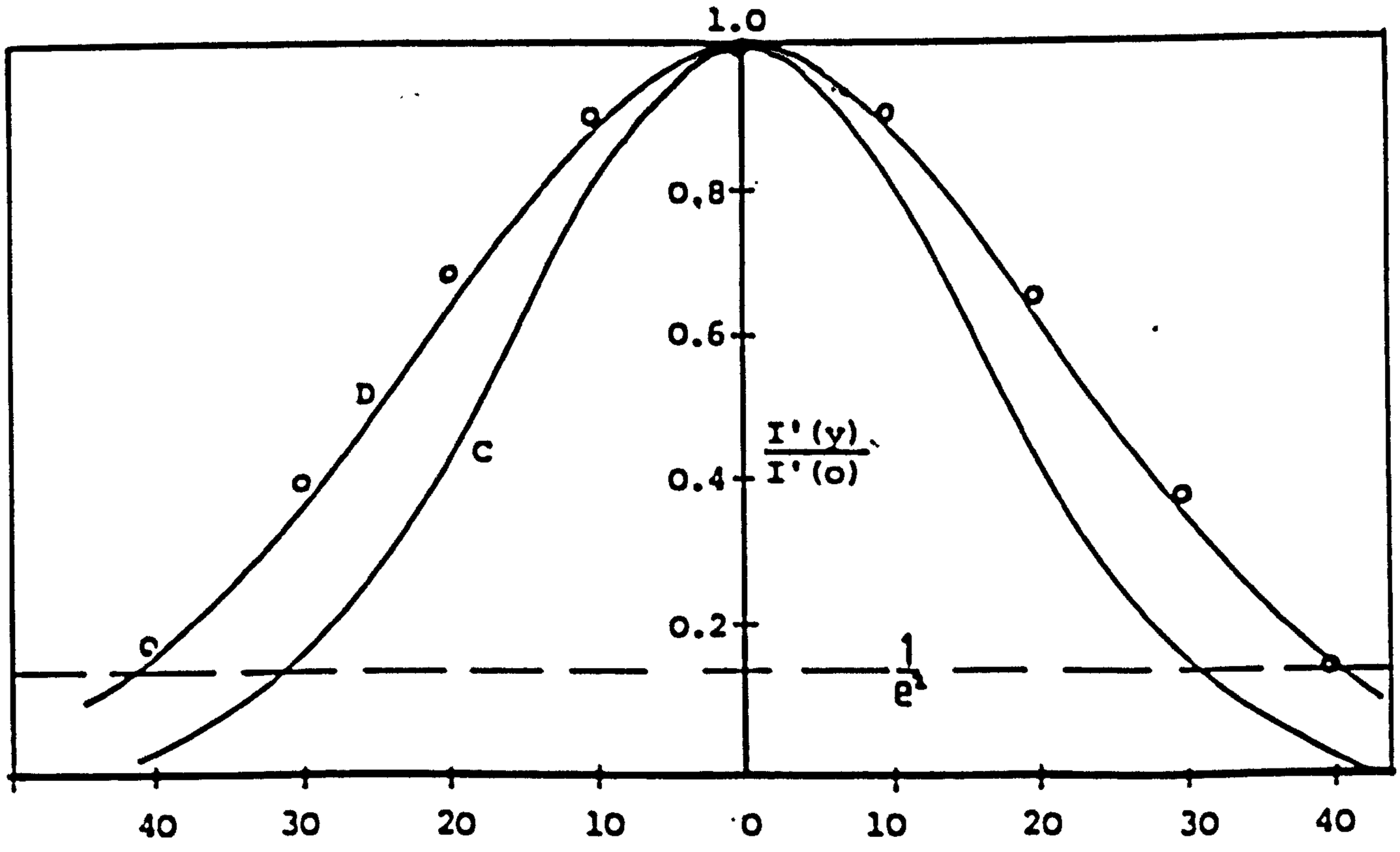

(b)

Figure 2.33 Dimensions of probe volume. A and C: equations (2.19) and (2.20) with b_o = 31.3 μm; B and D: equations (2.19) and (2.20) with b_o = 41.3 μm; o: experiment.

position (A), where it intersects both beams at b and c.

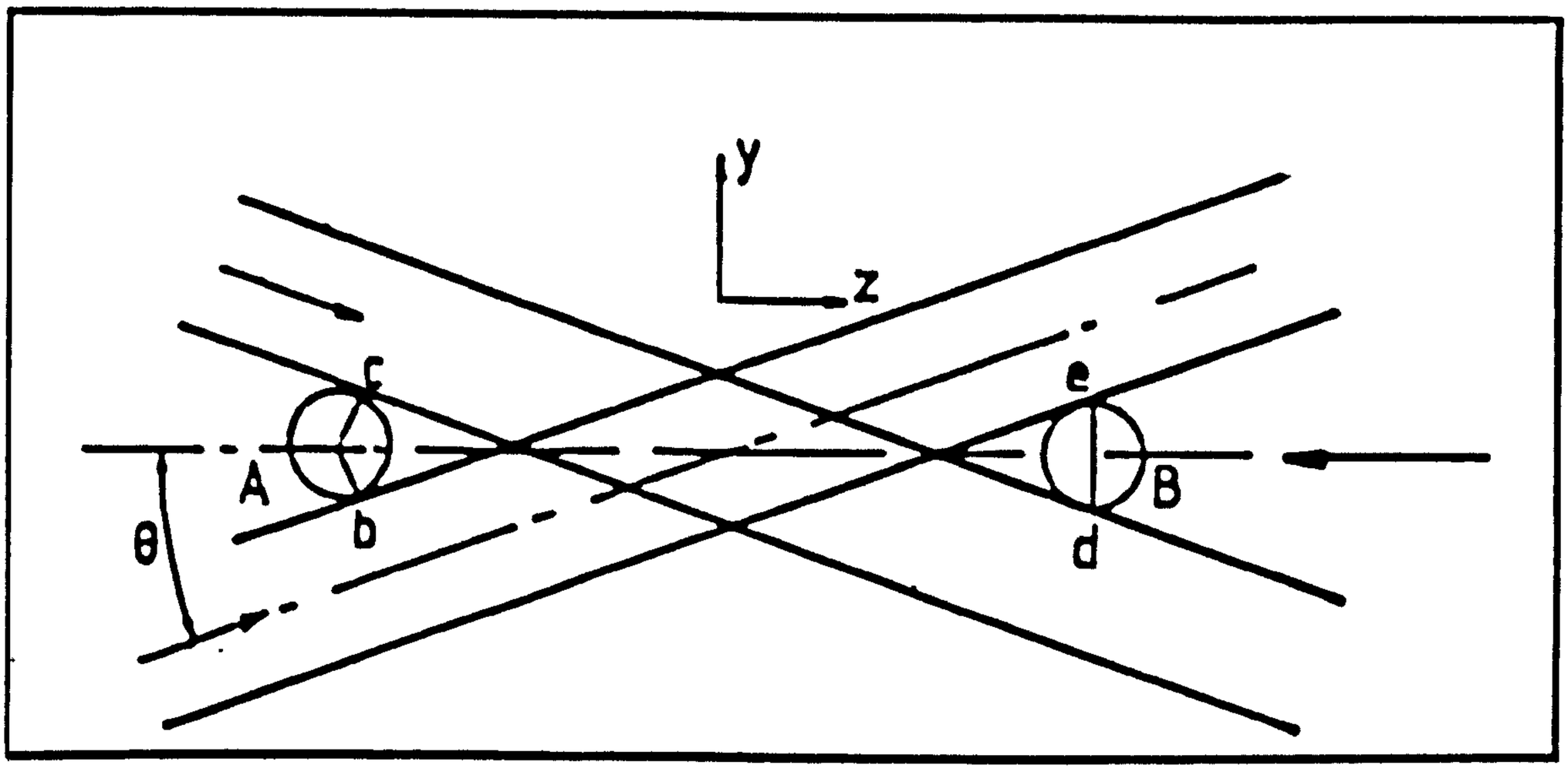

Figure 2.33 Probe volume length measurement using frequency shifting

This was confirmed by using wires of large radii to allow visual observation. At position (B) corresponding to the end of the Doppler signal, the end points of a wire diameter, parallel to the y axis, lie on the $\frac{1}{e^2}$ contour of the beams at d and e. It can be shown that from position (A) to position (B) the wire will have traversed a distance z given by

$$z = \Delta z + a\left(\frac{1}{\sin\theta} + \frac{1}{\tan\theta}\right)$$

If θ is small as is usually the case, then

$$z' = \Delta z + \frac{2a}{\theta} \qquad (2.34)$$

where θ is in radians. In a similar manner it can be shown that the measured length of the y-diagonal of the intersection region is:

$$y = \Delta y + \frac{2a}{\sin(\frac{\pi}{2} - \theta)}$$

which for a small angle θ becomes

$$y = \Delta y + 2a \qquad (2.35)$$

Using the results $z = 943$ μm and $y = 82$ μm it is found from equations (2.34) and (2.35) that $\Delta z = 710$ μm and $\Delta y = 62$ μm, results which are in good agreement with theoretical ones and those in (a).

Expressions (2.34) and (2.35) indicate that the results from this type of measurement are similar to what theory would predict if the $\frac{1}{e^2}$ beam diameters were equal to $(2b_o + 2a)$.

In figure 2.33, curves B and D are plots of equations (2.19) and (2.20) with the beam radius, b_o, equal to $(b_o + a)$ i.e. 41.3 μm.

2.8.6 Concluding remarks

When the power ratio method is used for measuring beam diameters, any size wire is, in theory, suitable provided its diameter does not exceed that of the beam. In

practice the best wire sizes were found to be in the region $\frac{1}{4}$ to $\frac{3}{4}$ of the beam diameter, since when using large wires P_m was too small and when the wire diameter was small, P_m differed very little from P_o. In both these extreme cases disproportionate errors arose.

When the beam diameter was small (focused beams) an estimate of it, based on equation (2.12), was necessary, to ensure that the sizes of the wires available were suitable.

Special care was taken to minimise background light and light scattered from the lenses, in order to reduce errors in the laser power measurements.

When a large area photodiode was used to measure laser power, a collecting lens was not necessary. Consistent results were obtained with and without such lens.

The method described in section 2.8.5(b) for measuring the probe dimensions, required very careful alignment of the collecting optics.

The pinhole method, also used in this work, is reliable, as long as the beam diameter is large compared with the pinhole size, but even so, due to significiant gradients in the Gaussian intensity distribution, the centre of the pinhole cannot be considered as the point of measurement.

The power ratio method is thought to be simple and reliable. Measurements made under various laboratory conditions were

consistent and repeatable. The orientation of the wire relative to the beam is not critical, the only condition being that the wire must be straight, clean and of constant diameter. Extensive use was made of this method for determining the position of the beam waist. To do this, it was only necessary to take readings of P_m, as P_m is directly proportional to beam diameter, provided that P_o remains constant. Visual observation of the beams by means of smoke was found to be a useful aid.

REFERENCES

[1] Durst F and Whitelaw J H 1971 Optimization of optical anemometers. Proc. Roy. Soc. Lond. A.324 157-181.

[2] Blake K A and Jespersen K I The NEL laser velocimeter. Dept. of Trade and Industry, National Engineering Laboratory Report No. 510, May 1972

[3] Goldstein R J Measurement of fluid velocity by laser-Doppler techniques. Appl. Mech. Reviews 753-760, 1974

[4] Svelto O 1976 Principles of lasers. Published by Heyden.

[5] Kogelnik H 1965 Imaging of optical modes - resonators with internal lenses. The Bell System Tech. J. 455-494.

[6] Kogelnik H and Li T 1966 Laser beams and resonators. Appl. Opt. 5 10 1550-1567.

[7] Kogelnik H 1965 On the propagation of Gaussian beams of light through lens like media including those with a loss or gain variation. Appl. Opt. 4 12 1562-1569.

[8] Dickson L D 1970 Characteristics of a propagating Gaussian beam. Appl. Opt. 9 8 1854-1861.

[9] Yeh Y and Cummins H Z 1964 Localised fluid flow measurements with an He-Ne laser spectrometer. Appl. Phys. Letters 4 10 176-178.

[10] Wang C P and Snyder D 1974 Laser Doppler velocimetry: experimental study. Appl. Opt. 13 1 98-103.

[11] Durst F, Melling A and Whitelaw J H 1976 Principles and practice of laser-Doppler anemometry. Academic Press.

[12] Greated C A 1971 Resolution and back scattering optical geometry of laser Doppler systems. J. Phys. E: Sci. Instrum. 4 585-588.

[13] Spectra Physics Laser Review 1977 4 2.

[14] Russo A J 1975 Laser anemometer for large high velocity particles. Appl. Opt. 14 1 18-19.

[15] Coghe A and Ghezzi U 1978 LDA signal analysis. Proc. of the Dynamic Flow Conference 825-249.

[16] Brayton D B, Kalb H T and Crosswy F L 1973 Two-component dual scatter laser Doppler velocimeter with frequency burst signal readout. Appl. Opt. 12 6 1145-1156.

[17] Makatani N, Nishikawa T and Yamada T Y 1980 LDV optical system with multifrequency shifting for simultaneous measurement.of flow velocities at several points. J. Phys. E: Sci. Instrum. 13 172-173.

[18] Deters O J and Friedman M H 1980 Simple directionally sensitive two component laser Doppler anemometer. Appl. Opt. 19 8 1221.

[19] Greated C 1970 Measurement of Reynolds stresses using an improved laser flowmeter. J. Phys. E: Sci. Instrum. 3 753-756.

[20] Oldengarm J 1975 Two-dimensional laser Doppler velocimetry. Proc. of LDA Symposium Copenhagen 553-564.

[21] Dubnistchev N and Vasilenko G 1976 A laser Doppler velocimeter which measures the three components of velocity. Opt. and Laser Technology 129-131.

[22] Abbiss J B, Chubb T W and Pike E R 1974 Laser Doppler anemometry. Optics and Laser Technology 249-261.

[23] Hanson S 1973 Broadening of the measured frequency spectrum in a differential laser anemometer due to interference plane gradients. J. Phys. D: Appl. Phys. 6 164-171.

[24] Durst F and Stevenson W H 1976 Visual modelling of laser Doppler anemometer signals by moiré fringes. Appl. Opt. 15 1 137-144.

[25] Edwards R V, Angus J C, French M J and Dunning J W 1971 Spectral analysis of the signal from the laser Doppler flowmeter: time independent systems. J. Appl. Phys. 42 2 837-850.

[26] Owen J M and Rogers R H 1975 Velocity biasing in laser Doppler anemometers. Proc. LDA Symposium Copenhagen 89-114.

[27] Kreid D K 1974 Laser-Doppler velocimeter measurements in nonuniform flow: error estimates. Appl. Opt. 13 8 1872-1881.

[28] Oldengarm J, van Krieken A H and van der Klooster 1975 Velocity profile measurements in a liquid film flow using the laser Doppler technique. J. Phys. E: Sci. Instrum. 8 203-205.

[29] Eliasson B and Dandliker R 1974 A theoretical analysis of laser Doppler flowmeters. Optica Acta 21 2 119-149.

[30] Adrian R J and Orloff K L 1977 Laser anemometer signals: visibility characteristics and application to particle sizing. Appl. Opt. 6 3 677-684.

[31] Brayton D B and Goethert W H 1971 A new dual-scatter laser Doppler-shift velocity measuring technique. ISA Transactions 10 40-50.

[32] Tridimas Y T, Lalor M J and Woolley N H 1978 Beam waist location and measurement in a dual-beam laser Doppler anemometer. J. Phys. E: Sci. Instrum. 11 203-206.

[33] Oldengarm J 1975 The use of rotating radial diffraction gratings in laser Doppler velocimetry. Proc. AGARD Conf. on applications of non-intrusive instrumentation in fluid flow reseach (Neuilly sur Seine: NATO Advisory Group for Aerospace Research and Development) paper no 193 pp 23/1 - 23/6.

[34] Hobson C A 1978 Digital analysis of opto-electronic data. PhD Thesis, Department of Electrical and Control Engineering, Liverpool Polytechnic.

[35] George W K Jr 1975 Limitations to measuring accuracy inherent in the laser Doppler signal. Proc. LDA Symposium, Copenhagen 20-63.

[36] Hanson S 1975 Visualization of alignment errors and heterodyning constraints in laser Doppler velocimetry. Proc. LDA Symposium, Copenhagen 176-182.

[37] Yoshida A and Asakura T 1976 A simple technique for quickly measuring the spot size of Gaussian laser beams. Optics and Laser Technology 273-274.

[38] Skinner D R and Whitcher R E 1972 Measurement of the radius of a high-power laser beam near the focus of a lens. J. Phys. E: Sci. Instrum. 5 237-238.

[39] Suzaki Y and Tachibana A 1975 Measurement of the μm sized radius of Gaussian laser beam using the scanning knife-edge. Appl. Opt. 14 12 2809-2810.

[40] Goosens L H J and van Dagee J A 1976 Electronic mixing device in laser Doppler velocimetry. J. Phys. E: Sci. Instrum. 9 554-556.

CHAPTER 3

PRACTICAL ASPECTS OF VELOCITY MEASUREMENTS USING LDA

3.1 VELOCITY MEASUREMENTS IN FLUIDS - EFFECTS OF REFRACTIVE INDEX

3.1.1 Probe traverse

When velocity measurements are carried out in ducts, the laser beams usually pass through a glass wall and the probe volume is formed in the fluid in the duct. The distance traversed by the probe in the fluid can be different from the distance traversed by the optics, due to the different refractive indices involved [1,2]. Assuming a plane duct wall, refraction theory gives:

$$n_a \sin\theta = n_g \sin\phi = n_f \sin\alpha$$

and

$$\sin\alpha = \frac{\sin\theta}{n_f}$$

where n_a, n_g and n_f are the refractive indices of air, duct material (glass usually) and fluid in duct respectively.

If A and B are two positions of the focused beam, then the distance traversed by the optics, MN and the distance traversed by the measuring probe, KL, are related as follows (see Figure 3.1):

$$KL = QL - QK = \frac{1}{\tan\alpha}\,(QP - QE)$$

where $QK = \frac{QE}{\tan\alpha}$, $QL = \frac{QP}{\tan\alpha}$

also $QP - QE = MN \tan\alpha$

$$\text{thus} \quad KL = MN \frac{\tan \theta}{\tan \alpha}$$

$$= MN \, n_f \frac{\cos \alpha}{\cos \theta}$$

$$\text{or} \quad \frac{KL}{MN} = \frac{\sqrt{n_f^2 - \sin^2 \theta}}{\cos \theta} \qquad (3.1)$$

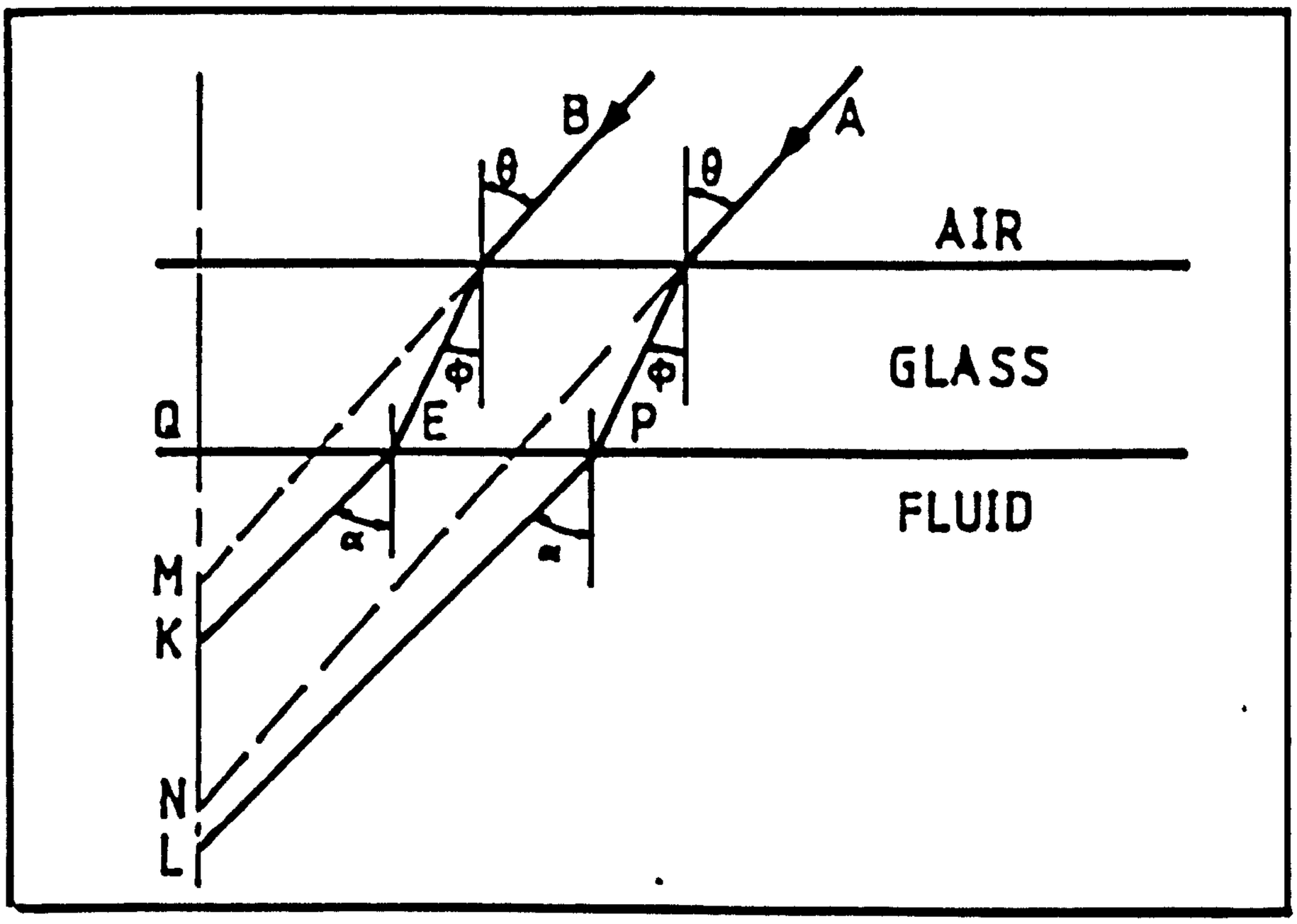

Figure 3.1 Effects of refraction on focused beams

If, as usually is the case, θ is small, the above reduces to

$$\frac{KL}{MN} = \frac{1}{n_f} \qquad (3.2)$$

Hence the distance traversed by the probe relative to the distance traversed by the optics is independent of the thickness of the glass wall and its refractive index. It follows that when the fluid in the duct is air ($n_f = 1$), no correction is necessary for the probe traverse.

The addition of solids would result in a different index for the suspension. In this work, only dilute suspensions were used, and no significant change in the refractive index was observed.

3.1.2 Fringe spacing (fringe mode anemometer)

With reference to figure 3.1,

$$\frac{\sin \alpha}{\sin \theta} = \frac{V'}{V} = \frac{\lambda'}{\lambda}$$

where V' and λ' are the velocity and wavelength of light in the fluid and V and λ are the velocity and wavelength of the light in air.

For the refracted beams within the fluid

$$\text{fringe spacing} = \frac{\lambda'}{2 \sin \alpha} .$$

Substituting for sin α from above:

$$\text{fringe spacing} = \frac{\lambda}{2 \sin \theta} .$$

This expression is identical with equation (2.4), which gives the fringe spacing for the case when the surrounding medium is air.

Hence for velocity measurements in fluids, the signal frequency is independent of the refractive index of the fluid.

3.2 FREQUENCY SHIFTING

3.2.1 Introduction

It was noted in section 2.2.3 that the signal obtained from a laser anemometer gives the magnitude of the velocity of the scattering particle normal to the fringes, but not its direction. Hence the inherent directional ambiguity of such signals is 180^{o}. This is of no consequence in situations where the direction of the mean velocity is known, e.g. laminar flow in ducts, linear translation of a solid surface, turbulent flow with low turbulence intensity etc. However, in cases such as highly turbulent flows, where the direction of the velocity changes with time, oscillating or recirculating flows, information about the direction of the velocity vector is as important as information about its magnitude. Assuming Gaussian velocity probability density distribution, estimates of possible errors in the calculation of the mean velocity and turbulence intensity in highly turbulent flows, as a result of directional ambiguity, have been presented by Durst and Zaré [3].

The most common technique for the removal of directional ambiguity in laser anemometry consists of adding a frequency shift to the laser beams. The effect of this is that the zero velocity level of the scatterers is represented by the shift frequency and positive or negative velocities will appear above or below this shifted frequency.

Buchhave [4] has pointed out that, for frequency counter based LDA systems, the velocity offset must be greater than

the largest velocity component along the measuring direction by an amount such that the number of fringe crossings by the particle is larger than the number of cycles over which the frequency counter operates. He has also noted that the accuracy of the measurement would be reduced by introducing too large a frequency shift.

Measurements in low velocity flows are facilitated if frequency shifting is used, as low frequency noise from the laser and photodetector and low frequency mechanical vibrations can be present. Frequency bias also allows matching of the heterodyne frequency to the characteristics of the signal processing equipment [5].

Another function of frequency shifting is the removal of the pedestal part of the signal. The photodetector signal consists of (i) a Gaussian pedestal waveform produced by the light scattered from the beams by a scatterer and (ii) a sinusoidal signal, containing the velocity information, with Gaussian amplitude variation, produced by interference of the light scattered from the two beams. Durst and Zaré [3] have shown that in highly turbulent flows the frequency spectrum of the pedestal can interfere with the sinusoidal frequency spectrum of the signal, when scatterers of widely differing velocities are present. In this case electronic filtering is not sufficient to attenuate the pedestal. A constant frequency bias will shift the sinusoidal frequency without affecting the pedestal frequency and electronic

filtering can then remove the pedestal. Measurements in flows with varying velocity require continuous resetting of the high pass filter or an initial setting of the filter covering the largest part of the expected frequency range. This is a major limitation of this pedestal removal technique and other more effective methods have been proposed [3].

3.2.2 Effect of frequency shifting on counter processed signals

There are three main factors to be considered when frequency shifting is employed. First directional ambiguity must be removed, second the number of cycles in the signals must be made sufficient for the counter to process the signal and third the signal must be efficiently filtered.

Depending on the level of turbulence, particle trajectories through the probe volume can vary between two extremes: that normal to the fringes when the measured velocity component equals the absolute velocity of the scatterer, and that parallel to the fringes, producing a zero velocity component in the direction of measurement.

As the angle between the interference planes and the particle trajectories becomes smaller so the probability of obtaining a valid signal diminishes, the limiting case being when the number of signal cycles falls below the preset number over which the frequency counter operates. It is thus obvious that the signal generating process

discriminates against fluctuating velocity components, which deviate appreciably from the mean flow direction, thus truncating the low frequency end of the frequency spectrum.

Particles passing through various parts of the probe volume and at various angles to the orientation of the fringes, may or may not produce a signal containing sufficient cycles for the counter to process that signal. Thus counters suffer from "dead zones", i.e. particle trajectories which give an insufficient number of signal cycles. Buchhave [4] has presented analytical estimates of particle trajectories which give rise to dead zones. Frequency shift can remedy these problems by artificially producing sufficient fringe crossings from particles, whose path may even be parallel to the fringes.

In a moving fringe system the total signal frequency f, is made up of the Doppler signal frequency f_d, and the shift frequency f_s, i.e.

$$f = f_d + f_s \tag{3.3}$$

It is noted that when the particle path is parallel to the fringes then $f = f_s$. The transit time for any particular particle path through the probe volume is independent of the frequency shift. Frequency shift can either increase the Doppler frequency, in which case the fringes move in a direction opposite to that of the particle, or reduce it,

when the fringes move in the same direction as the particle.

3.2.3 Removal of directional ambiguity

Consider a flow where the instantaneous velocity u, consists of a known mean velocity $\bar{u}$ and a fluctuating component u'. If $\bar{u} > |u'|$ then the measured value of u can be either greater than $\bar{u}$, which implies that the measured component u' has the same direction as $\bar{u}$, or $u < \bar{u}$ in which case $\bar{u}$ and u' have opposite directions. In these cases there is no directional ambiguity. If on the other hand $\bar{u} < |u'|$ or when $\bar{u} = 0$, the direction of u' will not be known and a velocity bias will be necessary to overcome this difficulty.

For removal of directional ambiguity the measured frequency f, must not change sign during measurements. Hence the directional ambiguity can be removed by applying a frequency bias larger than the maximum absolute value of the fluctuating Doppler frequency. In practice an estimate of the maximum value of the velocity fluctuations is necessary before the shift frequency can be set.

Frequency shifting, if not properly controlled, can have detrimental effects when used in conjunction with frequency counting techniques. Frequency counters process signals which exceed a preset threshold voltage, if the number of zero crossings and several other conditions are correct (see chapter 4). It is possible, with improper setting of

the shift frequency to either reduce the number of signal cycles to less than that required by the counter, or to increase them to such an extent that the time duration of the measurement cycles is only a small fraction of the particle transit time.

In pipe flows with moderate turbulence intensities, frequency shifting is necessary in the region near the wall, when measuring the axial velocity component and throughout the pipe radius when measuring in the radial direction.

In this work upshifting, i.e. adding a positive frequency shift to the signal frequency, was often used and the Doppler frequency was then obtained by subtracting the shift frequency, i.e. $f_d = f - f_s$, see equation (3.3).

3.2.4 Effects of frequency shift on signal filtering

It is possible using frequency shift to upshift or downshift the signal frequencies so that optimum filtering can be obtained from an available filterband.

Figure 3.2 illustrates the usefulness of frequency shift in cases where part of the frequency spectrum lies close to the filter cut-off and is thus attenuated. The bimodal distribution was obtained from an air-solids suspension flow. The solids were glass ballotini, size 10, producing the low frequency part of the histogram. Smoke was injected, which together with fine dust present in the air, produced the high frequency signals. In figure 3.2(a) the

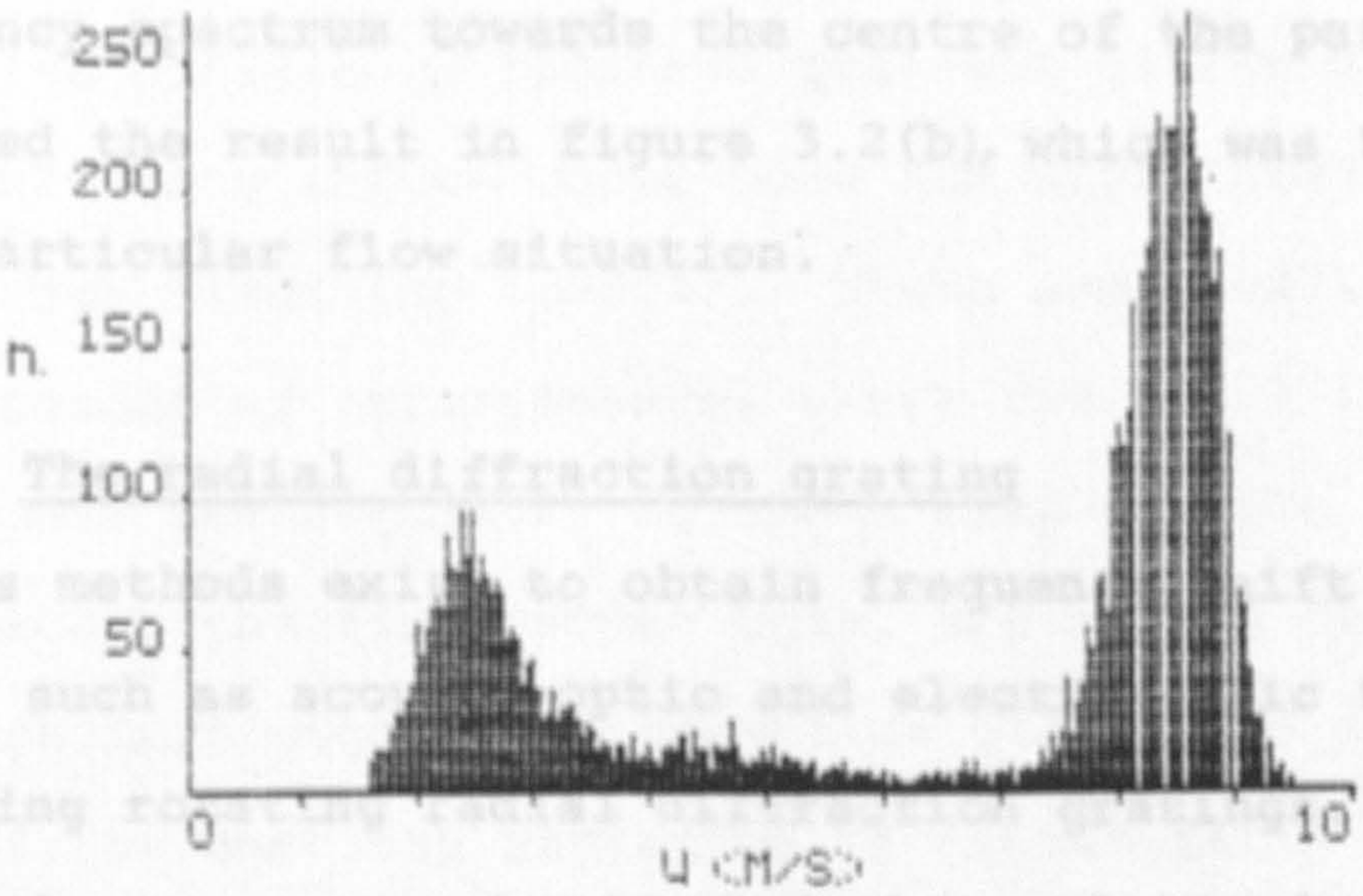

(a) no shift

(b) frequency shift = 1.2 MHz

Figure 3.2 Effect of frequency shift on velocity measurements. Glass ballotini, 210-325 μm; filter band: 0.5-8 MHz (corresponding to 1-16 m/s).

low frequencies were attenuated by the high pass filter. Upshifting of the frequency by 1.2 MHz moved the whole frequency spectrum towards the centre of the pass band and produced the result in figure 3.2(b), which was typical for that particular flow situation.

3.2.5 The radial diffraction grating

Various methods exist to obtain frequency shift of light beams, such as acousto-optic and electro-optic techniques and using rotating radial diffraction gratings. The latter is a very popular method when relatively low pre-shift frequencies are needed and the budget is limited.

A radial diffraction grating consists of a glass disc with line pairs etched on it. The disc can be mounted on a d.c. motor whose speed can be accurately controlled. Thus a rotating radial diffraction grating performs two functions, namely that of splitting the incident beam and also as a frequency shifting device.

The grating divides the incident laser beam into one undiffracted zeroth-order beam and pairs of higher order diffracted beams. The diffraction angles for the diffracted beams are given [5,6,7] by

$$\sin \theta_p = p \frac{\lambda}{d_r}$$

where θ_p is the angle between the p^{th} order beams and the zeroth-order beam, λ is the incident light wavelength and d_r is the line pair width of the grating.

There are two main types of gratings with different diffraction efficiencies [8].

(a) High efficiency bleached gratings giving a low intensity zeroth-order beam and high intensity first-order beams (up to 65%). These are used in dual beam anemometer arrangements, where two equal intensity beams are required, in which case all the other beams except the first-order ones, are masked out.

(b) Gratings with low diffraction efficiency in which most of the emerging radiation is contained in the zeroth-order beam (up to 85%). This type of grating is used in the reference beam mode optical anemometer.

When the radial diffraction grating is rotated, it produces a light frequency shift in the diffracted beams given [7,9] by

$$f_{s(p)} = \pm p N_d f_r$$

where N_d is the number of line pairs on the grating, f_r is the frequency of rotation (rev/s) and p is the diffraction order. The total frequency shift produced from two beams of the p^{th} order is then

$$f_s = 2pN_d f_r \qquad (3.4)$$

In the fringe model, the above represents a movement of the fringes which results in a signal from a stationary scatterer of frequency equal to f_s.

Due to the change in the line spacing along the radius of a

radial diffraction grating, the diffracted beams have an elliptical rather than circular cross-section; this is more prominent in the higher order beams, whereas the 1st order beams, usually employed in the fringe mode anemometers, suffer very little distortion. This distortion can be minimized if the incident beam is focused on to the grating [7], although this may result in an increase of the bandwidth of the frequency shift [6].

Some of the features of the radial diffraction grating as a beam splitting device [8,10] are:

(i) The two first order diffracted beams have equal intensities, regardless of the state of polarization of the incident light.

(ii) The beams have equal path lengths.

(iii) The beams lie in one plane and will cross each other when focused even if the optics are slightly misaligned.

(iv) A small angle between the plane of the grating and the optical axis does not affect the beam propagation.

(v) The shifted frequency of the diffracted beams is independent of the radial distance.

The performance of a radial grating can be limited by errors in the ruling, variations in the angular velocity and vibrations. These defects result in an increase of the frequency spread in the shifted signal although mean flow velocities remain unaffected [6]. To reduce the effect of

drift and random fluctuations in the diffraction grating velocity, Goossens and Pagee [11] used a separate photo-diode to monitor the preshift frequency and by electronic mixing with the signal frequency they improved the performance of the diffraction grating.

The electro-optic and acousto-optic frequency shifting methods, mentioned above, have inherent disadvantages when compared to the diffraction grating, in the frequency range where the latter is used; they both require expensive modulating devices [6] high frequency supplies and their alignment is critical [5]. A detailed account of these various methods of frequency shift has been presented by Durst and Zaré [3].

3.3 LIMITATIONS IN THE ACCURACY OF FREQUENCY MEASUREMENTS

3.3.1 Introduction

The accuracy of measurement of the Doppler signal frequency is limited by noise present in the processed signals and various biasing effects. Noise can exist in the optical signals, the scattering and detection process (shot noise) and in the resulting electronic signals (Johnson noise) [12].

Biasing of the measured frequencies may be due to variable fringe spacing, gradients in the flow field and statistical bias inherent in the sampling methods. Errors can

also be introduced into the measurements from the frequency measuring instruments.

3.3.2 Velocity biasing, sources and corrections

(a) General considerations

Velocity measurements by a laser Doppler anemometer are affected by errors which arise from a variety of sources. The main error is a random statistical error arising from a bias in favour of signals from the faster moving particles when the flow is turbulent. Another error arises from the velocity gradients that are present across the finite length of the velocity profile covered by the measuring volume [13,14,15]. In general more signals are recorded from faster particles than slow ones in a given time period [16,17,18,19,20,21,22,23]. Thus the velocity that exists at the geometric centre of the probe volume, is not necessarily the mean velocity calculated from all the signals collected at that position. Another source of error is due to the averaging properties of the photo-multiplier [16,23] with a biasing towards the lower velocities.

In the following investigation it is assumed that there is a uniform distribution of scatterers in the fluid.

(b) Sources of biasing errors

Consider a velocity distribution defined by a function $u = f(x)$ as shown in figure 3.3.

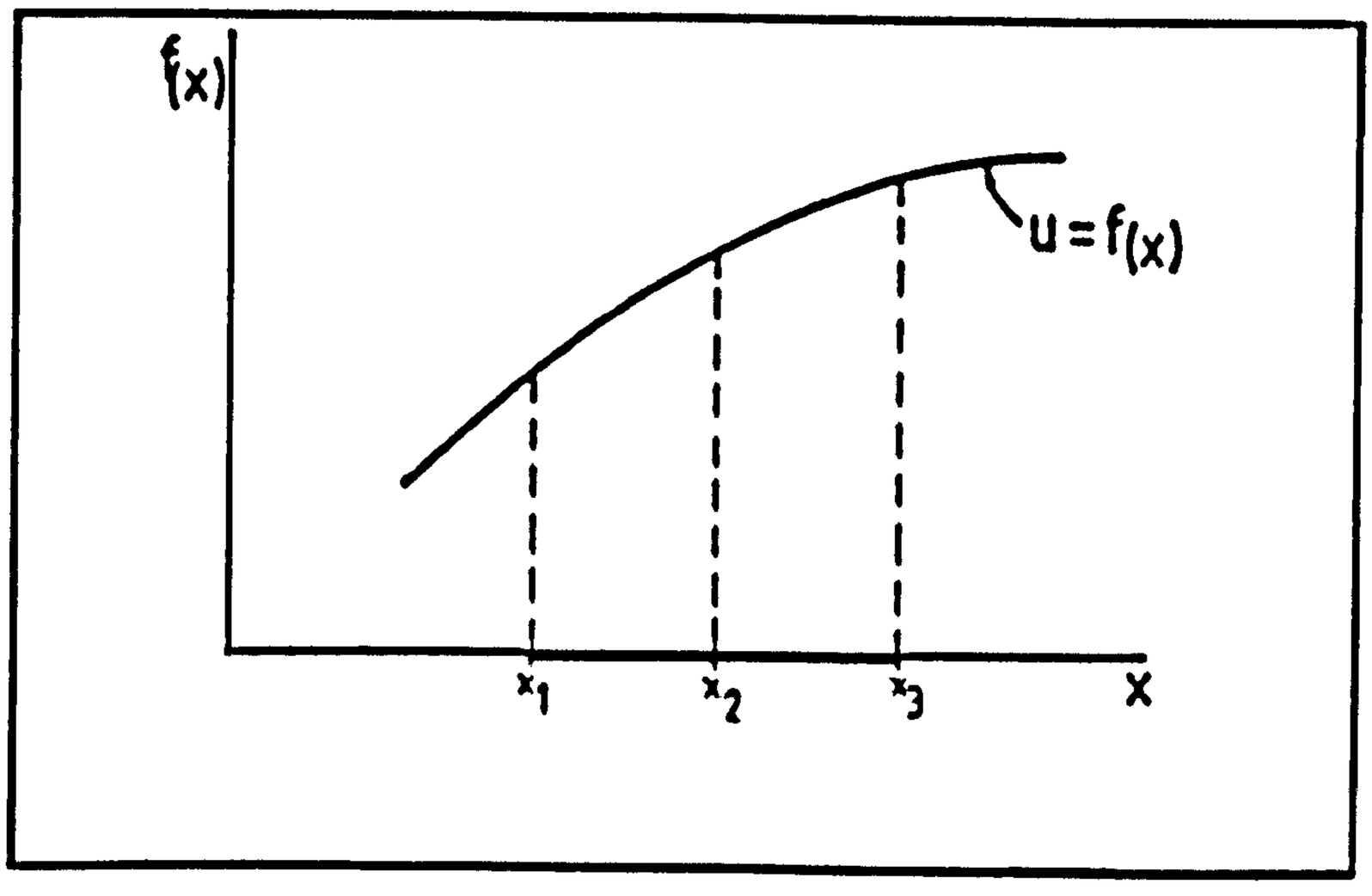

Figure 3.3 Velocity variation along measuring volume.

u = velocity, x = radial direction, $x_1 - x_3$ = probe length.

Assuming a two dimensional situation, let the probe volume be centred at x_2 and its length extend over a finite distance x_1 to x_3. When specifying the measuring point, one assumes this to coincide with the centre of the probe, i.e. located at x_2 and hence the mean velocity measured by the probe in that position would be expected to be

$$\bar{u}_r = f(x_2) \qquad (3.5)$$

In practice the measured velocity would not be equal to $\bar{u}_r$ but would deviate from it by an amount depending on the

type of flow, laminar or turbulent, and on the velocity gradient existing at that point. The following observations present a general view of the problem.

(1) <u>Flow past a point in steady flow</u>

(i) Laminar flow: All particles flowing past a point have identical velocities, hence there is no bias.

(ii) Turbulent flow: Particles flowing past a point have different velocities depending on the degree of turbulence. Since faster particles produce more signals, this gives rise to a bias in the measured mean velocity towards the higher signal frequencies, i.e. $n_i \propto u_i$, where n_i is the number of data points and u_i the corresponding velocities. Let this be type (a) bias.

Particles which have a small velocity component normal to the fringes suffer an added drawback, i.e. a lower probability of producing a measurement than particles which have a large component normal to the fringes, since the first might not, during their residence time in the probe volume, cross as many fringes as the preset number of measurement cycles, although the residence times for both cases may be of the same order of magnitude. Hence there is a minimum velocity component normal to the fringes, below which, no measurements take place due to the signal cycles being

fewer than the required measurement cycles. As previously mentioned, this error can be minimised by using frequency shifting.

Residence time and measurement time are different, in that the first is effectively equal to the time during which the signal exceeds a threshold amplitude and the latter is equal to the time of measurement over a preset number of cycles, which in the frequency meter used could be varied between 2 and 64.

(2) Flow over a finite length x_1 to x_3

Particles crossing the length $x_1 - x_3$ have different velocities according to the value of the function f(x) over that length.

(i) If equal numbers of crossings were obtained from every point along $x_1 - x_3$ then a bias would exist due to changes in the velocity gradient over that distance. Let this be type (b) bias. It can be shown that this bias would not exist in the case of a linear velocity profile.

(ii) In practice when sampling over time t, the number of crossings at every point along $x_1 - x_3$ is proportional to f(x), i.e. $n_i \propto u_i$. Let this be type (c) bias. It is noted that this type of bias is different from type (a), in that it exists in laminar flows as well as turbulent ones.

Hence it is seen that in turbulent flow there are three types of bias in the velocity measured by the LDA, types (a), (b) and (c). In laminar flow only the last two types. (b) and (c) can exist.

(c) Biasing error corrections

(1) Laminar flow

Assuming the idealised case (2)(i) above, the mean value of f(x) would be

$$\bar{u} = \frac{\int_{x_1}^{x_3} f(x)\ dx}{\int_{x_1}^{x_3} dx} \qquad (3.6)$$

or, in the case of discrete values

$$\bar{u} = \frac{\Sigma\ u_i\ n_i}{\Sigma\ n_i} \qquad (3.7)$$

and since n_i is constant,

$$\bar{u} = \frac{\Sigma\ u_i}{N_u} \qquad (3.8)$$

where N_u = number of data points.

Obviously $\bar{u} \neq \bar{u}_r$ (equation 3.5), except when f(x) is a straight line.

Using equations (3.5) and (3.6) the error in the measured results can be expressed as

$$\text{Error} = \frac{\int_{x_1}^{x_3} f(x)\ dx}{\int_{x_1}^{x_3} dx} - f(x_2)$$

Thus corrected value, $\bar{u}_c = \bar{u} - \text{error}$. (3.9)

For laminar flow, in case (2)(ii),

$$n_i = u_i \quad \text{or} \quad n_i = k\,u_i .$$

$$\text{Hence} \quad \bar{u} = \frac{\Sigma\ n_i\ u_i}{\Sigma\ n_i} = \frac{\Sigma\ k u_i^2}{\Sigma\ k u_i} = \frac{\Sigma\ u_i^2}{\Sigma\ u_i}$$

$$\text{For a continuous function } \bar{u} = \frac{\int_{x_1}^{x_3} (f(x))^2\ dx}{\int_{x_1}^{x_3} f(x)\ dx} \qquad (3.10)$$

To correct this bias the number of samples must be weighted down to compensate for the higher n_i values corresponding to higher values of u_i, i.e.

$$\text{corrected number of data } n_{ic} = k\,\frac{n_i}{u_i}$$

$$\text{Then, corrected mean, } \bar{u}_c = \frac{\Sigma\ n_{ic}\ u_i}{\Sigma\ n_{ic}} = \frac{\Sigma\ k\,\frac{n_i}{u_i}\,u_i}{\Sigma\ k\,\frac{n_i}{u_i}}$$

$$\text{or} \qquad \bar{u}_c = \frac{\Sigma\ n_i}{\Sigma\ \frac{n_i}{u_i}} . \qquad (3.11)$$

If $n_i = k\ u_i$ then the above expression gives

$$\bar{u} = \frac{\Sigma\ u_i}{N_u}$$

or as $N_u \to \infty$

$$\bar{u} = \frac{\int_{x_1}^{x_3} f(x)\ dx}{\int_{x_1}^{x_3} dx}$$

which is identical to equation (3.8). This shows that equation (3.11) corrects only for type (c) bias but not for bias type (b). Normally, equation (3.9) would be used for correcting type (b) bias, but this would assume prior knowledge of the velocity function. This is not practicable, especially in complex flow situations.

(2) <u>Turbulent flow</u>

In turbulent flow a similar argument leads to an expression similar to equation (3.11) for correcting bias type (a) and (c),

$$\text{i.e. } n_{ic} = k\frac{n_i}{|u_i|}$$

and

$$\bar{u}_c = \frac{\Sigma\ u_i\ n_{ic}}{\Sigma\ n_{ic}}$$

or

$$\bar{u}_c = \frac{\Sigma \frac{u_i}{|u_i|}\ n_i}{\Sigma\ n_i \frac{1}{|u_i|}} \qquad (3.12)$$

where $|u_i|$ is necessary due to possible negative values of u_i.

Type (b) bias would need a separate correction similar to that in equation (3.9).

(d) Velocity gradient bias corrections

As mentioned above correcting for bias due to velocity gradients assumes prior knowledge of the velocity function. This is of course possible in laminar flows where an exact expression for the velocity distribution exists, but in other situations, such as turbulent flow, this is not possible and empirical relationships have to be used. Some investigators [13,15] have used a parabolic profile for laminar flow and for turbulent flow they have used the 1/7 power law.

Assuming that the scatterers move with the fluid, that there is a uniform particle distribution and that the sample number is proportional to the velocity, i.e. $n_i = k\ u_i$, we can derive approximate expressions for the velocities, which are measured by the LDA in laminar flows and hence apply corrections, as follows:

Consider a velocity distribution in a laminar pipe flow as shown in figure 3.4.

The 3-dimensional velocity profile is given by $u = f(x,z)$, where

$$f(x,z) = U_m\left(1 - \frac{x^2 + z^2}{R^2}\right)$$

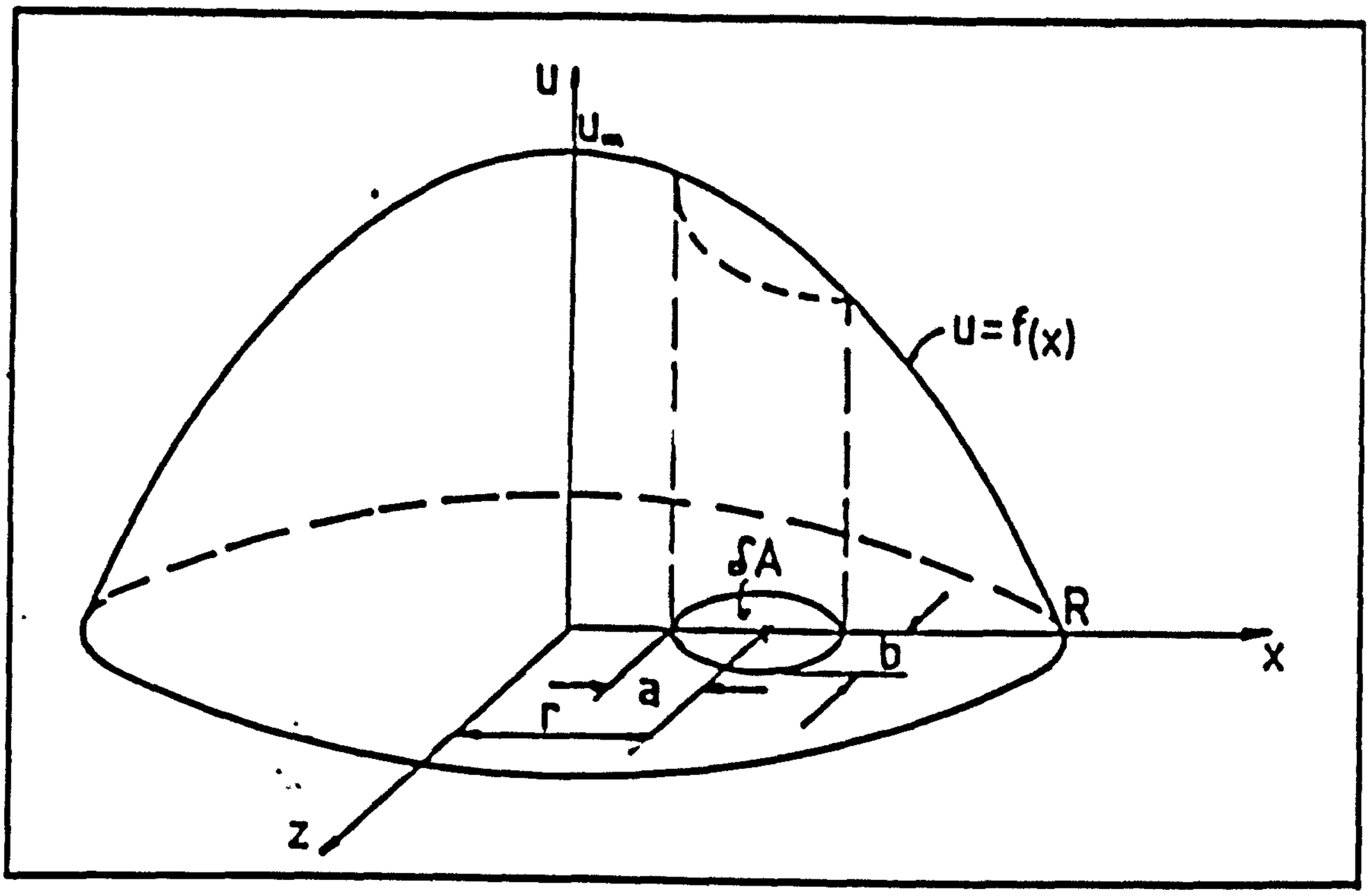

Figure 3.4 Laminar profile geometry

In figure 3.4 δA is the cross-sectional area of the probe volume normal to the flow direction (x-z plane) and the major axis of the ellipsoidal probe lies along a pipe diameter.

The ellipsoidal cross section is given by

$$\frac{(x - r)^2}{a^2} + \frac{z^2}{b^2} = 1$$

where a_1 and b are the major and minor semiaxes of the ellipse. Equation (3.10) can be written as

$$u = \frac{\iint_{\delta A} . [\, f(x,z)]^2}{\iint_{\delta A} f(x,z)}$$

The integration is performed between the limits

$$0 \leq z \leq b$$

and

$$r - a\sqrt{1 - \frac{z^2}{b^2}} \leq x \leq r + a\sqrt{1 - \frac{z^2}{b^2}} ,$$

$$\int_{z_1}^{z_2} dz \int_{x_1}^{x_2} [f(x,z)^2]\, dx$$

so that $\bar{u} = \dfrac{\int_{z_1}^{z_2} dz \int_{x_1}^{x_2} [f(x,z)^2]\, dx}{\int_{z_1}^{z_2} dz \int_{x_1}^{x_2} f(x,z)\, dx}$

where $z_1 = 0$, $z_2 = b$, $x_1 = r - a\sqrt{1 - \frac{z^2}{b^2}}$

and $x_2 = r + a\sqrt{1 - \frac{z^2}{b^2}}$.

Integration yields the following expression for the velocity $\bar{u}$, measured by the probe centred at distance r from the pipe centreline:

$$\frac{\bar{u}}{U_m} = \frac{(R^2 - r^2)^2 - \frac{R^2}{2}(a^2 + b^2) + \frac{r^2}{2}(3a^2 + b^2) + \frac{a^4}{8} + \frac{b^4}{8} + \frac{a^2 b^2}{12}}{R^2\left[R^2 - r^2 - \left(\frac{a}{2}\right)^2 - \left(\frac{b}{2}\right)^2\right]}$$

If the actual local velocity at the centre of the probe volume is $u_r = U_m(1 - r^2/R^2)$, then

$$\frac{\bar{u}_r}{U_m} - \frac{\bar{u}}{U_m} = \frac{\bar{u}_r - \bar{u}}{U_m} = 1 - \frac{r^2}{R^2} - \frac{\bar{u}}{U_m} \quad .$$

Referring to figure 3.4, the probe dimensions in the z-direction are small and if neglected, an approximate but

simpler expression can be obtained; so by putting b = 0, i.e. evaluating $\bar{u}$ along the major axis of the elliptical cross section of the probe volume one obtains the following 2-dimensional solution:

$$\frac{\bar{u}_r - \bar{u}}{U_m} = \frac{\left[\frac{(a/2)}{R}\right]^2 \left\{ 1 - 5\left(\frac{r}{R}\right)^2 - 2\left[\frac{(a/2)}{R}\right]^2 \right\}}{1 - \frac{r}{R}^2 - \frac{a/2}{R}^2} \qquad (3.13)$$

This last expression compares with equation (3.4) of reference [13].

The following observations are made about equation (3.13):

(i) At the centre line, $\frac{r}{R} = 0$,

$$\frac{\bar{u}_r - \bar{u}}{U_m} = \frac{1 - 2\left(\frac{a/2}{R}\right)^2}{\frac{1}{\left(\frac{a/2}{R}\right)^2} - 1}$$

Since $a < R$, $\frac{\bar{u}_r - \bar{u}}{U_m}$ is always positive at that position. Hence the average velocity at the centre line measured by the LDA is less than the actual one.

(ii) At the pipe wall, $\frac{r}{R} = 1$,

$$\frac{\bar{u}_r - \bar{u}}{U_m} = -4\left[1 + \frac{1}{2}\left(\frac{a/2}{R}\right)^2\right]$$

This implies that the measured velocity at the wall is higher than the actual velocity.

(iii) When $\frac{u_r - \bar{u}}{U_m} = 0$, i.e. no bias, then

$$\frac{r}{R} = \sqrt{0.2 - 0.1\left(\frac{a}{R}\right)^2}$$

Since $a \prec R$, this gives zero bias approximately halfway between the centreline and the pipe wall.

Thus it is concluded that the measured local mean velocities are too high near the wall, with no bias midway along the radius and too low around the pipe axis. Experiments carried out in laminar water flow were in agreement with these results.

There are some factors which tend to minimise velocity gradient bias:

(i) A small probe volume reduces the distribution of velocities about the true mean $\bar{u}_r$ [15]. For a small probe length $(x_1 - x_3)$, a linear velocity profile across it can be assumed. Equation (3.11) will fully correct linear profiles in the case of laminar flow.

(ii) The Gaussian distribution of the light intensity in the probe volume favours signals from crossings near its centre. Thus by setting a high threshold level in the frequency meter, only particles crossing near the centre, x_2, will be recorded. This effectively reduces the size of the probe volume.

Hence it can be concluded that type (b) bias is not as important as the sampling bias type (a) and (c) and can be kept to a minimum by proper optimization of the optics.

(e) Corrections used

In this work the uncorrected and corrected values of mean velocity, RMS and turbulence intensity were calculated as follows:

(1) Uncorrected values

$$\bar{u} = \frac{\Sigma\, u_i\, n_i}{\Sigma\, n_i}$$

$$RMS = \sqrt{u'^2} = \left[\frac{\Sigma (u_i - \bar{u})^2\, n_i}{\Sigma\, n_i}\right]^{1/2}$$

$$\text{Turbulence intensity} = \frac{RMS}{\bar{u}} \times 100\%.$$

(2) Corrected values

Here $n_{ic} = k \dfrac{n_i}{|u_i|}$

$$\bar{u}_c = \frac{\Sigma\, n_i \dfrac{u_i}{|u_i|}}{\Sigma\, n_i \dfrac{1}{|u_i|}}$$

$$RMS = \left[\frac{\Sigma (u_i - \bar{u}_c)^2 \dfrac{n_i}{|u_i|}}{\Sigma \dfrac{n_i}{|u_i|}}\right]^{\frac{1}{2}}$$

$$\text{Turbulence intensity} = \frac{RMS}{\bar{u}_c} \times 100\%$$

The above corrections are idential to the ones proposed by McLaughlin and Tiederman [20], although the author arrived at them by an intuitive approach.

The basic reasons for using these types of corrections, instead of more sophisticated ones, e.g. those proposed by Hoesel and Rodi [18], which take into account the dependence of the measured velocity component on residence time of the scatterers in the probe volume are:

(i) The level of turbulence encountered in the majority of experiments was moderate and no large scale fluctuations or flow reversals were expected, in which case McLaughlin and Tiederman's corrections should be sufficient [18].

(ii) The McLaughlin and Tiederman correction offers simplicity and does not require the measurement of residence time, which, being different from the measurement time, would require additional electronic circuitry.

In laminar flows or flows with low turbulence levels, when the particle velocity vectors deviate little from the mean flow direction, the measurement time is approximately a constant proportion of the residence time. In such case the correction proposed by Hoesel and Rodi [18],

$$\text{i.e.} \qquad \bar{u} = \frac{\Sigma\, u_i\, \Delta\tau_i\, n_i}{\Sigma\, \Delta\tau_i\, n_i}$$

where $\Delta\tau_i$ denotes the residence time, can be rewritten as

$$\bar{u} = \frac{\Sigma\, u_i\, n_i\, k\, \Delta\tau m_i}{\Sigma\, n_i\, k\, \Delta\tau m_i}$$

or $$\bar{u} = \frac{\Sigma\ u_i \quad n_i\ \Delta\tau_{m_i}}{\Sigma\ n_i\ \Delta\tau_{m_i}}$$

where the measurement time $\Delta\tau_{m_i}$, is equal to the number of measurement cycles N , divided by the signal frequency f_i, and $f_i = \frac{|u_i|}{\delta}$, where δ is the fringe spacing.

Hence $$\Delta\tau_{m_i} = \frac{N \quad \delta}{|u_i|}$$

and $$\bar{u} = \frac{\Sigma\ n_i\ u_i \dfrac{N \quad \delta}{|u_i|}}{\Sigma\ n_i \dfrac{N \quad \delta}{|u_i|}}$$

or $$\bar{u} = \frac{\Sigma\ n_i \dfrac{u_i}{|u_i|}}{\Sigma\ n_i \dfrac{1}{|u_i|}}$$

which is identical to equation (3.12). It has thus been demonstrated that at low turbulence intensities the corrections used in this work compare with the residence time correction proposed by Hoesel and Rodi.

3.3.3 Effects of noise

One of the main problems in signal processing is the elimination of noise which is always present in electronic signals. Such noise in the signals results from three main sources [1,24]:

(i) The light scattering process and the resulting optical signal.

(ii) The signal detection process and the conversion of the optical signal to an electronic signal.

(iii) The processing of the electronic signal.

High noise levels can cause a time shift in the zero crossings of the Doppler signal and the noise peaks may lead to additional zero crossings [24]. Since the measured frequency is proportional to the number of zero crossings when counters are used, large errors can be introduced into the measurement. Advanced frequency counters have detection circuits which minimize such possibilities (see chapter 4).

There are several factors which can lead to an increase in the noise levels and a deterioration of the signal, i.e. a decrease in the signal to noise ratio. Signal to noise ratio is a function of such factors [25] as:

(i) Available laser power.

(ii) Efficiency of the optical system employed. Noise in the optical signals can be minimised by optimising the design of the electrical components.

Differences in the intensities of the beams can also lead to a decrease in the signal to noise ratio [26].

(iii) Availability of suitable scattering particles of high scattering efficiency.

(iv) Selection of suitable photodetectors.

(v) Particle velocity and proper matching of particle size and fringe spacing, requirements which are often not possible to satisfy.

(vi) Mechanical vibrations may also result in deterioration of the signal quality.

An important consideration when setting up a LDA system is filtering of the electronic signals. High pass filters are used to remove the pedestal of the signal and low frequency noise; low pass filters are necessary in order to remove as much high frequency noise as possible. Improper setting of the filters can result in truncation and distortion of the Doppler signals [27] or not complete removal of low frequency and high frequency components, thus causing a broadening of the signal frequency spectrum.

Even after filtering there is always some noise left superimposed on the Doppler signals [1] . This noise has two components:

(i) Background noise, which is statistically independent of the signal and is produced by photodetector shot noise and thermal noise in the electronic components.

(ii) Pedestal shot noise which is uncorrelated with the signal although it is associated with the time dependent currents flowing when a particle is in the scattering volume.

One way to minimise errors in the measurements due to background noise is to process only signals of high amplitude,

i.e. to set the threshold voltage of the frequency meter high. This results in a reduction in the data rate and exclusion of signals with small a.c. amplitude, which, in gas-solid suspension flows may be a hindrance to the attempts to separate the velocities of the two phases (see chapter 5).

Although noise superimposed on the Doppler signal can be minimised by suitable filtering, this is best achieved in practice if the velocity fluctuations are small and the signal frequency spectrum is narrow, in which case a narrow filter band will cope with most of the noise. In cases where the velocity fluctuations are high or when different velocity fields exist between different phases (e.g. bimodal distribution), then filtering becomes more difficult and a compromise has to be found. To overcome such difficulties, Durst [28] employed an automatic filter-bank consisting of a number of filter bands which covered the whole range of frequencies likely to be encountered. A logic circuit selected the optimum pass band for every individual signal burst, thus ensuring good separation of noise and signal, even in signals with low signal to noise ratio.

3.4 COLLECTING OPTICS GEOMETRY

The geometry of the collecting optics determines the effective dimensions of the probe volume from which scattered light is collected by the photomultiplier. When forward paraxial light collection, as in this work, is used, the depth of field of view, i.e. the length of the probe volume is determined by the collecting lens f number. The transverse size of the probe is determined by the pinhole diameter, d_p [29].

Referring to figure 3.5, a pinhole of diameter $d_p = 4R_s(v/u)$ where u and v denote the object and image distances of the collecting lens, would only let through light collected from the probe volume of radius R. Thus the radius of the pinhole reduces the effective size of the probe volume by masking off light scattered by a particle outside radius R_s.

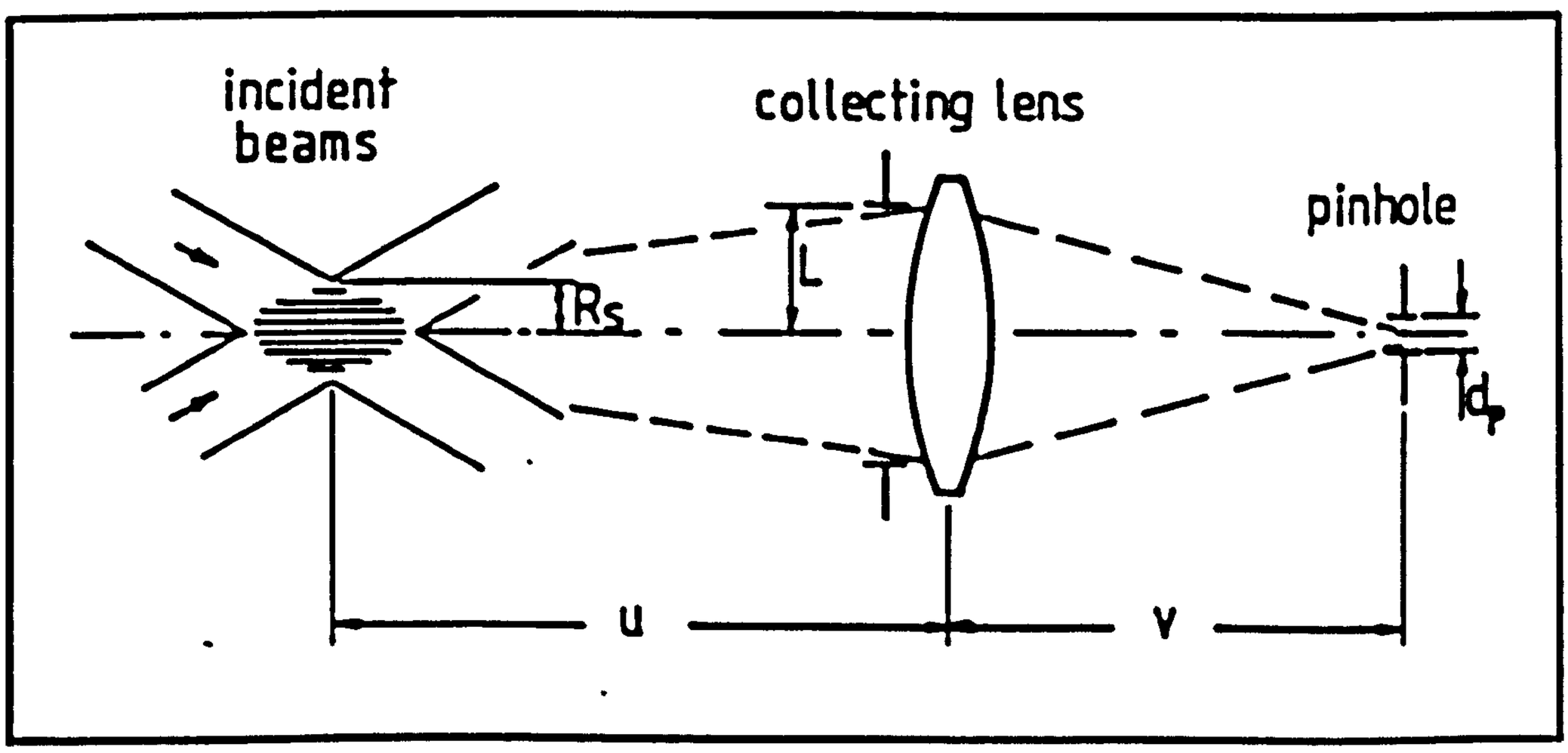

Figure 3.5 Collecting optics geometry

The effects of the collecting optics f number are discussed in detail in chapter 5, where the conflicting requirements of small collecting aperture for limiting noise and of large aperture for dependence of signal visibility on particle size, are investigated.

REFERENCES

[1] Blake K A and Jesperson K I The NEL laser velocimeter. Dept. of Trade and Industry, National Engineering Laboratory Report No 510, May 1972.

[2] Hobson C A 1978 Digital analysis of opto-electronic data. PhD Thesis, Dept. of Electr. and Control Engineering, Liverpool Polytechnic.

[3] Durst F and Zare M 1974 Removal of pedestals and directional ambiguity of optical anemometer signals. Appl. Opt. 13 11 2562-2579.

[4] Buchhave P 1975 Laser Doppler velocimeter with variable optical frequency shift. Optics and Laser Technology 11-16.

[5] Stevenson W H 1970 Optical frequency shifting by means of a rotating diffraction grating. Appl. Opt. 9 3 649-652.

[6] Wigley G 1974 The application of radial diffraction gratings to laser anemometry. AERE-R 7886.

[7] Oldengarm J 1975 The use of rotating radial diffraction gratings in laser Doppler velocimetry. Proc. AGARD Conf. on applications of non-intrusive instrumentation in fluid flow research (Neuilly sur Seine: NATO Advisory Group for Aerospace Research and Development) paper no 193 pp 23/1-23/6.

[8] Oldengarm J 1977 Development of rotating diffraction gratings and their use in laser anemometry. Optics and Laser Technology 69-71.

[9] Oldengarm J and Venkatesh P 1976 A simple two-component laser Doppler anemometer using a rotating radial diffraction grating. J. Phys. E: Sci. Instrum. 9 1009-1012.

[10] Oldengarm J, van Krieken A H and van der Klooster 1975 Velocity profile measurements in a liquid film flow using the laser Doppler technique. J. Phys. E: Sci. Instrum. 8 203-205.

[11] Goosens L H J and van Pagee J A 1976 Electronic mixing device in laser Doppler velocimetry. J. Phys. E: Sci. Instrum. 9 554-556.

[12] Hösel W and Rodi W 1975 Errors occurring in LDA-measurements with counter signal processing. Proc. LDA symposium Copenhagen 251-257.

[13] Owen L M and Rogers R H 1975 Velocity biasing in laser Doppler anemometers. Proc. LDA symposium Copenhagen 89-114.

[14] Edwards R V, Angus J C, French M J and Dunning J W 1971 Spectral analysis of the signal from the laser Doppler flowmeter: time independent systems. J. Appl. Phys. 42 2 837-850.

[15] Kreid D K 1974 Laser-Doppler velocimeter measurements in nonuniform flow: error estimates. Appl. Opt. 13 8 1872-1881.

[16] Durao D F G and Whitelaw J H 1979 Relationship between velocity and signal quality in laser Doppler anemometry. J. Phys. E: Sci. Instrum. 12 47-50.

[17] Buchhave P 1975 Biasing errors in individual particle measurements with the LDA-counter signal processor. Proc. LDA Symposium Copenhagen 259-278.

[18] Hoesel W and Rodi W 1977 New biasing elimination method for laser Doppler velocimeter counter processing processing. Ref. Sci. Instrum. 48 7 910-919.

[19] McDougall T J 1980 Bias correction for individual realisation LDA measurements. J. Phys. E: Sci. Instrum. 13 53-60.

[20] McLaughlin D K and Tiederman W G 1973 Biasing correction for individual realization of laser anemometer measurements in turbulent flows. The Physics of Fluids 16 k2 2082-2088.

[21] Durao D F G and Whitelaw J H 1975 The influence of sampling procedures on velocity bias in turbulent flows. Proc. LDA Symposium Copenhagen 138-149.

[22] George W K Jr 1975 Limitations to measuring accuracy inherent in the laser Doppler signal. Proc. LDA Symposium Copenhagen 20-63.

[23] Durao D F G, Laker J and Whitelaw J H 1980 Bias effects in laser Doppler anemometry. J. Phys. E: Sci. Instrum. 13 442-445.

[24] Hoesel W and Rodi W 1975 A highly accurate method for digital processing of laser-Doppler velocimeter signals. Universitat Karlsruhe.

[25] Durst F 1975 Electronic processing of optical anemometer signals. Proc. LDA Symposium Copenhagen 208-250.

[26] Durst F and Whitelaw J H 1971 Optimization of optical anemometers. Proc. Roy. Soc. London A 3211 157-181.

[27] Wang J C F 1975 Measurement accuracy of flow velocity via a digital-frequency-counter laser velocimeter processor. Proc. LDA Symposium Copenhagen 150-174.

[28] Durst F 1978 Studies of particle motion by laser Doppler techniques. Proc. Dynamic Flow Conference 345-372.

[29] Hong N S 1977 A method of particle sizing using crossed laser beams. PhD Thesis Dept. of Chem. Eng. and Chem. Tech. Imperial College, London.

CHAPTER 4

EXPERIMENTAL EQUIPMENT

4.1 INTRODUCTION

The main laser Doppler anemometer system used in this work was a counter based dual beam arrangement, operating in the paraxial forward scatter mode. Although a number of integrated laser Doppler anemometers are commercially available, the systems used in this work were designed and assembled from various components not specifically intended for this purpose. This offered the advantage of flexibility in the optimization of the laser optics and also had the added benefit of low cost, with, it is believed, as good a performance as that of more sophisticated equipment.

Besides the main two lens system, other single and multiple lens dual beam arrangements were used in the course of optimization of the laser anemometer. Also non paraxial and backscatter modes were tried.

A large number of various electronic and other instruments were used and several types of flow rigs were designed to meet the particular requirements of these studies.

Figure 4.1 gives a general view of the optical system and the associated instrumentation used in the investigation of two phase flows. Digital data storage methods using a microprocessor based system were developed and online data processing was considered indispensable due to the very high data acquisition rates. The data were finally stored on floppy discs for further analysis if necessary.

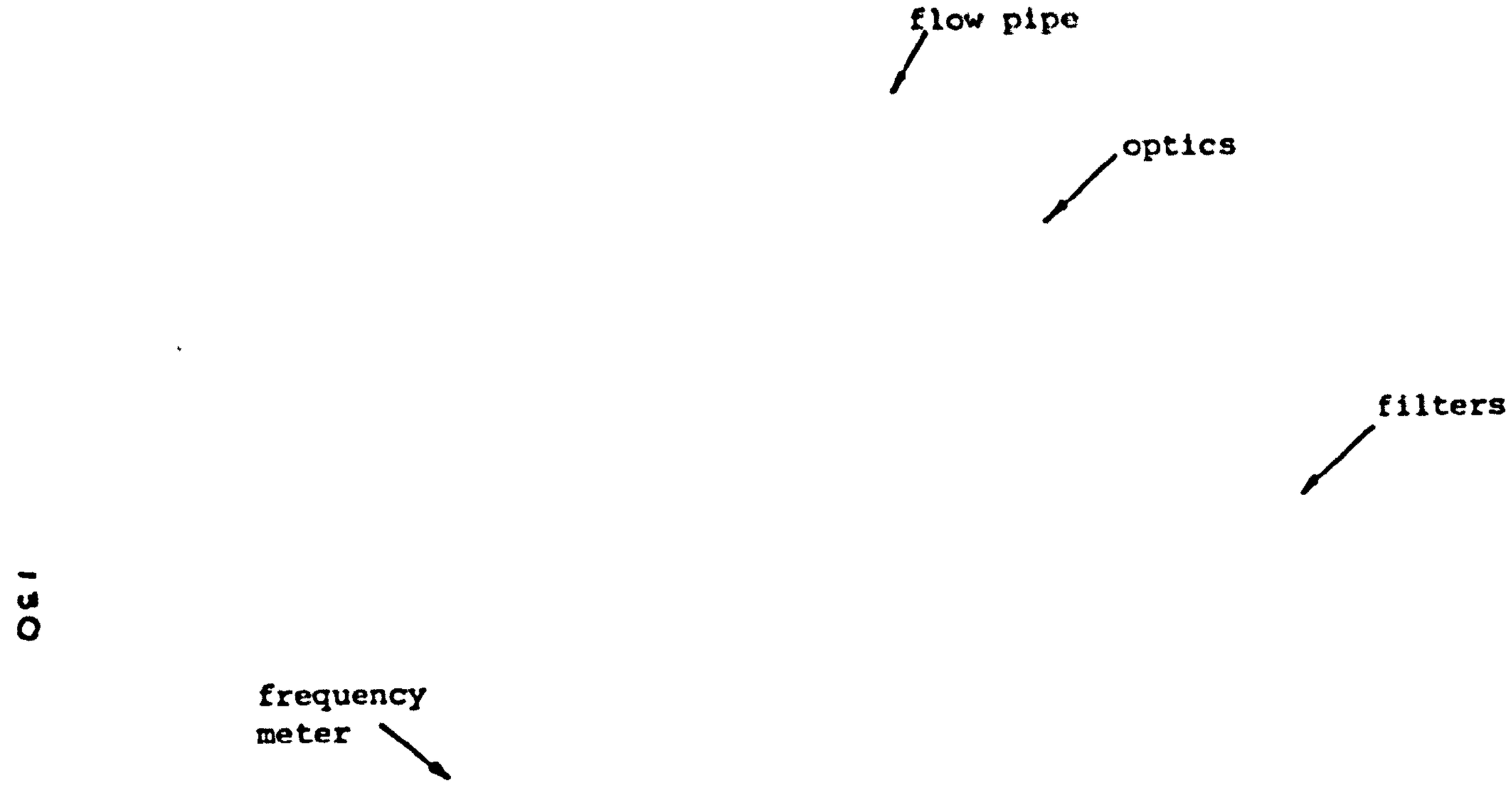

Figure 4.1 An overall view of the L.D.A. system

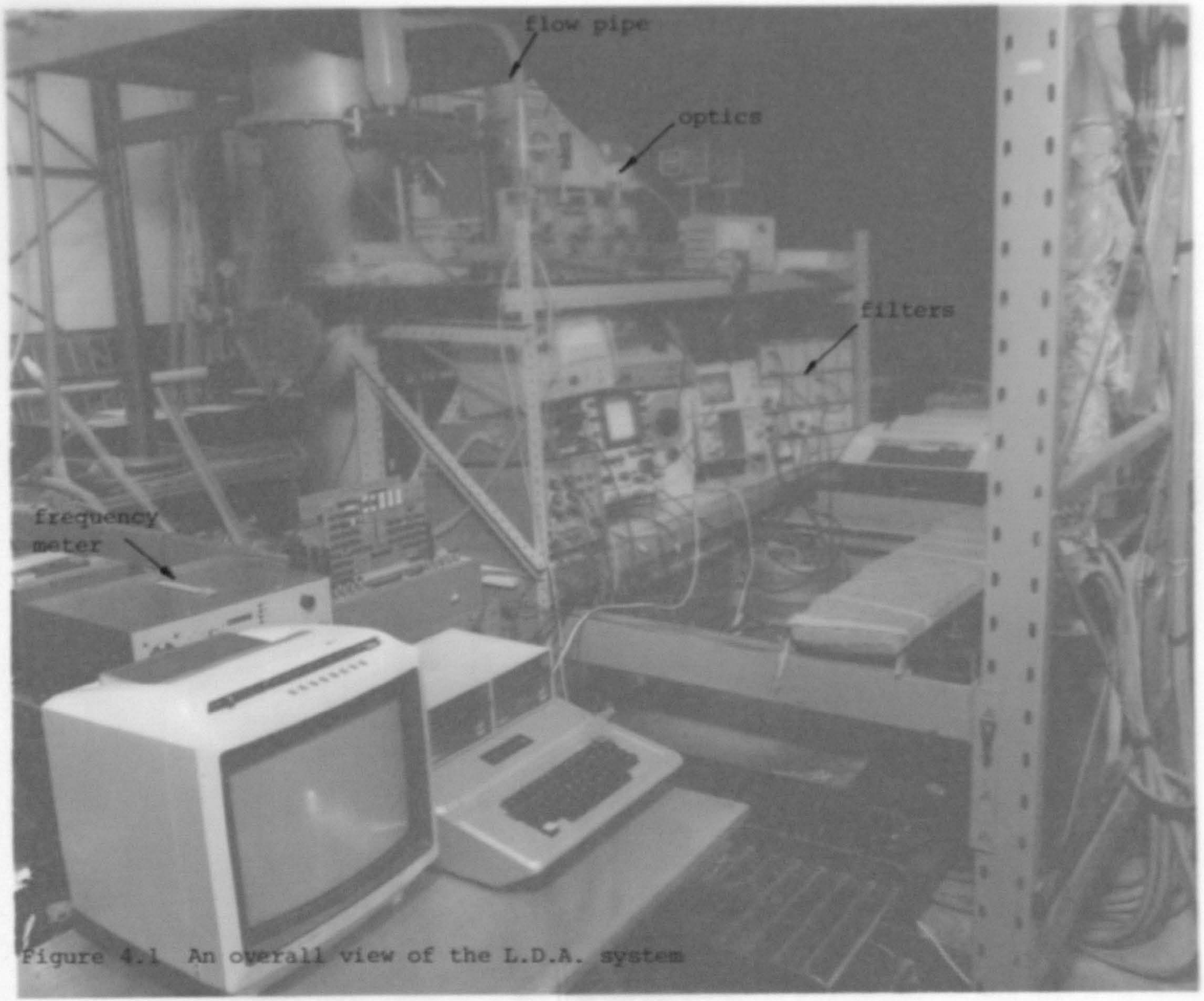

Figure 4.1 An overall view of the L.D.A. system

The results were normally displayed on a V.D.U. and hard copies obtained from a teletype if required.

4.2 LDA COMPONENTS

4.2.1 The laser

The laser used was a Spectra Physics, model 120, helium-neon laser, operating in the TEM_{oo} mode, with a 1.1 mrad beam divergence and a $\frac{1}{e^2}$ beam diameter of 0.8 mm at the exit from the resonator.

Figure 4.2 shows a schematic of the laser

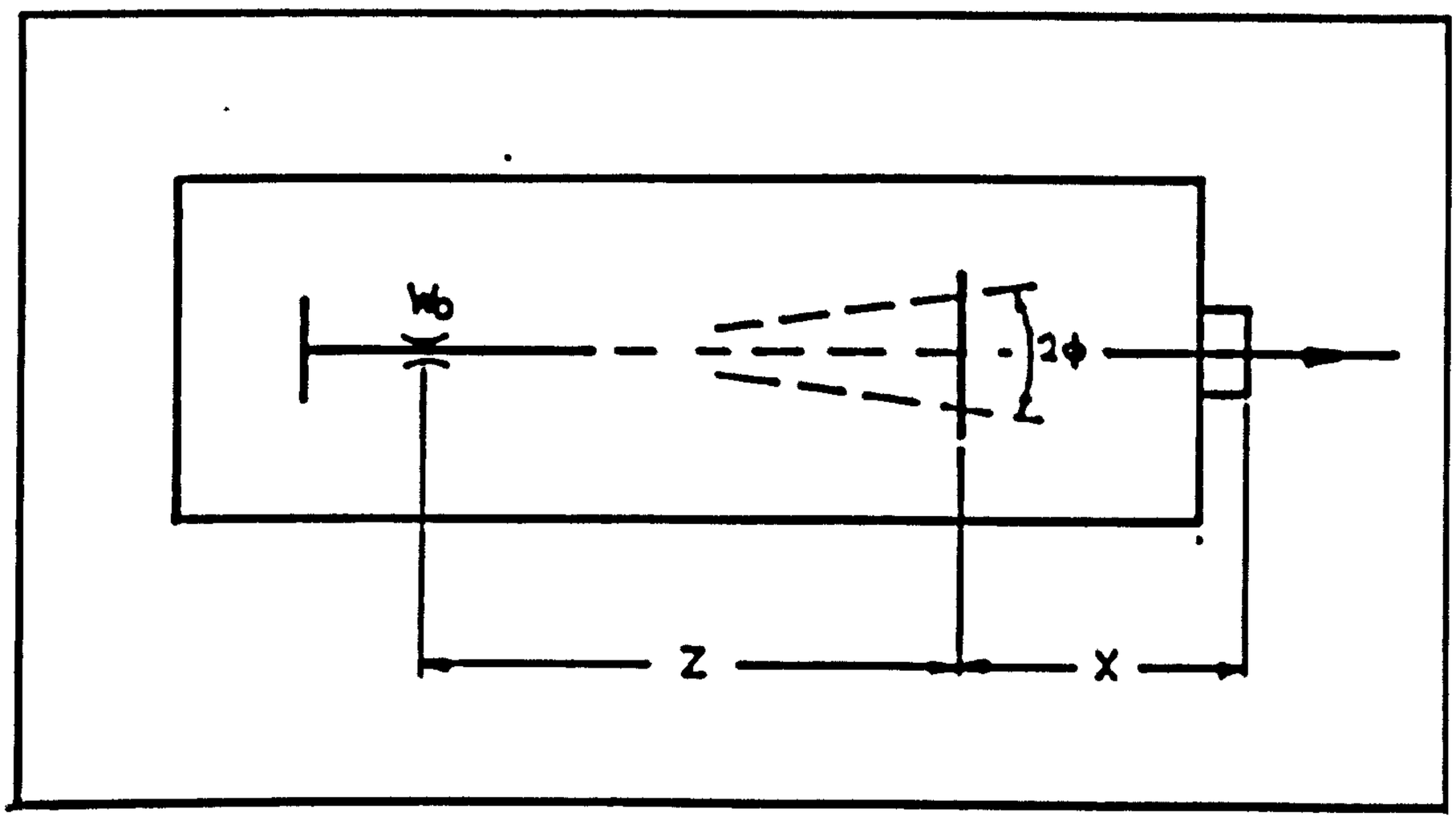

Figure 4.2 Laser parameters

The size and location of the minimum beam diameter (the waist) in the resonator were not included in the manufacturer's specification. They were estimated as follows:

The beam waist radius in the resonator, w_o, is given by equation (2.11) as

$$w_o = \frac{\lambda}{\pi \phi}$$

where 2ϕ = 1.1 mrad and λ = 0.6328 μm.

Thus w_o = 366 μm.

Equation (2.9) was used to estimate the distance of the waist from the exit, giving

$$z = \left[\left(\frac{w_z^2}{w_o^2} - 1\right)\left(\frac{\pi w_o^2}{\lambda}\right)^2\right]^{\frac{1}{2}}$$

After substituting the values w_z = 0.4 mm and w_o = 0.366 mm it was found that z = 293 mm.

The distance x was estimated to be 32 mm, thus giving an overall distance of 325 mm between the beam waist in the resonator and the front aperture in the casing.

The above values were verified by calculating w_o and z using the radius of curvature of the concave exit mirror.

Those laser parameters were subsequently used in all calculations involving the parameters of the focused beam.

4.2.2 Photomultiplier and collecting optics

An E.M.I., 51 mm photomultiplier tube, model 9658 B was mainly used. Some use was also made of a 30 mm tube,

model 9698 QB. Due to the relatively high signal frequencies involved, the divider network for the 9658 B dynode was arranged as for fast pulse applications with excellent results [1]. The photomultiplier was enclosed in a metal casing and a DISA telescope was attached to it to form the collecting optics.

The telescope had a 105 mm focal length objective lens, an adjustable iris diaphragm and a pinhole holder whose position could be adjusted along two axes. A number of additional lenses of various focal lengths could be attached to the telescope objective to alter the magnification. The importance of the collecting optics geometry, in relation to the Doppler signal characteristics is discussed in chapter 5.

As shown in figure 4.3 the distance between the objective and the pinhole was 105 mm. Table 4.1 shows a number of f number values for various magnifications and aperture openings, where

$$\text{f number} = \frac{u}{2L}$$

(see chapter 5). The focal lengths of the lens combinations were evaluated using the thin lens formula [2]

$$\frac{1}{f} = \frac{1}{f_1} + \frac{1}{f_2} + \cdots$$

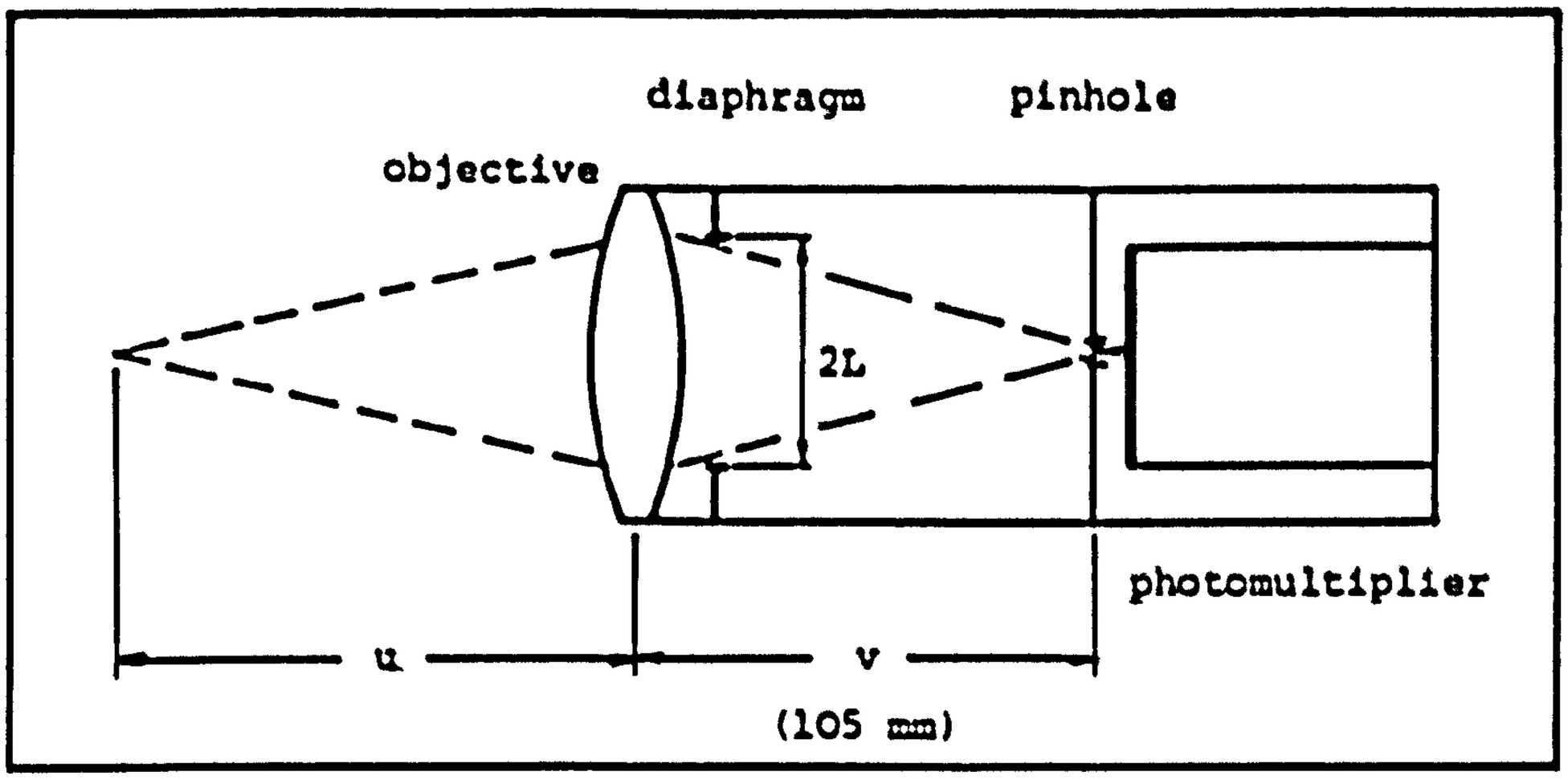

Figure 4.3 Collecting optics parameters

Aperture numbers / Collecting lenses	4	5.6	8	11	16	22	32	f (mm)	u (mm)
OB	∞	∞	∞	∞	∞	∞	∞	105	∞
OB + 3	12.8	17.9	25.6	35.2	51.2	70.4	102.4	80	336
OB + 4	9.6	13.4	19.1	26.3	38.2	52.6	76.5	74	251
OB + 5	7.6	10.7	15.3	21.1	30.6	42.1	61.3	69	201
OB + 3 + 4	5.3	7.5	10.7	14.7	21.3	29.3	42.7	60	140
OB + 3 + 5	4.8	6.7	9.5	13.1	19.0	26.2	38.1	57	125
OB + 4 + 5	4.2	5.9	8.5	11.6	16.9	23.3	33.8	54	111
OB + 3 + 4 + 5	3.1	4.4	6.2	8.6	12.5	17.2	25.0	46	82
OB + 3 + 4 + 4 + 5	2.4	3.3	4.7	6.5	9.4	13.0	18.9	39	62

Table 4.1 Values of $f\,no$ for telescope. OB = objective; f = focal length; lenses are numbered 3, 4 and 5, numbers indicate lens power $(\frac{1}{f})$; $f\,no = u/(\frac{f_{OB}}{\text{aperture no}})$

4.2.3 The radial diffraction grating

Two bleached type radial diffraction gratings were used, one with 18600 lines and the other with 36000 lines. The former was used during optimization of the optics whereas the latter was mainly used during investigations of two phase flows. The diffraction grating disc was mounted on the spindle of a variable speed motor controlled by a 'Motomatic' speed control, model E-550-m. The maximum speed of the motor was 5000 rpm. The 36000 line grating gave a shift frequency of 1.2 MHz/1000 rpm.

When assembling the optics it was found convenient to place the diffraction grating at a small angle to the incident beam so that the reflected zero order beam did not reenter the laser, as this could affect the coherence and polarization of the main beam [3]. It was also observed that if this was allowed to happen, reflections from the laser mirror produced faint beam spots in the vicinity of the crossover region with undesirable effects.

4.2.4 Other components

During the various stages of the work a large number of optical components and accessories were used such as: Triangular optical benches, carriers with adjustments in two directions, lens holders, iris diaphragms, angular displacement units.etc.

A number of glass lenses of various apertures and focal

lengths, mirrors and prisms were also used as required.

4.3 TRAVERSING MECHANISM

The laser Doppler anemometer was designed with the ultimate objective of being used in pipe flows; therefore a suitable traversing mechanism had to be designed, so that velocity profiles could be obtained.

Various methods for traversing have been used in the past, such as moving the focusing lens, moving the flow pipe, or moving the whole optical system. The first method was excluded, since movement of the focusing lens alone alters the position of the beam waist relative to the beam cross-over. The latter two methods preserve the beam geometry and require no readjustment of the collecting optics.

It was decided to adopt the third method, as being simpler to realise in practice than the second one. The components of the laser anemometer were arranged on a 2 m long optical bench, which was carried on two translation stages with micrometric movement. The micrometer provided a 65 mm traverse in one direction and was graduated in $\frac{1}{100}$ mm intervals. In this manner the optical system, once arranged, was left undisturbed, thus securing constancy of probe volume parameters.

Figure 4.4 shows the optical set up operating in the forward scatter mode. In order to accommodate the flow

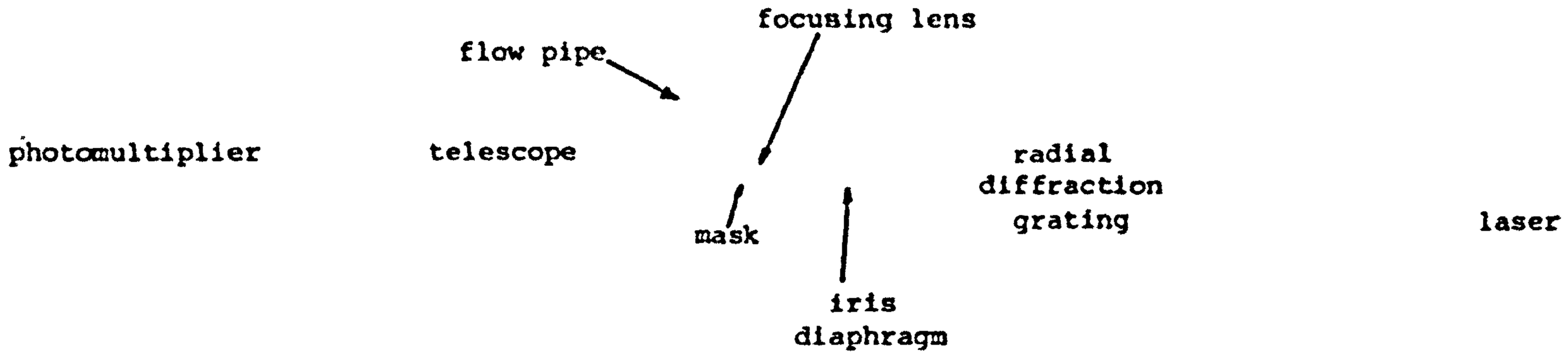

Figure 4.4 L.D.A. optical set-up

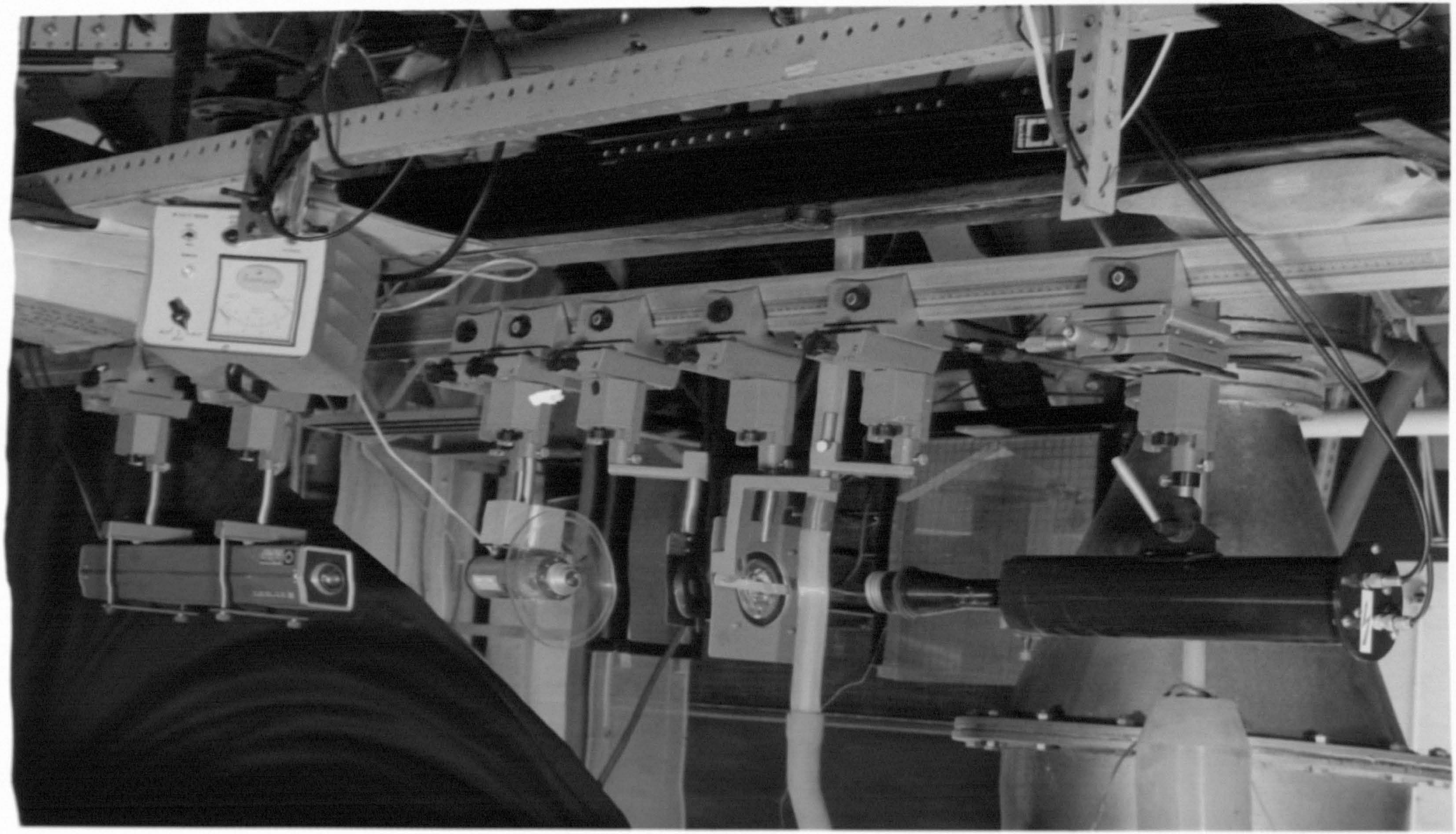

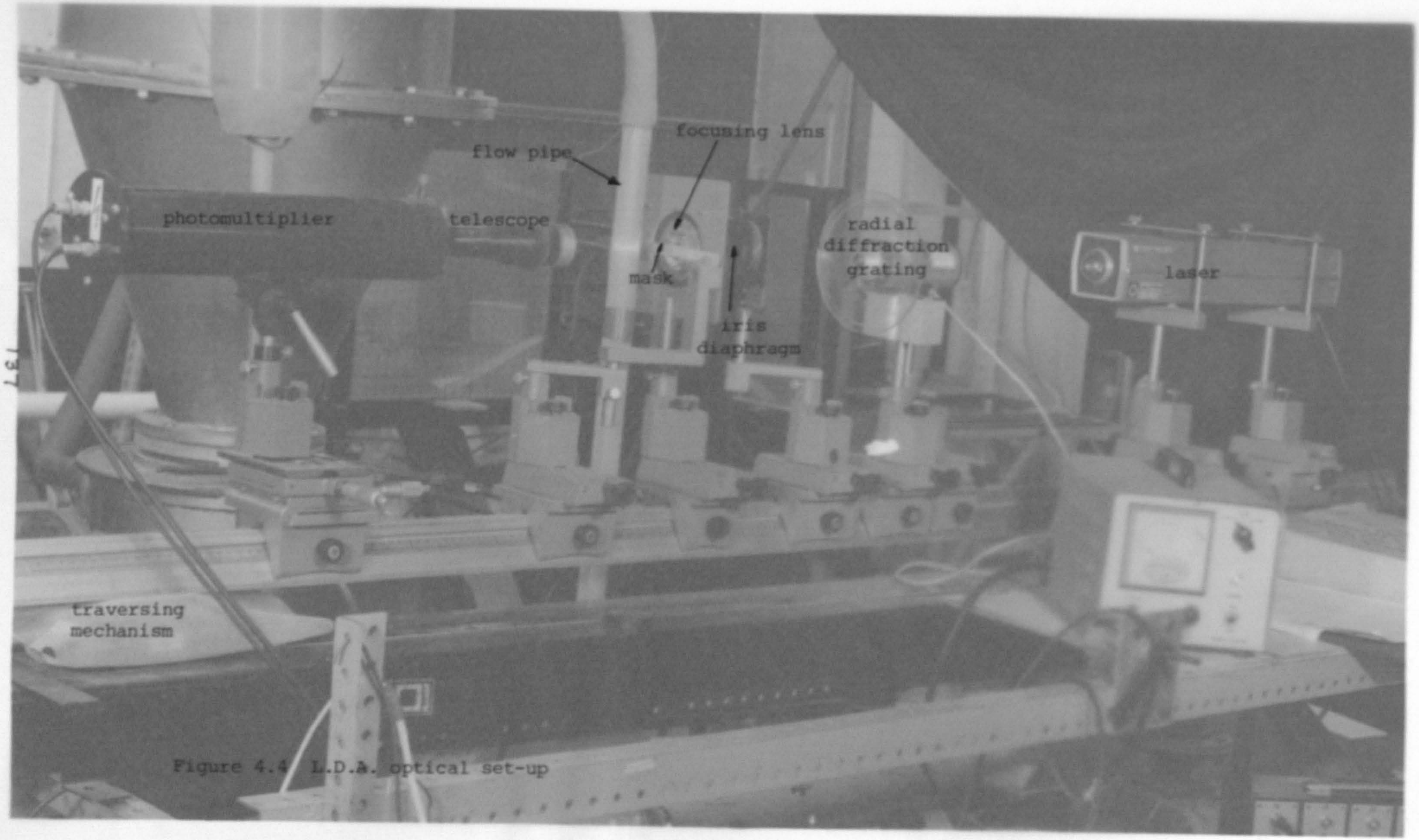

Figure 4.4 L.D.A. optical set-up

pipe, the components on the optical bench were offset by suitable modification of the carriers.

4.4 TWO LENS DUAL BEAM SYSTEM

A dual beam laser anemometer system based on the two lens arrangement discussed in chapter 2 was mainly used, operating in the forward scatter mode. Details of that system are shown in figure 4.5. That arrangement achieved coincidence of beam intersection and beam waist.

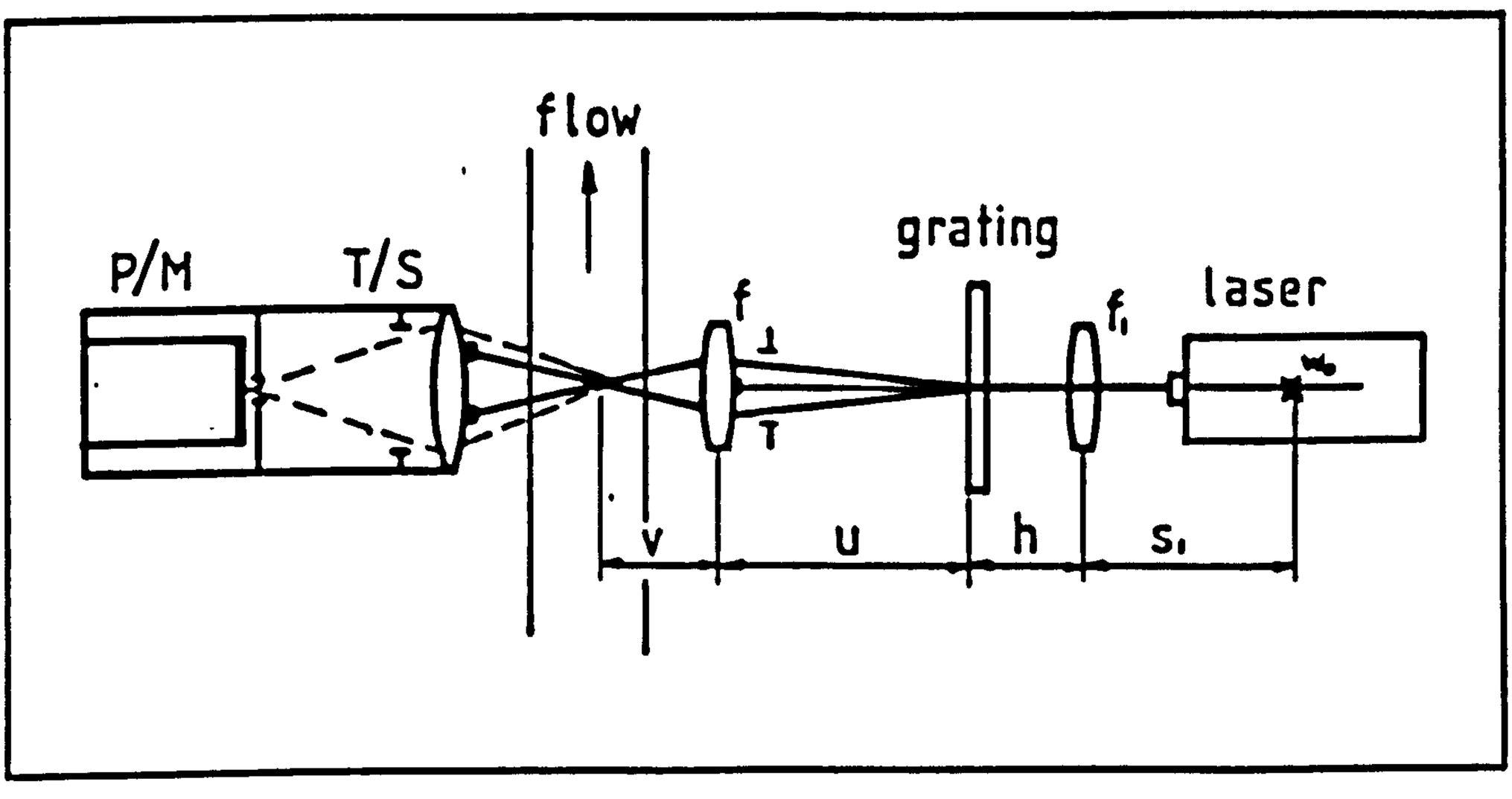

Figure 4.5 Two lens dual beam anemometer. S_1 = 64.2 cm, h = 15.3 cm, u = 20.5 cm, f_1 = 20 cm, f = 5 cm, v = 7.3 cm.

The angle between the beams was calculated by measuring the beam spacing at a known distance away from the crossover and

and was found to be 9.08^{o}. This, using equation (2.5), gave a fringe spacing $\delta \approx 2$ μm. The beam waist diameters at the crossover were measured using the power ratio method (see chapter 2) and were found to be approximately equal to 80 μm, which, using equation (2.16), gave the following probe volume dimensions:

$$\Delta z = 510 \text{ μm}$$

$$\Delta y = 81 \text{ μm} \quad .$$

Hence the number of fringes was approximately 40.

Figures 4.6 and 4.7 show the above system as used both in forward and back scatter modes. The back scatter mode was only used when investigating the signal characteristics in the development of discrimination techniques (see chapter 5).

One of the main experimental difficulties encountered was the measurement of velocities in the near wall region, due to reflections from the walls of the glass pipe, which led to excessive noise in the signals. As a wide collecting aperture had to be used in order to maintain dependance of signal parameters on particle size (see chapter 5), a different system was tried. In this system, which was similar to that reported by Koniuta, Dudermel and Adler [4], the beams were made to cross at a point by using two high quality mirrors and were each focused by a small aperture

Figure 4.6 Combined forward and backscatter modes

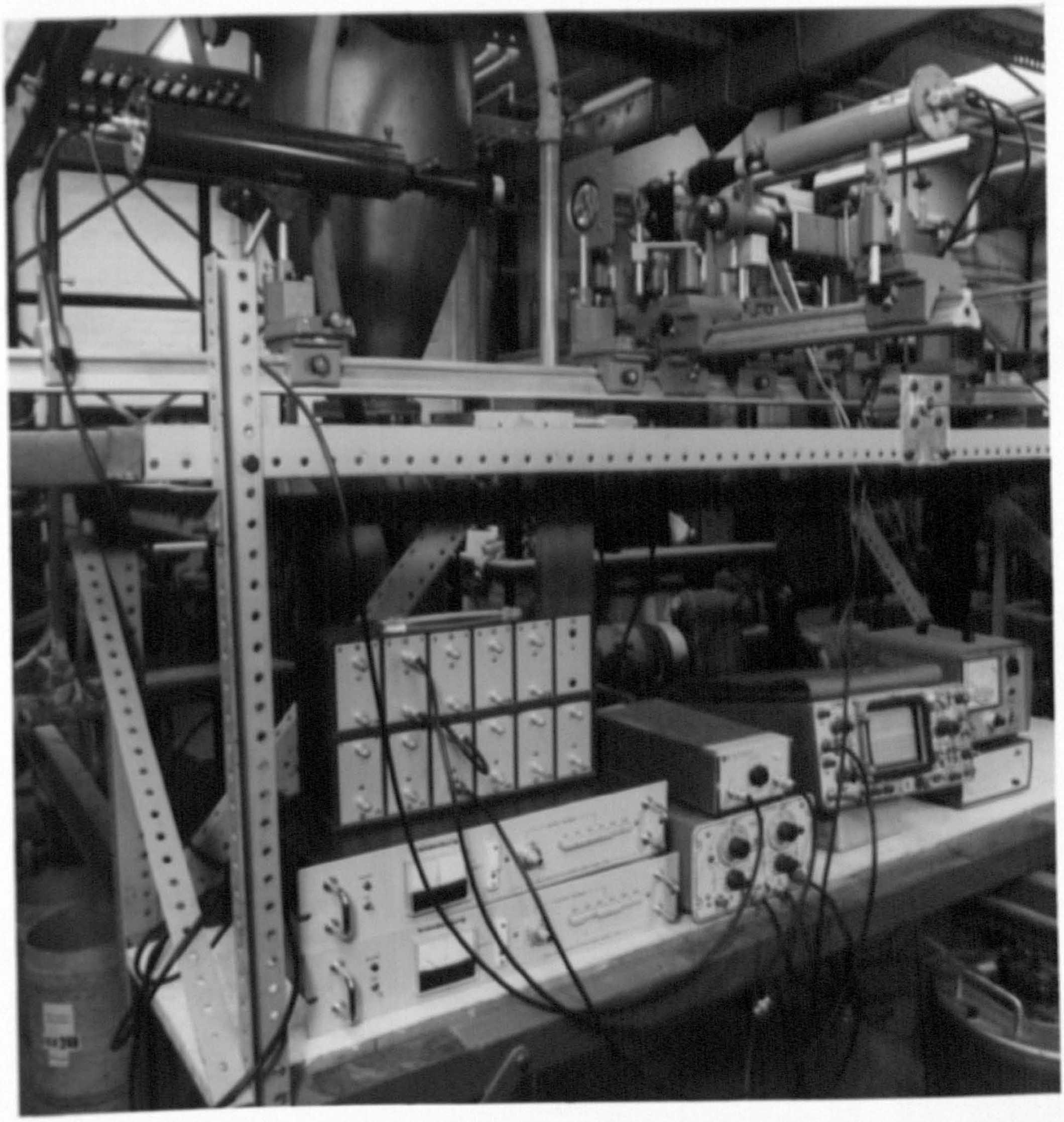

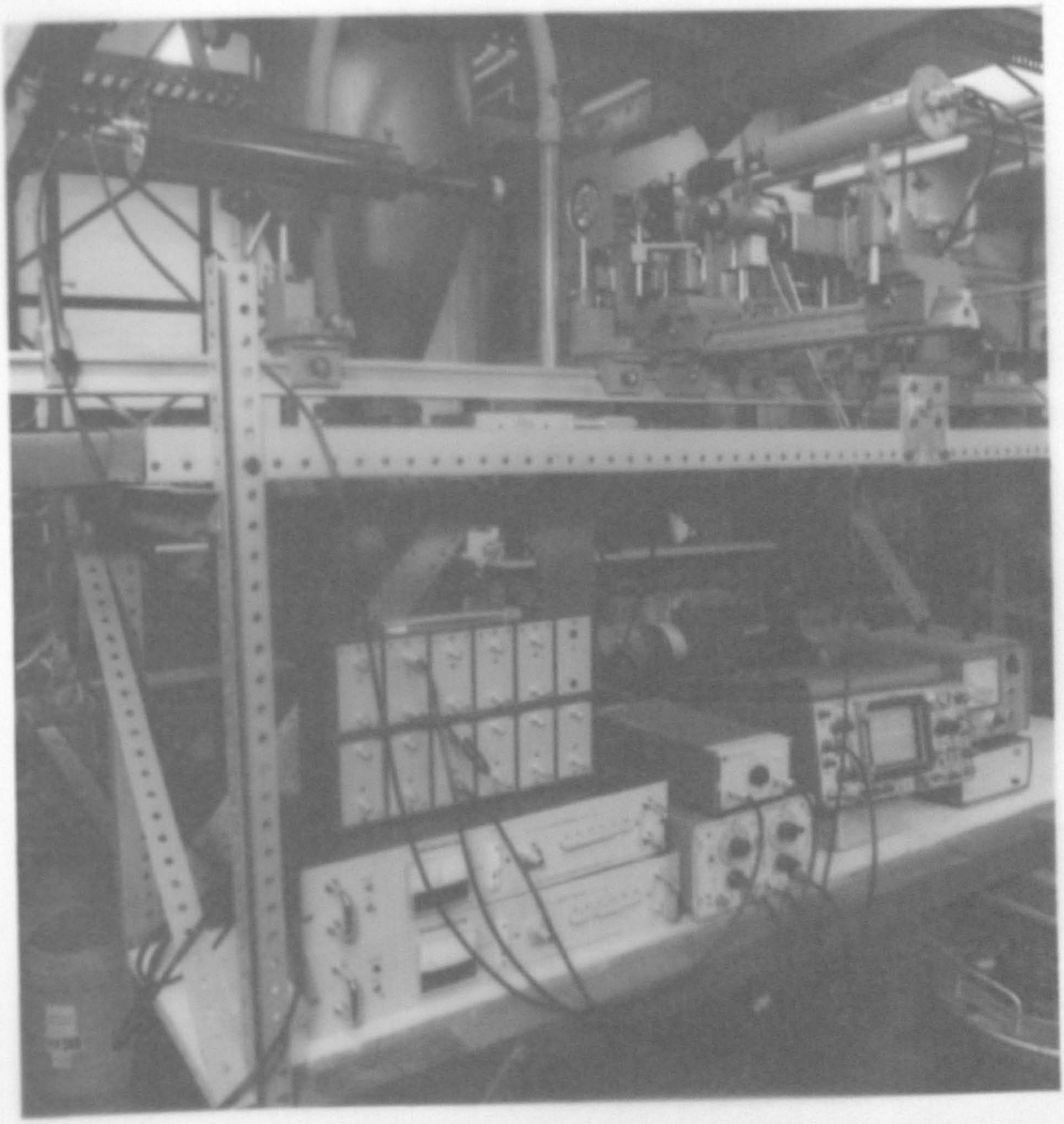

Figure 4.6 Combined forward and backscatter modes

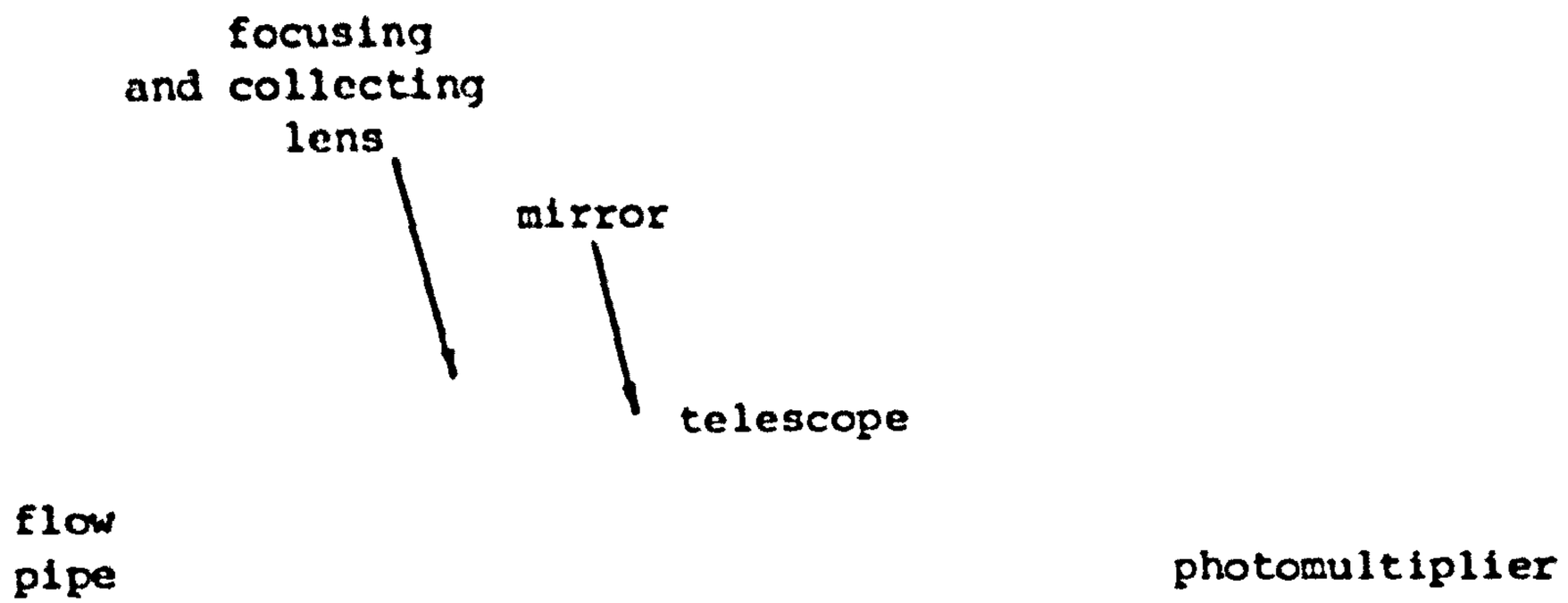

Figure 4.7 Details of the backscatter arrangement

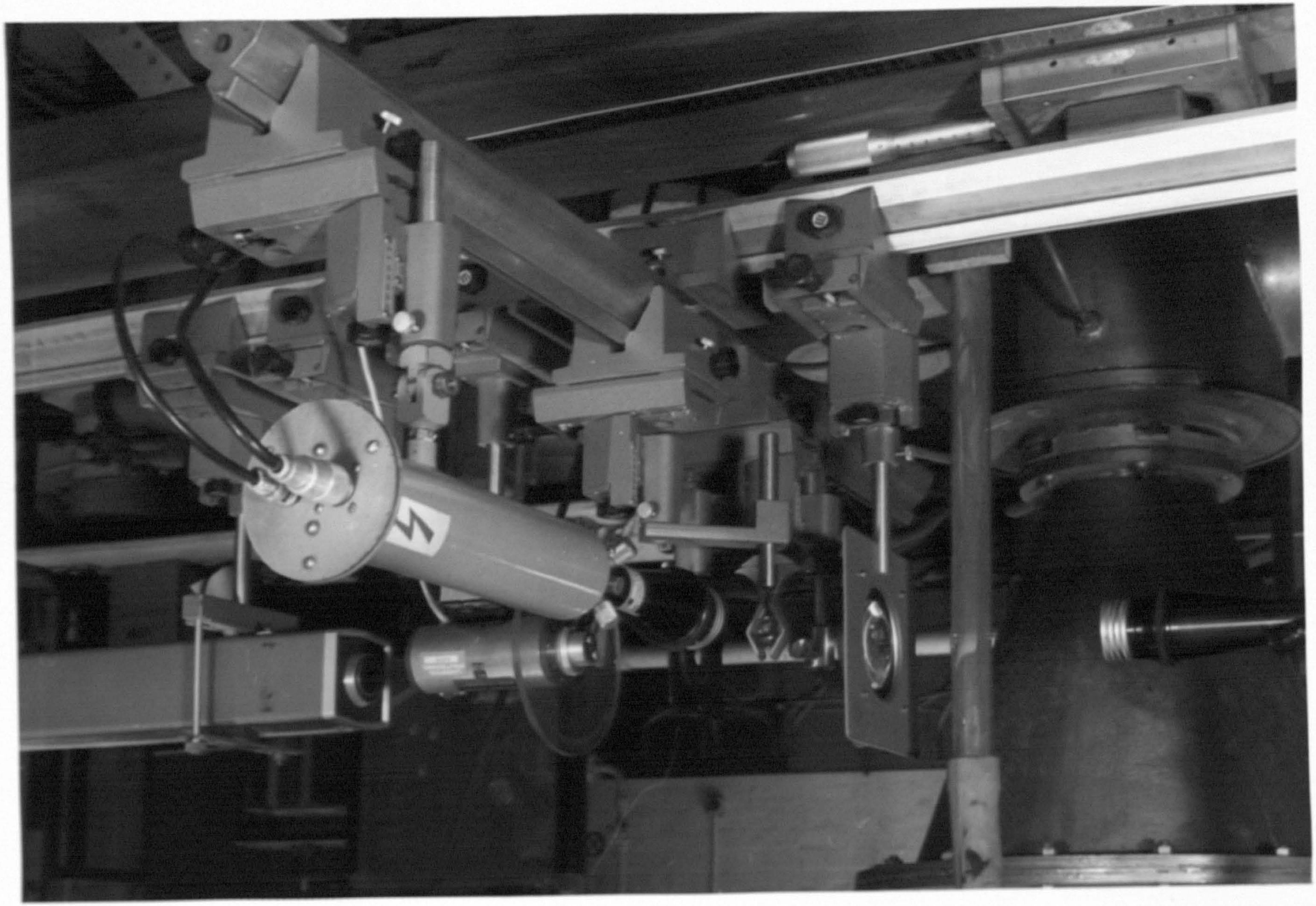

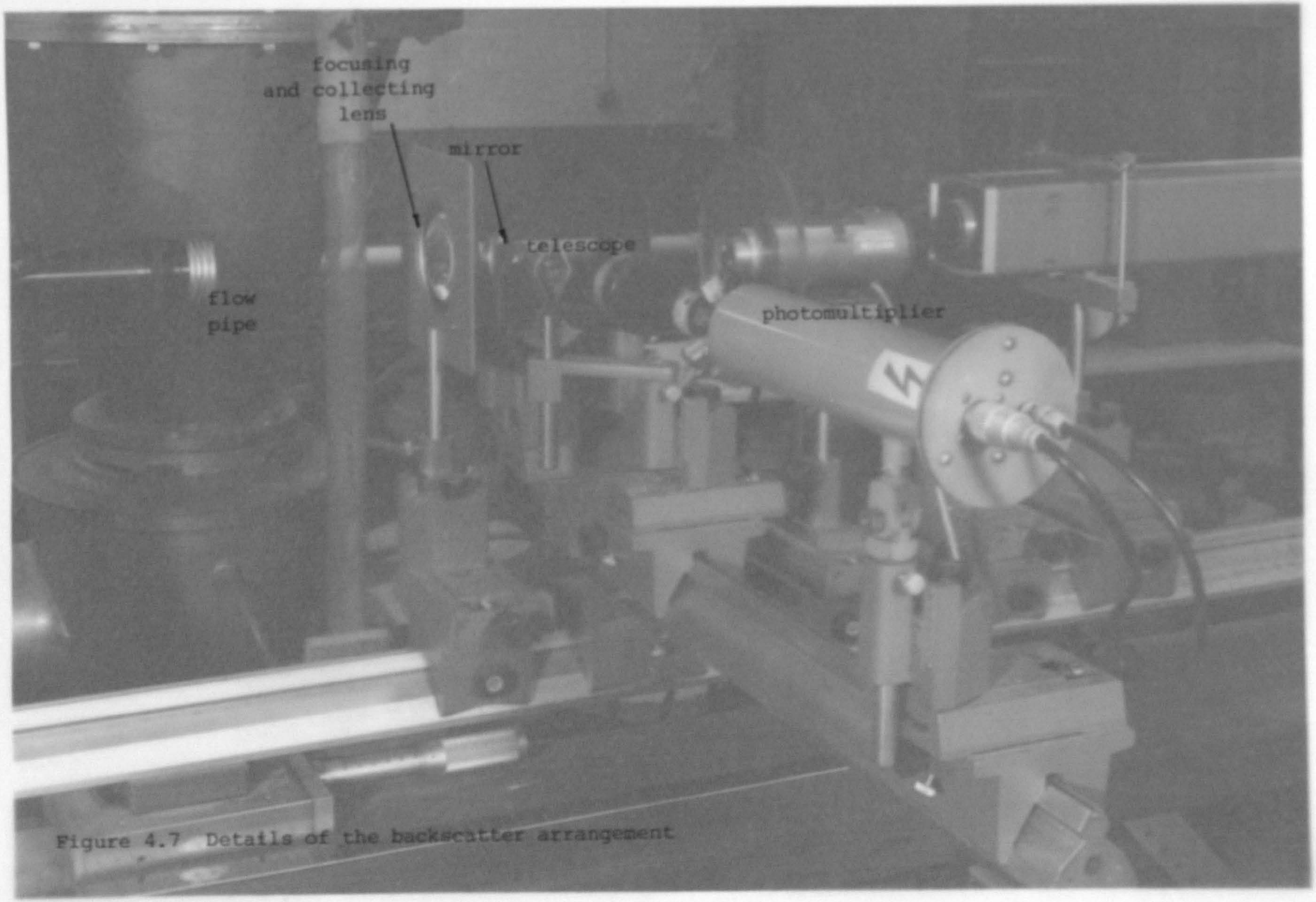

Figure 4.7 Details of the backscatter arrangement

lens. The resulting wide beam angle reduced the effects of reflected light and allowed measurements near the pipe wall to be made. The drawback was that the number of high visibility signals, resulting from small scatterers, decreased significantly. This was attributed to the very small fringe spacing (δ = 1 μm), approaching the wavelength λ, in which case the conditions $\lambda < D < \delta$ (see chapter 5), where D is the scatterer diameter, were not satisfied.

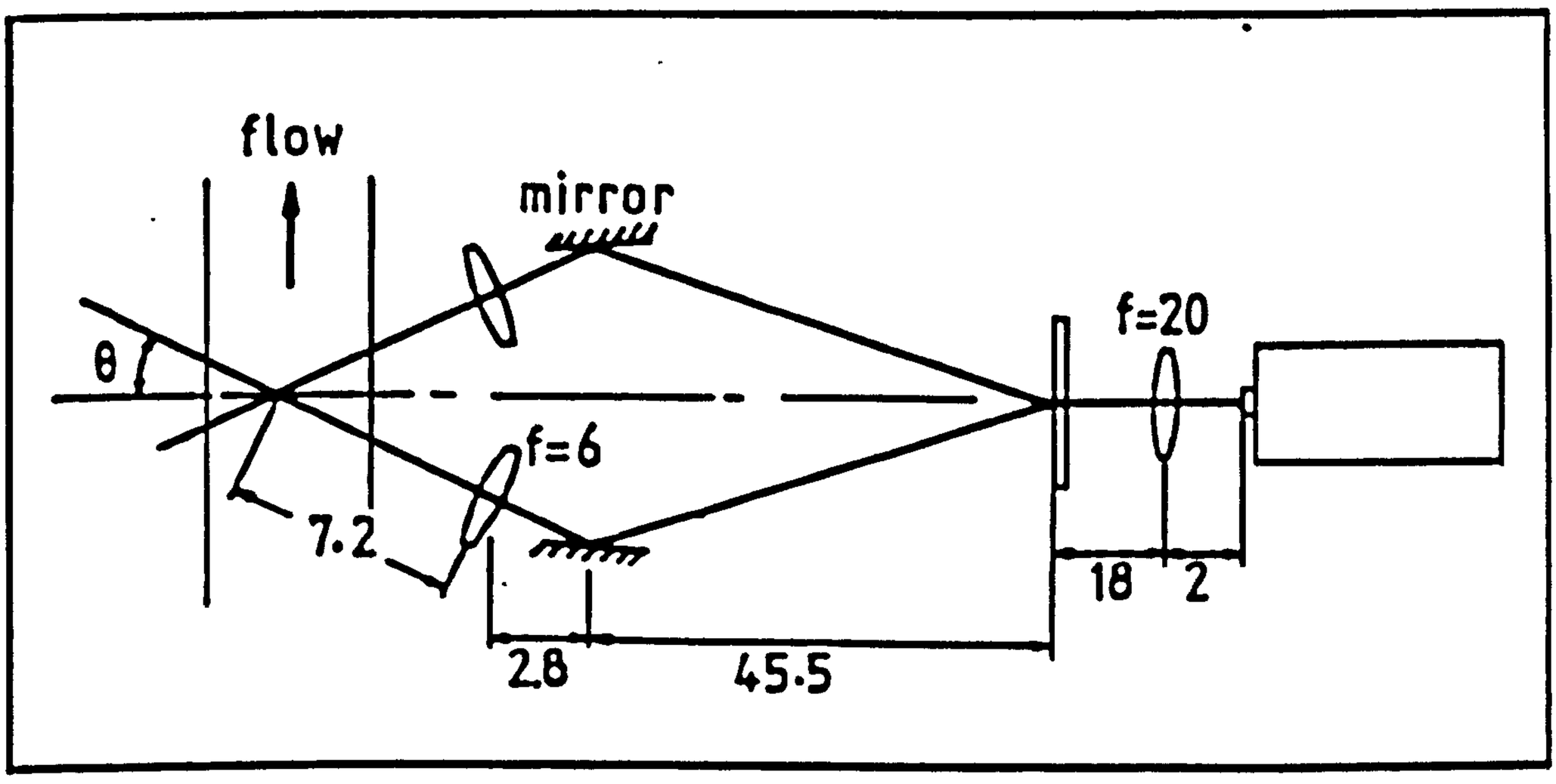

Figure 4.8 Illustrating the use of mirrors, and lenses in place of a focusing lens; dimensions in cm.

In view of the above, the two lens system was used in all measurements and the minimum distance from the pipe wall was kept to about 1 mm.

4.5 FLOW RIGS

A number of different flow rigs were designed and constructed during the course of this work. Descriptions, diagrams and a brief account of their role and usefulness follow.

4.5.1 Water flow rig

A water flow rig was designed to test different laser anemometer configurations and gain practical experience in aligning the optics. Figure 4.9 is a schematic of this flow rig. A centrifugal pump supplied a header tank in which the water level was kept constant by means of an overflow pipe. The flow pipe of 2" bore was horizontal; the working section was made of glass pipe of the same inside diameter. Dye injection into the flow was possible by means of a hypodermic needle in order to visually observe the flow. The flow was regulated by a gate valve downstream of the working section. The flowrate was evaluated by weighing a quantity of water over a measured time period.

4.5.2 Recirculating powder rig

The recirculating powder rig consisted of a vertical glass pipe connected via flexible rubber tubing to a blower. This constituted a closed system in which a fixed quantity of solids could be circulated with air. The blowers used were an axial fan driven by an a.c. motor, whose speed could be altered via a 'variac', and a centrifugal fan driven by a

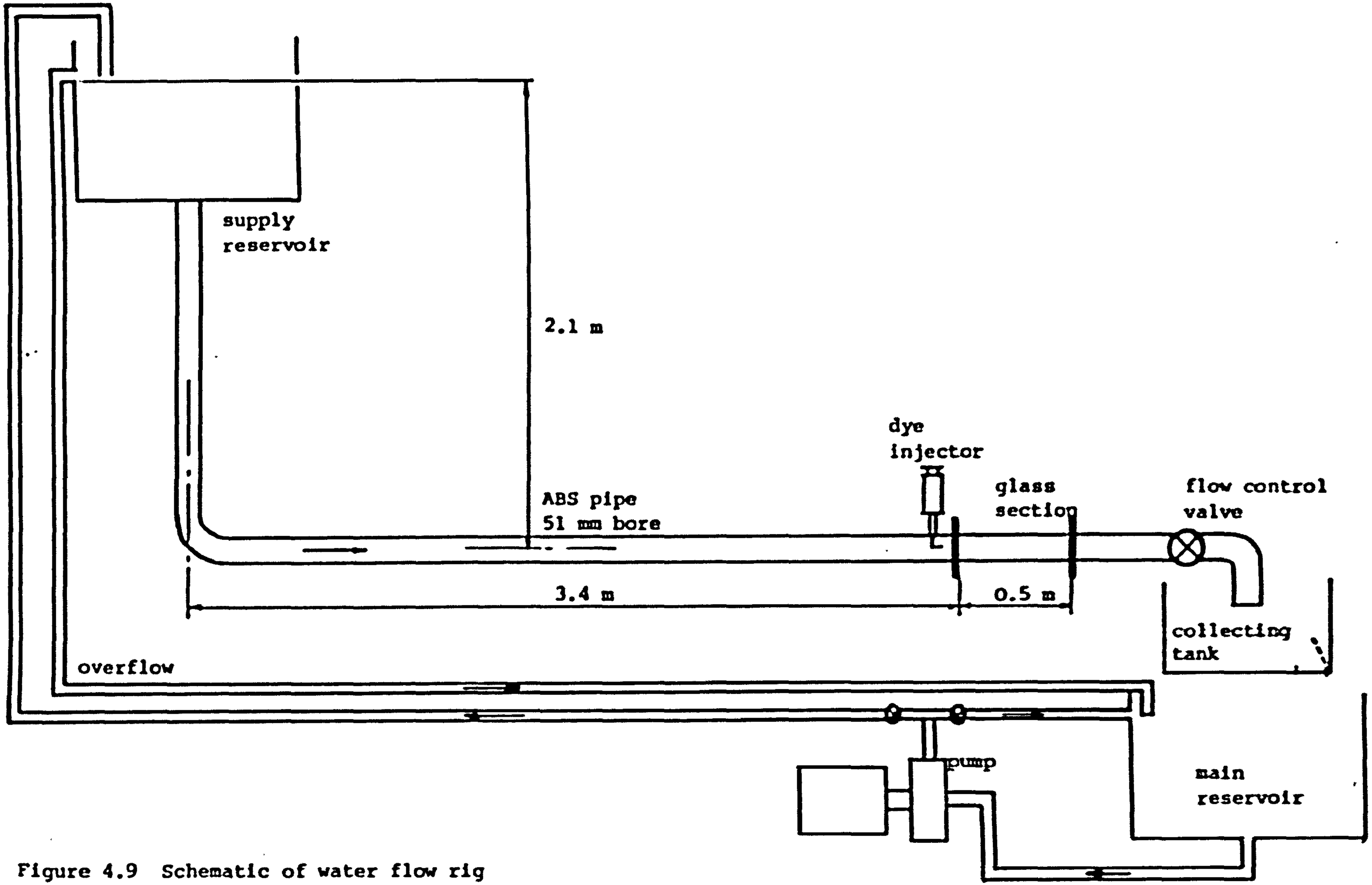

Figure 4.9 Schematic of water flow rig

d.c. motor with feedback for speed control. This rig was used for circulating mainly alumina, sand and smoke, for studying the signal dependence on particle size.

The drawbacks of this system were:

(i) unknown solids flowrate

(ii) breaking up of solids due to impact on the fan blades.

4.5.3 Large scale powder rig

A diagram of the large scale powder rig is shown in figure 4.10. It was basically the same as the flow rig used previously for heat transfer measurements [5], with some minor modifications. Air was supplied by a Roots blower and the solids were fed into a mixing chamber by a screw-feeder driven by a variable speed motor. The flow pipe was a vertical glass tube. Separation of air and solids was achieved by a cyclone, backed by bag filters. The powder then dropped under gravity to the supply hopper via two double sleeve pinch valves which were operated manually.

The flow pipe used initially was a 51 mm bore, 3 m long pyrex glass tube. As this required that the optics were mounted on a platform at an inconvenient height from the ground, in order to achieve fully developed flow, the pipe was changed to a smaller bore one. The drawbacks of this rig were the need for a large quantity of solids in the supply hopper and instability of the flow due to the large capacity of the blower and the small bore flow pipe.

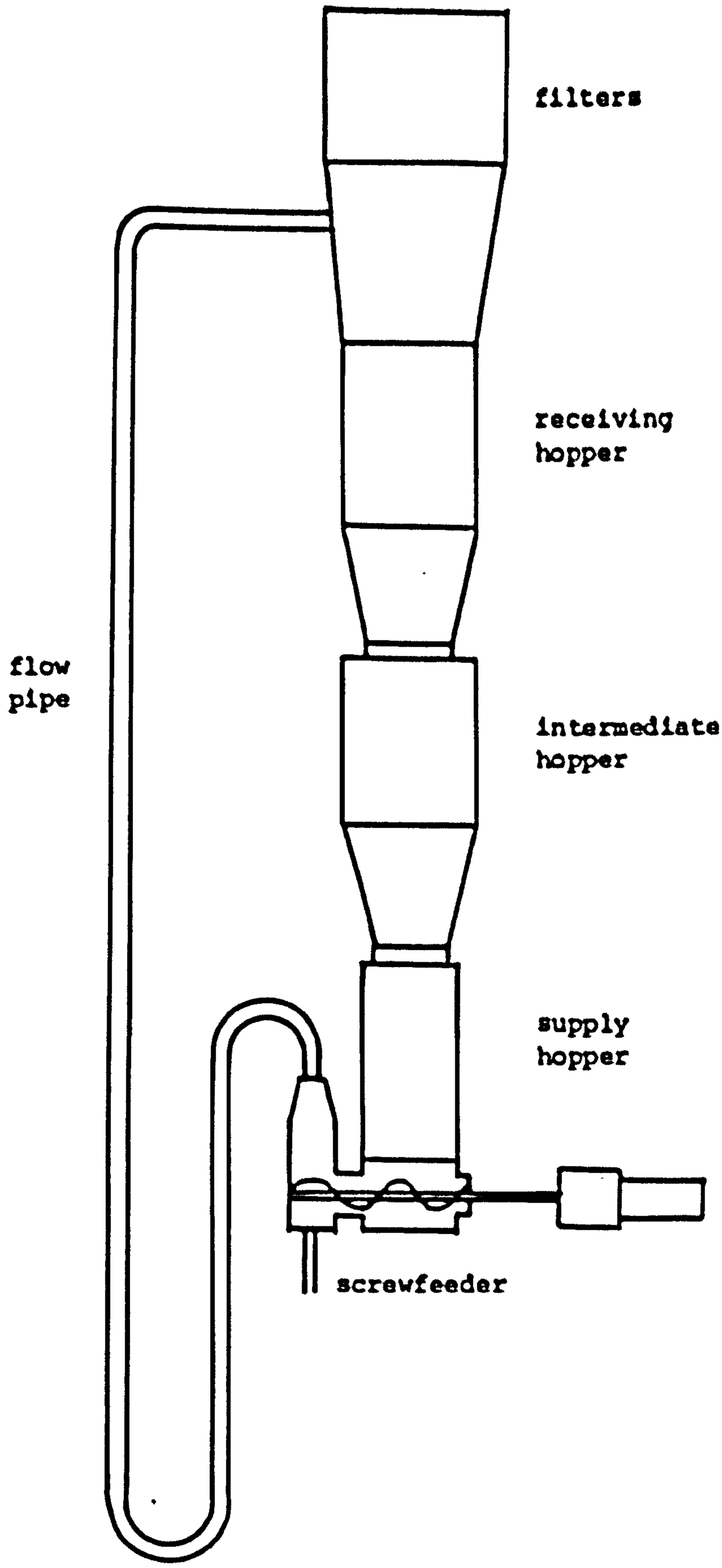

Figure 4.10 Schematic of the large scale flow rig

4.5.4 Open type flow rig

This flow rig was constructed in order to be able to circulate small quantities of solids of well defined size distribution without breaking up and with precise metering of the air and solids flowrates. As seen in figure 4.11 the flow rig consisted of an a.c. blower, whose speed was controlled by a 'variac', a vertical glass flowpipe, a cyclone separator, a solids feed and metering system and a smoke injection facility.

This rig was used during all the experiments involving velocity measurements in gas solid suspension flows. The solids flowrate was varied by using different size feed tips, which were calibrated for all the materials used (see appendix 2).

The solids feed device consisted of a venturi which created a slight pressure drop and allowed the solids to fall under gravity and mix with the air stream. Air and solids were separated by the cyclone and the solids fell freely into the reservoir above the metering orifice.

Smoke was produced by a T.E.M. smoke generator by vaporisation of silicon oil although for small amounts of dry smoke, tobacco and paper were burnt. The smoke was introduced into the flow by means of a pressure drop created by a venturi, situated upstream of the orifice plate.

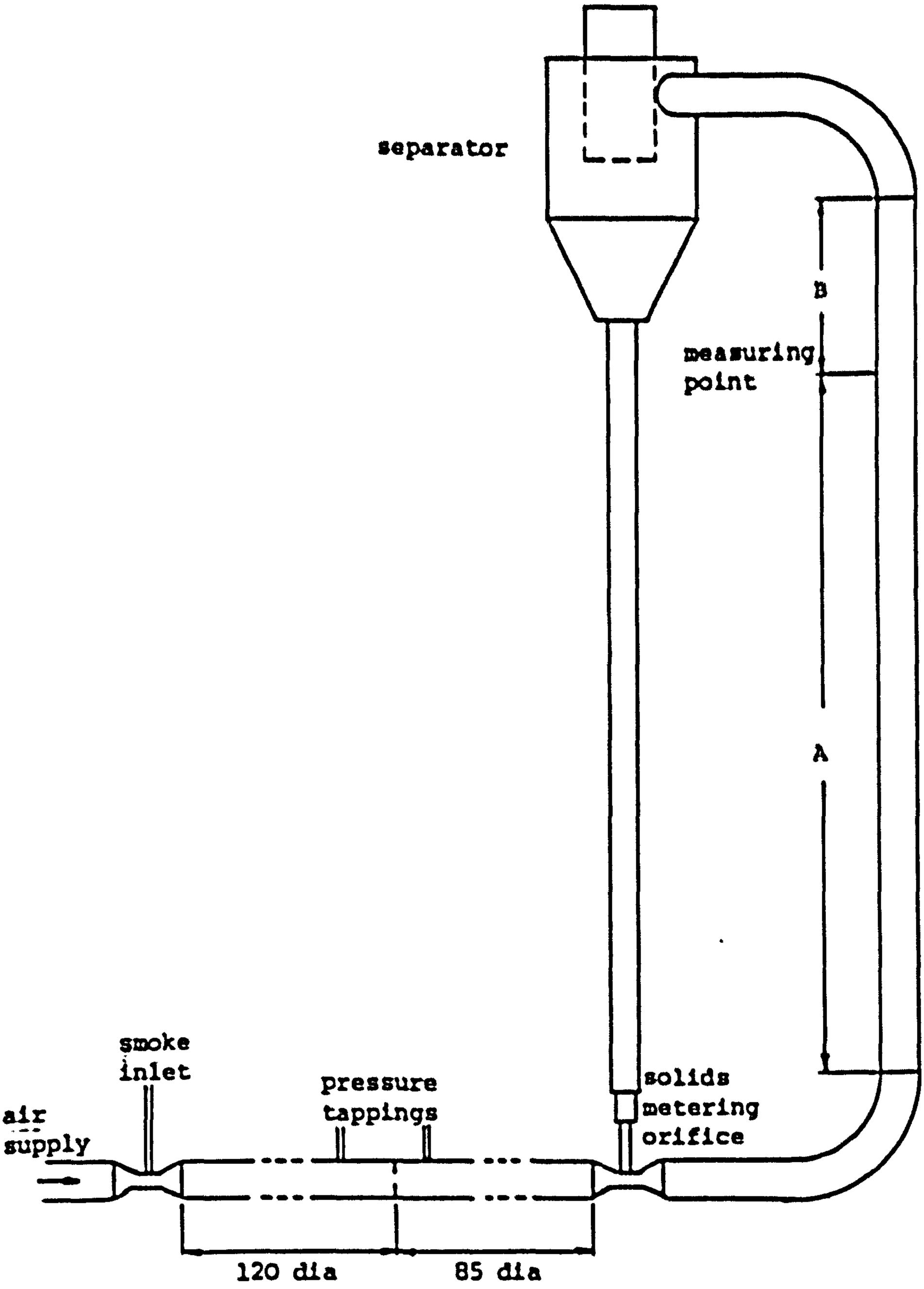

Figure 4.11 Open type flow rig; 25.8 mm bore pipe: A = 54 diameters, B = 6 diameters; 22 mm bore pipe: A = 63 diameters, B = 7 diameters

The orifice plate, designed to B.S.1042 was used to determine the air flowrate. The pressure drop across the orifice was measured using an electronic micromanometer. For calibration of the orifice plate see appendix 1.

The temperatures at the orifice and at the working section were recorded by means of thermocouples attached to the pipe walls.

4.6 SOLIDS USED

(a) White bauxilite abrasive
(white fused alumina),
supplied by Universal Abrasives Ltd.

Size designation	Mean size (μm)
F 230/53	53
F 240/45	44.5
F 500/13	12.8
F 800/7	6.5

Specific gravity = 3.94.

(b) Ballotini solid glass balls,

supplied by Jenkons (Scientific) Ltd.

Grade number	Approximate size (μm)
18	45- 70
13	90-135
10	210-325
8	440-530
5	675-935

Material: lead glass

Specific gravity: 2.95

(c) Titanium oxide

supplied by T.S.I. and BDH Ltd.

Size ≈ 0.2 μm.

(d) Silicon carbide

supplied by T.S.I.

Size ≈ 1.5 μm

(e) Tobacco

supplied by Mollins Ltd.

Sizes: < 250 μm

250-425 μm

425-600 μm

600 μm-1.8 mm

1.8-2.0 mm

> 2.0 mm

(f) Brown fused alumina (Brown Bauxilite), supplied by Universal Abrasives Ltd.

Size ≈ 300-430 μm

Specific gravity: 3.94

(g) Sand

Size ≈ 150-360 μm

Specific gravity: 2.60

4.7 THE FREQUENCY METER

The Doppler frequency meter used in this investigation was the final version of a series of instruments designed by C.A. Hobson [6], although in the initial stages of the work some earlier prototypes were used.

4.7.1 Principles of operation

The signal from the photomultiplier is high-pass filtered to remove the pedestal compoment and amplified. The resulting a.c. component of the signal (see figure 2.13) is fed into the frequency meter. This input voltage 'burst', which is effectively a sine wave with gaussian modulation, increases from a minimum value to reach a peak amplitude and then decays to the minimum value again. This minimum value is the noise level between bursts.

When the amplitude of the input voltage exceeds the preset threshold voltage V_{T1}, the envelope goes to logic 1, see

figure 4.12. The measurement starts on the first zero crossing after the input voltage exceeds the preset threshold voltage, i.e. after the envelope goes to logic 1. A counter is used to count the time for a predetermined number of cycles N, of the filtered Doppler signal, when the envelope is present. The envelope goes to level 0 at the first zero crossing after the stop voltage, which is equal to $\frac{2}{3} V_{T_1}$, has not been crossed. The O/P results pulse indicates that a measurement over the preset number of cycles, N, has been completed.

The number of measurement cycles, N, could be set to the values 2, 4, 8, 16, 32 and 64. In figure 4.13 the 'cycle count' waveform indicates a measurement over 8 cycles.

The period voltage is converted to frequency. At the end of each measurement the period is converted to an analogue voltage by a digital to analogue converter and it can be displayed on an oscilloscope screen if required.

4.7.2 Accuracy

The frequency counter is subjected to certain errors, such as period quantisation errors, arising during the calculation of the signal period and frequency quantisation errors arising from calculations of the frequency from the signal period. Figure 4.13 shows these instrument errors as a function of the full scale output. As it is seen, the quantisation errors are at a minimum near the middle of the range.

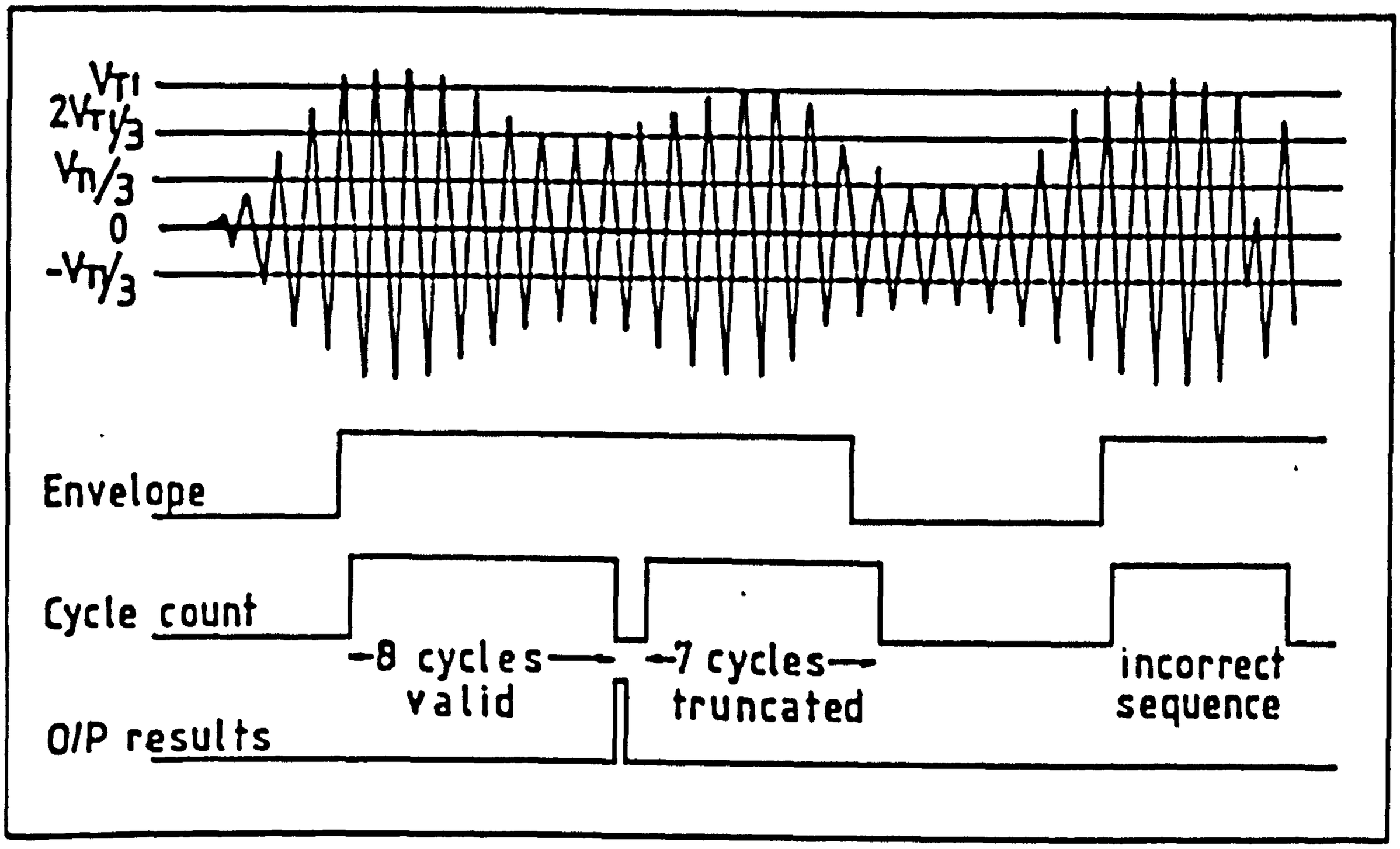

Figure 4.12 Frequency meter operation

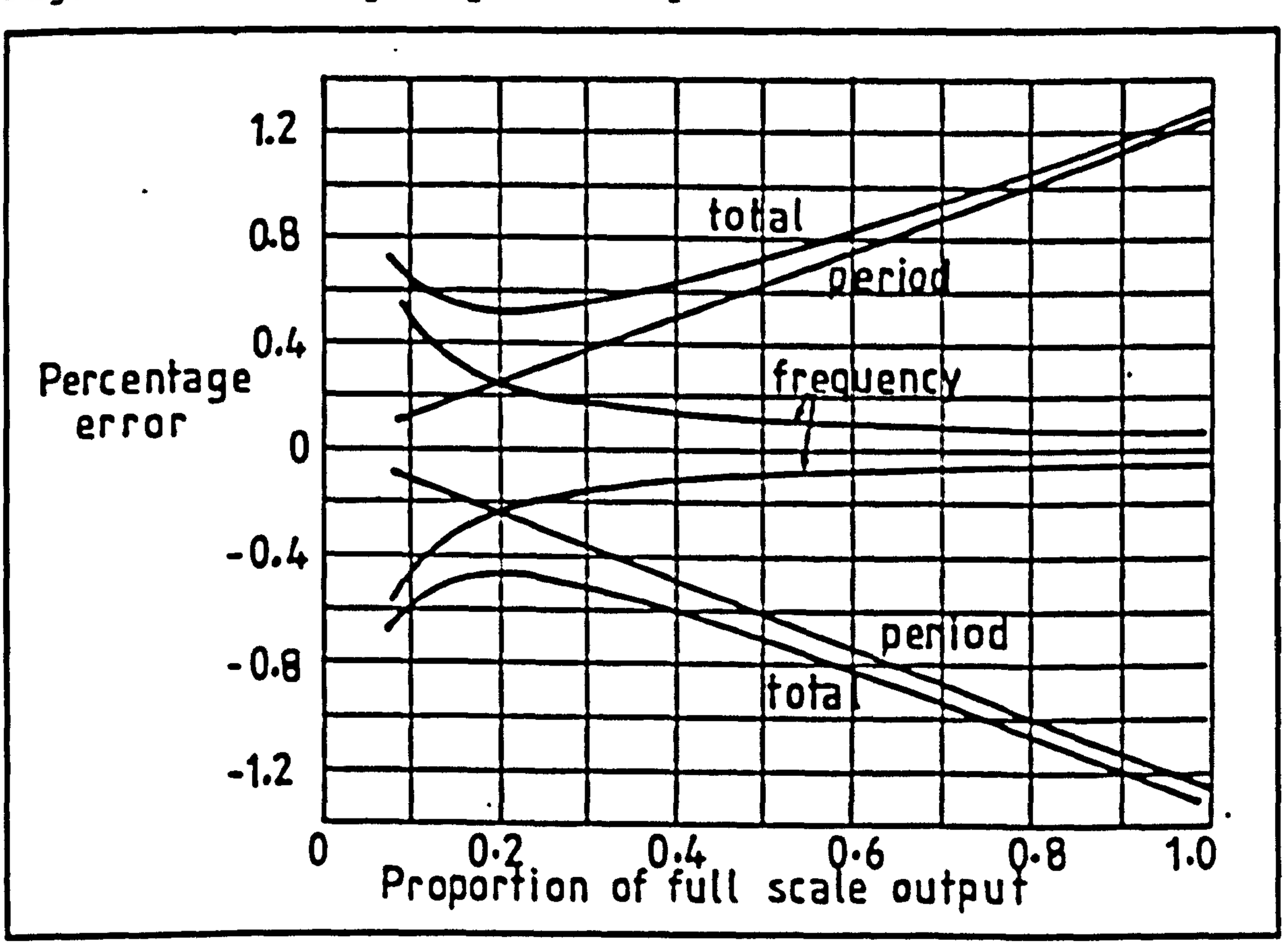

Figure 4.13 Maximum possible errors due to period and frequency quantisation

Errors in the measurement of frequency can also arise due to the presence of noise in the signals. Lowering of the threshold voltage V_{T1} can produce measurements with wider distribution, as this allows measurements from signals with low signal/noise to be taken.

In order to reduce the various errors, sequence detection and $^{N}/_{2}$:N comparison are employed.

When $^{N}/_{2}$:N comparison is used, the period of N cycles is calculated and compared with the period of the first $^{N}/_{2}$ cycles. If the two measurements differ by more than a specified amount, the measurement is rejected.

Sequencing ensures rejection of those signals in which additional zero crossings occur due to noise superimposed on the Doppler signal. Figure 5.12 shows the principle of operation of the sequence detection circuit. For a signal to be accepted, $^{V_{T1}}/_{3}$, 0 and $-^{V_{T1}}/_{3}$ must be crossed in sequence. If this is not the case the measurement is truncated.

4.7.3 Instrument capabilities

A summary of the main features of the frequency meter is given below:

(i) Analogue and digital frequency outputs.

(ii) Measurement of frequencies up to 10 MHz when measuring over 8 cycles.

(iii) Truncation of measurements not completed in one

Doppler burst. This is a very useful feature, as different signal bursts can have different frequencies (e.g. turbulent flow).

(iv) One measurement only from each burst. This is important in the calculation of fluid flow statistics. This facility is not necessary in measurements of velocities of solids and can be cancelled.

(v) Data validation which includes sequence detection and $^{N}/_{2}$:N comparison for minimisation of measurement errors.

(vi) The measurement ranges, number of measurement cycles and the corresponding maximum frequencies that can be measured are shown in table 4.2.

	Full scale output					
no of cycles / Range	2	4	8	16	32	64
0	1.25 kHz	2.5 kHz	5 kHz	10 kHz	20 kHz	40 kHz
1	2.5	5	10	20	40	80
2	7.5	25	50	100	200	400
3	15	50	100	200	400	800
4	75	250	500	1 MHz	2 MHz	4 MHz
5	150	500	1 MHz	2	4	8
6	750	2.5 MHz	5	10	20	
7	1.5 MHz	5	10	20		

Table 4.2 Full scale deflection as a function of range and number of cycles

4.8 DATA RECORDING AND PROCESSING SYSTEM

Figure 4.14 shows the basic principles of the data recording and processing system. The amplified photo-detector output was passed through two different filters to produce pedestal and Doppler components. The pedestal was then fed into a discrimination circuit (see 5.2) where it was compared with a d.c. level set by a potentiometer. The result of the comparison formed an enable input to an interface circuit, which was used to enter the Doppler frequency meter output into the memory of a microcomputer using direct memory access (d.m.a.).

The rate of data arrival depended on the overall experimental conditions. At the end of a measurement sequence, which occurred when 255 measurements of the same frequency were recorded, the results were available for processing and were transferred to an Apple computer, via an RS232 link. By operating a manual switch, the results could be stored in the microcomputer for as long as desired. After the results were transferred, the microcomputer was reset automatically and the system was ready to restart immediately. The 'Apple' computer was programmed in 'Basic' to receive the results, store them on disc and perform various calculations as well as display them in histogram form.

A flow diagram and listing of the 'Apple' data processing programme are shown in Appendix A5.

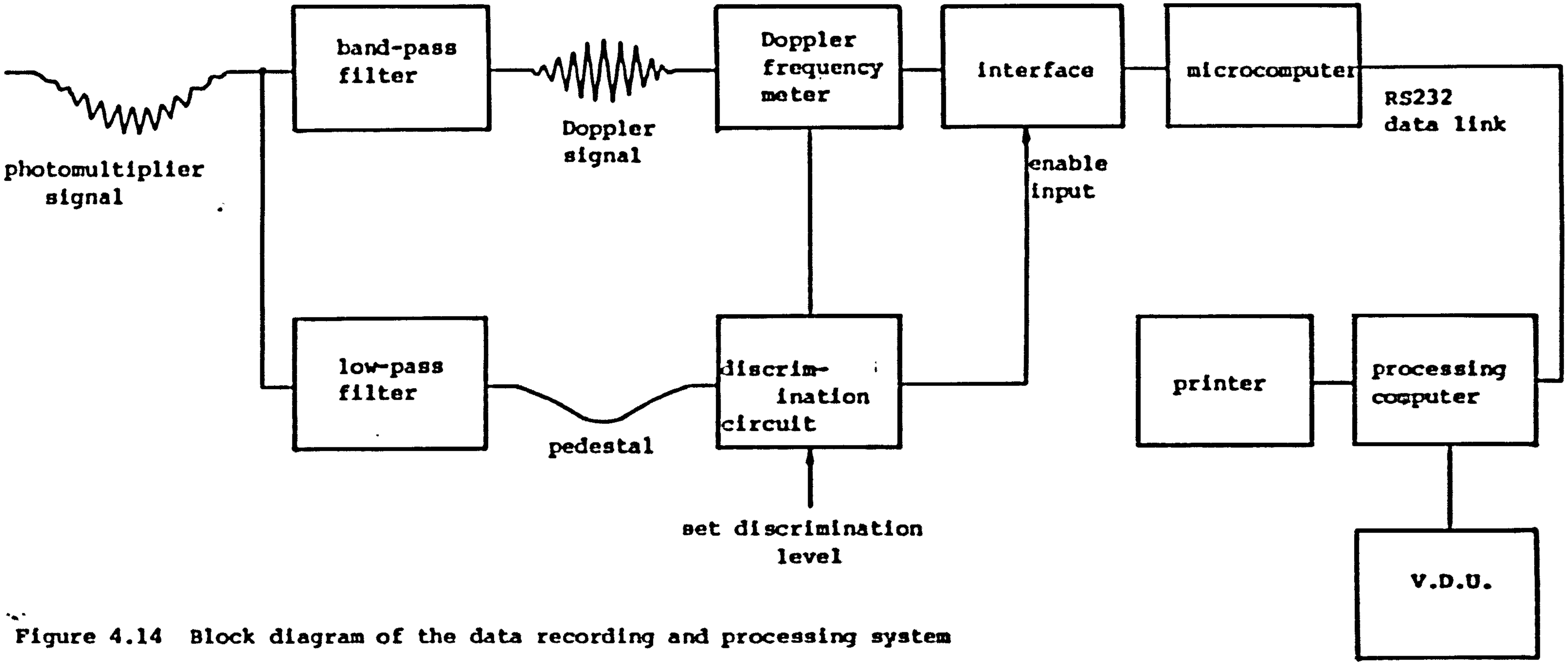

Figure 4.14 Block diagram of the data recording and processing system

4.9 LIST OF OTHER INSTRUMENTS

Storage Oscilloscope Tectronix, model 7633.

Oscilloscope, S.E. Labs.

Quarndon QMS system with 8080 microprocessor

Wide band amplifiers, HewlettPackard,model 461 A

Electronic micromanometer, Furness Controls Ltd.

Photomultiplier power supply, Budenburg, model 475 R

Teletype, Peripheral Hardware, model 43

Stabilised power supplies, Farnell Instruments, model E30/2

Laser power monitor, Scientifica and Cook Electronics

Smoke generator, T.E.M. Engineering, type FVSP 204

Timer counter, S.E., model Sm 200 Mk 2, with remote gate triggering

Low noise amplifier, Variable band amplifier, AIM Electronics Ltd.

High frequency signal generator, Advance Electronics Ltd.

Electronic filters, for design see appendix 4

Microcomputer, ITT 2020, 48 k RAM with monitor, twin disc drives, RS232 serial interface

Microcomputer, APPLE II, 48 k RAM, with monitor, two disc drives, RS232 serial interface, language card.

REFERENCES

[1] EMI Photomultipliers Catalogue, EMI Electronics Ltd. 1975.

[2] Jenkins and White Fundamentals of Optics, 4th Edition, International Student Edition.

[3] Durst F and Zare M 1974 Removal of pedestals and directional ambiguity of optical anemometer signals. Appl. Opt. 13 11 2562-2579.

[4] Koniuta A, Dundermel M T and Adler P M 1979 A laser Doppler anemometer with microscopic intersection volume. J. Phys. E: Sci. Instrum. 12 918-920.

[5] Muskett W J 1977 A study of rates of heat transfer to flowing gas-solid suspensions. MPhil Thesis Mech. Marine and Prod. Eng, Liverpool Polytechnic.

[6] Hobson C A 1978 Digital analysis of opto-electronic data. PhD Thesis Dept. of Elect. and Control Eng. Liverpool Polytechnic.

CHAPTER 5

DEVELOPMENT OF DISCRIMINATION TECHNIQUES

5.1 INTRODUCTION

One of the main problems encountered in the study of two phase flows, using LDA, is distinguishing between signals from the fluid and the solid phases. The object of this investigation was to develop a method which would solve the above problem. This could lead to a better understanding of two phase flows, for which insufficient experimental data exist, due mainly to the lack of suitable measurement methods.

'Discrimination' was based on the dependence of signal visibility and of absolute signal amplitude on particle size (see section 5.2). This method, which is not a particle sizing technique, utilized the marked difference, which exists between two distinct regions of the scattering visibility. One region corresponds to the 'small' scatterers, whose diameter is smaller than the fringe spacing and the other corresponds to scatterers whose diameter is greater than the fringe spacing. Doppler signals representing the fluid phase are those obtained from micron sized scatterers, which follow the flow, without appreciable slip.

The fringe spacing obtained from the LDA apparatus used in this investigation was approximately 2 μm. Therefore it was assumed that all scatterers satisfying the condition (particle diameter) $<$ (fringe spacing) would have the fluid velocities everywhere in the flow.

5.2 LDA SIGNAL CHARACTERISTICS

5.2.1 Signal visibility

The two basic components of the signal from a laser Doppler anemometer are the low frequency component or pedestal, (d.c.) and the high frequency Doppler component, (a.c.). Typical such signals obtained from a photomultiplier were shown in figures 2.12 and 2.13. The amplitude of the pedestal and Doppler components depends on the size of the scatterer, the fringe spacing, the refractive index of the scatterer material and the collecting optics geometry [1,2, 3].

The ratio of the a.c. amplitude to the d.c. amplitude is called the scattering visibility V_{sca}, or modulation depth [4,5,6]. Thus with reference to figure 5.1,

$$V_{sca} = \frac{I_{max} - I_{min}}{I_{max} + I_{min}} = \frac{\frac{1}{2}(I_{max} - I_{min})}{I_{min} + \frac{1}{2}(I_{max} - I_{min})}$$

$$= \frac{\text{a.c. amplitude}}{\text{d.c. amplitude}}$$

where I_{max} is the scattered intensity when the scatterer is centred on a bright fringe and I_{min} is the scattered intensity when the scatterer is centred on a dark fringe.

In a study of signal visibility, using Mie scattering theory, Farmer [5] showed that the signal visibility is a unique function of particle shape and depends upon the ratio of the particle size to the fringe spacing. In a later paper, Robinson and Chu [1] using scalar diffraction theory,

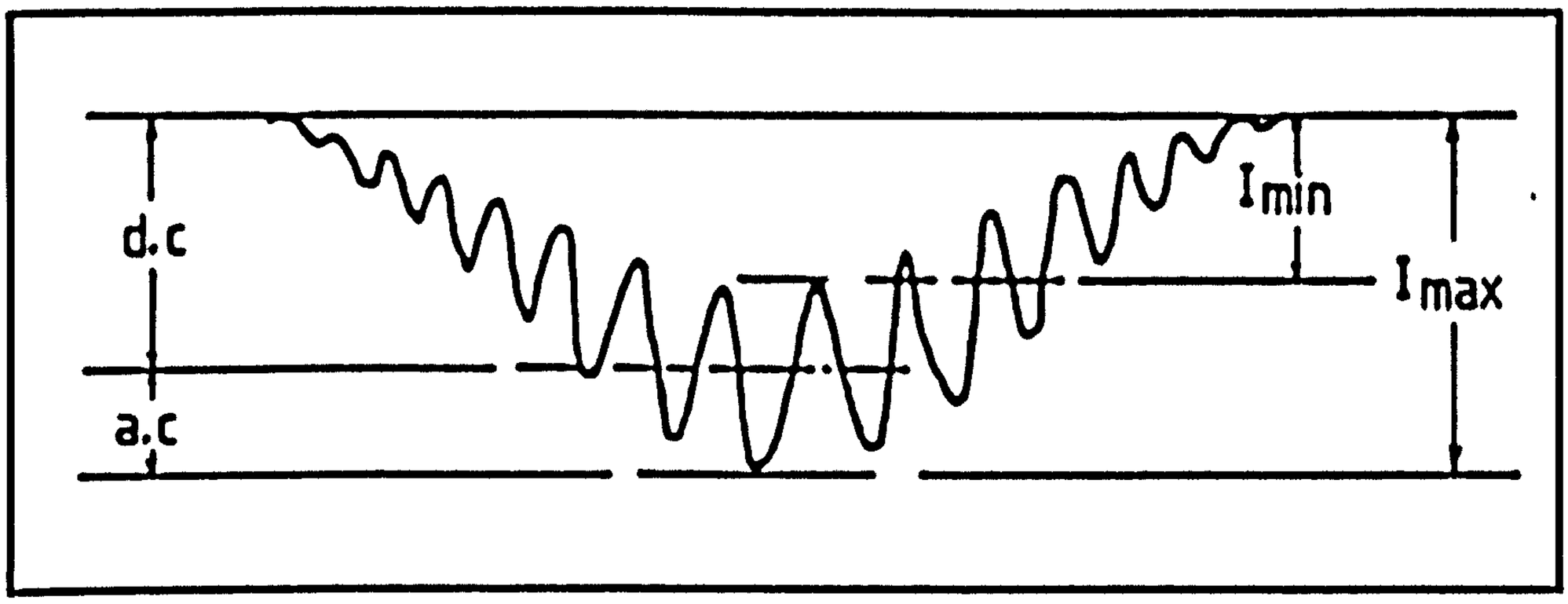

Figure 5.1 Doppler signal parameters

showed that this dependence of signal visibility on the size parameter D/δ, is true only for on axis forward light collection and with a wide collecting optics aperture, for $\lambda < D < \delta$, where D denotes particle diameter and δ is the fringe spacing. Figure 5.2 shows the dependence of visibility upon particle size for spherical and cylindrical particles as presented by Farmer [5], where for a cylinder of length D,

$$V_{sca}\ (\text{cylinder}) \simeq \frac{\sin(\pi\ D/\delta)}{(\pi\ D/\delta)}$$

and for a sphere of diameter D,

$$V_{sca}\ (\text{sphere}) \simeq \frac{2J_1\ (\pi\ D/\delta)}{(\pi\ D/\delta)}$$

where $J_1(\pi\ D/\delta)$ is a first order Bessel function of the first kind.

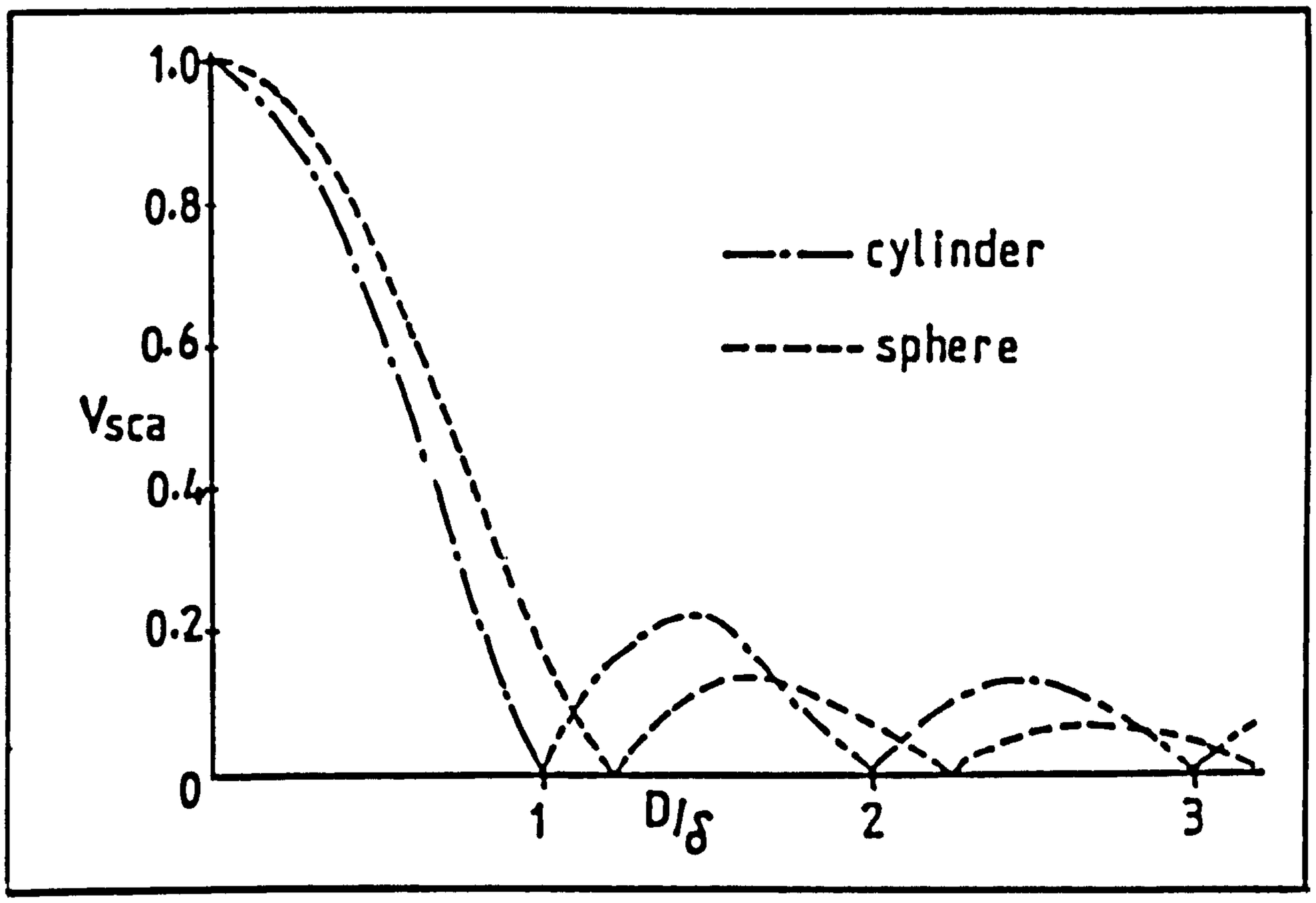

Figure 5.2 Theoretical visibility vs size parameter

Similar results were presented in reference [1] for a spherical and a square section scatterer.

The dependence of the signal visibility on the size of the collecting optics aperture is explained as follows: According to diffraction theory, most of the energy scattered from a particle is contained within the first forward lobe of the diffraction pattern [1,7] ; this lobe subtends an angle approximately equal to $2\lambda/D$ as shown in figure 5.3.

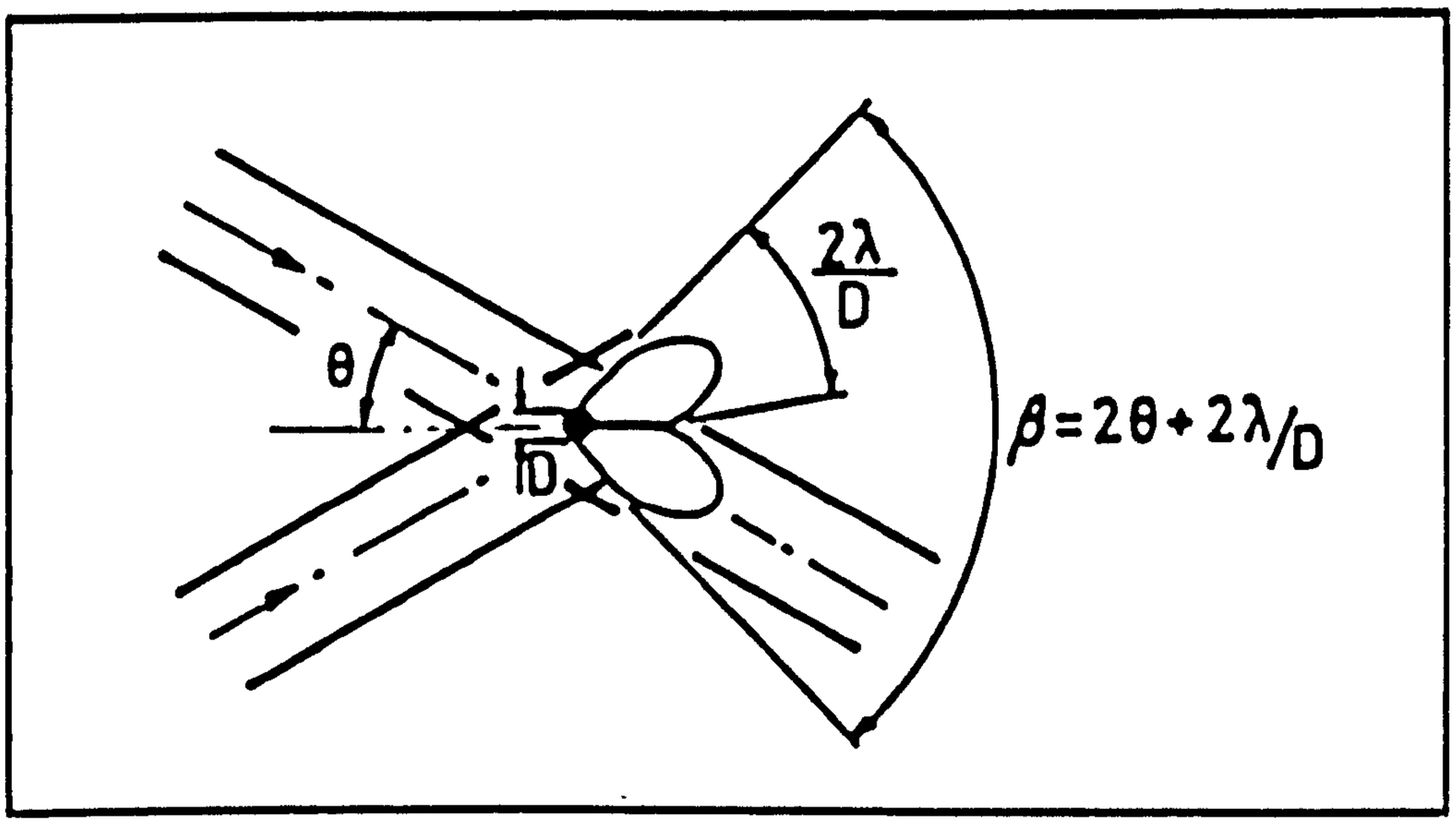

Figure 5.3 Light scattering by a particle in the beam cross over region

In the case of an infinite collecting aperture both main diffraction lobes are collected and thus the scattered visibility depends on the interference between those two lobes; this interference is in turn a function of the ratio D/δ [1,4]. Referring to figure 5.3, the angle containing both main forward diffraction lobes is given by

$$\beta \approx \frac{\lambda}{\delta} + \frac{2\lambda}{D} = \frac{2\lambda}{D}\left(1 + \frac{D}{2\lambda}\right),$$

where the fringe spacing is $\delta \approx \frac{\lambda}{2\theta}$ and θ is the half-angle between the two incident beams. A collecting aperture of diameter 2L will collect both main lobes if $\beta/2 < \phi/2$, see figure 5.4.

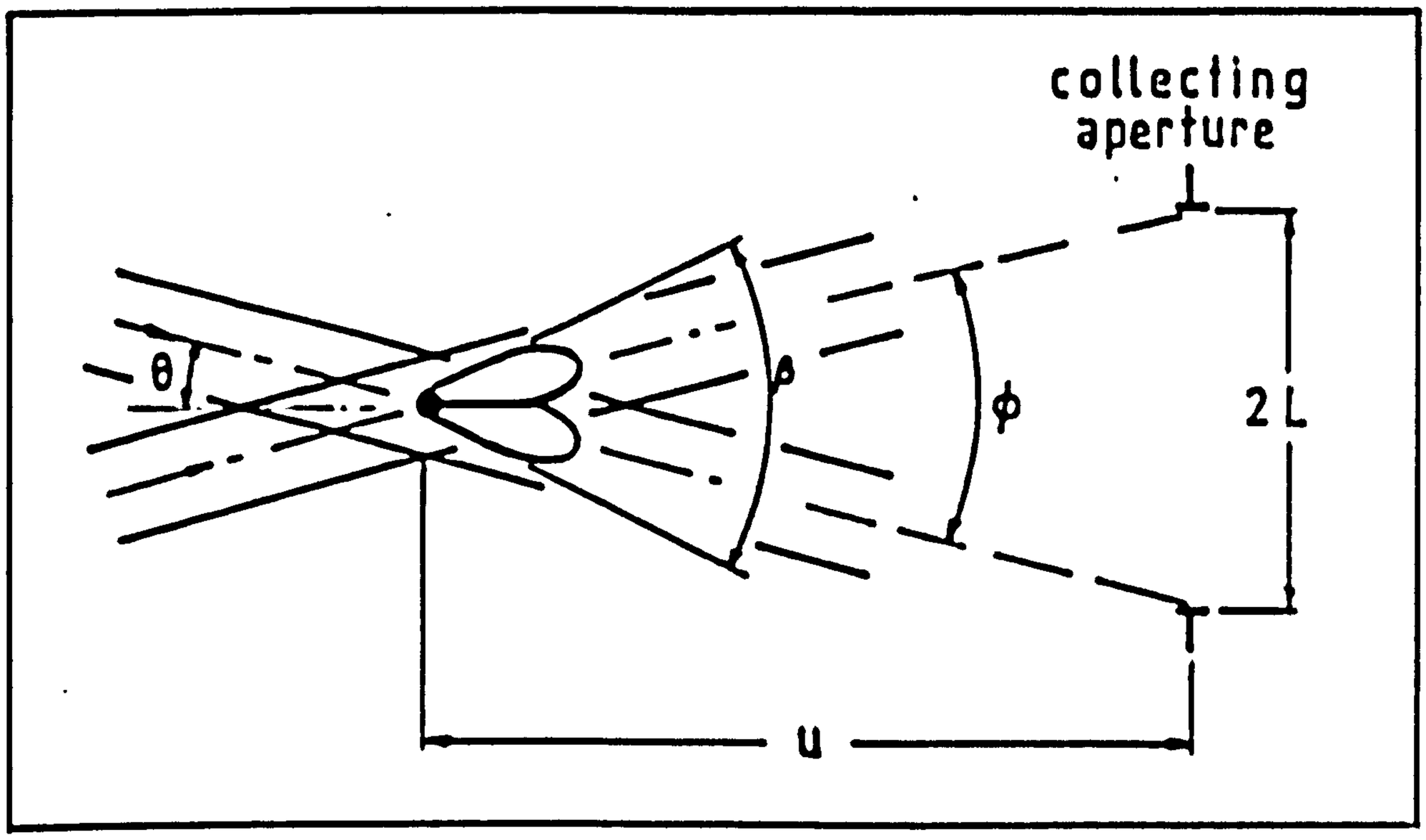

Figure 5.4 Collecting optics parameters

Since $\frac{\phi}{2} \approx \frac{L}{u}$, then $\frac{\beta}{2} < \frac{L}{u}$

If the collecting aperture f no is defined as $u/2L$, where u is the object distance, then

$$f \text{ number} = \frac{u}{2L} < \frac{1}{\beta} = \frac{D}{2\lambda(1 + \frac{D}{2\delta})}$$

It was shown by Robinson and Chu that the above requirement was met for values of f_{no} of 4 or less. They also showed that for a small aperture, the scattering visibility tends to unity regardless of particle size [8].

The validity of the above argument was confirmed by

Robinson and Chu in a later investigation [2] of light scattering based on Mie theory,'in which a strong dependence of visibility on refractive index was shown to exist.

It has thus been estblished that when all the forward scattered light is collected, small particles ($D < \delta$), produce signals of high visibility and larger particles produce signals with low visibility. Experiments have also shown that signals from small scatterers have a small d.c. signal component whereas large particles produce signals of large pedestal. An experimental investigation of the above signal characteristics now follows.

5.2.2 Experimental investigation of LDA signal characteristics

(a) Using an oscilloscope

The object of this experimental investigation was to verify that small particles, ($D < \delta$), produce signals of high visibility and of low pedestal amplitude and that large particles, ($D > \delta$), produce signals of large pedestal amplitude but with low visibility.

The optical arrangement used was a two lens system with forward light collection as shown in figure 4.5

A very large number of signals from known particle sizes were observed using an oscilloscope and photographs of representative signals were taken. The solids used were of

various sizes and by varying the size of the scatterer, relationships were established between particle size and signal characteristics. Whenever difficulty arose in determining the size of the scatterers, more indirect methods, such as observing the average signal characteristics from a class of particles, were employed. Among the materials used for that purpose were tobacco smoke, silicon oil smoke, silicon carbide powder (1.5 μm diameter) natural dust, glass ballotini of various sizes up to 1 mm diameter, sand, tobacco flakes etc.

It was not always possible to make the collecting optics aperture as large as it was desired, due mainly to the need to cut out reflections from the pipe walls. The resulting dependence of signal characteristics on aperture size was not thought to be as critical in this type of work, as it might have been if particle sizing was undertaken.

The experiments can be divided into two broad categories:

(i) observation of overall signal amplitude from photomultiplier,

(ii) observation of the relative magnitudes of the a.c. (high pass filtered) component and of the d.c. (low pass filtered) component, as well as of the unfiltered photomultiplier signal.

In case (i), signals from the photomultiplier were observed on an oscilloscope screen. In case (ii) the trigger

facility of the oscilloscope was utilised in order to correlate the d.c. and a.c. amplitudes. The trigger was set alternately on either input and the signals were observed using a two-channel display.

A number of representative signals are shown in figures 5.5 to 5.14. Figures 5.5 to 5.8 show photomultiplier signals obtained from scatterers of various sizes. Figures 5.9 to 5.14 show simultaneous traces of the photomultiplier signals - upper trace - and high pass filtered signals - lower trace, in chop mode.

It is seen from figures 5.5 to 5.12 that small particles produce high visibility, low amplitude signals, whereas large particles produce signals with large pedestal amplitude but with low visibility. Figures 5.13 and 5.14 clearly show that a large a.c. amplitude is associated with a low pedestal amplitude, high visibility signal, and high pedestal amplitude signals are invariably associated with a low amplitude a.c. component.

These results are a representative sample of a very large number of observations.

(b) <u>Using velocity histograms</u>

The dependence of the signal arrival rate on the number of scatterers present in the flow and on the geometry of the collecting optics (f no and pinhole size), were investigated by obtaining velocity measurements for various flow

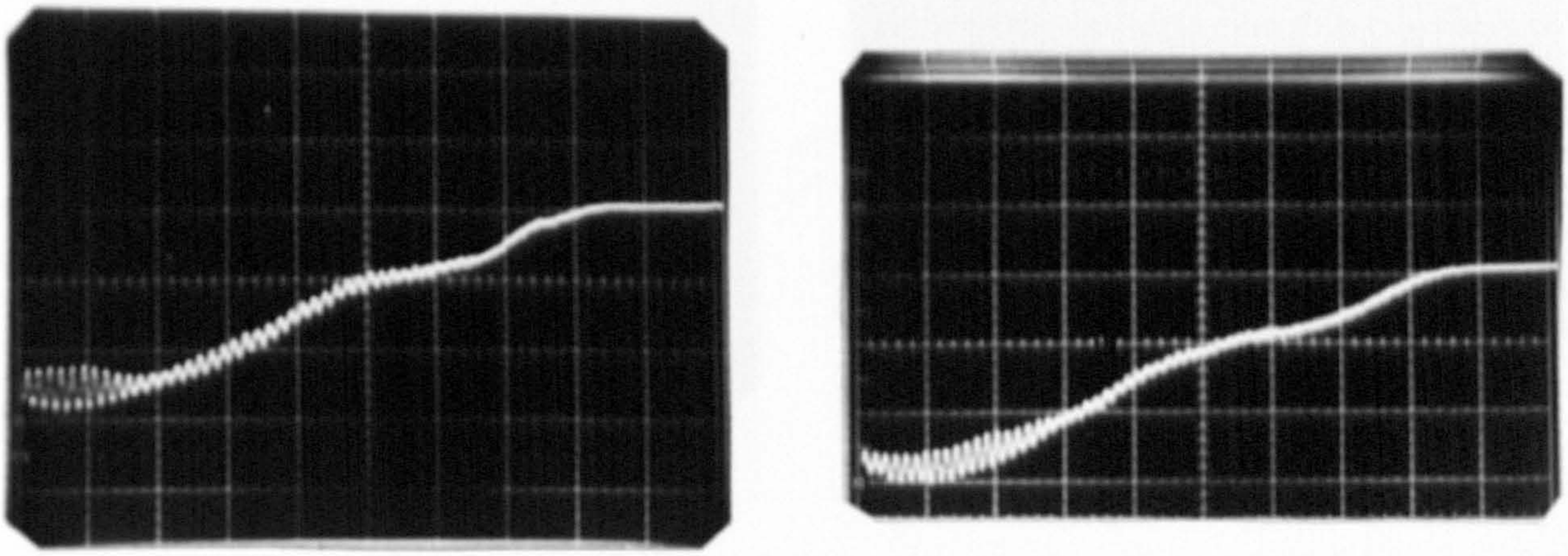

(a) (b)

Figure 5.5 Photomultiplier signals. Glass ballotini, size 210-235 m; telescope f no = 6.7; pinhole dia = 100 μm; 0.1 V, 5 μs/div.

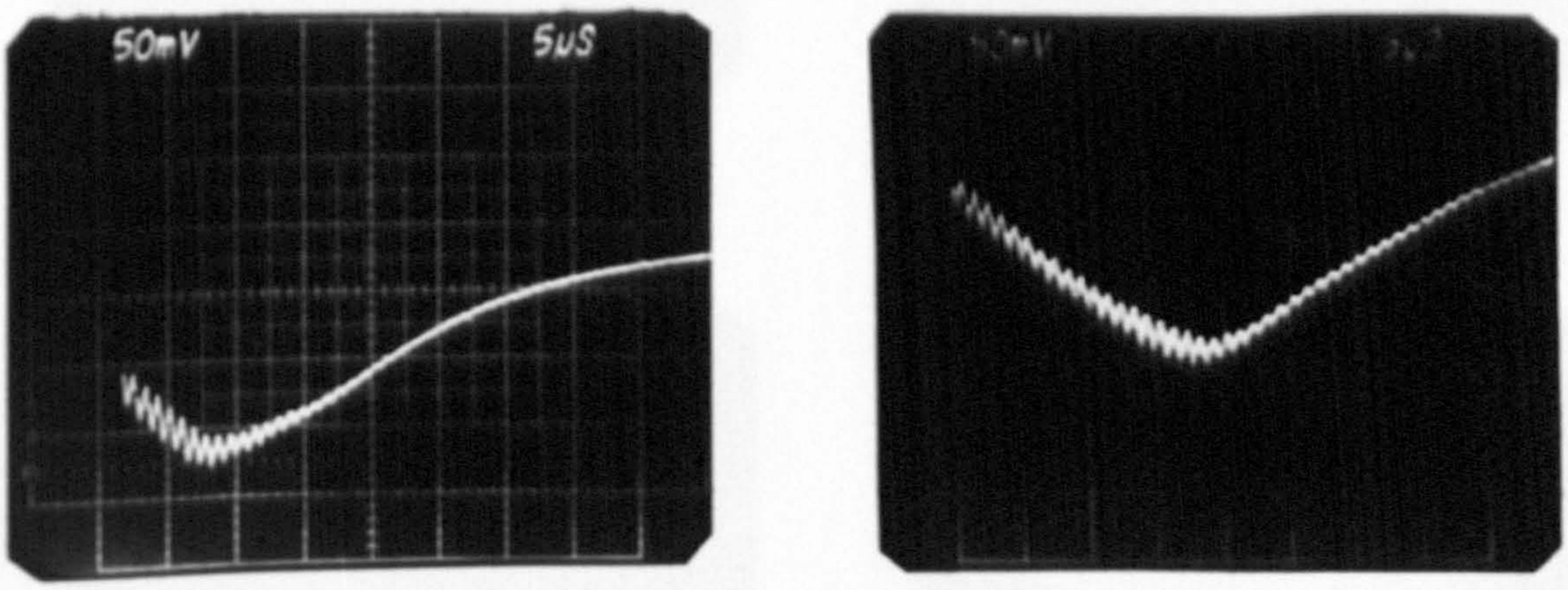

(a) (b)

Figure 5.6 Photomultiplier signals. Glass ballotini, size 90-135 μm; telescope f no = 4.74; pinhole dia = 200 μm

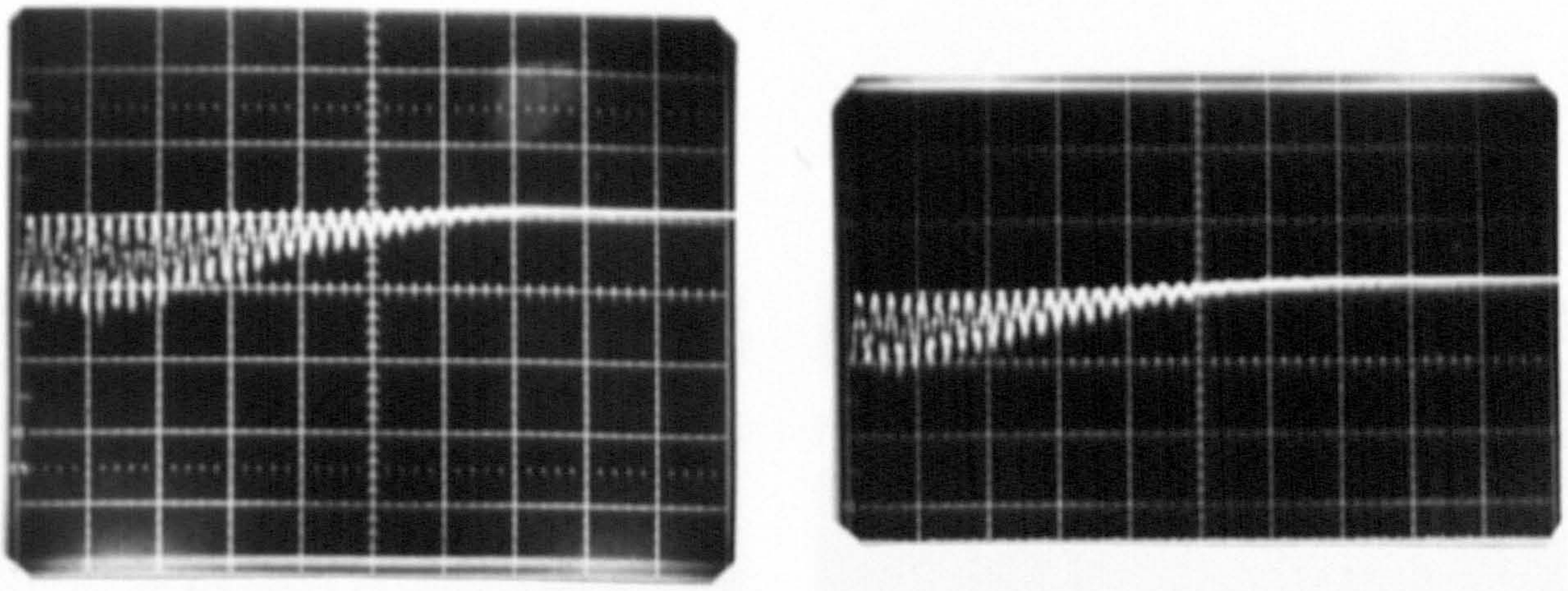

(a) (b)

Figure 5.7 Photomultiplier signals. Dust; telescope f no = 6.70; pinhole dia = 100 μm; 20 mV, 5 μs/div

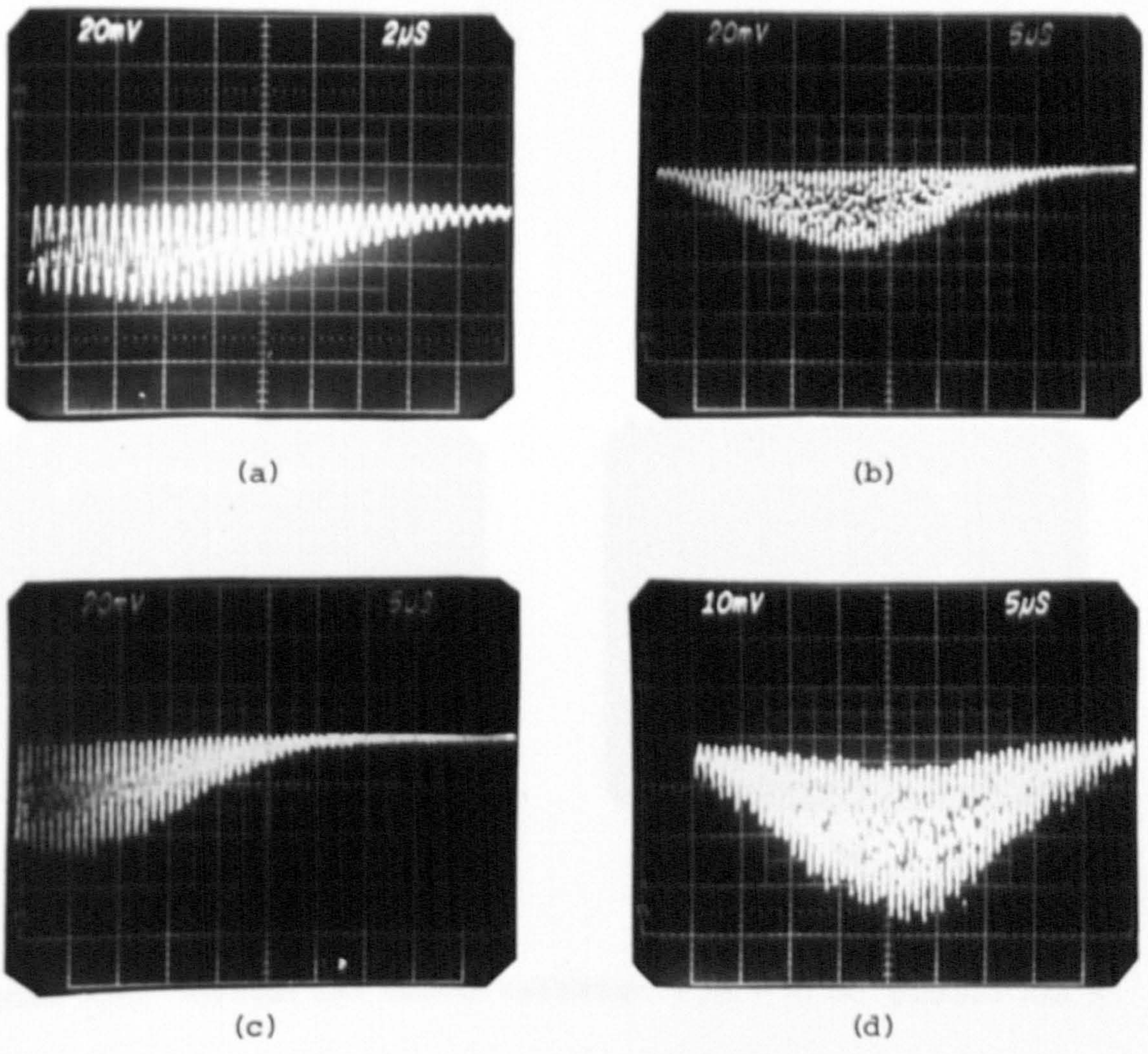

(a) (b)

(c) (d)

Figure 5.8 Photomultiplier signals. Silicon oil smoke; telescope f no = 4.74; pinhole diameter = 200 μm

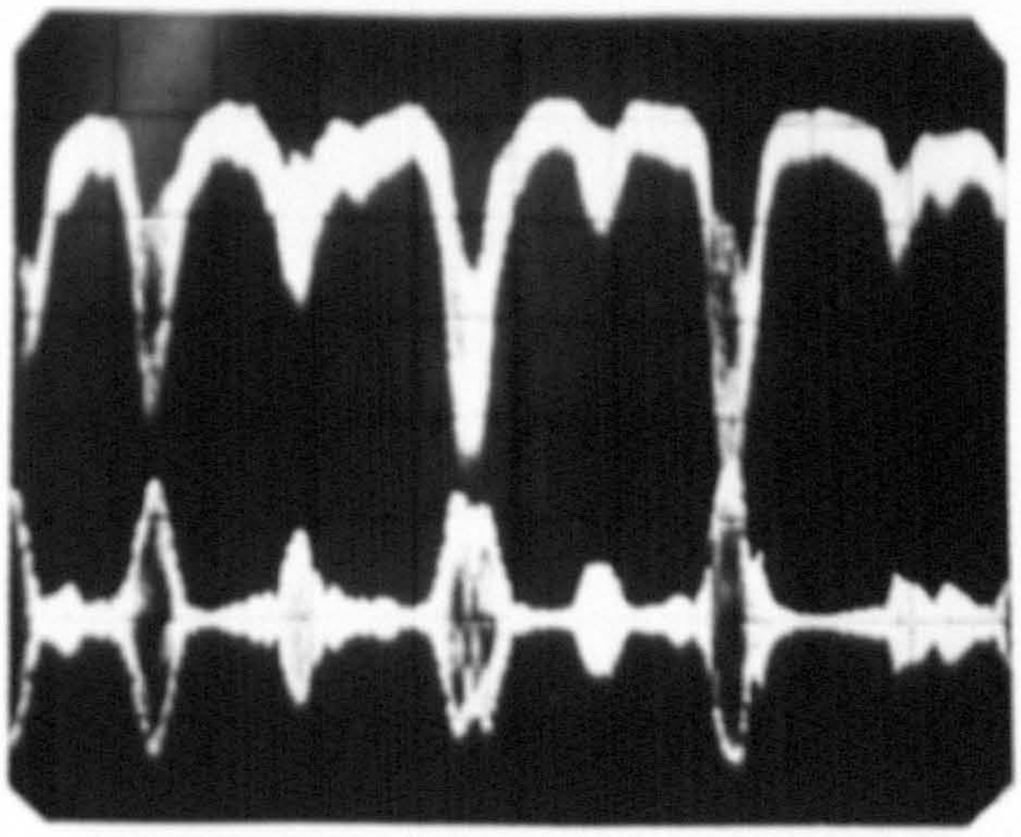

Figure 5.9 Tobacco smoke; 0.5 ms/div ms/div; Top: 5 mV; Bottom: 0.2 V; telescope f no = 6.7; pinhole dia = 100 μm

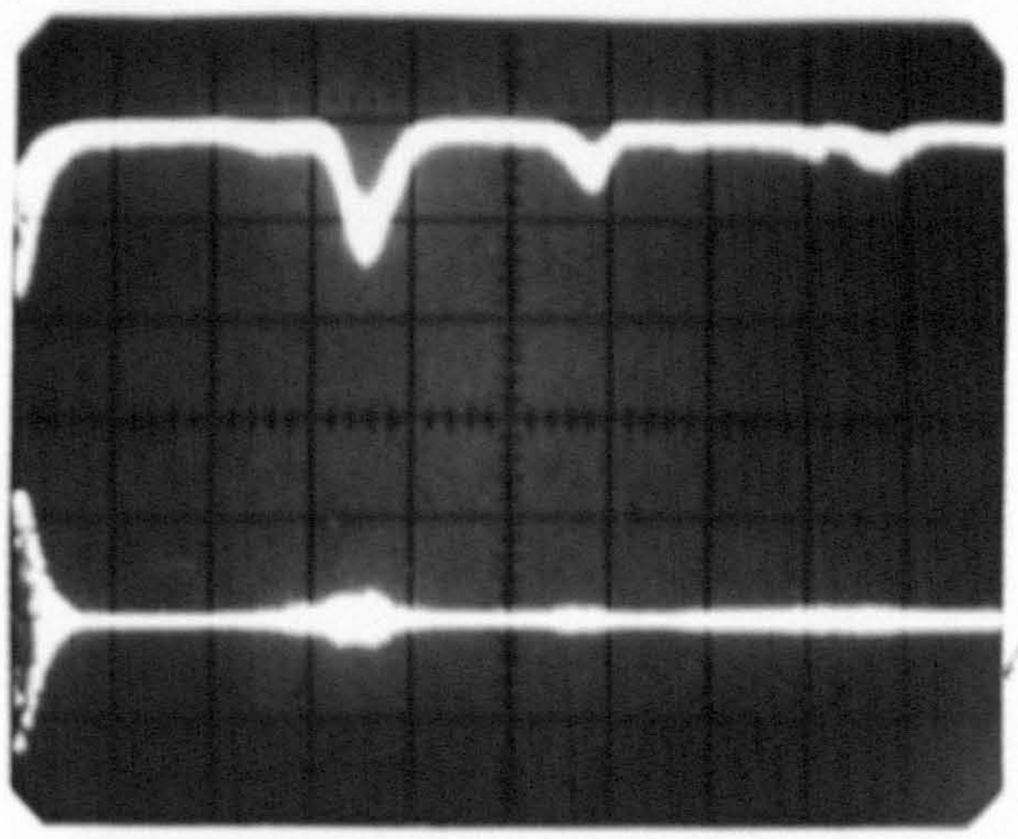

Figure 5.10 Silicon carbide (1.5 μm), 1 ms/div; Top: 10 mV; Bottom: 0.5 V; telescope f no = 6.7; pinhole dia = 100 μm

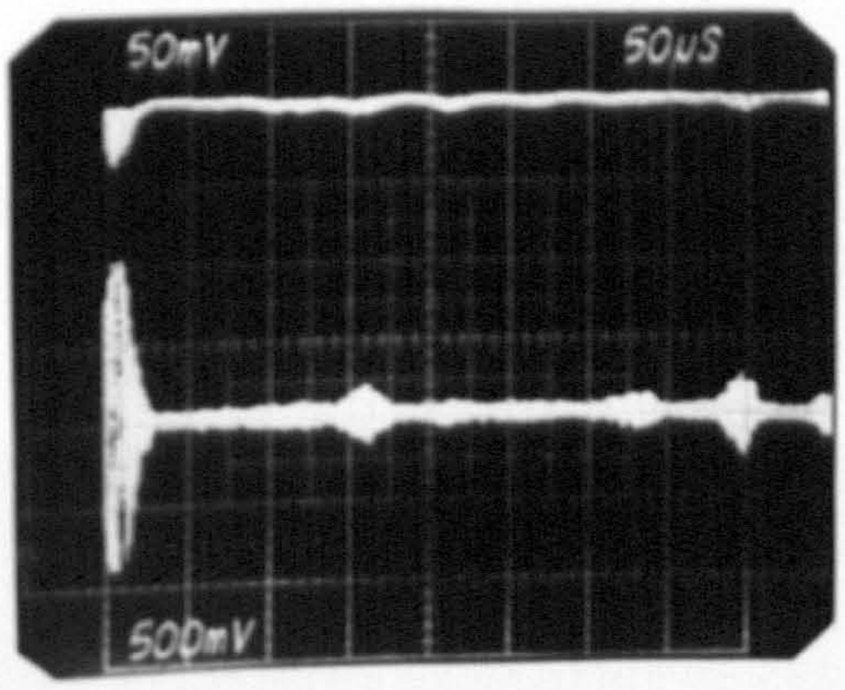

(a)

trigger on lower trace

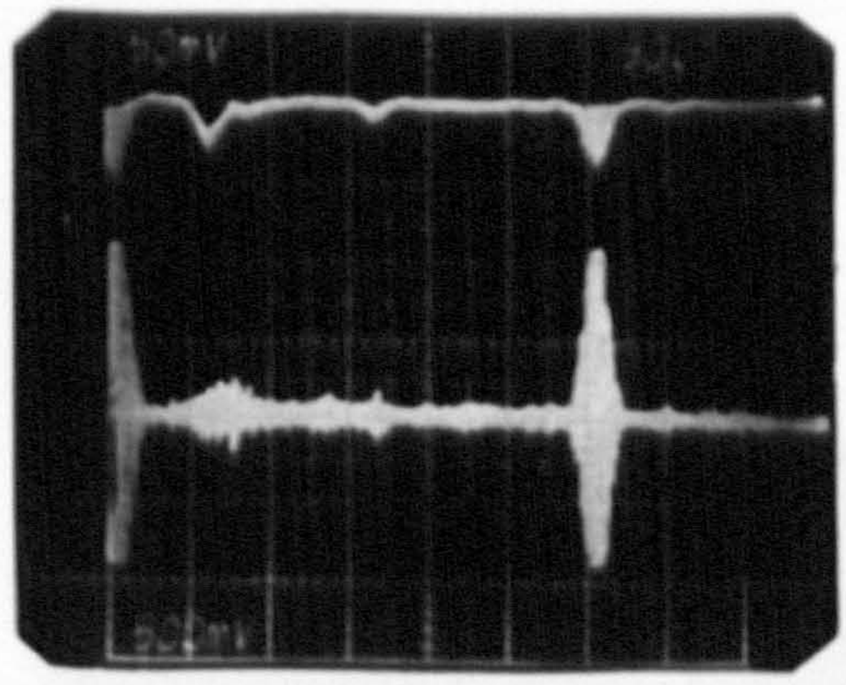

(b)

trigger on upper trace

Figure 5.11 Silicon oil smoke; telescope f no = 4.74; pinhole dia = 200 μm

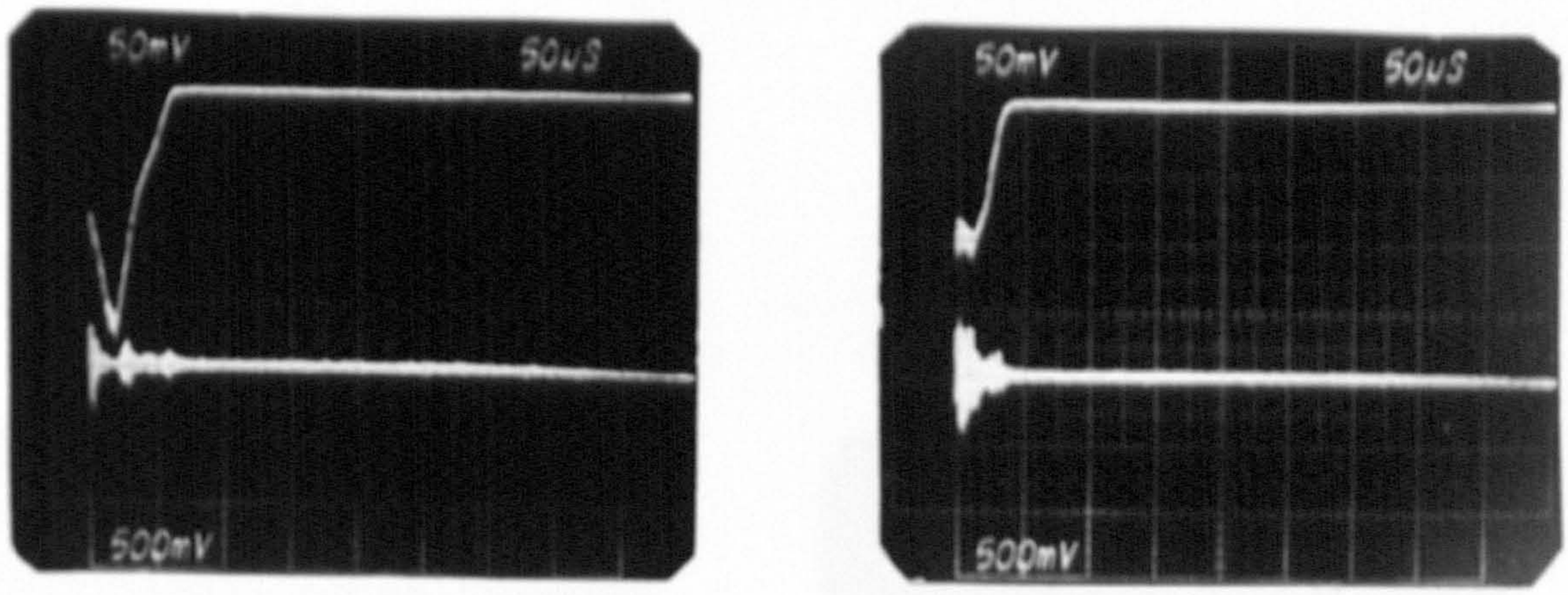

(a) (b)

Trigger on lower trace

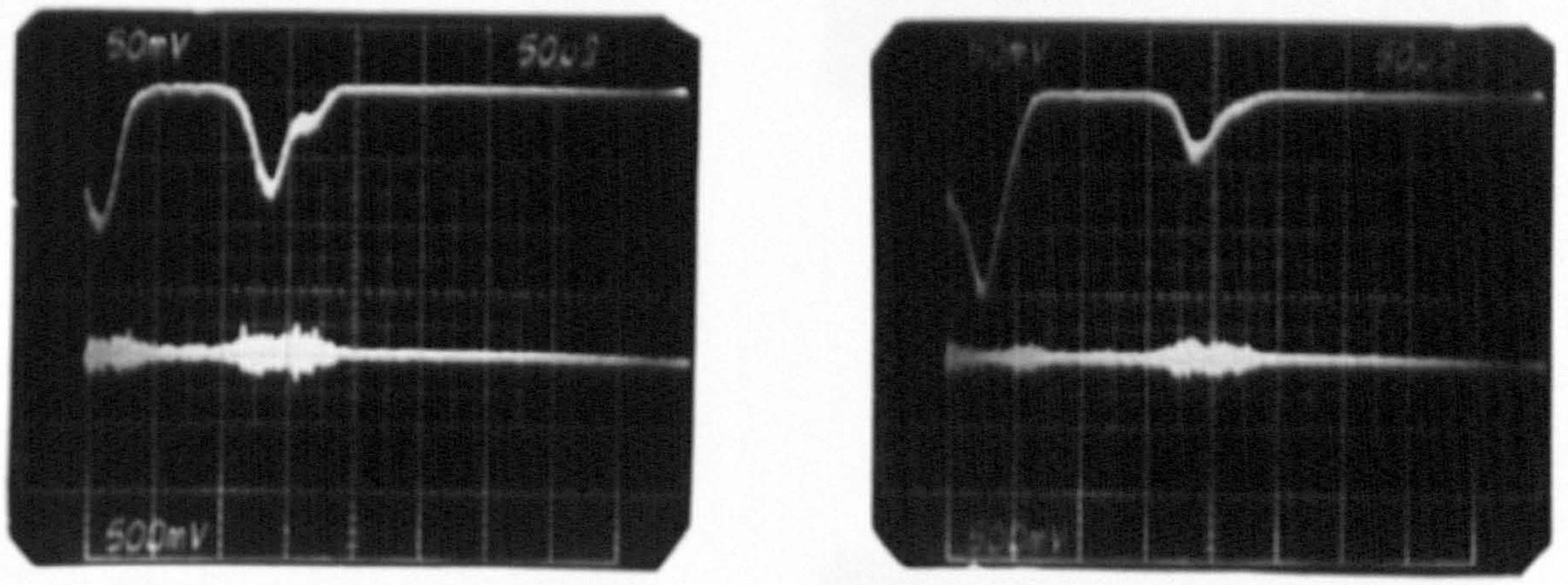

(c) (d)

Trigger on upper trace

Figure 5.12 Glass ballotini, 95-135 μm; telescope f no = 4.74; pinhole dia = 200 μm

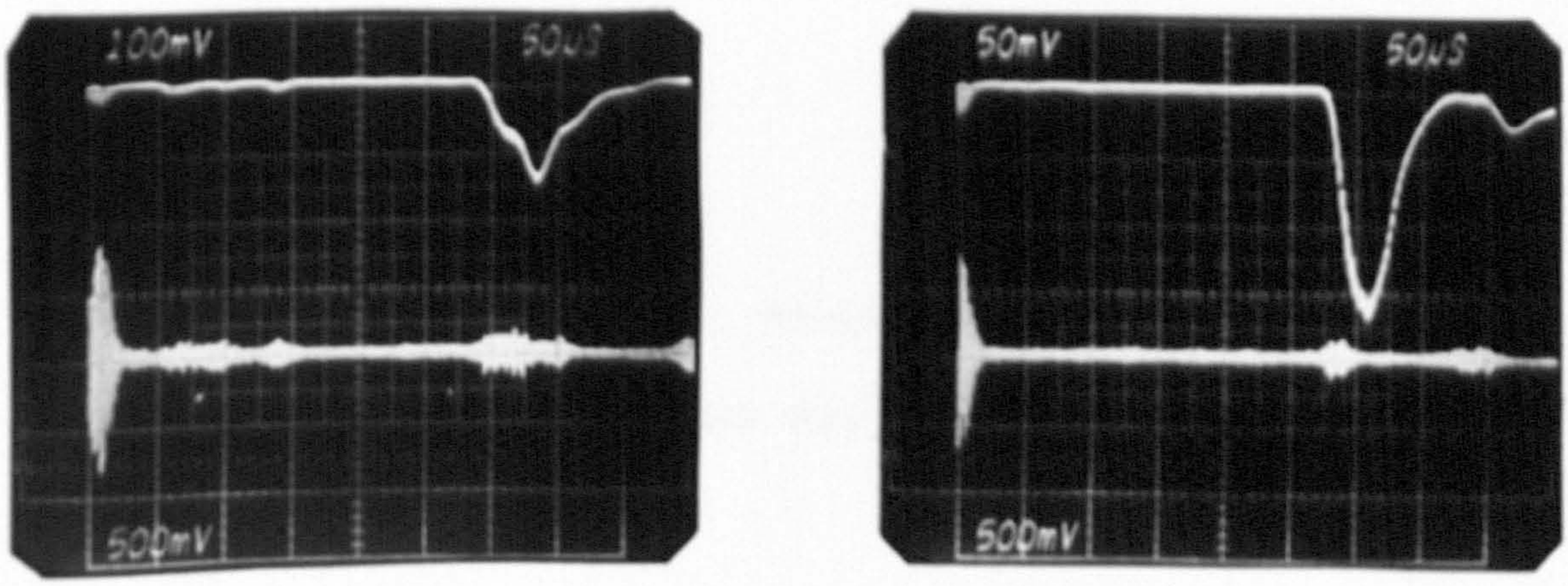

(a) (b)

Figure 5.13 Glass ballotini, 95-135 μm with silicon oil smoke; trigger on lower trace; telescope f no = 4.74; pinhole dia = 200 μm

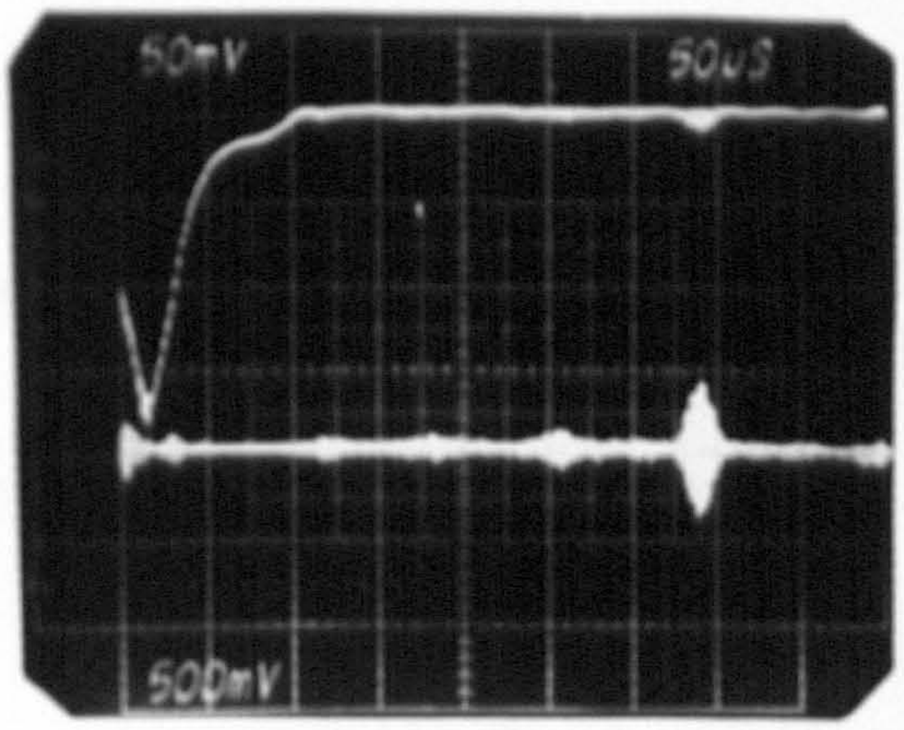

(a)

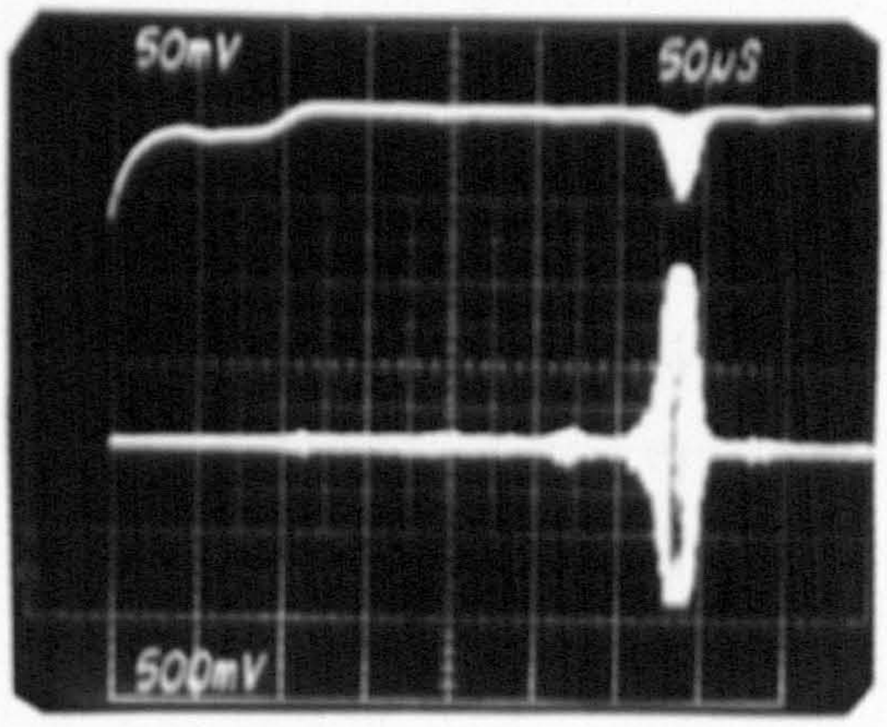

(b)

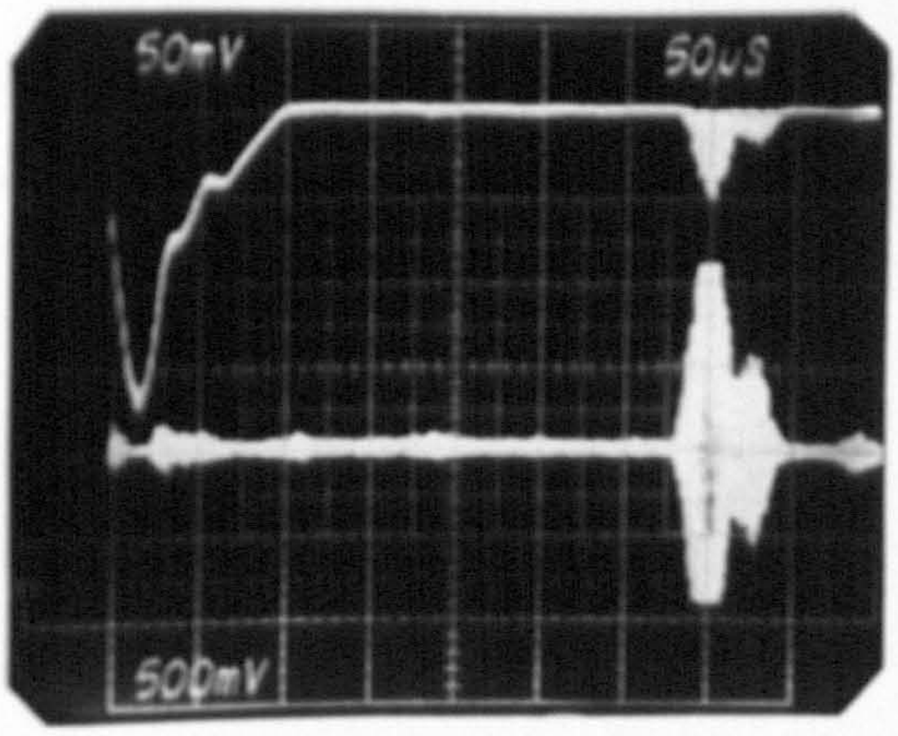

(c)

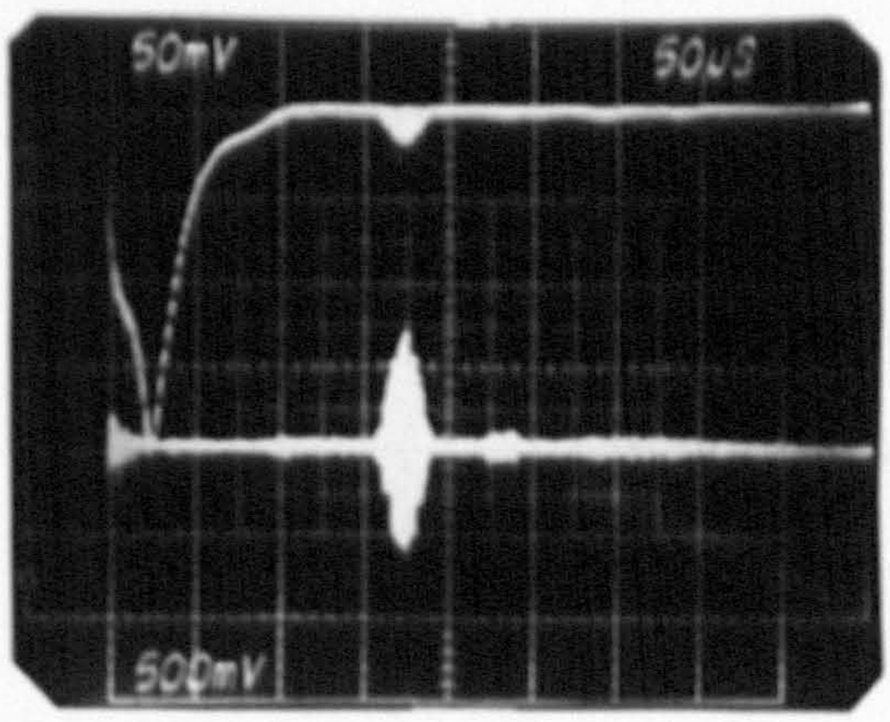

(d)

Figure 5.14 Glass ballotini, 95-135 μm with silicon oil smoke; telescope f no = 4.74; pinhole dia = 200 μm; trigger on upper trace

conditions and observing the resulting velocity histograms. The size comparability between smoke and naturally occurring dust was also investigated.

Figures 5.15 and 5.16 show velocity histograms from flows in which the small scatterers were smoke particles (from tobacco and silicon oil) and dust. As it can be seen the high frequency part of the histogram indicates no change in the small particle velocity with the type of small scatterer used. It is also noted that the naturally occurring small scatterers were outnumbered by the large scatterers. This demonstrates the need for artificial seeding in similar flow situations, in order to achieve an acceptable data arrival rate.

Figures 5.17 and 5.16 (c) and (d) show that the presence of a large number of small scatterers results in a faster growth of the high frequency part of the histogram.

The dependence of the signal visibility on collecting optics geometry is demonstrated by figure 5.18. Since the flow was not artificially seeded there was a far greater number of large scatterers present than small ones.

It is noted that as the collecting optics aperture decreased, the rate of signal arrivals from large particles increased so that for a small aperture, as in figure 5.18 (b) and (f), only signals from larger scatterers were recorded. This can be explained as follows:

As shown in section 5.2.1, for small collecting apertures (large f no) the visibility tends to unity, independent of particle size. Thus as the size of the collecting aperture is reduced the visibility of large particle signals increases, with an associated increase in the amplitude of the a.c. component of the signals. This in turn increases the number of signals from large scatterers which exceed VT_1, and the low frequency part of the histogram builds up faster.

The remarkable and to some extent unexpected result, was that a reduction in the pinhole size had a similar effect on signal visibility as a reduction of the collecting aperture size, see figures 5.18(c) and (d).

5.2.3 Concluding remarks

The experimental results of the previous paragraph, which were in complete agreement with the arguments presented in section 5.2.1, lead to the conclusion that in the forward scatter mode the signal parameters (a.c. and d.c. amplitudes) exhibit the following average characteristics with respect to the size of the scatterer:

(i) Small scatterer ($D < \delta$): small d.c. component amplitude, high visibility.

(ii) Large scatterer ($D \gg \delta$): large d.c. component amplitude, low visibility.

As an exception to the above, the absolute value of the scattered light intensity in any direction may depend on a

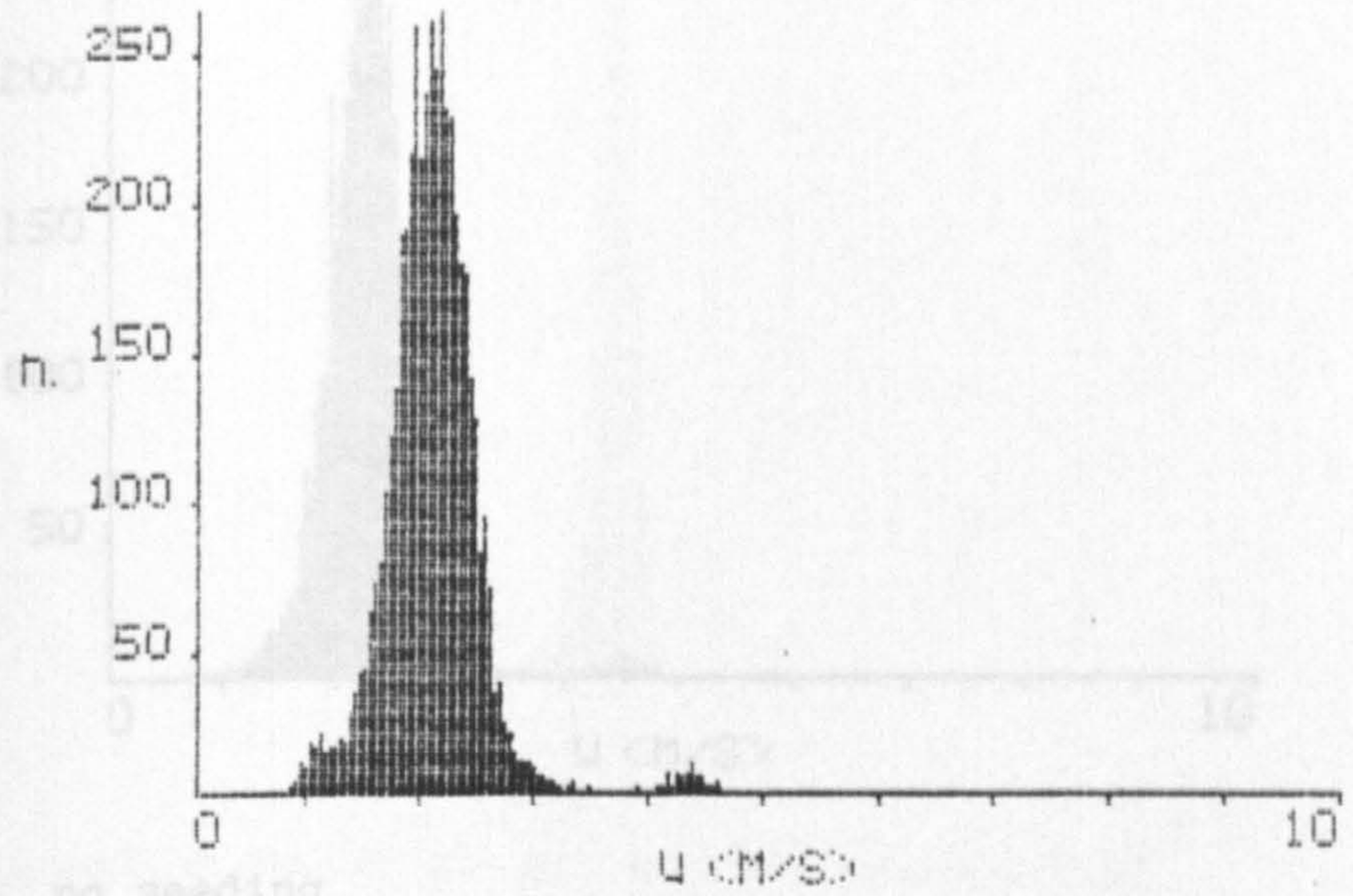

(a) no seeding

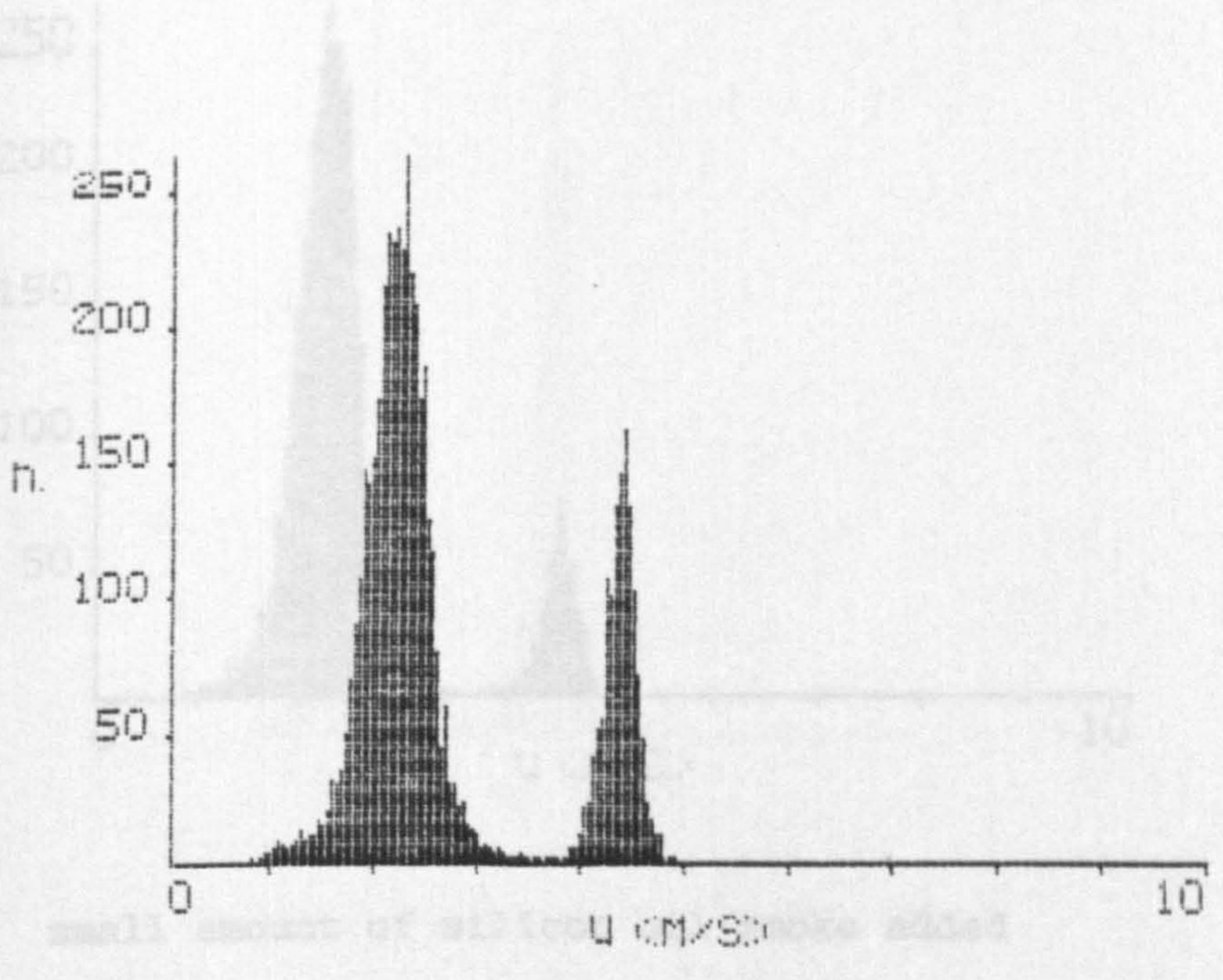

(b) seeded with tobacco smoke

Figure 5.15 Glass ballotini, 210-235 μm; f no = 6.7; pinhole dia ≒ 100 μm; VT_1 ≒ 0.1 V.

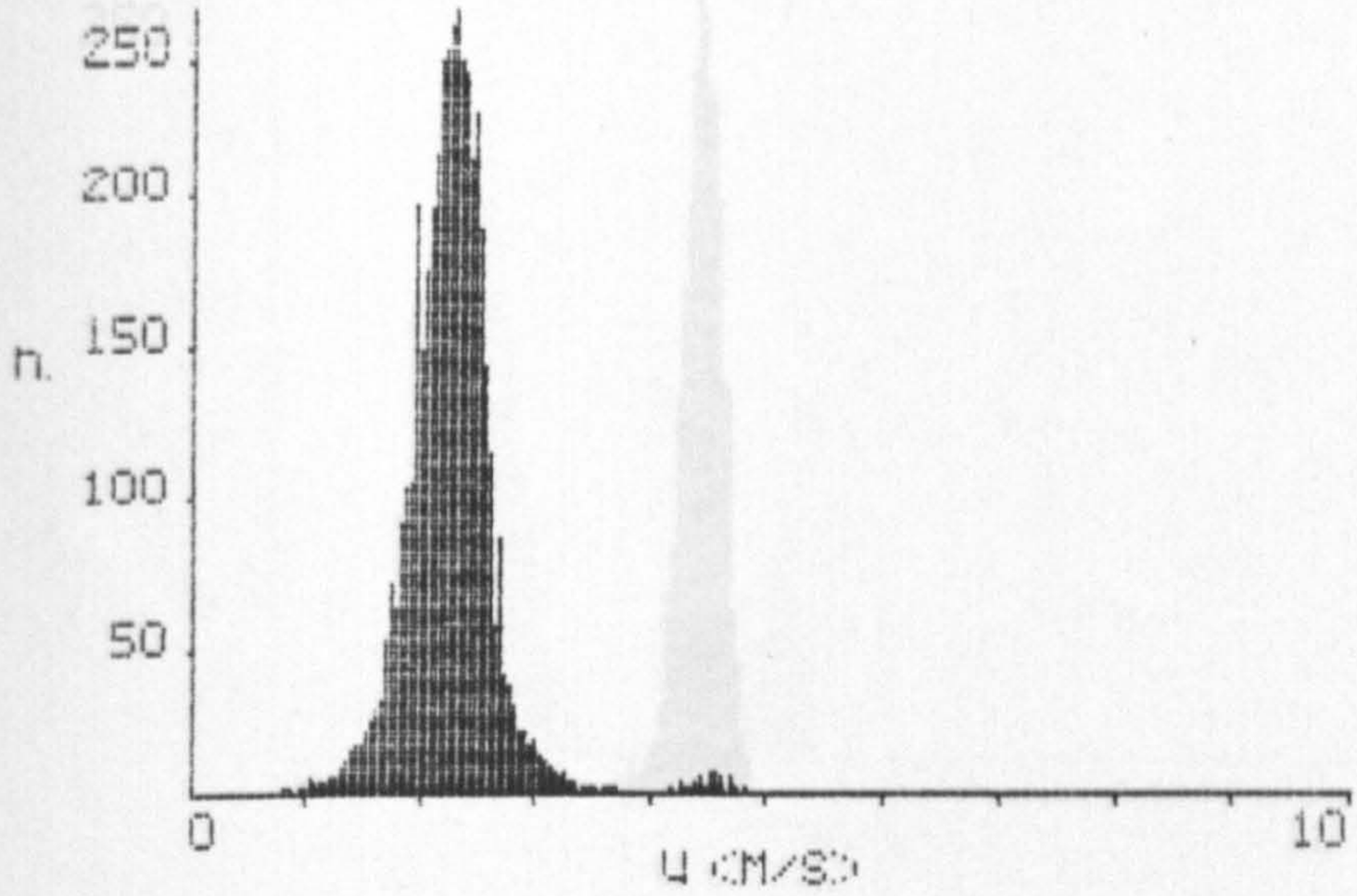

(a) no seeding

(b) small amount of silicon oil smoke added

part of figure 5.16.

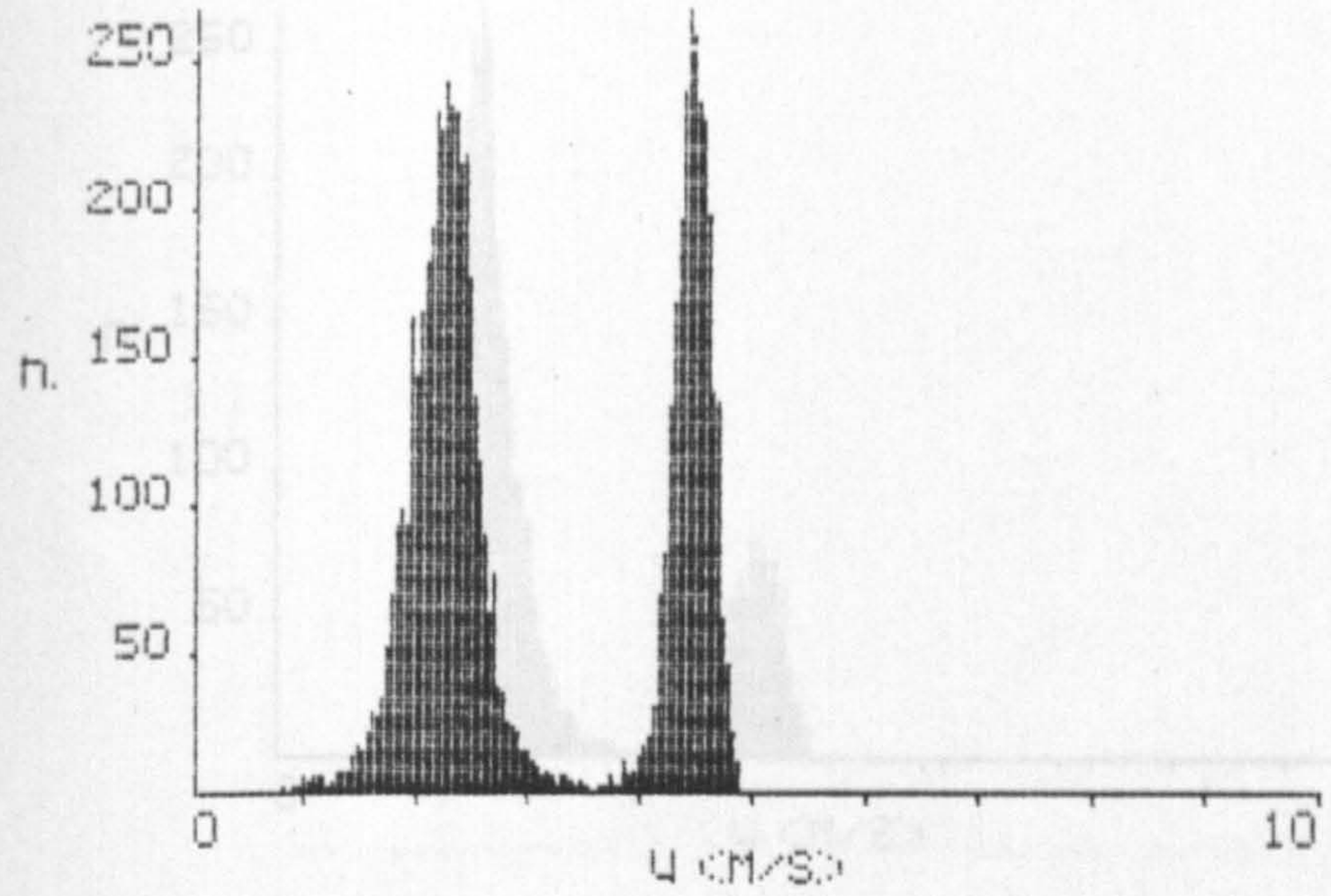

(c) Medium amount of silicon oil smoke added

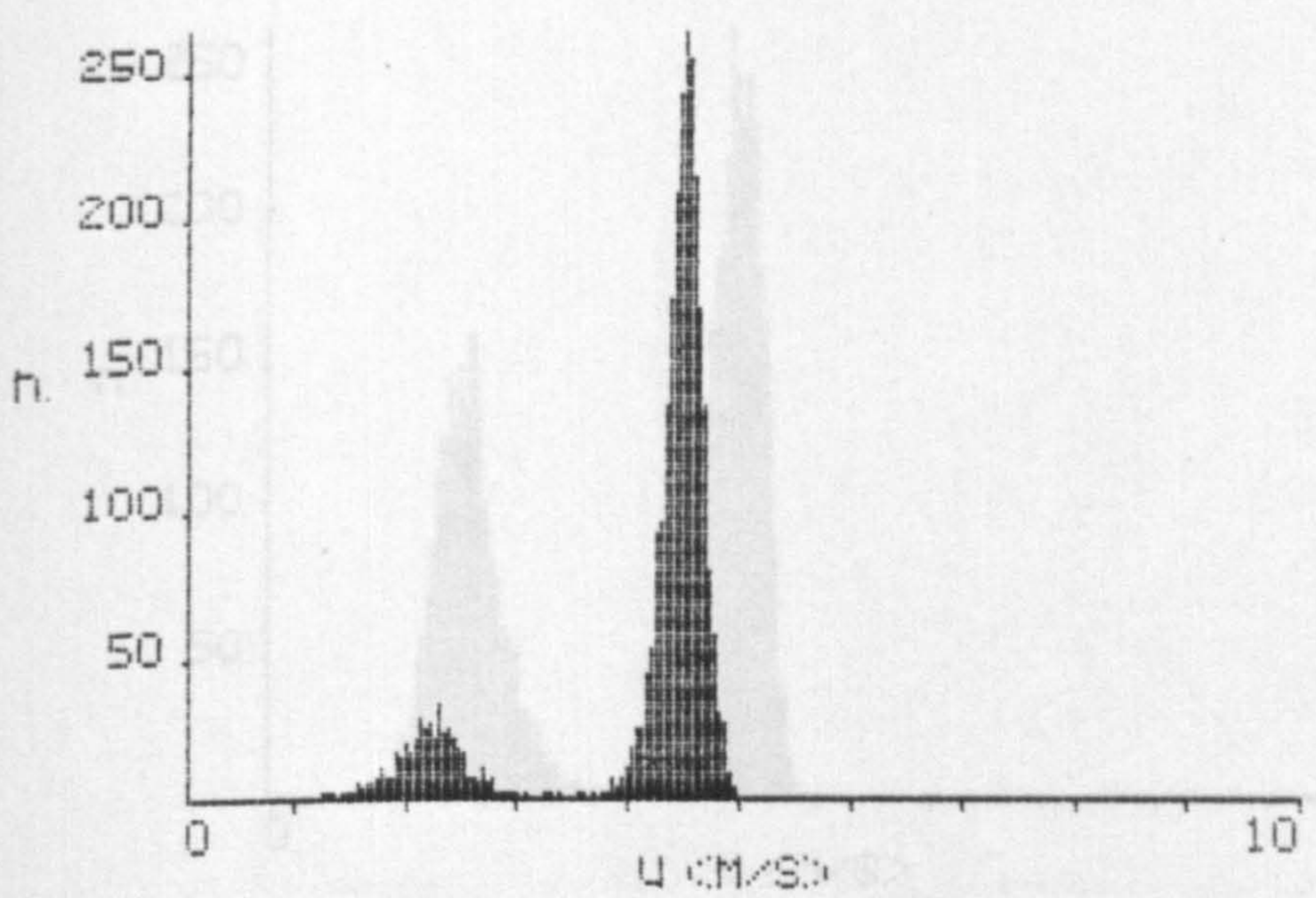

(d) Large amount of silicon oil smoke added.

Figure 5.16 Glass ballotini, 210-325 μm; f no = 6.7; pinhole dia = 100 μm; VT_1 = 0.07 V.

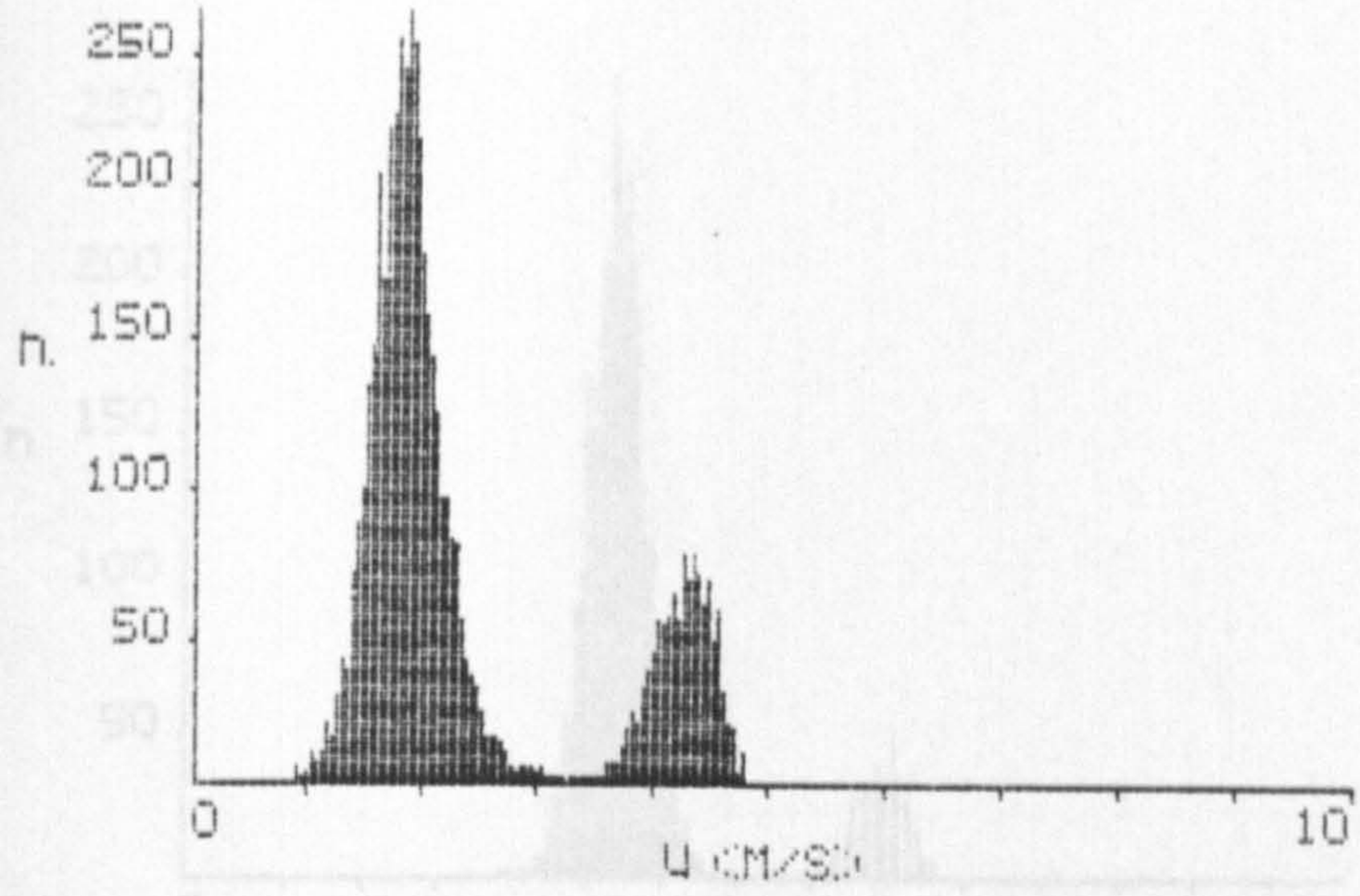

(a) small amount of smoke added

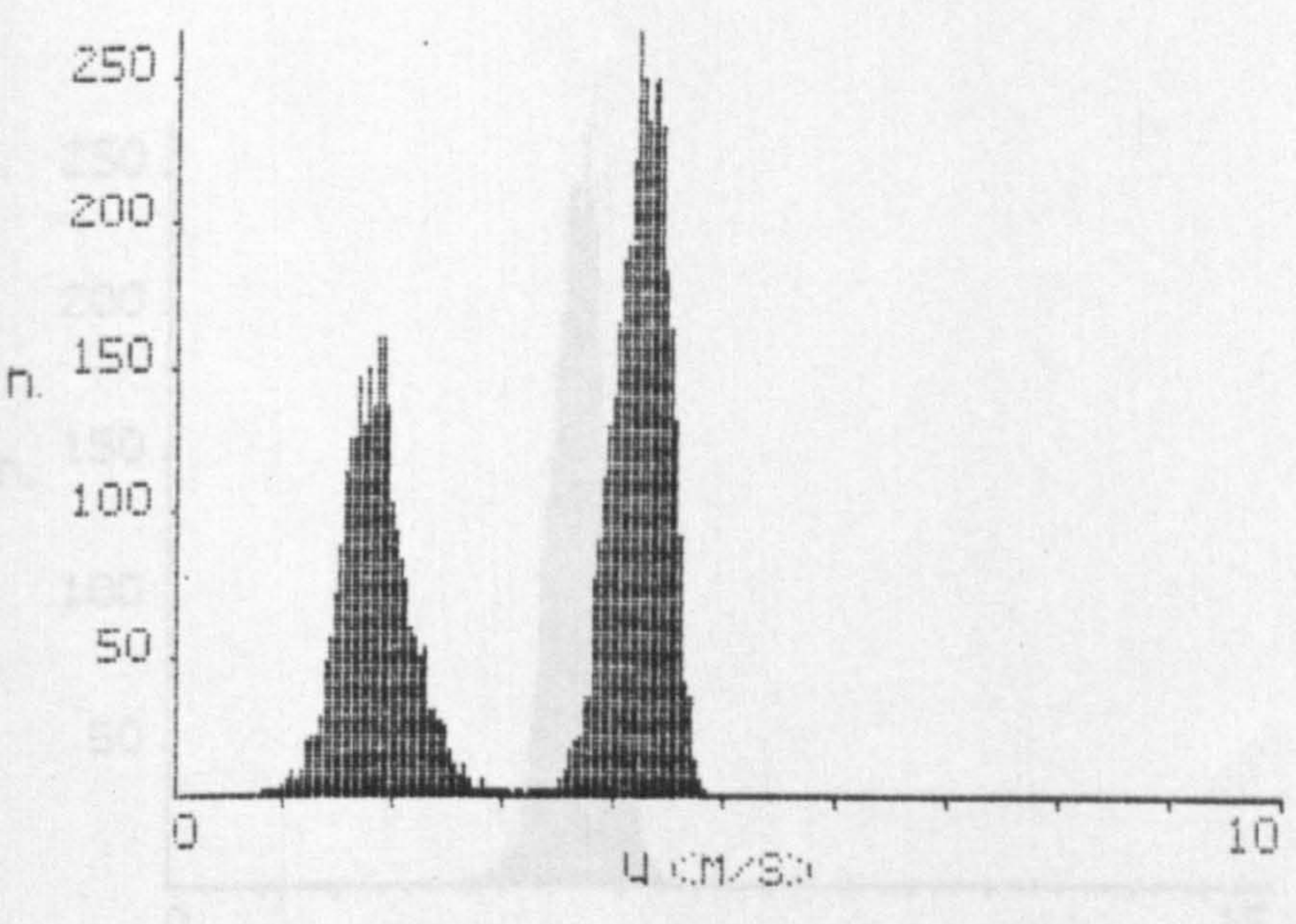

(b) large amount of smoke added

Figure 5.17 Glass ballotini, 210-325 μm and silicon oil smoke; telescope f no = 6.7; pinhole dia = 100 μm; $VT_1 \doteq 0.07$ V.

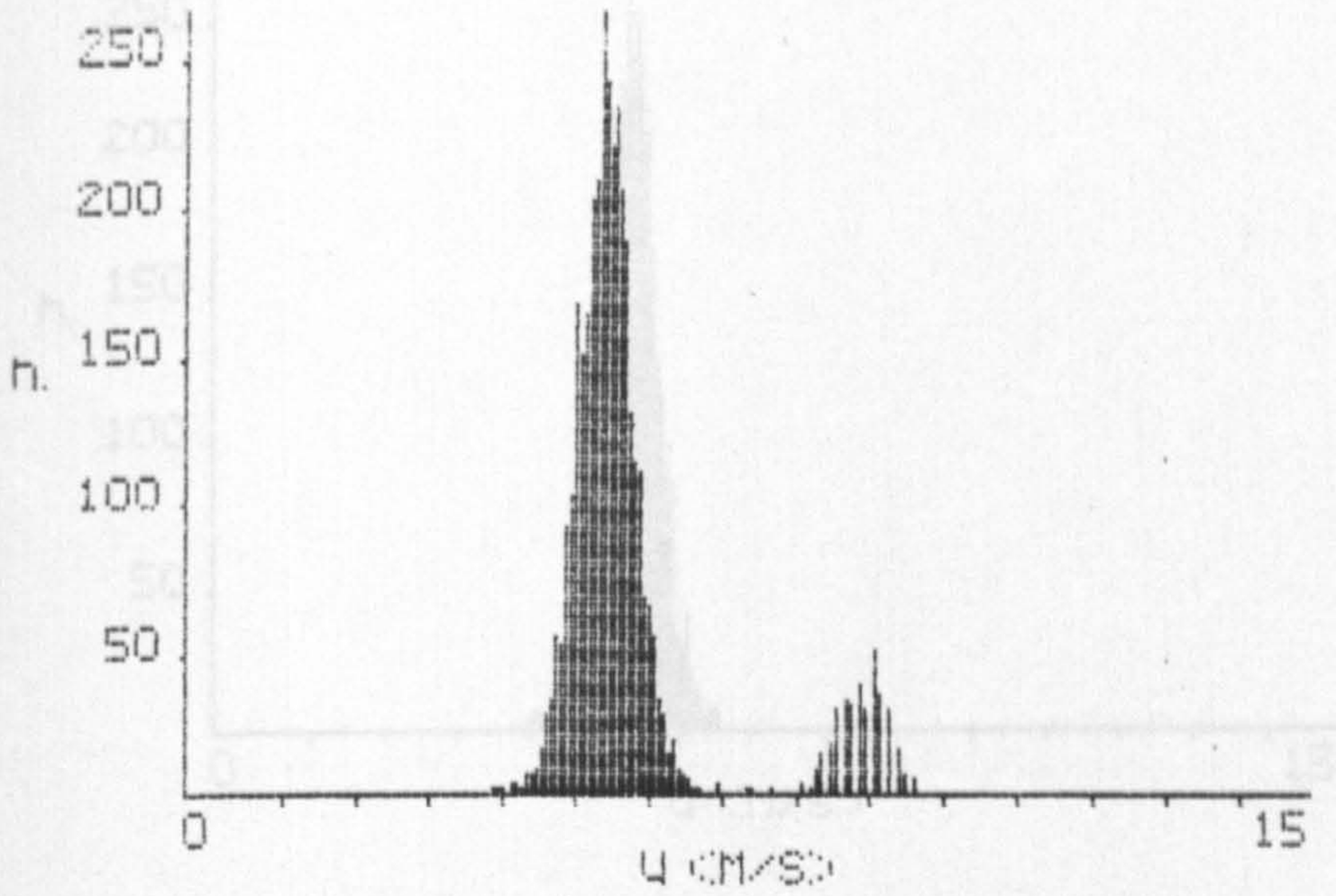

(a) f no = 2.4; pinhole dia = 100 μm

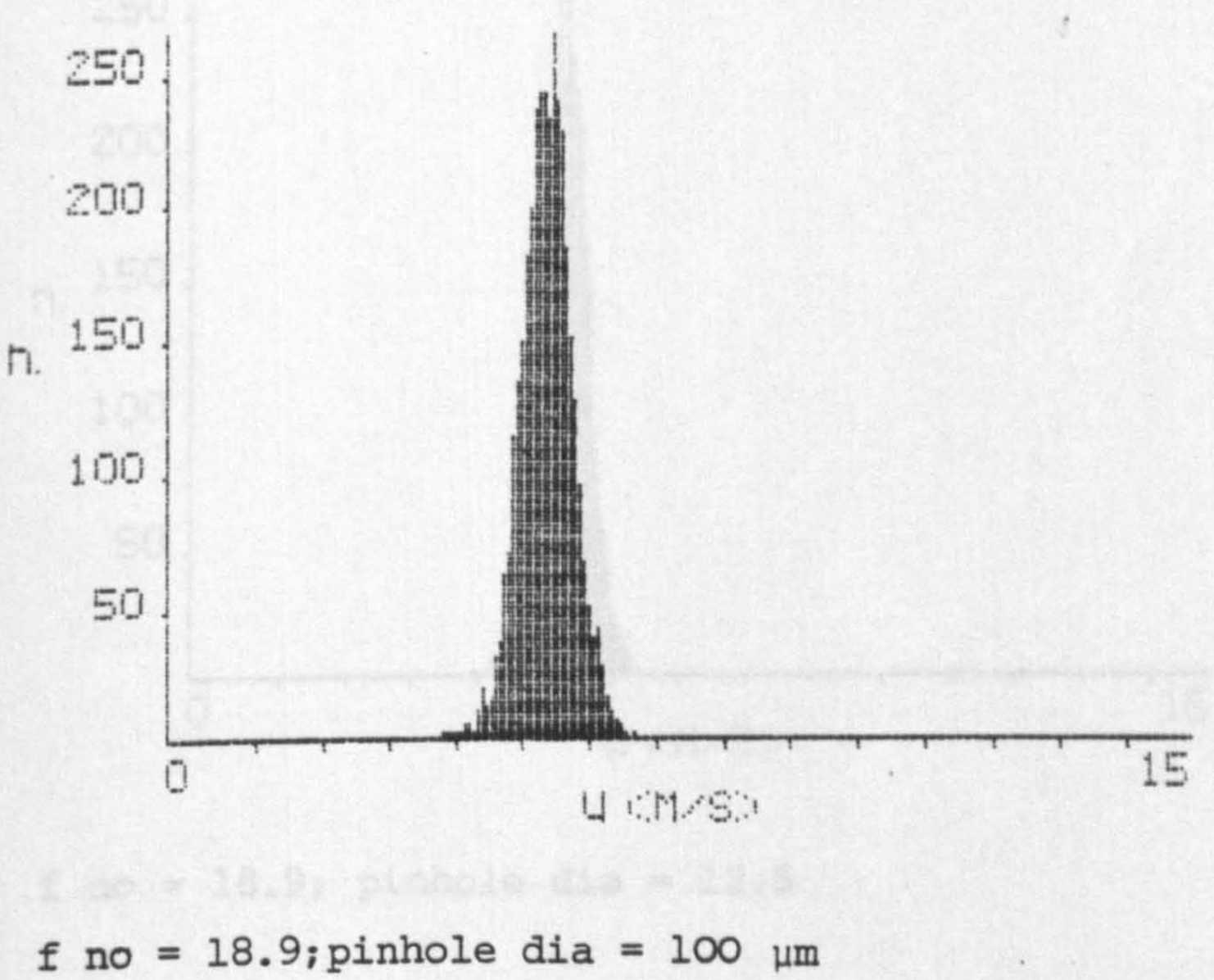

(b) f no = 18.9;pinhole dia = 100 μm

part of figure 5.18.

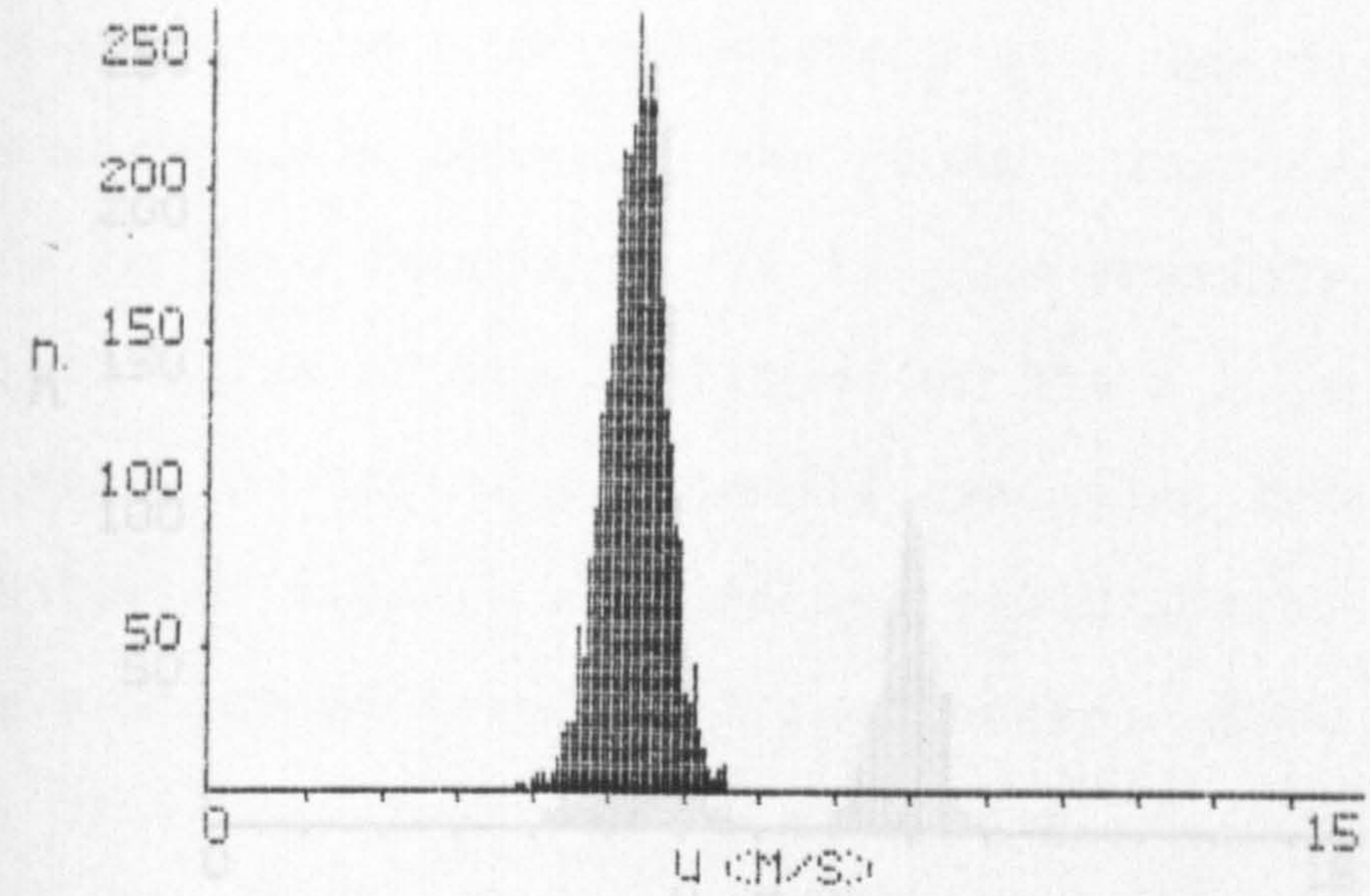

(c) f no = 2.4; pinhole dia = 12.5 μm

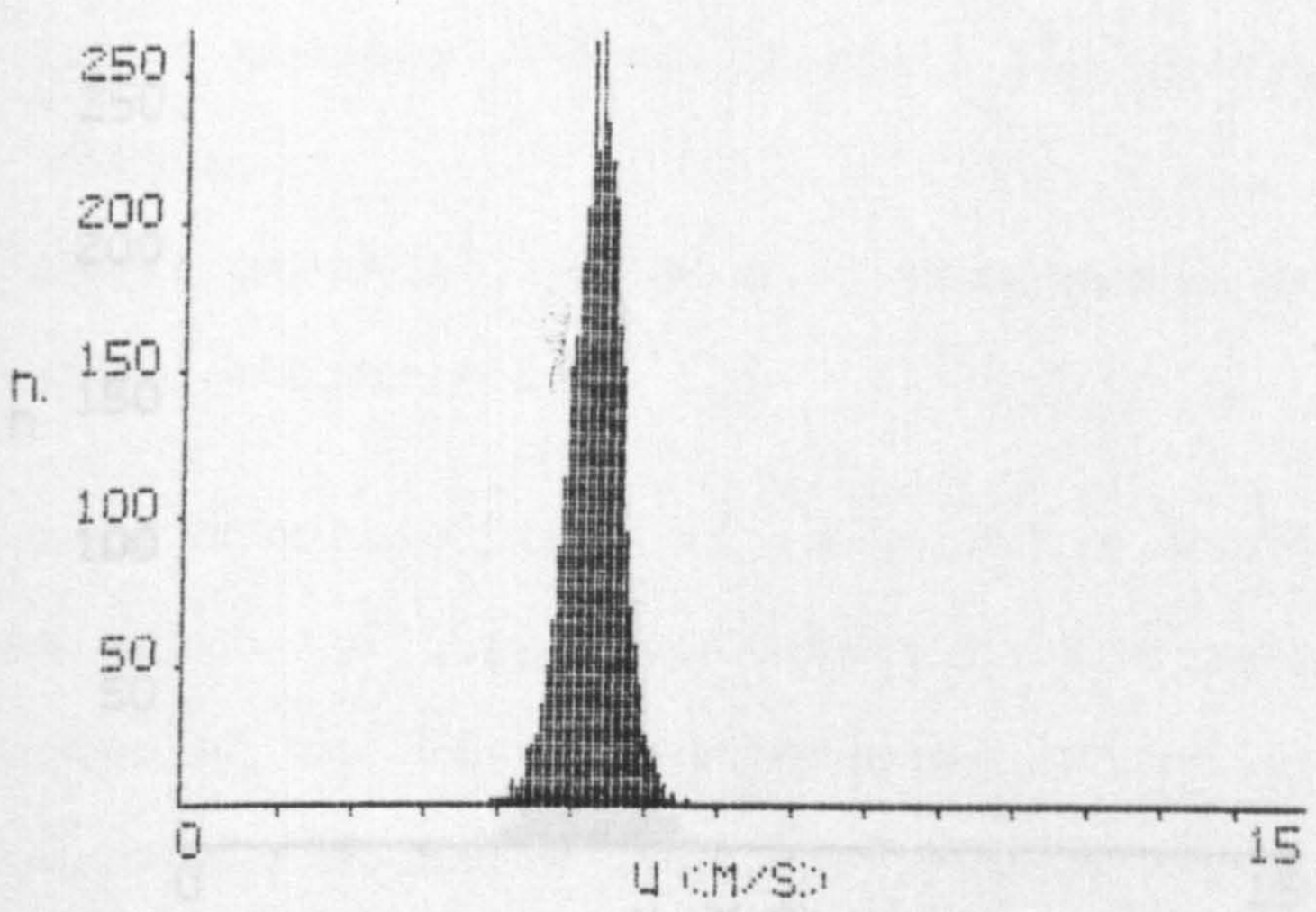

(d) f no = 18.9; pinhole dia = 12.5

part of figure 5.18.

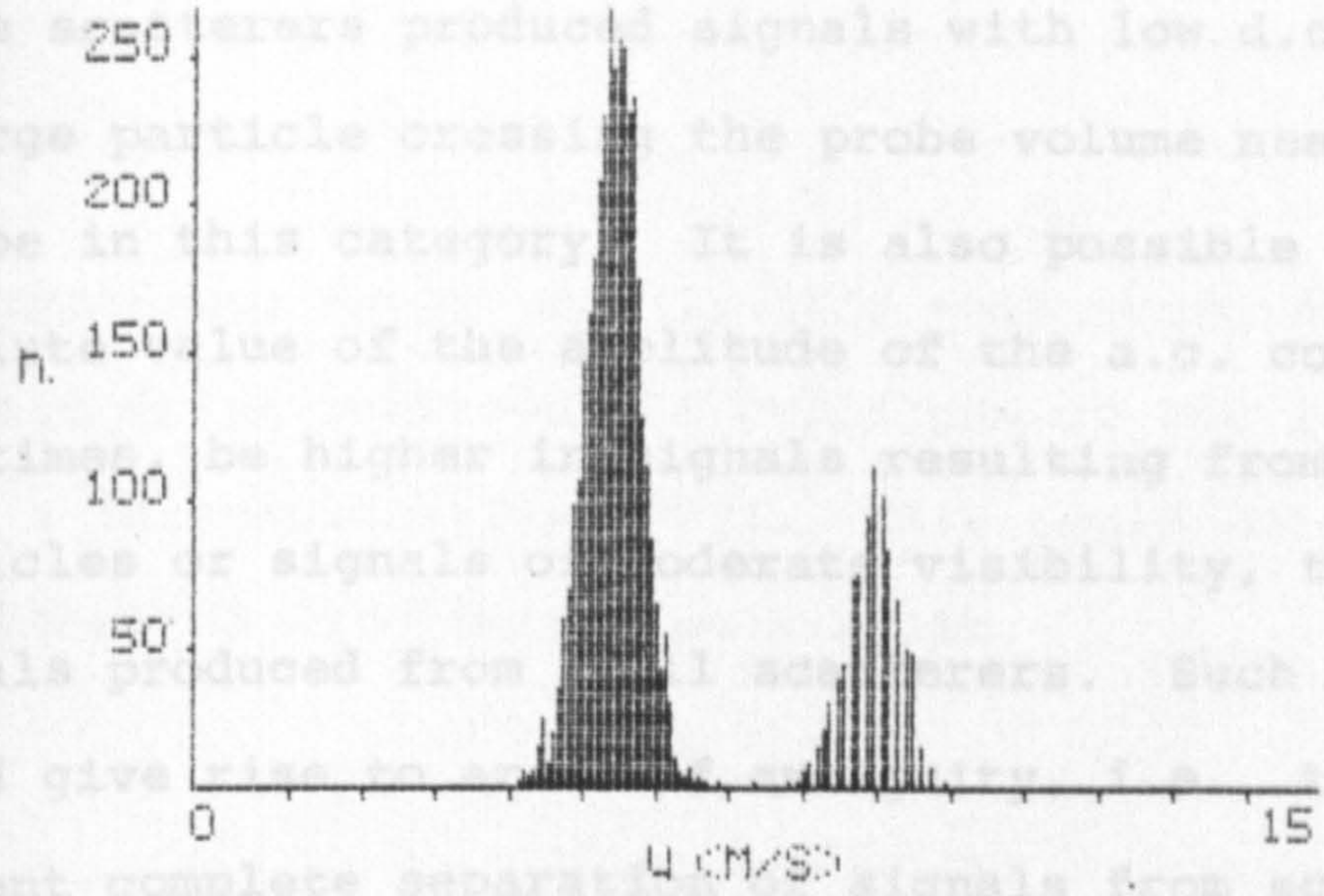

(e) fnσ = 2.4; pinhole dia = 150 μm

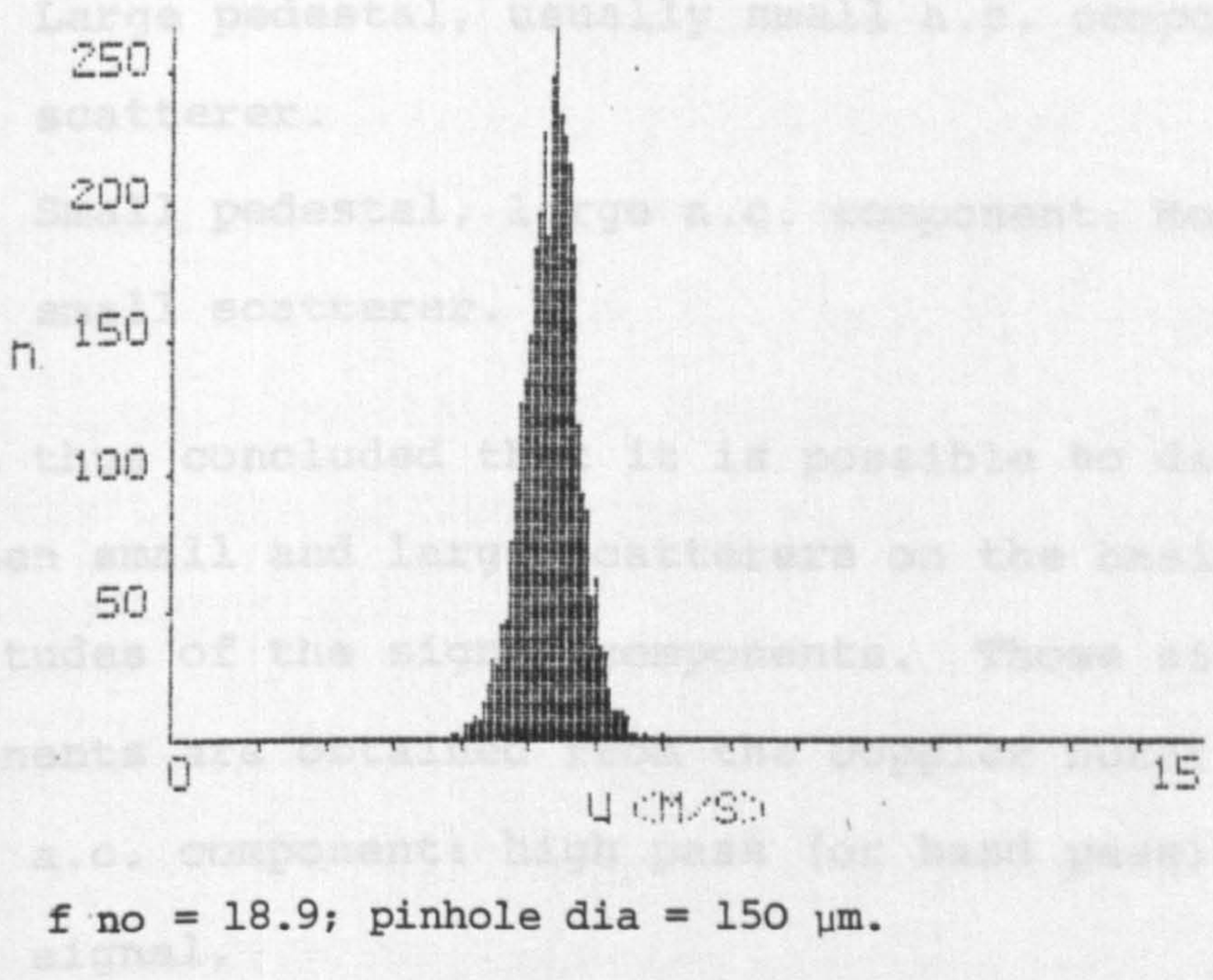

(f) f no = 18.9; pinhole dia = 150 μm.

Figure 5.18 Glass ballotini; 210-325 m; no seeding; VT_1 = 0.13 V.

multitude of conditions, i.e. there could be cases where large scatterers produced signals with low d.c. amplitude; a large particle crossing the probe volume near the edge may be in this category. It is also possible that the absolute value of the amplitude of the a.c. component may, sometimes, be higher in signals resulting from large particles or signals of moderate visibility, than in signals produced from small scatterers. Such possibilities would give rise to areas of ambiguity, i.e. they would prevent complete separation of signals from scatterers of different sizes.

From the above, the following are deduced with regard to the signal components:

(i) Large pedestal, usually small a.c. component: large scatterer.

(ii) Small pedestal, large a.c. component: Most probably small scatterer.

It is thus concluded that it is possible to discriminate between small and large scatterers on the basis of the amplitudes of the signal components. Those signal components are obtained from the Doppler burst as follows:

(i) a.c. component: high pass (or band pass) filtered signal,

(ii) d.c. component: low pass filtered signal.

It was therefore decided to introduce a logic circuit into the LDA system which would compare the amplitude of the

two signal components with preset threshold voltages and would either accept or reject signals resulting from large or small scatterers.

The frequency meter used in this work employed a logic circuit which compared the amplitude of the a.c. component with a threshold voltage VT_1. This could become part of the proposed discriminating circuit.

5.3 THE DISCRIMINATOR

5.3.1 Principles of operation

Figure 5.19 shows the principles of operation of the discriminator circuit. The pedestal signal is compared with a d.c. level, VT_2, and produces a pulse output, as shown by the waveforms in figure 5.20, if the pedestal is larger than the set level VT_2. A pulse output from the discriminator sets the memory output at a logic 1, a value which it will retain until completion of the measurement. Thus the length of time during which the pedestal exceeds VT_2 is unimportant.

At the completion of a measurement the memory contents are entered into a D-type flip-flop using the 'output results' pulse. The flip flop has two complementary outputs, one of which indicates a large scatterer since it sets to logic 1 when the memory output is 1, and the other indicates a small particle since it sets to 1 when the memory output is 0.

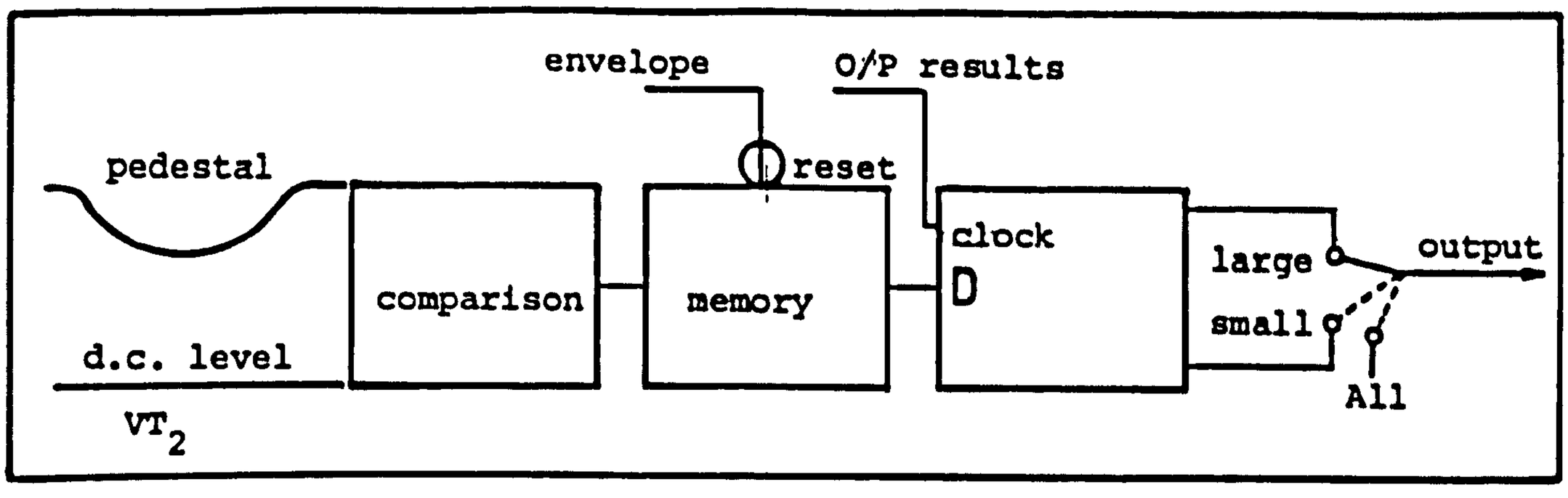

Figure 5.19 Block diagram of the discriminator

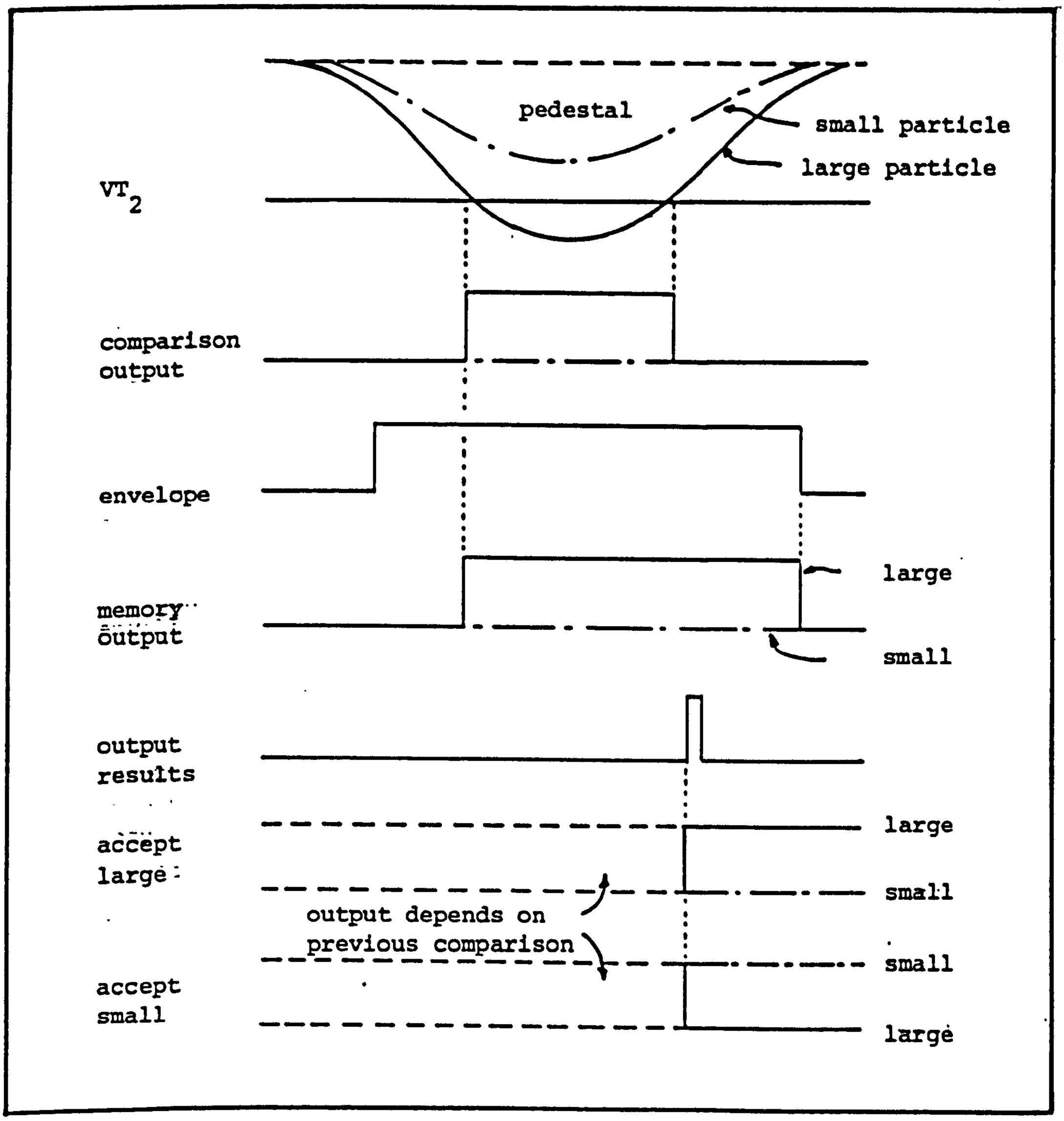

Figure 5.20 Waveforms for discriminator operation

A three way manually operated switch is used to select the output of the discriminator, the switch positions being:

(i) All: no discrimination; all results outputed from the Doppler frequency meter are recorded.

(ii) Accept small: Signals are accepted if the amplitude of the signal envelope does not exceed VT_2.

(iii) Accept large: Signals are accepted if the amplitude of the signal envelope exceeds the preset level VT_2.

5.3.2 Testing of circuit operation

(a) Using simulated signals

Simulated Doppler signals were produced using a high frequency signal generator with a modulated sine wave output. In order to make the simulated signal as realistic as possible, half wave rectification was applied to the modulated signal envelope, see figure 5.21. The purpose of this investigation was to evaluate the performance of the logic circuits and not an attempt to fully simulate LDA signals. Information about Doppler signal simulation can be found in the literature [9].

The frequency meter threshold voltage, VT_1, was set to less than the maximum a.c. signal amplitude and the discriminator threshold, VT_2, was set to about half the value of the peak envelope amplitude.

When the discriminator was switched to accept small particle

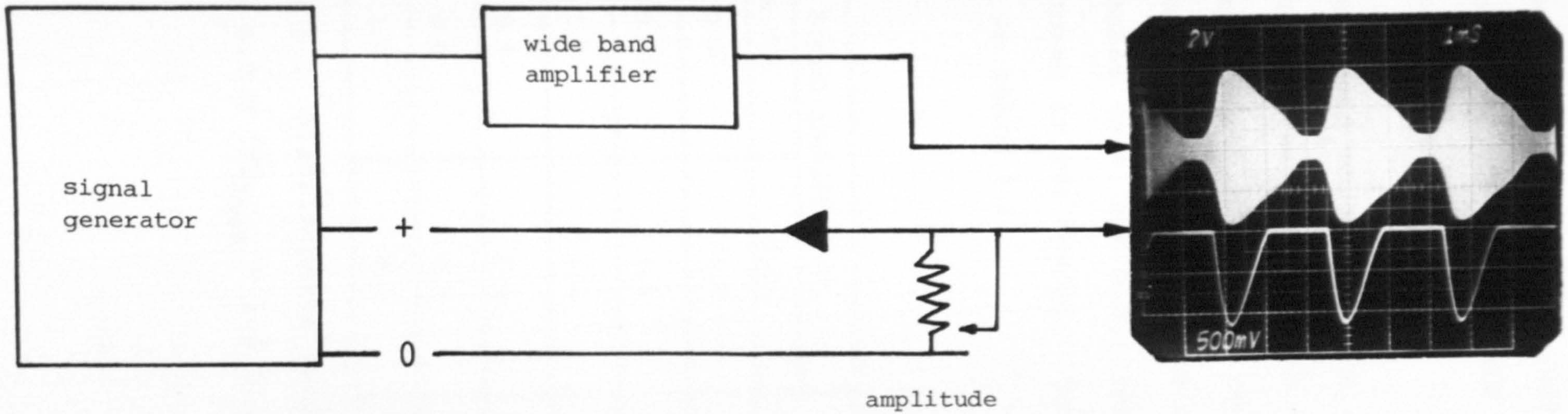

(a)

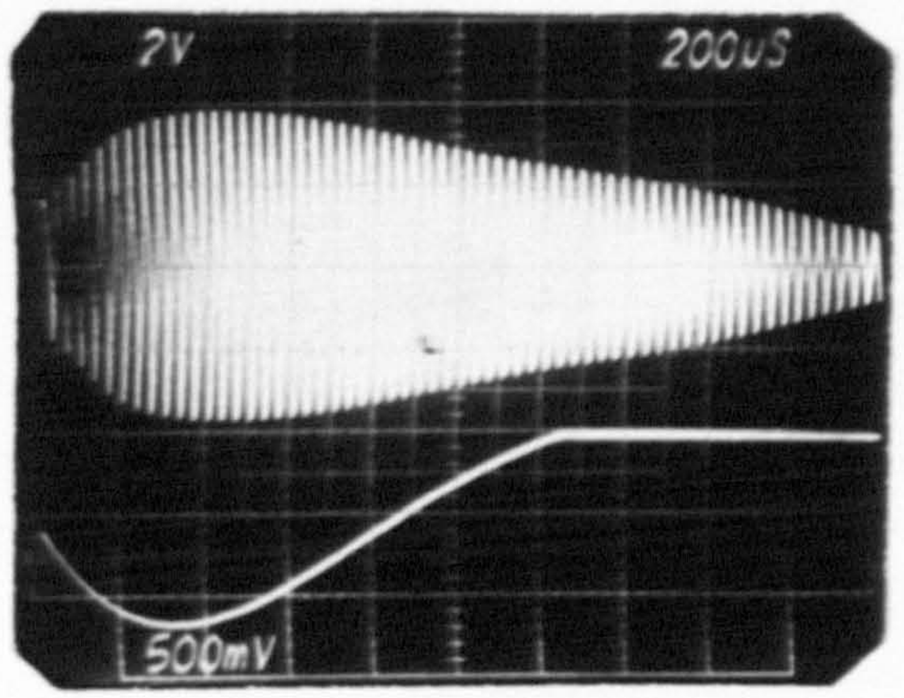

(b)

Figure 5.21 Doppler signal simulation

(a) circuit diagram; (b) signal details showing a.c. component and pedestal

signals, the logic output remained at state '0', i.e. no signals were accepted and when switched to accept large particle signals, all signals were accepted, as all pedestals exceeded VT_2.

The threshold voltage levels, VT_1 and VT_2, were varied and it was observed in all cases that the discriminator output corresponded to the design requirements. Alternatively the threshold voltages were kept constant and the signal amplitudes (a.c. and d.c.) were varied; again the circuit functioned as per design. Some representative results are shown in table 5.1.

Signal amplitude (V)		Large	Small
a.c.	d.c.		
0.4	1.4	-	-
0.6	1.4	All accepted	All rejected
1.0	1.4	All accepted	All rejected
0.4	0.4	-	-
0.6	0.4	All rejected	All accepted
1.0	0.4	All rejected	All accepted

Table 5.1 Discriminator output for simulated signals; $VT_1 = 0.5$ V ($VT_{1max} \simeq 1.4$ V); $VT_2 = 0.5$ V ($VT_{2max} \simeq 1.5$ V).

(b) Using signals from a gas-solid suspension flow

In order to investigate the relationship between the number of valid measurements and the threshold levels VT_1 and VT_2, the following procedure was followed:

The number of results from the Doppler frequency meter was measured by a counter, triggered by the 'output results' pulse. At the same time the data acquisition and processing system was operated and the number of measurements accepted by the discriminator was calculated by executing a short program on the computer. A large number of such tests was carried out using the recirculating type flow rig and a variety of solids. The signal component amplitudes were set so that their values were less than the maximum values of the threshold levels VT_1 and VT_2.

It was observed that as the value of VT_1 was increased the data arrival rate decreased. High settings of VT_2 caused all signals to be accepted as small particle signals, and low values of VT_2 caused all signals to be accepted as large particle signals.

Since the above depend on the signal amplification and the overall instrument settings, graphical representation of such results would be of limited value. The graphs in figure 5.22 show the dependence of the data arrival rate and hence the overall experiment time, on the settings of VT_1 and VT_2 for one particular situation.

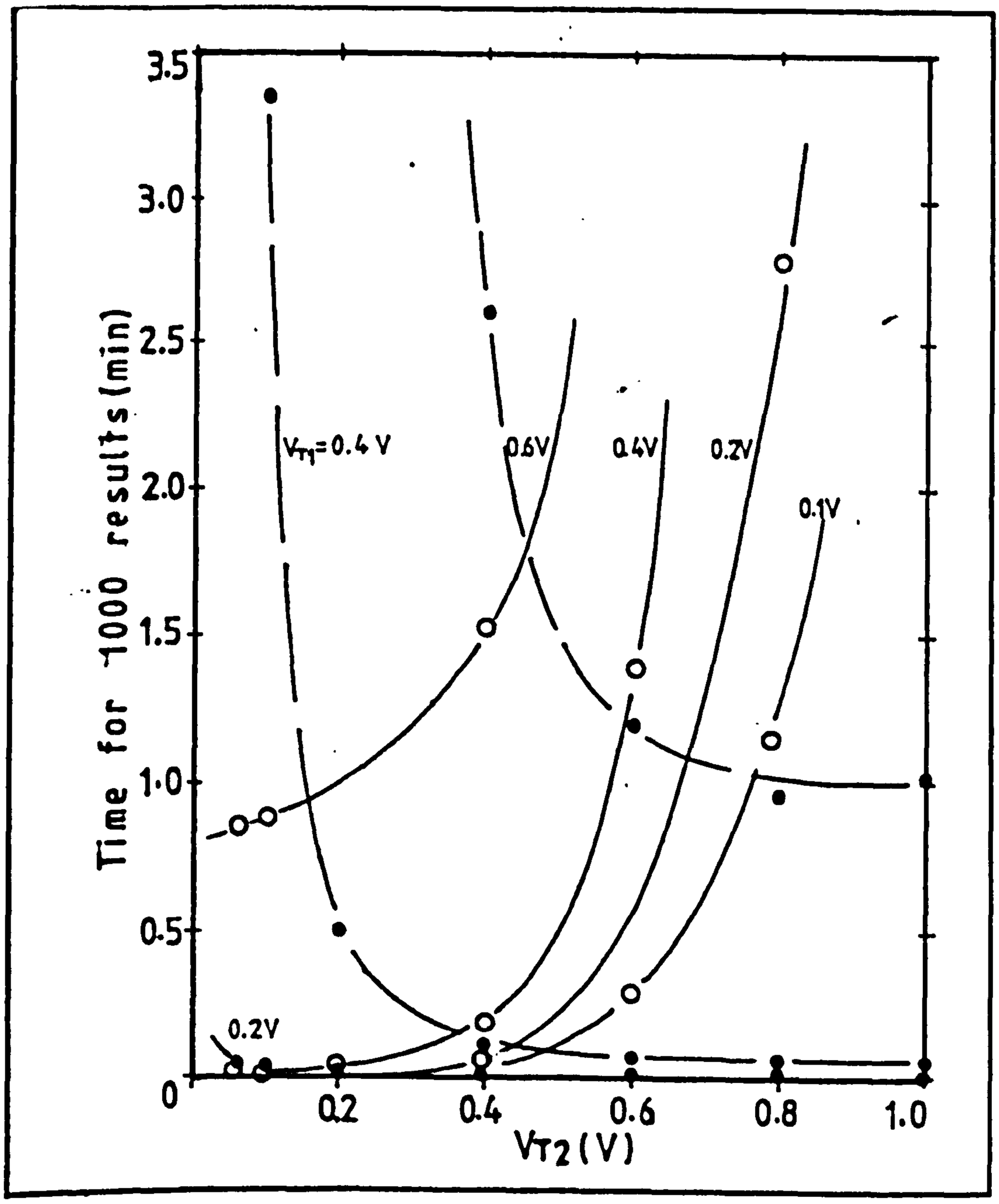

Figure 5.22 Variation of data arrival rate with VT_1 and VT_2; —•— small particle signals; —o— large particle signals.

5.3.3 Assessment of discriminator performance

Tests were carried out with the object of assessing the dependence of the effectiveness of the discriminator on the values of the threshold voltages VT_1 and VT_2. The open type flow rig was used and solids of known size distribution

were circulated. Seeding, when necessary, was provided by means of smoke from tobacco, paper and silicon oil.

Velocity measurements at a point were carried out and histograms of the results were plotted. Figure 5.23 to 5.28 show such velocity histograms for three values of VT_1 and two values of VT_2. In this experimental situation the small scatterers were more numerous than the large ones, as the results show. The majority of the signal amplitudes were estimated to be: a.c. $\leq$ 0.3 V; d.c. $\leq$ 0.4 V.

It is observed from figure 5.23 (b) that the low setting of VT_2 drastically reduced the number of large particle signals recorded. It is apparent from figure 5.23 (c) that with a low setting of VT_2, no exclusion of signals from small scatterers was possible.

On comparing figure 5.24 with fiture 5.23 it becomes apparent that the low setting of VT_1 gave rise to a wide distribution of frequencies. This may be attributed to noise and also to a reduction in the discrimination against large scatterers which normally have a low amplitude a.c. component. Figure 5.24 (b) clearly shows that raising of VT_1 improved discrimination in comparison with figure 5.23 (b).

It is seen from figure 5.25 that raising of VT_1 significantly reduced the number of signals recorded from large scatterers, as expected. Figure 5.25 (b) clearly

demonstrates the validity of the discrimination principles and is typical of many results obtained under a variety of conditions; a high VT_1 combined with a low VT_2 almost completely excluded signals produced by large scatterers.

Comparison of figures 5.26 (b) and 5.23 (b) verifies that large scatterers produce signals, whose pedestal amplitudes are larger than those of the small scatterers. Figure 5.26 (c) shows that when the discriminator is set to accept large particle signals, a high VT_2 virtually eliminates small particle signals.

Figure 5.27 (c) shows that a medium VT_1 setting combined with a high VT_2 is the optimum combination for discrimination against small particle signals.

It was noticed that when obtaining the results shown in figure 5.28 (c) the data arrival rate was unacceptably slow. To remedy this, the receiving optics f number was increased to 4.7, with a marked increase in the data rate. As explained earlier, this is due to an increase of the signal visibility, which in effect increases the number of signals with a.c. amplitudes exceeding VT_1.

Figure 5.29 gives another demonstration of the discriminator performance. Although a small number of low frequency signals is observed in figure 5.29 (c) this number could have been reduced by lowering VT_2 to about 0.08 V.

Figures 5.30 and 5.31 demonstrate the dependence of the

discrimination on VT_1. It is observed that for a fixed VT_2, raising of VT_1 reduces the number of large particle signals present in the histogram. Figures 5.20 (c) and (d) indicate that there is no real gain in making $VT_1 >$ 0.15 V. With reference to figure 5.31 it is noted that the results shown in (b) were obtained without the addition of smoke initially, for approximately one hour; smoke was then added and the data rate was considerably increased, so that the histogram was completed in a very short time. It is remarkable that even under those conditions there was such a small number of low frequency signals accepted. The time taken for the results shown in figure 5.31 (c) was approximately 10 minutes.

It is observed from figure 5.32 that the addition of a large number of small scatterers in the form of smoke in no way affected the discrimination against small particle signals. It is also noted that the much higher setting of VT_2 in figures 5.32 (c) and (d) offer no real benefit; it, in fact, resulted in a much slower data arrival rate.

5.4 CONCLUSIONS

From the results presented in section 5.2 as well as from a study of a large number of similar situations, the following conclusions were made, regarding the performance of the discrimination technique, presented in this chapter:

(a) A high setting of VT_1 results in exclusion of most large particle signals and thus VT_1 could, to some degree, be used alone as a discriminator for accepting small particle signals only; but a high VT_1 significantly reduces the data arrival rate. Combining VT_1 and VT_2 achieves discrimination with lower VT_1 settings, hence allowing for a higher data rate.

(b) In order to discriminate against small particle signals, the combination of VT_1 and VT_2 is indispensable, and use of VT_1 only, could not achieve this type of discrimination.

(c) The average threshold voltage settings necessary for good discriminator performance were found to be as follows:

(i) accepting small particle signals: low VT_2, high VT_1

(ii) accepting large particle signals: high VT_2, medium-low VT_1.

No actual values can be specified as the amplitudes of the a.c. and d.c. components depend on particular experimental conditions.

(d) Discrimination against small particles was found to be free from ambiguities, i.e. no small particle signals were accepted with those from large scatterers, since

the former invariably possess a pedestal of very much smaller amplitude than that of the latter.

(e) When discriminating against large particles, it was noticed that often some signals of low frequency were present in the histogram. Possible explanations for this could be as follows:

(i) Signals from large scatterers which have small pedestal may also sometimes have a sizeable visibility, in which case they qualify as small particle signals.

(ii) Those low frequency signals may results from genuinely small scatterers which have adhered to large ones and hence move with the velocity of the latter, although otherwise the signal characteristics are those corresponding to small particles.

(iii) Those signals could result from small particles, which, due to impacts with other - possibly large - scatterers have been deflected so that their velocity lies well outside the average range of that of the small particles.

(iv) It has been observed that often signals of significantly high visibility are obtained from the leading and trailing edges of large scatterers. Some of these signals may qualify as small particle signals.

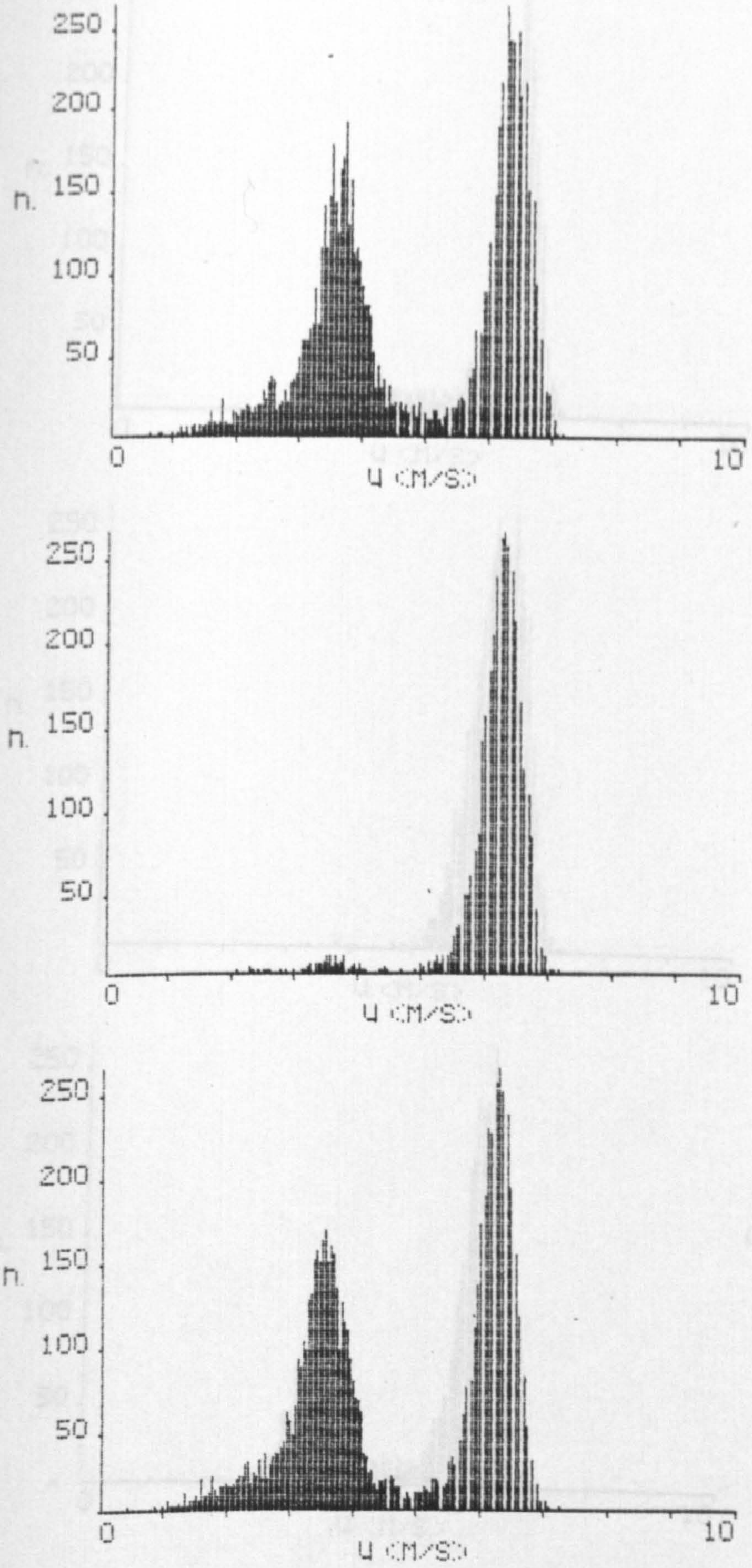

(a) no discrimination

(b) accept small particle signals

(c) accept large particle signals

Figure 5.23 Glass ballotini, 210-235 μm and paper smoke; telescope f no = 3.3; pinhole dia = 200 μm; VT_1 = 0.1 V; VT_2 = 0.08 V

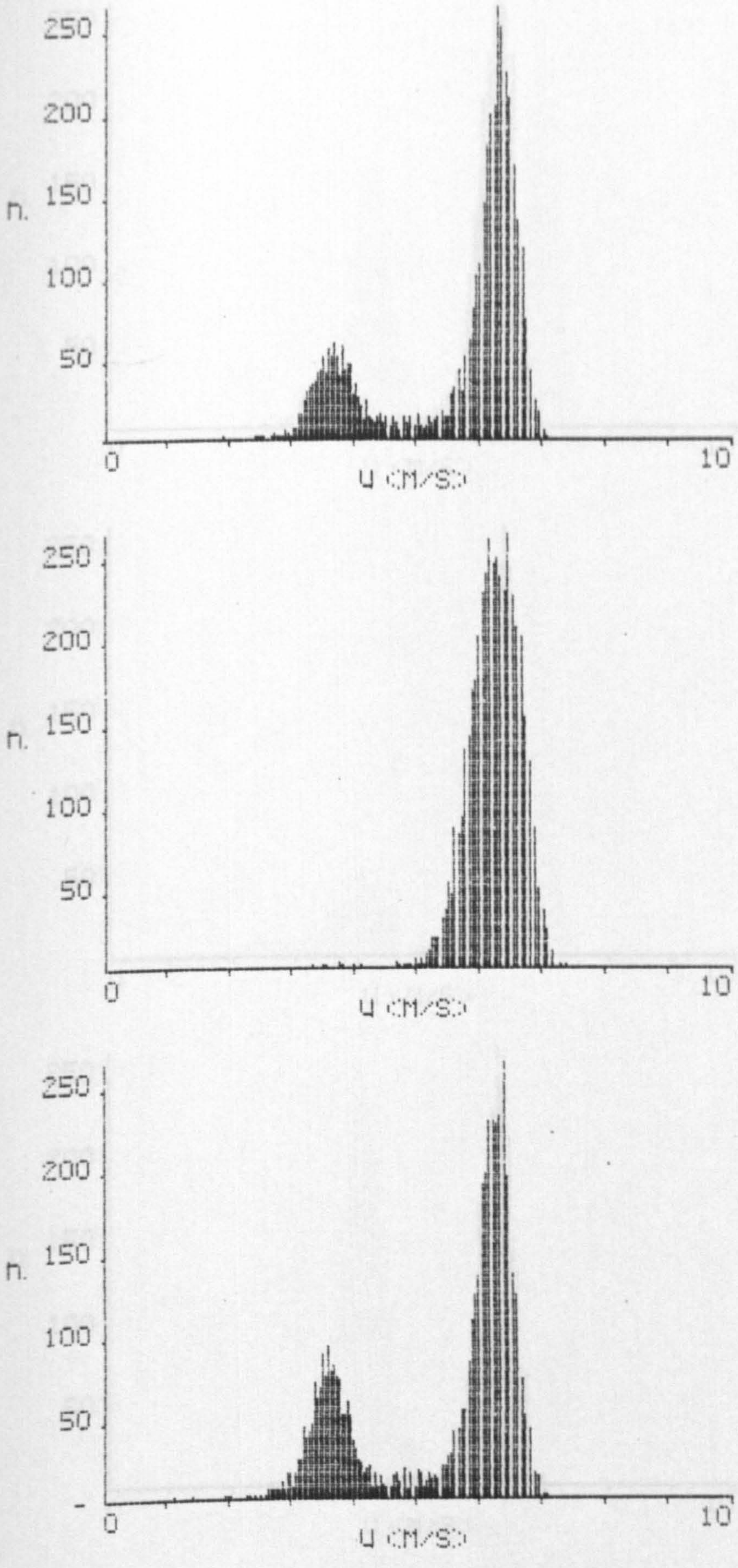

(a) no discrimination

(b) accept small particle signals

(c) accept large particle signals

Figure 5.24 Glass ballotini, 210-325 μm and paper smoke; telescope f no = 3.3; pinhole dia = 200; VT_1 = 0.14 V; VT_2 = 0.08 V.

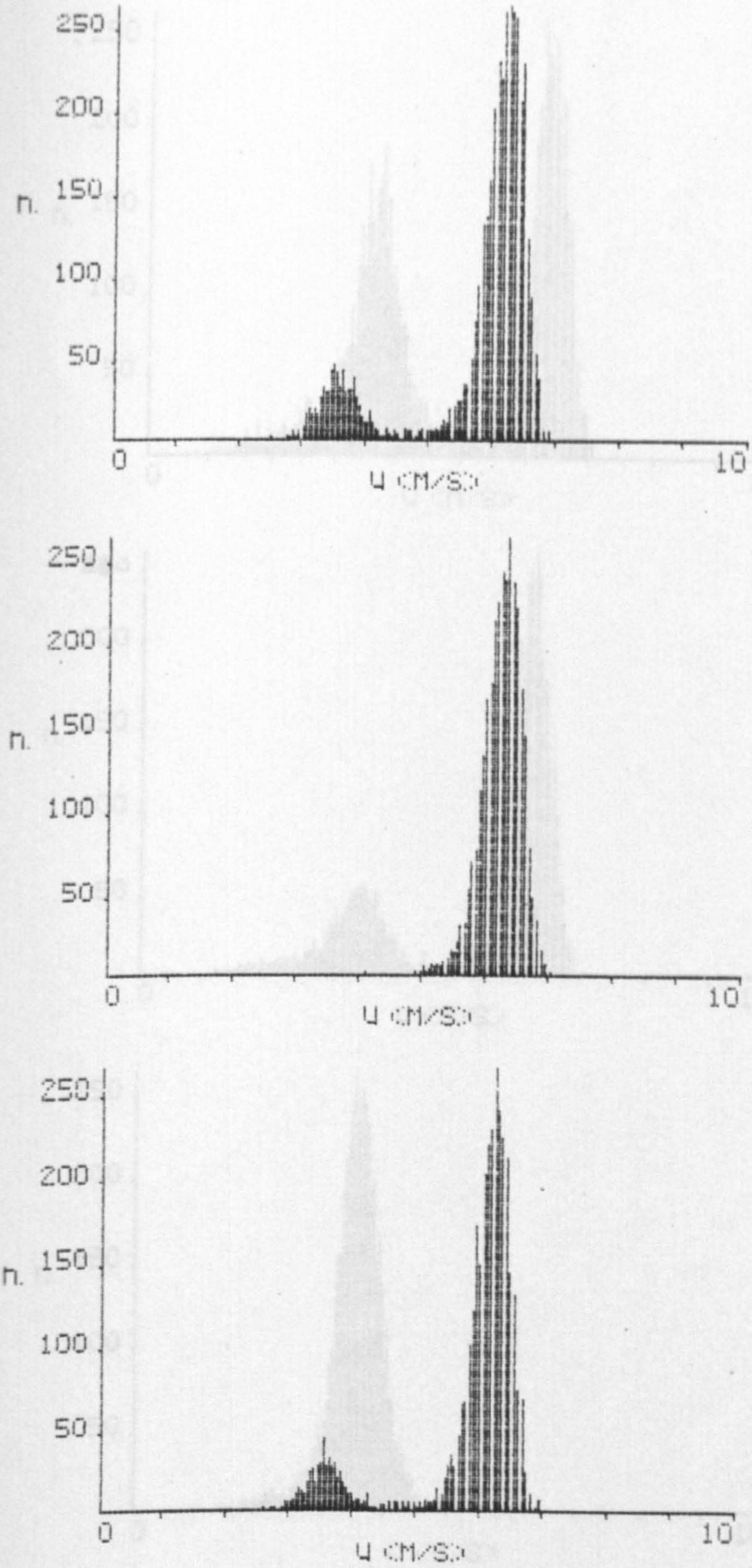

Figure 5.25 Glass ballotini, 210-325 μm and paper smoke; telescope f no = 3.3; pinhole dia = 200 μm; VT_1 = 0.2 V, VT_2 = 0.08 V.

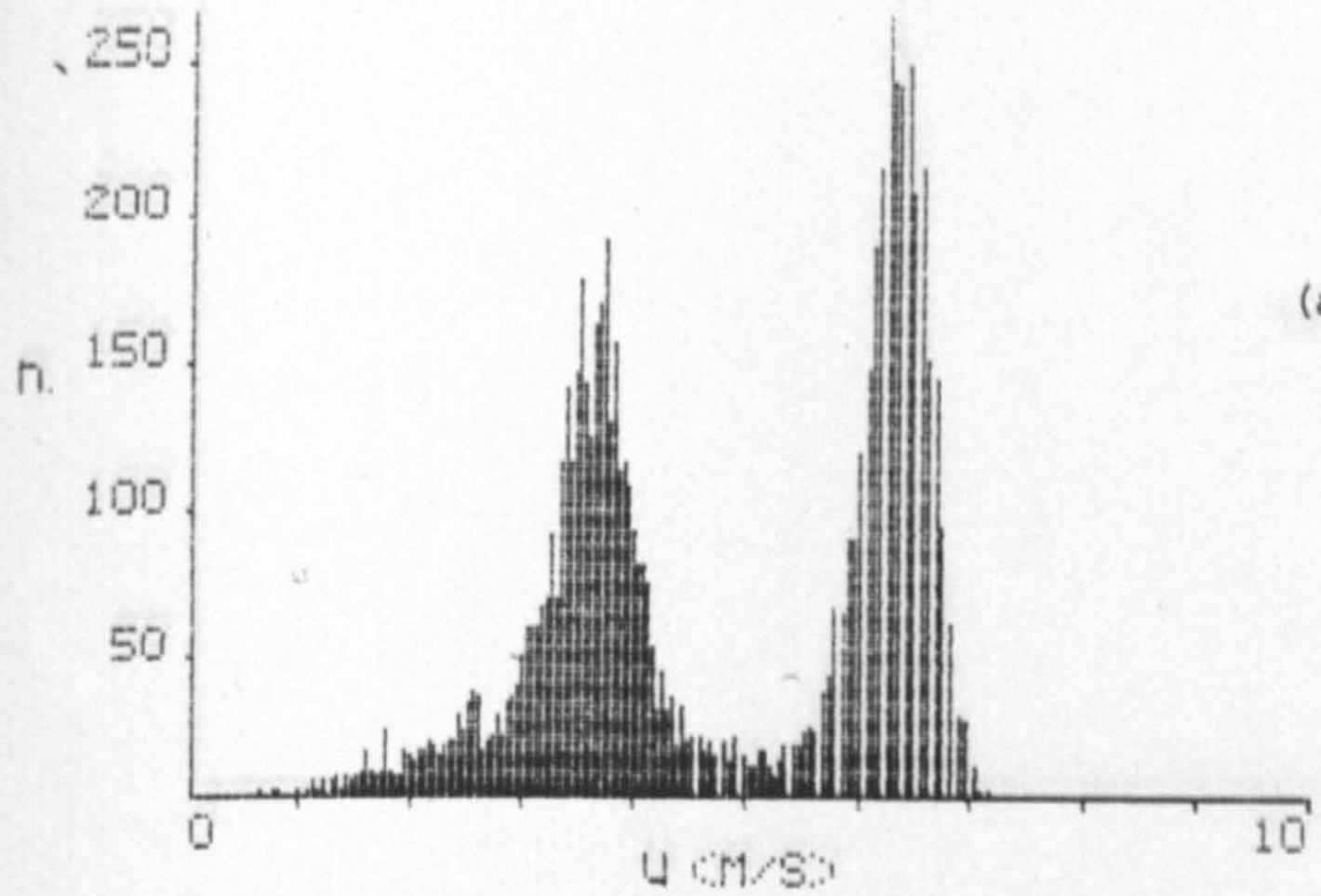

(a) no discrimination

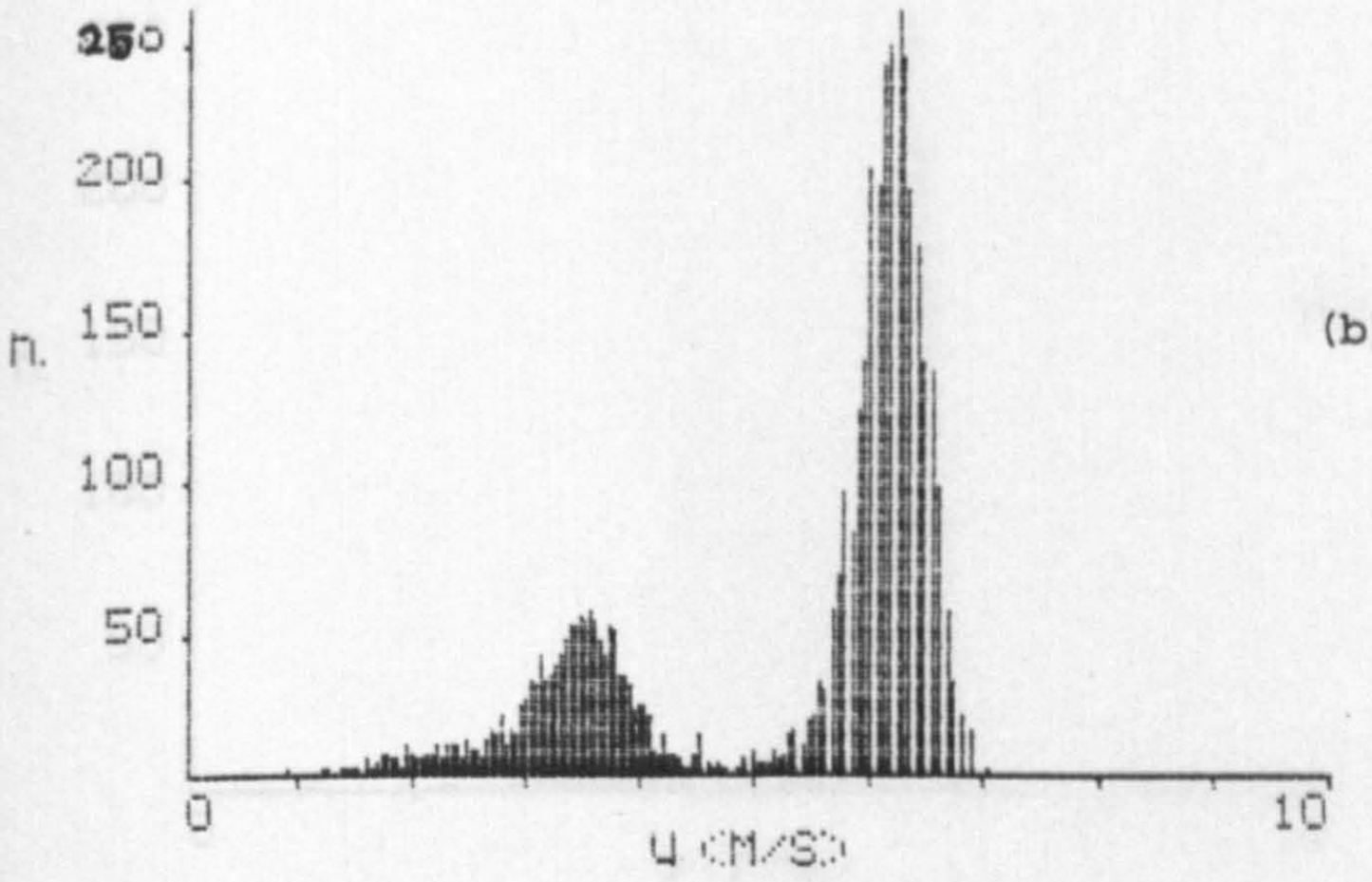

(b) accept small particle signals

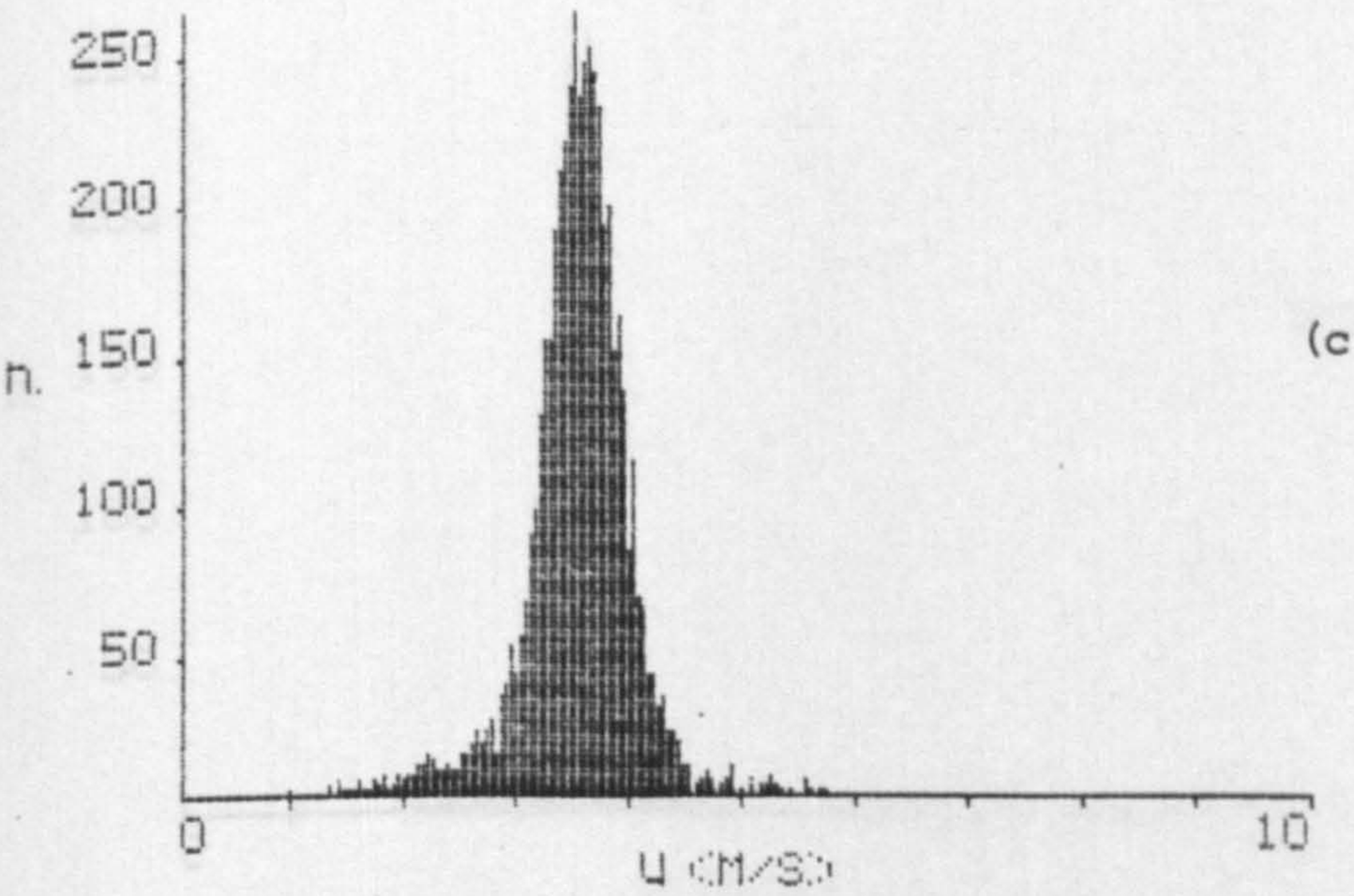

(c) accept large particle signals

Figure 5.26 Glass ballotini, 210-325 μm, and paper smoke; telescope f no = 3.3; pinhole dia = 200 μm; VT_1 = 0.1 V; VT_2 = 0.26 V.

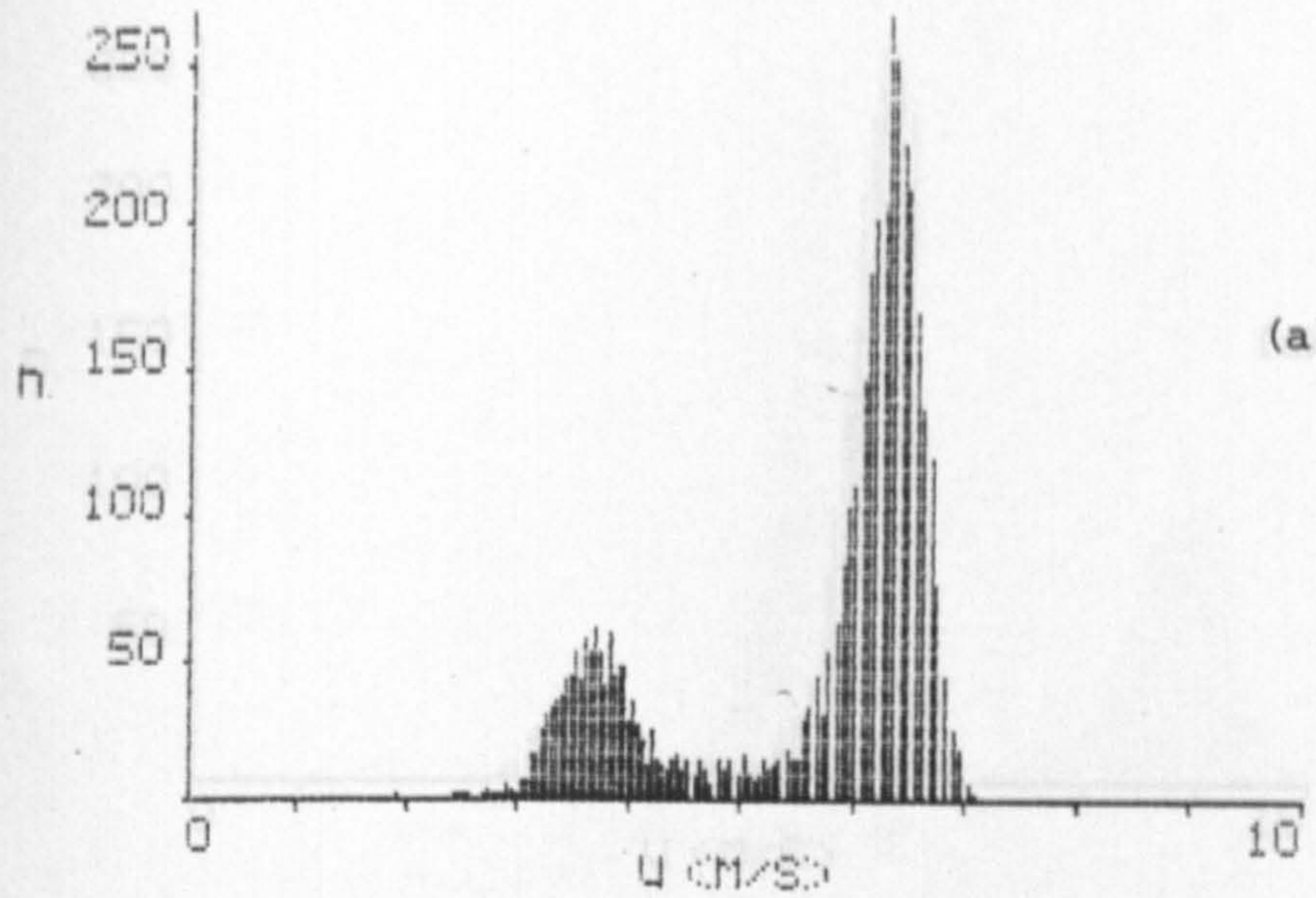

(a) no discrimination

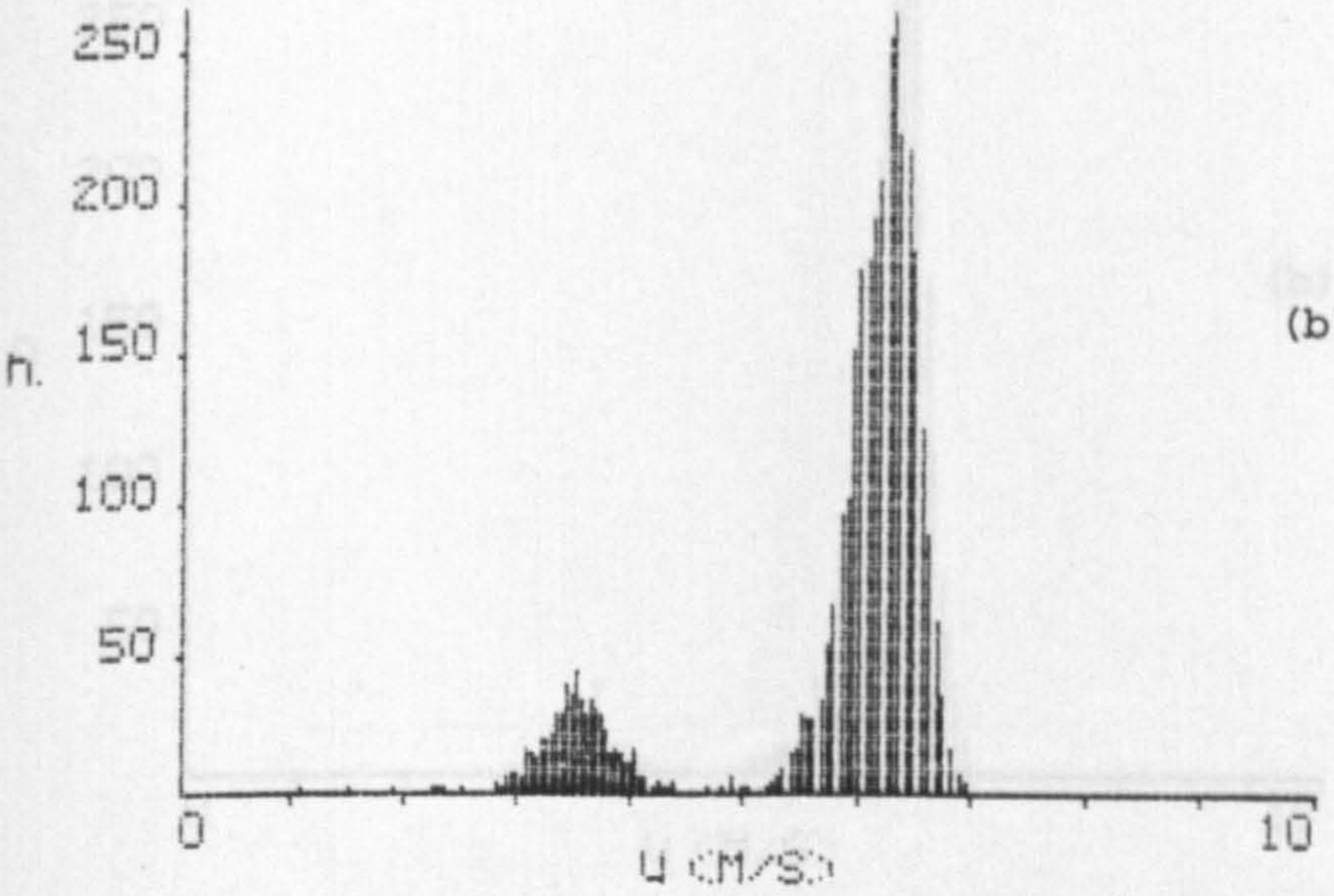

(b) accept small particle signals

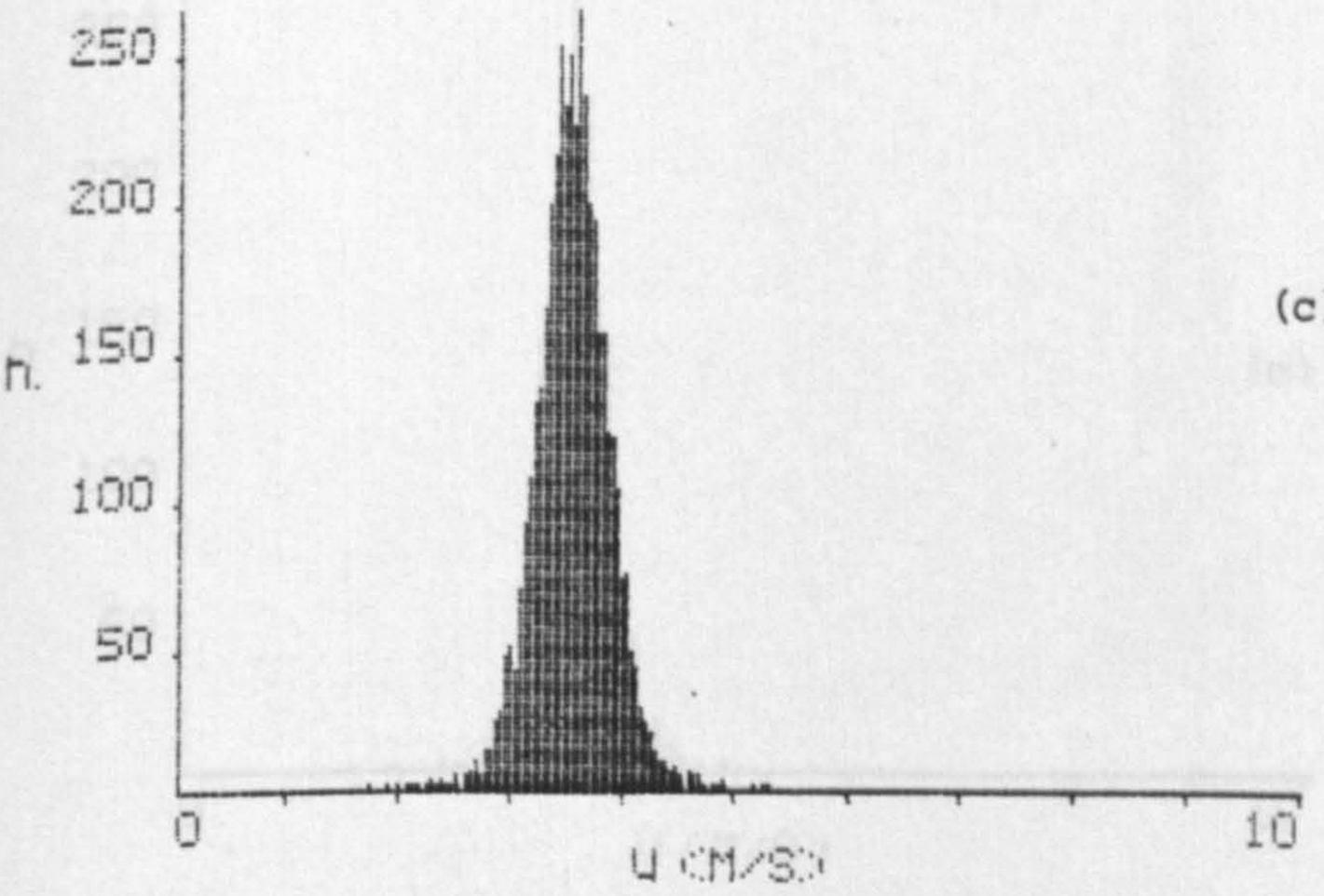

(c) accept large particle signals

Figure 5.27 Glass ballotini, 210-325 μm and paper smoke; telescope f no = 3.3; pinhole dia = 200 μm; VT_1 = 0.14 V; VT_2 = 0.26 V.

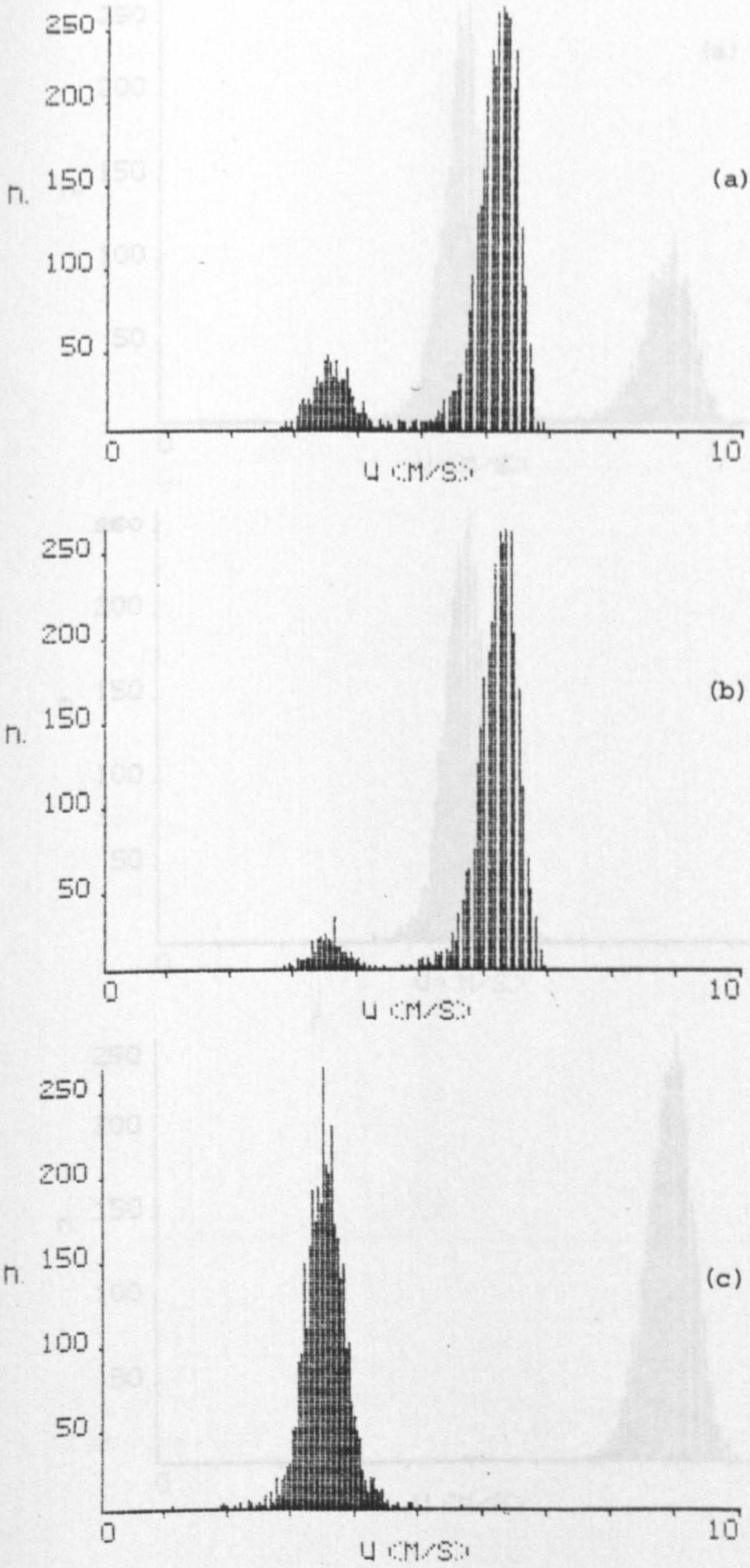

(a) no discrimination

(b) accept small particle signals

(c) accept large particle signals

Figure 5.28 Glass ballotini, 210-325 μm and paper smoke; telescope f_{no} = 3.3; pinhole dia = 200 μm; VT_1 = 0.2 V; VT_2 = 0.26 V.

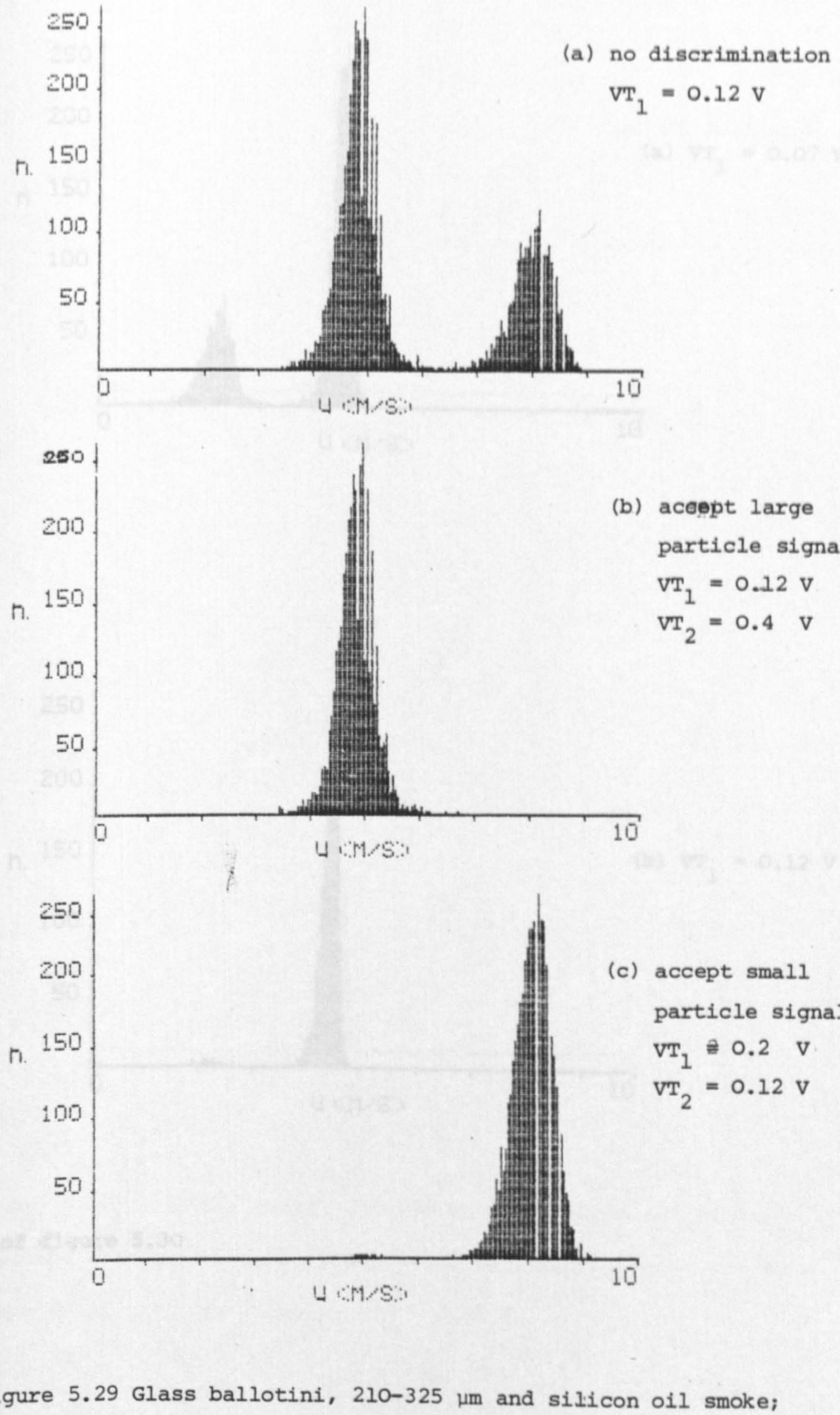

Figure 5.29 Glass ballotini, 210-325 μm and silicon oil smoke; telescope f no = 6.7; pinhole dia = 100 μm

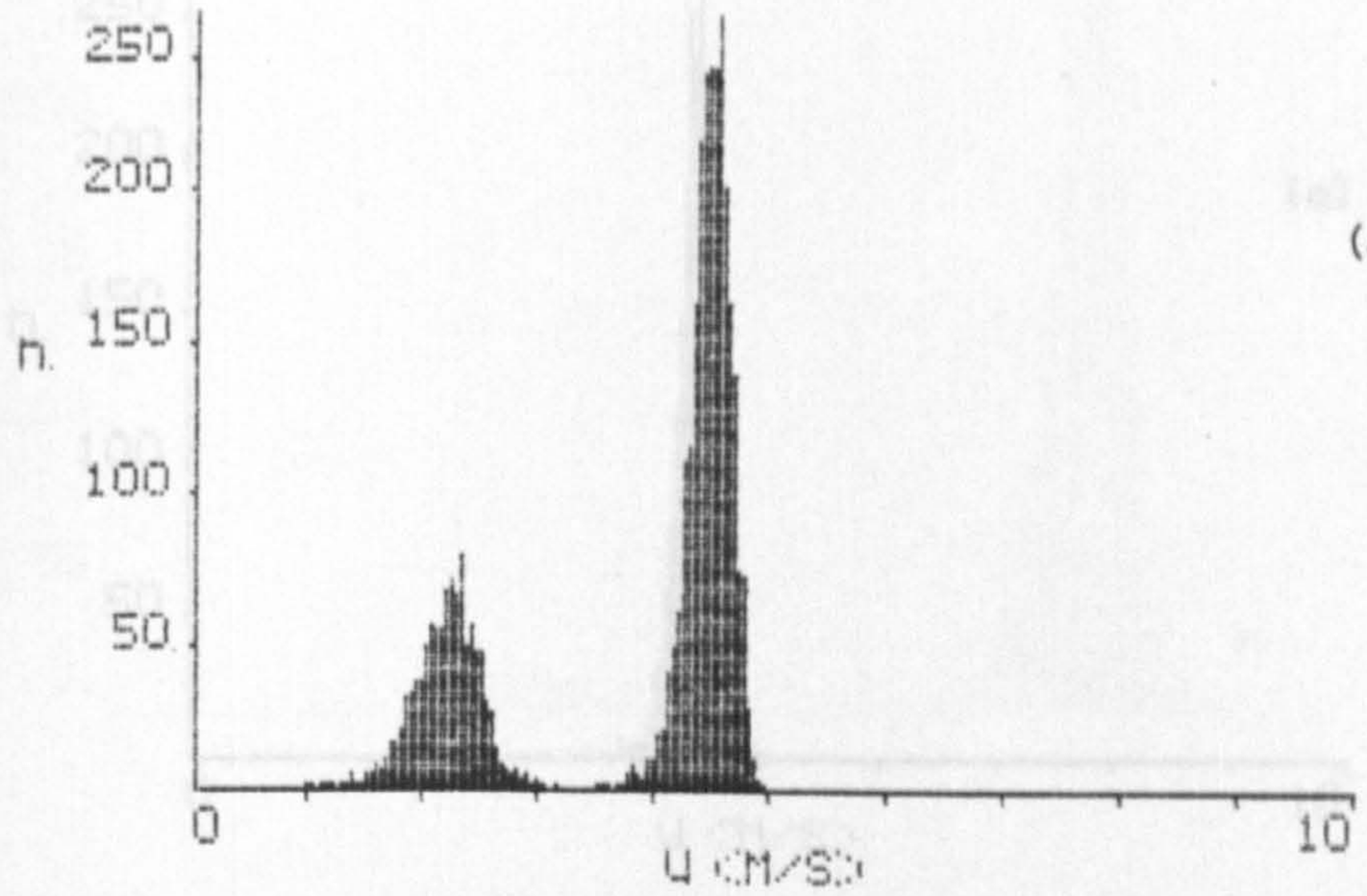

(a) VT_1 = 0.07 v

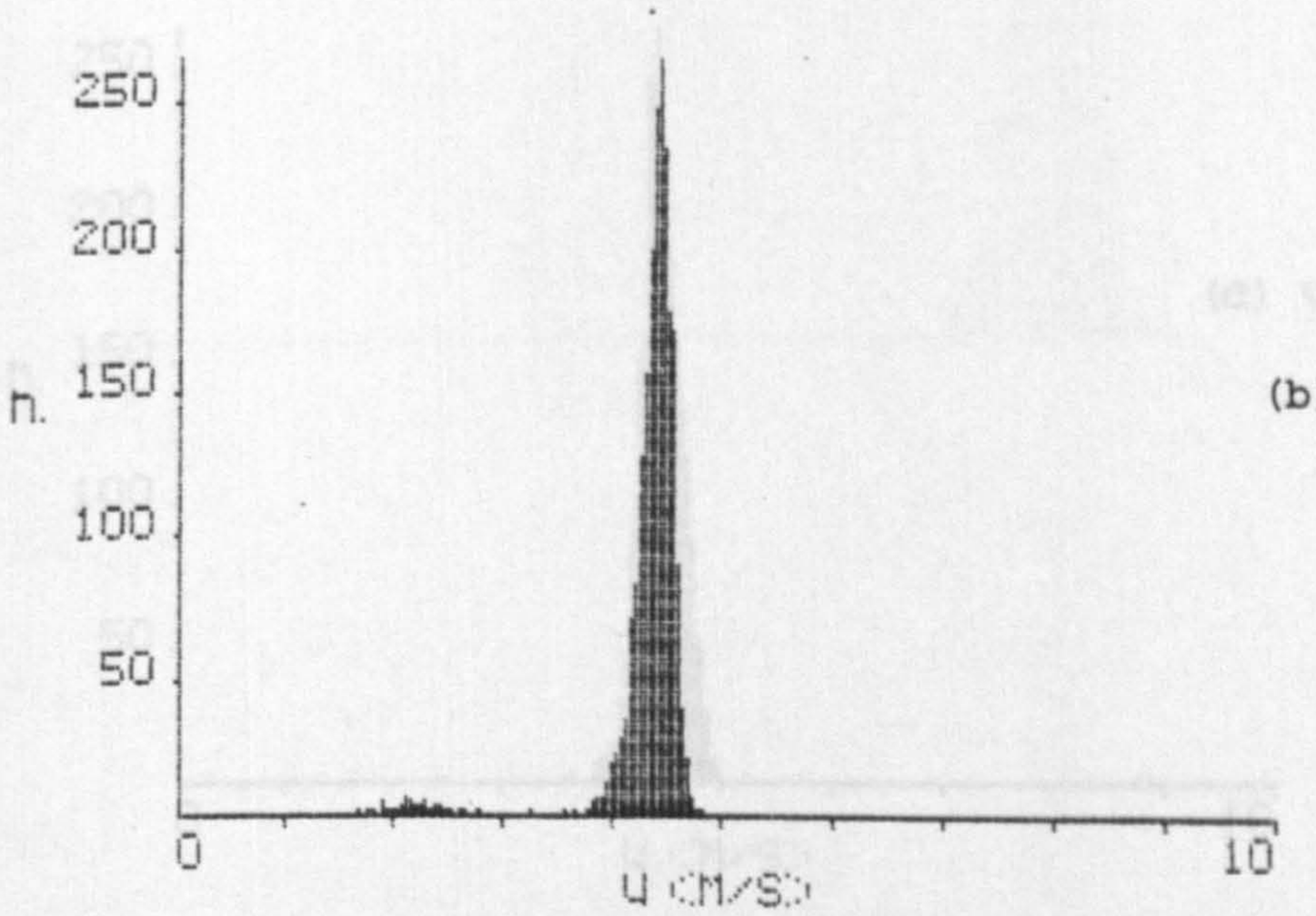

(b) VT_1 = 0.12 v

Part of figure 5.30

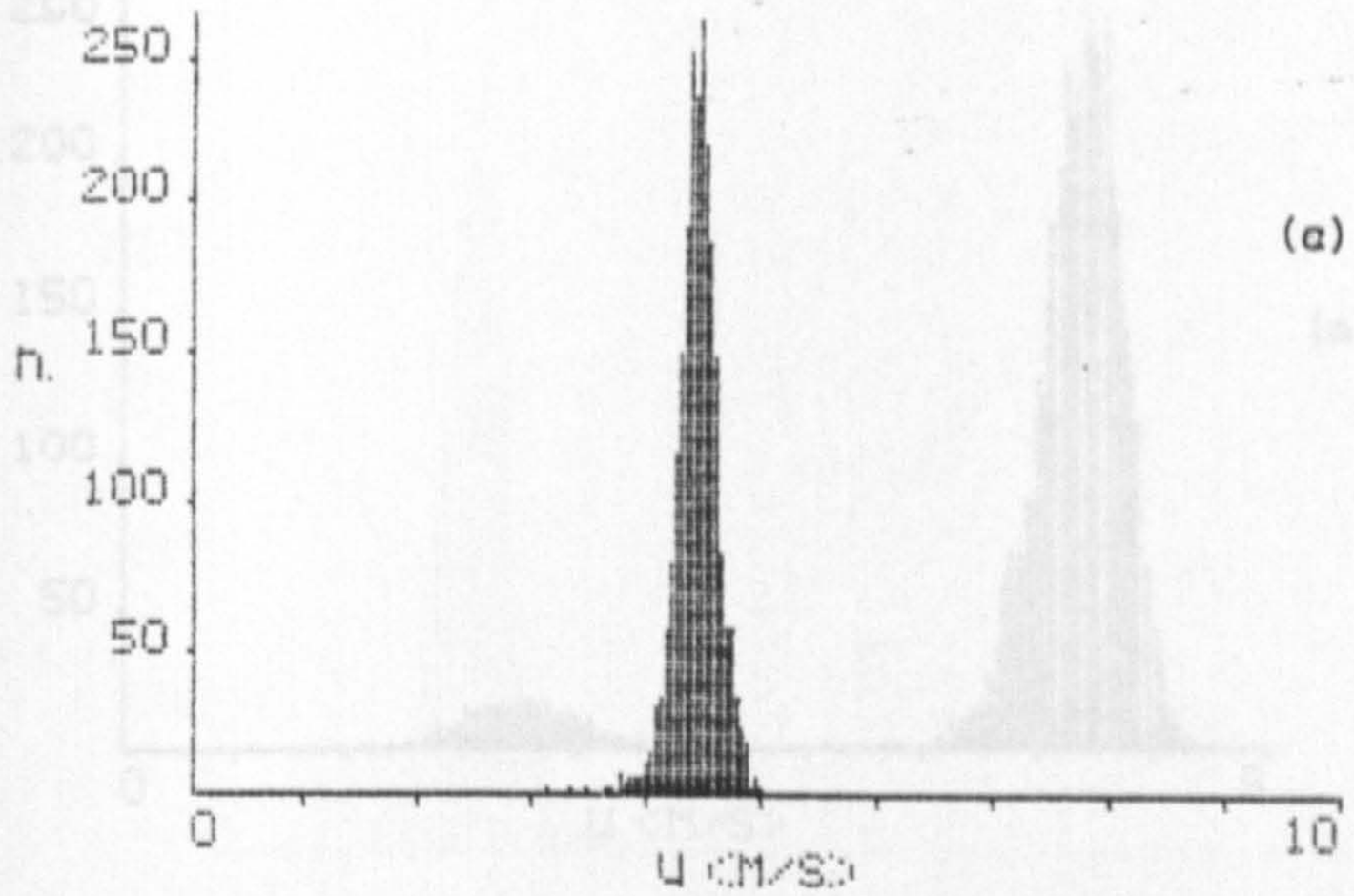

(a) VT_1 = 0.15 V

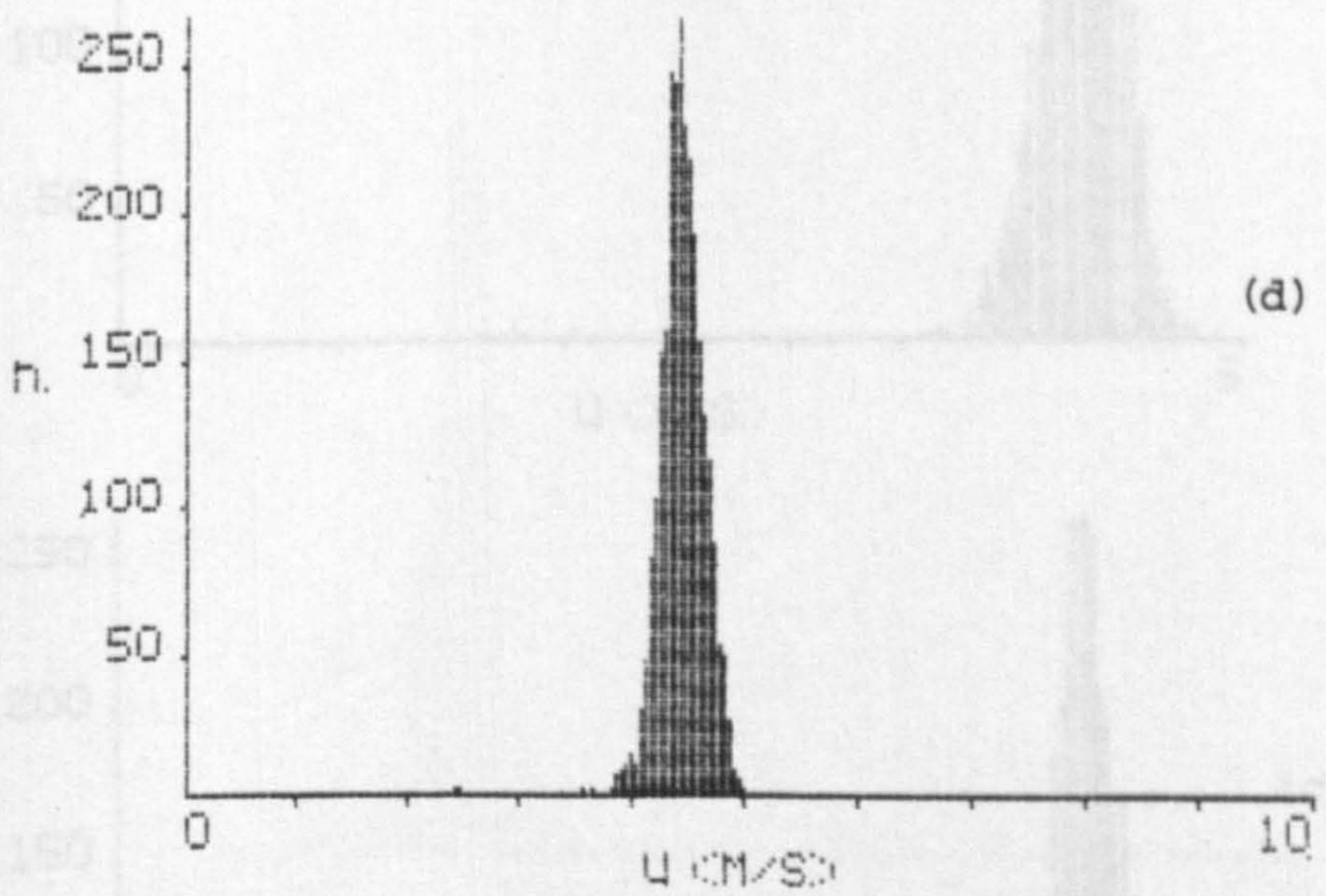

(d) VT_1 = 0.2 V

Figure 5.30 Glass ballotini, 210-235 μm and silicon oil smoke; telescope f/no = 6.7; pinhole dia = 100 μm; discriminator set to accept small particle signals; VT_2 = 0.08 V

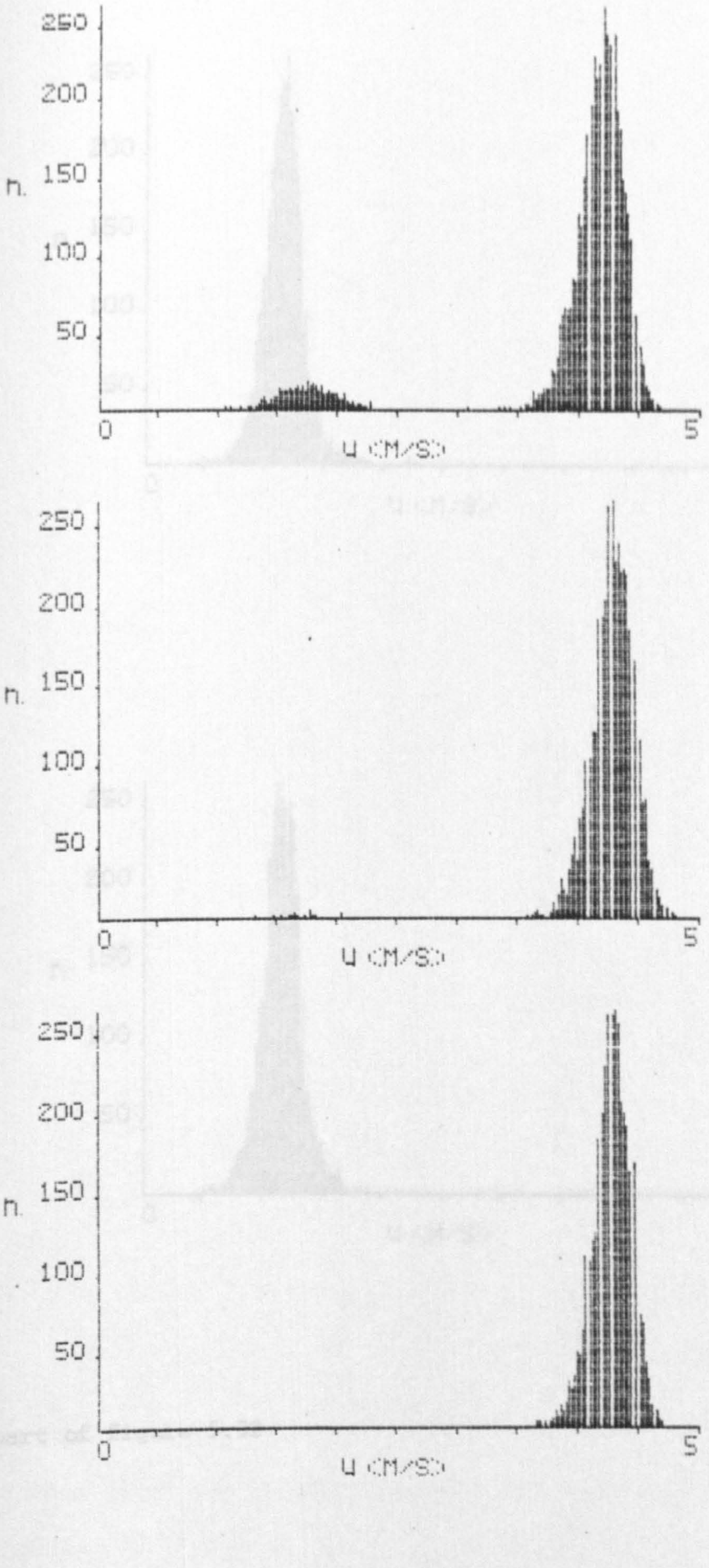

Figure 5.31 Glass ballotini, 210-325 μm and silicon oil smoke; telescope f no = 6.7; pinhole dia = 100 μm; discriminator set to accept small particle signals; VT_2 = 0.1 V.

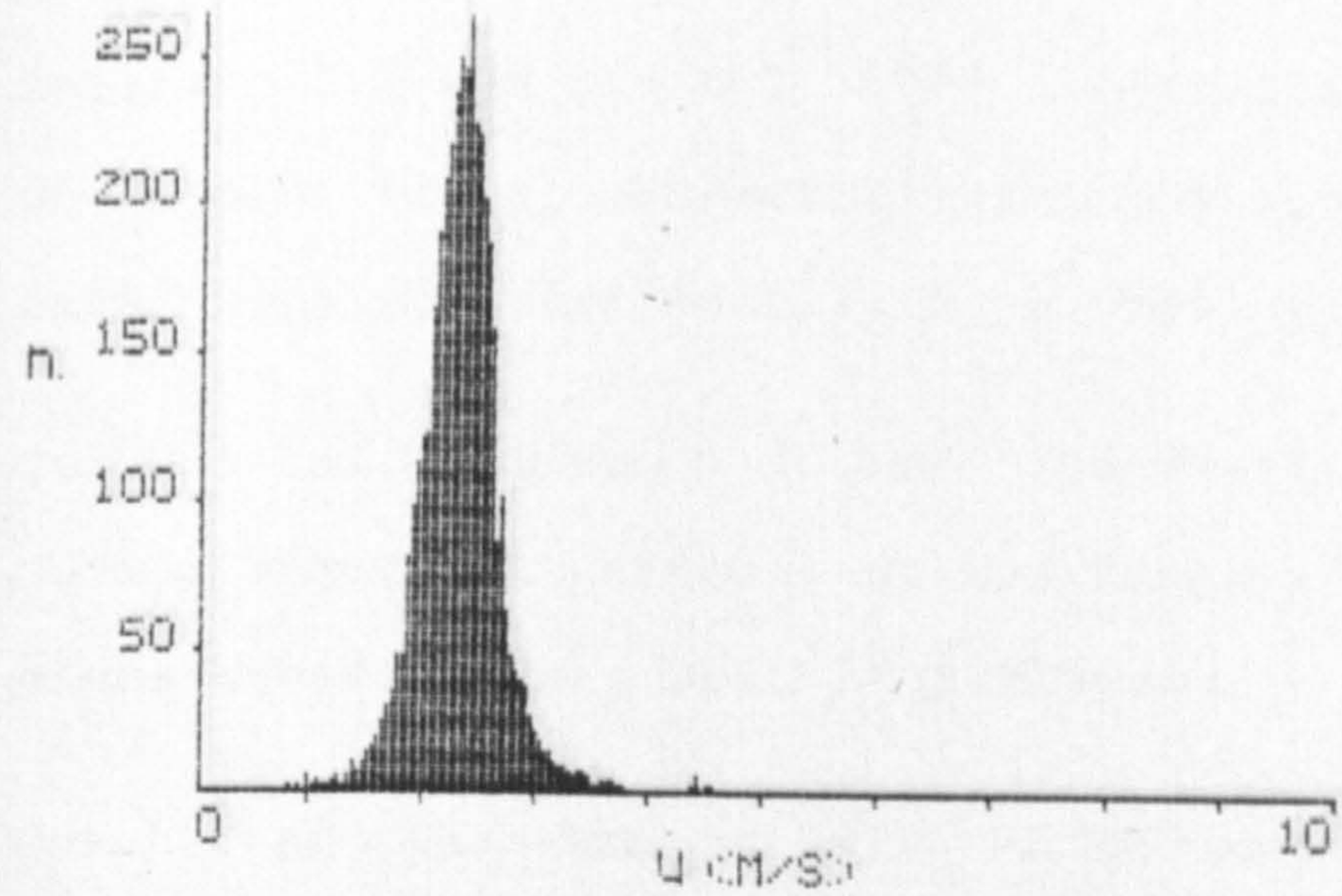

(a) no seeding

VT_2 = 0.2 V

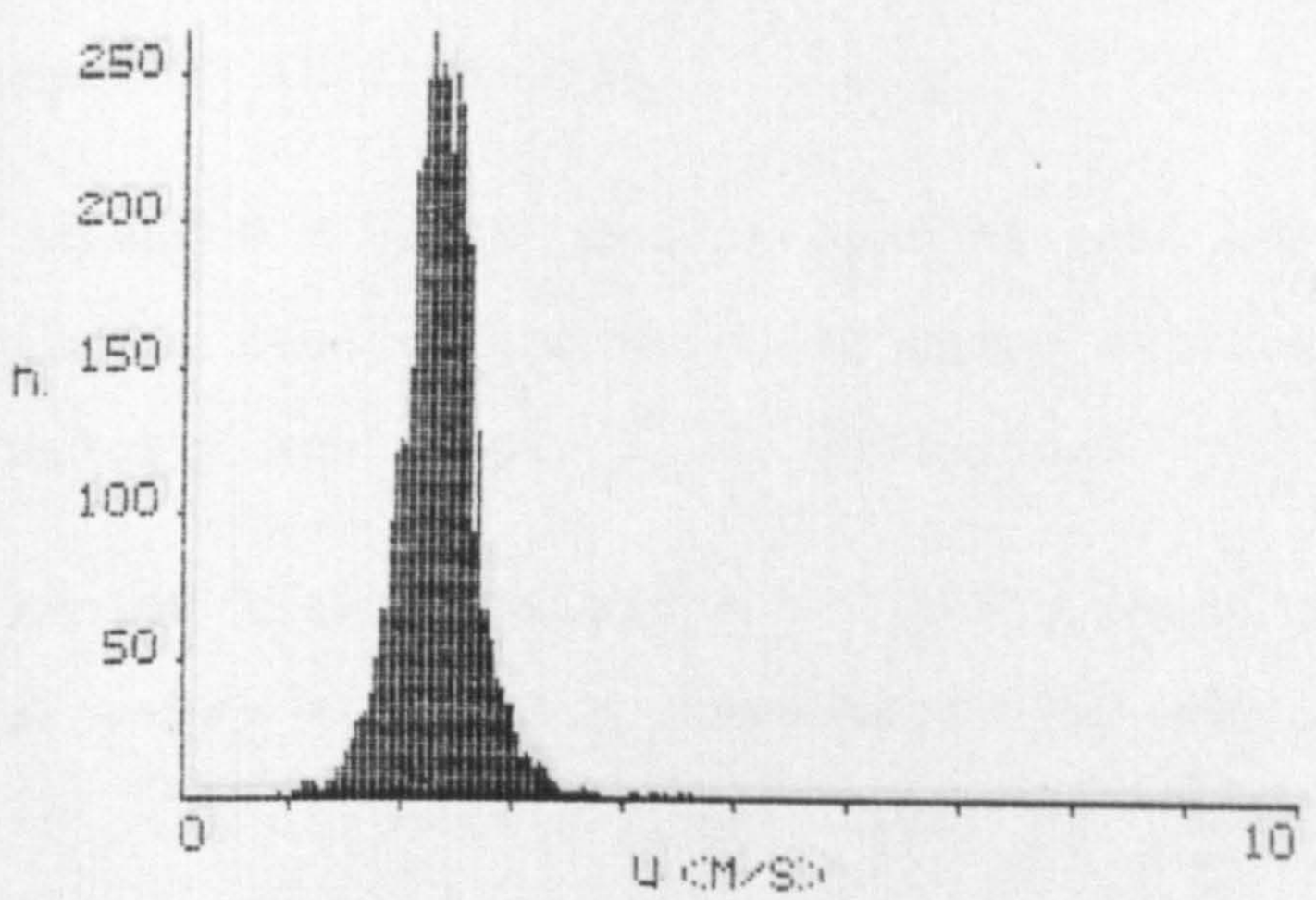

(b) seeded with tobacco smoke

VT_2 = 0.2 V

part of figure 5.32

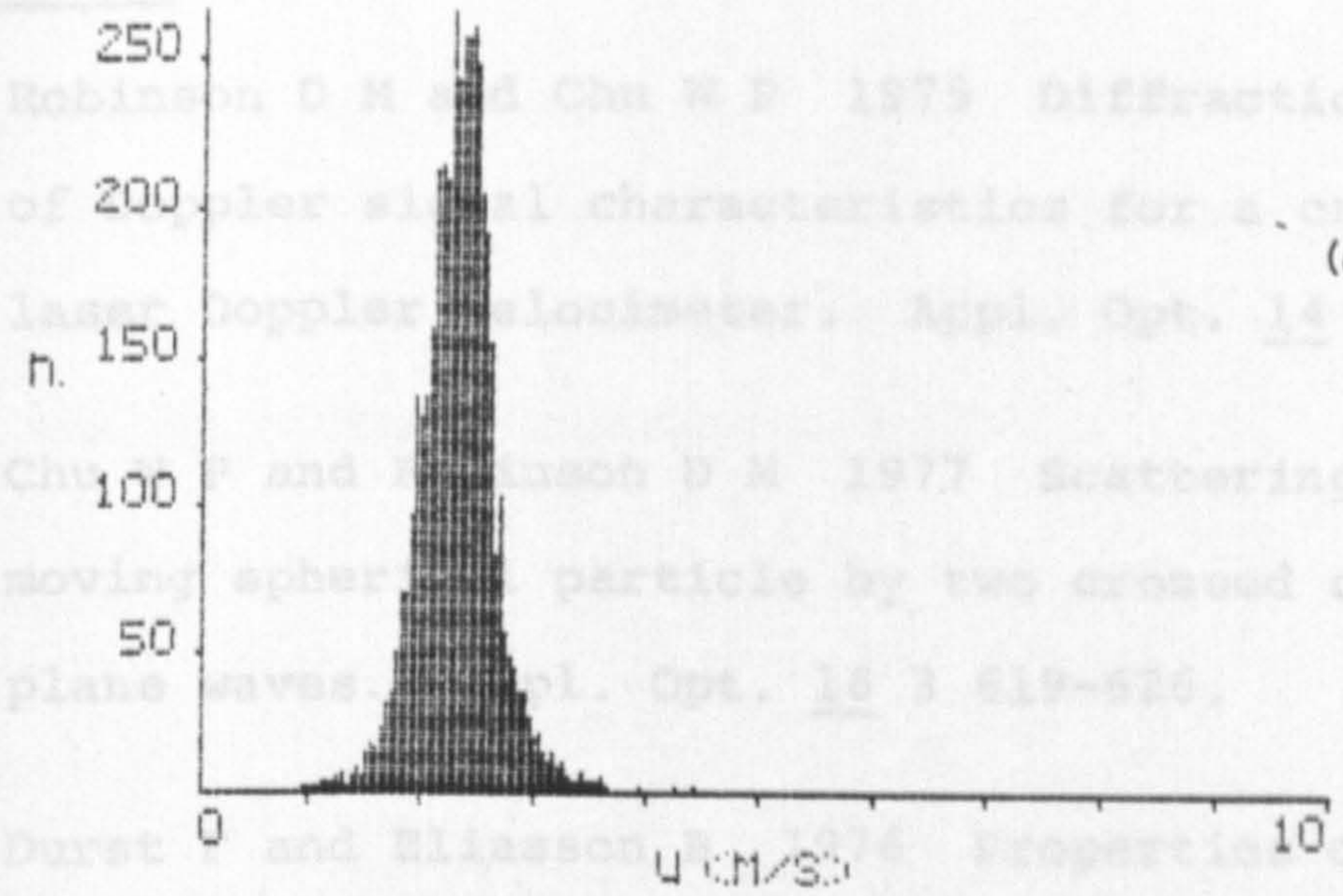

(a) no seeding

VT_2 = 0.4 V

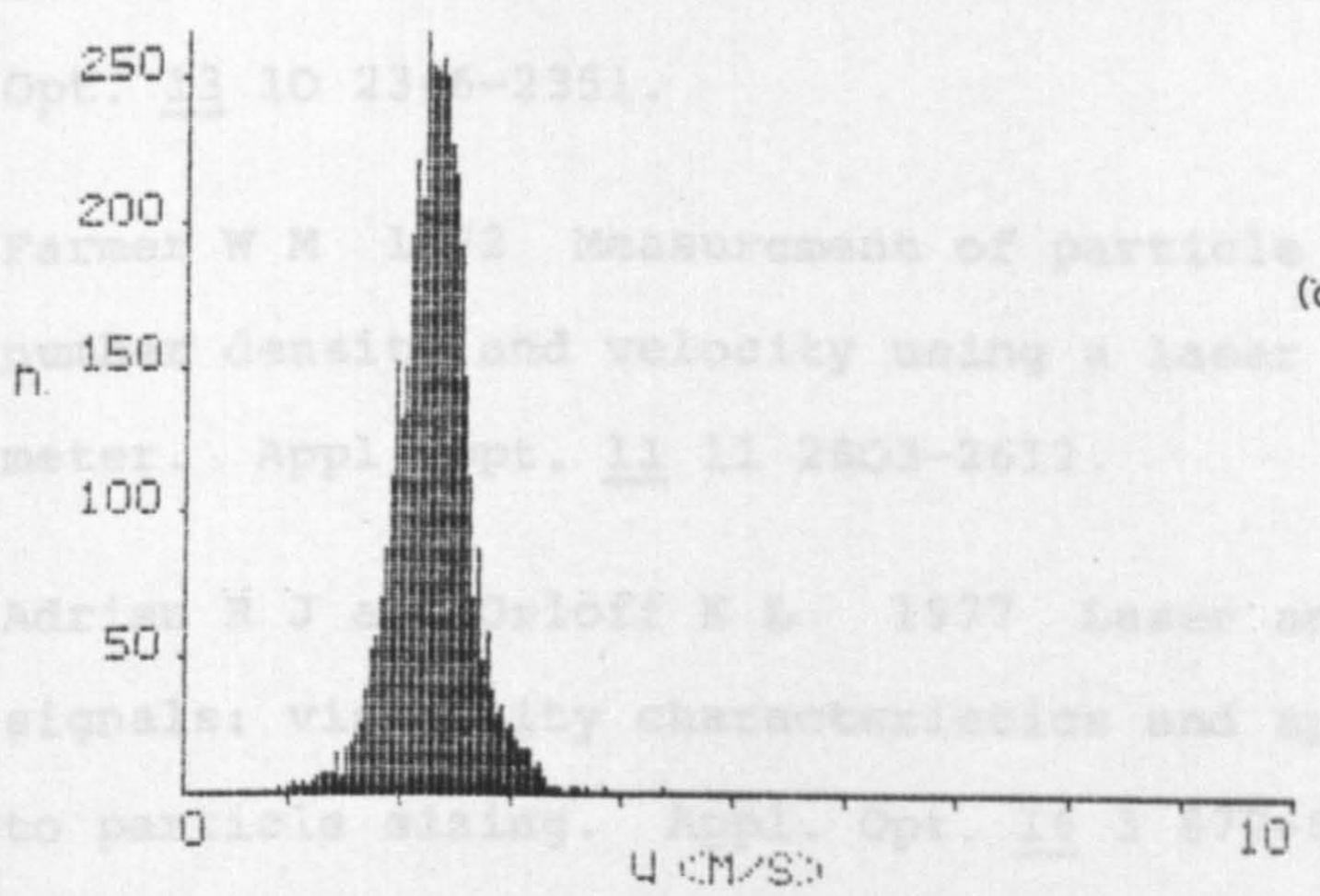

(d) seeded with tobacco smoke

VT_2 = 0.4 V

Figure 5.32 Glass ballotini, 210-325 μm; telescope f no = 6.7; pinhole dia = 100 μm; discriminator set to accept large particle signals; VT_1 = 0.05 V

REFERENCES

[1] Robinson D M and Chu W P 1975 Diffraction analysis of Doppler signal characteristics for a cross-beam laser Doppler velocimeter. Appl. Opt. 14 9 2177-2183.

[2] Chu W P and Robinson D M 1977 Scattering from a moving spherical particle by two crossed coherent plane waves. Appl. Opt. 16 3 619-626.

[3] Durst F and Eliasson B 1976 Properties of laser Doppler signals and their exploitation for particle size measurements, Universität Karlsruhe.

[4] Brayton D B 1974 Small particle signal characteristics of a dual-scatter laser velocimeter. Appl. Opt. 13 10 2346-2351.

[5] Farmer W M 1972 Measurement of particle size, number density and velocity using a laser interferometer. Appl. Opt. 11 11 2603-2612.

[6] Adrian R J and Orloff K L 1977 Laser anemometer signals: visibility characteristics and application to particle sizing. Appl. Opt. 16 3 677-684.

[7] Blake K A and Jespersen K I 19 The NEL laser velocimeter. Dept. of Trade and Industry, National Engineering Laboratory Report No 510, May 1972

[8] Farmer M W 1978 Measurement of particle size and concentrations using LDV techniques. Proc. Dynamic

Flow Conference 373-396.

[9] Lading L and Edwards R V 1975 The effect of measurement volume on laser Doppler anemometer measurements as measured on simulated signals. Proc. LDA Symposium, Copenhagen 64-80.

CHAPTER 6

VELOCITY MEASUREMENTS IN GAS-SOLID SUSPENSION FLOWS

6.1 INTRODUCTION

It was shown in chapter 5 that the "discriminating" circuits which were developed, made possible the separation of signals produced by particles whose diameter was smaller than the fringe spacing, from those produced by larger solids. Particles such as the former, whose size is approximately 1 micron and which, under normal circumstances will follow the air flow everywhere [1], are used as seeding particles and as such they represent the carrier fluid.

Following the development of discrimination techniques, velocity measurements in gas-solid suspensions were carried out, with the object of studying the flow characteristics of the two phases and investigating the influence of the presence of solids on the air flow.

The solids used ranged from 40 μm to 1 mm in diameter and consisted mainly of glass ballotini beads of spherical shape. Brown fused alumina of irregular shape was also used.

All the measurements were carried out in upward flow in vertical circular pipes. Glass pipes of inside diameter 22, 25.8 and 31.4 mm were used. The pipe Reynold's numbers varied from approximately 5000 to 31,000.

The aim was to obtain results from fully developed flows. Thus, a straight length of 50 to 60 diameters was allowed upstream of the working section. Positioning of the instruments high above the laboratory floor was not

considered practical. Due to this limitation, only small bore pipes could be used, although larger diameters would have been more advantageous in studying the flow close to the pipe wall. Large diameter pipes produce less distortion of the incident beams, since the curvature of the walls is less than that of small diameter pipes. Also the ratio of a given wall distance to the various flow scales is smaller in thecase of a large bore pipe than a small bore one.

The results presented in this chapter were obtained using the open type flow rig (see section 4.5.4), as it offered the advantage of continuous operation with a small amount of recirculated solids, whose flowrate was precisely metered.

The experiments can be divided into two categories:

(i) velocity profiles across the flowpipe were obtained for each phase of the suspension

(ii) Centreline velocity measurements were carried out for a variety of flow conditions.

Velocity measurements for the air and the solids were thus taken consecutively, with the flow conditions maintained the same. Simultaneous measurements were not possible as this would have required duplication of the signal processing instruments.

Seeding of the flow with small scatterers, which would follow the air flow, was achieved by using smoke (micron size particles), produced by either vaporising silicon oil or by burning tobacco and paper. Fine silicon carbide powder

(1.5 μm diameter) was also used. In many instances, no artificial seeding was employed and the dust particles present in the air were utilised. In those cases, of course, the data arrival rate was slower.

The duration of some of the experiments was rather long, since many thousands of results were recorded at each point. The microprocessor data recording system stored the measurements in histogram form and released them to the on line computer, after 255 measurements had accumulated in one histogram bar. This meant that in cases when the data arrival rate was slow, or the velocity spread was large, a long time elapsed before a set of results was completed. As the prototype electronic circuity did not include a facility for manually terminating a measurement cycle, this was achieved, when necessary, by feeding into the Doppler frequency meter a modulated sinusoidal signal from a signal generator. The single frequency of that signal, which was set well outside the range of the measured Doppler frequencies, was then excluded from the calculations, by using a modified version of the computer programme, which processed only those results contained within specified limits.

Electrostatic forces presented a problem mainly with the solids supply system, which was initially made of perspex and clear pvc tubes. Since the solids were gravity fed, flow was often interrupted, as the solids were attracted to the tube walls. The pvc tube was changed to an earthed

copper pipe. This almost completely eliminated electrostatic effects.

6.2 EXPERIMENTAL PROCEDURE

The laser was switched on approximately one hour before the commencement of the experiments, to allow its power output to become stable. The rest of the instruments needed no settling period. The air blower was started 15 to 20 minutes before measurements were taken, so that the air temperature reached a steady state.

The solids were initially fed into the system; their flowrate was determined by the size of the solids feed orifice. The air flowrate was set by varying the voltage supply to the a.c. blower motor and observing the pressure drop across the orifice on the micromanometer.

The solids loading ratio, defined as the ratio of the mass flowrate of the solids to the mass flowrate of the air was thus dependent on the size of the solids feed tip and the blower speed setting.

The position of the measuring probe in the flowpipe was determined by observing the beam spots on the inner pipe walls focused by the telescope on the pinhole plate. When the centre of the measuring volume coincided with the inner surface of the pipe wall, the two beams converged to a single spot. The pipe bore was also determined

in this manner.

The two incident beams were made to lie on a plane parallel to the pipe axis and passing through the pipe centre, by observing the reflections from the pipe walls.

The photomultiplier power supply voltage was set at -1000 volts throughout the experiments.

The photomultiplier with a telescope attached to it was carried on a translation stage. Its position was adjusted by means of micrometers in two orthogonal horizontal directions, along the optical axis and at right angles to it. Vertical movement was also possible. Care was taken to ensure proper focusing of the probe volume on the pin-hole by observing the image of the crossover region on the pinhole plate.

The pinhole position could be adjusted in a plane normal to the incident light by means of two screws.

The aperture of the telescope objective was varied by means of a diaphragm. Although small apertures normally reduce noise in the signals, it was necessary, for reasons explained in chapter 5, to maintain as wide an aperture as possible without excessive noise. The setting of the collecting optics was checked by observing the quality of the signals on an oscilloscope screen.

The range of signal frequencies for a particular flow speed was first estimated by observing the photomultiplier

signals on an oscilloscope. A wide filter band was set and a few results were recorded and displayed in histogram form. The filters were then adjusted until optimum setting was obtained. Frequency shifting was also added when necessary, so that the frequency spectrum was contained within the filter pass band. When moving from the centreline towards the wall, the filters were readjusted to match the signal frequency changes and minimize noise.

Two wide band amplifiers were used to amplify the signal, each normally set at a gain of 20 dB, although different experimental conditions often dictated different settings. Normally amplification was such that no saturation or distortion of the signals took place. A separate set of filters and amplifiers was used for the low pass filtered signal fed into the discriminator.

The a.c. and d.c. signal components were both displayed on an oscilloscope together with the corresponding threshold voltages VT_1 and VT_2. Normally the amplitudes of those two signal components were made less than the maximum threshold values. As the signal amplitudes depended on the particular experimental conditions, no fixed values could be assigned to them, and the threshold settings were broadly defined as 'high' or 'low' relative to the signal amplitudes. Often, when starting a new set of experiments, adjustments were made on VT_1 and VT_2 until the effective-

ness of the discriminator was satisfactory. In doing this, consideration was given to the often conflicting requirement of short time duration of each test.

Normally three sets of results were taken at each point in the flowing suspension, one without discrimination, one for small and one for large particles. In some cases, in order to save time, results without discrimination were not recorded. Switching of the discriminator as well as resetting of the threshold voltages was done manually.

After the end of a set of measurements in a particular suspension, the solids were taken out and a velocity profile of the air alone was recorded by seeding the air with smoke. To maintain comparable conditions between such pairs of tests the same pressure drop across the orifice was maintained (see appendix A1). This gave approximately the same air mass flowrate in both cases, since an increased back pressure due to the addition of solids was invariably accompanied by an increase in air temperature; the two effects counteracted one another and the air density was not significantly altered.

Traversing across the pipe was achieved by means of high precision translation stages, on which the whole optical system was mounted.

The average duration of each test was 5 to 10 minutes, except near the wall where longer times were necessary. While new data were being collected by the data

acquisition system, the online 'Apple' computer stored the previous set of results on disc, performed statistical calculations and displayed velocity histograms on a VDU. In this manner the results were continuously monitored and corrective action could be taken, if necessary. Use of a shorter computer program which only stored results on disc for later analysis, was limited to a few cases of measurements in air alone, where the data arrival rate was high.

For each set of results the following information was recorded:

Type of solids and orifice size.

Manometer reading.

Type of seeding used, if any.

Ambient air temperature.

Air temperature at the orifice.

Air temperature of the working section.

Doppler meter settings (Range, cycles).

Frequency shift.

Threshold voltage settings (VT_1 and VT_2)

Filter settings.

A hard copy of the results and the calculated flow statistics - corrected and uncorrected - was obtained for every measurement point in the flow. Only the corrected results were subsequently used for analysis.

In most cases, readings were taken across half the pipe -

from the wall to the centreline. Some traverses were carried out along the pipe diameter and they indicated that the flow was axisymmetric.

6.3 RESULTS AND COMMENTS

Before examining in detail the experimental results, it may be appropriate at this point to consider the physical interactions between the carrier fluid - in this case air - and the solids, in an upward gas-solid suspension flow in a vertical pipe.

The main parameters which may be considered in this type of flow, are the particle concentration, the size of the particles relative to the scale of turbulence and the solids mass density.

The sphere of influence of these parameters may be assumed to contain:

Velocities of both phases and their relative (slip) velocity

Air turbulence.

Particle turbulence.

(a) Slip velocity

Due to the flow being in the upward direction a finite slip takes place between the particles and the air. If the flow is fully developed, this slip is directly related to the particle weight. Consequently one would expect increased slip for increased particle size, for a given

particle mass density. For solids whose mass density is much greater than that of the fluid, buoyancy forces can be neglected. The drag force is then approximately equal to the particle weight. In addition, in an accelerating flow, the particle inertia will contribute to the slip. An increase in particle concentration will lead to more particle-particle collisions with a consequent probable loss of particle momentum. This in turn should result in an increase of slip velocity.

In pipe flow the fluid velocity decreases from a maximum value at the centreline to zero at the wall. The velocity profile of the solids should be similar to that of the air with the exception at the wall where a finite average velocity would be expected. Even small solid particles in contact with the pipe wall extend some distance from it, so that one cannot, strictly speaking, assign the term "at the wall" to them. Solids at that position may exchange energy with the air and with other particles with which they collide and thus maintain a velocity greater than zero. particles approaching the wall with a significant axial velocity component would also have a finite velocity at the instant of impact with the wall.

From the above, it follows that the velocity profiles of the air and of the particulate phase will cross, giving rise to negative slip in the near wall region. One would expect a 'flatter' solids velocity profile with greater slip as the

size of the particles increases, due to the higher inertia of the large particles and the consequent reduction of influence of the air. The width of the negative slip region should thus reduce with increasing particle size.

(b) Air turbulence

The level of turbulence of both the gas and the particulate phase in a gas-solid suspension flow may be influenced by the size of the particulates in relation to the eddy size. In an upward flow where considerable slip between the solids and the air takes place, heavy particles act like screens and thus they might enhance turbulence. In particular they might increase the transverse component of the turbulence intensity, due to the wake formed behind each particle. On the other hand, by penetrating and breaking up larger eddies they may encourage the cascade of energy towards the smaller scales, promoting dissipation and thus reducing the level of turbulence [2].

Large particles may be more effective in reducing turbulence since they break up larger eddies. Consequently it is rather difficult to accurately predict the effect of the solids on the air turbulence, because of the number of possibly conflicting physical effects, since

(i) by breaking up the eddies they accelerate dissipation which results in the suppression of turbulence shear and turbulence energy. Large particles should be more effective in reducing the turbulence in this way as they will be capable of breaking up larger, high energy

eddies.

(ii) depending on such factors as shape, size and particle Reynold's number the turbulence energy may increase in the wake of the particles. One might expect again that the larger particles are the most important with regards to this effect.

The two effects are additive and the result could either be a net drop or an increase in the turbulence intensity of the conveying fluid.

Increased particle concentration should cause a decrease in particle turbulence (see below). This could lead to a reduction of air turbulence compared to that produced with lower solids loadings, as the turbulent wakes formed behind particles may now be of lower intensity.

Alternatively, one may consider the suspension as a continuum, in which high particle concentrations are analogous to high viscosities. High fluid viscosity would, of course, result in a low level of turbulence.

(c) Particle turbulence

The turbulence of the solids should increase with eddy size, as large eddies would transfer some of their energy to particles whereas the effect of small eddies on particles larger than themselves would be very small. The turbulence of the solids would thus be greater in the centreline region than near the wall, where the scale of turbulence will probably be smaller than the particle diameter.

Two additional factors to be considered here are the variation of air turbulence intensity along the pipe radius and the influence of the wall on particle turbulence.

In turbulent pipe flow, the region of maximum energy production lies near the wall at the edge of the laminar sublayer [3] where the bulk of the viscous dissipation also takes place. There, the various energy rates (production, diffusion and dissipation) reach a sharp maximum.

It thus seems that the turbulence of the solids will be at a relatively high level in the centreline region, it will increase towards the wall due to the increase of air turbulence and would then decrease very close to the wall, but not as sharply as the air turbulence at that point. A damping influence by the wall on the turbulence of the solids would be expected due to particle wall collisions.

Although particles which are small compared with the scale of turbulence are strongly influenced by the gas phase, large particles are not affected as much due to the large inertia which they possess.

High solids concentrations would give rise to increased interactions between the solids. This could result in an increase of the lower velocities and a decrease of the higher velocities of the particles, thus reducing the r.m.s. deviations. At low loading ratios the frequency of collisions between particles would be small compared to that

at higher loadings and as a consequence the value of the r.m.s. velocity would be relatively high.

Summarising the above observations on the mutual influences between the two phases of a gas-solid suspension, it may be reasonable to conclude that probably the strongest air-particle interactions take place when the length scale of the eddies is comparable to the particle diameter.

Rotation of the solids due to impact with the pipe wall or other particles and due to shearing of the surrounding fluid may be of importance. Due to rotation the solids experience transverse forces and they may thus move at right angles to the wall.

Brownian effects can be neglected for relatively large particles, such as the ones used in this work.

Thermophoretic forces, i.e. forces due to temperature gradients in the fluid may be considered to be negligible as no significant temperature gradients existed in the flow.

Electrostatic charging may have some effect on the flow of the solids although this would be difficult to quantify. In this work an effort was made to minimize electrostatic charging. The distribution of the particulates in the flow was assumed uniform, although there is evidence that electrostatic forces might affect this uniformity.

Graphs of the results obtained from the velocity measurements are shown in figures 6.1 to 6.19 and 6.21 to 6.31, at the

end of this section. Further experimental details are listed in the tables in Appendix A6.

Three graphs were plotted for each set of results, using values corrected for biasing errors (see section 3.3.2(e)), i.e.

(i) velocity profiles, U against R, where $U = \bar{u}_c/U_m$ and R = r/a denote nondimensionalised velocity and radial distance respectively.

a denotes pipe radius

r denotes radial distance

$\bar{u}_c$ denotes corrected mean velocity and

U_m denotes the centreline velocity of the air while solids were present.

(ii) r.m.s. velocity, $\sqrt{\overline{u'^2}}$, versus nondimensionalised radius R, where $\sqrt{\overline{u'^2}}$ is the corrected r.m.s. velocity, as defined in section 3.3.2(e).

(iii) turbulence intensity, $(\sqrt{\overline{u'^2}}/u_c) \times 100\%$ versus nondimensionalised radius.

The results consist of velocities of the solids (o), velocities of the air while the solids were being conveyed (•) and velocities of the air alone (x). The dotted lines in the graphs of the velocity profiles are smooth curves joining the points for the air (with solids) and for the solids.

The results shown in figures 6.1 to 6.19 contain groups of readings obtained by varying the loading ratio and keeping

the particle diameter, the air flowrate and the pipe bore constant. Numerical details for these results are shown in table 6.1.

Figures 6.21 to 6.31 show results obtained from a number of particle sizes, corresponding to various solid loading ratios and air flowrates.

It is observed from the above mentioned results that there is a slip between the solids and the air, which increases with increasing particle size as expected. This, for example, is demonstrated by the results shown in figures 6.22, 6.13, 6.16, 6.26 and 6.30, in which the particle diameter increases from an average of 112.5 μm to 805 μm.

The slip velocity of the solids varies across the pipe. In the near-wall region the particle velocity decays at a much slower rate than that of the air. Consequently the velocity profiles of the two phases may cross. This is clearly demonstrated by results obtained close to the pipe wall (see figures 6.9, 6.10, 6.12, 6.22 and 6.26). As mentioned previously, the negative slip region becomes wider as the particle diameter decreases. This, for example, can be observed from the results shown in figures 6.22 and 6.26, which correspond to two very different particle sizes.

In the case of small particles, the velocity profiles cross high up on the velocity scale, where the air profile slopes away from the wall. In the case of large particles the

profiles cross near the wall, where the air velocity gradient is high. The present results are in agreement with those reported by Durst [3].

No real conclusion can be drawn from the results about the effects of particle concentration on slip velocity. Perhaps the main reason for this is that in all the tests relatively dilute suspensions were used and other, smaller effects, including experimental errors, may have overshadowed slip velocity variations. In dilute suspensions the particle-particle interactions are not so important. Consequently, changes in the air turbulence may predominate. As previously mentioned, the air turbulence can be either increased or decreased by the presence of solids. This in turn may affect the relative velocity between the phases in a similar manner.

Results exhibiting such characteristics are shown in figure 6.20, which contains graphs of slip velocity, U_σ and air velocity, U_m, at the pipe axis, against loading ratio. These results, which are grouped according to the pressure drop across the orifice, as indicated by the numbers on the graph, are centreline values extracted from the results shown in figures 6.1 to 6.19. Further experimental details can be found in table 6.1. Although only a small number of points make up the various graphs it is noted that a drop as well as an increase in slip velocity occurred with solids loading. The air velocity at the centreline showed a similar pattern.

The turbulence intensity of the solids is, on average, greater than that of the air. This is the case even when the r.m.s. velocity of the solids is of similar magnitude as that of the air or even smaller. The reason lies in the way turbulence intensity is calculated - i.e. the ratio of r.m.s. velocity to the local mean velocity. Since the solid phase usually has a relatively low local mean velocity, this consequently results in higher turbulence intensity values. For this reason, graphs of both r.m.s. velocity and turbulence intensity have been plotted, so that the absolute values of the fluctuating components as well as their magnitude relative to the local mean velocity can be examined.

The r.m.s. velocity of the solids has been found to be higher than that of the air in the centreline region in all but a few cases (figures 6.25, 6.26, 6.28 and 6.29) in which, as it can be observed, the loading ratio was relatively high. No significant influence on the r.m.s. velocity and turbulence intensity profiles from particle concentration has been observed.

A decrease in the r.m.s. velocity and turbulence intensity of the solids with increasing loading ratio, at the pipe centreline, can be observed from figures 6.17, 6.18, 6.19 and 6.16 for fused alumina, 300-430 μm diameter. A similar trend is exhibited by the results from glass spheres, size 210-325 μm, where a low loading ratio is accompanied by a

relatively high turbulence intensity (e.g. figures 6.8, 6.11 and 6.12) and a higher loading ratio is accompanied by a lower turbulence intensity (e.g. figures 6.7, 6.10, 6.13 and 6.25).

An additional increase in the spread of the velocity spectrum is expected to have been introduced into the results from the fact that the solids were polydisperse i.e. the size distribution covered a finite range about a mean (for size distribution of solids see section 4.6). Such a spread of velocities would have existed even in the case when all particles had only axial velocity components, due to different slip velocities resulting from particles of different weights and giving rise to a range of deviations from the mean. It is thus expected that the value of the r.m.s. velocity in the case of monodisperse solids would have been smaller.

The r.m.s. velocity of the air increases from the centreline towards the wall, as can be observed from figures 6.1 to 6.8, 6.12 to 6.19, 6.21 to 6.23, 6.25 and 6.27 to 6.31; it reaches a peak value near the wall as can be seen from results obtained very close to the wall, shown in figures 6.9 to 6.11, 6.24 and 6.26, and it then drops sharply. Hence the results are in agreement with those reported by Laufer [4]. Similar results have also been reported by, among others, Durst [3] and Zisselmar and Molerus [5]. According to thelatter, an increase of turbulence intensity of the

gas phase in the edge of the viscous sublayer takes place, due to interactions between the two phases as the size of the turbulent eddies becomes of the same order of magnitude as the solids.

This has been verified by the results presented in figures 6.11, 6.13 to 6.16, 6.22, 6.23 and 6.31, although an opposite effect can be observed from the results shown in figures 6.1 to 6.10, 6.12, 6.18, 6.19, 6.21, 6.25, 6.28, 6.29 and 6.30. There is very little or no change in the turbulence intensity of the air caused by the larger solids used, as can be seen from figures 6.26 to 6.31. On the other hand, there is a significant decrease of the turbulence intensity of the air caused by smaller particles, e.g. figures 6.21 and 6.22.

An increase in the level of turbulence of the solids in the direction of decreasing eddy size, i.e. towards the wall, is observed from many of the results. As the eddies become more comparable in size with the solids - this happens at different wall distances for different size particles - a strong interaction takes place between the two phases [5] and as a consequence, some of the turbulence energy of the gas is transferred to the solids. Thus the turbulence of the solids is seen to be increasing up to the near-wall region in the case of glass spheres, size 90-135 μm and 210-325 μm (figures 6.1 to 6.13 and 6.21 to 6.25), whereas in the case of larger solids, i.e. fused alumina, size 300-430 μm (figures 6.14 to 6.19) and glass

spheres, size 440 to 530 and 675-935 μm (figures 6.28 to 6.31) the turbulence intensity levels off and often falls near the pipe wall.

In the majority of cases (figures 6.2 to 6.9, 6.11, 6.14 to 6.21 and 6.27 to 6.31) the velocity of the air (with solids) at the pipe centreline was greater than that of air alone. This would indicate a reduction in the level of air turbulence and as a result, a more parabolic velocity profile. A significant increase of the centreline velocity resulting from narrowing of the effective flow area due to the presence of solids in the flow is ruled out since, as shown in Appendix A1, the ratio volume of air to volume of solids was, on average, in the region 1000:1. Hence the above mentioned increase of the centreline air velocity is probably due to a suppression of the air turbulence, resulting from the addition of solids. An increase of the centreline air velocity in suspension flows has been reported by Reddy and Pei [6].

A decrease in the centreline air velocity with the addition of solids has been observed in the results shown in figures 6.10, 6.12, 6.13 and 6.23. Such a decrease of the centre-line velocity, which results in a flatter velocity profile has been reported by Chandok and Pei [7].

An increase in the centreline air velocity due to the addition of solids would be expected to be accompanied by a drop in the turbulence intensity in the near-wall region.

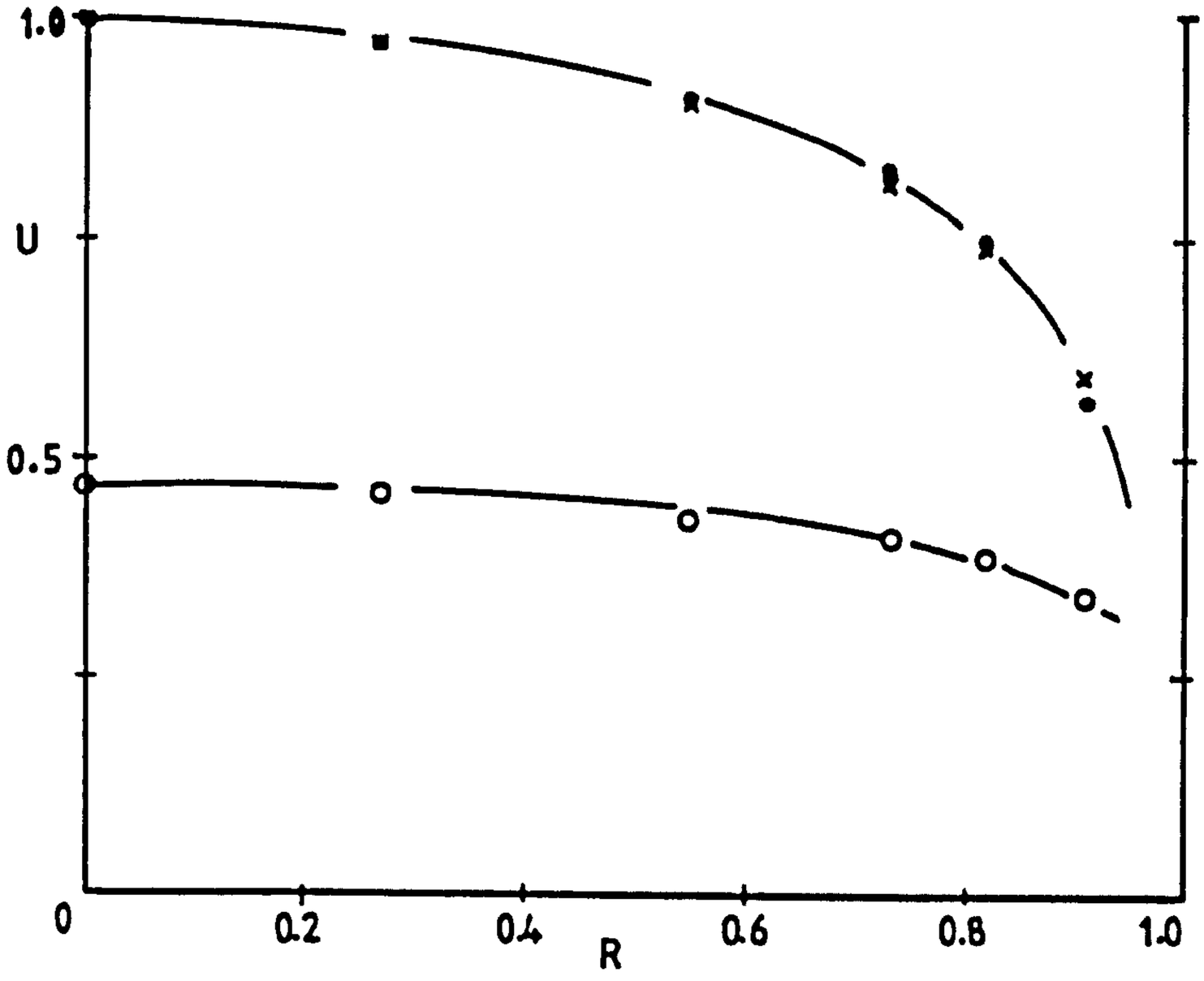

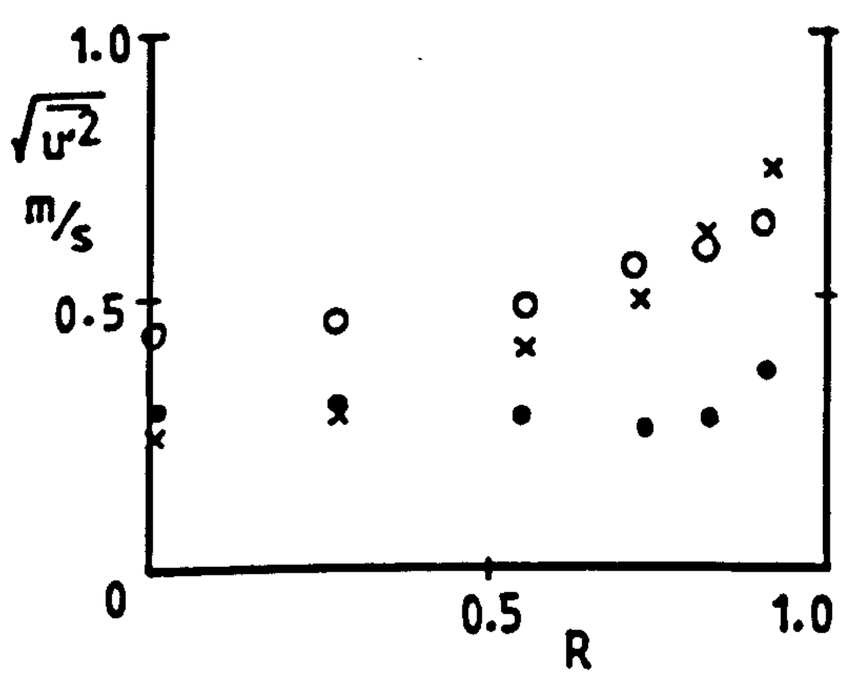

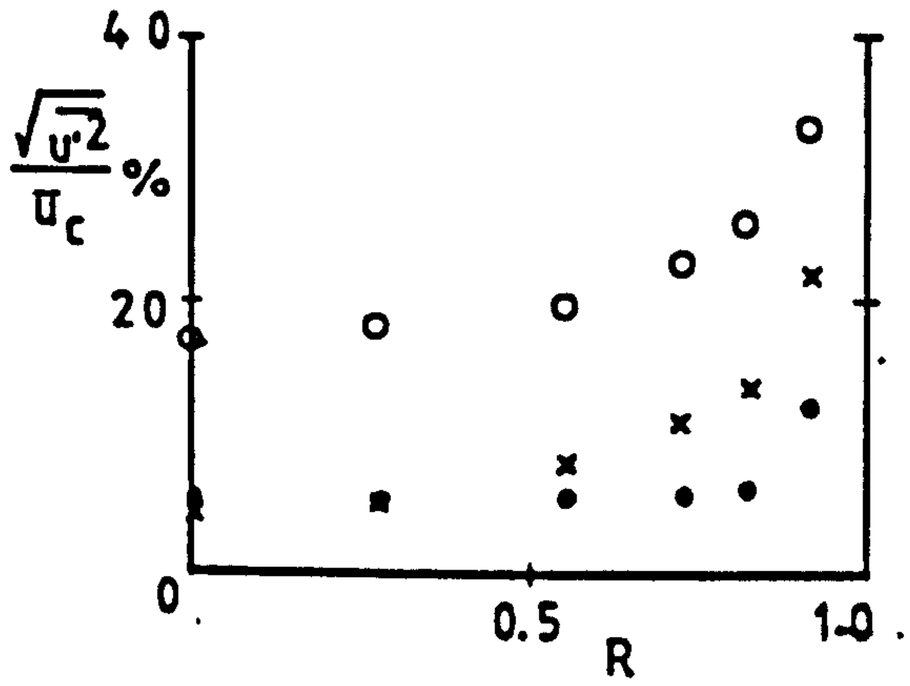

Figure 6.1 Glass ballotini, 210-325 μm; loading ratio 2.44; pipe diameter = 22 mm; U_m = 5.59 m/s

• air; o solids; × air alone

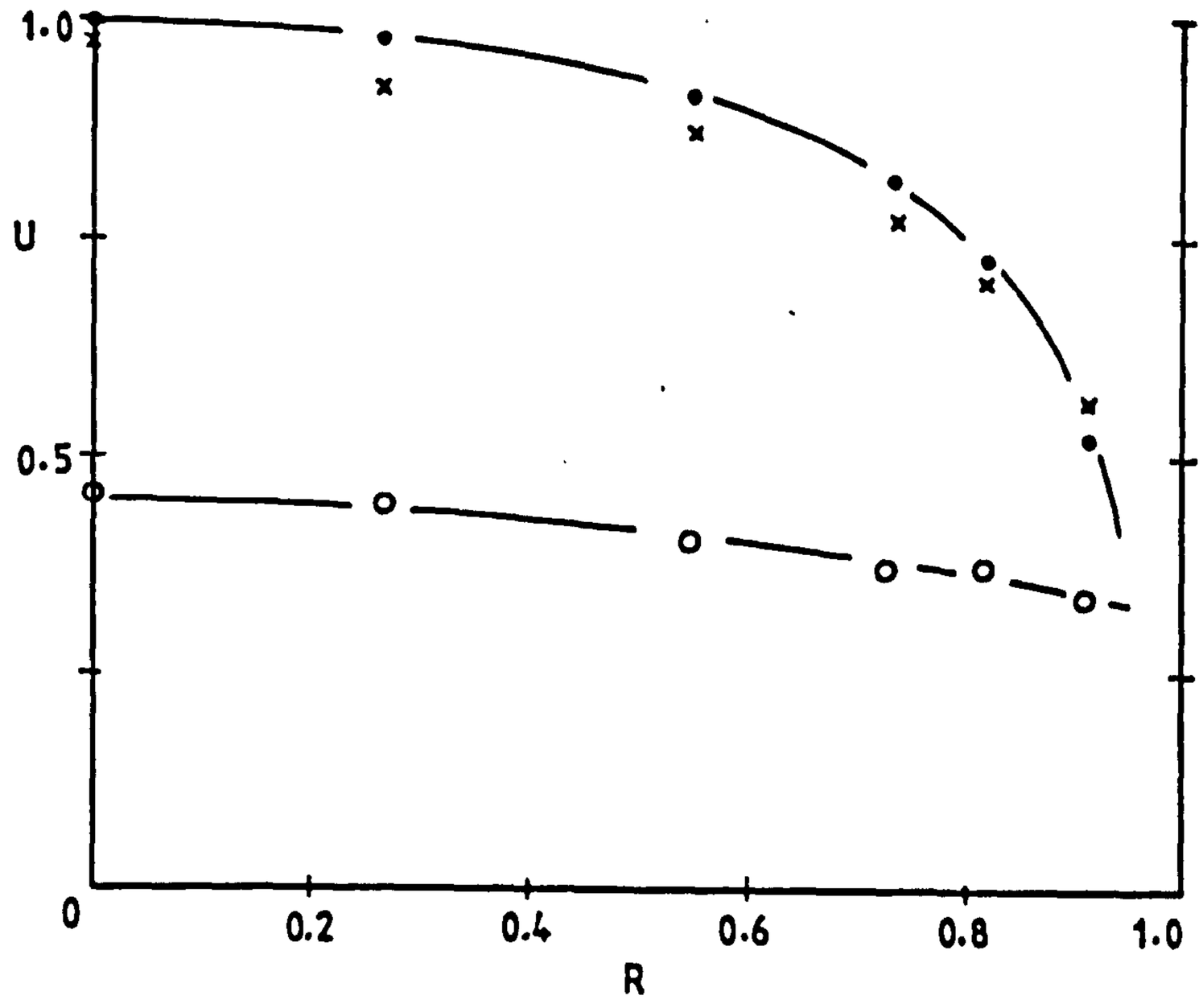

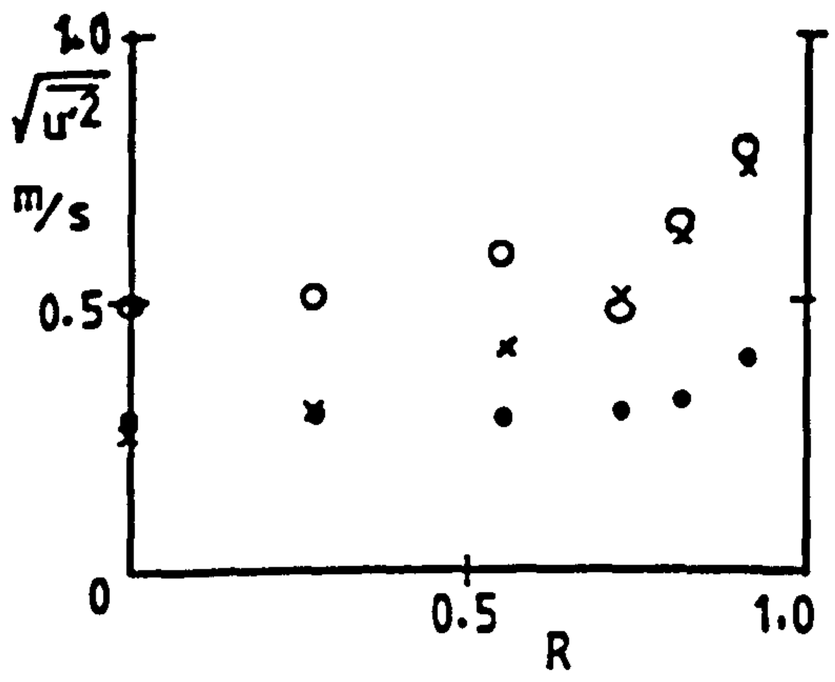

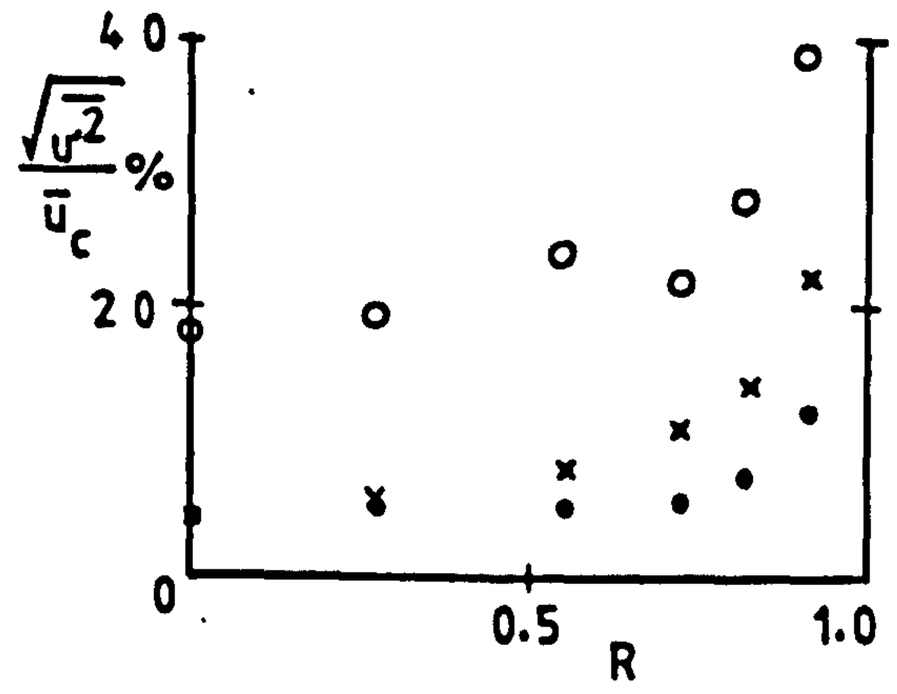

Figure 6.2 Glass ballotini, 210-325 μm; loading ratio 3.73; pipe diameter = 22 mm; U_m = 5.93 m/s

• air; o solids; × air alone

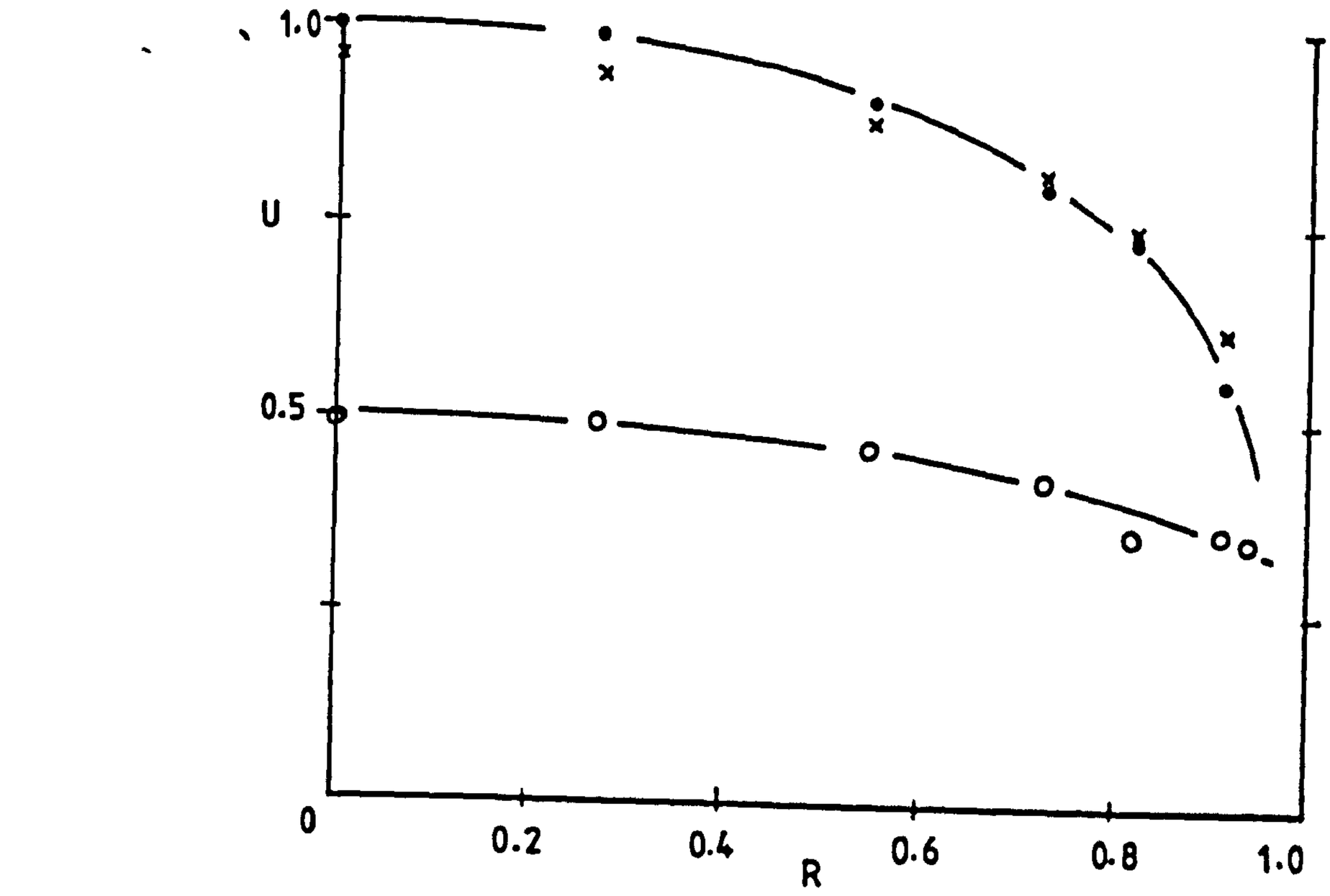

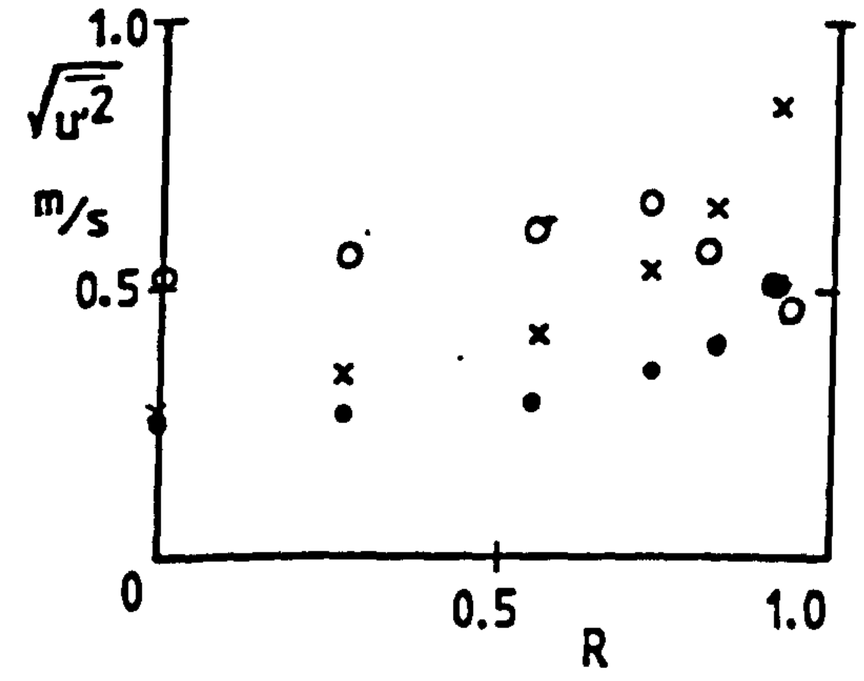

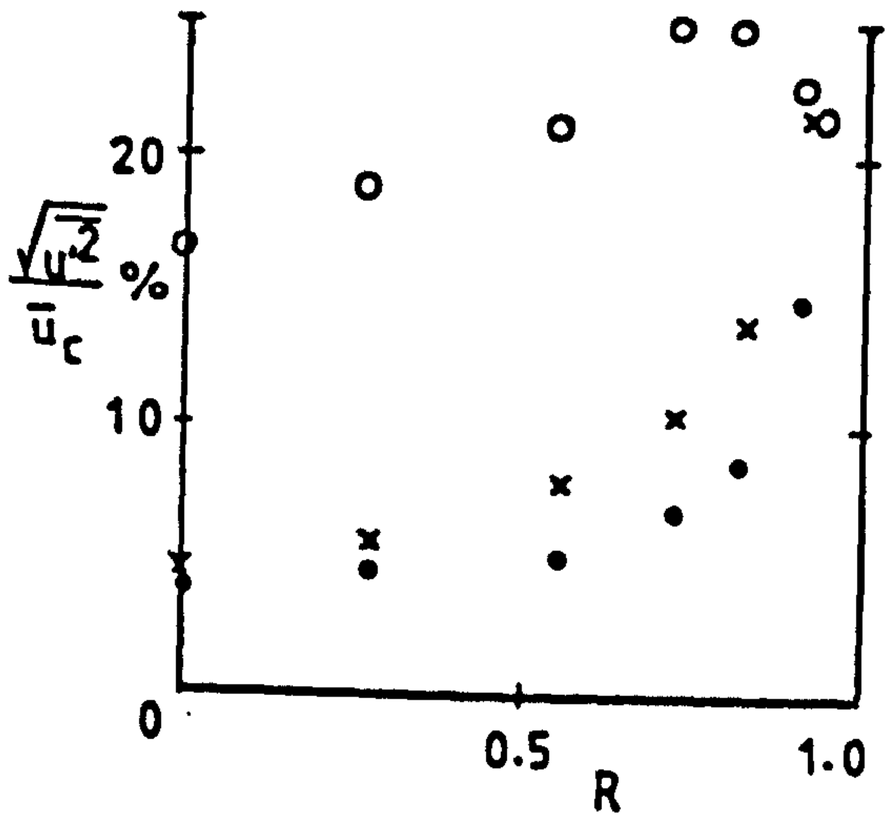

Figure 6.3 Glass ballotini, 210-325 μm; loading ratio 2.24; pipe diameter = 22 mm; U_m = 6.29 m/s

• air; o solids; x air alone

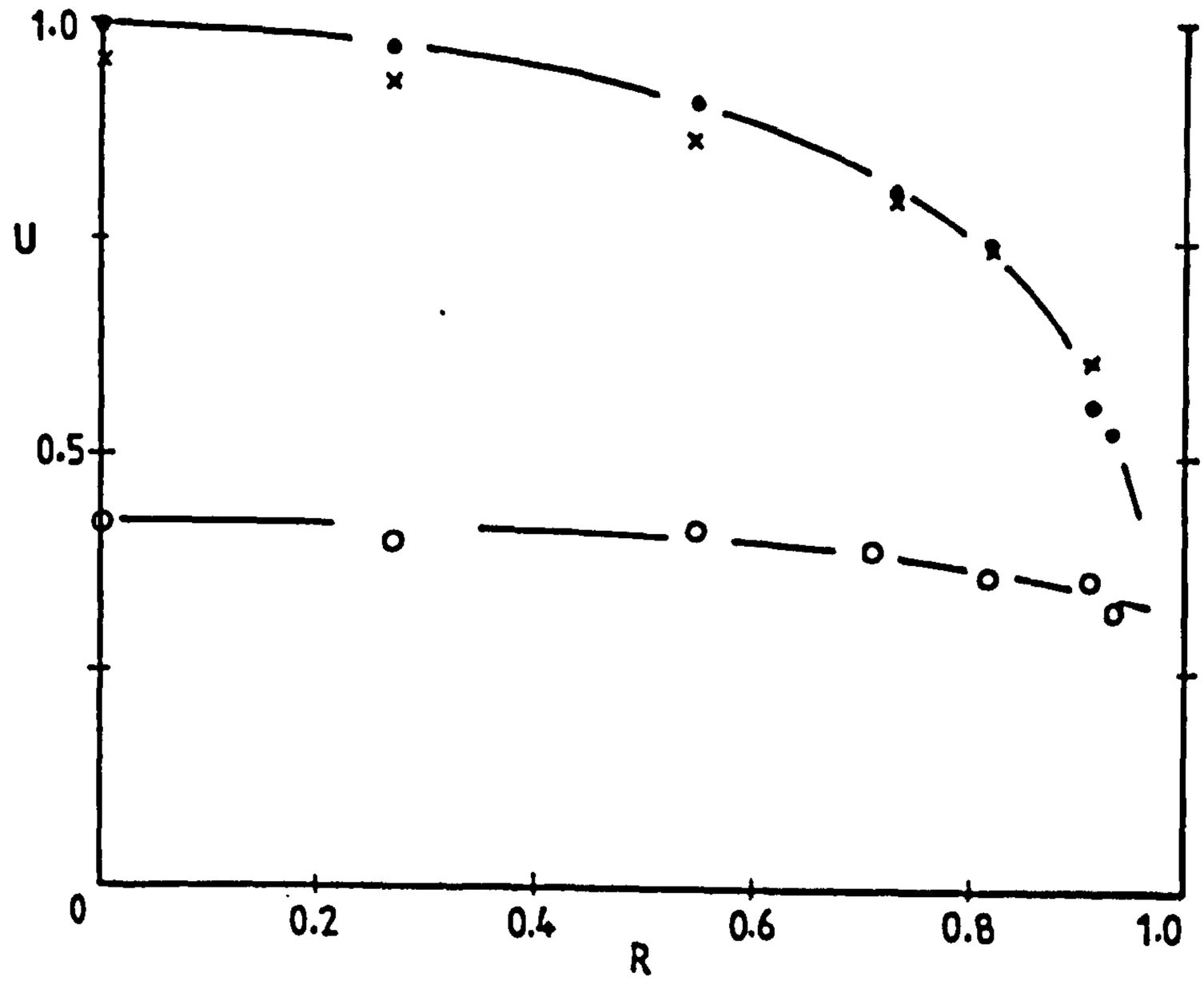

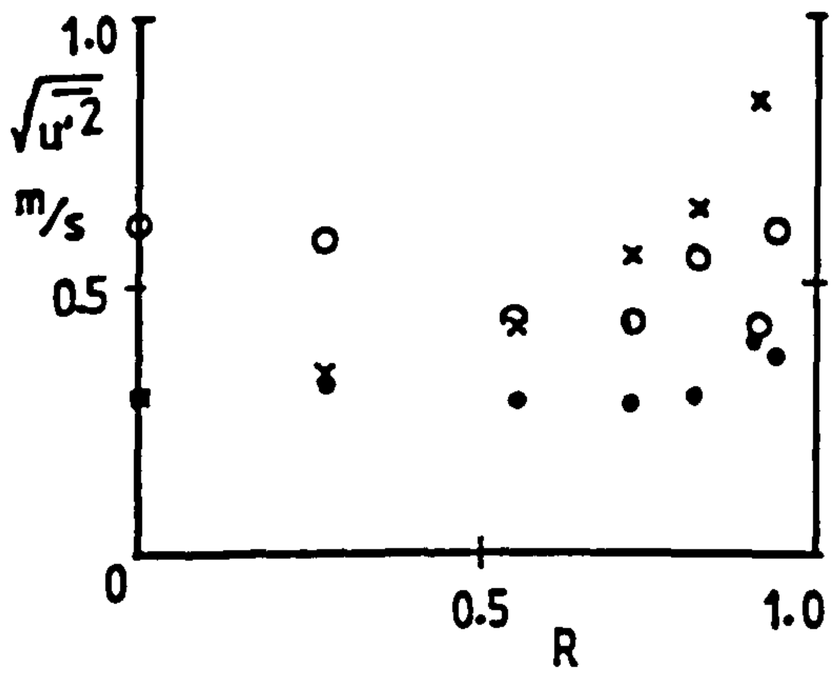

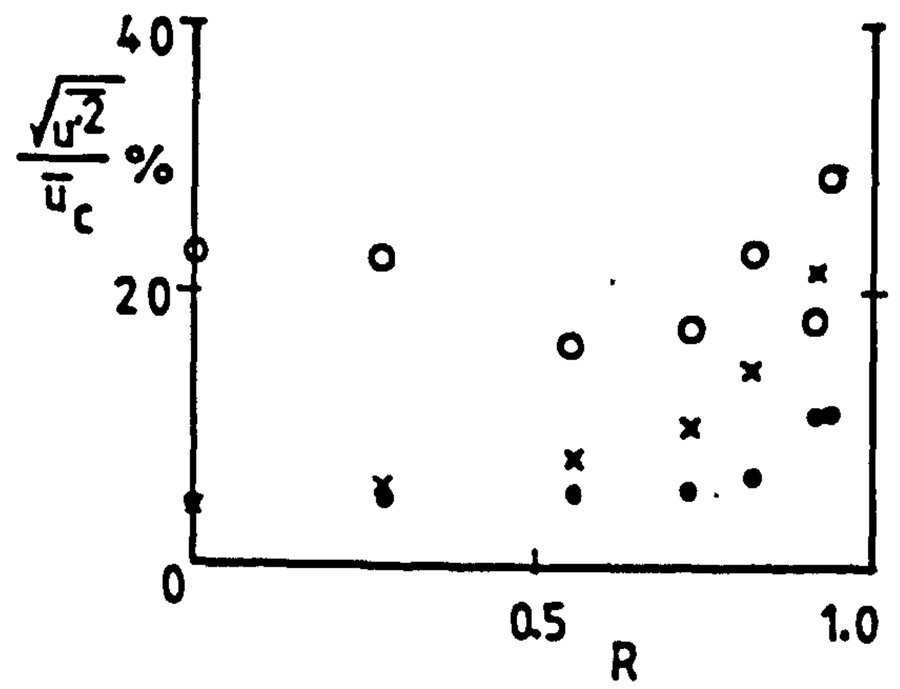

Figure 6.4 Glass ballotini, 210–325 μm; loading ratio 3.42; pipe diameter = 22 mm; U_m = 6.37 m/s

• air; o solids; × air alone

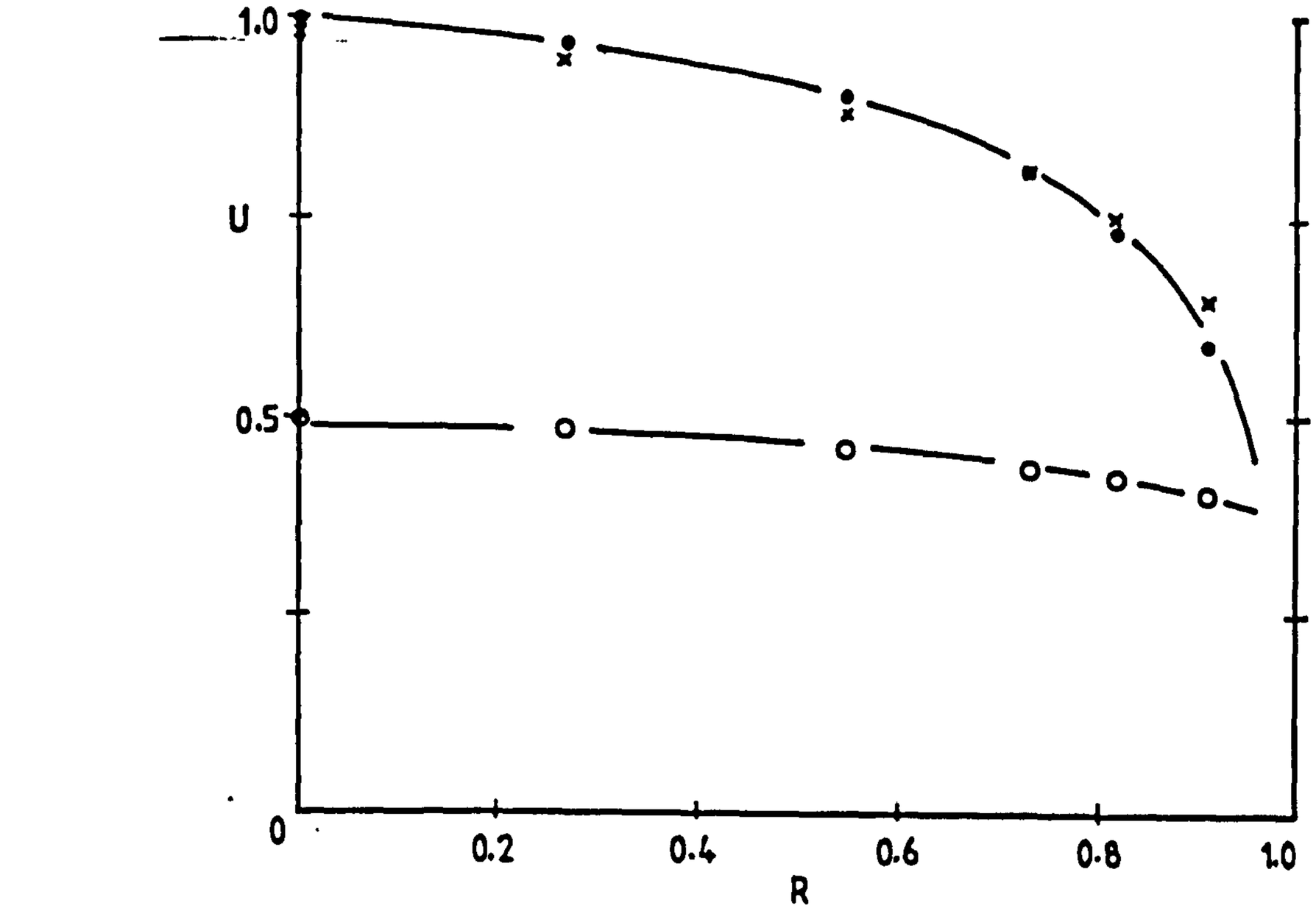

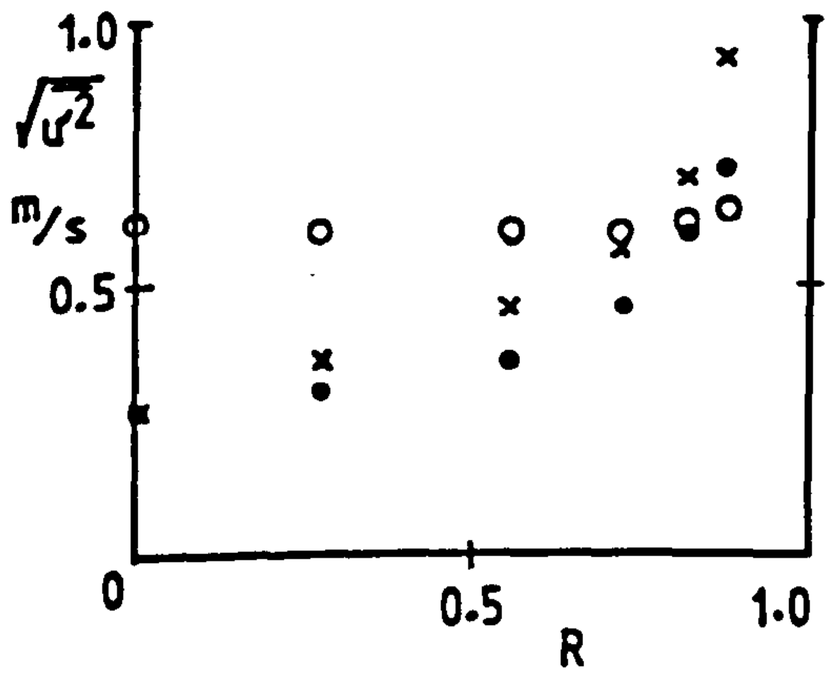

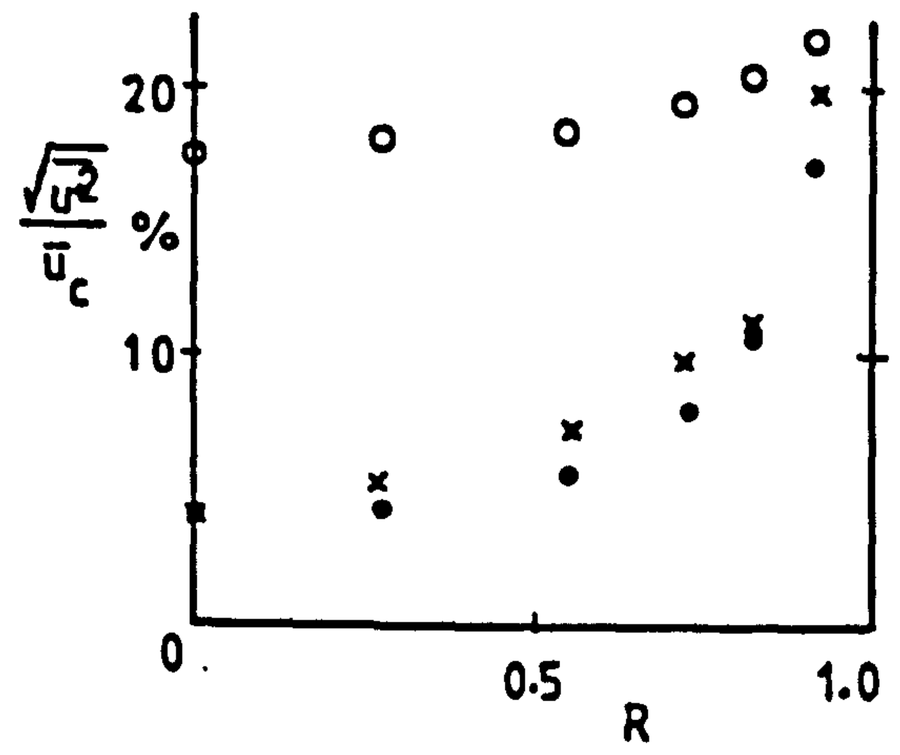

Figure 6.5 Glass ballotini, 210-325 μm; loading ratio 1.99; pipe diameter = 22 mm; U_m = 7.08 m/s

• air; o solids; × air alone

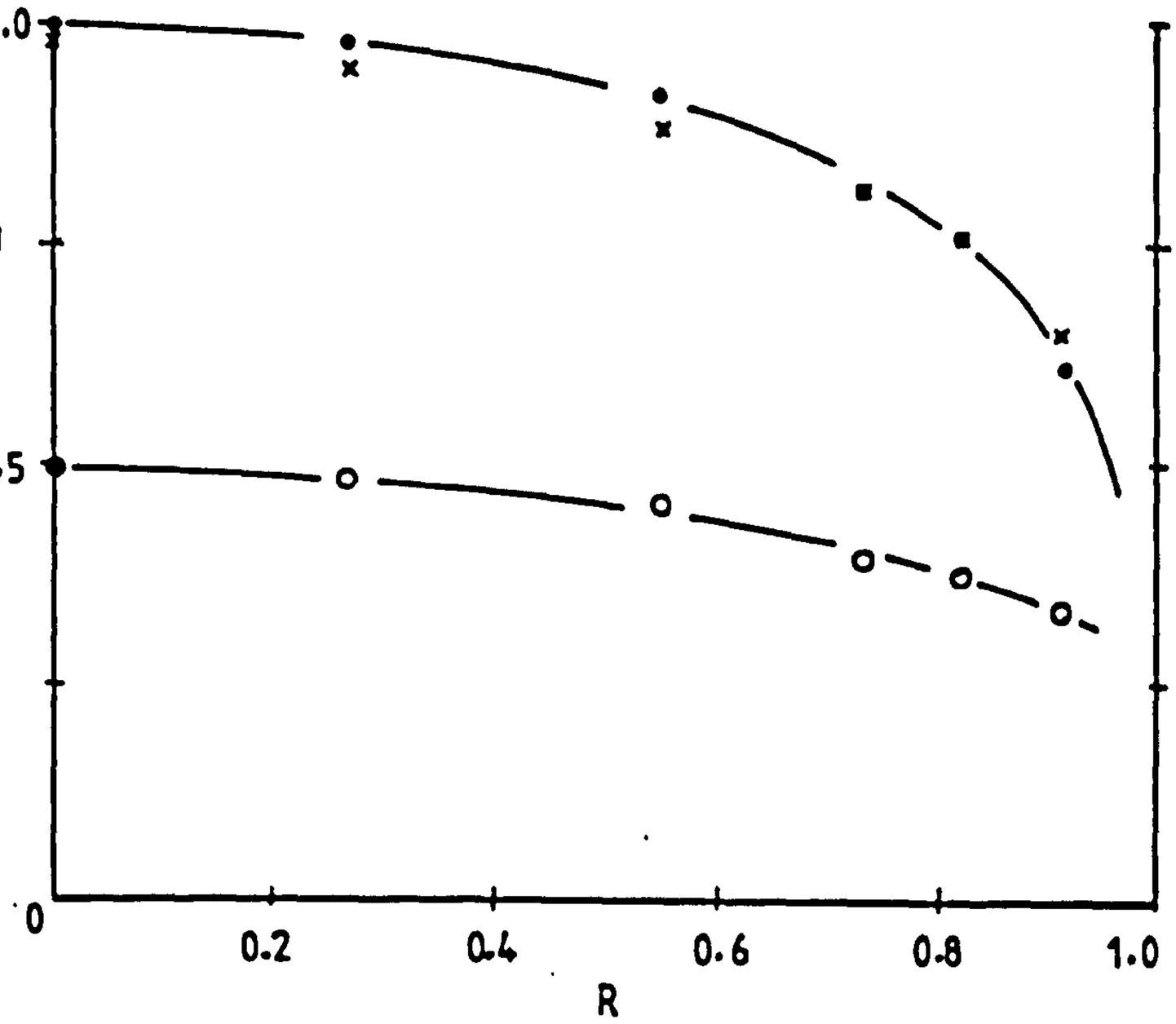

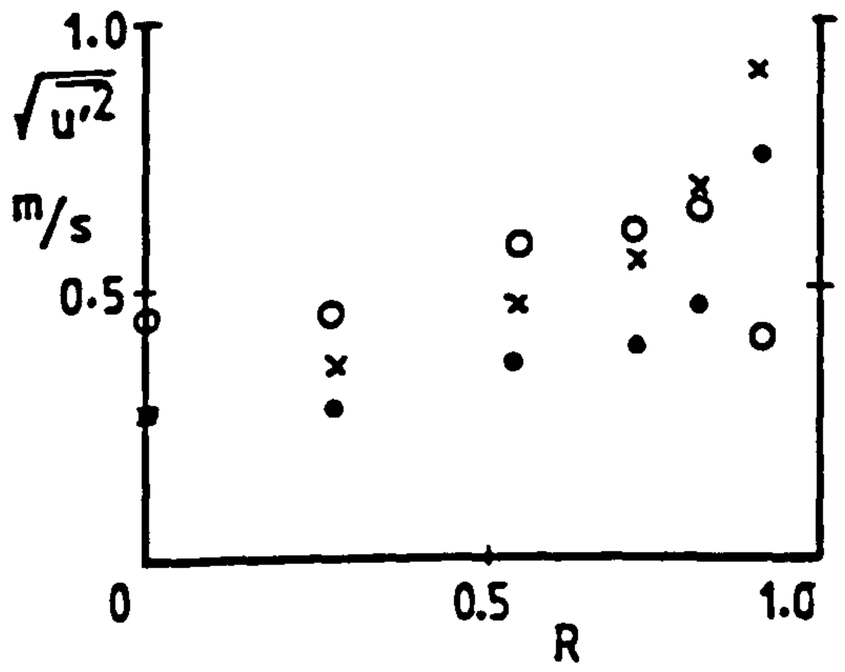

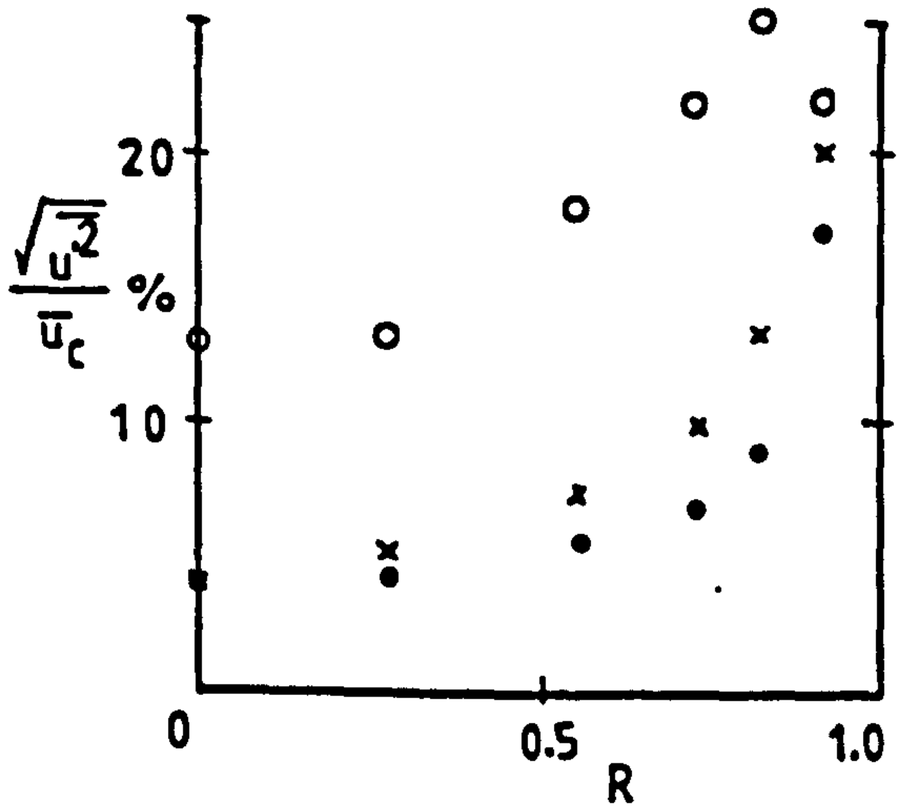

Figure 6.6 Glass ballotini, 210-325 μm; loading ratio 3.05; pipe diameter = 22 mm; U_m = 7.08 m/s

• air; o solids; × air alone

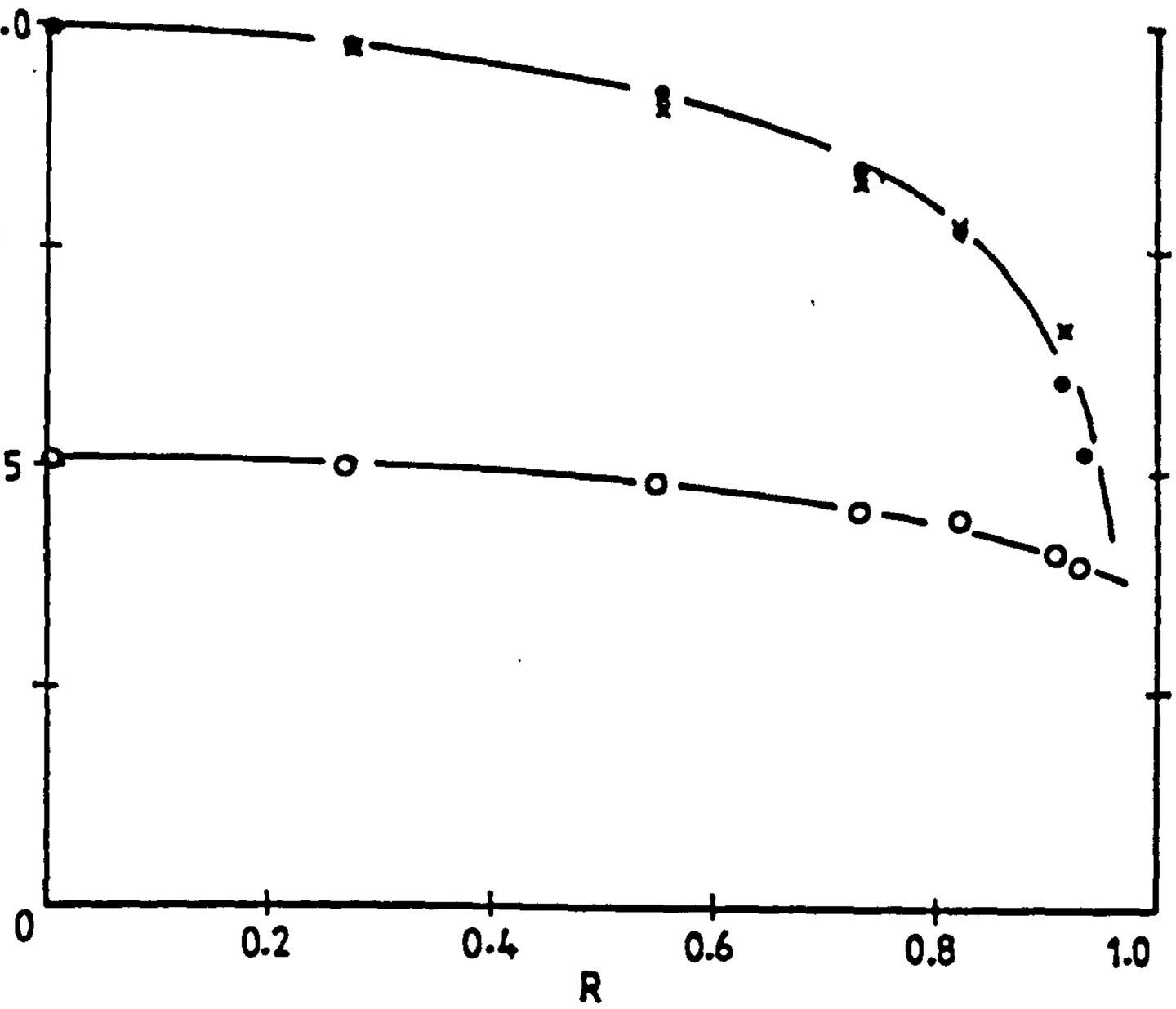

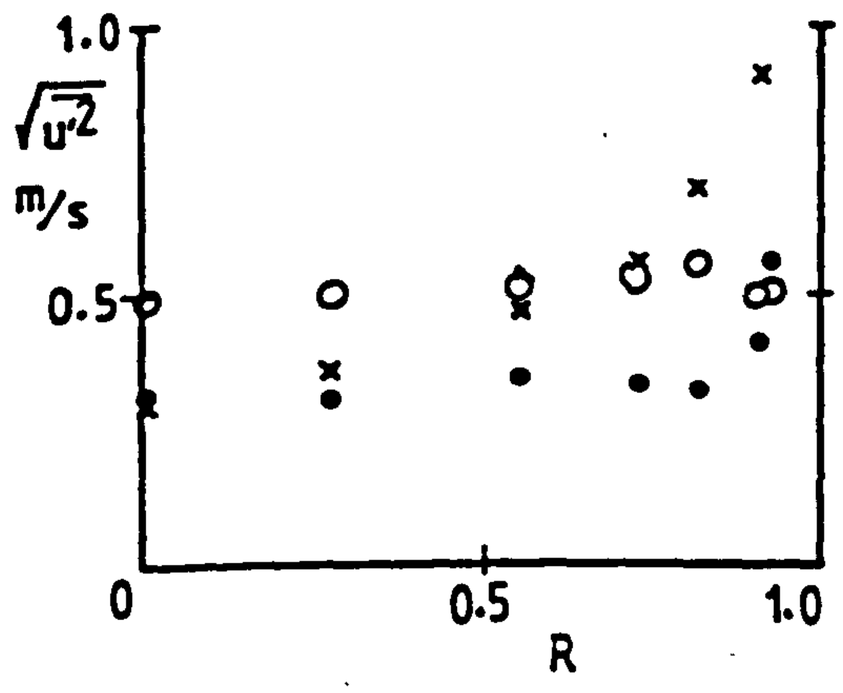

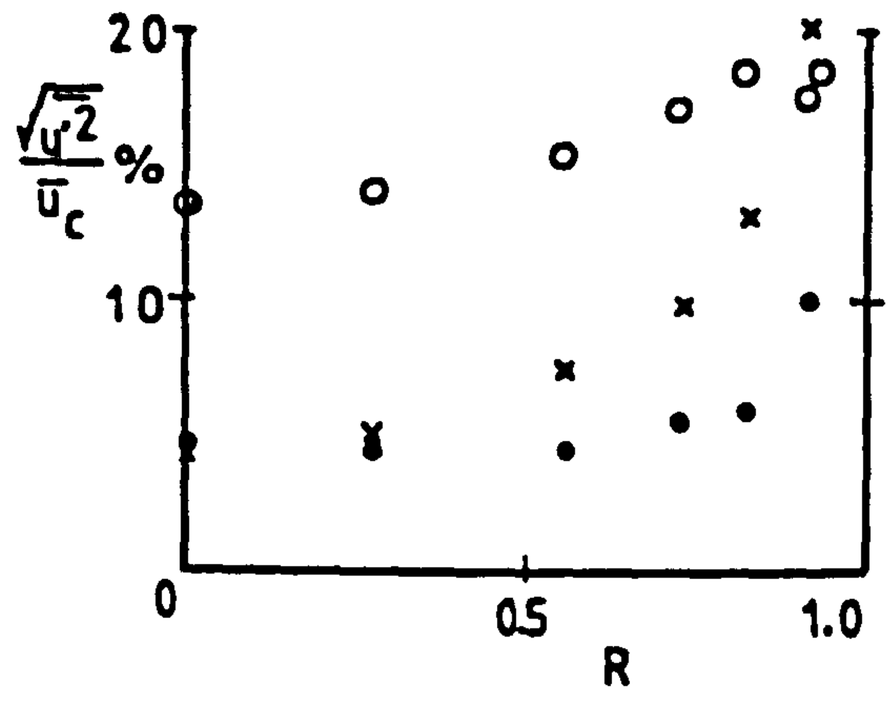

Figure 6.7 Glass ballotini, 210-325 μm; loading ratio 4.99; pipe diameter = 22 mm; U_m = 6.(o m/s

• air; o solids; × air alone

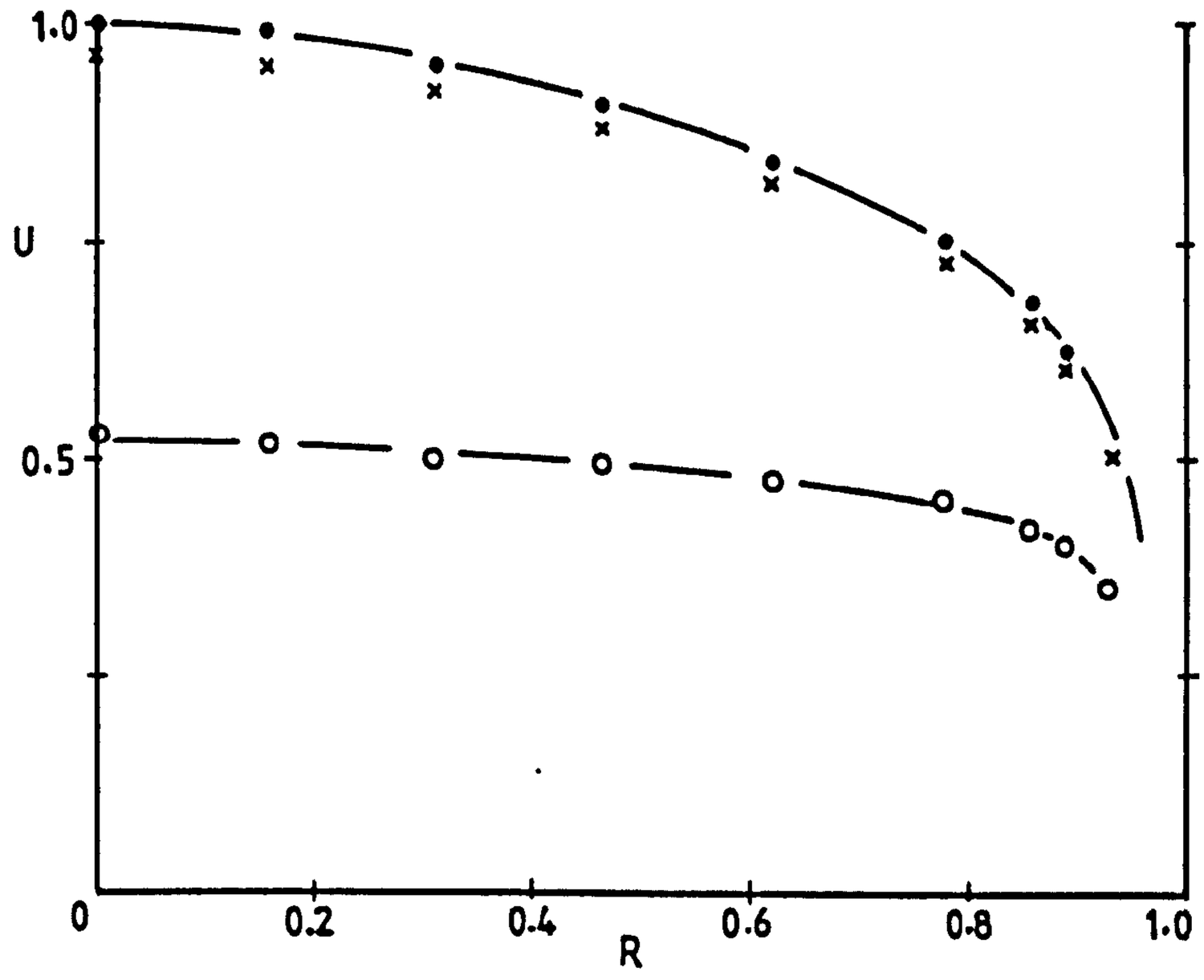

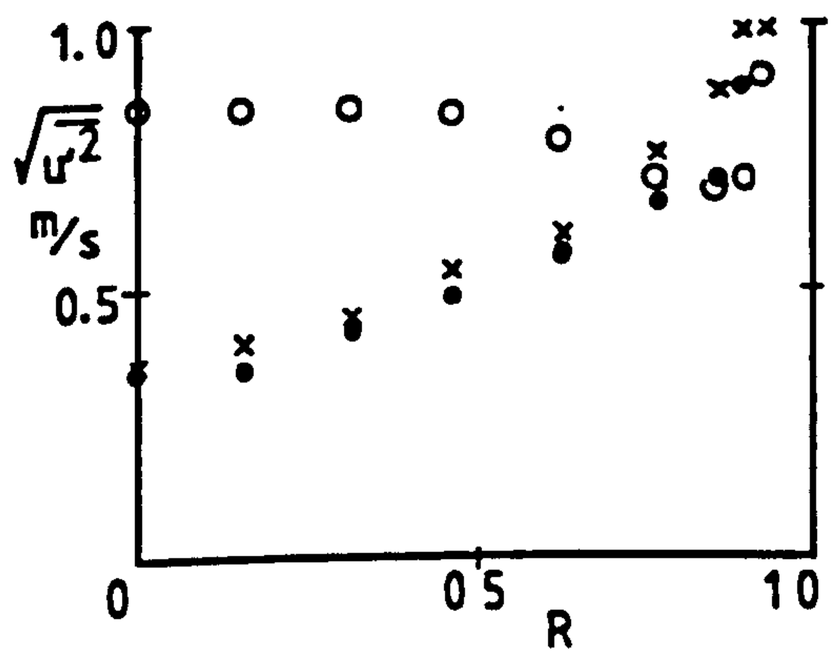

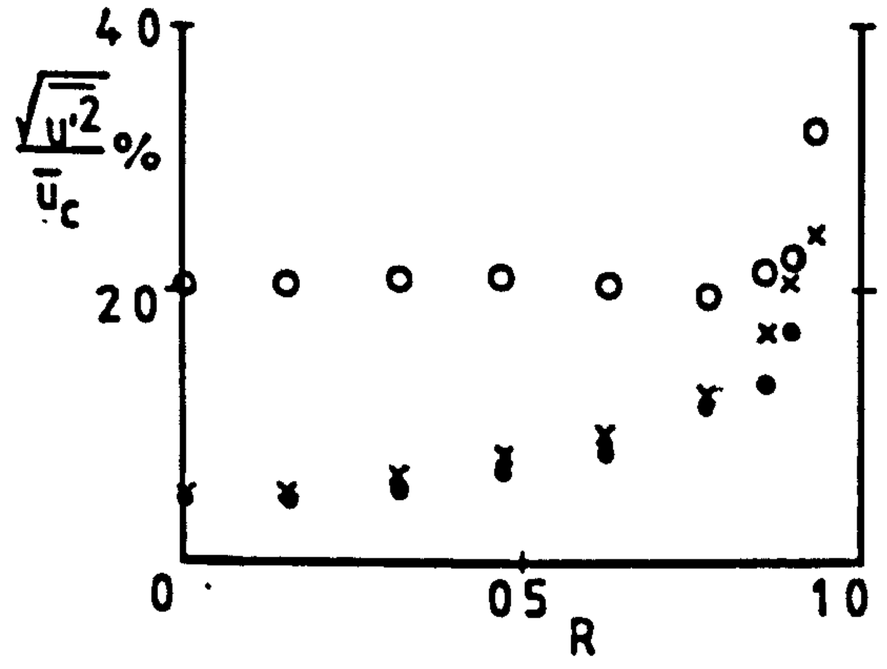

Figure 6.8 Glass ballotini, 210-325 μm; loading ratio 0.69; pipe diameter = 25.8 mm; U_m = 8.00 m/s

• air; o solids; × air alone

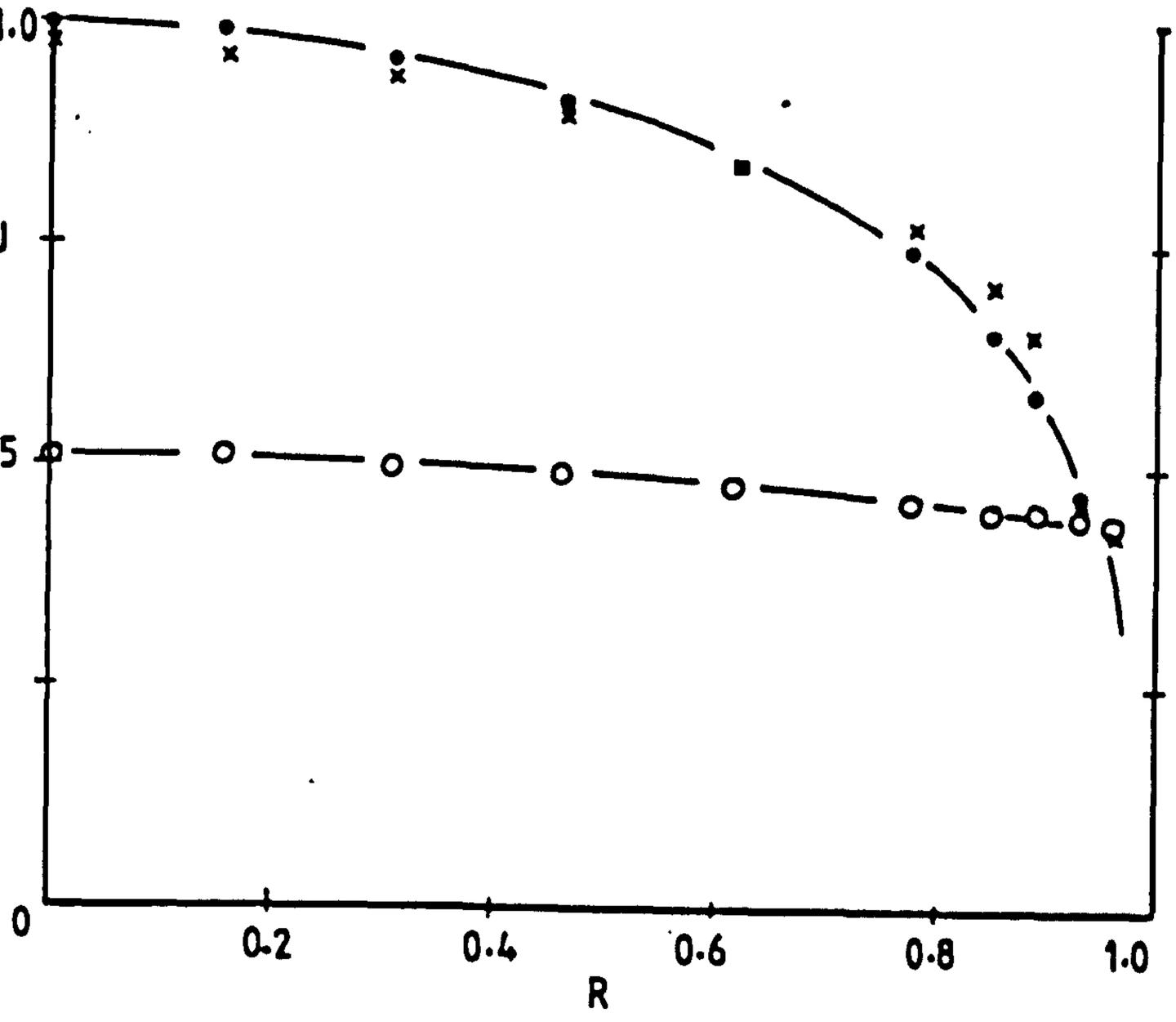

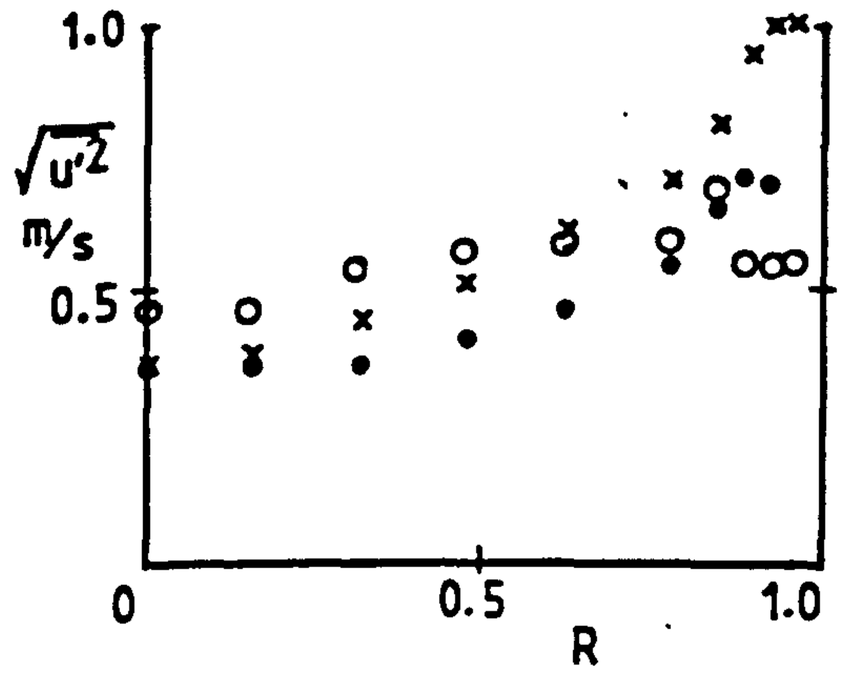

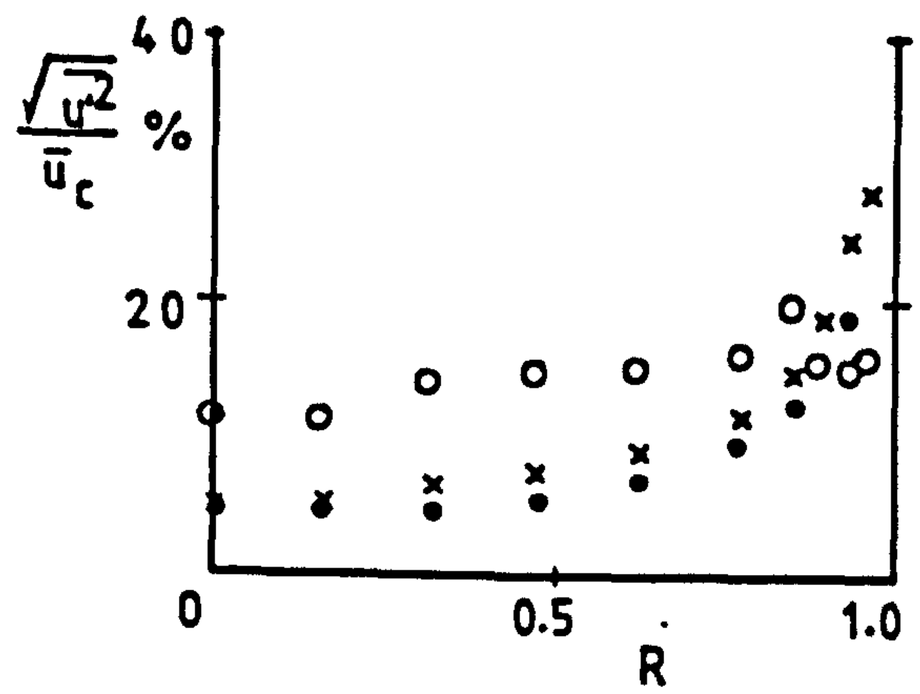

Figure 6.9 Glass ballotini, 210-325 μm; loading ratio 2.0; pipe diameter = 25.8 mm; U_m = 7.95

• air; o solids; x air alone

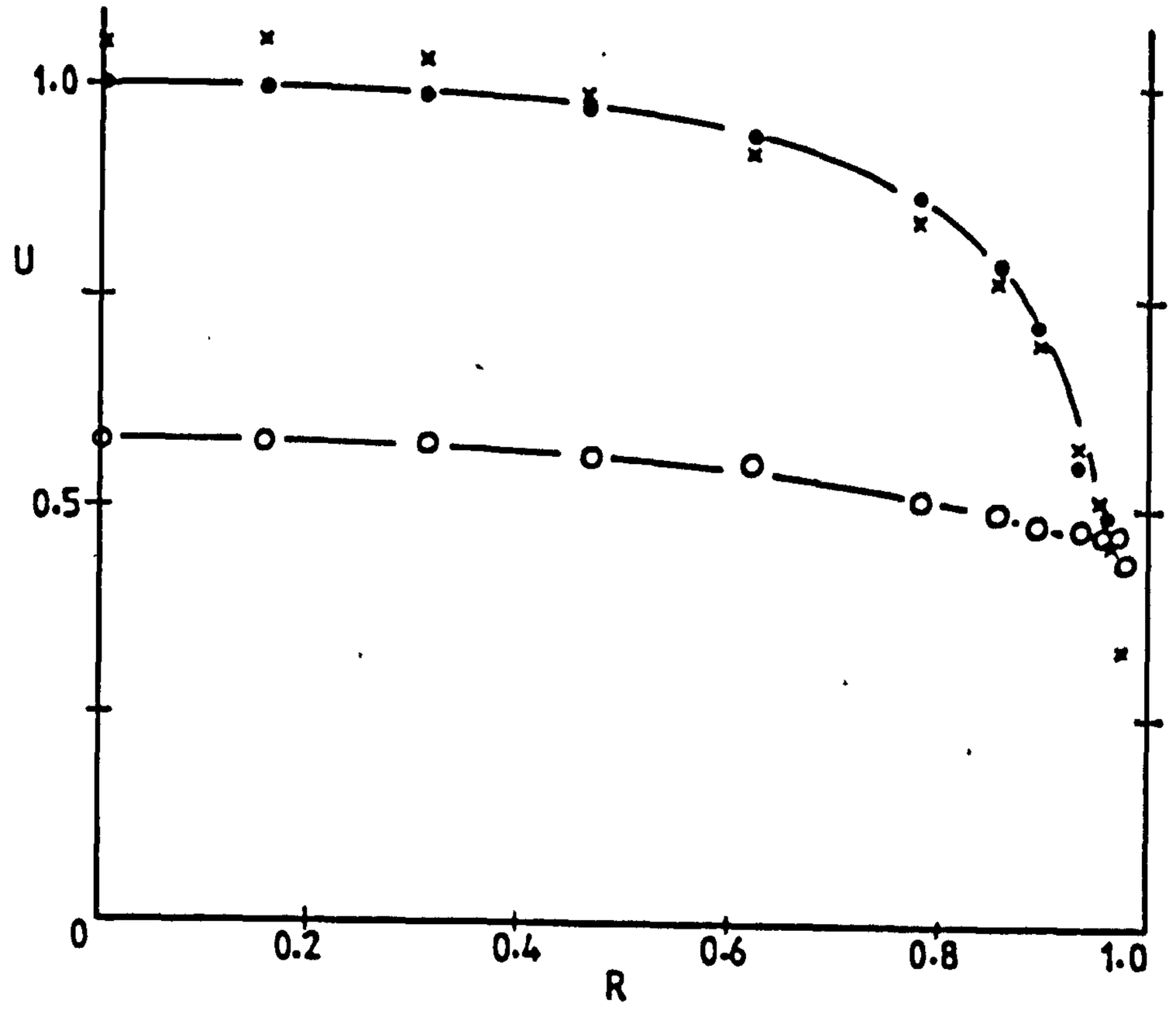

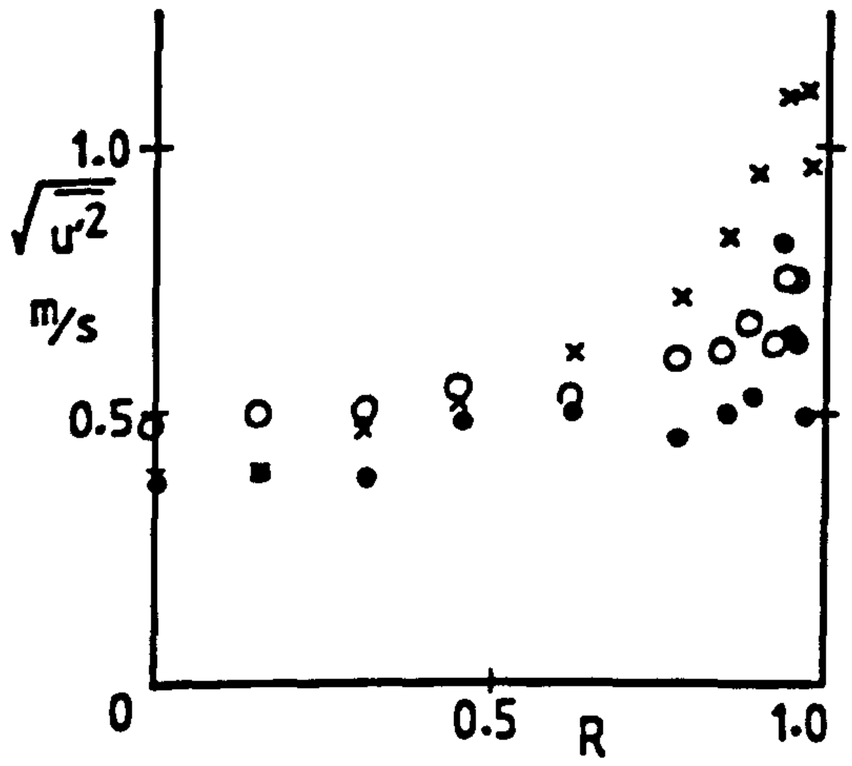

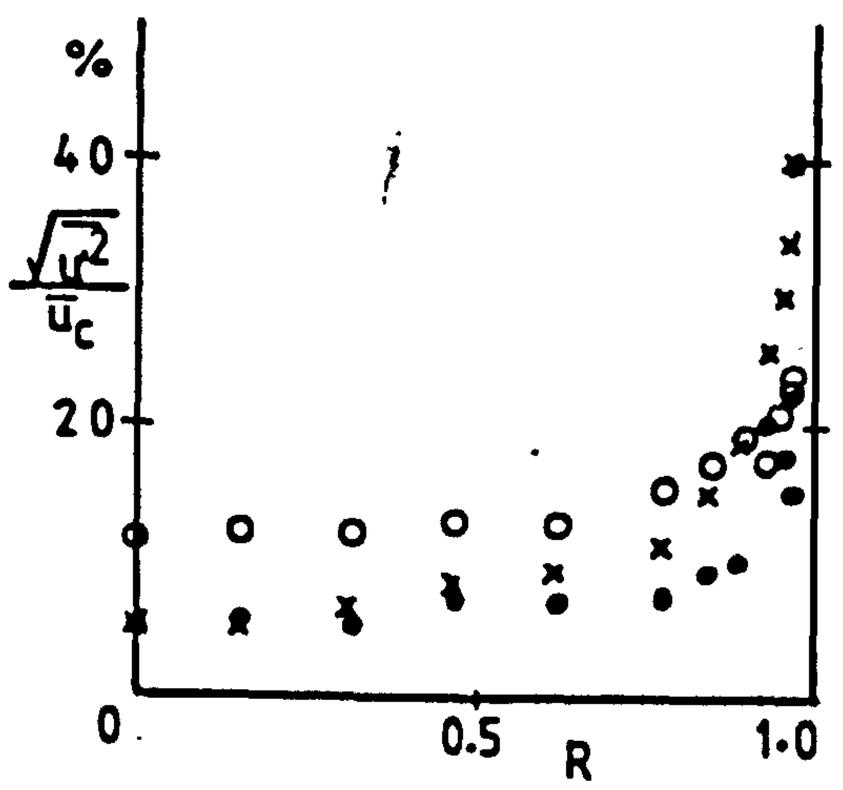

Figure 6.10 Glass ballotini, 210–325 μm; loading ratio 5.65; pipe diameter 25.8 mm; U_m = 7.26 m/s

• air; o solids; × air alone

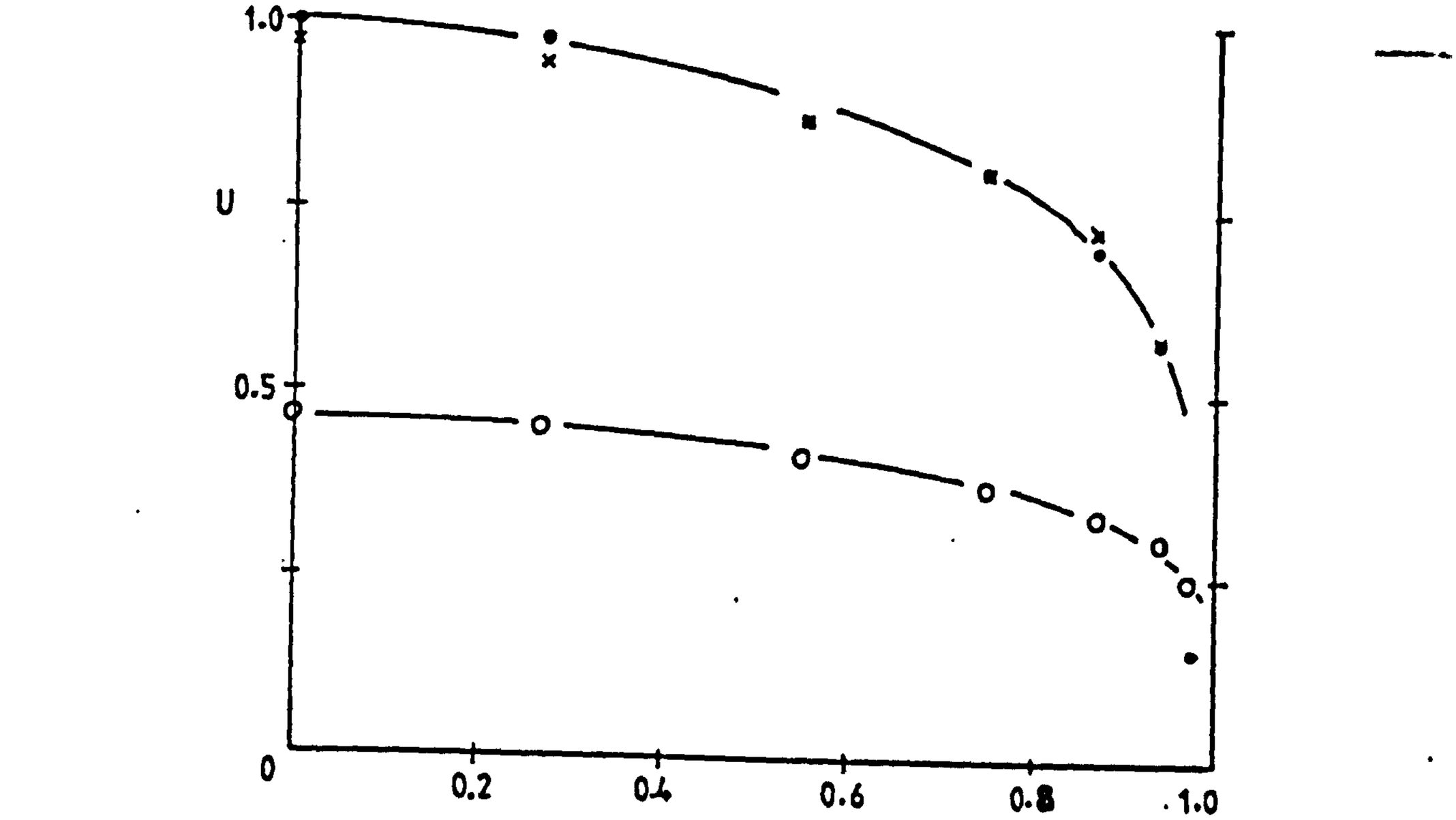

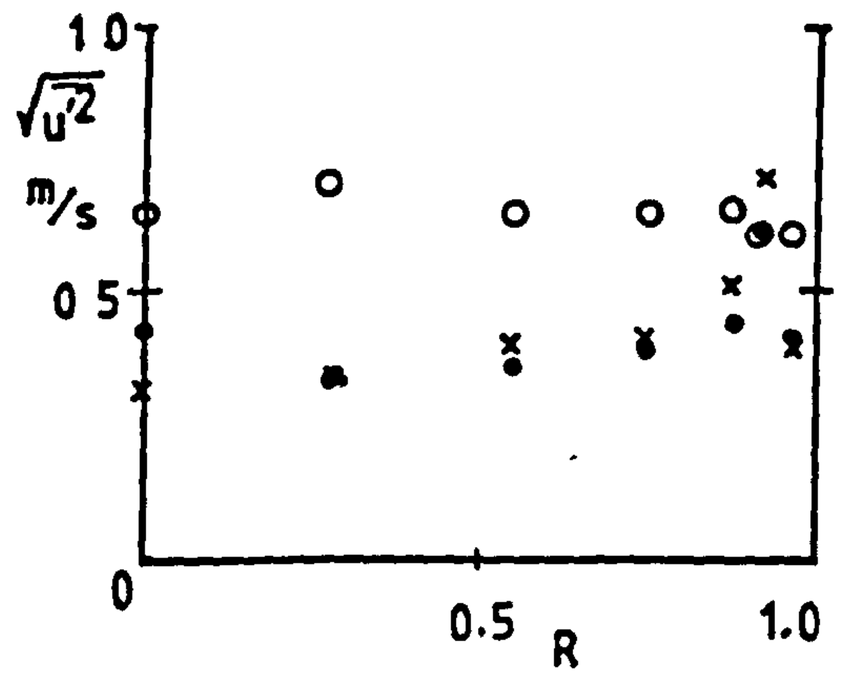

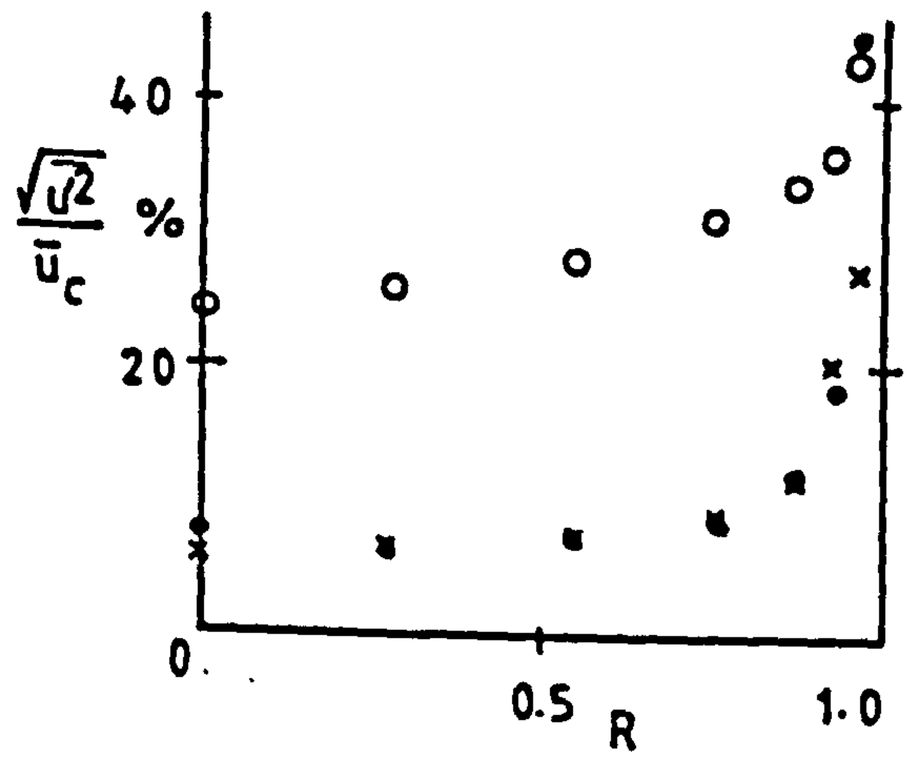

Figure 6.11 Glass ballotini, 210-325 μm; loading ratio 0.61; pipe diameter = 31.4 mm; U_m 5.71 m/s.

• air; o solids; x air alone

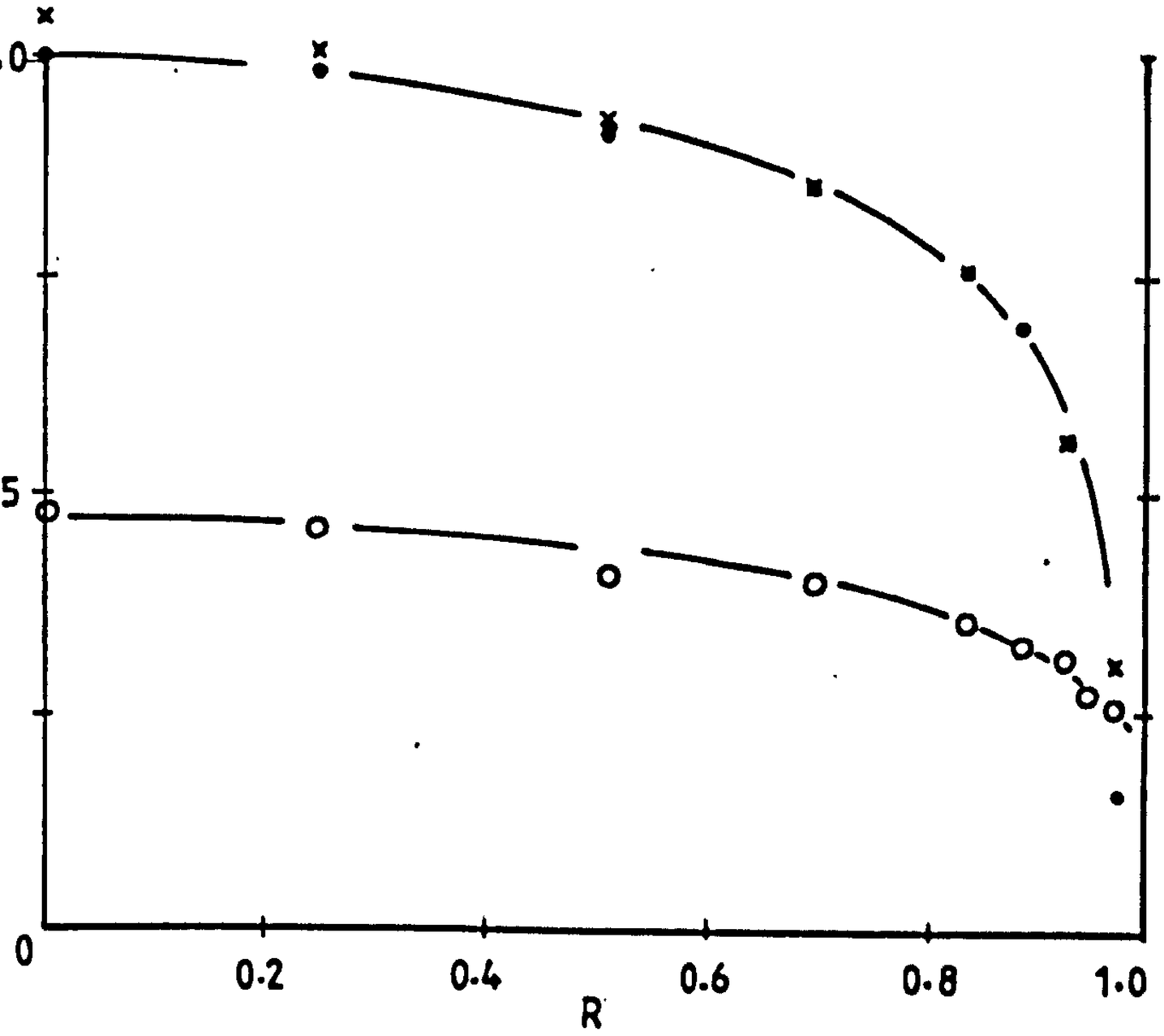

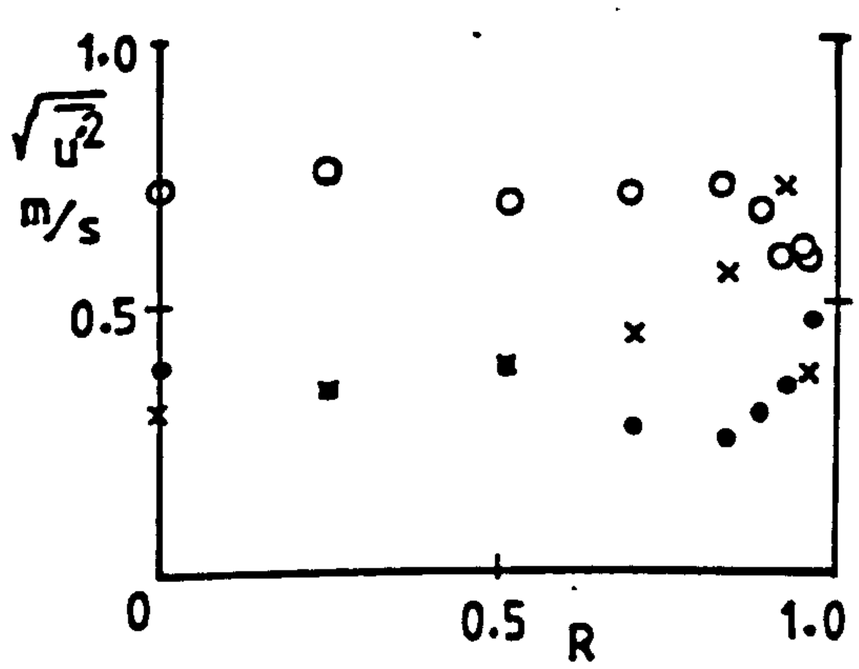

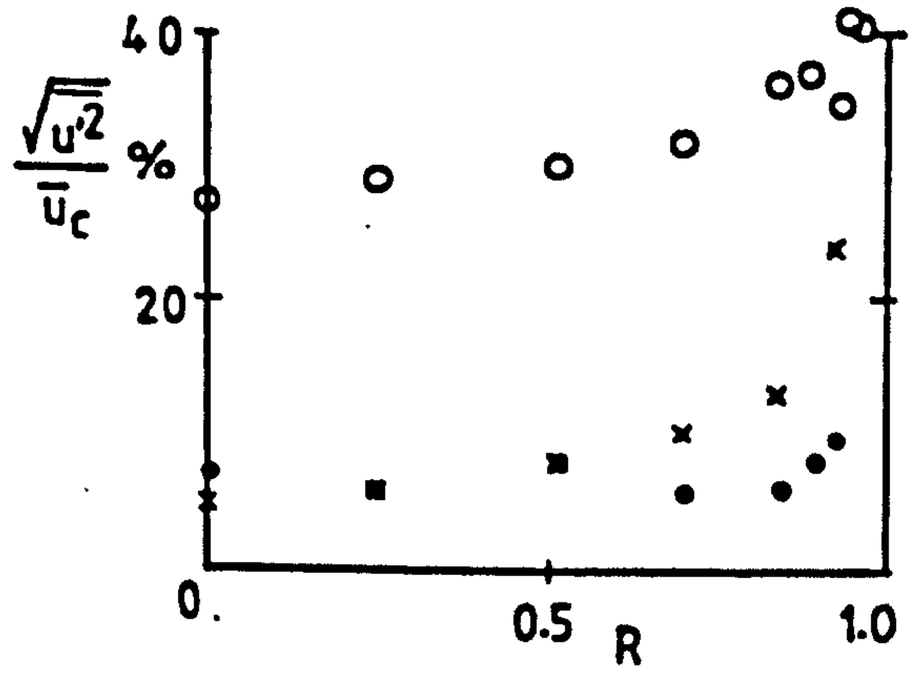

Figure 6.12 Glass ballotini, 210-325 μm; loading ratio 1.81; pipe diameter = 31.4 mm; U_m = 5.38 m/s

• air; o solids; x air alone

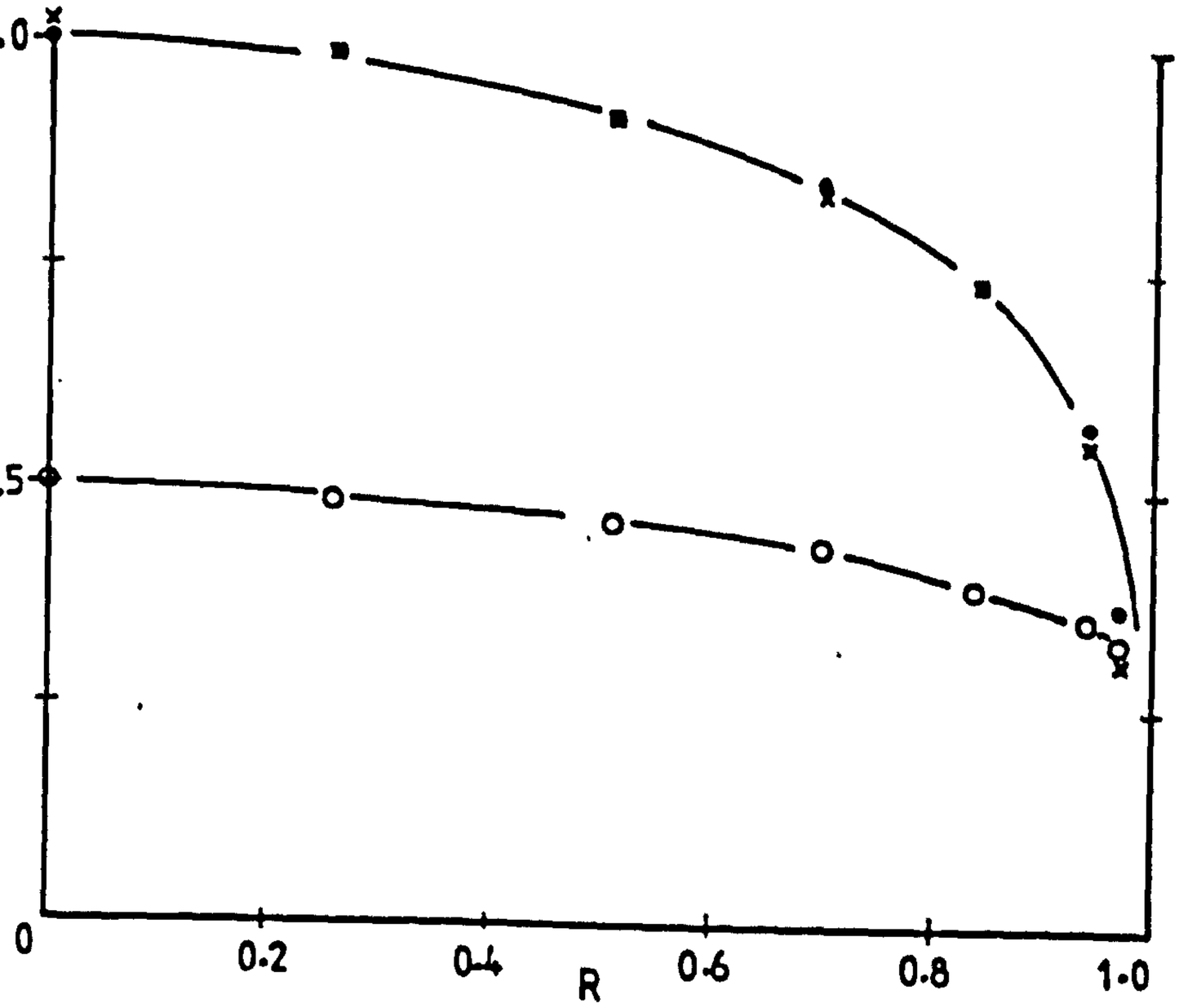

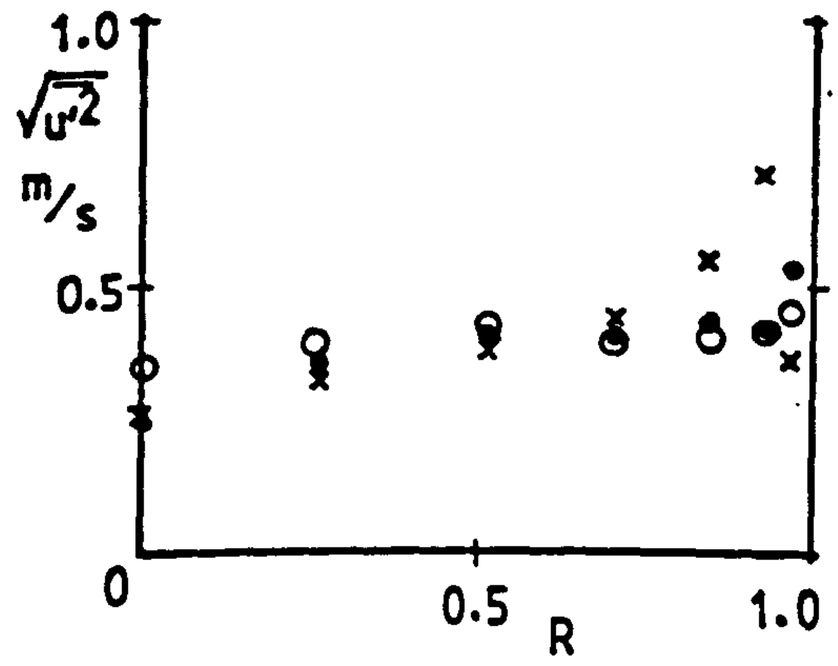

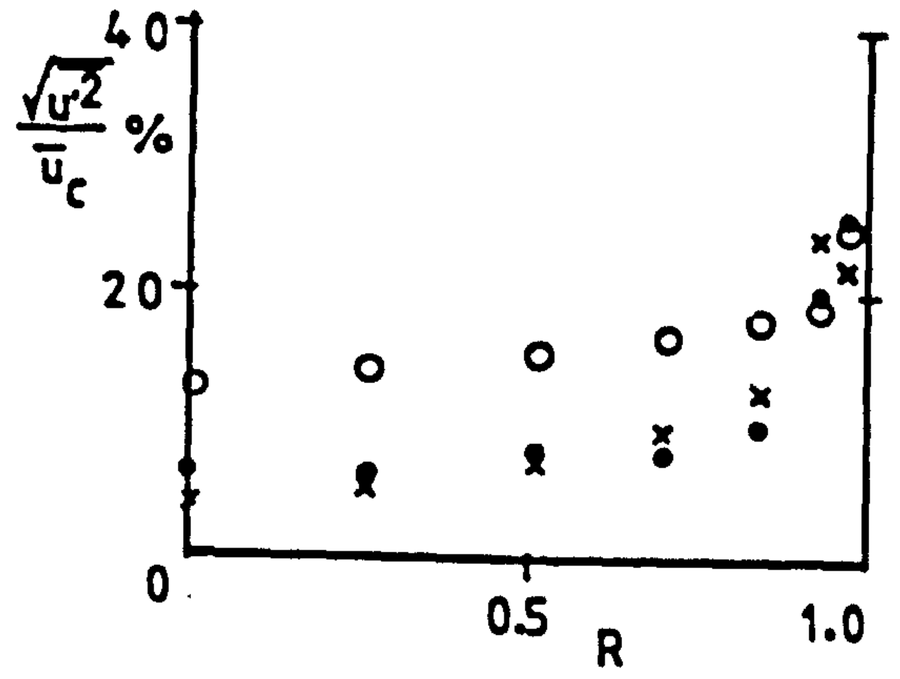

Figure 6.13 Glass ballotini, 210-325 μm; loading ratio 5.03; pipe diameter = 31.4 mm; U_m = 5.54 m/s

• air; o solids; × air alone

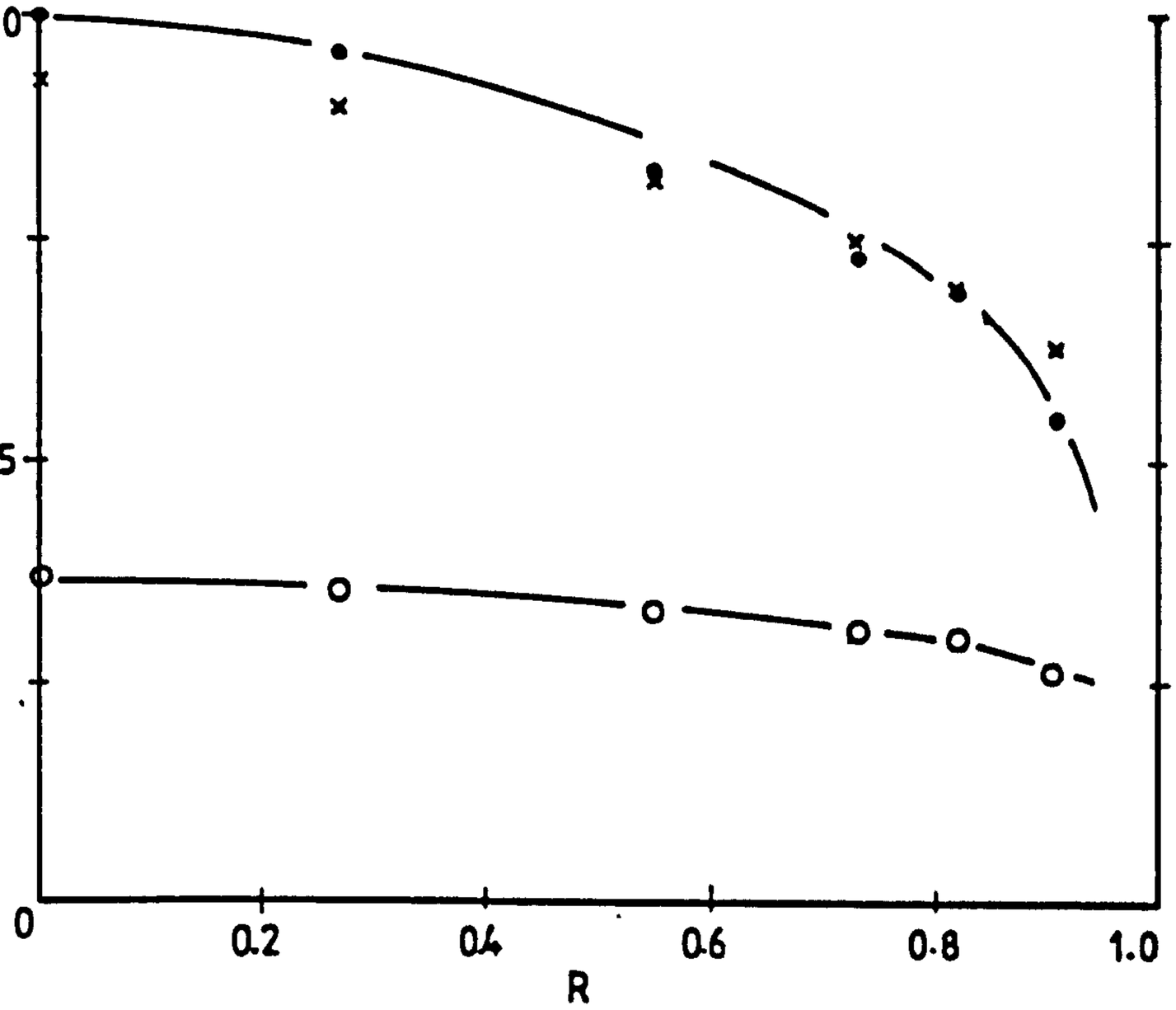

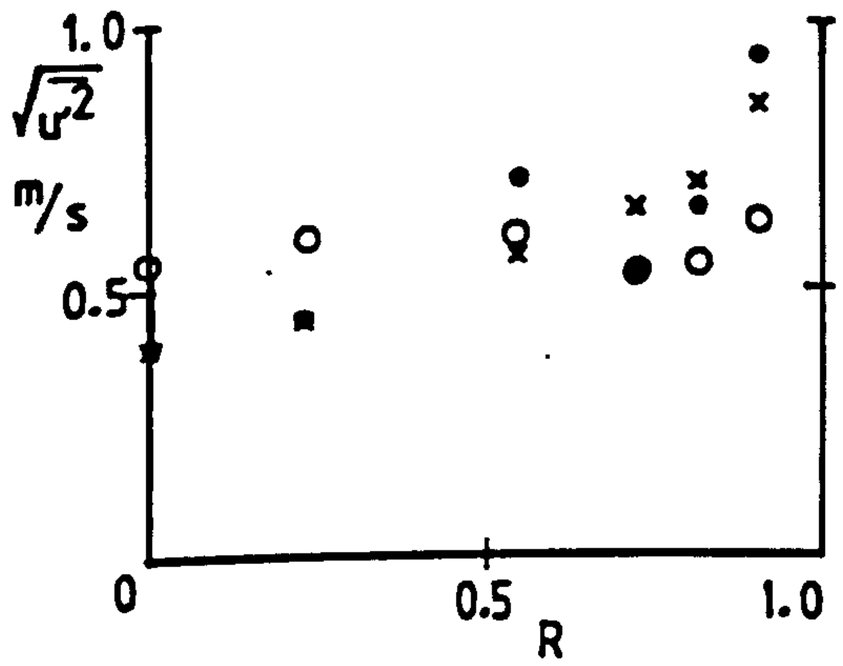

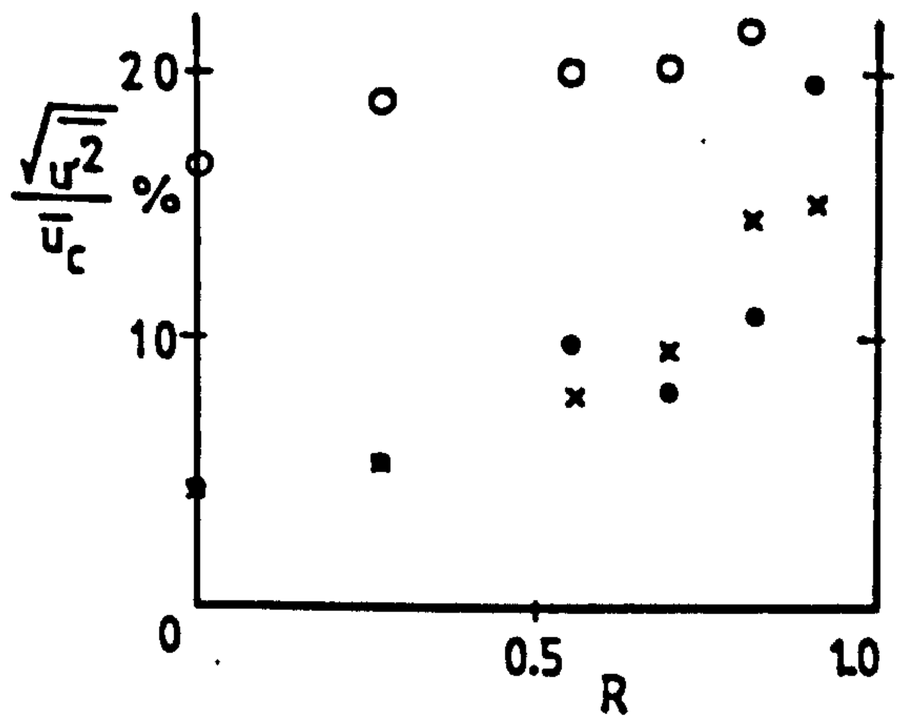

Figure 6.14 Fused alumina, 300-430 μm; loading ratio 1.64; pipe diameter = 22 mm; U_m = 8.72 m/s

• air; o solids; × air alone

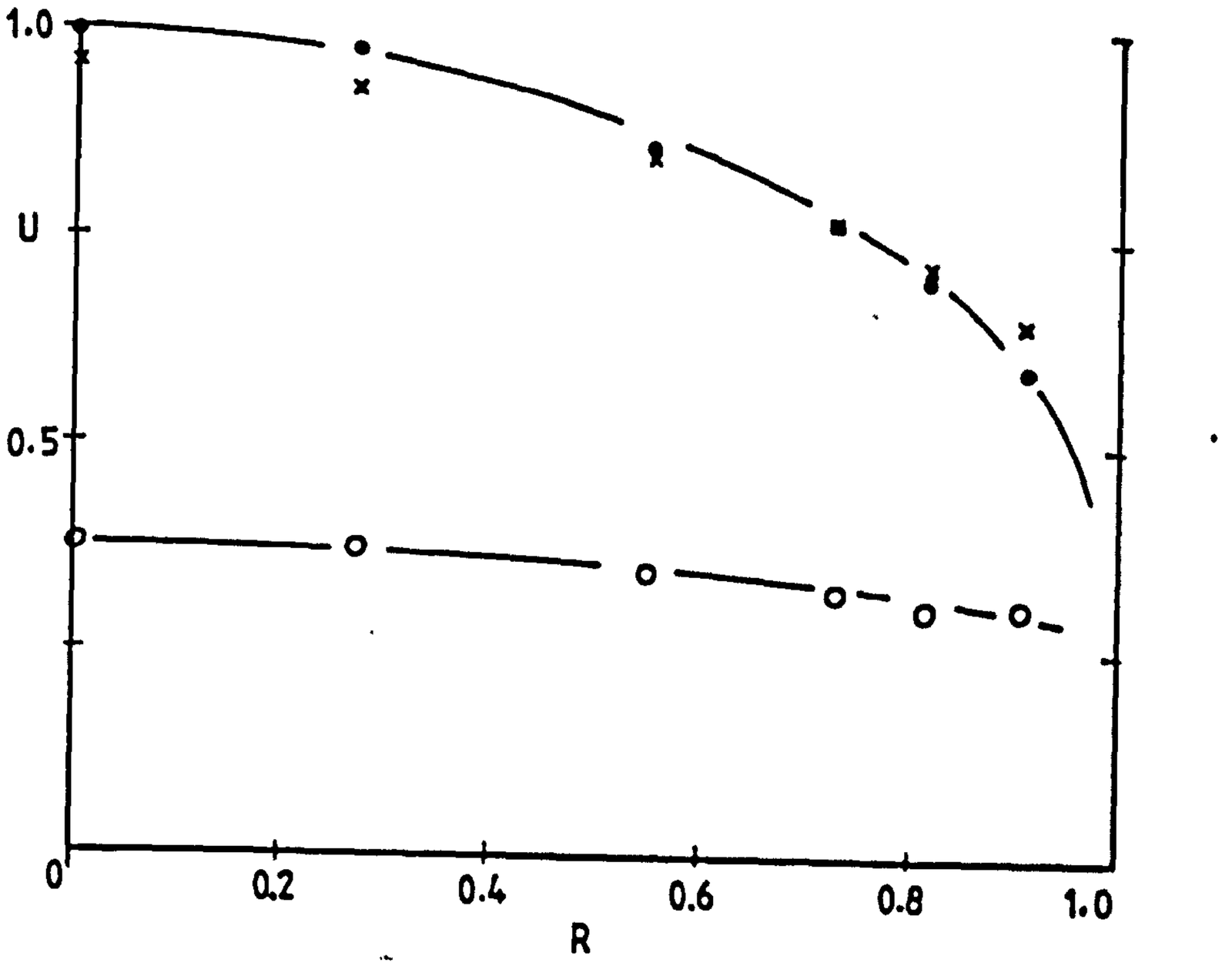

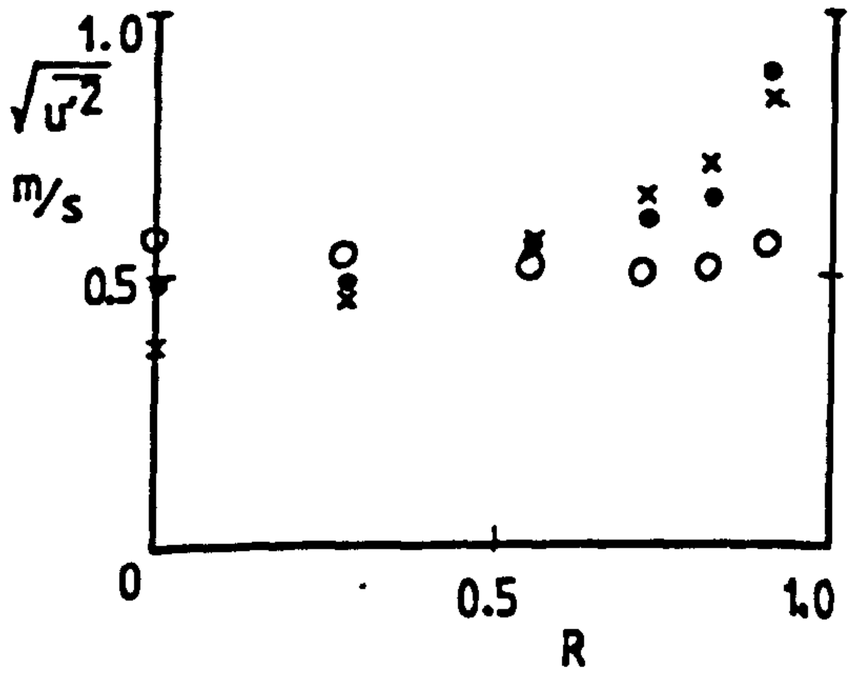

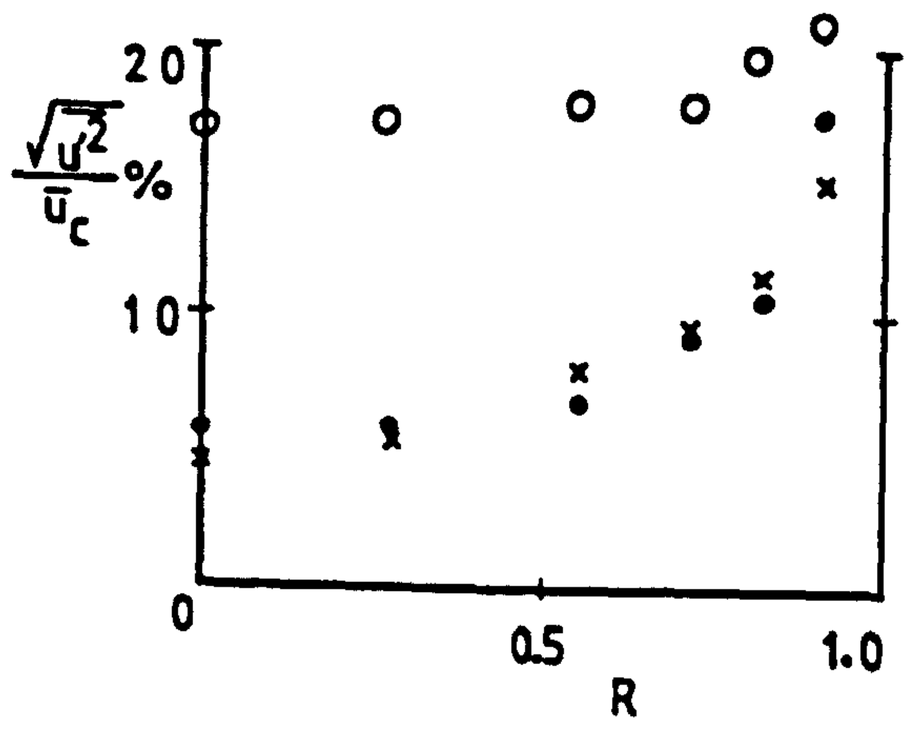

Figure 6.15 Fused alumina; 300–430 μm; loading ratio 2.63; pipe diameter = 23 mm; U_m = 8.49

• air; o solids; × air alone

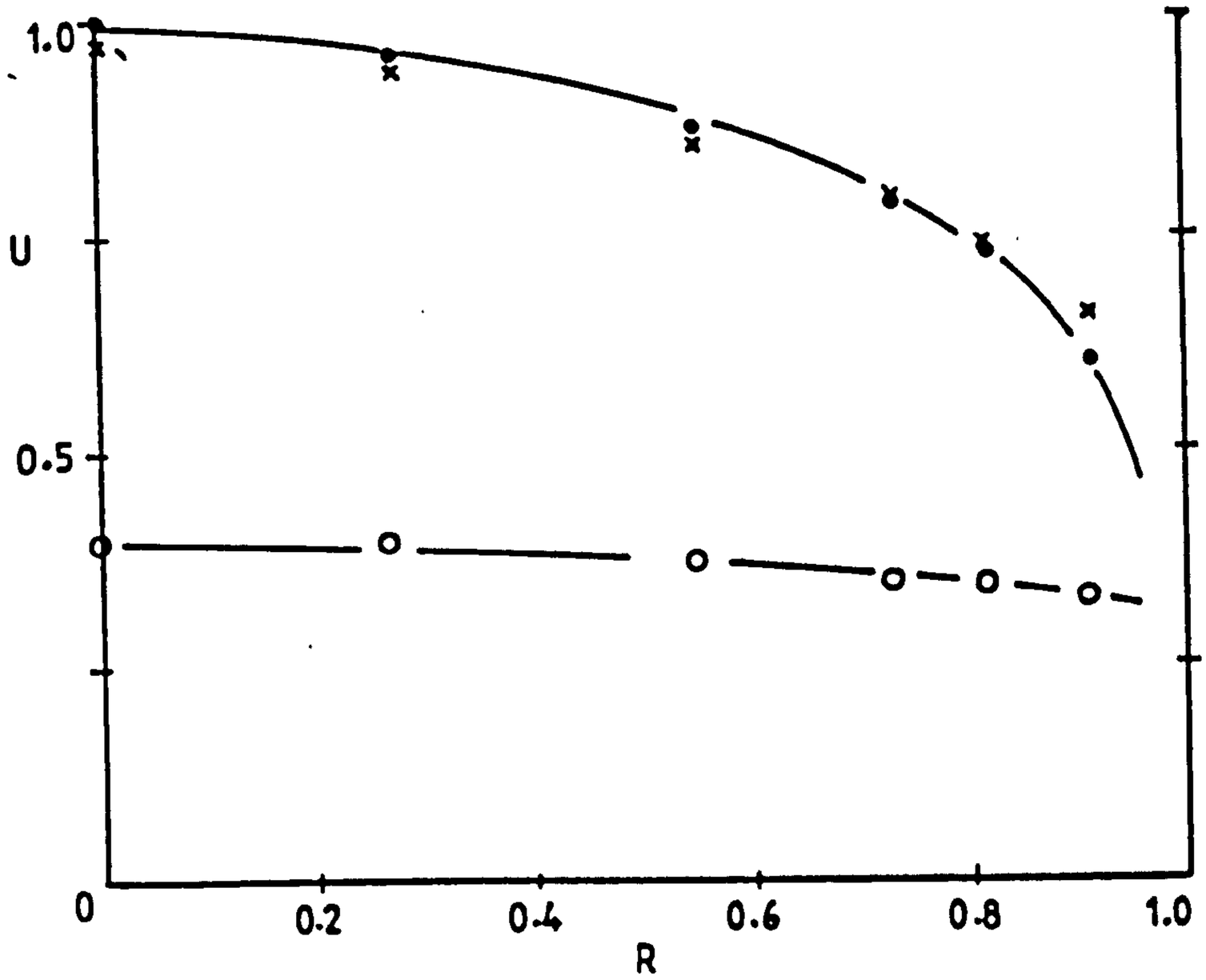

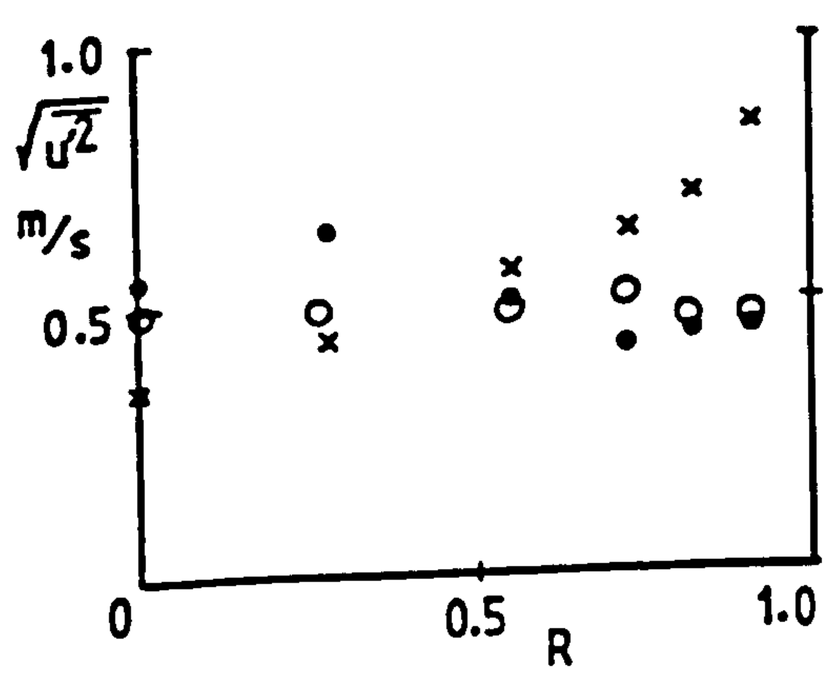

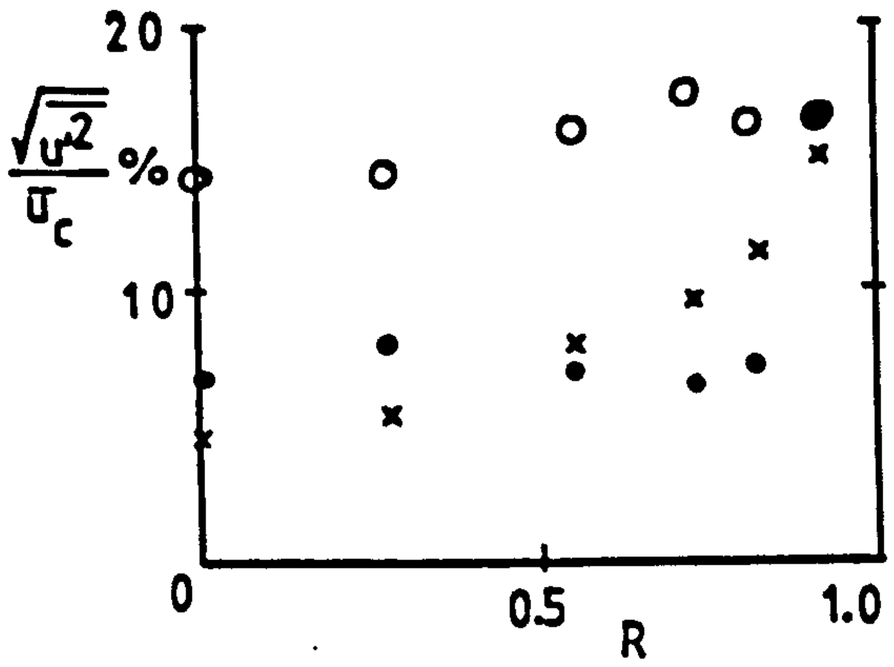

Figure 6.16 Fused alumina, 300-430 μm; loading ratio 4.25; pipe diameter = 22 mm; U_m = 8.31 m/s

• air; o solids; × air alone

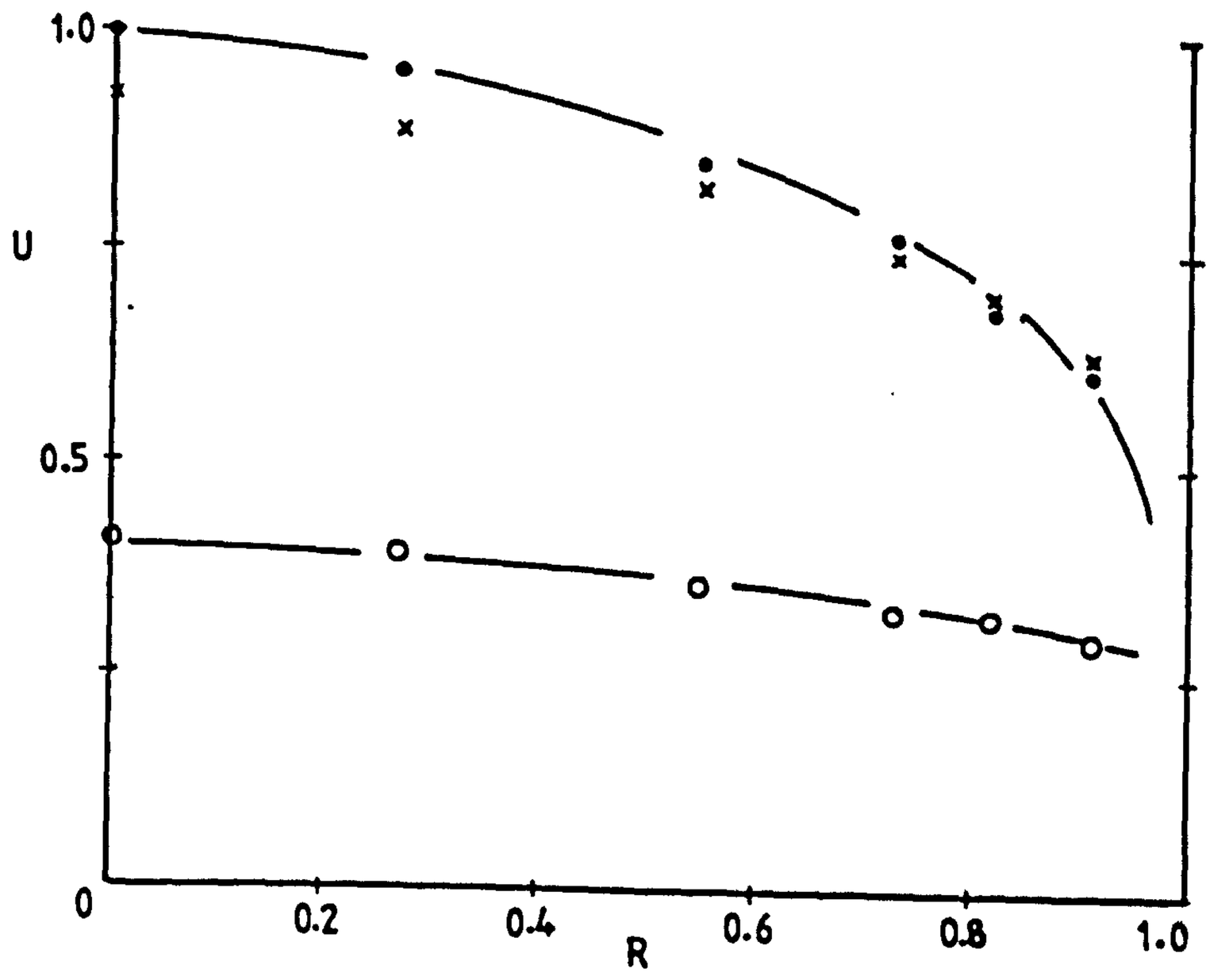

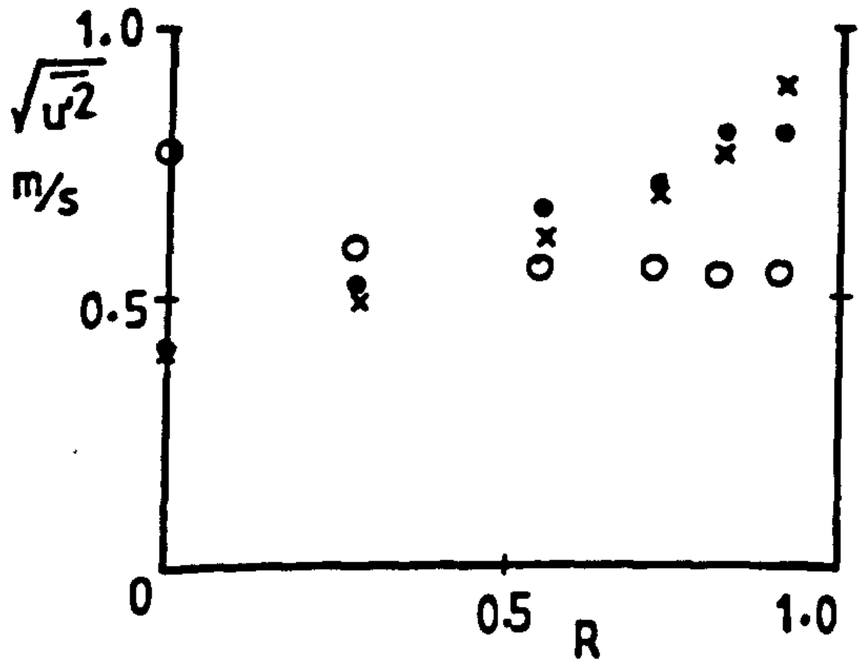

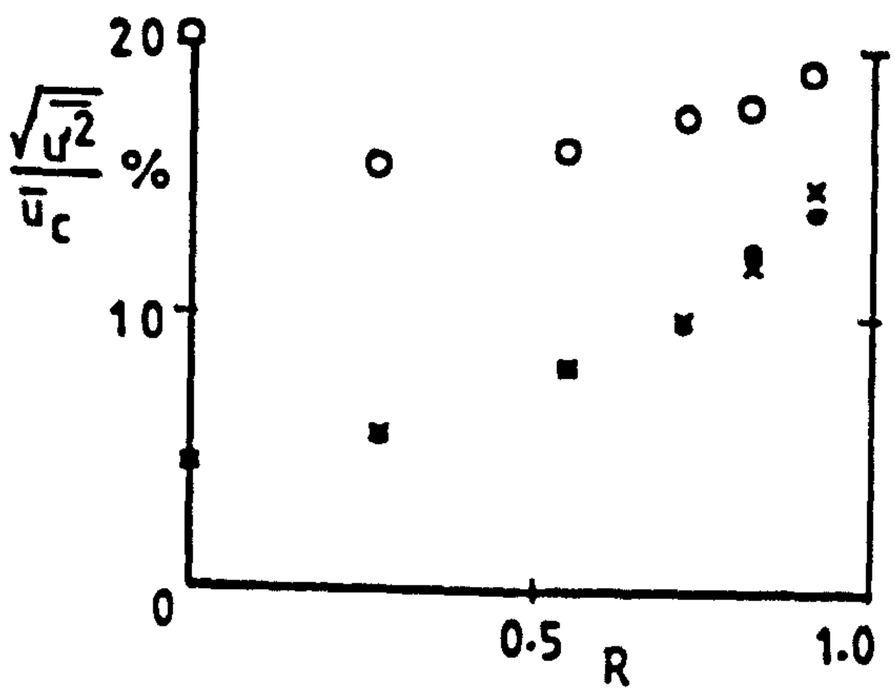

Figure 6.17 Fused alumina, 300-430 μm; loading ratio 1.49; pipe diameter = 22 mm; U_m = 9.45 m/s

• air; o solids; × air alone

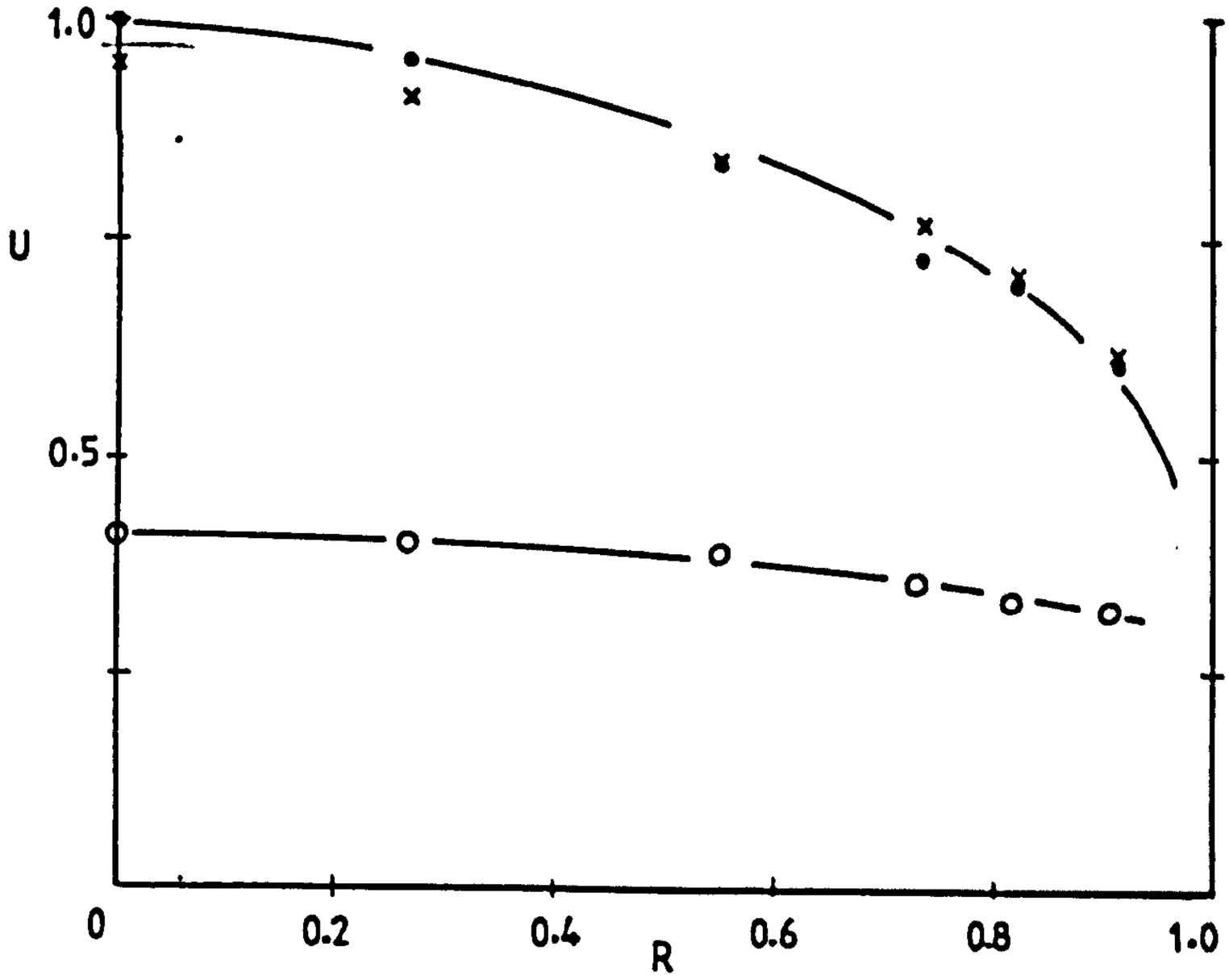

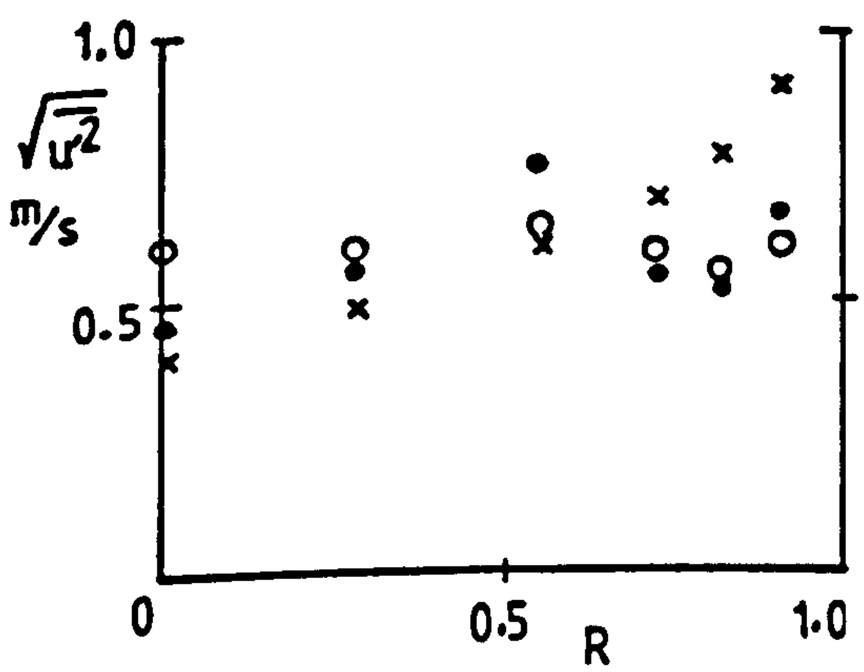

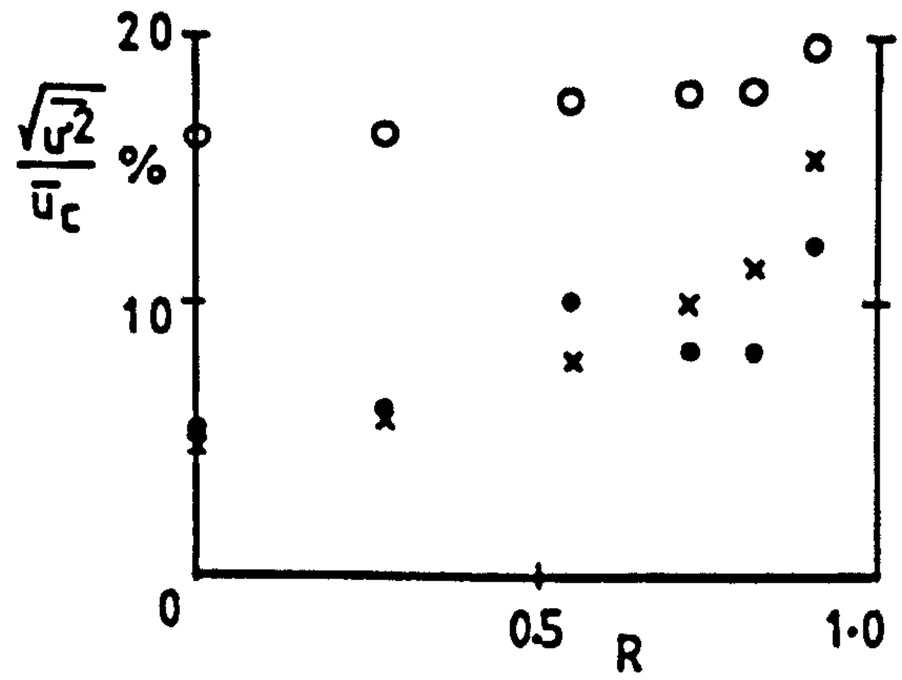

Figure 6.18 Fused alumina, 300-430 μm; loading ratio 2.40; pipe diameter = 22 mm; U_m = 9.26 m/s

• air; o solids; x air alone

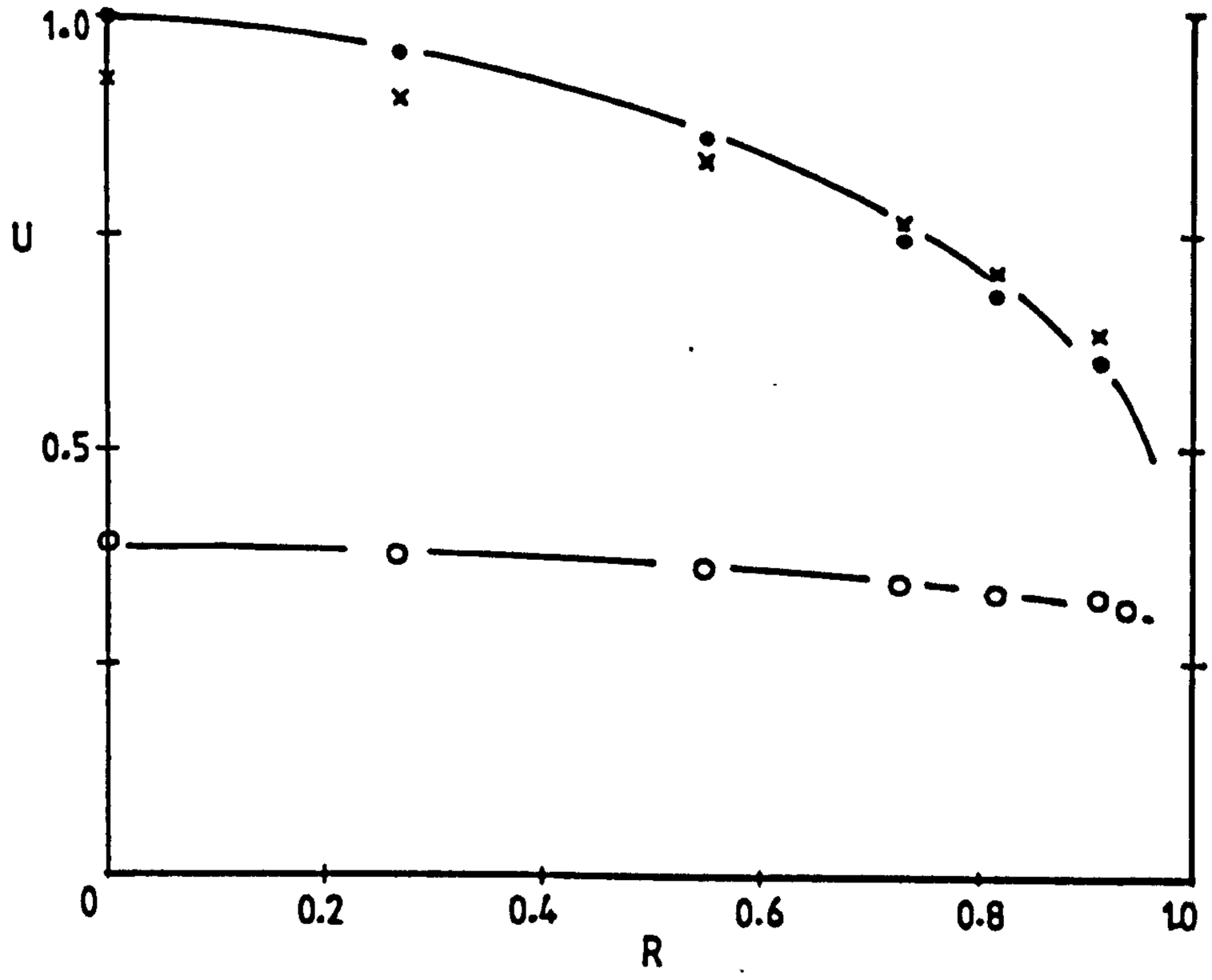

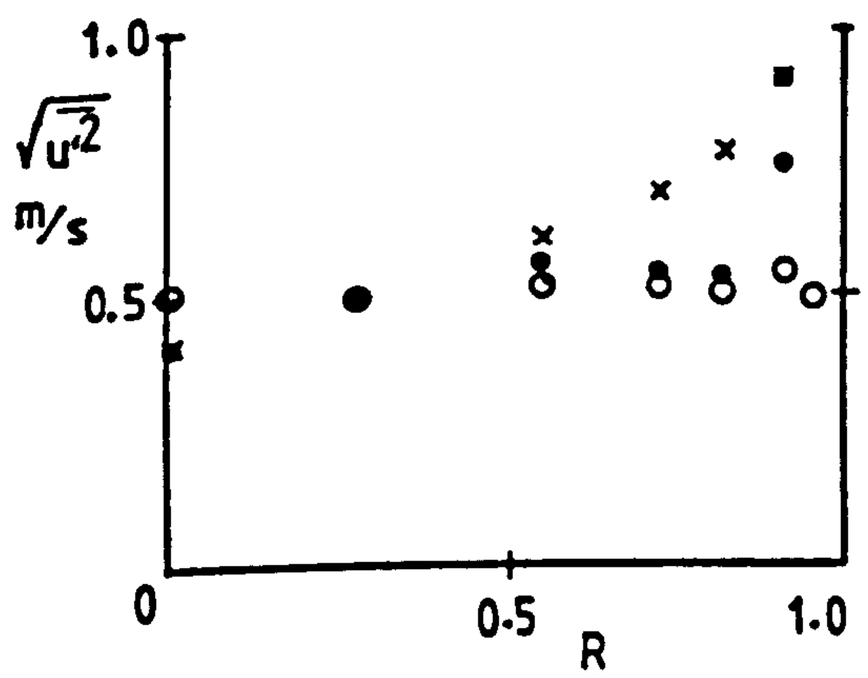

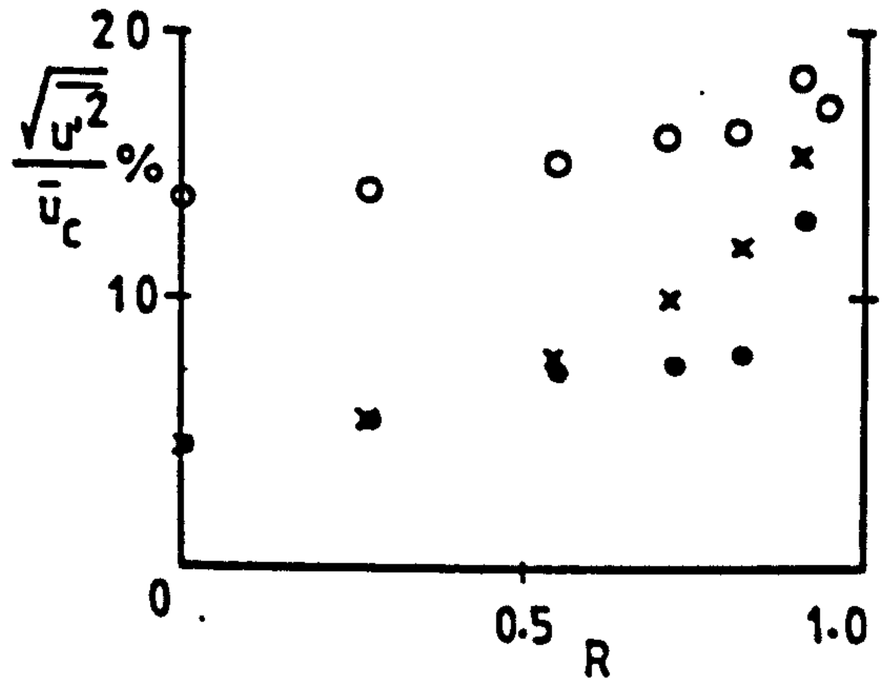

Figure 6.19 Fused alumina, 300–430 μm; loading ratio 3.88; pipe diameter = 22 mm; U_m = 9.40 m/s

• air; o solids; × air alone

pipe diameter mm	solids	pressure drop at orifice mm H_2O	loading ratio	ρ_f kg/m³	μ_f kg/m-s $\times 10^6$	U_m m/s	figure
22	Glass ballotini size 10	12	2.44	1.196	18.20	5.59	6.1
22	"	12	3.73	1.192	18.25	5.93	6.2
22	"	14	2.24	1.199	18.18	6.29	6.3
22	"	14	3.42	1.200	18.15	6.37	6.4
22	"	18	1.99	1.199	18.18	7.08	6.5
22	"	18	3.05	1.199	18.18	7.08	6.6
22	"	18	4.99	1.198	18.30	6.90	6.7
25.8	"	40	0.69	1.196	18.20	8.00	6.8
25.8	"	40	2.0	1.209	18.06	7.95	6.9
25.8	"	40	5.65	1.213	18.00	7.26	6.10
31.4	"	50	0.61	1.186	18.33	5.71	6.11
31.4	"	50	1.81	1.180	18.40	5.38	6.12
31.4	"	50	5.03	1.179	18.41	5.54	6.13
22	Fused alumina	25	1.64	1.192	18.25	8.72	6.14
22	"	25	2.63	1.188	18.30	8.49	6.15
22	"	25	4.25	1.192	18.25	8.31	6.16
22	"	30	1.49	1.190	18.28	9.45	6.17
22	"	30	2.40	1.188	18.30	9.26	6.18
22	"	30	3.88	1.188	18.30	9.40	6.19

Table 6.1 Experimental details for the results shown in figures 6.1 to 6.19

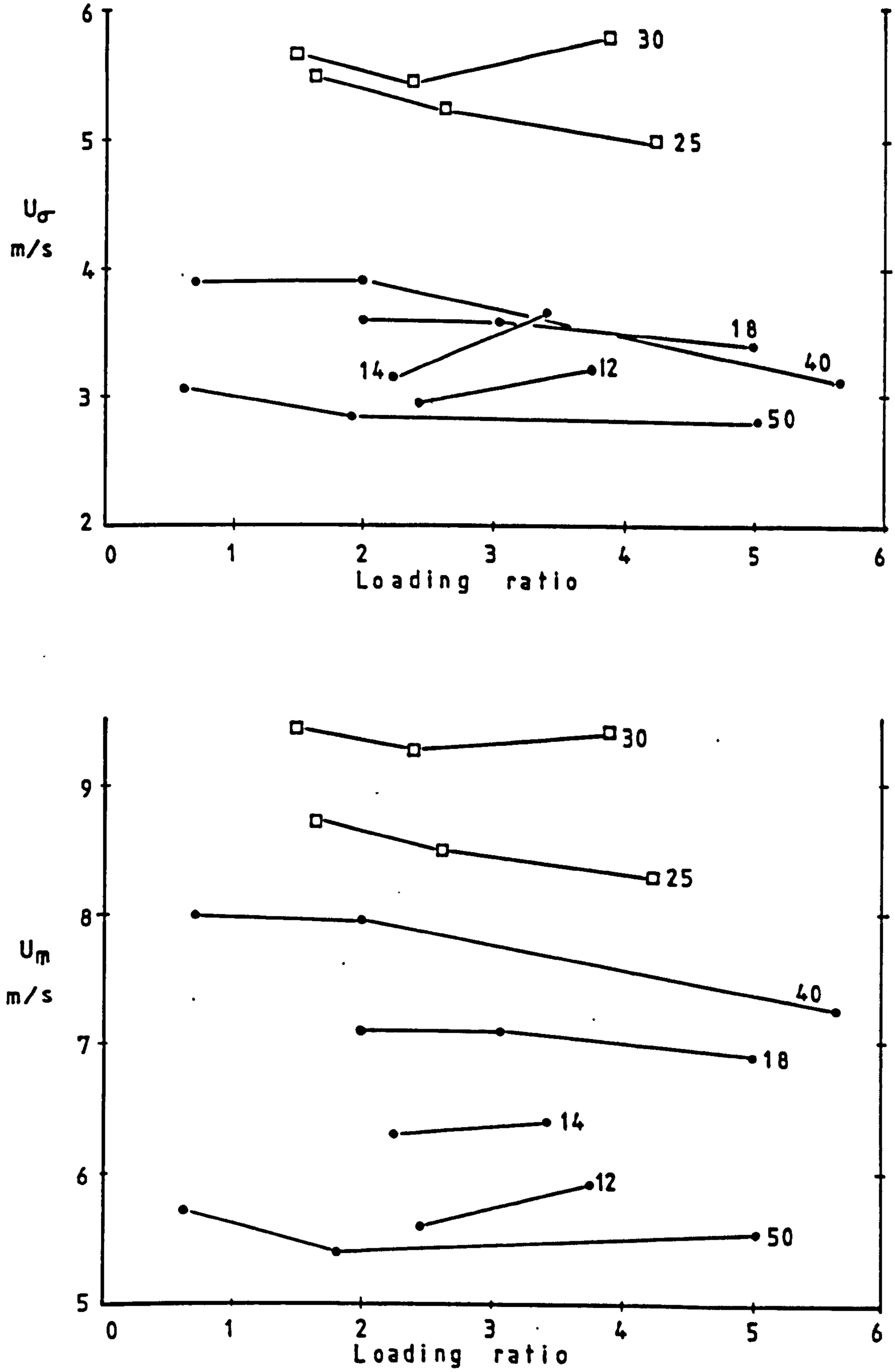

Figure 6.20 Variation of particle slip velocity and air velocity with loading ratio at the pipe centreline

• glass ballotini size 10; □ brown fused alumina

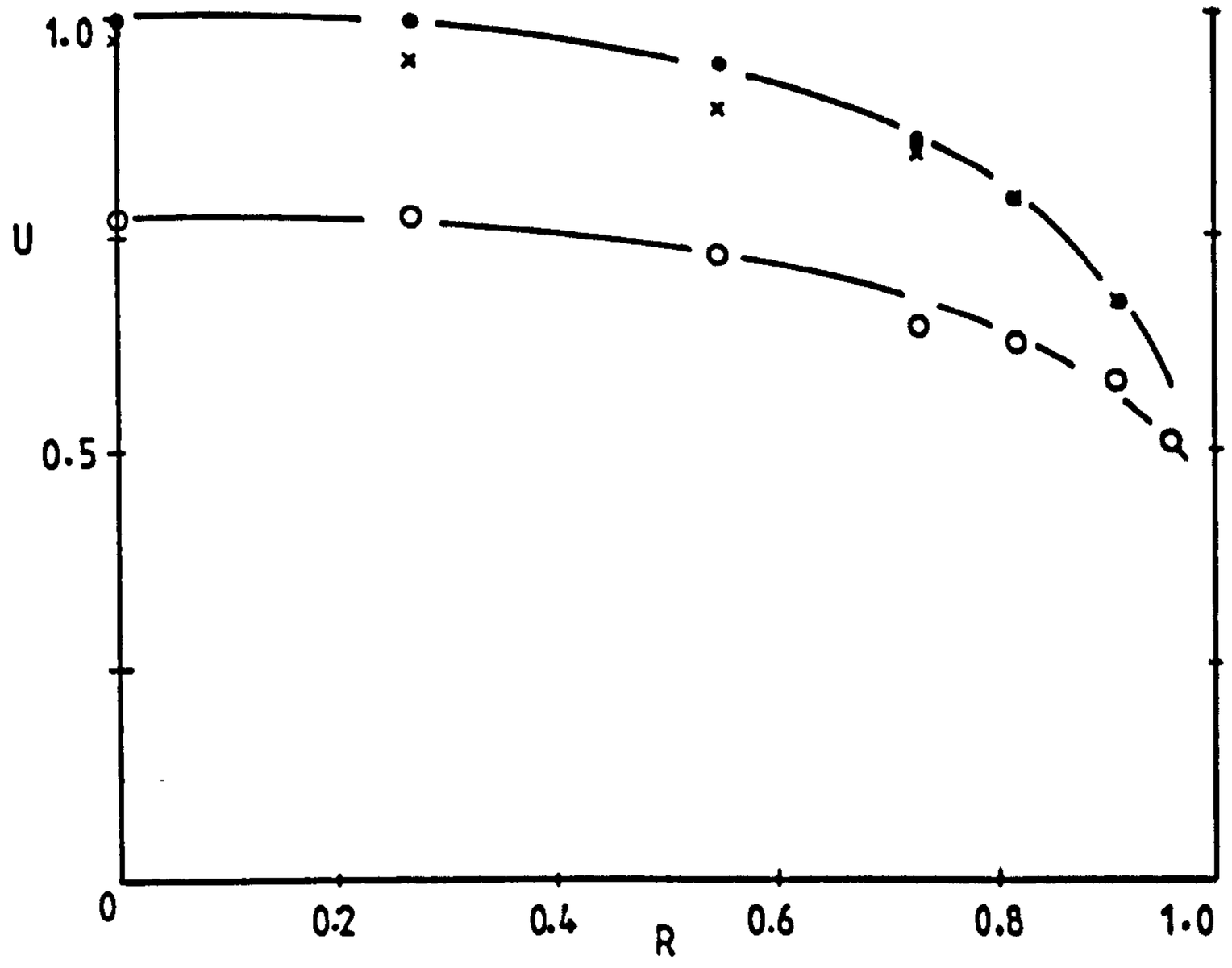

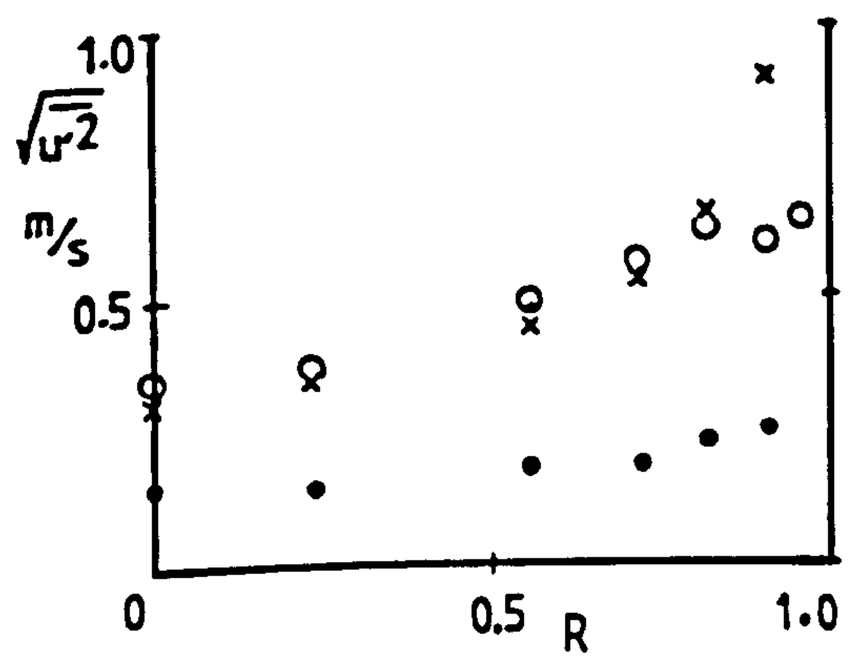

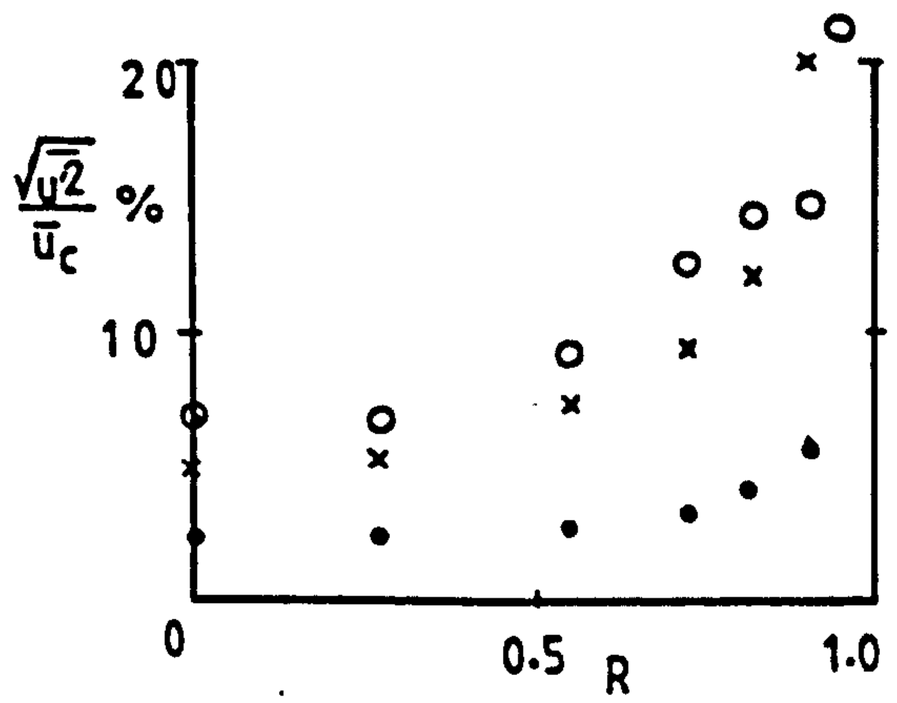

Figure 6.21 Glass ballotini, 90-135 μm; loading ratio 3.07; pipe diameter = 22 mm; U_m = 6.90 m/s

• air; o solids; × air alone

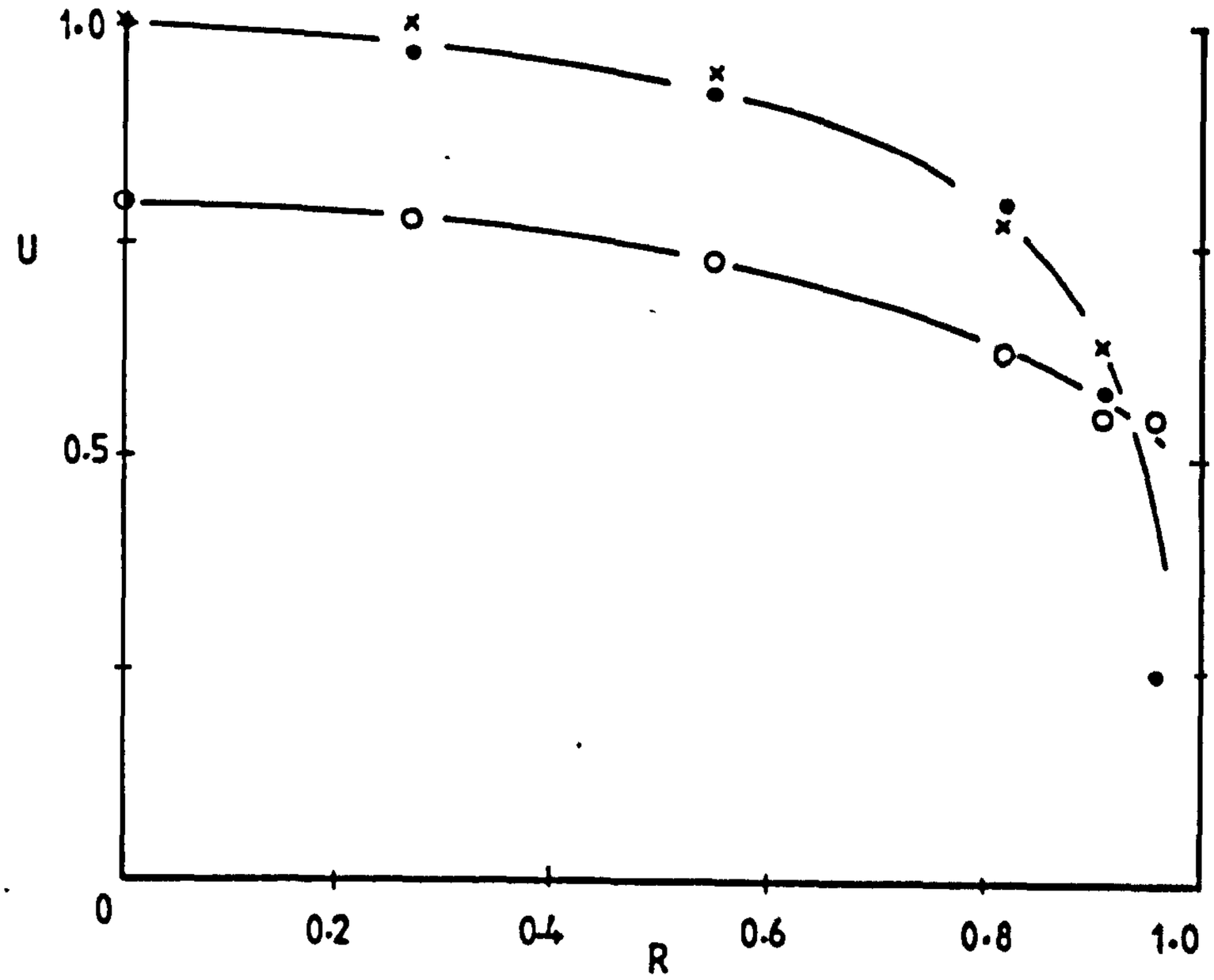

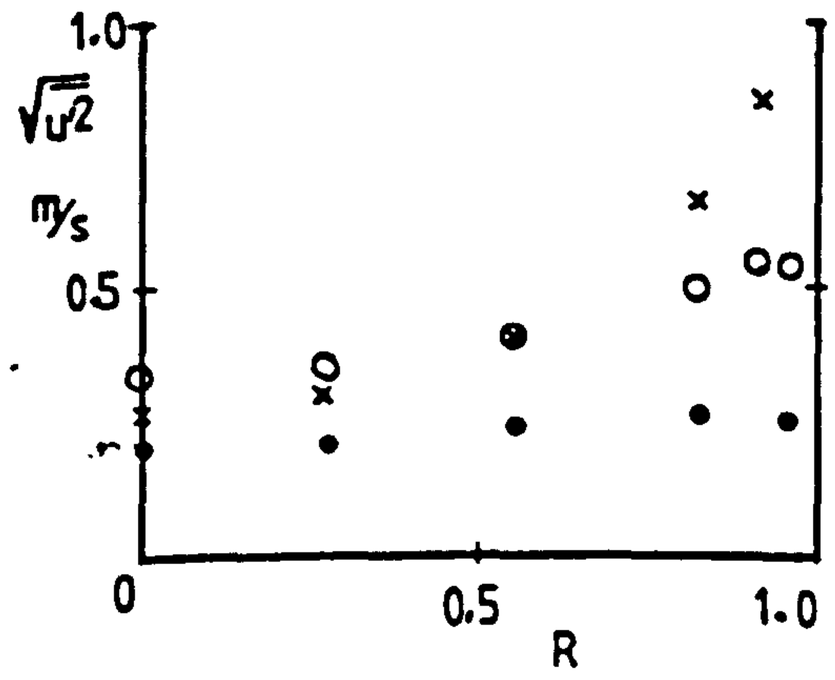

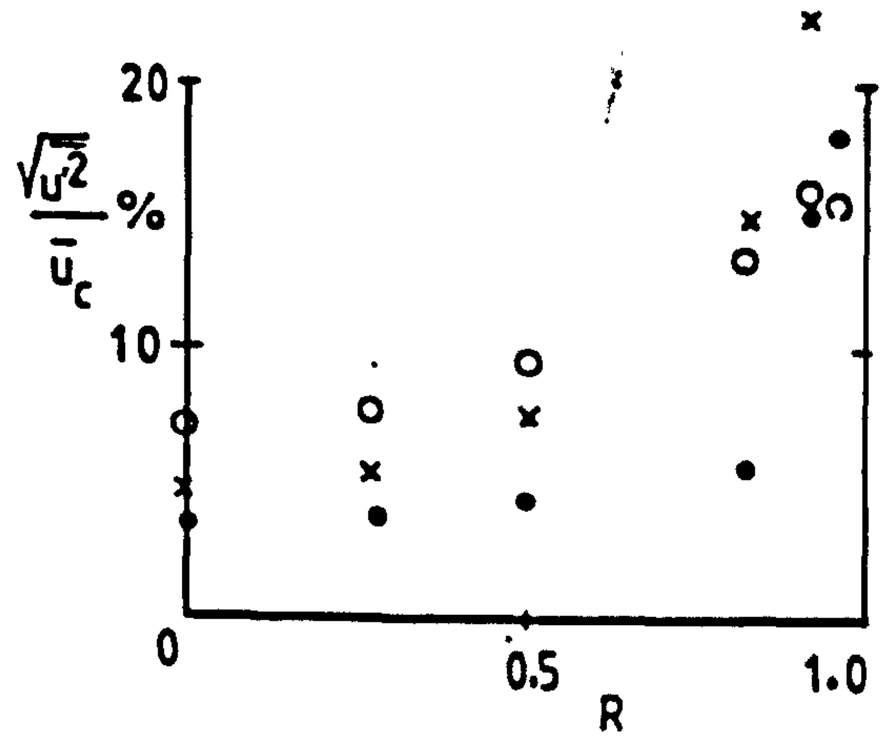

Figure 6.22 Glass ballotini, 90-135 μm; loading ratio 5.64; pipe diameter = 22 mm; U_m = 5.91 m/s

• air; o solids; × air alone

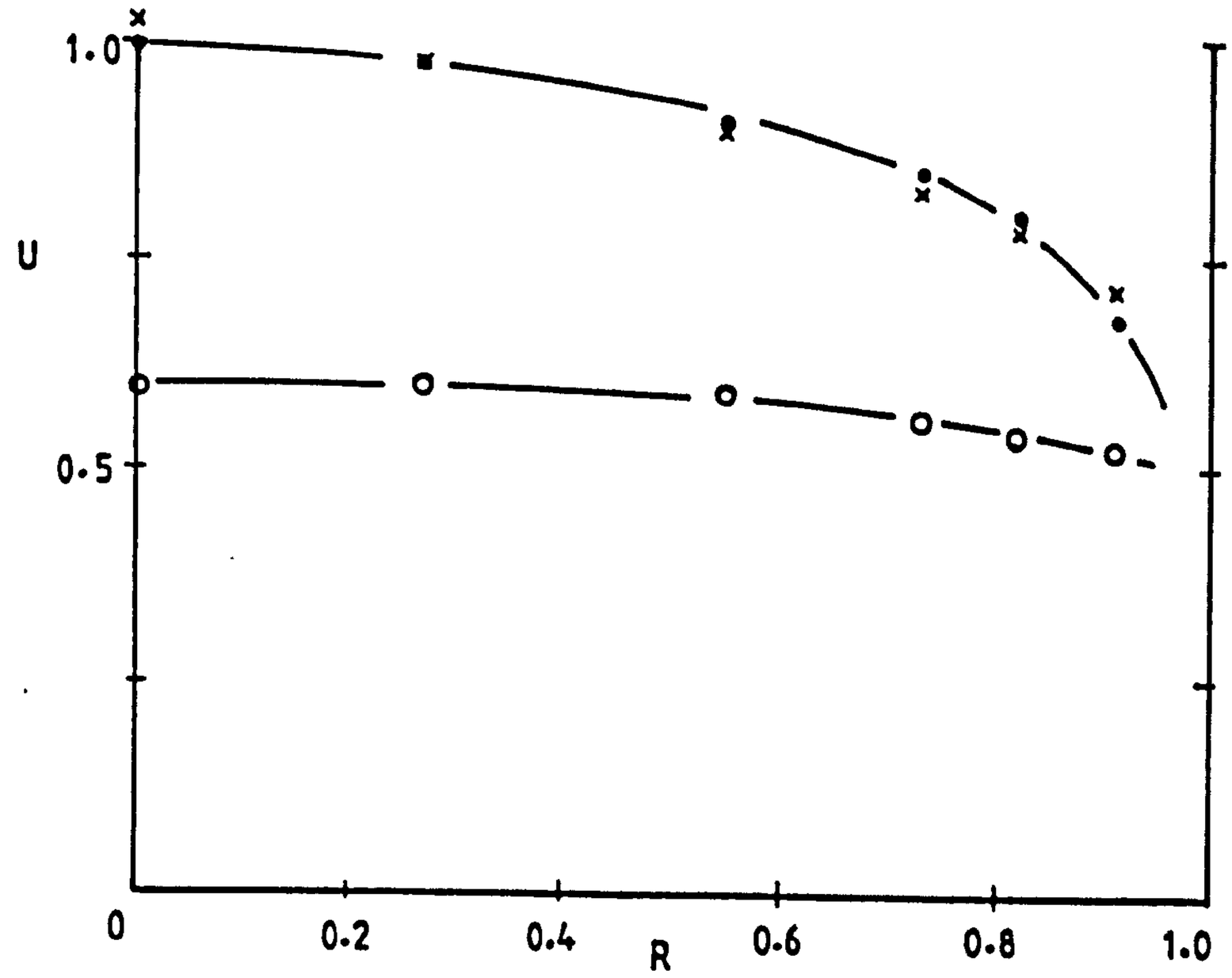

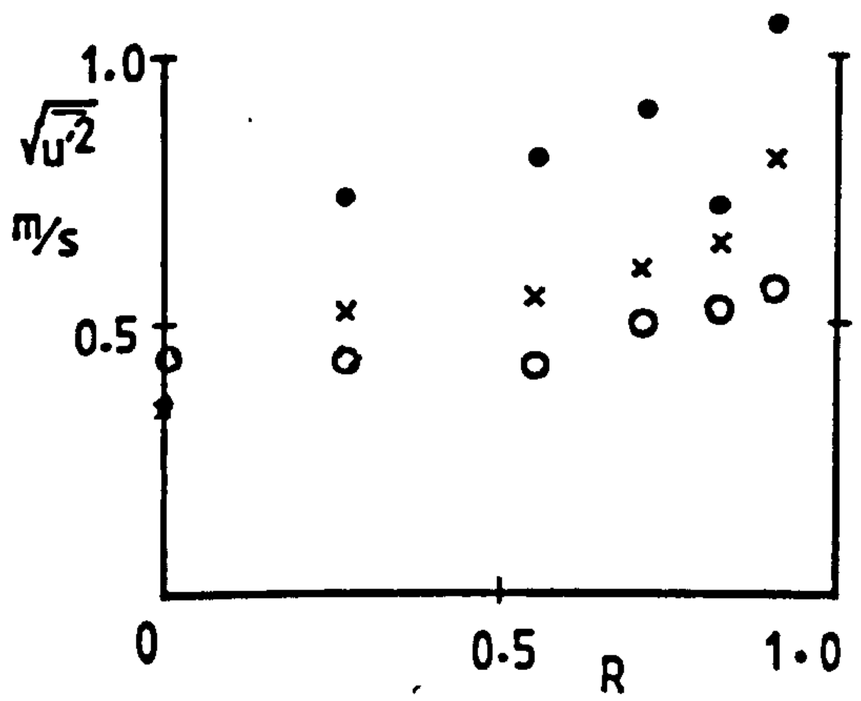

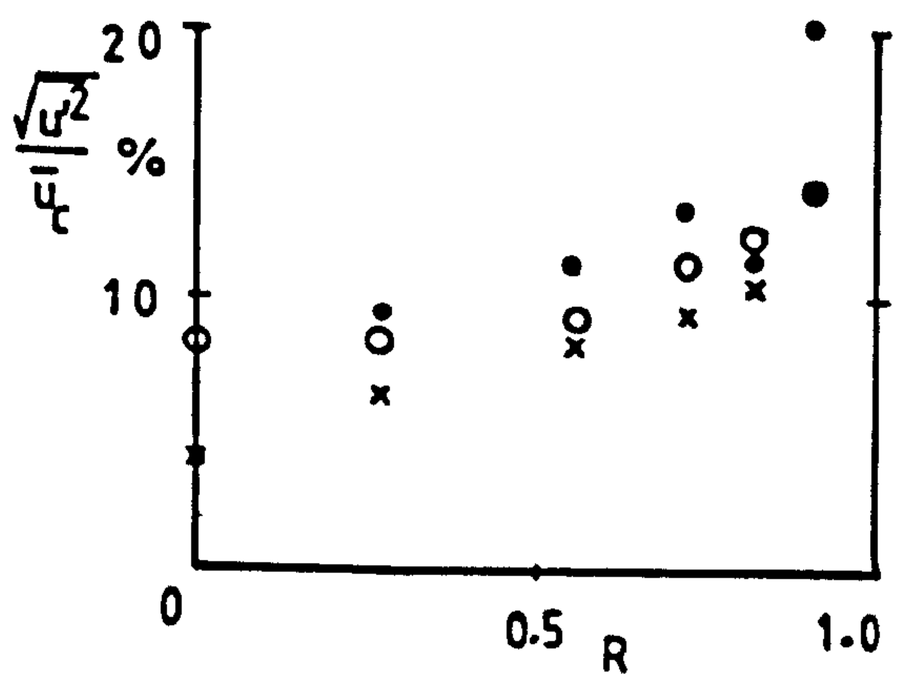

Figure 6.23 Glass ballotini, 210-325 μm; loading ratio 4.22; pipe diameter = 22 mm; U_m = 7.79 m/s

• air; o solid; x air alone

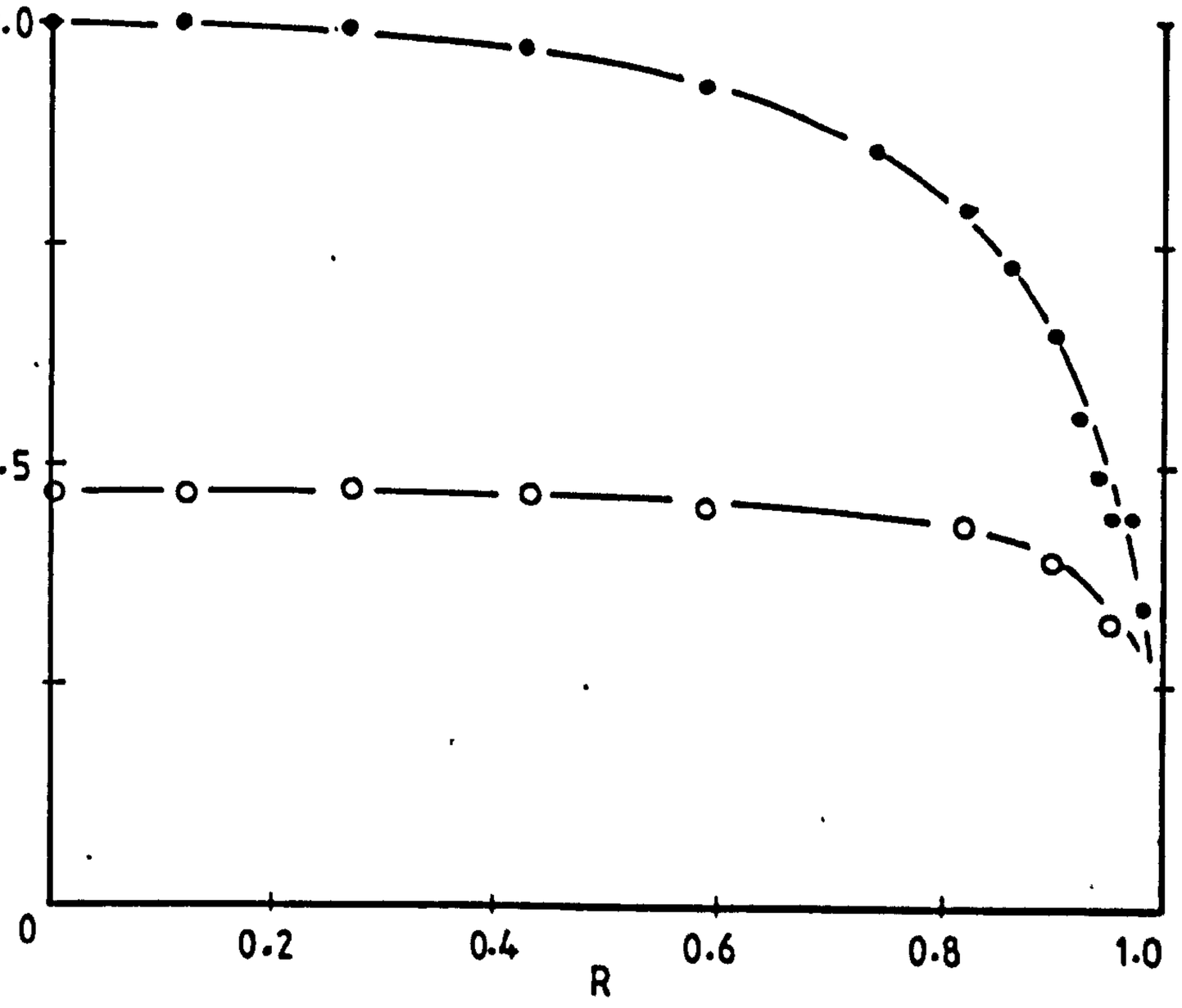

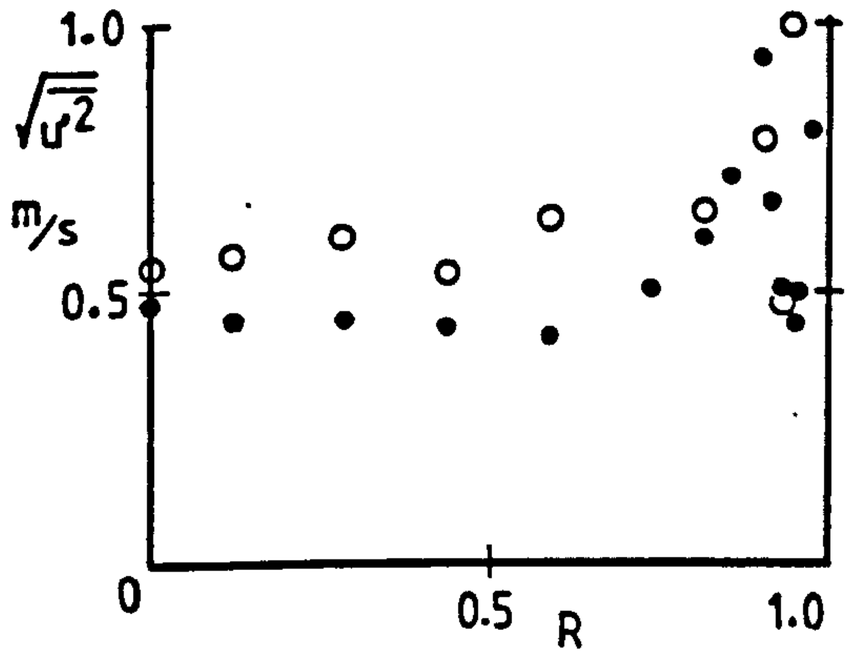

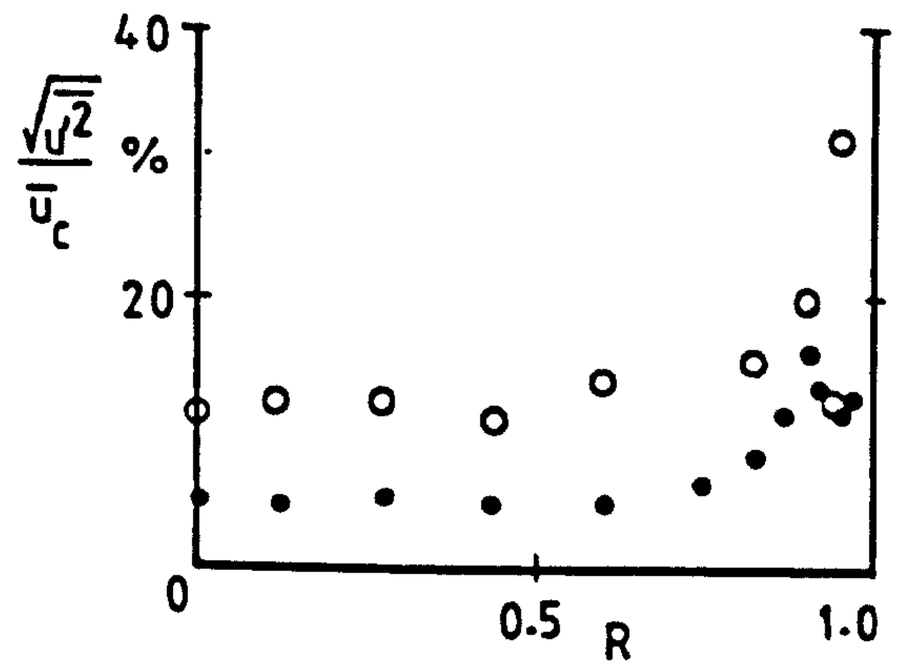

Figure 6.24 Glass ballotini, 210-325 μm; loading ratio 4.62; pipe diameter = 25.8 mm; U_m = 9.14 m/s

• air; o solids; × air alone

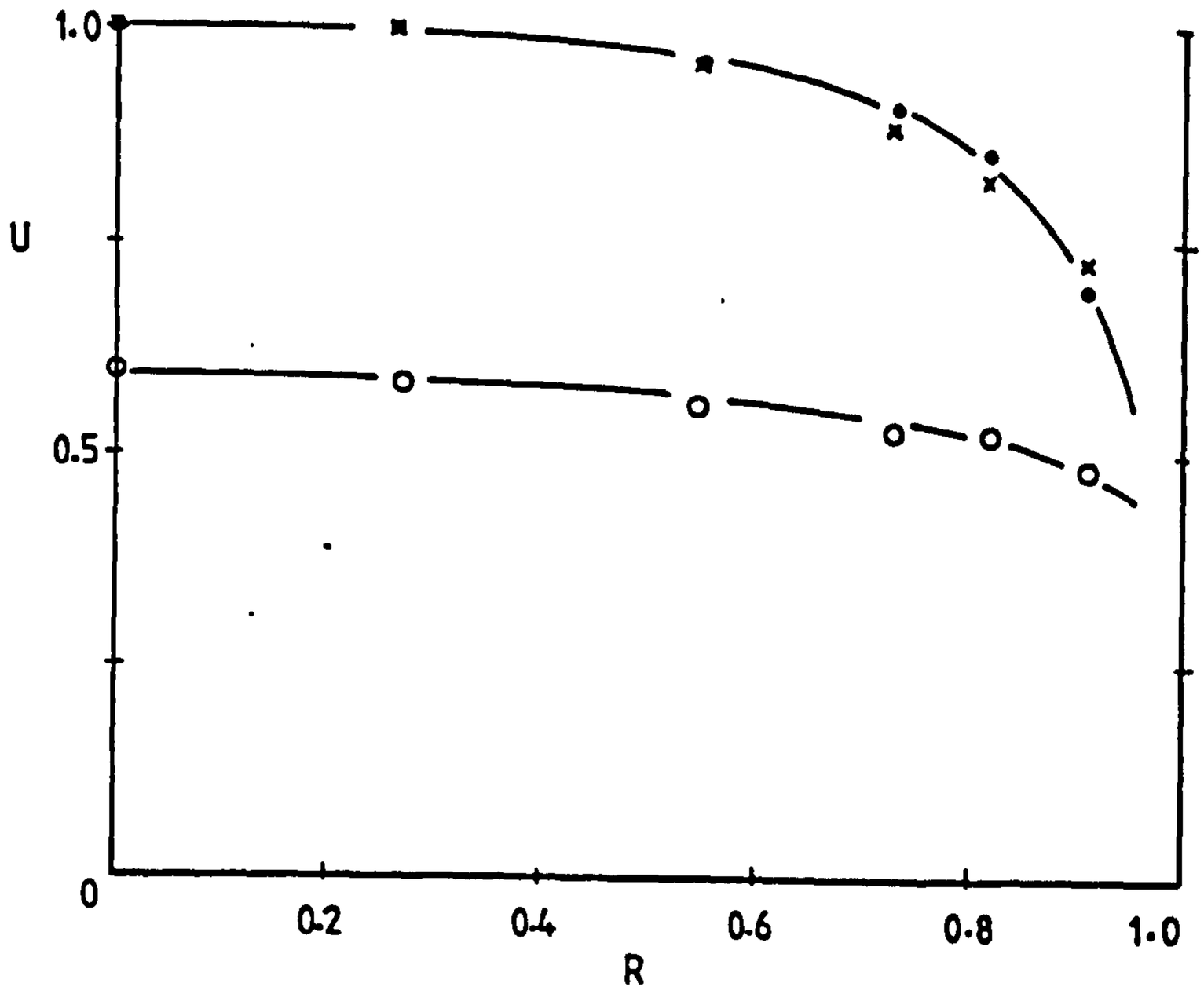

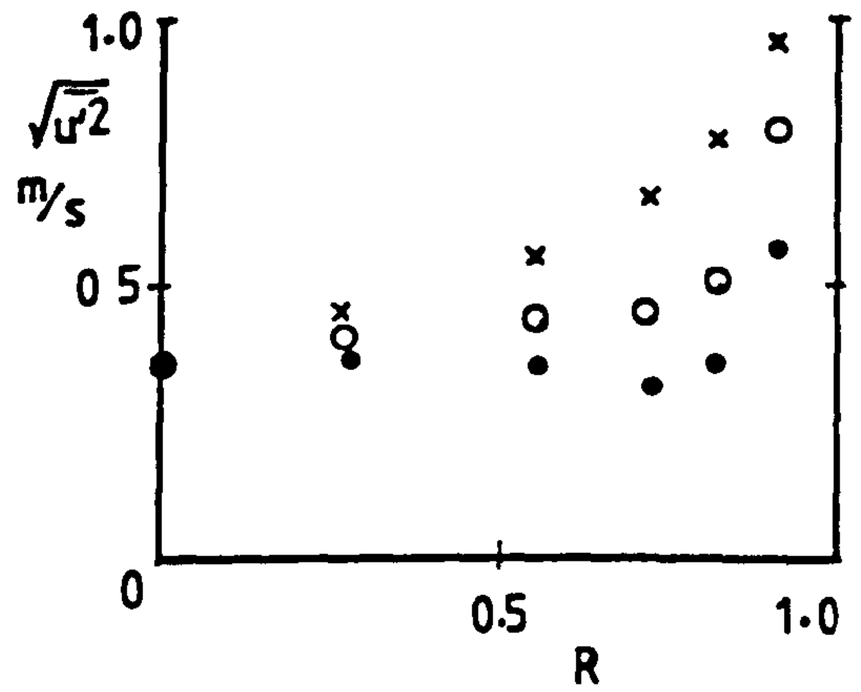

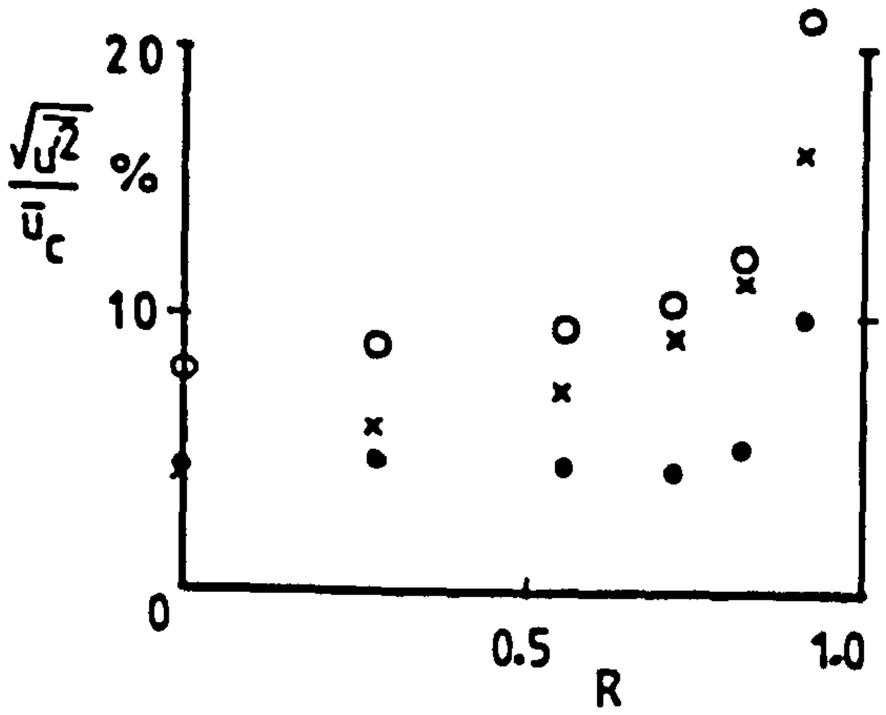

Figure 6.25 Glass ballotini; 210-325 μm; loading ratio 6.80; pipe diameter 22 mm; U_m = 8.06 m/s

• air; o solids; × air alone

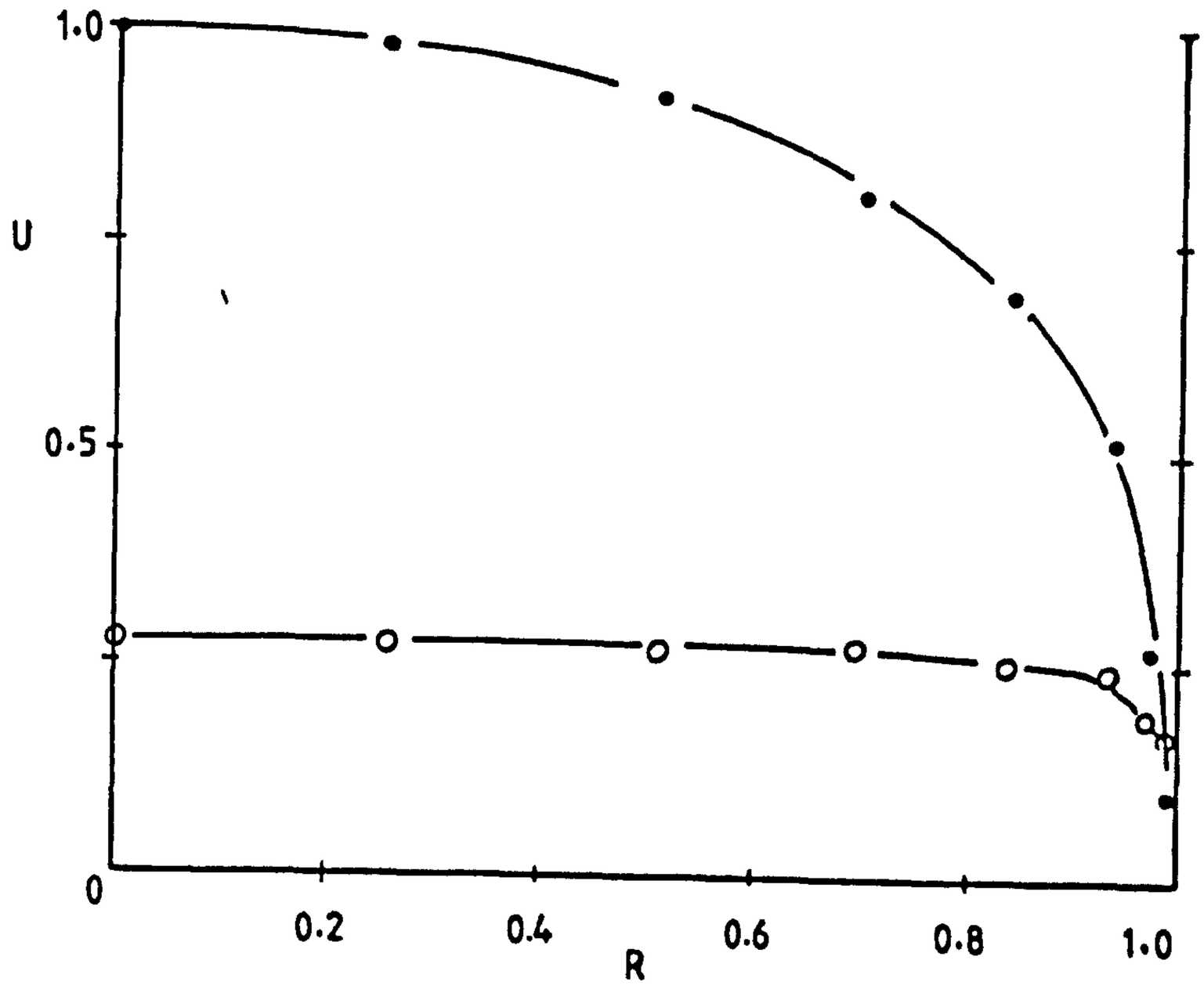

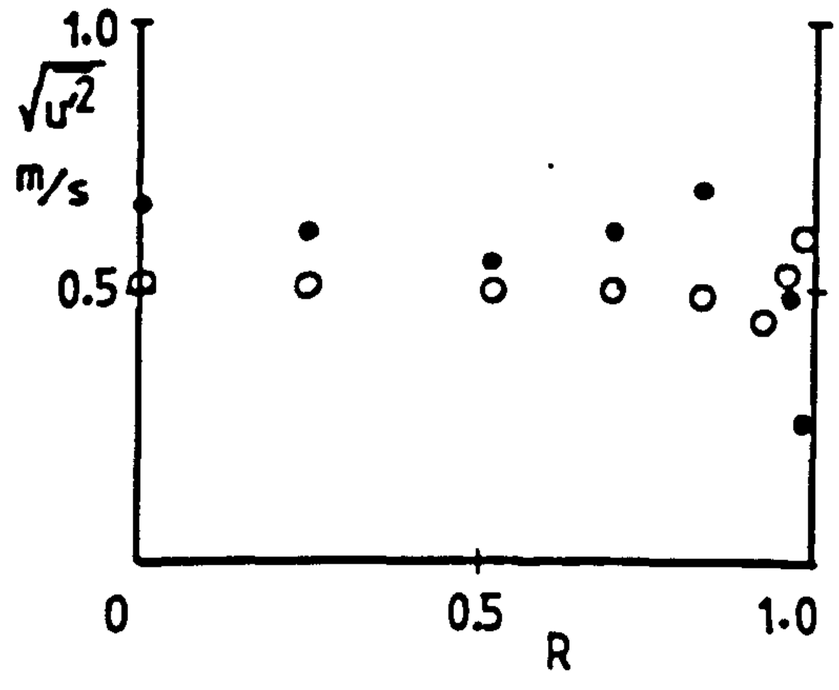

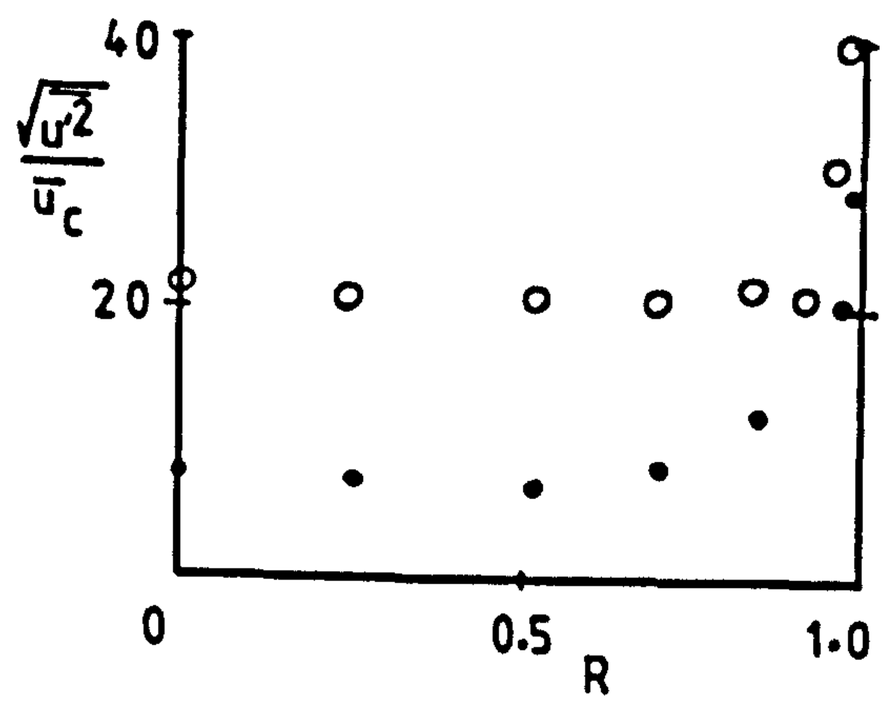

Figure 6.26 Glass ballotini, 440-530 μm; loading ratio 3.29; pipe diameter = 31.4 mm; U_m = 8.82 m/s

• air; o solids; × air alone

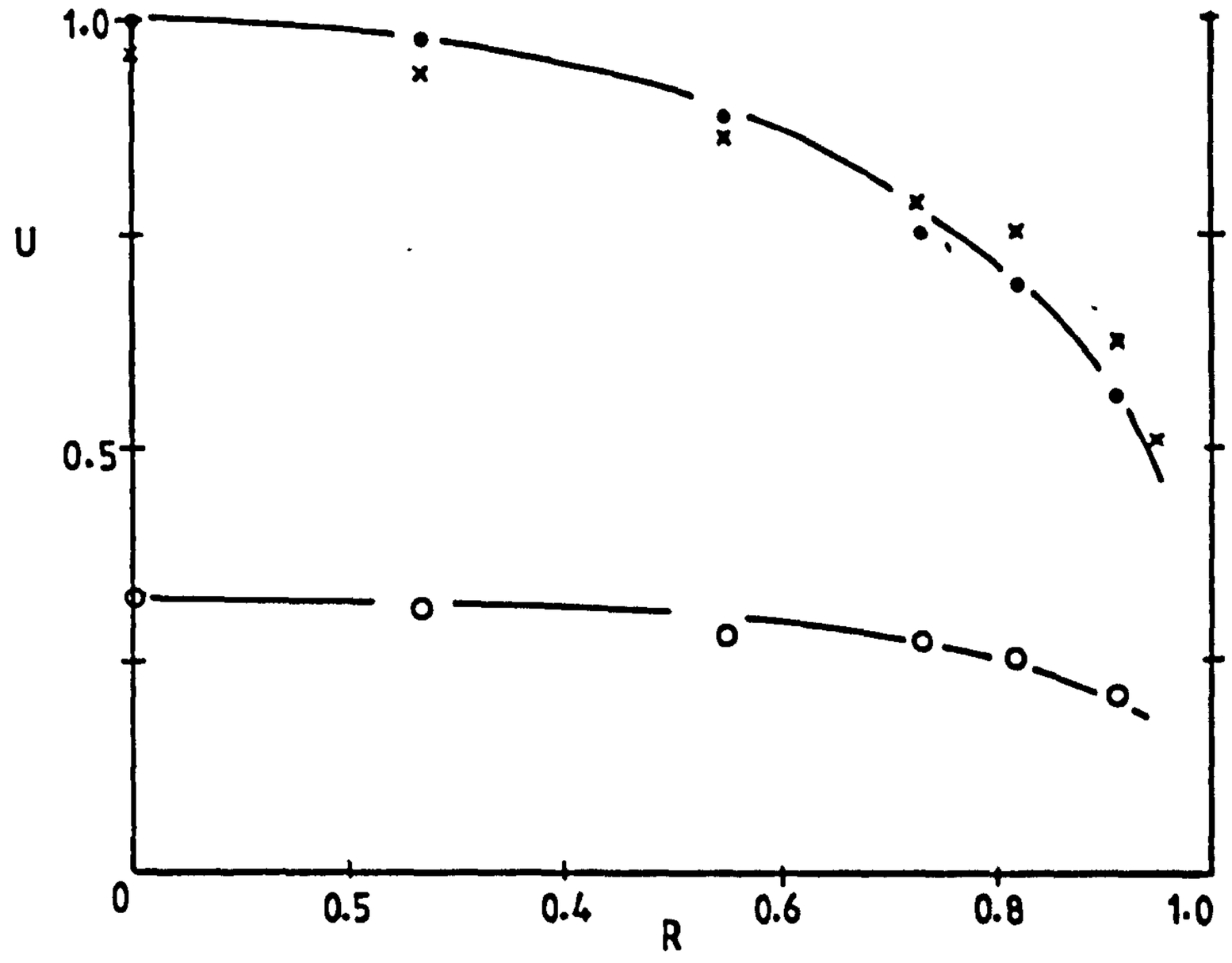

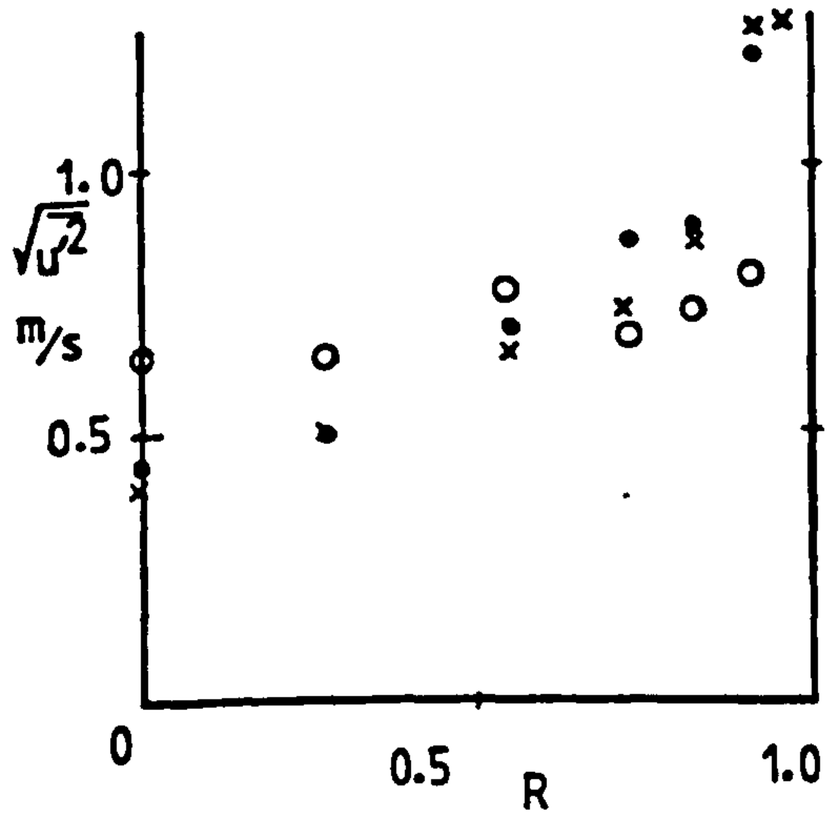

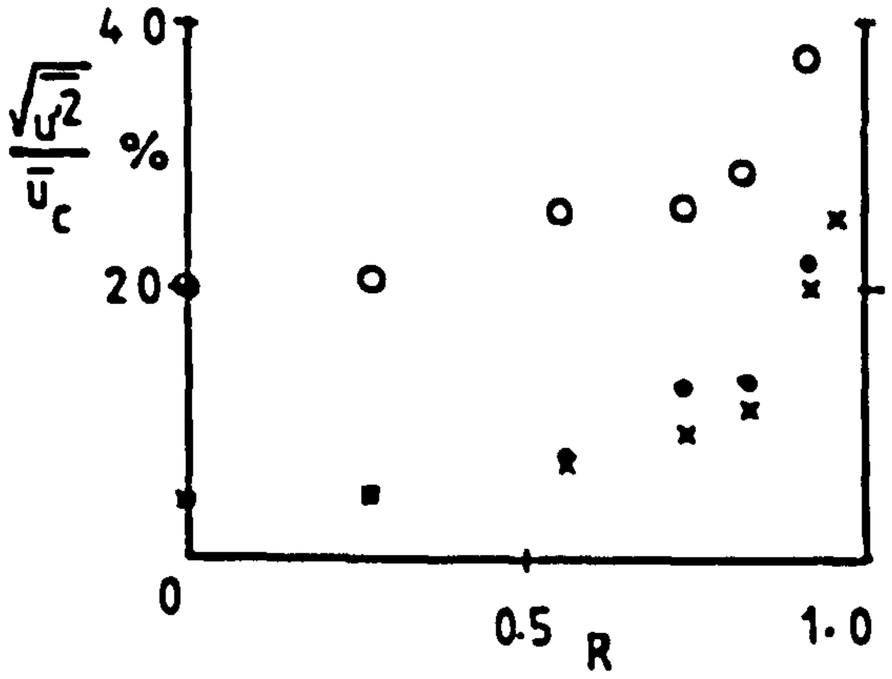

Figure 6.27 Glass ballotini, 440-530 μm; loading ratio 3.41; pipe diameter = 22 mm; U_m = 9.97 m/s.

• air; o solids; x air alone

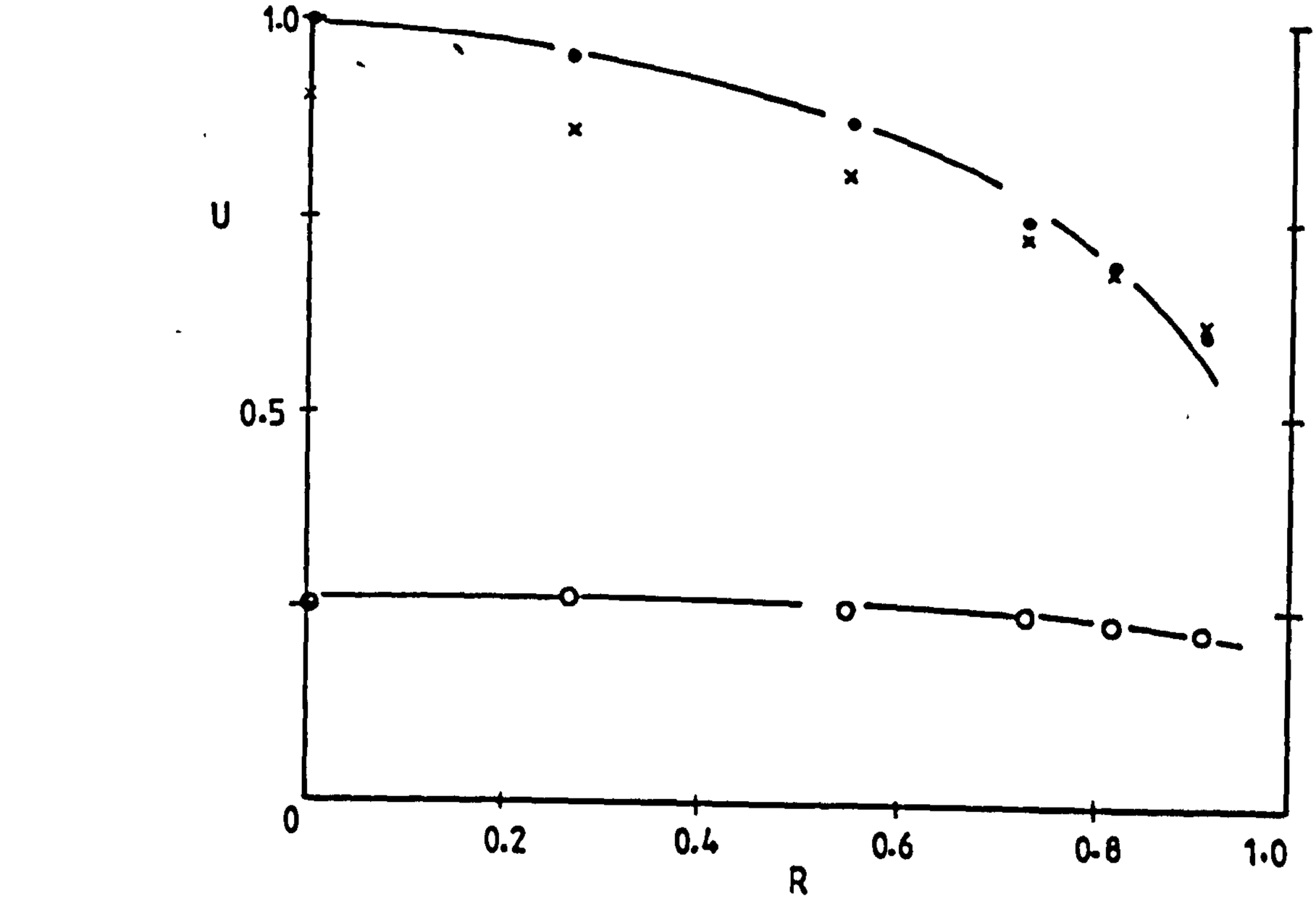

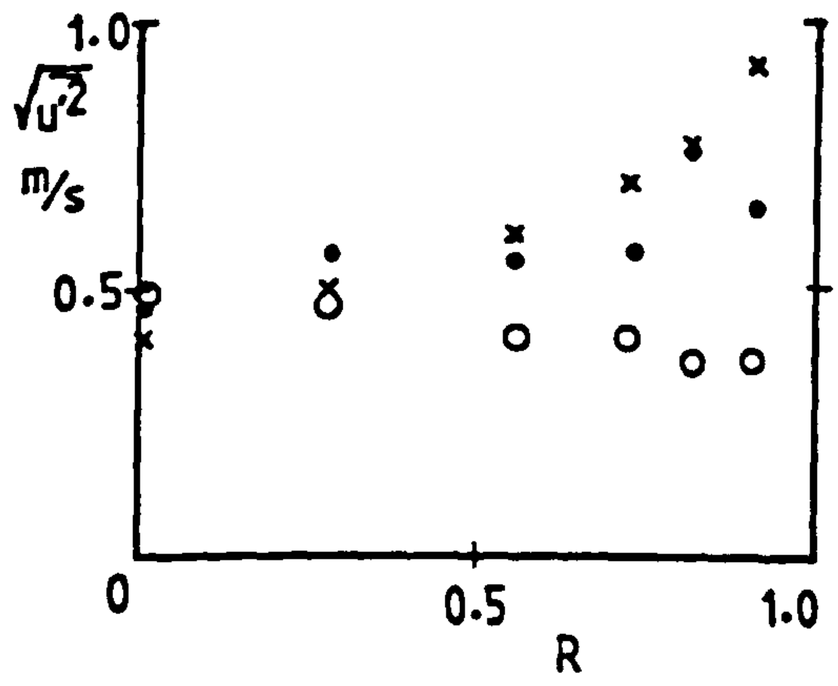

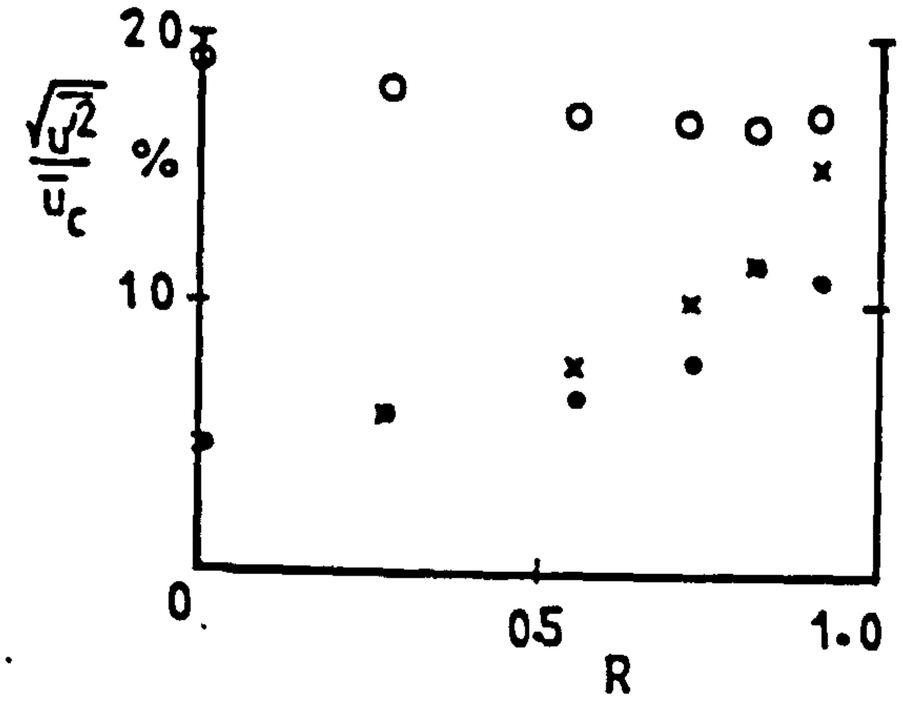

Figure 6.28 Glass ballotini, 440-530 μm; loading ratio 3.67; pipe diameter = 22 mm; U_m = 9.74 m/s.

• air; o solids; x air alone

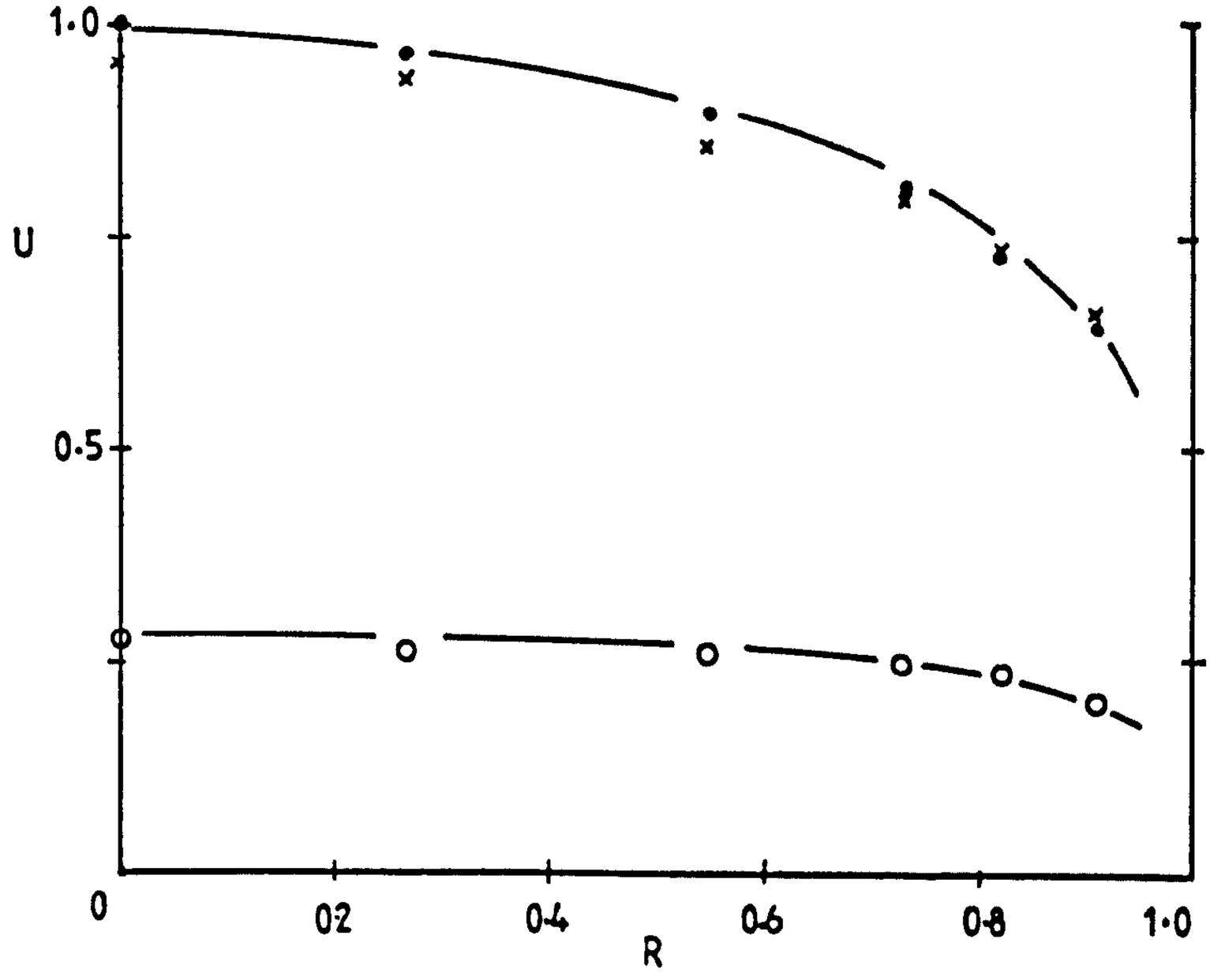

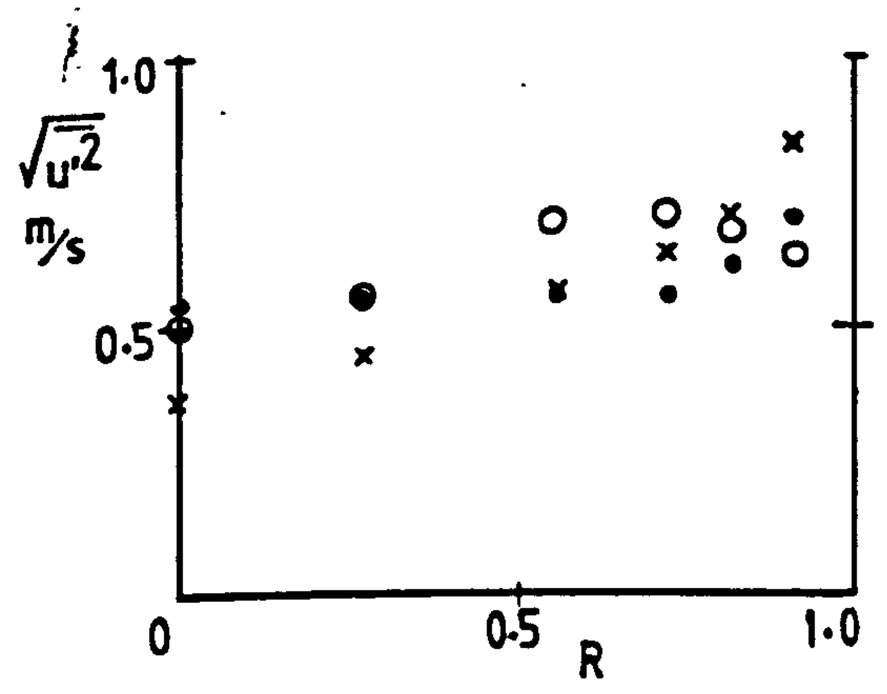

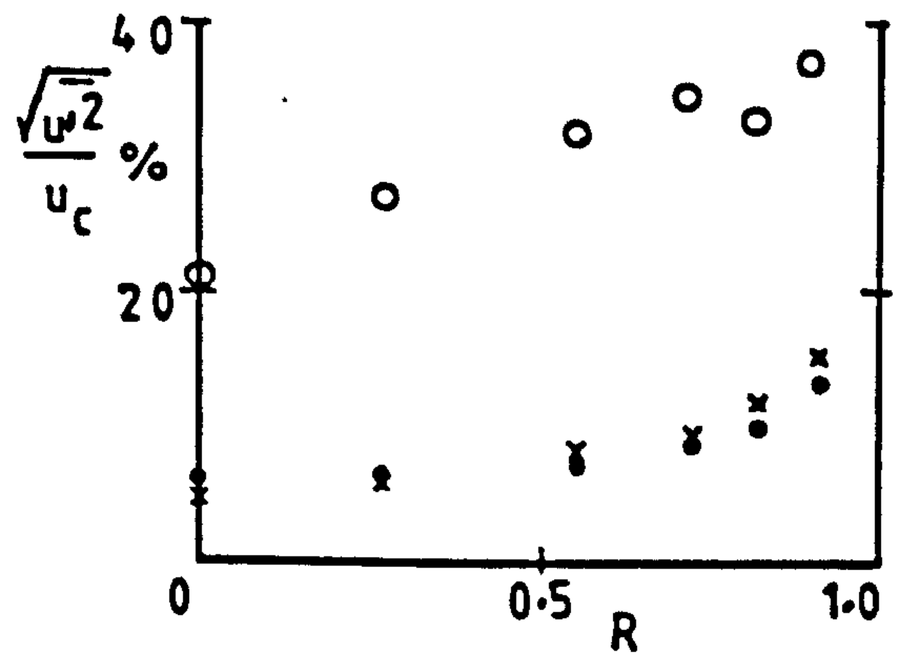

Figure 6.29 Glass ballotini, 440-530 μm; loading ratio 4.02; pipe diameter = 22 mm; U_m = 8.37 m/s

• air; o solids; × air alone

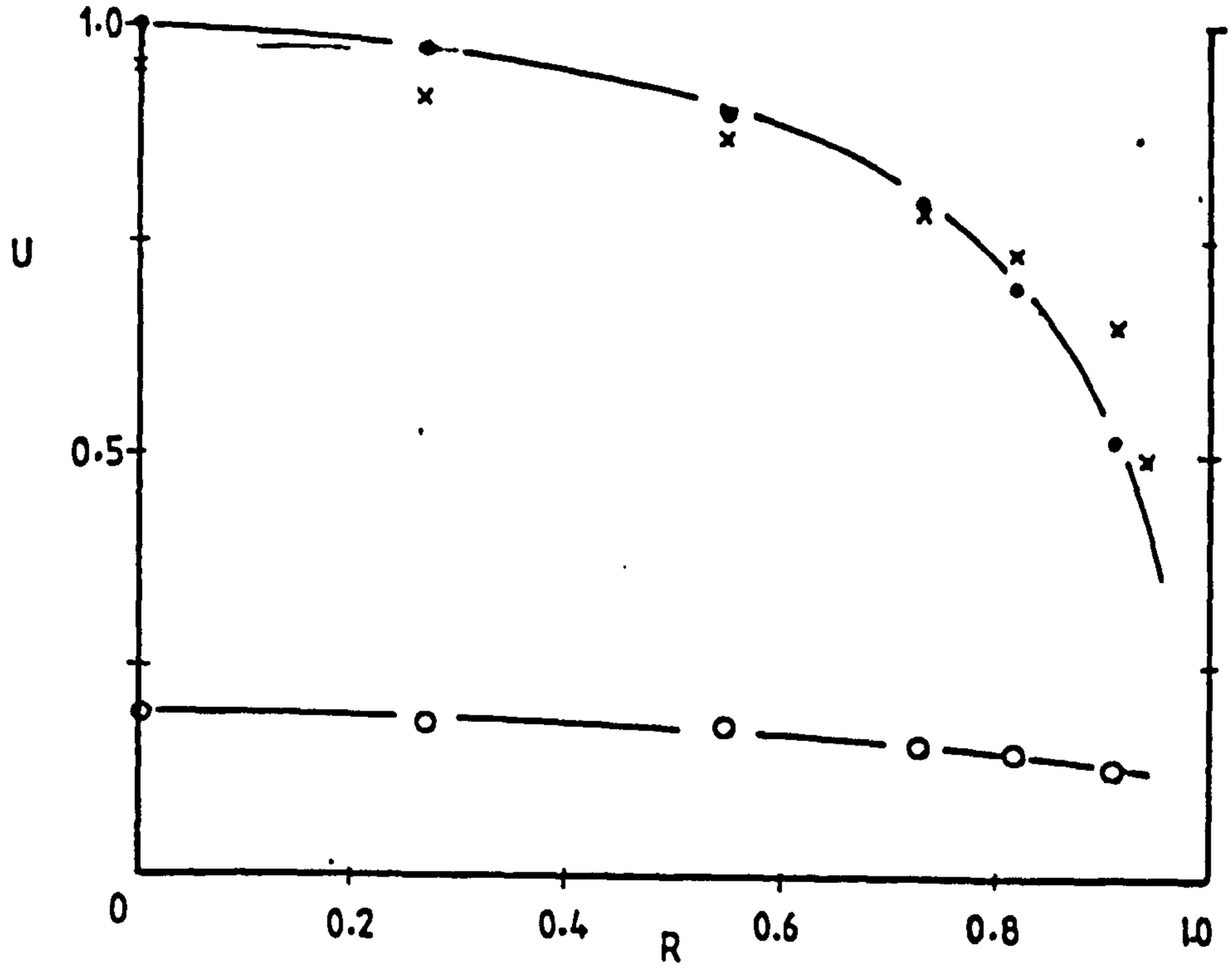

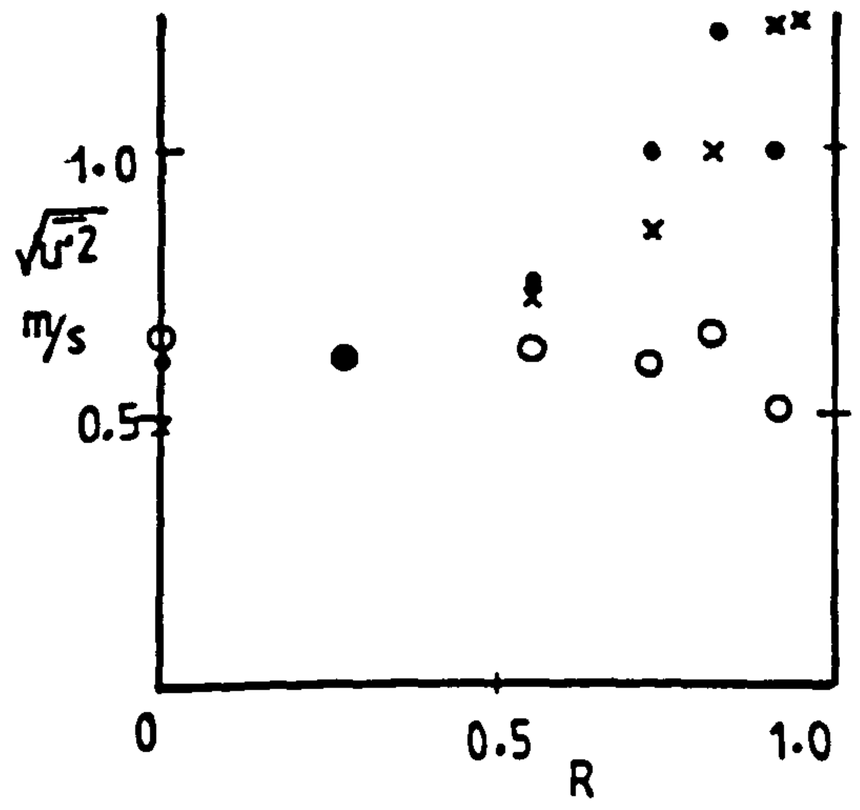

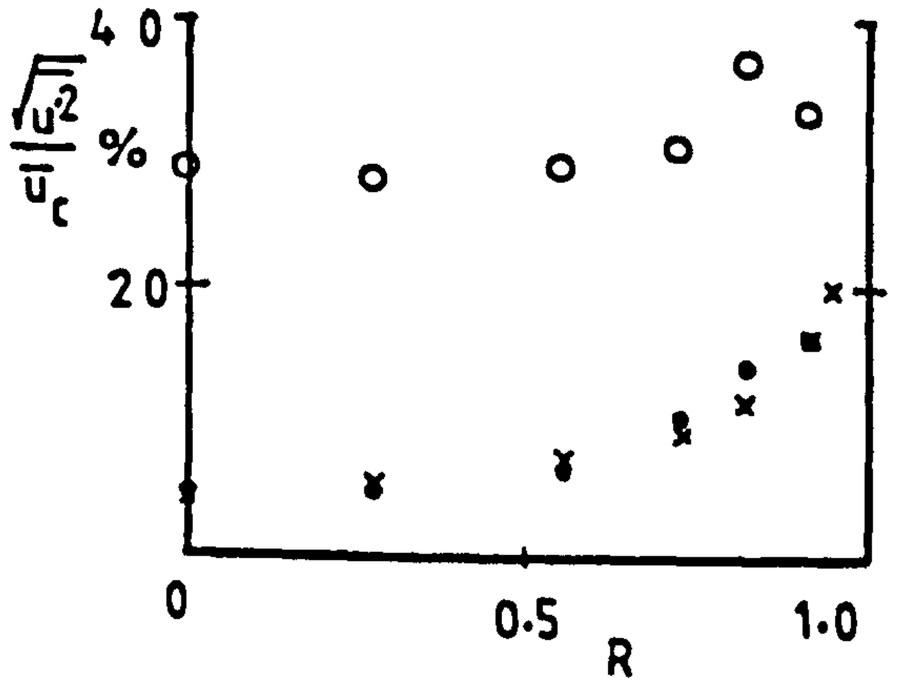

Figure 6.30 Glass ballotini, 675-935 μm; loading ratio 2.24; pipe diameter = 22 mm; U_m = 12 m/s.

• air; o solids; x air alone.

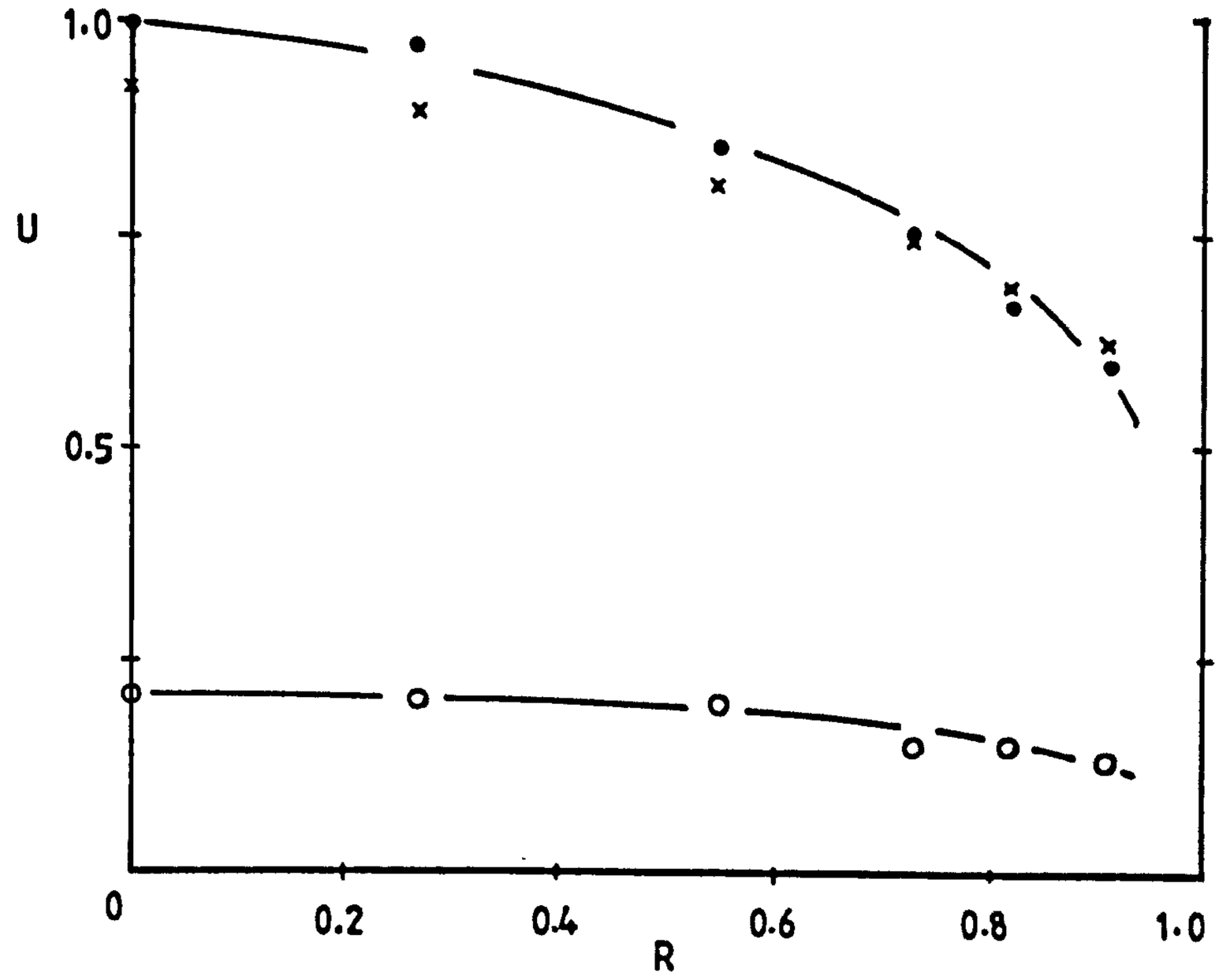

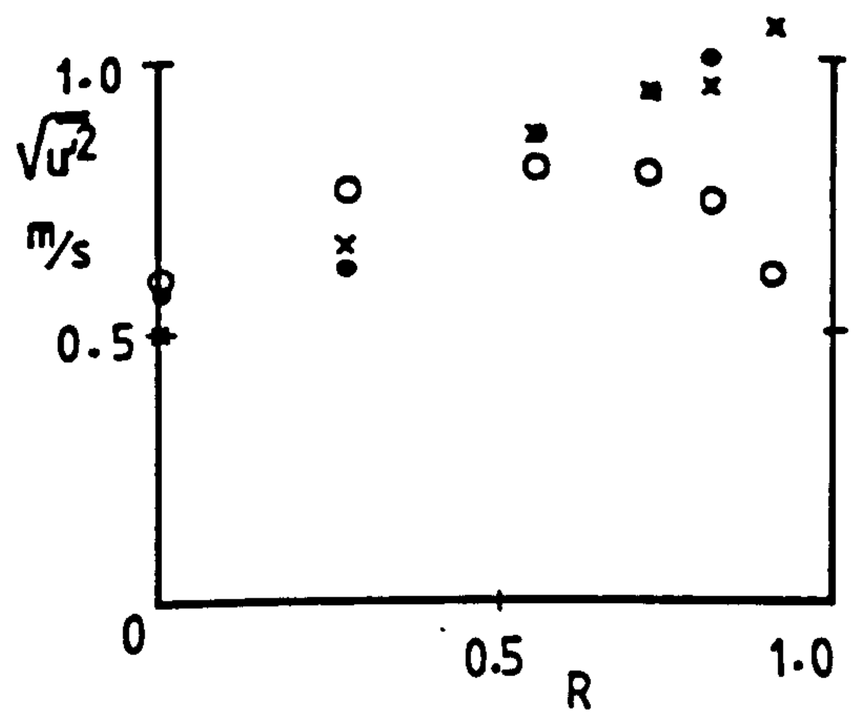

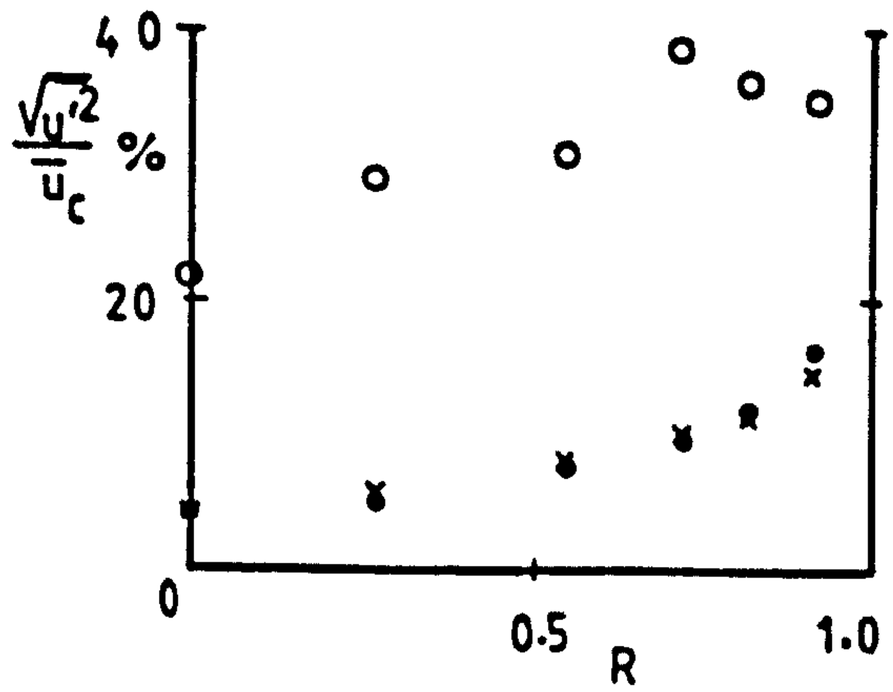

Figure 6.31 Glass ballotini, 675-935 μm; loading ratio 3.78; pipe diameter = 22 mm; U_m = 13.09 m/s.

• air; o solids; x air alone.

This has been verified by the majority of the results in which an increase of the air velocity in the pipe axis was observed (see figures 6.2 to 6.9, 6.17 to 6.21 and 6.27 to 6.30). The opposite effect has also been observed from figures 6.11, 6.14 to 6.16 and 6.31.

A decrease in the centreline air velocity would be associated with an increase in the near-wall turbulence. This has been the case in half the results for which a decrease in the centreline air velocity has been observed, i.e. those shown in figures 6.13 and 6.23, whereas a decrease in turbulence intensity is observed from the results shown in figures 6.10 and 6.12.

6.4 ANALYSIS OF RESULTS

Extensive theoretical analysis of two phase flows has been carried out by many workers in this field [6,7,8,9,10,11, 12,13,14,15]. In this work, the results obtained are compared with some established empirical relationships.

6.4.1 Particle slip velocity and drag coefficient

The particle drag coefficient is defined as

$$C_D = \frac{F_D}{\frac{1}{2}\rho_f U_\sigma^2 \pi D^2/4} \qquad (6.1)$$

The particle Reynold's number is given by

$$Re_p = \frac{\rho_f U_\sigma D}{\mu_f} \qquad (6.2)$$

where F_D is the drag force acting on the particle,

U_σ is the particle slip velocity

D is the particle diameter

ρ_f is the fluid density

μ_f is the dynamic viscosity of the fluid.

Combining equations (6.1) and (6.2) gives

$$C_D = \frac{8F_D}{\pi \mu_f^2/\rho_f} \cdot \frac{1}{Re_p^2} \qquad (6.3)$$

When a particle is moving upwards with constant slip velocity U_σ, the drag force F_D is equal to the weight of the particle less the buoyancy forces, i.e.

$$F_D = \rho_p g \frac{4}{3} \pi \left(\frac{D}{2}\right)^3 - \rho_f g \frac{4}{3} \pi \left(\frac{D}{2}\right)^3$$

or

$$F_D = \frac{\pi D^3}{6} g(\rho_p - \rho_f) \qquad (6.4)$$

When $\rho_p \gg \rho_f$ the buoyancy force can be neglected, and equation (6.4) reduces to

$$F_D = \frac{\pi D^3}{6} g \rho_p \qquad (6.5)$$

Combining equations (6.3) and (6.5) gives

$$C_D = \frac{4}{3} \frac{\rho_f g}{\mu_f} \rho_p D^3 \frac{1}{Re_p^2} \qquad (6.6)$$

Using the average values $\rho_f = 1.20$ kg/m^3 and $\mu_f = 18.2 \times 10^{-6}$ kg/m s in equation (6.6) gives

$$C_D = 0.04738 \times 10^{-6} \rho_p D^3 \frac{1}{Re_p^2} \qquad (6.7)$$

Figure 6.32 shows a plot of the particle drag coefficient against particle Reynold's number. Values of C_D and Re_p were computed using the average values of particle diameter and values of slip velocity at the pipe centre-line. Details of the relevant data are listed in appendix A6. The dotted lines in figure 6.32 represent plots of equation (6.7) for the varidus particle sizes used.

Many empirical relationships between particle drag coefficient and Reynold's number have been proposed by various investigators. Boothroyd [16] has presented a list of several such relationships.

The three main regions [17] are:

(i) $Re_p < 0.2$; Stoke's law:

$$C_D = \frac{24}{Re_p} \qquad (6.8)$$

(ii) $0.2 < Re_p < 500$; Chand [8]:

$$C_D = \frac{24}{Re_p} + \frac{3.4}{Re_p^{0.3056}} \qquad (6.9)$$

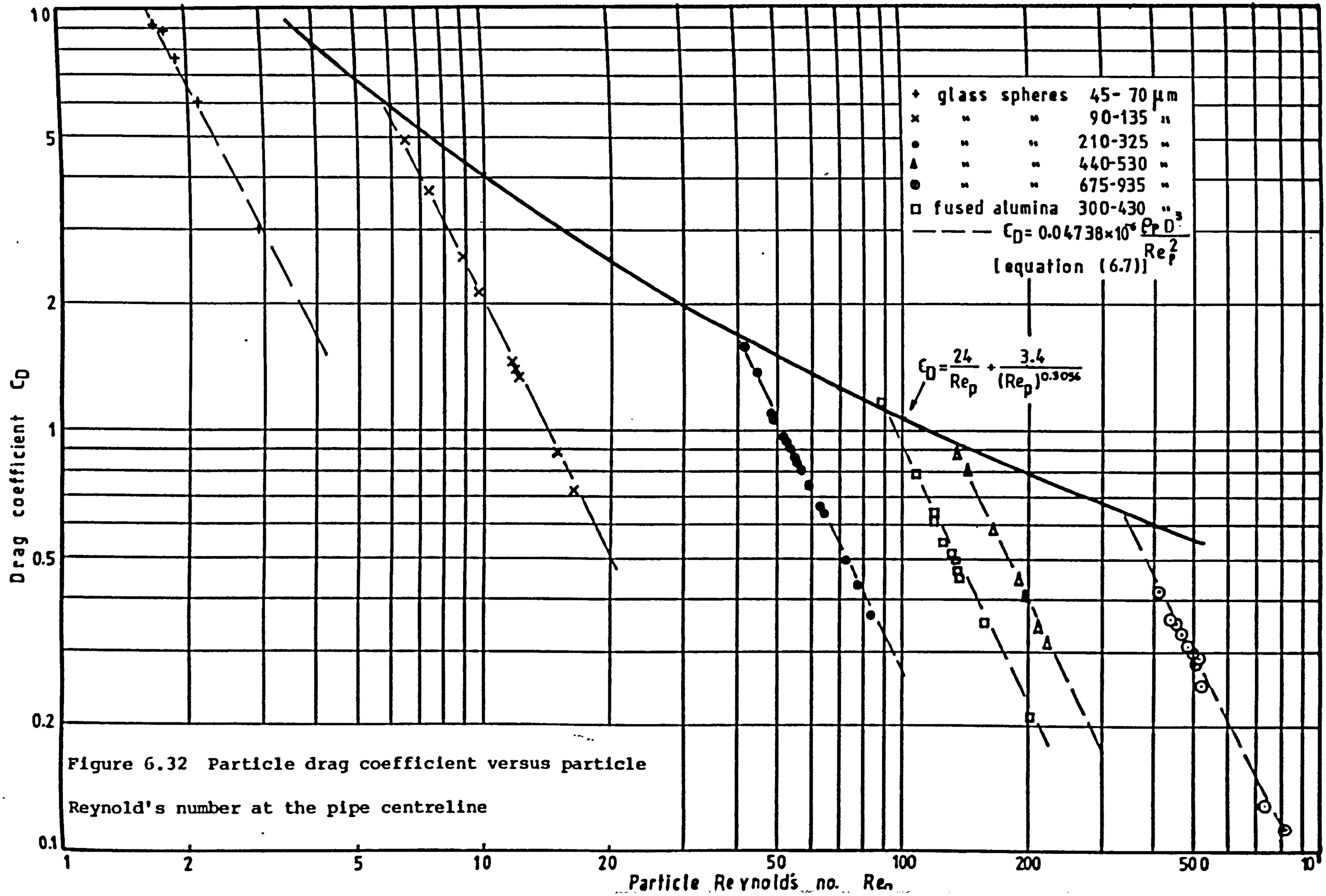

Figure 6.32 Particle drag coefficient versus particle Reynold's number at the pipe centreline

(iii) $500 < Re_p < 300,000$; Newton's law:

$$C_D = 0.44 \tag{6.10}$$

In figure (6.32), the solid line is a plot of equation (6.9), which applies to a free falling spherical particle, i.e. falling with terminal velocity.

The experimental results indicated that the slip velocity and hence C_D, was not constant. An attempt to explain that variation follows later in this section. It is observed from figure 6.32 that the experimental points corresponding to the lowest values of slip velocity (highest C_D values) for each particle size, fall close to the standard drag curve (equation 6.9). Those slip velocities were obtained from the lowest possible particle flow velocities; further drop in the air velocity caused the flow of particles to become unsteady and the particles to fall out of suspension.

The terminal velocity of a freely falling particle can be compared with the air velocity in an upward flowing suspension, at the instant when the solids cease to move up. Figure 6.32 verifies this observation.

A dependence of particle slip velocity on loading ratio has been reported by, among others, Reddy and Pei [6] and Chandok and Pei [7]. In the present investigation changes in slip velocity have been observed, although it is not clear whether the sole cause is a change in the loading ratio, or changes in air velocity and air

Reynold's number. Further investigation into thi$ area is needed.

Figure 6.33 shows graphs of particle slip velocity against air velocity dt the pipe centreline, for different particle sizes. It is observed that the slip velocity increases with flow velocity. The slope of the curves decreases with particle size. It is expected that for very small particles the change of the slip velocity with flow velocity, as well as the slip velocity itself, tend to zero, as the particles follow the flow completely.

Figure 6.34 shows graphs of particle slip velocity at the pipe centreline against loading ratio. A drop in the slip velocity is observed, mainly in the case of the larger solids. This result disagrees with the ones obtained by Chandok and Pei [7], who observed a decrease of the particle drag coefficient (i.e. an increase of slip velocity). It is also apparent from the same figure that there is a slight dependence of slip velocity on pipe diameter - pipe diameters are indicated by the numbers on the graphs. Obviously, in the absence of external influences, such as electrostatic forces, pipe diameter could not affect the slip velocity provided all other parameters remained constant.

It is possible that changes in the flow velocity, which in most tests could not be kept separate from changes in solids loadings, played a role in the slip velocity variations.

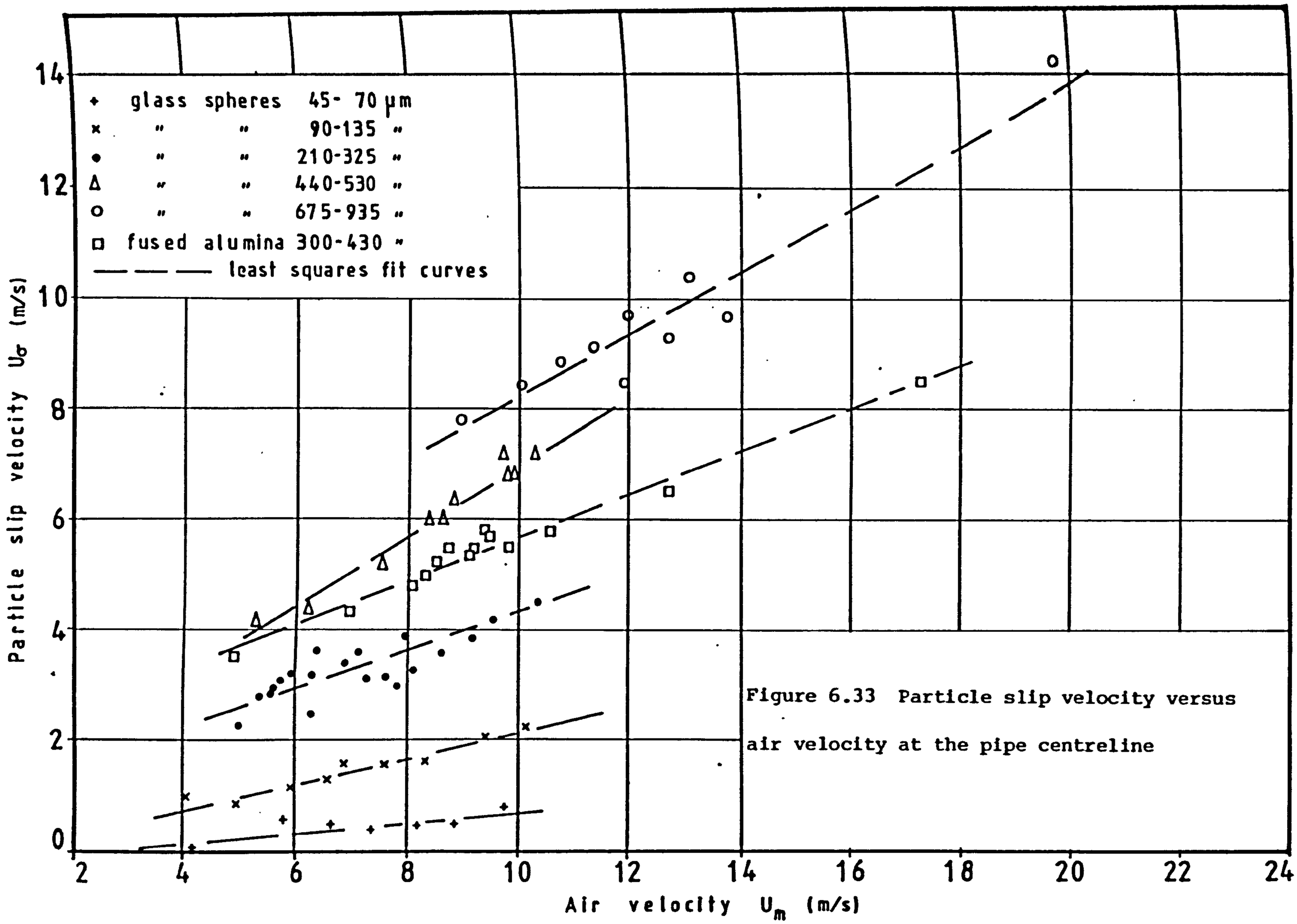

Figure 6.33 Particle slip velocity versus air velocity at the pipe centreline

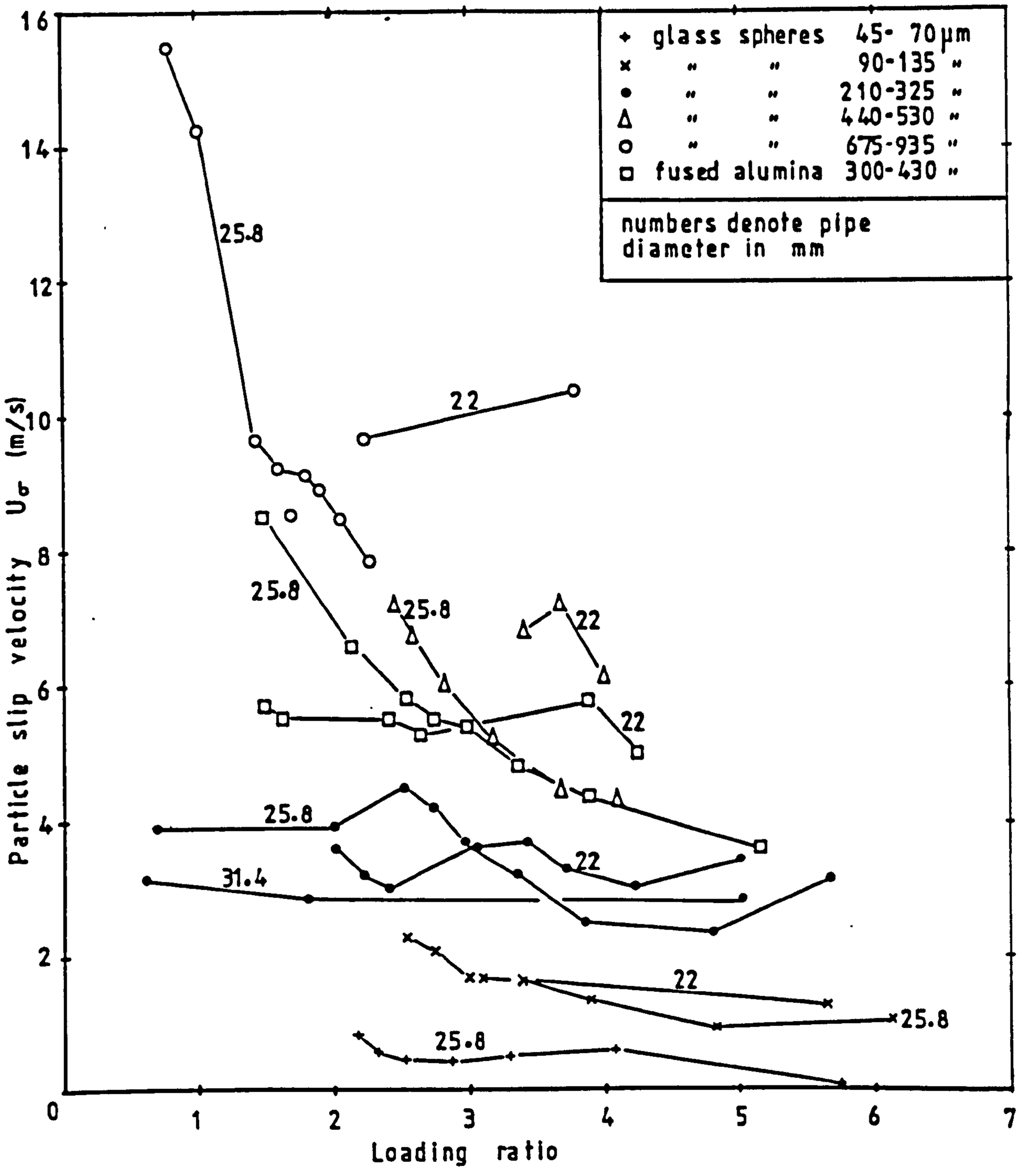

Figure 6.34 Graphs of particle slip velocity against loading ratio

Figure 6.35 shows plots of slip velocity against pipe Reynold's number. A dependence of slip velocity on pipe Reynold's number, similar to that on flow velocity can be observed.

The strongest correlation observed is that between particle slip velocity U_σ, and air velocity U_m, at the pipe axis, as seen in figure 6.33. Since loading ratio depends on solids mass flowrate as well as air mass flow-rate and hence air velocity, dependence of C_D on the latter would have obscured the variation of C_D with loading ratio. Varying the loading ratio and the air flowrate separately is necessary, in order to fully investigate changes in drag coefficient.

If the drag coefficient is a function of the particle Reynold's number only, i.e. $C_D = f(Re_p)$, then for a given particle diameter, D, U_σ must be constant. If this is not the case then

(i) The flow may not be fully developed, hence the solids are still accelerating upwards, and

(ii) the drag coefficient is not a function of Re_p only, but also perhaps of Re_f and solids loading. Electrostatic forces may also be important.

In order to investigate case (i), i.e. whether fully developed flow had been established at the working section, velocity measurements were carried out, using two different pipe lengths. Two 25.8 mm bore pipes were used,

Figure 6.35 Particle slip velocity against pipe Reynold's number

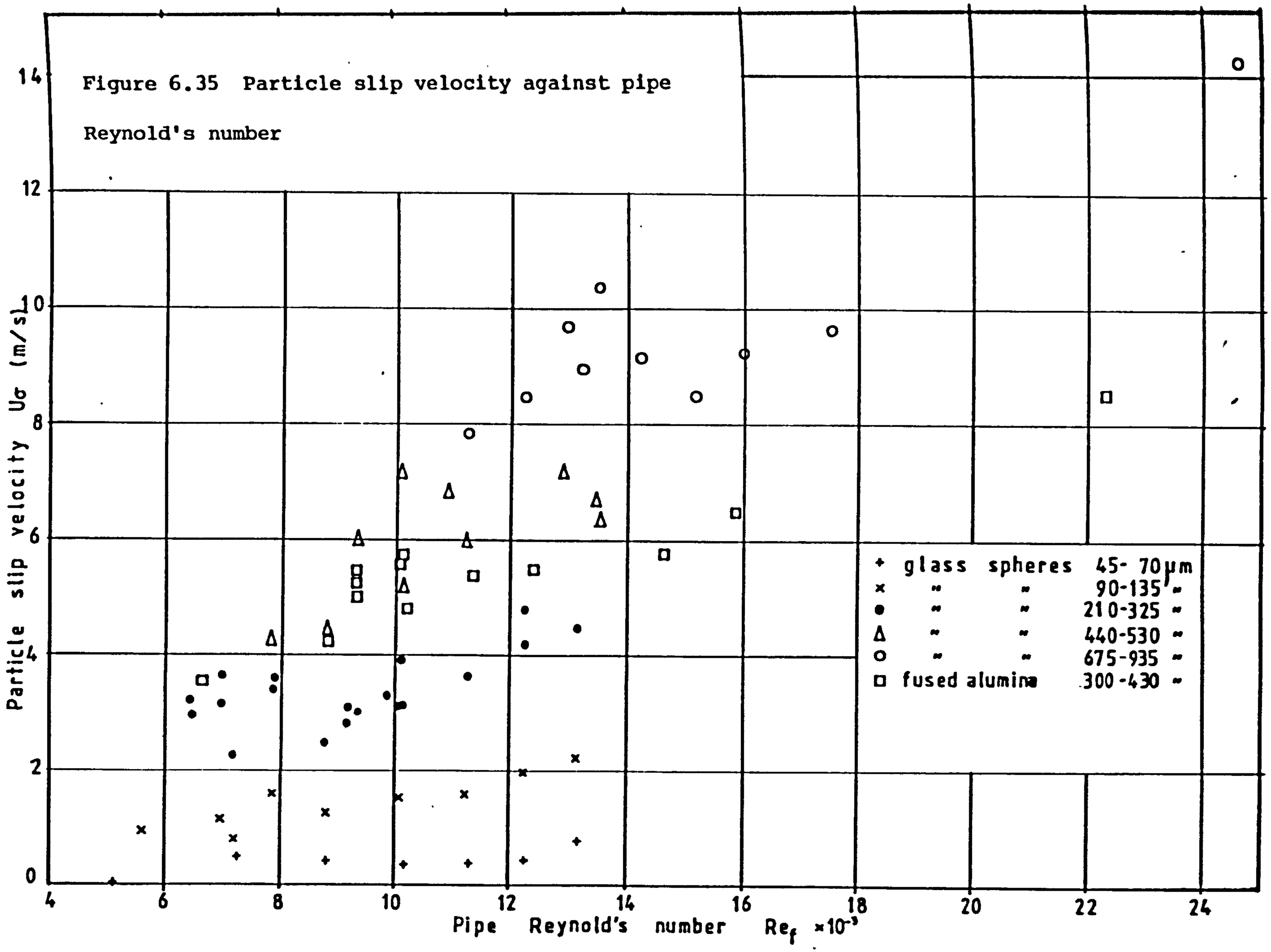

giving 54 and 67 diameters upstream of the working section. Due to space limitations longer pipes could not be used. Measurements were taken at two air mass flow-rates for each pipe length, a low and a high one. No significant difference was observed between the speeds of the solids at the centreline for the two pipe lengths. It was thus concluded that the solids had reached their maximum velocity.

The variation of the particle slip velocity with particle diameter is shown in figure 6.36. The results obtained with fused alumina have been omitted from that graph, since there is a difference in mass density between glass and alumina, and slip velocity depends on both, size and weight.

After combining equations (6.1), (6.2) and (6.9), and using the average values $\rho_f = 1.20$ kg/m^3 and $\mu = 18.2 \times 10^{-6}$ kg/m-s, the following result is obtained:

$$10.9\rho_p D^3 - 0.364 \times 10^{-3} D\, U\sigma - 0.1145(U_\sigma D)^{1.694} = 0 \qquad (6.10)$$

A plot of the above equation is shown in figure 6.36 (solid line).

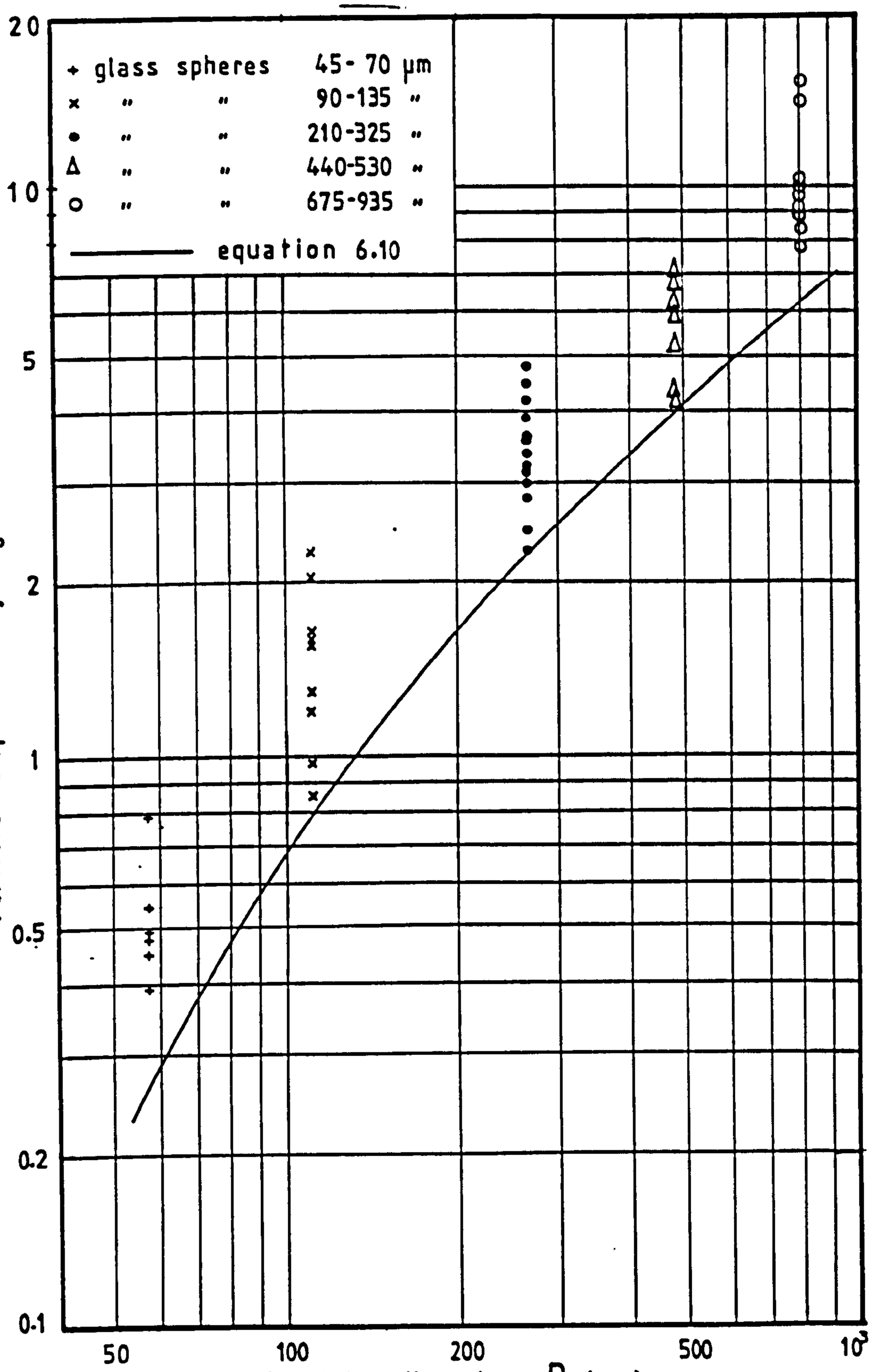

Figure 6.36 Particle slip velocity versus particle diameter

6.4.2 Particle velocity profiles

The particle velocity distribution across the pipe can be described by a power law [7], i.e.

$$\frac{U_p - U_{pw}}{U_{po} - U_{pw}} = \left(\frac{y - D/2}{a - D/2}\right)^{1/n}$$

where U_p denotes particle velocity, suffices o and w refer to the centreline and the wall respectively, y denotes wall distance, a pipe radius and D particle diameter.

By letting $V_p = U_p/U_m$, $y = 1 - r$, where r is the radial distance, and $R = r/a$, the above expression can be written as

$$\frac{V_p - V_{pw}}{V_{po} - V_{pw}} = \left(1 - \frac{R}{1 - \frac{D}{2a}}\right)^{1/n} \qquad (6.11)$$

The boundary conditions are:

(i) $R = 0$, $V_p = V_{po}$

(ii) $R = 1 - \frac{D}{2a}$, $V_p = V_{pw}$.

Unlike the velocity of the fluid phase, the particle velocity at the wall is not zero. Graphs of $(V_p - V_{pw})/(V_{po} - V_{pw})$ against $1 - R/[1 - (D/2a)]$ are shown in figure 6.37. V_p values were obtained from the graphs shown in figures 6.1 to 6.19 and 6.21 to 6.31, after fitting smooth curves over the points. An estimate of V_{pw} for each

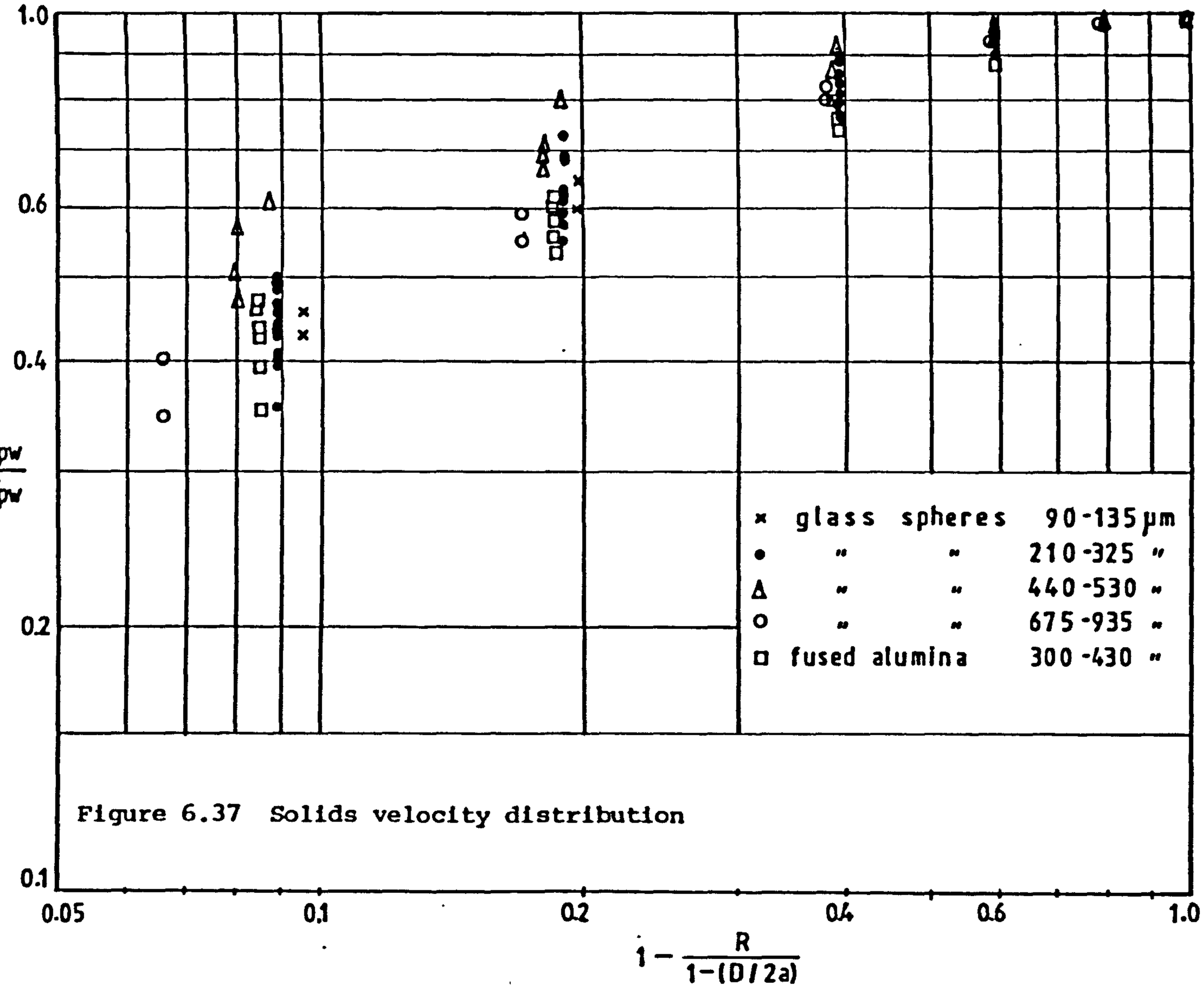

Figure 6.37 Solids velocity distribution

velocity profile was made by extending the curve up to R = 1. Although this method for obtaining particle velocity at the wall is likely to introduce errors, it is not thought that the simple power law assumed by Reddy and Pei [6] would lead to more accurate estimates of particle wall velocities.

It is seen from figure 6.37 that the index m is not a constant, but varies with radial distance. Chandok and Pei [7] found m to be a function of particle Reynold's number, Re_p, i.e.

$$m = 3.78 - 0,007Re_p \quad .$$

The present results indicate a dependence of m on particle Reynold's number, but as it can be seen from figure 6.38, that relationship, unlike the one above, is a more complex function of Reynold's number and particle size.

For each particle size, a parabolic relationship exists between the index m and Reynold's number, of the form

$$m = a\, Re_p^b + C \qquad (6.12)$$

The constant C was estimated to be equal to 2, and the index b equal to 4.5, for all particle sizes. The values of the coefficient a are shown in table 6.2.

Solids	a
Glass spheres 90 - 135 μm	1.63×10^{-4}
Glass spheres 210 - 325 μm	8.65×10^{-8}
Glass spheres 440 - 530 μm	4.85×10^{-10}
Glass spheres 675 - 935 μm	3.40×10^{-12}
Fused alumina 300 - 430 μm	2.10×10^{-9}

Table 6.2 Values for equation (6.12)

Further to the above, it was thought that the coefficient 'a' would be a function of particle diameter, of the form

$$a = A\, D^{n} \qquad (6.13)$$

where the constants were estimated to be n = -8.71 and $A = 1.2 \times 10^{12}$.

This agreed very well with the results obtained from glass ballotini, size 13, 10 and 8, but not with those from glass ballotini, size 5, and fused alumina. The latter, of course, being of different mass density than glass and of irregular shape, is expected to require a different value for the constant A. Weight is probably the third parameter upon which the index m depends.

Figure 6.38 Index m against particle Reynolds number. —— —— —— equation (6.12) with values for a as in table 6.2

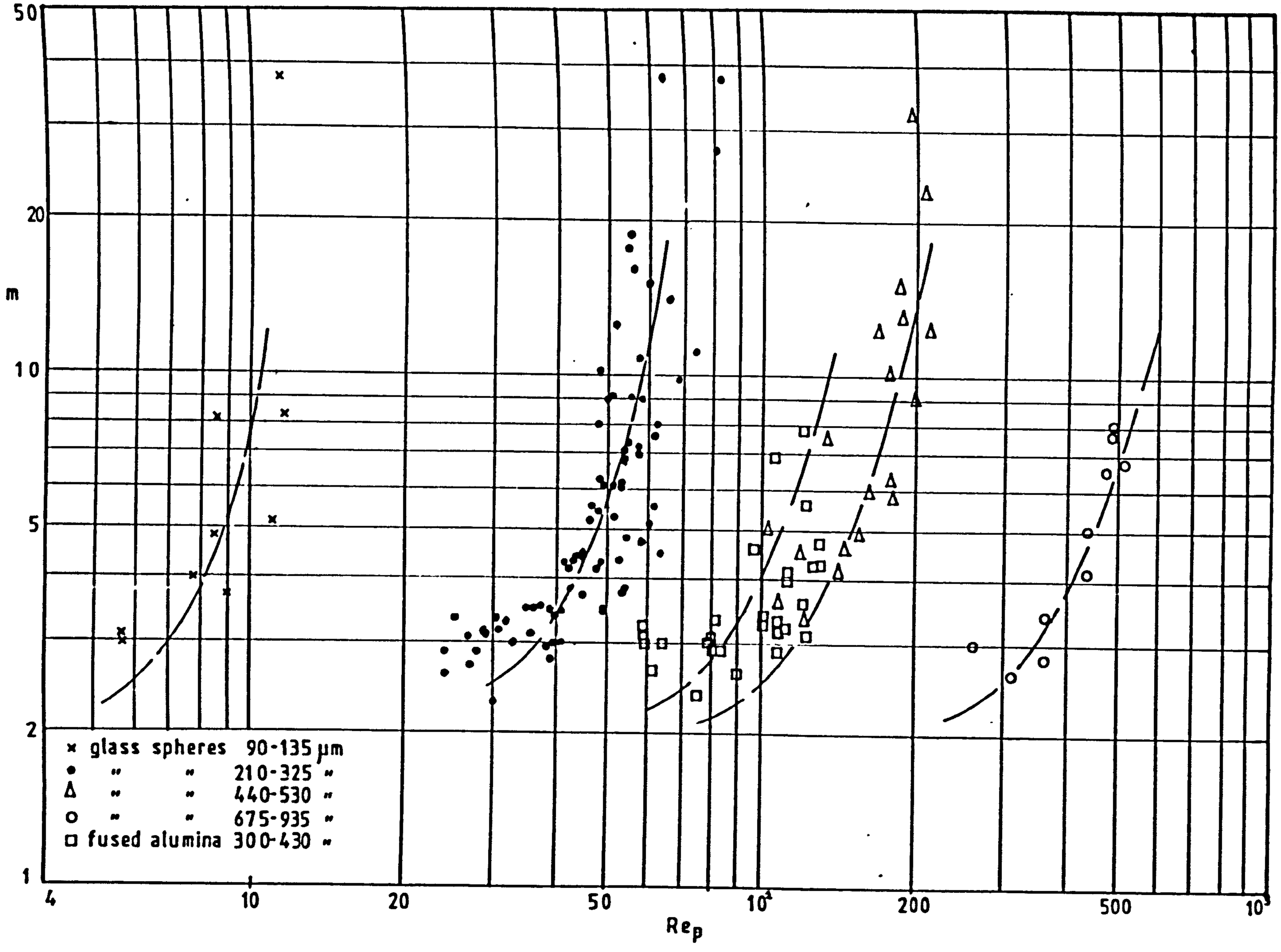

REFERENCES

[1] Melling A and Whitelaw J H 1973 Seeding of gas flows for Laser Anemometry. DISA Information, no 15, pp 5-14.

[2] Koronakiz P S 1973 Reduction of turbulent energy and shear by particulates in a homologous turbulent shear flow field of low Reynold's number. Ph.D. thesis, University of Illinois, USA.

[3] Durst F 1978 Studies of particle motion by laser Doppler techniques. Proc. Dyn. Flow Conference 345-372.

[4] Laufer J 1954 The structure of turbulence in fully developed pipe flow. Reprt 1174 NACA.

[5] Zisselmar R and Molerus O 1978 Investigation of solid-liquid pipe flow with regard to turbulence modification. Intl. seminar on Momentum, Heat and Mass Transfer, Dubrovnik.

[6] Reddy R V S and Pei D C 1969 Particle dynamics in solid-gas flow in a vertical pipe. I & CE Fundamentals 8 3 390-497.

[7] Chandok S S and Pei D C 1971 Particle dynamics in solid-gas flow in a vertical pipe. Pneumotransport 1, conf. Cambridge, B5-53-67.

[8] Chand P 1973 A theoretical model of the pneumatic-conveying drying system. Pneumotransport 2 Conf. paper C2 (Guildford: BHRA), C2-15-27.

[9] Migdal D and Agosta V D 1967 A source flow model for continuum gas-particle flow. ASME Trans. 860-865.

[10] Syamala R C 1975 A pressure drop correlation for gas-solid flow through similarity analysis. Indian J. Tech. 13, 435-437.

[11] Syamala R C 1976 Study of thd mechanism of turbulent gas-solids flow pressure drop: Part II solids phase momentum equations for turbulent flow. Indian J. Tech. 14 365-368.

[12] Ahmadi G 1973 Motion of particles in a turbulent fluid - on the effect of rotation on the dispersion coefficient. Pneumotransport 2, conf. Paper C1, Guildford: BHRA.

[13] Tirumalesa D and Channapragada R S 1969 Turbulent mixing of gas-particle and pure gas streams. Astronautica Acta, 14, 665-679, Pergamon Press.

[14] Soo S L 1969 Pipe flow of suspensions. Appl. Sci. Res. 21, 60-84.

[15] Baw P S H and Peskin R L 1971 Some aspects of gas-solid suspension turbulence, ASME Trans.

[16] Boothroyd R G 1971 Flowing gas-solid suspensions, Chapman and Hall

[17] Arundel P A, Hobson C A, Lalor M J and Weston W 1974 Measurements of individual alumina particle velocities and the relative slip of different sized particles in a gas-solid suspension flow using a laser anemometer system. J. Phys. D: Appl. Phys. 7 2288-2300

CHAPTER 7

CONCLUSIONS AND RECOMMENDATIONS

7.1 CONCLUSIONS

The previous lack of experimental results for two phase flows has been pointed out by many authors [1,2,3,4] as mentioned in the introduction. Various reasons for that were also given, such as absence of suitable instruments, which would effectively separate signals from the two phases and which would be able to cope with such a basically hostile environment, without at the same time causing a flow disturbance.

It can now be concluded that the use of LDA for the study of two phase flows seems very promising, as the results presented in this work show.

The outstanding points of this investigation can be summarised as follows:

(a) A study of the beam propagation characteristics in a dual beam laser Doppler anemometer, was followed by the development of a method for measuring beam diameter, hence determining the exact position of the minimum beam cross section - the waist. Inexpensive and relatively simple optical arrangements were thus designed, in which the beam crossover region coincided with the beam waist.

(b) The dependence of Doppler signal visibility on scatterer size was investigated, and as a result a "discrimination" technique, was developed which allowed separation of signals obtained from each of

the two phases of a flowing gas-solid suspension. The basis of this technique was formed by a digital logic circuit, together with a Doppler frequency meter. In this arrangement signals could at will be accepted or rejected, depending on the amplitudes of the Doppler signal components. The discriminator was tested and its performance was found to be satisfactory.

(c) Velocity measurements were carried out in upward flow of gas-solid suspensions in the axial direction in vertical circular pipes. An optimized dual beam optical anemometer was used, with a prototype Doppler frequency meter and discrimination logic. A microprocessor based data collection system and an on line computer for data processing were used. The conveying medium in the flowing gas-solid suspension was air. Solids, of mainly spherical shape, and diameters between 400 to 1000 μm were conveyed, in an open type flow rig, with a cyclone separator and continuous recycling of the solids. Velocity profiles across the pipe and centreline velocity measurements were obtained for both the solid and the gas phases of the suspension. The results indicated that:

(i) The velocity profiles of the air and of the solids were distinctly different, the difference depending on the average size of the solids. The solids velocity profiles were 'flatter'

than those of the air. Although the centreline particle velocities were lower than those of the air, the velocity profiles crossed over near the wall, as the solids maintained a finite velocity at the wall.

(ii) The slip velocities of the solids were found to depend on particle size as well as pipe Reynold's number and possibly loading ratio.

(iii) An increase as well as a decrease of air turbulence was observed. These conflicting results were attributed to the many different ways in which the presence of solids in an air flow affect turbulence. Depending on particle shape, size and concentration and flow velocity, the manifestation of the mutual influences between the phases can vary.

(iv) The level of turbulence of the solids was on average higher than that of the air, except in the near wall region, where a sharp increase in the air turbulence was observed.

Due to the very complex nature of two phase flows and the large number of variables involved, it is felt that more exhaustive experimentation is necessary in order to fully explain the mechanisms of the air-solids interactions. Such thorough coverage of all the possible combinations will require additional lengthy experimental work and was not possible to carry out in the present project.

7.2 RECOMMENDATIONS FOR FUTURE WORK

7.2.1 Experimental Techniques

Several problems were encountered during the course of the experimental work, many of which could not be solved at that time due to practical limitations. An outline of those problems now follows, together with suggested remedies and improvements of the experimental techniques.

a) Flow pipe diameter

Due to space limitations only small bore flowpipes were used. This made difficult taking measurements near the wall, due to laser light scattering from the wall. It is recommended that in order to study the flow close to the solid boundary, large diameter pipes be used, in which case wall distances are smaller fractions of the pipe diameter. Pipe diameters in excess of 50 mm are recommended.

b) Laser power

Although the 5 mW laser used produced about 10 mW, it was noticed that natural seeding of the flow with small scatterers was not sufficient, due to the low scattered intensity. A more powerful laser would be an added benefit to the signal quality.

c) Air supply

One of the main difficulties experienced in this investigation was maintaining a steady air flow speed. This was due to the use of electric blowers, whose motor speed fluctuated. In order to minimise flow fluctuations it is

recommended to use a large air reservoir, charged by a compressor, via a heat exchanger. An automatic bleed valve could then maintain the air supply within close tolerances.

d) Electronic filtering

The signal frequency distributions obtained from the flowing suspensions were wide - usually bimodal. This presented difficulties in filtering out noise, since a wide filter band had to be used, to avoid truncating the frequency spectrum. An automatic filterbank, such as the one developed by Durst and Heidbreder [5], which would allow individual filtering of each signal burst, could improve signal quality and reduce measurement errors due to noise.

e) Radial diffraction grating

The problems associated with the radial diffraction grating were speed fluctuations and eccentricity of the grating disc. Although these may leave the mean velocity unaffected, they tend to increase the frequency spread. It is thought that a mixing device [6] for electronically subtracting the preshift frequency would solve the above problem and would also eliminate errors due to inaccurate speed settings.

f) Electrostatic charging

Electrostatic forces, often prevented the solids from flowing smoothly. The effect was reduced by using earthed metal tubes, wherever possible, particularly in the solids feed system. It is recommended that the air humidity be controlled in order to obtain optimum conditions.

g) Collecting optics

It was observed that incorrect adjustment of the collecting telescope, affected signal visibility, upon which discrimination was based. It is of great importance to focus the collecting optics correctly; this can be facilitated by observing the resulting photomultiplier signal on an oscilloscope screen.

h) Small particle seeding

Due to the small laser power and the need to obtain results in a short time, artificial seeding with small scatterers was employed. This was achieved by various types of smoke. It was noticed that smoke, in particular oil smoke droplets, tended to adhere to the solids and to the pipe walls, thus impeding the smooth flow of the solids. This was particularly severe, as the solids were gravity fed.

It is thought that use of a more powerful laser would eliminate the need for seeding and the problems associated with it.

i) Solids flow characteristics

A number of fixed size solids feed tips were used to vary the solids flowrate. Since the solids to air loading ratio can be altered by altering the flow of either the solids or the air, or both, this meant that the loading ratio could not always be set independent of the air flowrate.

It is recommended that in order to study possible dependence of particle drag coefficient on loading ratio and pipe

Reynold's number, a variable solids feed orifice must be used.

j) Velocity bias corrections

The velocity bias corrections used were similar to those proposed by McLaughlin and Tiederman [7]. These corrections only consider that particle velocity component, which is normal to the fringes, and do not take into account the fact that the flow through the probe volume is three dimensional.

It is recommended that in future work, the bias correction proposed by Hoesel and Rodi [8] be used. This correction considers the particle velocity vector, not one component only by taking into account the residence time of the particle in the probe volume.

7.2.2 Organisation of future experimental work

It is now understood that it is not possible to fully separate the variables involved in a two phase flow while carrying out experimental work. For example a change in the solids flowrate only, would bring about changes in the distribution of velocities in the duct, hence the centre-line air velocity would be altered. Nevertheless one can vary one of the controllable variables at a time and thus obtain a better understanding of this type of flow than has been possible up to now.

The variables to be considered are:

Air flowrate and air mean velocity.

Solids mass loadings

Particle size.

Solids concentration would be a consequence of the latter two conditions.

The above three parameters should be varied one at a time, over a wide range of values and measurements of local mean velocities as well as fluctuating components carried out.

Pipe diameter would be a possible fourth parameter to be considered. Since particle contact with the pipe wall and particle-wall collisions are likely to exert a damping influence on the flow of the solids, the variation of the volume to wall area ratio, with pipe diameter, may be of significance.

Two component velocity measurements should be considered as a necessary step, following a comprehensive series of axial velocity measurements.

REFERENCES

[1] Reddy K V S and Pei D C 1969 Particle dynamics in solid-gas flow in a vertical pipe. I & CE Fundamentals 8 3 390-497.

[2] Boothroyd R G 1971 Flowing gas-solid suspensions, Chapman and Hall.

[3] Moller R E K and Norman B 1978 Simultaneous measurement of velocity and concentration in fibre suspension flow. Proc. Dyn. Flow Conference Marseille & Baltimore 745-754

[4] Spalding D B 1980 Recent advances in numerical methods in fluids Vol 1, Pineridge Press, Swansea

[5] Durst F and Heidbreder J 1979 Eine automatische Filterbank für LDA-Signale Sonderforschungsbereich 80, SFB 80/M/140, Universität Karlsruhe

[6] Goossens L H J and van Pagee J A 1980 Electronic mixing device in laser Doppler velocimetry J. Phys. E: Sci. Instrum. 9 554-556.

[7] McLaughlin D K and Tiederman W G 1973 Biasing correction for individual realization of laser anemometer measurements in turbulent flows. The Physics of Fluids 16 12 2082-2088

[8] Hoesel W and Rodi W 1977 New biasing elimination method for laser-Doppler velocimeter counter processing. Rev. Sci. Instrum. 48 7 910-919.

APPENDICES

APPENDIX A1. CALIBRATION OF THE ORIFICE PLATE

APPENDIX A2. CALIBRATION OF SOLIDS FEED-TIPS

APPENDIX A3. PUBLISHED WORK

APPENDIX A4. ELECTRONIC FILTER DESIGN

APPENDIX A5. COMPUTER PROGRAMMES

APPENDIX A6. VELOCITY MEASUREMENT RESULTS

APPENDIX A1

CALIBRATION OF THE ORIFICE PLATE

Although the orifice plate was designed to BS 1042 it was decided to carry out a calibration rather than rely on manufacturing accuracy.

The flowrates corresponding to a large number of manometer readings were determined from velocity profiles as follows:

The volume flowrate is given by $2\pi \int_{r=0}^{r=a} \bar{u}\, r\, dr$ where $\bar{u}$ and r denote local mean velocity and radial position respectively. When the velocities and radii are non-dimensionalised,

i.e. $$U = \frac{\bar{u}}{U_m} \quad \text{and} \quad R = \frac{r}{a} \ ,$$

where U_m is the centreline velocity and a the pipe radius, the above expression for the volume flowrate becomes:

$$\dot{V} = 2\pi\, U_m\, a^2 \int_{R=0}^{R=1} U\, R\, dR \qquad \text{(A1.1)}$$

Also mass flowrate $\dot{m} = \rho \dot{V}$ (A1.2)

where $\rho = \frac{p}{RT}$ is the air density at the point of measurement. The pressure p, at that position was assumed to be atmospheric. The temperature was measured by a thermocouple attached to the pipe wall. R = 287 J/(kg K), is the specific gas constant for air.

The integral $\int U\,R\,dR$ was evaluated using Simpson's Rule for numerical integration as follows: a smooth curve was fitted over the experimental points of the velocity distribution and the product UR was evaluated at nine equidistant positions up to R = 0.8 and at a further seven positions from R = 0.8 to R = 1.0. Hence the volume and mass flow-rates were computed using equations (A1.1) and (A1.2).

As one of the objectives of this work was to investigate the effects of the presence of solids on the flow of air through a vertical pipe, pairs of experiments, i.e. air and solids and air alone under comparable flow conditions, had to be carried out. Setting the differential head across the orifice the same for both tests in each pair was thought to give comparability of flow conditions, but an investigation was carried out in order to quantify the influences on the air mass flowrate resulting from:

(i) narrowing of the effective flow area due to the presence of solids in the flow

(ii) increased back pressure caused by the added resistance to the flow from the conveyed solids, i.e. possible increase of the absolute pressure at the orifice with an associated increase in the air density.

To investigate the effects of increased pressure drop the following test was carried out:

Maximum solids flowrate was set, using solids feed-tip no.8 and glass ballotini, size 10 (see Appendix A2). The blower

was set at maximum speed giving a differential head at the orifice of approximately 60 mm H_2O. The gauge pressure at the tapping upstream of the orifice was then 300 mm H_2O. For the same differential head, when air alone was flowing, the tapping upstream of the orifice read 170 mm H_2O. Thus the net pressure increase at the upstream tapping of the orifice between the two flow conditions was 130 mm H_2O. This would result in an increase in air density of approximately 1.2%. Since no heat exchanger was used to maintain constant air temperature, an increased pressure drop was always accompanied by an increase in the air temperature at the orifice, of a few ^{o}C. This would reduce air density and the two effects should more or less cancel one another out.

To quantify this argument, two velocity profiles with air alone were obtained, using smoke as seeding, with a 50 mm H_2O differential head in each case, but with different back pressures, achieved by means of a restriction placed between the working section and the orifice plate. The gauge pressures upstream of the orifice were 128 and 315 mm H_2O values which compared with those at maximum solids loadings. The air mass flowrates were computed from the velocity profiles, as explained previously, with no significant difference between the two values.

It was thus concluded that for the conditions encountered in the present work, changes in the air density at the orifice due to pressure and temperature variations could be ignored

without significant error.

As regards the narrowing of the flow area due to the presence of solids, the maximum solids mass flowrate was 20.89 g/s (see Appendix A2). The corresponding volume flowrate was

$$\dot{v} = \frac{\dot{m}}{\rho} = \frac{20.89 \times 10^{-3}}{2950} = 7.1 \times 10^{-6} \ m^3/s \quad .$$

This, compared with the volume flow of air (see table A1.1) is smaller by a factor of about one thousand and can be neglected as insignificant.

Hence it was concluded that comparable flow conditions prevailed if the differential head was kept constant for experiments involving air alone and air with solids.

The mass flowrate through the orifice was expressed as

$$\dot{m} = k\sqrt{\rho \ h}$$

where k is a constant

ρ the air density at the orifice

and h the differential head across the orifice (m H_2O)

Since the pressure changes were not significant, the air density was taken as

$$\rho = \frac{p_{at}}{RT}$$

where p_{at} denotes atmospheric pressure

and T was taken as 300 K, which was an average value for a number of experiments.

Hence $\dot{m} = C\sqrt{h}$

where $C = k\sqrt{\frac{101.3}{0.287 \times 300}}$

A graph of $\dot{m}$ against $\sqrt{h}$ is shown in figure A1.1, for a number of flow conditions as shown in detail in table A1.1.

From the slope of the calibration curve it was found that

$C = 0.0185$.

Hence $\dot{m} = 0.0185\sqrt{h}$ (A1.3)

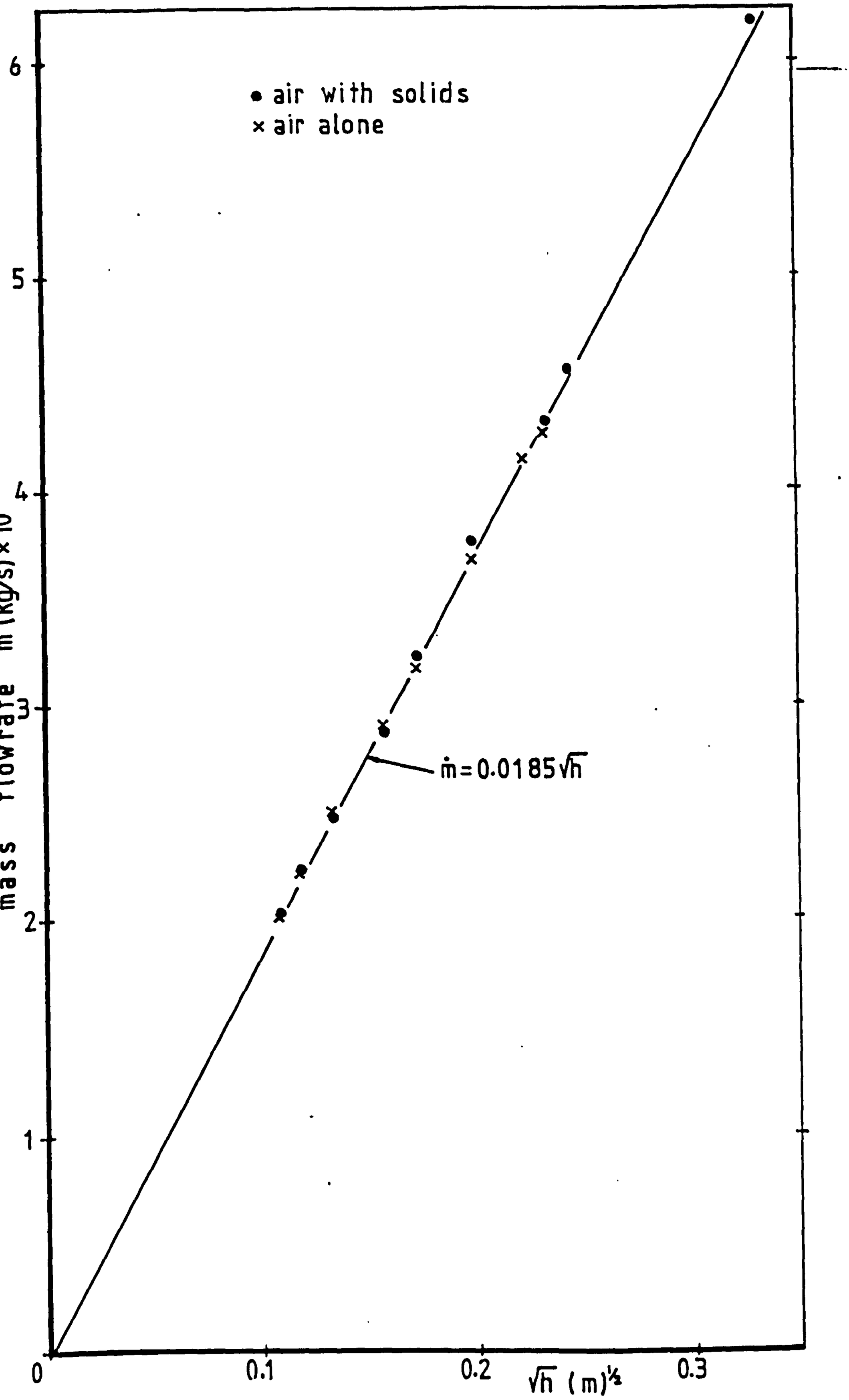

Figure A1.1 Calibration of the orifice plate

$\sqrt{h}$ $m^{\frac{1}{2}}$	air alone				air with solids			
	air temperature (^{o}C)		$\dot{V}$ $\frac{m^3}{s} \times 10^3$	$\dot{m}$ $\frac{kg}{s} \times 10^3$	air temperature (^{o}C)		$\dot{V}$ $\frac{m^3}{s} \times 10^3$	$\dot{m}$ $\frac{kg}{s} \times 10^3$
	orifice	working section			orifice	working section		
0,109	24	22	1.651	1.976	25.3	23	1.705	2.035
0.118	24	21	1.828	2.202	24.5	21	1.861	2.234
0.134	25	21	2.085	2.503	26	21.5	2.051	2.458
0.158	29	23	2.448	2.919	28	23	2.383	2.871
0.173	29	23	2.645	3.154	29.5	23.5	2.709	3.225
0.200	29	21.5	3.052	3.657	30	22	3.154	3.773
0.224	31	22	3.459	4.138				
0.234	35	26.5	3.616	4.261	38	29.5	3.702	4.319
0.245					37	24	3.834	4.557
0.332					30.5	24	5.211	6.193

Table A1.1 Data for calibration of orifice plate

APPENDIX A2

CALIBRATION OF SOLIDS FEED-TIPS

Calibration of the solids flowrate through the different sizes of solids feed-tips used was carried out as follows:

The flow of the solids through each tip was timed and the amount collected in a beaker was weighed to determine the mass. This procedure was repeated three times. Average values are shown in table A2.1.

material \ tip		mass flowrate (g/s)				
		8	7	6	5	4
glass ballotini	18	19.48	10.52	6.29	4.60	2.42
glass ballotini	13	20.08	12.41	7.59	5.23	2.74
glass ballotini	10	20.89	12.33	7.53	4.92	2.54
glass ballotini	8	20.14	11.74	6.86	4.48	2.23
glass ballotini	5	16.31	9.31	5.25	3.35	1.56
sand		13.98	9.05	5.69	3.75	1.99
burnt alumina		19.48	12.92	7.69	4.78	2.48

Table A2.1 Solids mass flowrates

APPENDIX A3

PUBLISHED WORK

A3.1

Phys. E: Sci. Instrum., Vol. 11, 1978. Printed in Great Britain

Beam waist location and measurement in a dual-beam laser Doppler anemometer

Tridimas, M J Lalor and N H Woolley
Department of Mechanical, Marine and Production Engineering, Liverpool Polytechnic, Byrom Street, Liverpool L3 3AF, UK

Received 22 July 1977, in final form 19 October 1977

Abstract A method is described for measuring Gaussian laser beam diameters and, in particular, determining the location of the beam waist in a dual-beam laser Doppler anemometer. Results of measurements carried out by different techniques and theoretical predictions are presented as a check to the validity of that method. The associated problem of the beam waist location is also discussed. The method, called here the 'power ratio method', offers itself as a simple and reliable way of measuring beam diameters and locating beam waists, tasks which, otherwise, are cumbersome and time-consuming.

1 Introduction

The most common laser Doppler anemometer (LDA) system is of the dual-beam type in which a laser beam is split into two equal-intensity parts, which are made to intersect by means of a simple converging lens. Figure 1 shows such a system where a radial diffraction grating is used as beam splitter. In the intersection region interferences fringes are formed. Attention has recently been drawn to the fact that the waist does not usually occur at the intersection and hence the spacing of these interference fringes may not be constant throughout the crossover region (Hanson 1973). This can lead to errors which can be significant when the frequencies of the observed 'Doppler' signals are related to the velocities of the scattering particles passing through the fringes. Doppler signals from particles crossing the probe volume at different points and with the same velocity can have frequencies differing by 10% or more (Abbiss *et al* 1974, Durst and Stevenson 1975).

It is, therefore, important to minimise this effect by arranging the optical system so as to produce constant fringe spacing in the intersection region. This is normally done by locating the waists of the focused Gaussian beams at that point – the practical problem being to achieve this condition quickly and easily. A related problem is the necessity to know the physical dimensions of the probe volume, which is important when making biasing corrections in turbulent flow studies (George 1975).

2 Beam propagation

In general, for a Gaussian beam having a waist of radius r_0, the beam radius r_x at a distance x from the waist is given by (Kogelnik 1965, Dickson 1970)

$$r_x = r_0\left[1+\left(\frac{\lambda x}{\pi r_0^2}\right)^2\right]^{1/2}. \tag{1}$$

When that beam is focused by a lens (Durst and Stevenson 1975),

$$r_1 = \frac{r_0 f}{[(x_0-f)^2+(\pi r_0^2/\lambda)^2]^{1/2}} \tag{2}$$

$$x_1 = f+\frac{(x_0-f)f^2}{(x_0-f)^2+(\pi r_0^2/\lambda)^2} \tag{3}$$

where r_1 is the radius of the focused beam waist, f is the paraxial focal length of the lens, x_1 is the distance between the lens and the focused beam waist and x_0 is the distance between the lens and the beam waist before the lens, as shown in figure 2. For a lens free of spherical aberration, equation (3) gives $x_1 = f$ if $x_0 = f$ or $x_0 \to \infty$.

Equation (1) applies equally to the focused beam shown in figure 2 by changing r_0 to r_1 and measuring x from the focused beam waist. If the beams intersect at a distance x from the waist then r_x/r_1 will be greater than unity. It is necessary to have a reliable method of measuring beam radius and reducing r_x/r_1 to as close to unity as possible. For the Spectra Physics model 120 He–Ne laser used in this work the beam waist radius in the resonator has been calculated from the specification data as 0·366 mm at a distance of 325 mm from the beam exit end of the case.

3 Measurement of beam diameter – power ratio method

A technique for measuring the spot size of Gaussian beams (Yoshida and Asakura 1976) has been adapted and applied to the location and measurement of the beam waist. The theoretical basis of the method is as follows. The intensity

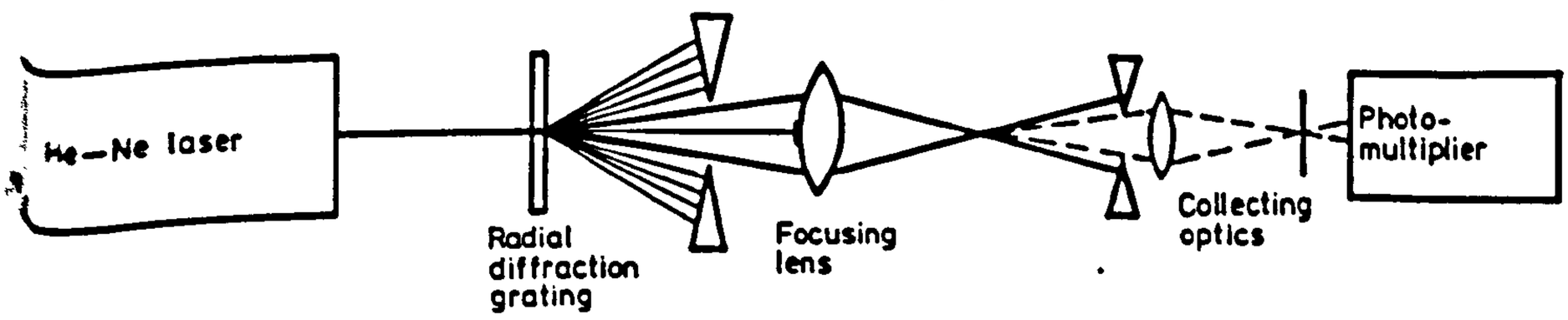

Figure 1 Dual-beam laser anemometer.

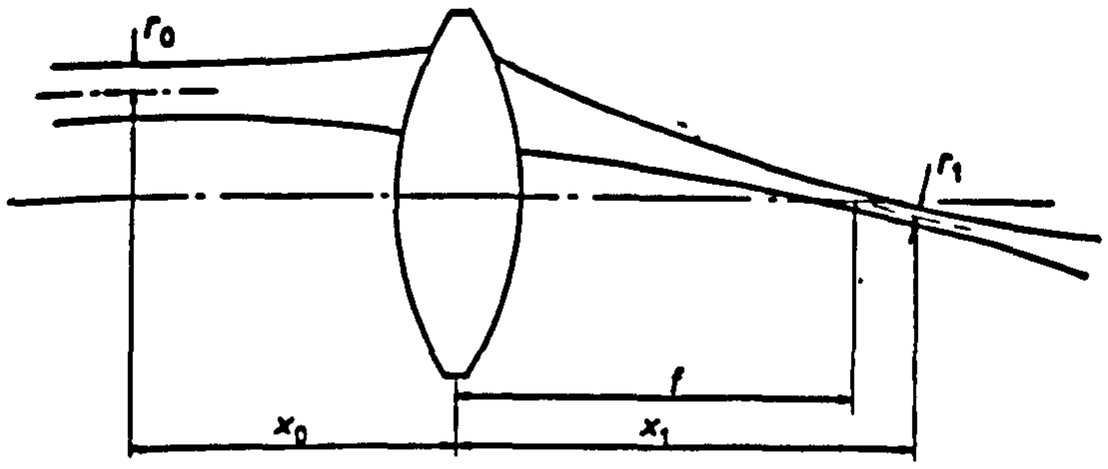

Figure 2 Focused laser beam.

$I(x, y)$ of a Gaussian beam is given by (Skinner and Whitcher 1972, Suzaki and Tachibana 1975)

$$I(x,y)=\frac{2P_0}{\pi r^2}\exp\left(-2\frac{x^2+y^2}{r^2}\right) \tag{4}$$

where P_0 denotes the total beam power and r denotes the beam radius at the $1/e^2$ intensity points. The beam power is $\iint I(x, y)\,dx\,dy$.

If a thin wire of radius α is placed symmetrically about a diameter of the beam cross section, the detected beam power becomes a minimum, P_m, and is given by

$$P_m=2\frac{2P_0}{\pi r^2}\int_{x=-\alpha}^{x=\infty}\int_{y=-\infty}^{y=\infty}\exp\left(-2\frac{x^2+y^2}{r^2}\right)dy\,dx. \tag{5}$$

This can be reduced to

$$\frac{P_m}{P_0}=\operatorname{erfc}\left(\frac{\alpha}{r}\sqrt{2}\right). \tag{6}$$

Having measured P_m and P_0 and knowing α, we may calculate r.

4 Experimental determination of unfocused beam radius

Measurements were carried out at a distance of 7·10 m from the laser. Three wires of different diameters and three steel strips of corresponding widths were used as indicated in table 1. It is seen from the results that:

(i) there is no difference between readings obtained with flat strips and wires of similar dimensions;

(ii) the different-sized wires and strips gave results which are in close agreement;

(iii) the beam diameter was about 7·8 mm.

A similar result was obtained using the traversing pinhole technique with which it was also verified that the intensity distribution in the beam was Gaussian. For measurements near the laser it was found necessary to place a small-aperture iris diaphragm before the wire and so minimise background radiation.

Table 1 Results from unfocused beam measurements. 2α, wire diameter or strip width; r, beam radius.

	Wires			Flat strips		
2α (mm)	P_m (mW)	P_0 (mW)	$2r$ (mm)	P_m (mW)	P_0 (mW)	$2r$ (mm)
4·83	1·69	8·50	7·51	1·65	8·50	7·48
2·57	4·40	8·53	7·99	4·40	8·53	7·99
1·10	6·72	8·60	7·86	6·73	8·60	7·89

5 Experimental determination of beam waist dimensions

5.1 *Using the power ratio technique*

The layout is shown in figure 3, where the focal lengths of L_1, L_2 and L_3 are 15, 8 and 5 cm respectively, and the number of lines in the radial diffraction grating is 21 600. The wires used were stretched along a diameter of a small hole drilled on a thin steel plate.

By suitable positioning of L_1 and L_2 the first-order beam waists were made to coincide with the point of intersection. The diffraction grating was rotated at approximately 350 rev min^{-1} to average out any variations in transmissivity. Three different-sized wires were used and their dimensions and the results obtained are shown in table 2. From these results it is seen that the beam waist diameter was about 61·5 μm.

Table 2 Results from beam waist measurements. α, wire radius; r, beam radius.

2α (μm)	P_m (mW)	P_0 (mW)	$2r$ (μm)
20	0·945	1·835	62
30	0·580	1·815	60
40	0·350	1·800	62

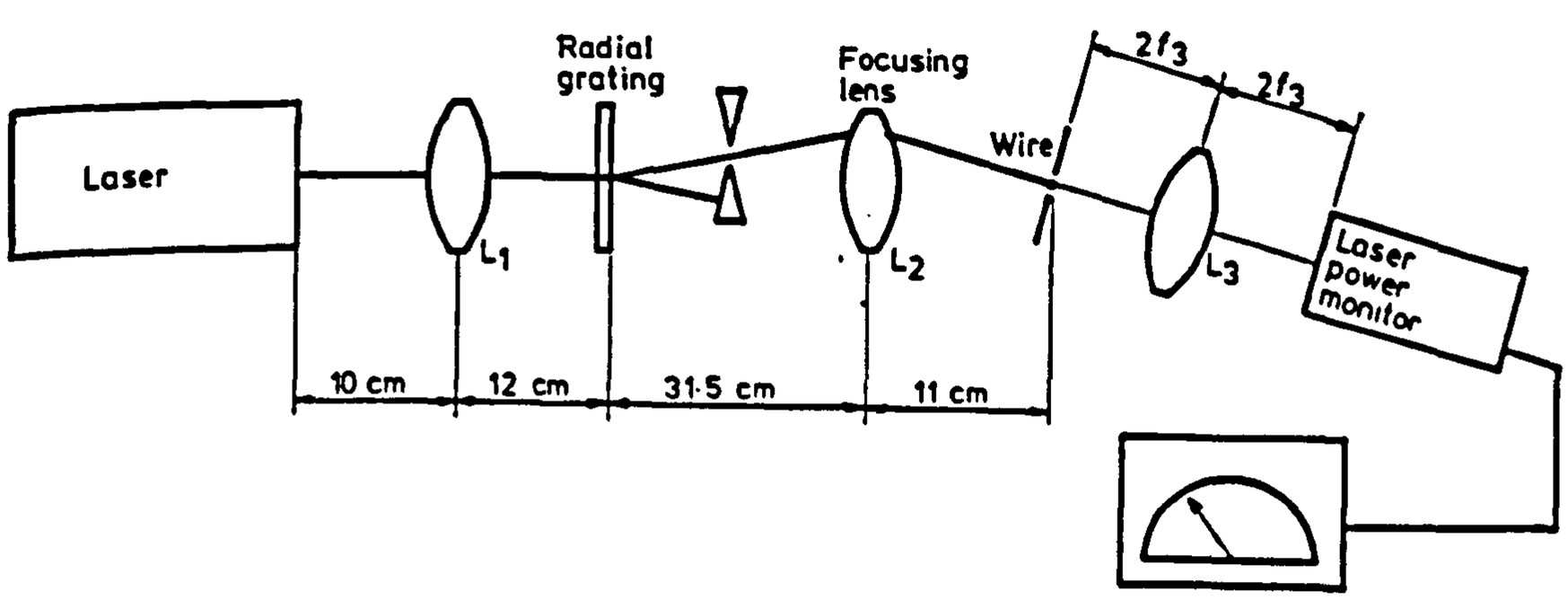

Figure 3 Set-up for measuring beam waist diameter.

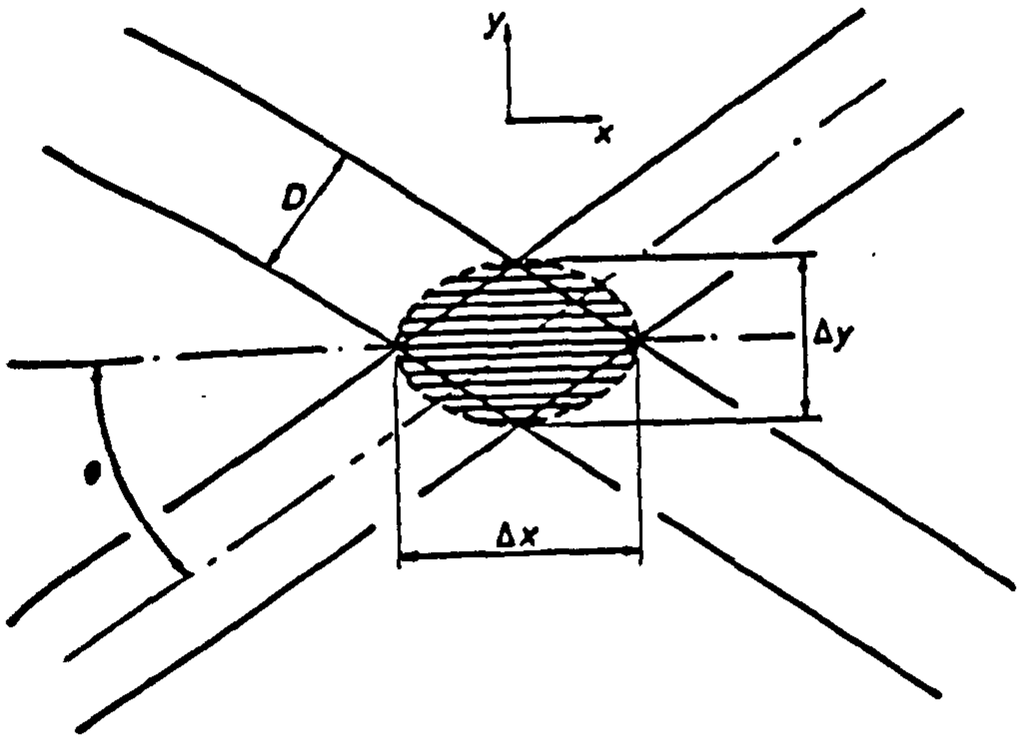

Figure 4 Beam intersection region, showing $1/e^2$ intensity ellipsoid.

In the dual-beam anemometer the beam intersection region at the $1/e^2$ intensity points is an ellipsoid (Brayton and Goethert 1971, Kreid 1974), as shown in figure 4, where $\Delta x = D/\sin\theta$ and $\Delta y = D/\cos\theta$. The angle θ was measured as 4·92°. Thus the probe dimensions are $\Delta x = 730\,\mu$m and $\Delta y = 62{\cdot}8\,\mu$m.

5.2 *Using frequency shifting*

The apparatus was arranged as in figure 3 with a photomultiplier replacing the photodiode and allowing both first-order beams through the iris diaphragm. Frequency shifting was provided by a radial diffraction grating. A wire of 20 μm diameter was placed in the intersection at right angles to the x–y plane defined in figure 4. A telescope was attached to the photomultiplier with a combination of objectives, a diaphragm and an adjustable-position pinhole.

Readings of the photomultiplier AC voltage output were taken, using a digital voltmeter, at a number of positions along the x and y axes. These readings divided by the estimated peak value are shown in figure 5, from which the x and y dimensions of the intersection region were estimated as being 943 μm and 82 μm respectively. Theoretical curves are also shown (see appendix).

The discrepancy between the results obtained here and those in §5.1 can be explained as follows. Figure 6 shows two intersecting beams. A wire of radius α traversing the intersection region in the x direction will first produce a signal of intensity ratio equal to $1/e^2$ at position A where it touches both beams at b and c. This was confirmed by using wires of large radii to allow visual observation. At position B corresponding to the end of the Doppler signal, the end-points of a wire diameter parallel to the y axis lie on the $1/e^2$ contour of the beams, at d and e. It can be shown by geometry that from position A to position B the wire will have traversed a distance x given by

$$x = \Delta x + \alpha\left(\frac{1}{\sin\theta} + \frac{1}{\tan\theta}\right).$$

If θ is small, as is usually the case, then

$$x = \Delta x + 2\alpha/\theta \qquad (7)$$

where θ is in radians. In a similar manner it can be shown that the measured length of the other diagonal of the intersection region is

$$y = \Delta y + \frac{2\alpha}{\sin(\frac{1}{2}\pi - \theta)}$$

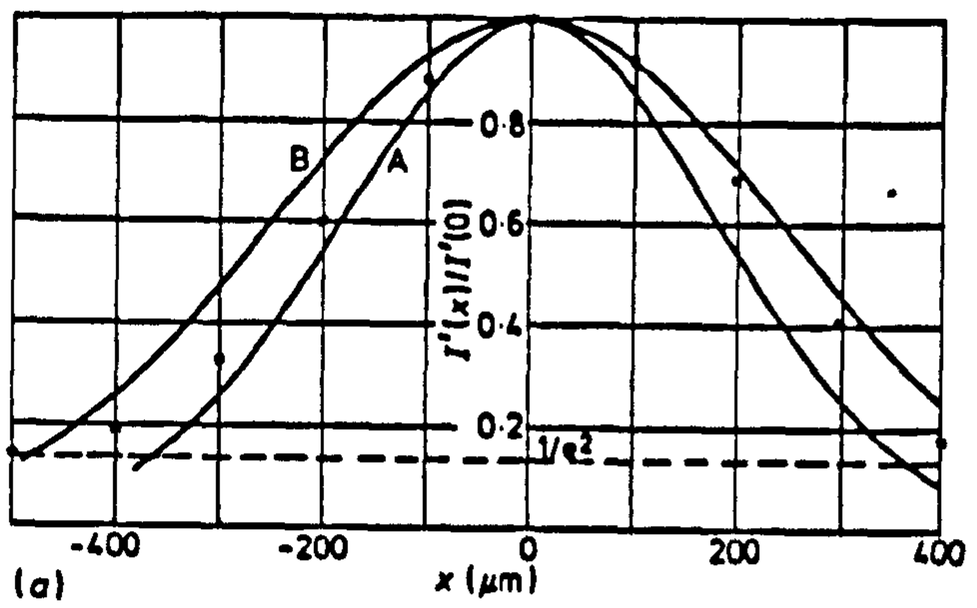

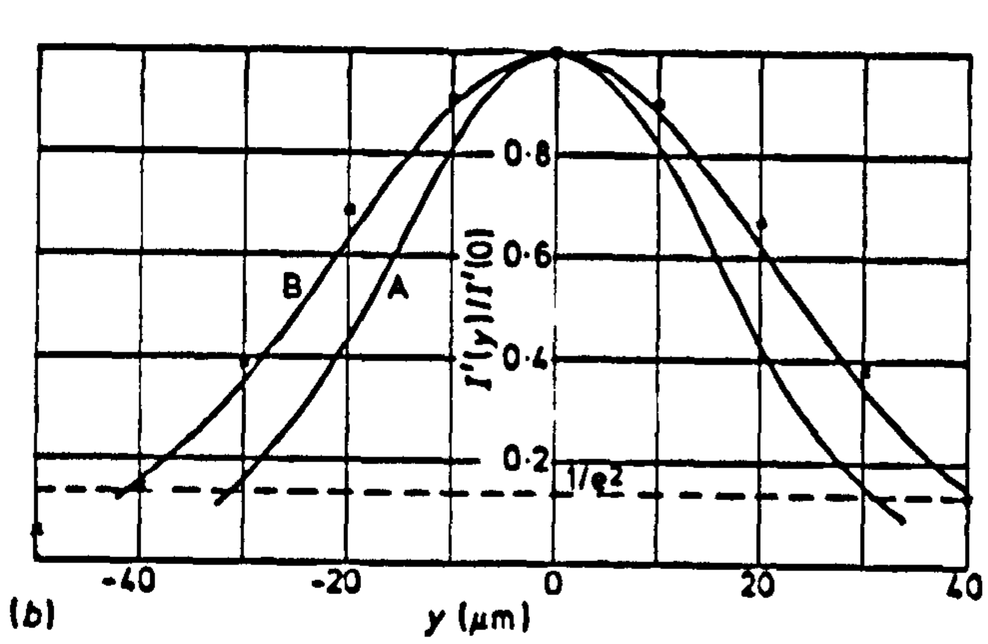

Figure 5 Dimensions of probe volume. A, equations (A.3) and (A.4) with $r = 31{\cdot}3\,\mu$m; B, equations (A.3) and (A.4) with $r = 41{\cdot}3\,\mu$m. ×, experiment.

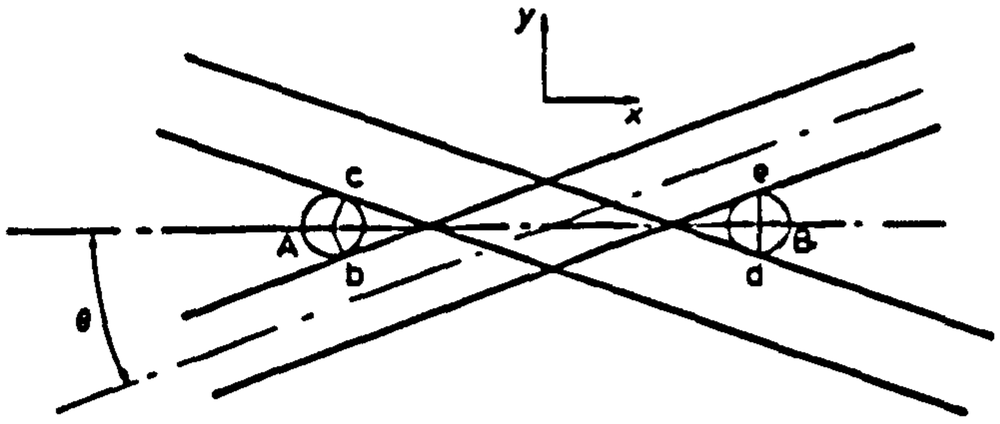

Figure 6 Relative wire–beam positions for Doppler signal limits. A, signal commences; B, signal ends.

which for small θ becomes

$$y = \Delta y + 2\alpha. \qquad (8)$$

Using the results $x = 943\,\mu$m and $y = 82\,\mu$m it is found from (7) and (8) that $\Delta x = 710\,\mu$m and $\Delta y = 62\,\mu$m, which agree well with the previous values.

Expressions (7) and (8) indicate that the results from such a measurement are similar to what theory would predict if the beams had $1/e^2$ intensity diameters equal to $D + 2\alpha$. In figure 5, curve B is a plot of equations (11) and (12) with the beam radius $r = \frac{1}{2}(D + 2\alpha)$, i.e. 41·3 μm.

6 Beam waist location

The layout shown in figure 3 gives good control over the waist position as it allows the waist and beam intersection to coincide for a variety of positions at L_1 and L_2. The laser, grating and L_2 can be fixed to give the desired distance of the beam intersection from L_2, and angle θ. Small movements of L_1 will alter the position of the beam waists. Visual observation is usually possible by means of smoke. Using the power ratio technique the position of the waist can be accurately

adjusted by taking readings of P_m only (P_m is directly proportional to beam diameter) provided that P_0 remains constant.

This set-up requires that in velocity measurements the whole apparatus be traversed and not lens L_2 only. Arrangements in which a third lens is placed between the grating and L_2 to make the beams parallel allow traversing of only L_2; but it must be pointed out that although any movement of L_2 will not affect the distance between L_2 and the intersection and the angle between the beams, it will certainly alter the position of the waist relative to the intersection

It has been suggested (Oldengarm 1975) that focusing of the laser beam on the diffraction grating ensures coincidence of the beam waist and measuring volume in such a set-up. This could only be true if the parallel beams were collimated. Measurements concerning the geometry of the parallel beams using the power ratio method indicated that a waist occurs after the intermediate lens at a distance from it proportional to its focal length. Thus the position of L_2 relative to that lens will determine the position of the beam waist in the focused beams. Focusing of the single beam on the grating of course has the advantage that the shape of the cross section of the diffracted beams suffers the minimum of distortion (Oldengarm 1975).

7 Discussion

When the power ratio method is used for measuring beam diameters, a wire of any size, is, in theory, suitable provided that its diameter does not exceed that of the beam. In practice the best wire sizes were found to be in the region $\frac{1}{4}$–$\frac{1}{2}$ of the beam diameter, since when large wires were used P_m was too small on the analogue meter scale, and when the wire was small P_m differed very little from P_0. In these extreme cases disproportionate errors arose. When the beam is of very small diameter (focused beams) an estimation of the theoretical diameter of the beam may be necessary to ensure that the sizes of the wires available are suitable.

Special care must be taken to minimise background light and light scattered from the lenses, since with the presence of large amounts of such light one might obtain erroneous results. When a large-area photodiode is used to measure laser power a collecting lens is not necessary. The authors obtained consistent results with and without this lens.

The power ratio method is thought to be simple and reliable. Measurements made under different laboratory conditions were consistent and repeatable. The orientation of the wire relative to the beam is not critical, the only condition being that the wire must be straight, clean and of constant diameter.

Acknowledgments

The authors are pleased to acknowledge the support of the Science Research Council for the work presented in this paper.

Appendix Intensity distribution along x and y diagonals of beam intersection region

Referring to figure 7, the intensity distribution $I(z', y')$ in the Gaussian laser beam is given by

$$I(z', y') = \frac{2P_0}{\pi r^2} \exp\left(-2\frac{z'^2 + y'^2}{r^2}\right)$$

where P_0 denotes total beam power and r is the $1/e^2$ intensity radius.

For the intensity distribution along the x and y diagonals of the intersection region the above expression can be transformed to

$$I'(x) = \frac{4P_0}{\pi r^2} \exp\left(-2\frac{x^2 \sin^2\theta}{r^2}\right) \tag{A.1}$$

$$I'(y) = \frac{4P_0}{\pi r^2} \exp\left(-2\frac{y^2 \cos^2\theta}{r^2}\right) \tag{A.2}$$

(note that the contribution from each beam is one-half of this).

Dividing equations (A.1) and (A.2) by $I'(0)$, i.e. $4P_0/\pi r^2$, the non-dimensionalised intensity distribution becomes

$$I'(x)/I'(0) = [\exp(-2\sin^2\theta)]^{x^2/r^2} \tag{A.3}$$

$$I'(y)/I'(0) = [\exp(-2\cos^2\theta)]^{y^2/r^2}. \tag{A.4}$$

If the beams intersect at or near the waist, r is approximately constant along the diagonals. However, if this is not the case account must be taken of the radius variation in equations (A.3) and (A.4).

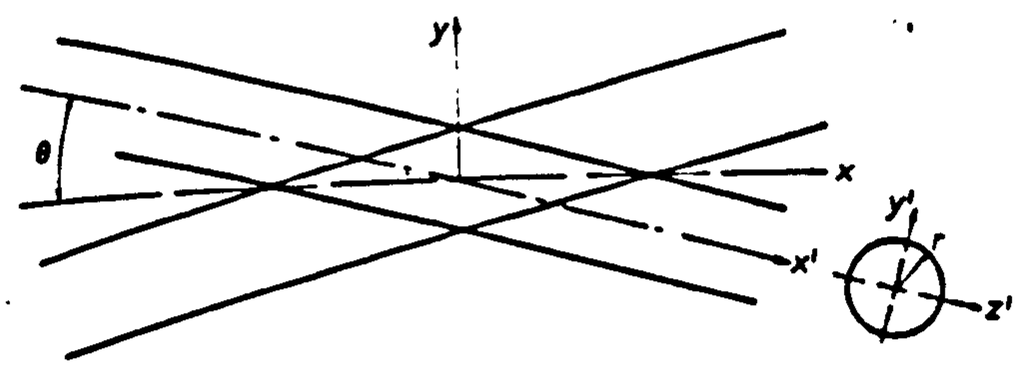

Figure 7 Coordinate system for intensity distribution in beam intersection region.

References

Abbiss J B, Chubb T W and Pike E R 1974 *Opt. Laser Technol.* 6 249–61

Brayton D B and Goethert W H 1971 *ISA Trans.* 10 40–50

Dickson L D 1970 *Appl. Opt.* 9 1854–61

Durst F and Stevenson W H 1975 *Proc. LDA Symp., University of Minnesota* (Minnesota: University) pp 373–83

George W K 1975 *Proc. LDA Symp., Copenhagen* pp 21–63

Hanson S 1973 *J. Phys. D: Appl. Phys.* 6 164–71

Kogelnik J 1965 *Bell Syst. Tech. J.* 44 455–94

Kreid D K 1974 *Appl. Opt.* 13 1872–81

Oldengarm J 1975 *Proc. AGARD Conf. on Applications of Non-intrusive Instrumentation in Fluid Flow Research* (Neuilly sur Seine: NATO Advisory Group for Aerospace Research and Development) Paper No. 193 pp 23/1–23/6

Skinner D R and Whitcher R E 1972 *J. Phys. E: Sci. Instrum.* 5 237–8

Suzaki Y and Tachibana A 1975 *J. Appl. Opt.* 14 2809–10

Yoshida A and Asakura T 1976 *Opt. Laser Technol.* 8 273–4

J. Phys. E: Sci. Instrum., Vol. 12, 1979. Printed in Great Britain

Criteria for achieving coincidence of beam waist and crossover region in a dual-beam laser Doppler anemometer

Y Tridimas, M J Lalor and N H Woolley
Department of Mechanical, Marine and Production Engineering, Liverpool Polytechnic, Byrom Street, Liverpool L3 3AF, UK

Received 1 August 1978, in final form 15 May 1979

Abstract The imaging laws for a laser beam waist and crossover region of two laser beams have been studied with reference to a dual-beam laser Doppler anemometer. Mathematical expressions relating the various parameters of the system geometry are presented as well as conditions for achieving coincidence of beam waist and measuring volume.

1 Introduction

A simple dual-beam laser anemometer consists of a laser, a beam splitter and a lens. The single beam, which has a waist in the laser resonator, is divided into two by the beam splitter. The two beams may be parallel, diverging or converging, depending on the type of beam splitter used. The lens produces images of the waist and intersection of the incoming (input) beams. The imaging laws for the waist and intersection are different and as a result the waist and intersection of the focused (output) beams will not normally coincide unless the overall optical system is arranged to achieve this. Coincidence is important because, for example,

(i) it eliminates interference plane gradients which cause signal broadening (Abbiss *et al* 1974, Hanson 1973, Durst and Stevenson 1975);

(ii) it produces a small crossover region and thus minimises velocity gradient broadening (Edwards *et al* 1971, Owen and Rogers 1975, Kreid 1974) and improves measurements in some flow situations, e.g. film flows (Oldengarm *et al* 1975).

This investigation is of particular importance when a diffraction grating is used as a beam splitter. As will be shown later it is not possible to achieve coincidence with a single lens placed after the grating, so a system comprising two lens has been examined. Beam radii are measured to the $1/e^2$ intensity beam contour and equal path lengths for the two beams are assumed.

2 Imaging of beam waist and intersection

The position and size of the image of a Gaussian beam waist produced by a lens are given by (Kogelnik and Li 1966, Dickson 1970)

$$(z_2/f-1)\,|\,(f/f_F)=\frac{(z_1/f-1)(f/f_F)}{1+(z_1/f-1)^2(f/f_F)^2} \tag{1}$$

$$\left(\frac{w_2}{w_1}\right)\left|\left(\frac{f}{f_F}\right)=[1+(z_1/f-1)^2(f/f_F)^2]^{-1/2}\right. \tag{2}$$

where $f_F=\pi w_1^2/\lambda$, λ denotes the wavelength, w_1 and w_2 represent the input and output waist radii and z_1 and z_2 are as shown in figure 1.

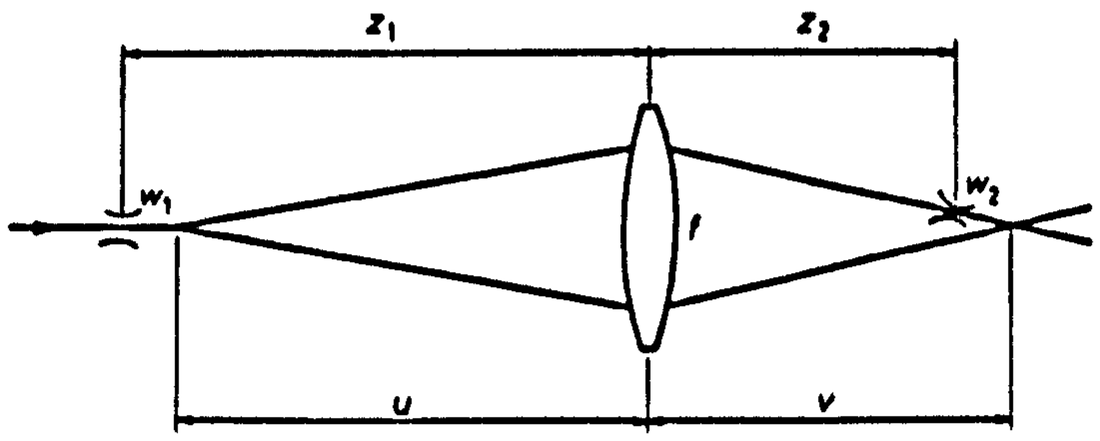

Figure 1 One-lens system. u, v, z_1 and z_2 are positive as shown.

If two coplanar beams pass through a converging lens the distance of their point of intersection from the lens, real or virtual, is imaged according to the geometric optics relationship

$$\frac{1}{u}+\frac{1}{v}=\frac{1}{f}. \tag{3}$$

u and v are positive as shown in figure 1. As $u\to\infty$ the input beams are parallel; $u>0$ gives diverging beams; $u<0$ gives converging beams.

If a prism-type beam splitter is used one can with suitable adjustments obtain parallel, converging or diverging beams whose intersection lies some distance from the beam splitter. With a diffraction grating only diverging beams are obtained and their intersection lies on the grating.

3 Conditions for coincidence of output waist and intersection

Coincidence of output beam waist and intersection is achieved if $v/f=z_2/f$. Hence

$$\left(\frac{u}{f}-1\right)\frac{f}{f_F}=\frac{1+(z_1/f-1)^2(f/f_F)^2}{(z_1/f-1)(f/f_F)} \tag{4}$$

$$\left(\frac{z_2}{f}-1\right)=\frac{1}{(u/f-1)}. \tag{5}$$

A summary of the relationships between the output variables z_2, w_2 and the input variables z_1, w_1, u is given in table 1.

Table 1 Relationships between input and output variables.

z_1/f	z_2/f	u/f	w_2/w_1
$-\infty$	1	$-\infty$	0
$1-\frac{1}{f/f_F}$	$1-\frac{1}{2}\frac{f}{f_F}$ (min)	$1-\frac{2}{f/f_F}$ (max)	$\frac{f/f_F}{\sqrt{2}}$
1	1	∞	$\frac{f}{f_F}$ max
$1+\frac{1}{f/f_F}$	$1+\frac{1}{2}\frac{f}{f_F}$ (max)	$1+\frac{2}{f/f_F}$ (min)	$\frac{f/f_F}{\sqrt{2}}$
∞	1	∞	0

Graphs of equations (1) and (2) have been presented by Kogelnik and Li (1966) and Dickson (1970). It is observed

0022-3735/79/121176+03 $01.00

that for finite values of f/f_F, $|u/f| > |z_1/f|$. This implies that if a diffraction grating is used as a beam splitter it is not possible to achieve coincidence although this is not necessarily the case with other types of beam splitting device. As an example let $z_1 = 600$ mm and $f = 150$ mm. Then $z_2/f = 1{\cdot}11$ and for coincidence u/f must be 10·55. If the lens focuses the two beams, the input intersection u must lie about 1·6 m in front of the lens – this is not possible with a diffraction grating. In this last case if we set $u = 250$ mm then $v/f = 2{\cdot}5$. The distance between the output waists and the intersection is 210 mm.

4 Two-lens system

To achieve coincidence of output beam waist and intersection when a diffraction grating is used a second lens is placed between the laser and the grating. A new beam waist is formed whose position can be adjusted so that the condition $u > z_1$ is satisfied. The effect of this intermediate lens is to increase f/f_F in equation (1) since w_1 decreases. As f/f_F increases the difference between the values of u and z_1 decreases and thus the input waist to the second lens can be located near the grating. This gives the added advantage that if a radial grating is used the beam incident upon it has a small spot size and hence the emerging beams suffer the minimum of distortion (Oldengarm 1975).

A two-lens system designed to achieve coincidence is shown in figure 2. It consists of simple glass lenses and a radial

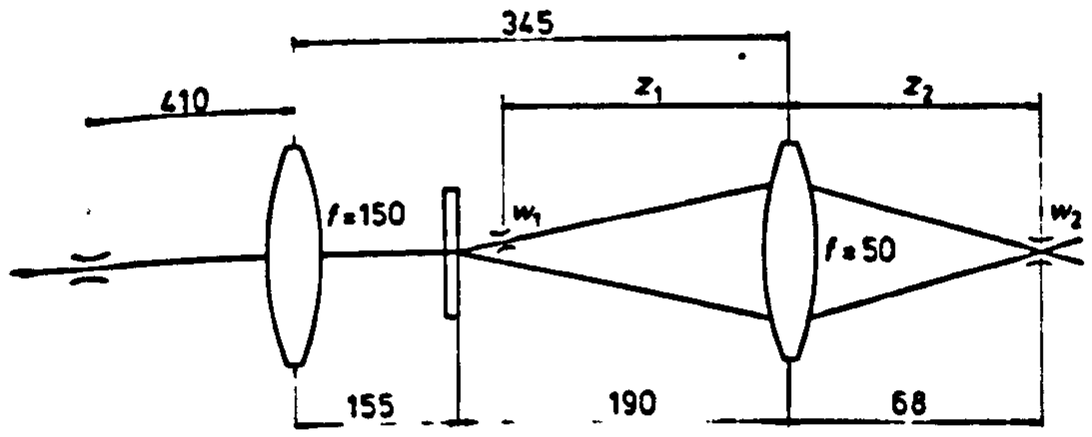

Figure 2 Two-lens system (dimensions in millimetres).

diffraction grating with 36 000 lines and a diffraction angle for the first-order beams of 3·14°. The dimensions shown were calculated using equations (1), (2) and (5). The overall size of the system was chosen according to practical considerations. A Spectra Physics 120 He–Ne laser was used for which the distance of the waist from the laser exit was estimated to be 325 mm and the waist radius 0·366 mm. The components were arranged on an optical bench and length measurements were carried out using a ruler graduated in millimetres. By use of the 'power ratio' technique (Tridimas *et al* 1978) it was found that the output waists of the beams were situated 2 mm from the intersection (towards the left in figure 2). The grating was then moved away from the second lens by about 8 mm to obtain coincidence. The discrepancy is attributed to the low accuracy of measurements using a ruler, a possible difference between the actual and nominal focal lengths of the lenses, non-paraxial focusing and probable error in estimating the location of the beam waist in the laser resonator. The calculated and measured values for the output waist diameter were 56 and 60 μm respectively and the fringe spacing was 2 μm.

By applying equations (1) and (2) to the two lenses successively an expression can be derived relating the output variables of the second lens to the input variables of the first lens and the lens spacing. Combining the result with equation (3) one obtains an expression of the same form as equation (4) for the two-lens system. The authors solved numerically such an equation for a wide range of variables and a number of solutions were tested with similar results as in the above example. Accurate measurement of distances between components is not necessary since corrections are carried out easily as indicated.

5 Practical considerations

In a practical laser Doppler anemometer some of the variables are limited to a particular range of values.

(*a*) A positive distance of output waist from lens is necessary, i.e. $z_2/f > 0$. It can be shown that $z_2/f \leqslant 0$ if $f/f_F \geqslant 2$. The corresponding z_1/f range lies between the two values of $\frac{1}{2}(1 \pm \{1 - [2/(f/f_F)]^2\}^{1/2})$. This condition also satisfies the requirement for a real beam intersection image ($v > 0$).

(*b*) It is usually required that $w_2/w_1 < 1$, which holds if $f/f_F < 1$ (all z_1/f), and also if $f/f_F > 1$ and z_1/f lies outside the range of values given by $1 \pm [1 - 1/(f/f_F)^2]^{1/2}$.

(*c*) The minimum value of z_1/f (determined by the distance from the waist to the laser exit), the lens aperture, the value of u, the angle between the input beams, the value of z_2 and the angle between the output beams must all be taken into account when designing a laser anemometer.

6 Discussion and conclusions

When a small probe volume is required with narrow fringe spacing it is necessary to use a lens of short focal length to focus the two beams rather than focus the single beam prior to splitting. In this latter arrangement, proposed by Abbis *et al* (1974), the focused beam is split into two converging beams and coincidence of beam waist and intersection is achieved by suitable adjustment of the beam splitter. Although simple, this arrangement excludes lenses of short focal length because of the length of the prism-type beam splitter.

It is thus concluded that the two-lens system is indispensable when a diffraction grating is used as a beam splitter and also when a small probe volume and small fringe spacing are required.

Acknowledgment

The authors are pleased to acknowledge the support of the Science Research Council for the work presented in this paper.

References

Abbiss J B, Chubb T W and Pike E R 1974 Laser Doppler anemometry
Opt. Laser Technol. 6 249–61

Dickson L D 1970 Characteristics of a propagating Gaussian beam
Appl. Opt. 9 1854–61

Durst F and Stevenson W H 1975 Properties of focused laser beams and their influence on optical anemometer signals
Proc. LDA Symp., University of Minnesota (Minnesota: University Press) pp 373–83

Edwards R V, Angus J C, French M J, Dunning J W 1971 Spectral analysis of the signal from the laser Doppler flowmeter: Time-independent systems
J. Appl. Phys. 42 837–50

Hanson S 1973 Broadening of the measured frequency spectrum in a differential laser anemometer due to interference plane gradients
J. Phys. D: Appl. Phys. 6 164–71

Kogelnik H and Li T 1966 Laser beams and resonators
Appl. Opt. 5 1550–67

Kried D K 1974 Laser Doppler velocimeter measurements in non-uniform flow: Error estimates
Appl. Opt. 13 1872–81

Oldengarm J 1975 The use of rotating radial diffraction gratings in laser Doppler velocimetry
Proc. AGARD Conf. on Application of Non-intrusive Instrumentation in Fluid Flow Research (Neuilly sur Seine: NATO Advisory Group for Aerospace Research and Development) Paper 193 pp 23/1–23/6

Oldengarm J, van Krieken A H, van der Klooster H W 1975 Velocity profile measurements in a liquid film flow using the laser Doppler technique
J. Phys. E: Sci. Instrum. 8 203–5

Owen J M and Rogers R H 1975 Velocity biasing in laser Doppler anemometers
Proc. LDA Symp., Copenhagen pp 89–114

Tridimas Y, Lalor M J and Woolley N H 1978 Beam waist location and measurement in a dual-beam laser Doppler anemometer
J. Phys. E: Sci. Instrum. 11 203–6

APPENDIX A4

ELECTRONIC FILTER DESIGN [A4.1] (L-C FILTER)

A4.1 General Considerations

The design was based on a combination of prototype and m-derived 'T' sections in order to obtain a good attenuation in the attenuation band and a sharp cut-off.

The final filters consisted of:

(i) one m-derived section (m = 0.35), for sharp cut-off

(ii) one prototype section (m = 1), giving high attenuation far beyond the cut off frequency

(iii) two terminating half-sections (m = 0.6), giving attenuation equal to that of a complete m-derived section with m = 0.6.

The design requirements were:

(i) Impedance, R_o = 50 Ω

(ii) Cut off frequency, f_o - varied.

The relationships between the filter components and the design parameters are given by:

Low pass filters

$$R_o = \sqrt{\frac{L}{C}}$$

$$f_o = \frac{1}{\pi\sqrt{LC}}$$

High pass filters

$$R_o = \sqrt{\frac{L}{C}}$$

$$f_o = \frac{1}{4\pi\sqrt{LC}}$$

where L and C denote inductance and capacitance respectively.

A4.2 Low pass filter

$$L = \frac{R}{\pi f_o}$$

and

$$C = \frac{1}{\pi R_o f_o}$$

Also

$$m = \sqrt{1 - \left(\frac{f_o}{f_\infty}\right)^2}$$

Hence

$$f_\infty = \frac{f_o}{\sqrt{1 - m^2}}$$

The circuit diagram and the filter characteristics are shown in figure A4.1.

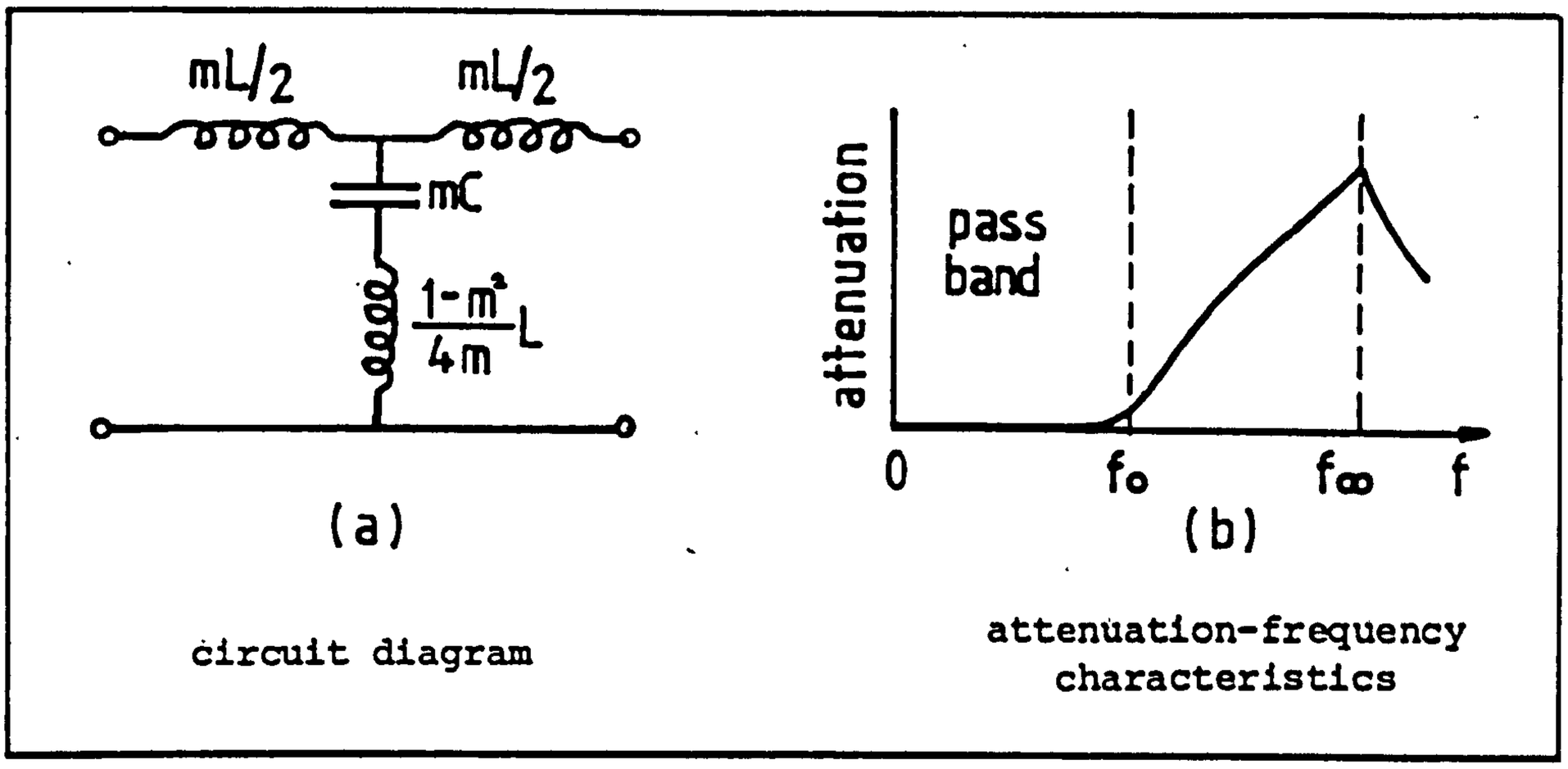

Figure A4.1 m-derived low pass T-section

For m = 0.6, $f_\infty = \frac{f_o}{\sqrt{1 - 0.6^2}} = 1.25 f_o$

For m = 0.35, $f_\infty = \frac{f_o}{\sqrt{1.035^2}} = 1.07 f_o$

For a prototype section, where m = 1, $f_\infty \to \infty$ (see figure A4.2)

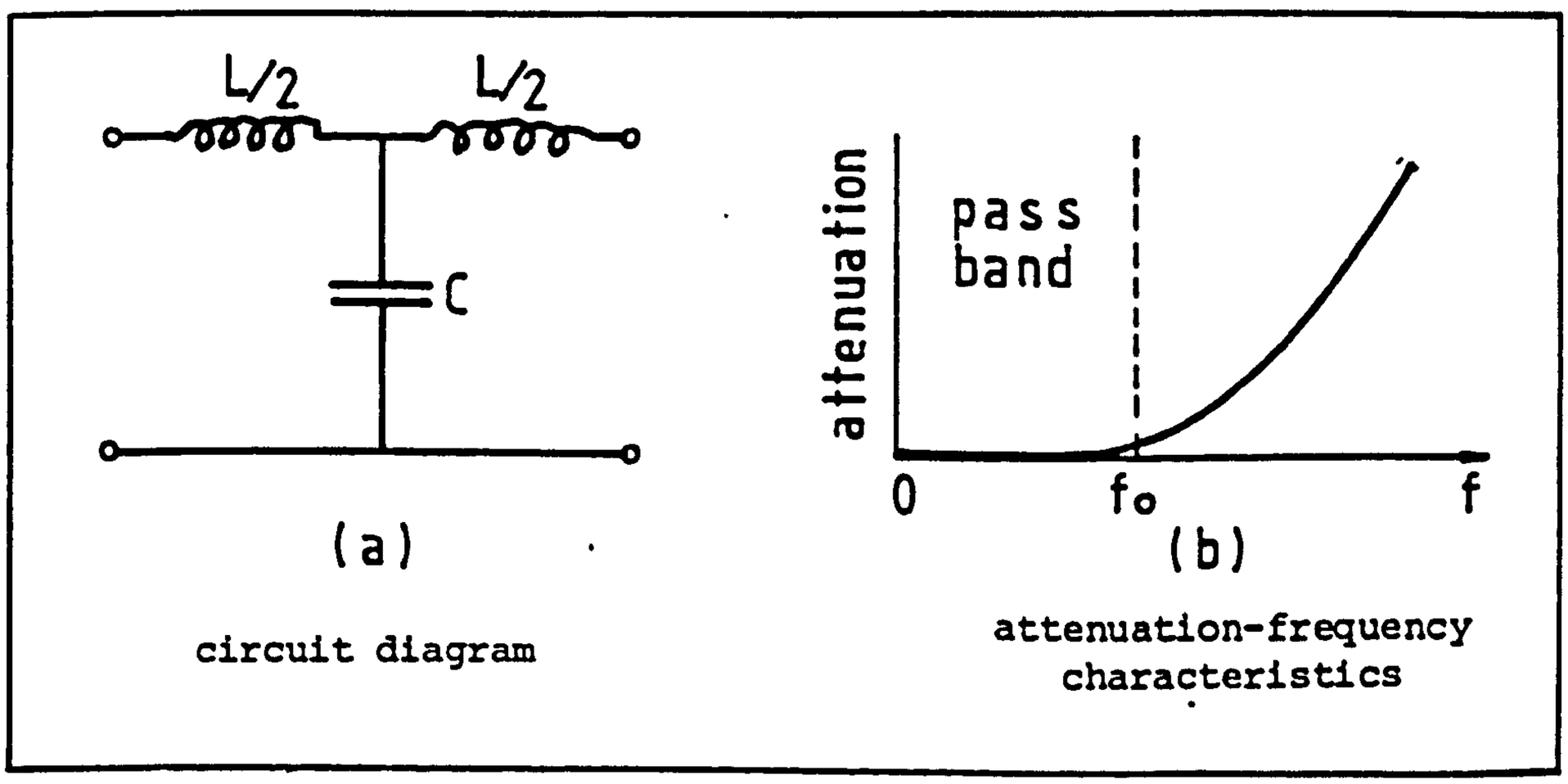

Figure A4.2 Prototype low pass 'T' section

The final design of the complete low pass filter is as shown in figure A4.3(a). Since for series elements $L = L_1 + L_2 + \ldots$ then the circuit simplifies to that shown in figure A4.3(b)

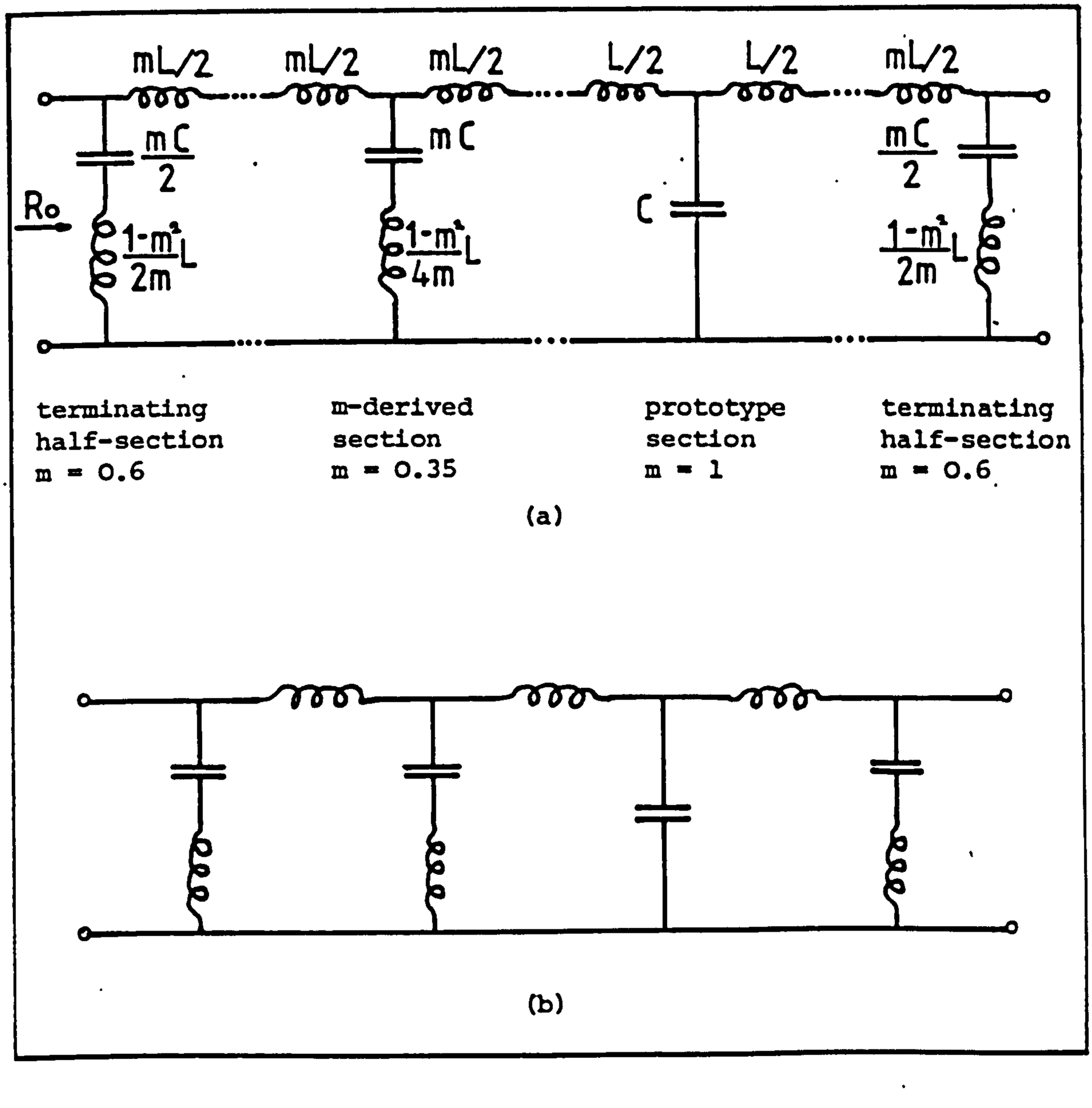

Figure A4.3 Final circuit for low pass filter

A4.3 High pass filter

$$L = \frac{R_o}{4 f_o}$$

and

$$C = \frac{1}{4 R_o f_o}$$

Also

$$m = \sqrt{1 - \left(\frac{f_o}{f_\infty}\right)^2}$$

Hence

$$f_\infty = \frac{f_o}{\sqrt{1 - m^2}}$$

The circuit diagram and the filter characteristics are shown in figure A4.4.

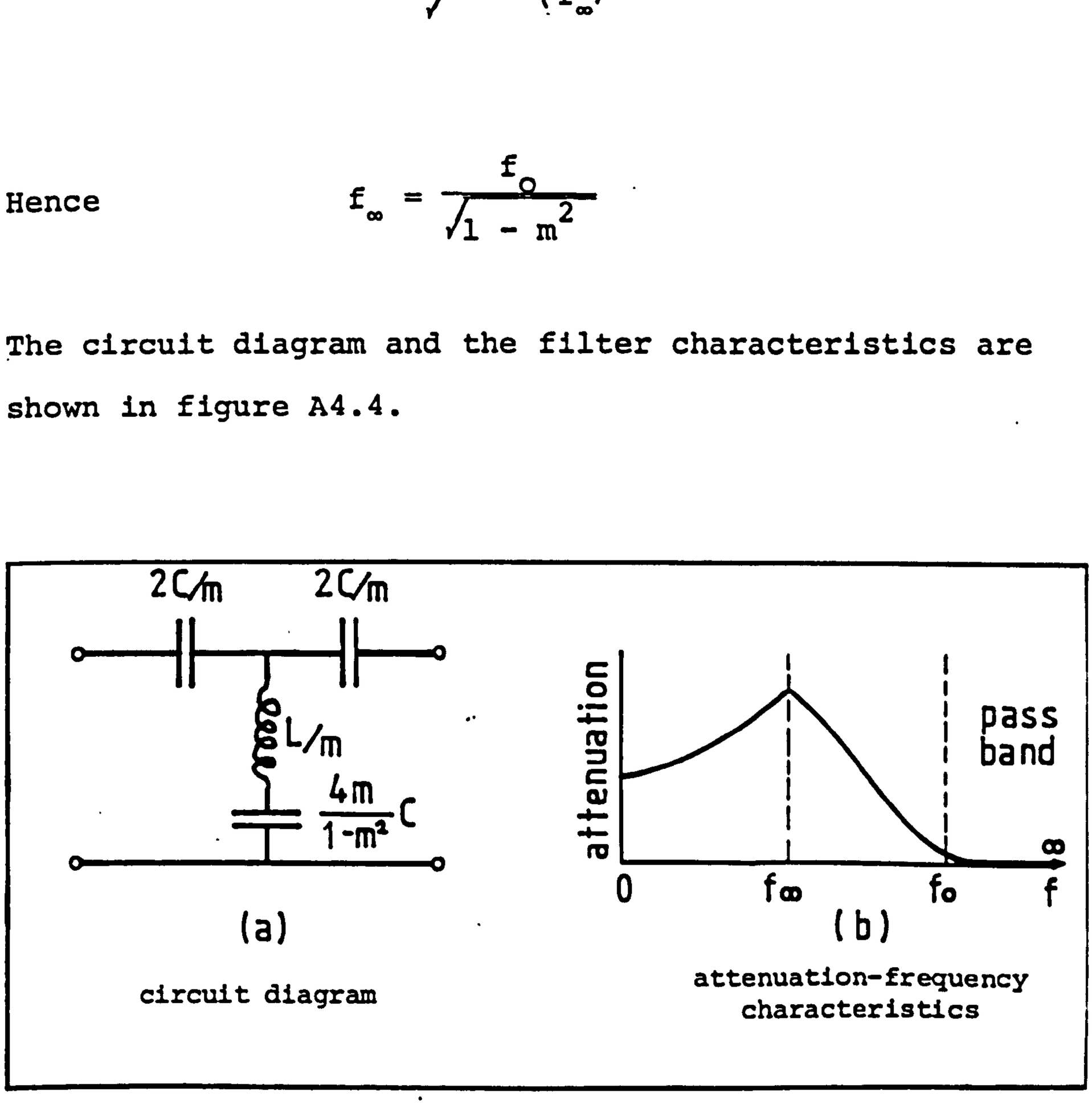

Figure A4.4 m-derived high-pass T-section

For m = 0.6, $f_\infty = 0.8f_o$ and

for m = 0.35, $f_\infty = 0.94f_o$

For the prototype section (m = 1), $f_\infty \to 0$ (see figure A4.5)

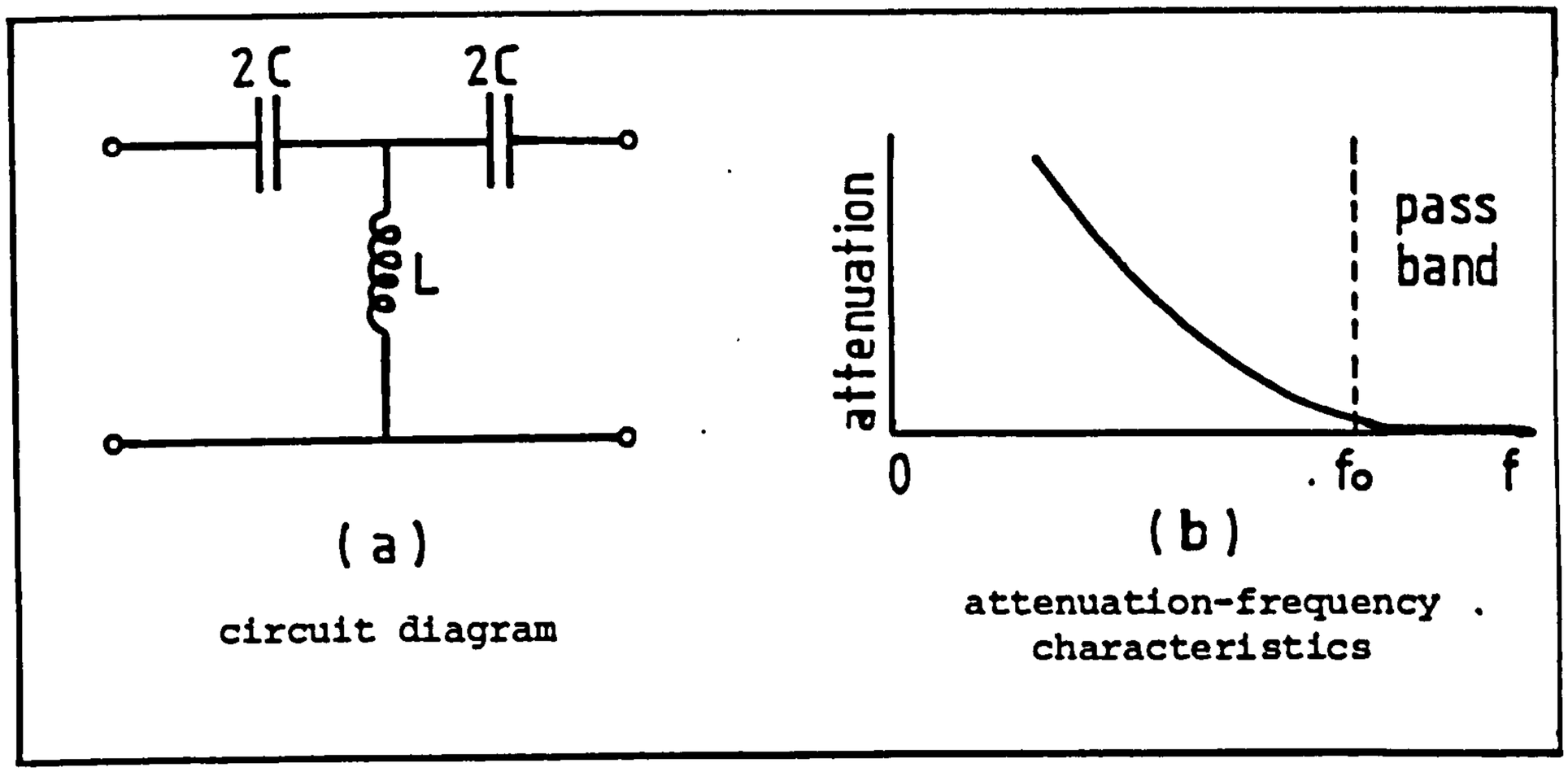

Figure A4.5 Prototype high pass 'T' section

The final design of the complete high pass filter is shown in figure A4.6(a). For the capacitors in series,

$\frac{1}{C} = \frac{1}{C_1} + \frac{1}{C_2} + \ldots$ and the circuit simplifies to that shown in figure A4.6(b).

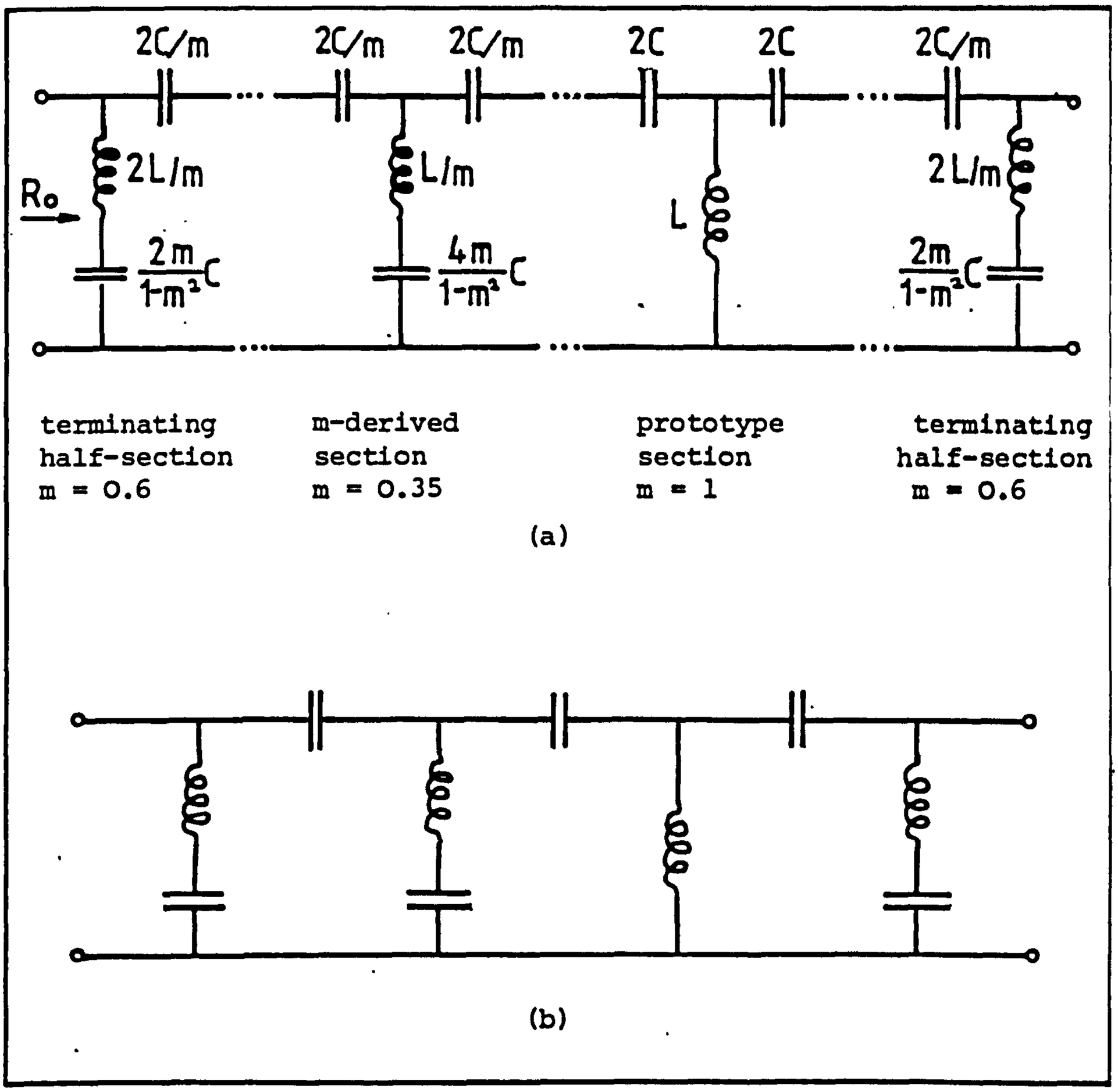

Figure A4.6 Final circuit for high pass filter

A4.4 Construction and testing

A number of low-pass and high-pass filters were designed with cut off frequencies ranging from 0.1 MHz to 30 MHz, which covered the range of frequencies encountered in this work.

The filters were assembled as individual circuits on printed circuit boards and arranged in a specially constructed framework with b.n.c. terminations. Band selection was manual.

The components used were capacitors of the silvered mica type and shielded printed circuit coils of variable inductance. After assembly each unit was tested, using a high frequency signal generator, and its cut off frequency and attenuation characteristics adjusted.

It was found that the performance of these filters was excellent and met all signal filtering requirements.

REFERENCES

[A4.1] The Royal Signals Handbook of Line Communication, 1974, Vol 1, H.M. Stationery Office.

APPENDIX A5

COMPUTER PROGRAMMES.

A5.1 Introduction

The results from the signal frequency measurements were transferred from the microcomputer memory to the processing computer via an RS232 link, as soon as one memory location accumulated 255 results. Figure A5.1 shows one such set of results, together with various calculated flow statistics.

The octal numbers in the first column denote frequency and the decimal numbers in the other eight columns indicate numbers of events. The results are arranged in a histogram form, starting from the lowest occurring frequency. The frequency corresponding to the first decimal number in each line is given by the first (octal) number in that line and the frequencies corresponding to the remaining seven decimal numbers are obtained by incrementing the octal frequency number by 1 for every successive column.

The computer performed calculations of flow statistics and stored the data on discs. Two disc drives were used, one containing the programmes and the other used to store the data files.

The main computer programme was used either to accept new data or to access existing files from discs. Other, smaller versions of that programme were used for specific purposes, e.g. for calculating the sample size only, accepting and

storing data on discs without processing, etc.

The main programme was accompanied by a programme for plotting histograms using high resolution graphics. Listings of these programmes are shown later.

```
0270 000 000 000 000 001 000 000 000
0310 001 000 000 000 000 000 000 000
0320 000 000 000 000 000 001 000 001
0330 000 000 000 000 000 000 001 002
0340 000 000 000 001 000 000 002 002
0350 003 001 001 001 001 000 002 001
0360 000 001 001 007 000 000 006 003
0370 002 007 002 006 007 004 006 002
0400 011 003 003 009 006 018 009 007
0410 006 012 015 009 019 007 009 018
0420 010 012 015 031 011 014 024 021
0430 016 020 022 027 024 029 026 020
0440 027 025 027 034 034 034 051 042
0450 038 000 053 045 051 046 051 060
0460 064 058 066 000 067 063 066 083
0470 097 103 000 100 088 089 099 000
0500 089 089 113 107 000 110 114 130
0510 000 133 105 142 000 137 117 128
0520 000 154 129 000 149 153 170 000
0530 153 159 000 157 174 000 182 190
0540 000 191 194 000 212 207 000 214
0550 000 204 211 000 228 220 000 199
0560 000 237 210 000 231 000 228 255
0570 000 231 000 218 000 196 212 000
0600 203 000 230 000 213 000 198 000
0610 234 199 000 172 000 191 000 198
0620 000 175 000 147 000 150 000 147
0630 000 141 000 112 000 109 000 090
0640 000 000 085 000 112 000 091 000
0650 061 000 052 000 000 036 000 034
0660 000 037 000 026 000 000 031 000
0670 017 000 023 000 000 015 000 011
0700 000 000 007 000 005 000 000 007
0710 000 006 000 000 001 000 002 000
0720 000 001 000 000 001 000 001 000
0730 000 000 000 000 001 000 000 002
DATA FILE NAME:D1409
UNCORRECTED MEAN VEL.=7.04761001M/S
R.M.S. VEL.=.758055473M/S
TURB.INT.=10.7562063%

APPLYING BIASING CORRECTIONS
CORRECTED MEAN VEL.=6.96140282M/S
CORRECTED R.M.S. VEL.=.774676035M/S
CORRECTED TURB.INT.=11.1281599%

SAMPLE SIZE: 13176
```

Note: the zeros occur as a result of the numerical division process within the frequency meter, in which, quantities are rounded to the nearest integer.

Figure A5.1 Experimental results and calculated flow statistics

A5.2 Programme structure

A flow diagram of the programme is shown in figure A5.2.

The two main parameters of the laser anemometer, the wavelength, λ and the beam angle, θ, were among the initial statements. From them the fringe spacing was computed as $\delta = \frac{\lambda}{2 \sin \theta}$.

As the programme was very often used to access existing data files the first decision making concerned this point. The number of measurement cycles, N, the full scale output of the Doppler frequency meter, F.S.D., and the frequency shift were fed in manually unless conditions remained identical as in the previous programme execution.

Once the various input parameters had been set, the RS232 link was initialised to accept data from the microcomputer. The end of a set of results was recognised by an additional line feed.

A copy of the result could be produced by a printer on request. After this a file name was assigned to that set, which was then saved on disc.

The first part of the calculations performed on the results concerned the conversion of the octal frequency numbers to velocities and the creation of two arrays containing velocities and corresponding numbers of events. Conversion was carried out using the formula

$$u_i = \frac{f_i}{1024} \times FSD \times \frac{N}{8} \times \delta$$

where f_i is the decimal frequency number and δ the fringe spacing. The frequency shift, when employed, was subtracted before velocities were computed. Corrected values for the numbers of data (see section 3.3.2(c)) were also computed and stored in array form, so that uncorrected and corrected histograms could be displayed.

The various flow statistics - corrected and uncorrected, were computed using the expressions in section 3.3.2(3). These results could be printed on request; an example is shown in figure A5.1.

The programmes, listings of which are shown in figure A5.3, were written in 'Applesoft' Basic. The first of the two programmes ('TEST') was used to process the results and the second, ('GRAPH'), to plot velocity histograms when required.

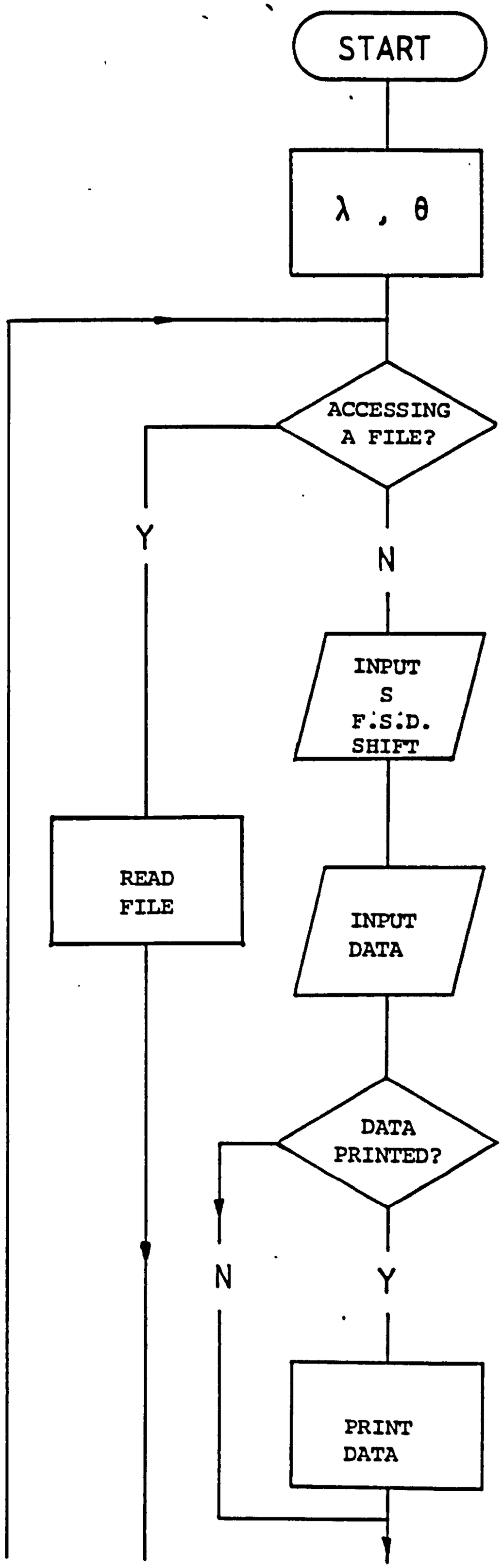

part of figure A5.2

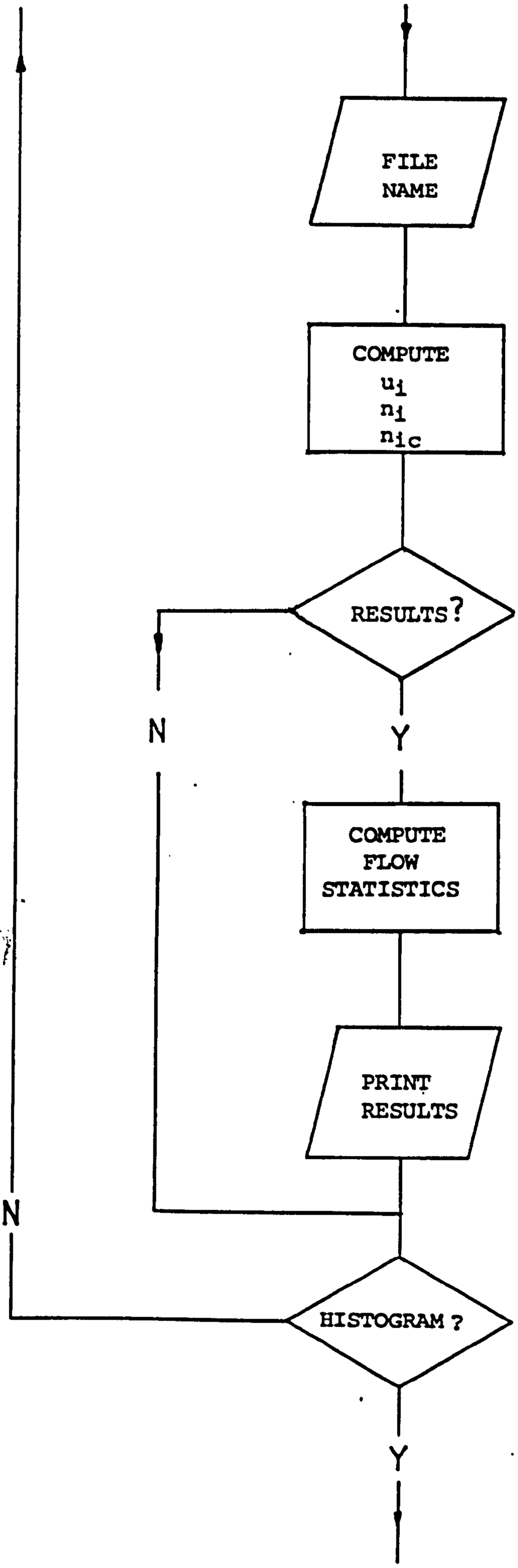

part of figure A5.2

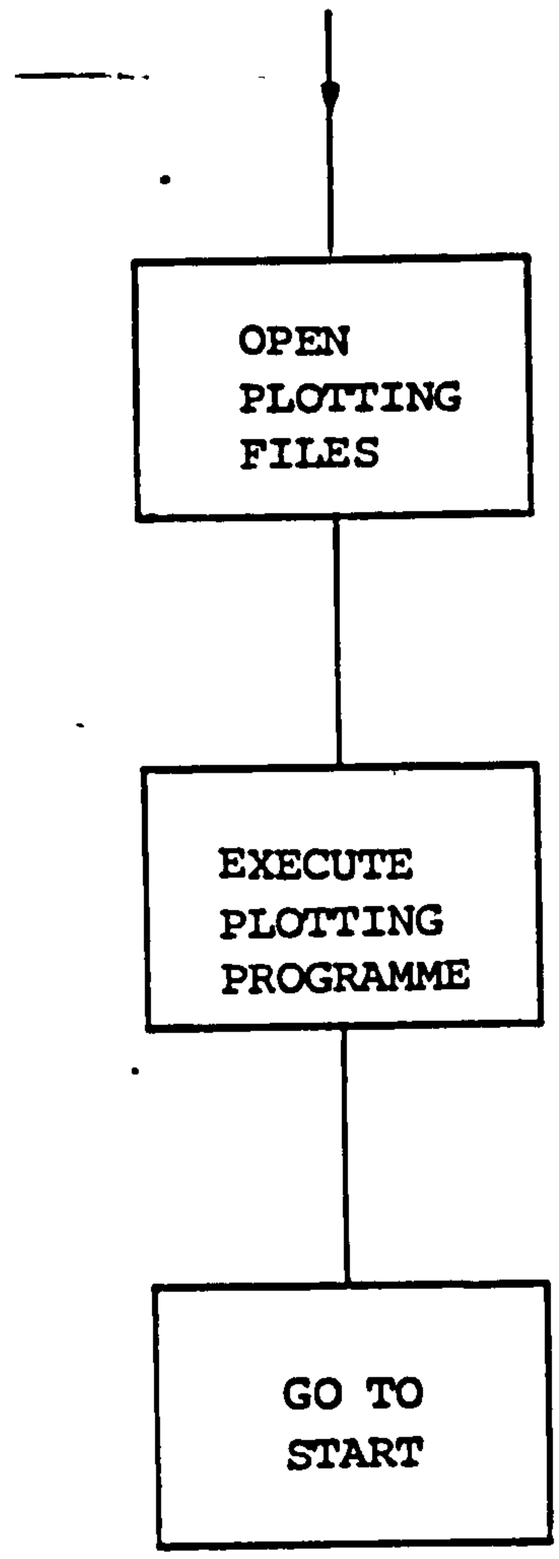

Figure A5.2 Flow diagram

```
1  HIMEM: 32768
2  REM   THIS PROGRAMME IS WRITTEN IN APPLESOFT BASIC FOR THE
      APPLE II
5  REM   THIS PROGGRAMME CAN BE USED FOR ON-LINE COLLECTION A
     ND PROCESSING OF RESULTS OR FOR ACCESSING EXISTING FILES

30 D$ = ""
40  DIM DA$(150),F(1200),NB(1200),U(1200),CN(1200)
50 LM = 0.6328E - 6:BA = 9.0750:BR = BA * 3.14159 / 180:B7 =
      SIN (BR):B8 = 2 * B7
55 L8 = LM / B8
60  PRINT "DO YOU WANT TO ACCESSA N EXISTING DATA FILE (Y/N)"
     : INPUT DH$
62  IF DH$ = "Y" THEN 66
64 I = 1: GOTO 68
66 I = 2
68  ON I GOSUB 930,1350
100 L1 = 512:L2 = 64:L3 = 8
110  FOR I = 1 TO N
120 A$ =  STR$ (F(I)):DC$ =  MID$ (A$,2,1):BC$ =  MID$ (A$,3,
     1):CC$ =  MID$ (A$,4,1):EC$ =  RIGHT$ (A$,1)
130 F(I) =  VAL (DC$) * L1 +  VAL (BC$) * L2 +  VAL (CC$) * L
     3 +  VAL (EC$)
140  NEXT
500 SM = SS * 1000000:WW = 8192
505 NF = FS * NC / WW
560  FOR I = 1 TO N
570 F(I) = F(I) * NF:F(I) = F(I) - SM:U(I) = F(I) * L8:F(I) =
     U(I):CN(I) = NB(I) /  ABS (F(I))
580  NEXT
582  PRINT
583  PRINT "DO YOU WANT TO SEE TH E RESULTS? (Y/N)"
584  INPUT W$
585  IF W$ = "N" THEN 912
590 S1 = 0:S2 = 0:S3 = 0:S8 = 0
592 S4 = 0
600  FOR I = 1 TO N
610 S1 = S1 + NB(I):S2 = S2 + (F(I) * NB(I)):S8 = S8 + CN(I):
     S4 = S4 + (F(I) * CN(I))
620  NEXT
630 U1 = S2 / S1:U9 = S4 / S8
674  GOTO 680
675  PRINT D$;"PR#5"
680  PRINT "..................... ............."
682  PRINT "DATAFILENAME:"B$
685  PRINT
690  PRINT "UNCORRECTED MEAN VEL.=";U1;"M/S"
700  FOR I = 1 TO N
710 S3 = S3 + ((F(I) - U1) ^ 2 * NB(I) / S1)
720  NEXT I
730 S3 =  SQR (S3)
740  PRINT "R.M.S. VEL.=";S3;"M/S"
750  PRINT "TURB.INT.=";S3 * 100 / U1;"%"
760  PRINT
770  PRINT "APPLYING BIASING CORRECTIONS"
780  PRINT "CORRECTED MEAN VEL.=";U9;"M/S"
```

part of figure A5.3(a)

```
790 SA = 0
800  FOR I = 1 TO N
810 SA = SA + ((F(I) - U9) ^ 2) * CN(I)
820  NEXT I
830 SA = SA / S8
850 SA =  SQR (SA)
860  PRINT "CORRECTED R.M.S. VEL.=";SA;"M/S"
870  PRINT "CORRECTED TURB.INT.=";100 * SA / U9;"%"
880  PRINT
890  PRINT "SAMPLE SIZE: ";S1
900  PRINT "....................................."
911  PRINT : PRINT D$;"PR#0"
912  PRINT "IS A HISTOGRAM REQUIRED?(Y/N)"
914  INPUT Y$: IF Y$ = "N" THEN 60
916  GOSUB 1461
930  PRINT "HAVE THE OPERATING PARAMETERS CHANGED   SINCE THE
      LAST RUN OR HAS A HISTOGRAM BEEN PLOTTED (Y/N)"
940  INPUT RP$
950  IF RP$ = "N" THEN 1030
960  PRINT "NUMBER OF CYCLES"
970  INPUT NC
980  PRINT "FULL SCALE DEFLECTION IN MHZ"
990  INPUT FS
1000 FS = FS * 1000000
1010  PRINT "FREQUENCY SHIFT IN MHZ"
1020  INPUT SS
1030  PRINT "START MICROPROCESSOR INPUT"
1040  PRINT D$;"IN#5"
1050  INPUT "";XX$
1060 I = 0
1070 I = I + 1
1080  INPUT "";DA$(I)
1090  IF  LEN (DA$(I)) = 36 THEN 1070
1100  PRINT D$;"IN#0"
1110 I = I - 1
1120  PRINT "DO YOU WANT THE DATA PRINTED? (/N)"
1130  INPUT DD$: IF DD$ = "N" THEN 1200
1140  PRINT D$;"PR#5"
1150  PRINT
1160  FOR Z = 1 TO I
1170  PRINT DA$(Z)
1180  NEXT Z
1190  PRINT D$;"PR#0"
1200  PRINT "DATA FILE NAME ?": INPUT B$: PRINT D$;"OPEN"B$",
     D2": PRINT D$;"WRITE"B$:N = 8 * I
1210  PRINT N: PRINT NC: PRINT FS: PRINT LM: PRINT BA: PRINT
     SS:K = 0
1220  FOR I = 1 TO N STEP 8
1230 M = 6
1240 K = K + 1
1250 F(I) =  VAL ( LEFT$ (DA$(K),4)): PRINT F(I):F(I) = F(I) +
     10000
1260  FOR J = I TO I + 7
1270 NB(J) =  VAL ( MID$ (DA$(K),M,3)): PRINT NB(J):M = M + 4

1280  NEXT J
1290  FOR K1 = I TO I + 6
1300 F(K1 + 1) = F(K1) + 1
1310  NEXT K1
1320  NEXT I
```

part of figure A5.3(a)

```
1330  PRINT D$;"CLOSE"B$""
1340  RETURN
1350  PRINT "DATA FILE NAME TO ACCESSED": INPUT B$: PRINT D$;
     "OPEN"B$",D2": PRINT D$;"  READ"B$: INPUT N: INPUT NC: INPUT
     FS: INPUT LM: INPUT BA: INPUT SS:K = 0
1360  FOR I = 1 TO N STEP 8
1370 M = 6:K = K + 1: INPUT F(I):F(I) = F(I) + 10000
1380  FOR J = I TO I + 7
1390  INPUT NB(J):M = M + 4
1400  NEXT J
1410  FOR K1 = I TO I + 6
1420 F(K1 + 1) = F(K1) + 1
1430  NEXT K1
1440  NEXT I
1450  PRINT D$;"CLOSE"B$""
1460  RETURN
1461  PRINT "YOU WILL NOW SEE A H ISTOGRAM OF THE VELOCITY DI
     STRIBUTION"
1463 PY = 157:PX = 230: PRINT "LIMIT REQUIRED ON X-AXIS(M/S)"
     : INPUT MX
1464 MY = 0:MZ = 0
1465  FOR I = 1 TO N
1466  IF MZ >  = CN(I) THEN 1468
1467 MZ = CN(I)
1468  NEXT
1469  FOR I = 1 TO N
1470  IF MY >  = NB(I) THEN 1472
1471 MY = NB(I)
1472  NEXT
1474  FOR I = 1 TO N:NB(I) = PY -  INT (NB(I) * PY / MY):F(I)
     =  INT (F(I) * PX / MX) + 50
1475 CN(I) = PY -  INT (CN(I) * PY / MZ)
1476  NEXT I
1478  PRINT D$;"OPEN LASERFILE,D1"
1480  PRINT D$;"WRITE LASERFILE"
1490  PRINT N
1495  PRINT MX
1500  FOR I = 1 TO N
1510  PRINT F(I): PRINT NB(I)
1520  NEXT I
1530  PRINT D$;"CLOSE LASERFILE"
1540  PRINT D$;"OPEN CORRFILE"
1550  PRINT D$;"WRITE CORRFILE"
1560  PRINT N
1565  PRINT MX
1570  FOR I = 1 TO N
1580  PRINT F(I): PRINT CN(I)
1590  NEXT I
1600  PRINT D$;"CLOSECORRFILE"
1610  PRINT D$;"RUN GRAPH,D1"
1620  END
```

(a) Data procedsing programme

```
5  HIMEM: 16384
7 D$ = ""
10  DIM F(800),NB(800),CN(800)
50  PRINT D$;"OPEN LASERFILE,D1"
60  PRINT D$;"READ LASERFILE"
70  INPUT N
75  INPUT MX
80  FOR I = 1 TO N
90  INPUT F(I): INPUT NB(I)
100  NEXT I
110  PRINT D$;"CLOSE LASERFILE"
111  PRINT D$;"OPENCORRFILE"
112  PRINT D$;"READCORRFILE"
113  INPUT N: INPUT MX
114  FOR I = 1 TO N
115  INPUT F(I): INPUT CN(I)
116  NEXT I
117  PRINT D$;"CLOSECORRFILE"
120 PY = 157:PX = 230
161  CALL  - 936
162  PRINT
163  PRINT
164  PRINT "DO YOU WISH TO SEE:-"
165  PRINT
166  PRINT "1.   UNCORRECTED HISTOGRAM-U"
167  PRINT "2.   CORRECTED HISTOGRAM  -C"
168  PRINT "    PRESS<SPACE>TO ESC"
169  PRINT "ENTER LETTER:": INPUT C$
170  HGR2 : HCOLOR= 7
171  ROT= 0: SCALE= 1
172  FOR I = 9 TO 129 STEP 30
174  DRAW 1 AT 40,I
176  NEXT I
178  FOR I = 9 TO 129 STEP 60
180  DRAW 4 AT 34,I
182  NEXT I
183  FOR I = 39 TO 99 STEP 60
184  DRAW 1 AT 34,I
185  NEXT I
186  FOR I = 69 TO 99 STEP 30
187  DRAW 2 AT 28,I
188  NEXT I
189  HPLOT 50,0 TO 50,157 TO 279,157
190  FOR I = 9 TO 129 STEP 30
200  HPLOT 49,I TO 50,I
210  NEXT I
212  IF MX = 15 THEN 242
220  FOR I = 72 TO 279 STEP 23
230  HPLOT I,157 TO I,159
240  NEXT I
241  GOTO 250
242  FOR I = 70 TO 279 STEP 15
244  HPLOT I,157 TO I,159
246  NEXT I
250  FOR I = 9 TO 39 STEP 30
260  DRAW 3 AT 32,I
270  NEXT I
```

part of figure A5.3(b)

```
280  DRAW 1 AT 50,167
282 Z = MX / 5
284  ON Z GOSUB 286,288,290,292
285  GOTO 300
286  DRAW 4 AT 274,167: RETURN
288  DRAW 2 AT 268,167: DRAW 1 AT 274,167: RETURN
290  DRAW 2 AT 268,167: DRAW 4 AT 274,167: RETURN
292  DRAW 3 AT 268,167: DRAW 1 AT 274,167: RETURN
300  DRAW 5 AT 15,74
310  HPLOT 21,74
320  DRAW 6 AT 148,175: DRAW 9 AT 154,175: DRAW 8 AT 160,175:
      DRAW 11 AT 166,175: DRAW 7 AT 172,175: DRAW 10 AT 178,1
     75
340  IF C$ = "C" THEN 390
350  FOR I = 1 TO N
360  HPLOT F(I),NB(I) TO F(I),157
370  NEXT I
380  GOTO 420
390  FOR I = 1 TO N
400  HPLOT F(I),CN(I) TO F(I),157
410  NEXT I
420  INPUT C$
425  IF C$ = "" THEN 505
440  FOR I = 1 TO 229
450  HCOLOR= 0
460  HPLOT I + 50,0 TO I + 50,156
470  NEXT I
480  HCOLOR= 7
490  IF C$ = "U" THEN 350
500  GOTO 390
505  TEXT
510  PRINT "HARD COPY? (Y/N)";: INPUT TT$
520  IF TT$ = "N" THEN 700
565 Q$ = ""
570  PRINT D$;"PR#1": PRINT Q$
580  PRINT D$;"PR#0"
700  PRINT D$;"RUN TEST"
710  END
```

(b) Histogram plotting programme

Figure A5.3 Programme listing

APPENDIX A6

RESULTS FROM VELOCITY MEASUREMENTS

Details of the various flow conditions and the results obtained from the velocity measurements are given in the following tables.

The values of the particle drag coefficient, C_D and particle Reholds number, Re_p, are based on mean particle diameter.

The pipe Reynolds number is based on the mean air velocity in the pipe, obtained by dividing the air volumetric flowrate by the pipe cross-sectional area.

pipe diameter mm	pressure drop at orifice mm H_2O	solids flowrate g/s	loading ratio	air temperature °C	ρ_f kg/m³	μ_f kg/m-s $\times 10^6$	U_m m/s	Re_f	U_p m/s	U_σ m/s	C_D	Re_p	comments
Glass ballotini, size 18, 45-70 µm													
25.8	70	10.52	2.16	25	1.184	18.35	9.75	13,164	8.96	0.79	3.00	2.93	Centre line only
"	60	"	2.33	23	1.192	18.25	8.90	12,254	8.42	0.48	8.08	1.80	"
"	50	"	2.53	22	1.196	18.20	8.20	11,217	7.75	0.45	9.16	1.70	"
"	40	"	2.86	20	1.205	18.10	7.35	10,088	6.96	0.39	12.10	1.49	"
"	30	"	3.29	19	1.209	18.06	6.62	8.756	6.13	0.49	7.64	1.89	"
"	20	"	4.08	17.5	1.215	17.98	5.82	7,181	5.27	0.55	6.03	2.14	"
"	10	"	5.75	16.5	1.219	17.94	4.17	5,089	4.11	0.06	5.06	0.23	"
Glass ballotini, size 13, 90-135 µm													
25.8	70	12.41	2.54	26	1.180	18.40	10.12	13,128	7.86	2.26	0.72	16.30	Centre line only
"	60	"	2.74	24	1.188	18.30	9.39	12,220	7.35	2.04	0.88	14.90	"
"	50	"	2.99	22.5	1.194	18.22	8.34	11,205	6.69	1.65	1.34	12.16	"
22.0	18	7.59	3.07	23.5	1.190	18.28	6.90	7,858	5.29	1.61	1.41	11.77	Velocity profile
25.8	40	12.41	3.37	21	1.201	18.16	7.57	10,055	6.00	1.57	1.46	11.68	Centre line only
"	30	"	3.88	20	1.205	18.10	6.58	8,737	5.28	1.30	2.13	9.74	"
"	20	"	4.81	19	1.209	18.06	4.98	7,149	4.12	0.86	4.85	6.48	"
22.0	14	"	5.64	23.5	1.190	18.28	5.91	6,930	4.72	1.19	2.56	8.74	Velocity profile
25.8	12	"	6.14	18.5	1.211	18.04	4.09	5,544	3.11	0.98	3.73	7.40	Centre line only

Glass ballotini, size 10, 210-325 μm													
pipe diameter mm	pressure drop at orifice mm H_2O	solids flowrate g/s	loading ratio	air temperature °C	ρ_f kg/m³	μ_f kg/m-s $\times 10^6$	U_m m/s	Re_f	U_p m/s	U_σ m/s	C_D	Re_p	comments
31.4	50	2.54	0.61	24.5	1.186	18.33	5.71	9,151	2.63	3.08	0.92	53.36	Velocity profile
25.8	40	2.54	0.69	22.0	1.196	18.20	8.00	10,033	4.11	3.89	0.57	68.40	"
31.4	50	7.53	1.81	26.0	1.180	18.40	5.38	9,116	2.53	2.85	1.08	48.82	"
22.0	18	4.92	1.99	21.5	1.199	18.18	7.08	7,901	3.49	3.59	0.67	63.33	"
25.8	40	7.38	2.00	19.0	1.209	18.06	7.95	10,111	4.05	3.90	0.56	69.80	"
22.0	14	4.92	2.24	21.5	1.199	18.18	6.29	6,968	3.12	3.17	0.86	53.92	"
22.0	12	4.92	2.41	22.0	1.196	18.20	5.59	6,444	2.63	2.96	0.98	52.08	"
25.8	70	12.33	2.53	25.0	1.184	18.35	10.35	13,164	5.88	4.47	0.435	77.15	Centre line only
"	60	12.33	2.73	23.5	1.190	18.28	9.53	12,234	5.35	4.18	0.50	72.79	"
"	50	12.33	2.97	22.5	1.194	18.20	8.59	11,217	4.99	3.60	0.66	63.18	"
22.0	18	7.53	3.05	21.5	1.199	18.18	7.08	7,901	3.49	3.59	0.63	63.33	Velocity profile
25.8	40	12.33	3.35	21.5	1.199	18.18	7.56	10,044	4.41	3.15	0.87	55.57	Centre line only
22.0	14	7.53	3.42	21.0	1.200	18.15	6.37	6,980	2.71	3.66	0.64	64.66	Velocity profile
22.0	12	7.53	3.73	23.0	1.192	18.25	5.93	6,405	2.71	3.21	0.84	56.15	"
25.8	30	12.33	3.85	20.0	1.205	18.10	6.28	8,737	3.80	2.48	1.39	44.16	Centre line only
22.0	25	12.33	4.22	22.0	1.196	18.20	7.79	9,302	4.77	3.01	0.95	53.00	Velocity profile
25.8	60	20.89	4.62	24.0	1.188	18.30	9.14	12,220	4.29	4.84	0.37	84.12	"
25.8	20	12.33	4.78	18.5	1.211	18.04	5.01	7,157	2.71	2.30	1.61	41.30	Centre line only
22.0	18	12.33	4.99	24.0	1.188	18.30	6.90	7,850	3.50	3.40	0.75	59.08	Velocity profile
31.4	50	20.89	5.03	26.5	1.179	18.41	5.54	9,111	2.73	2.81	1.11	48.20	"
25.8	40	20.89	5.65	18.0	1.213	18.00	7.26	10,141	4.14	3.12	0.87	56.20	"
22.0	28	20.89	6.80	23.5	1.190	18.28	8.06	9,801	4.79	3.27	0.81	56.98	"

pipe diameter mm	pressure drop at orifice mm H_2O	solids flowrate g/s	loading ratio	air temperature °C	ρ_f kg/m³	μ_f kg/m-s $\times 10^6$	U_m m/s	Re_f	U_p m/s	U_σ m/s	C_D	Re_p	comments
Glass ballotini, size 8, 440-530 µm													
25.8	66.5	11.74	2.46	23.0	1.192	18.25	10.35	12,901	3.22	7.13	0.31	225.9	Centreline only
"	60.0	"	2.60	21.5	1.199	18.18	9.76	13,473	3.04	6.72	0.34	215.0	"
"	50.0	"	2.83	20.5	1.203	18.12	8.65	11,266	2.70	5.95	0.44	191.6	"
"	40.0	"	3.18	20.0	1.205	18.10	7.54	10,088	2.35	5.19	0.58	166.9	"
31.4	110.0	20.14	3.29	24.0	1.188	18.30	8.82	13,596	2.51	6.30	0.40	198.4	Velocity profile
22.0	35.0	11.74	3.41	24.5	1.186	18.33	9.97	10,928	3.19	6.78	0.34	212.8	"
25.8	30.0	"	3.67	18.0	1.213	18.00	6.20	8,785	1.80	4.40	0.80	143.9	Centreline only
22.0	30.0	"	3.67	26.0	1.180	18.40	9.74	10,079	2.59	7.15	0.31	222.4	Velocity profile
22.0	25.0	"	4.02	21.5	1.199	18.18	8.37	9,312	2.39	5.98	0.44	191.2	"
25.8	24.0	"	4.12	18.5	1.211	18.04	5.22	7,840	1.02	4.20	0.88	136.8	Centreline only
Glass ballotini, size 5, 675-935 µm													
25.8	400	9.31	0.80	31.5	1.159	18.66	23.33	30,944	7.81	15.52	0.11	776	Centreline only
"	245	"	1.02	25.0	1.184	18.35	19.79	24,627	5.59	14.20	0.13	738	"
"	120	"	1.45	19.0	1.209	18.06	13.76	17,512	4.13	9.63	0.28	519	"
"	100	"	1.59	18.5	1.211	18.04	12.76	16,004	3.50	9.26	0.30	500	"
"	90	"	1.68	18.0	1.213	18.00	11.95	15,216	3.46	8.49	0.35	461	"
"	80	"	1.78	20.0	1.205	18.10	11.73	14,267	2.24	9.13	0.31	489	"
"	70	"	1.91	22.0	1.196	18.20	10.74	13,272	1.82	8.92	0.33	472	"
"	60	"	2.06	24.0	1.188	18.30	10.06	12,220	1.58	8.40	0.36	443	"
"	50	"	2.24	21.5	1.199	18.18	8.98	11,229	1.17	7.81	0.42	415	"
22.0	50	16.31	2.24	26.0	1.180	18.40	12.00	13,011	2.29	9.71	0.28	501	Velocity profile
22.0	55	9.31	3.78	29.5	1.167	18.56	13.09	13,529	2.72	10.37	0.25	525	"

Brown Fused Alumina, 300-430 μm													
pipe diameter mm	pressure drop at orifice mm H_2O	solids flowrate g/s	loading ratio	air temperature °C	ρ_f kg/m³	μ_f kg/m-s $\times 10^6$	U_m m/s	Re_f	U_p m/s	U_σ m/s	C_D	Re_p	comments
22.0	30	4.78	1.49	23.5	1.190	18.28	9.45	10,145	3.78	5.67	0.47	134.7	Velocity profile
25.8	200	12.42	1.50	23.0	1.192	18.25	17.32	22,372	8.82	8.50	0.21	202.1	Centre line only
22.0	25	4.78	1.64	23.0	1.192	18.25	8.72	9,276	3.23	5.48	0.50	130.6	Velocity profile
25.8	100	12.42	2.12	20.5	1.203	18.12	12.70	15,933	6.19	6.51	0.35	157.8	Centre line only
22.0	30	7.69	2.40	24.0	1.188	18.30	9.26	10,134	3.80	5.46	0.51	129.4	Velocity profile
25.8	70	12.42	2.54	19.5	1.207	18.08	10.56	14,634	4.79	5.77	0.45	135.2	Centre line only
22.0	25	7.69	2.63	24.0	1.188	18.30	8.49	9,251	3.29	5.25	0.55	124.4	Velocity profile
25.8	60	12.42	2.75	17.5	1.215	17.98	9.85	12,438	4.38	5.47	0.50	134.9	Centre line only
25.8	50	12.42	2.99	17.0	1.217	17.96	9.14	11,367	3.81	5.33	0.52	131.8	Centre line only
25.8	40	12.42	3.37	16.0	1.221	17.90	8.06	10,201	3.27	4.79	0.64	119.3	Centre line only
25.8	30	12.42	3.88	16.0	1.221	17.90	6.94	8,834	2.60	4.34	0.79	108.0	Centre line only
22.0	30	12.42	3.88	24.0	1.188	18.30	9.40	10,134	3.63	5.77	0.45	136.7	Velocity profile
22.0	25	12.42	4.25	23.0	1.192	18.25	8.31	9,276	3.33	4.98	0.61	118.7	Centre line only
25.8	17	12.42	5.15	16.0	1.221	17.90	4.88	6,650	1.34	3.54	1.18	88.1	Centre line only